# UC Santa Cruz
**UC Santa Cruz Electronic Theses and Dissertations**

**Title**

Discovery and Investigation of the First Unsupported Monomeric Stibine Oxides

**Permalink**

**Author**

Wenger, John Stephen

**Publication Date**

2024

Peer reviewed|Thesis/dissertation

UNIVERSITY OF CALIFORNIA
SANTA CRUZ

**DISCOVERY AND INVESTIGATION OF THE FIRST UNSUPPORTED MONOMERIC STIBINE OXIDES**

A dissertation submitted in partial satisfaction
of the requirements for the degree of

DOCTOR OF PHILOSOPHY
in
CHEMISTRY

By

**John S. Wenger**

June 2024

The Dissertation of John S. Wenger is approved:

Professor Timothy Johnstone, chair

Professor Scott Oliver

Professor Shaun McKinnie

Peter Biehl
Vice Provost and Dean of Graduate Studies

**Table of Contents**

**List of Figures**

**Chapter 3**

bonds, (I) methyl C–H bonds, and (J) S–O bonds derived from the MM. Real space

functions corresponding to the hydrogen bonding oxygen are shown in red.

**Appendix B**

showing major components and summed outer-shell C components; the inset in B

shows the core used to model the spectra.

**Appendix C**

**Appendix D**

**Appendix E**

**List of Tables**

**Appendix B**

**Appendix C**

**Appendix D**

**Appendix E**

**Abstract**

The work presented herein describes the isolation and investigation of the first unsupported monomeric stibine oxides. In Chapter 1, I introduce the topic by discussing synthetic strategies for the isolation of novel, highly reactive main-group motifs, applications of pnictogen-containing species, advances in the isolation and investigation of monomeric pnictinidene chalcogenides and pnictine chalcogenides, and the currently accepted model for pnictoryl bonding (Pn=O/Pn⁺–O⁻). In this discussion, we rationalize why monomeric stibine oxides with the unperturbed stiboryl group had remained undiscovered. Chapter 2 focuses on a reinvestigation of previously reported monomeric stibine oxides. I collected new data on these species, including crystallographic, spectral, and computational experiments, which provide unambiguous evidence that these species are in fact hydroxystibonium salts and not monomeric stibine oxides. This chapter is heavily centered on the diffraction and refinement methods we employed, including neutron diffraction, multipole modeling, and Hirschfeld atom refinement with *NoSpherA2*. In Chapter 3, I present the isolation and investigation of the first monomeric stibine oxide Dipp₃SbO (Dipp = 2,6-diisopropylphenyl), as well as its

directly comparable lighter congeners, Dipp$_3$PO and Dipp$_3$AsO. Dipp$_3$SbO exists as a bench-stable monomer because the reactive stiboryl group is sterically shielded (i.e., kinetically stabilized) by the bulky Dipp groups. Theoretical analyses of Dipp$_3$PnO (Pn = P, As, Sb) are consistent with our expectation that Dipp$_3$SbO features the most highly polarized pnictoryl bond of the series, arising from inefficient back-bonding between O-centered p-orbitals and Sb–C σ* orbitals. Dipp$_3$SbO was found to engage in several distinct classes of reactivity, including H-bonding, Brønsted base chemistry, coordination chemistry with first, second, and third row transition metals, 1,2-addition chemistry, and oxo transfer. In each case, Dipp$_3$SbO was dramatically more reactive than Dipp$_3$PO or Dipp$_3$AsO. In Chapter 4, I quantify the enhanced Brønsted basicity of Dipp$_3$SbO relative to Dipp$_3$PO or Dipp$_3$AsO that arises from modulations of the electronic structure of the pnictoryl bond. We performed a series of stoichiometric reactions that involved the isolation of hydroxypnictonium salts to provide limiting values for the p$K_{aH}$ of each pnictine oxide. We then conducted a $^1$H NMR spectrometric titration experiment and determined that Dipp$_3$SbO boasts an approximately one-million fold increase in basicity relative to Dipp$_3$AsO, with p$K_{aH,MeCN}$ values of 19.81(5) and 13.89(13), respectively. The enhanced basicity of Dipp$_3$SbO enables it to catalyze a selected transesterification reaction efficiently, in contrast to the lighter congeners. In Chapter 5, I describe the isolation of Dipp$_3$Bi. Dipp$_3$Bi exhibited very distinct oxidative halogenation reactivity relative to Mes$_3$Bi, as well as Dipp$_3$Sb and Mes$_3$Sb (Mes = mesityl). Our work highlighted the drastic impact that bulky substituents can impose on the reactivity of heavy pnictines. The isolation of Dipp$_3$SbCl$_2$ serves as a curious example of this, as it exhibits a highly unusual square pyramidal geometry in solid state. Finally, Chapter 6 contains an investigation into the chemistry of Mes$_3$SbO, a less sterically encumbered monomeric stibine oxide relative

to Dipp$_3$SbO. Mes$_3$SbO is only stable under an inert atmosphere; atmospheric water will readily add across the stiboryl group to form a dihydroxystiborane. Mes$_3$SbO engaged with PbMe$_3$Cl and SnMe$_3$Cl to form classical Lewis adducts. In contrast, GeMe$_3$Cl SiMe$_3$Cl and CPh$_3$Cl added across the unsaturated stiboryl group to form five-coordinate stiboranes. This biphilic reactivity encouraged us to pursue more challenging substrate activations. Mes$_3$SbO was found to similarly activate the C–F and Si–F bonds of C($p$-MeOPh)$_3$F and SiEt$_3$F, respectively. Thus, by tuning the steric environment, the reactivity of the genuine stiboryl group could be accessed in a new way to activate among the strongest polar covalent single bonds in chemistry.

In conclusion, the use of sterically demanding organic groups has enabled us to access a highly reactive and previously undiscovered class of molecule, monomeric stibine oxides. I hope that this work will inspire other researchers in this area to elucidate novel functional groups that advance periodic trends and expand the frontier of modern chemistry. Gaining insights into fundamental structure and bonding and unlocking new reactivity at Earth-abundant main-group elements holds the promise of practical advances in sustainable catalysis.

**Chapter 1**

**Isolation and reactivity of monomeric stibinidene chalcogenides and stibine chalcogenides**

**1.1 – Isolation of main-group compounds with *unquenched reactivity***

The elucidation of novel chemical motifs provides an opportunity to extend periodic trends in chemistry and provide fundamental insights into chemical behavior. The results of these endeavors guide chemical research, inform chemical education strategies, and expand the frontier of modern chemistry. The chemistry of main-group elements is currently under intense investigation to discover novel molecular motifs that can be leveraged for small molecule activation and provide new insights into chemical bonding and reactivity.[1-2] Many synthetic processes for modern pharmaceuticals, agrochemicals, and polymers require the use of catalytic technologies, and these catalysts often exploit the chemistry of precious metals such as palladium, platinum, iridium, and rhodium.[3] In many cases, catalysis involves a metal center accessing different coordination numbers and oxidation states to facilitate substrate activation and transformation. There is, however, growing concern over the sustainability and ethics of global mining and consumption of precious metals, driving innovation to access useful substrate activations at the earth-abundant elements, including many within the p block.[4]

The isolation of chemically interesting, highly reactive, main-group species can be achieved with different synthetic strategies. These strategies often involve the development of molecular systems that possess *unquenched reactivity*. This unquenched reactivity may be leveraged in the activation of small molecules. If a molecular motif or system exhibits sufficient ambiphilicity, then self-association may occur to form stable adducts, dimers, or oligomers and deactivate the species. However, self-association does not necessarily preclude interesting reactivity, and there are many instances where stable adducts engage in useful reactions,[5] especially if the adduct is in equilibrium with the dissociated or monomeric form

in solution.[6-8] Some of the most prominent main-group frameworks that possess unquenched reactivity include Frustrated Lewis Pairs (FLPs),[9] molecules with low-valent centers,[10] geometrically constrained molecules,[11] and unsaturated bonds involving heavy elements.[12] The focus of this thesis will be on unsaturated bonds between a heavy element and a light element, such as occurs in the pnictine chalcogenides ($R_3PnCh$) and pnictinidene chalcogenides (RPnCh) (Figure 1.1a). In pnictine chalcogenides, the Pn center has no lone pairs and a valence of 5 ($\lambda^5$), whereas in pnictinidene chalcogenides, the Pn center has one lone pair and a valence of 3 ($\lambda^3$).

Unsaturated bonds between heavier electropositive elements and lighter electronegative elements are often highly polarized (Figure 1.1a) and competent in small molecule activation. The electronic structures of molecules with heavy main-group elements vary significantly from their first octal row congeners.[13] The increased size and diffuseness of the valence orbitals of heavier atoms results in diminished overlap with the relevant orbitals of bonding partners. Thus, π bonding tends to be less efficient with heavier main-group elements, causing a greater separation of charge in



**Figure 1.1.** General strategies for the stabilization of pnictinidene chalcogenides and pnictine chalcogenides. (a) Resonance structures for unsaturated pnictogen–chalcogen bonding. (b) Self-association of pnictine chalcogenides or pnictinidene chalcogenides. (c) Self-association can be prevented via thermodynamic stabilization afforded by a Lewis acid or base. (d) Self-association can be prevented via kinetic stabilization using sterically demanding substituents

unsaturated bonding situations. Dimers or oligomers may be more thermodynamically stable than monomers in such situations as head-to-tail self-association attenuates the separation of charge, exploiting the larger atomic radius of the heavy element to access an expanded coordination sphere (Figure 1.1b).

Insight into the bonding and reactivity of compounds containing highly reactive polar covalent bonds featuring heavy elements can be gained by using fast spectroscopic methods or matrix isolation experiments.[14-15] As valuable as this information can be, the isolation of highly reactive motifs within stable, tractable materials allows for a much wider range of experimental studies to be performed. To isolate highly reactive molecular fragments, chemists may thermodynamically stabilize the species by employing an external Lewis acid or base to form an adduct with the reactive motif (Figure 1.1c).[16] However, by engaging the loci of unquenched reactivity, this strategy modulates the reactive molecule and stifles direct investigation of its reactivity. The added acid or base can be a main-group compound but could also be a transition-metal complex and many reactive main-group bonding motifs have been captured for the first time in the primary coordination sphere of a metal atom.[17]

A kinetic stabilization approach may also be taken, in which reactive motifs are sterically protected using bulky substituents to prevent undesirable decomposition or self-association reactions (Figure 1.1d).[18] The strategy of kinetic stabilization offers a significant advantage in that it enables access to unperturbed bonds. However, steric protection is a double-edged sword in that it stabilizes the molecules from decomposition, but may simultaneously prevent the species from engaging in desirable substrate activations. Furthermore, sterically encumbered species are often challenging to design and synthesize. Bulky substituents can also engage in significant attractive London dispersion interactions that

4

provide a driving force *toward* self-association, and the stability of some molecules bearing bulky substituents may be more appropriately attributed to stabilizing attractive forces rather than kinetic stabilization.[19] It is important to note that thermodynamic and kinetic stabilization strategies are not mutually exclusive; molecules can be both sterically protected by bulky substituents and thermodynamically stabilized by donor–acceptor interactions. Furthermore, the extent of thermodynamic or kinetic stabilization is highly variable and tunable.

**1.2 – Applications of pnictogen chemistry**

Among p-block compounds, organopnictogen species are increasingly being recognized as optimal candidates to engage in main-group redox catalysis.[11] Oxidative addition is readily achieved by species of Groups 13 and 14, and reductive elimination is often observed for Group 16 and 17 species. Group 15, the pnictogen family, seems optimally positioned for molecules to catalytically cycle through oxidative additions and reductive eliminations in a manner that is reminiscent of transition metals.[20] Remarkable successes in this area include the activation of $C(sp^2)$–F bonds in catalytic hydrodefluorination by an N,C,N-pincer complex of Bi(I),[21] geometrically constrained phosphorous species,[20,22] and even simple phosphines.[23]

Pentavalent pnictine oxides (oxo-$\lambda^5$-pnictanes) of the general form $R_3Pn=O/R_3Pn^+–O^-$ (Pn = N, P, As, Sb, Bi) are an important class of molecules with diverse roles in chemistry. A prominent example of an amine *N*-oxide is trimethylamine *N*-oxide ($Me_3NO$), commonly used as an oxo transfer reagent in the decarbonylation of transition metal complexes through the loss of $CO_2$.[24]

Phosphine oxides are a commonplace laboratory reagent and feature in a wide array of chemical applications. The thermodynamic stability of the phosphoryl bond has been

utilized for over a century to drive forward the chemical reactions discovered by Wittig,[25] Mitsunobu,[26] Appel,[27] and Staudinger.[28] The competency of phosphine oxides as versatile hard Lewis bases arises from the O-centered lone-pairs. Synthetic access to structurally diverse phosphine oxides has unlocked their extensive development as fine-tuned organocatalysts for enantioselective transformations.[29] Phosphine oxides are commonly employed as ligands in s-block, d-block, and f-block metal coordination chemistry with successful application in catalysis,[30-31] supramolecular synthesis,[32] and uranium capture.[33] Triethylphosphine oxide is commonly used as a robust Lewis base to evaluate the strength of Lewis acids in the Gutmann-Beckett method, where the chemical shift of the $^{31}P$ nucleus serves as a convenient spectroscopic handle.[34] Arsine oxides are more basic and prone to reduction than phosphine oxides, but generally exhibit similar reactivity.[35-37] The bonding situation of the pnictoryl bond, which imbues these species with their characteristic reactivity, is discussed later in this chapter.

The chemistry of the pnictogens finds many application in traditional and modern medicine.[38-39] The drug brigatinib features a dimethylphosphine oxide group that serves as an H-bond acceptor that contributes favorable pharmacokinetic properties to the drug.[40] Beyond a long history in traditional Chinese medicine, arsenic trioxide is a clinically approved treatment for acute promyelocytic leukemia. Chemical research towards nanomaterial delivery platforms of arsenic trioxide show promise in expanding its medicinal applications and efficacy.[38] The antimonial drugs meglumine antimoniate (Glucantime) and sodium stibogluconate (Pentostam) are used to treat the neglected tropical disease leishmaniasis. Other members of the Johnstone Laboratory are currently pursuing the elucidation of the unknown molecular structures of these compounds.[41] Bismuth subsalicylate (Pepto-Bismol) is

a globally marketed gastrointestinal medication, and bismuth-containing species have also shown efficacy in the treatment of viral and bacterial infections.[42] $Bi^{3+}$ chelators have also been designed for the targeted delivery of α-emitting [213]Bi nuclei for cancer treatment.[43-44]

Among the pnictogens, antimony often exhibits characteristic and useful properties. For example, Lewis acidity of comparable pnictogen-containing species tends to be at a maximum for the antimony species.[45-47] The Lewis acidity of antimony compounds has been extensively studied in applications ranging from ion sensing to catalysis.[48-52] In this thesis, I will discuss my work on the reactivity of molecules with unsaturated bonds between lighter group 16 elements and heavy group 15 elements, particularly those that contain Sb–O bonds with relevance in medicinal and synthetic chemistry.[41,53-54]

## 1.3 – Monomeric stibinidene chalcogenides

Early studies on the alkaline hydrolysis of $RSbCl_2$ species afforded RSbO, but anomalous cryoscopic measurements, comparison to the analogous As species, and ultimately [121]Sb Mössbauer isomer shifts and single-crystal X-ray diffraction data supported its formulation as $(RSbO)_n$ oligomers with one aryl and two bridging oxide substituents, rather than monomers with unsaturated $Sb^+$–$O^-$ bonds.[55-60]

The application of bulky substituents at the Sb-center allowed for the isolation of well-defined multimeric and monomeric $\sigma^2,\lambda^3$-stibinidene chalcogenides. The sterically encumbered stibinidene chalcogenides $(RSbCh)_n$ (R = CH(SiMe$_3$)$_2$, Ch = S, Se, Te) predominantly exist in the trimeric form in solution, but are in equilibrium with dimeric and tetrameric forms.[61] In the late 1990s, the dimeric species $(L1Sb)_2$ with the bulky substituent **L1** (Figure 1.2) was isolated by the reduction of $(L1SbSe)_3$ wth $P(NMe_2)_3$ (Figure 1.3b).[62-63] $(L1SbSe)_3$ was

first generated by reaction of **L1**SbCl$_2$ with Li$_2$Se (Figure 1.3a) and exists as a trimeric species in which **L1**SbSe units associate in a head-to-tail fashion to form a 6-membered ring. Treatment of (**L1**Sb)$_2$ with oxygen quantitatively affords the corresponding dioxadistibetane (**L1**SbO)$_2$ (Figure 1.3c), and this reaction can occur in a single-crystal-to-single-crystal transformation.[63] Elemental sulfur will also oxidize (**L1**Sb)$_2$ and **L1**SbH$_2$, and these reactions likely proceed through an intermediate **L1**SbS, which was successfully trapped with MesCNO.[64-66] Other oxidation products can be obtained from the (**L1**Sb)$_2$ precursor including selenadistibiranes and telluradistibiranes.[67-70]
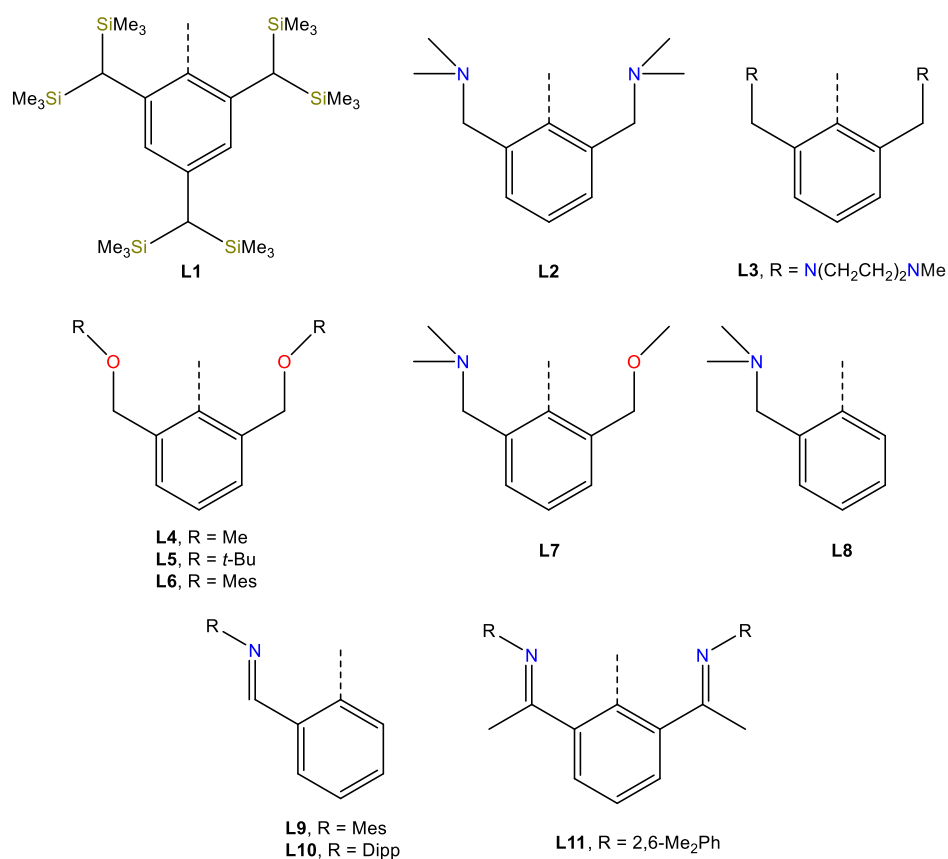


**Figure 1.2.** Ligands employed in the stabilization of stibinidene chalcogenides.

Beginning in the late 2000s, intense work on pnictinidene chalcogenide compounds with aryl substituents bearing pendent donor groups was conducted with exciting results.[71-73] For instance, a dehydrocoupling reaction between **L2**SbCl$_2$ (**L2** = C$_6$H$_3$-2,6-(CH$_2$NMe$_2$)$_2$) and two equivalents of K[B($i$-Bu)$_3$H] in THF afforded (Sb**L2**)$_4$ (Figure 1.3d).[74] From the reaction between these species, it was also possible to isolate Sb$_5$**L2**$_3$, which features a rare Group 15 trigonal bipyramidal cluster, Sb$_5^{3+}$, supported by three N,C,N-chelating substituents. Sb$_5$**L2**$_3$ decomposes in solution to form (Sb**L2**)$_4$ over the course of 24 h. (Sb**L2**)$_4$ can be understood as a tetramer of Sb**L2** stibinidene units. Although the pendent N-donors of the **L2** substituent
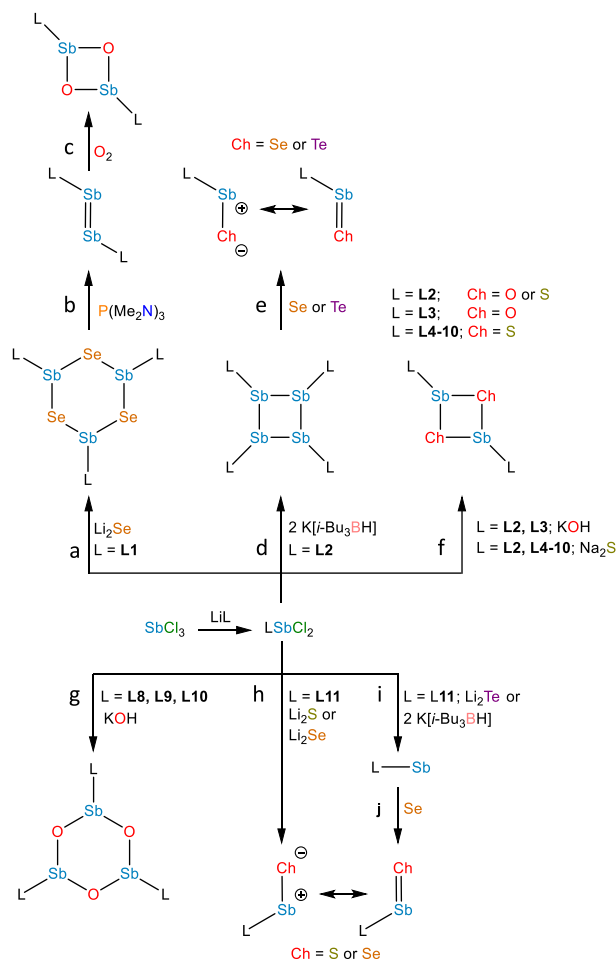


**Figure 1.3.** Strategies used to synthesize stibinidene chalcogenides.

9

interact with the Sb(I) centers, the donation is insufficient to prevent aggregation. The N-donor groups do, however, have a significant impact on the outcome of the oxidative chalcogenation of (Sb**L2**)₄. Oxidation of (Sb**L2**)₄ with elemental Se or Te resulted in clean formation of a product with the empirical formula **L2**SbCh (Ch = Se, Te) (Figure 1.3e).[75] Crystallographic analysis revealed these species to be monomeric with terminal Sb–Te and Sb–Se bonds (Figure 1.4a,b), unlike (**L1**SbSe)₃. These species are also monomeric in solution; comparison of the ⁷⁷Se chemical shift from NMR experiments in the solid state ($\delta_{iso}$ = −153 ppm) was similar to that in solution ($\delta$ = −197 ppm). If the compound oligomerized in solution, then the interaction between the Se atom and a Lewis acidic Sb center would be expected to result in a significant downfield shift, such as that of (**L1**SbSe)₃ at 179 ppm.[76]

The monomeric nature of **L2**SbCh stands in contrast to the trimeric nature of (**L1**SbCh)₃ (Ch = Se, Te). Despite the extreme steric protection afforded by **L1** relative to **L2**, **L2**SbCh is monomeric due to the presence of N-donors that quench the Lewis acidity of the
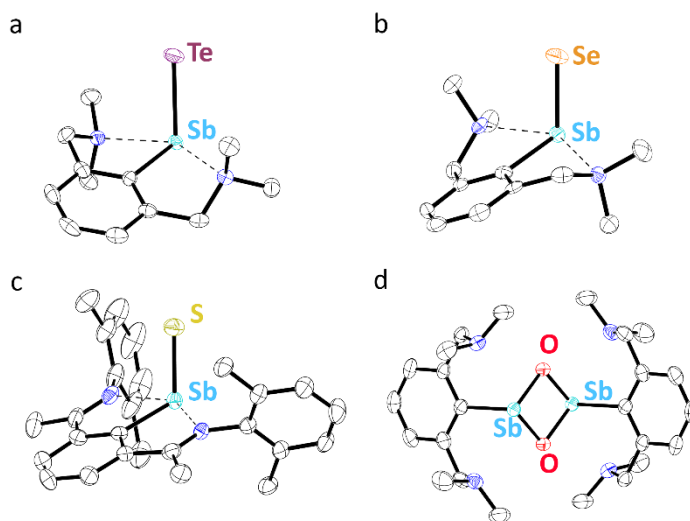


**Figure 1.4.** Thermal ellipsoid plots (50% probability) of (a) **L2**SbTe, (b) **L2**SbSe, (c) **L11**SbS, and (d) (**L2**SbO)₂. Color code: Sb teal, Te purple, Se orange, S yellow, O red, N blue, and C black. Hydrogen atoms are omitted for clarity.

10

antimony center and preclude oligomerization by nucleophilic attack of the chalcogen of one monomer on the pnictogen of another. Theoretical investigation of the terminal Sb–Se and Sb–Te suggested that the bonds are intermediate between polar-covalent single bonds and regular double bonds, with significant negative charge localized on the chalcogen atom. Significant back-donation from the Ch-centered lone pairs to vacant Sb-centered p orbitals was found. The positive charge localized on the Sb atom is reflected by the formation of strong N→Sb dative interactions. This donation from the N-donor atoms quenches the Lewis acidity of the Sb atom, thus attenuating back-bonding from the Ch atom and diminishing the multiple-bond character of the Sb–Ch bond in favor of a more polarized bond.

**L2**SbS was isolated by reaction of **L2**SbCl$_2$ with Na$_2$S (Figure 1.3f).[77] Crystallographic analysis found the species to exist in the dimeric form in the solid state, in contrast to the heavier stibinidene chalcogenides, **L2**SbSe and **L2**SbTe. However, NMR data collected on **L2**SbS were consistent with **L2**SbS existing as a monomer when dissolved in CHCl$_3$ or CDCl$_3$, and the most prominent ion in an electrospray ionization mass spectral measurement corresponded to the protonated monomer at *m/z* 345. Ebullioscopic experiments also found the molecular weight to approximate the mass expected for the monomer at 343 g/mol. **L2**SbS reacts with elemental sulfur (S$_8$) to yield a cyclic bis(pentasulfide), **L2**Sb(μ-S$_5$)$_2$Sb**L2**, highlighting the ambiphilic nature of the Sb–S bond (Figure 1.5a). Moreover, **L2**SbS undergoes a [2+2] cycloaddition reaction with CS$_2$ to form **L2**SbCS$_3$ (Figure 1.5b).[78]

Treatment of **L2**SbCl$_2$ with KOH resulted in the formation of (**L2**SbO)$_2$ (Figure 1.3f).[79] An SC-XRD experiment determined that (**L2**SbO)$_2$ exists as a centrosymmetric dimer with a central Sb$_2$O$_2$ core and the Ar ligands in an *anti* configuration with respect to the cyclic core (Figure 1.4d). ^{1}H and ^{13}C NMR analyses revealed two distinct sets of signals, consistent with

11
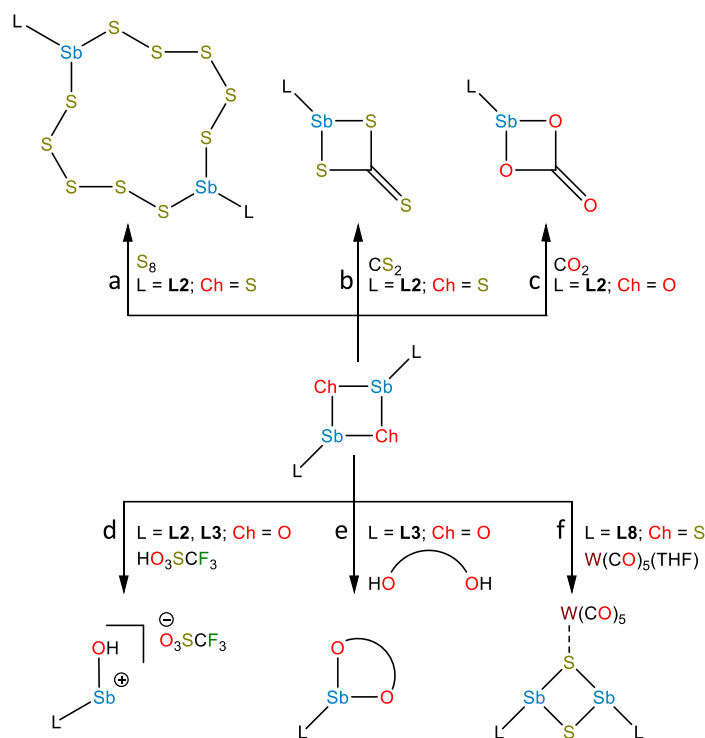
**Figure 1.5.** Reactivity of stibinidene chalcogenides.

persistence of the dimeric form in solution, existing in an equilibrium between the *syn* and

*anti* configurations with respect to the Ar groups, unlike (**L2**SbS)$_2$. Bubbling $CO_2$ into a toluene

solution of (**L2**SbO)$_2$ afforded **L2**SbCO$_3$, highlighting the polarity of the Sb$^+$–O$^-$ bond. **L2**SbCO$_3$

exists as a monomeric species with a 5-coordinate Sb(III) center bound by two O atoms of the

carbonate group (Figure 1.5c). Remarkably, heating a solution of **L2**SbCO$_3$ to 130 °C for 10 h

yielded the parent stibinidene oxide dimer, (**L2**SbO)$_2$. This heteroallene reactivity is

reminiscent of that of the corresponding stibinidene sulfide and $CS_2$. This may be a hint that

the predominantly dimeric (**L2**SbO)$_2$ is in equilibrium with a sufficient amount of monomeric

**L2**SbO for the addition of $CO_2$ to proceed readily. It was subsequently reported that treatment

of (**L2**SbO)$_2$ with trifluoromethanesulfonic or trifluoroacetic acid resulted in the disassociation

of the dimer to form monomeric hydroxyorganoantimony(III) salts of the form [**L2**SbOH][X]

(Figure 1.5d).[80] This reactivity was shared by the piperazinyl-substituted analogs (**L3**SbO)$_2$. (**L3**SbO)$_2$ can also react with pinacol and catechols to form pinacolato and catecholato species with the elimination of water (Figure 1.5e).[81] Ambiphilic reactivity of (**L2**SbO)$_2$ has been explored in response to other reagents, including phosphonic acids,[82] phosphoric acid,[83] arsenic oxides,[84] ChO$_2$ (Ch = S, Se),[85] silanols,[86] boronic acids,[87] and stannoxanes.[88]

These seminal works in the investigation of a completed series of stibinidene chalcogenides, **L2**SbCh (Ch = Te, Se, S, O), provide insight into periodic trends in polar, unsaturated bonding interactions involving heavy pnictogens. To summarize some key discoveries: **L2**SbTe and **L2**SbSe are monomers in both the solid state and solution, **L2**SbS is a dimer in the solid state and a monomer in solution, and (**L2**SbO)$_2$ is a dimer in both the solid state and solution. As the chalcogen atom becomes lighter, its electronegativity increases relative to the antimony center resulting in a more polarized Sb$^+$–Ch$^-$ bond and thus, increasing the thermodynamic driving force to self-aggregate to quench the separation of charge. The thermodynamic stabilization provided by the pendent N-donors does not sufficiently quench the Lewis acidity of the antimony center to prevent dimerization in the cases of **L2**SbS and **L2**SbO, suggesting that a different ligand that provides enhanced steric shielding or more potent Lewis basic donation would be necessary to preclude the observed self-association of these species.

Treatment of the stibinidene dichlorides LSbCl$_2$ (L = **L4**, **L5**, **L6**), which bear O,C,O-pincer ligands of varying steric bulk, with Na$_2$S, afforded dimeric species in both the solid state and in solution (Figure 1.3f).[89] The pendent O atoms of **L4**, **L5**, and **L6** are too weakly donating to prevent dimerization, despite their relatively large steric bulk. When the N,C,O-pincer ligand **L7** with a single NMe$_2$- pendent donor, **L8**, was employed, similar results were observed

(Figure 1.3f).[90-91] Treatment of (**L8**SbS)$_2$ with W(CO)$_5$(THF) does not result in disaggregation, but coordination to the W atom through a bridging sulfide (Figure 1.5f). Interestingly, (RSbCh)$_2$ (R = CH(SiMe$_3$)$_2$, Ch = S, Se) also bind W(CO)$_5$, but through the soft Sb(III) donors.[92-93] The variation in the binding mode may be attributed to donation from the pendent donor arms of **L8** to the Sb center. Treatment of LSbCl$_2$ (L = **L8**, **L9**, **L10**) with KOH afforded a cyclic trimeric stibinidene oxide (Figure 1.3g).[94]

Treatment of **L11**SbCl$_2$ with Li$_2$Se afforded the monomer **L11**SbSe (Figure 1.3h).[95] Similarly, treatment of **L11**SbCl$_2$ with Li$_2$S led to the stibinidene sulfide **L11**SbS. In contrast to **L2**SbS, **L11**SbS was confirmed to be monomeric using single-crystal X-ray diffraction and solution-phase NMR spectroscopy (Figure 1.3h, 1.4c).[95] In another contrast to the **L2** system, **L11**SbTe could not be isolated by reaction with Li$_2$Te; this reaction resulted in decomposition to **L11**Sb and elemental tellurium (Figure 1.3i). **L11**SbSe could also be isolated by reaction of **L11**Sb with elemental selenium (Figure 1.3j). Monomeric **L11**Sb could also be isolated by reduction of **L11**SbCl$_2$ by K[B(i-Bu)$_3$H] (Figure 1.3i).[96] Variations observed for the **L2** and **L11** systems may arise in part from the change in the N-donor strength, and in part from the much greater degree of steric protection afforded by the pendent arms of **L11**. Unsupported monomeric stibinidene and bismuthinidene compounds (i.e., without pendent N donors) have now been isolated with extremely sterically protecting substituents and may provide a platform for new types of reactivity and functional group elucidation.[97-99]

The Sb$^+$–S$^-$ and Sb$^+$–Se$^-$ bonds in **L11**SbCh were probed with theoretical methods. Comparison with the hypothetical monomeric molecules PhSbCh enabled the impact of the N-donor groups on stibinidene chalcogenide bonding to be assessed.[95] **L11**SbCh feature more polarized Sb$^+$–Ch$^-$ bonds with less unsaturated character than those of PhSbCh. The N-donors

quench the Lewis acidic Sb center and attenuate back-bonding from the Ch atom to the Sb atom, favoring a more negatively charged Ch atom. The use of bulky substituents to isolate the elusive monomeric stibinidene sulfide demonstrates the utility of the kinetic stabilization strategy to obtain polar unsaturated bonds involving heavy pnictogens. In the cases of **L2** and **L11**, however, donation of the pendent arms prevents direct study of unperturbed unsaturated stibinidene chalcogenide bonding.

Recently, a stibinidene with an aryl substituent bearing one imine donor and one amine donor (**L12**Sb) was oxidized by air to form a new species that is likely to have proceeded through a monomeric stibinidene oxide followed by a tautomerization whereby the NH amine proton migrated to the O atom (Figure 1.6).[100] Similar tautomerization was not observed when oxidized by heavier chalcogenide sources. This result highlights the extreme reactivity at the hitherto unobserved Sb$^+$–O$^-$ bond of a monomeric stibinidene oxide.



**Figure 1.6.** Oxidation of **L12**Sb to form a monomeric stibinidene oxide that undergoes a spontaneous NH to OH tautomerization.

## 1.4 – Monomeric stibine chalcogenides

Some $\sigma^4,\lambda^5$-stibine chalcogenides of the form $R_3SbCh$ (Ch = S, Se) exist as stable monomers with simple alkyl or aryl groups, but compared to common phosphine and arsine chalcogenides, there are very few examples. Reaction of $Ph_3SbBr_2$ with $H_2S$ affords $Ph_3SbS$ (Figure 1.7a).[101] [121]Sb Mössbauer spectroscopy and single-crystal X-ray diffraction unambiguously confirmed that $Ph_3SbS$ exists as the tetrahedral monomer.[102] $Me_3SbS$ can be synthesized by treatment of $Me_3SbO$ with $H_2S$. $Et_3SbS$ and $Cy_3SbS$ are accessible via reaction of the corresponding $R_3SbBr_2$ with $Na_2S$ (Figure 1.7b).[103] Trialkylstibine sulfides and selenides can also be prepared by reaction of the corresponding stibine with the elemental chalcogen; presumably, the more strongly donating alkyl groups relative to aryl groups enriches the Sb(III) center with electron density such that it is more susceptible to direct oxidation by a chalcogen source (Figure 1.7c).[104-105] Despite this known synthetic pathway to $Et_3SbS$ and $Et_3SbSe$, it was only within the last decade that their solid-state structures were determined (Figure 1.8a,b).[106]
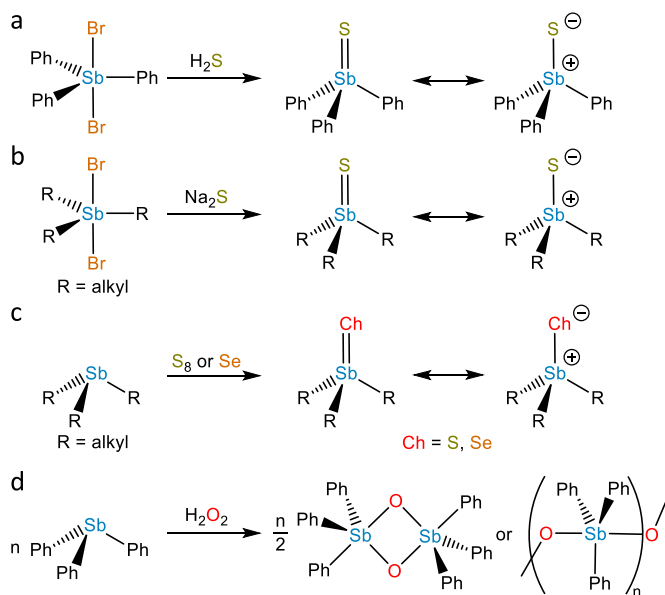


**Figure 1.7.** Synthesis of stibine chalcogenides.
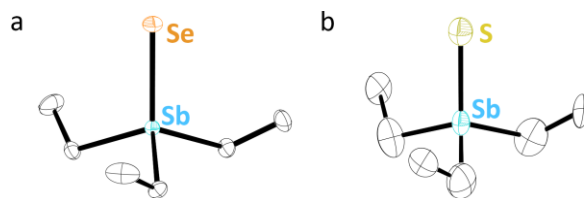
**Figure 1.8.** Thermal ellipsoid plots (50% probability) of (a) $Et_3SbSe$ and (b) $Et_3SbS$. Color code: Sb teal, Se orange, S yellow, and C black. Hydrogen atoms are omitted for clarity.

An electron-deficient triarylstibine, $(C_6F_5)_3Sb$, was purported to form $(C_6F_5)_3SbS$ by refluxing the stibine with elemental sulfur in MeCN or $C_6H_6$, however, more experiments to confirm this result are desirable.[107] I have personally been unsuccessful in producing $Ph_3SbS$ and $Mes_3SbS$ under similar conditions.

Trialkylstibine chalcogenides exhibit Sb–Ch stretching frequencies $\nu_{SbS}$ in the range of 422-440 cm$^{-1}$ and 272-300 cm$^{-1}$ for $\nu_{SbSe}$.[104,108] NMR and UV-vis spectroscopic studies on $Me_3SbS$ suggested that the Sb–S bond exists as a polar covalent bond.[109] NPA, NBO, and ELF (electron localization function) analyses of $Et_3SbCh$ (Ch = S, Se) were recently reported along with their solid-state structures, and these studies are consistent with the presence of polar covalent single bonds between the Sb and Ch atoms, with the Sb–S bond being more polarized than the Sb–Se bond.[106] The authors' interpretation of their data was incomplete in that they did not describe the extent of back-bonding between the Ch-centered lone pairs and the Sb–C σ* orbitals. Fortunately, the detailed output from the NBO analysis was published, allowing readers to interpret the theoretical data on their own. The Ch atom features two lone pairs of predominantly p character which are significantly depopulated. Furthermore, the HOMO and HOMO–1 have appreciable Sb–C σ* character, suggesting that there is indeed back-bonding from the Ch-centered lone pairs to the Sb–C σ* antibonding orbitals that is typical of pnictoryl bonding (*vide infra*). Well-characterized $R_3SbTe$ compounds have not yet been reported.

There is yet to be a systematic investigation into the reactivity of stibine sulfides. Their Lewis basicity is, however, made apparent by their facile coordination to p-block and d-block Lewis acids (Figure 1.9a).[103,110-112] Stibine selenides exhibit similar competency.[113-114] Treatment of $Me_3SbS$ with metal halides or alkyl halides was found to result in halodesulfurization in exchange for halide ions, in which the Sb center maintains its +5 oxidation state (Figure 1.9b,c),[111,115-116] and treatment with acyl halides resulted in 1,2-addition across the $Sb^+–S^-$ bond (Figure 1.9d).[117] Stibine sulfides have also been found to act as S-atom transfer reagents, both to substrates and in intramolecular S atom transfer (Figure 1.9e,f)[118-119]
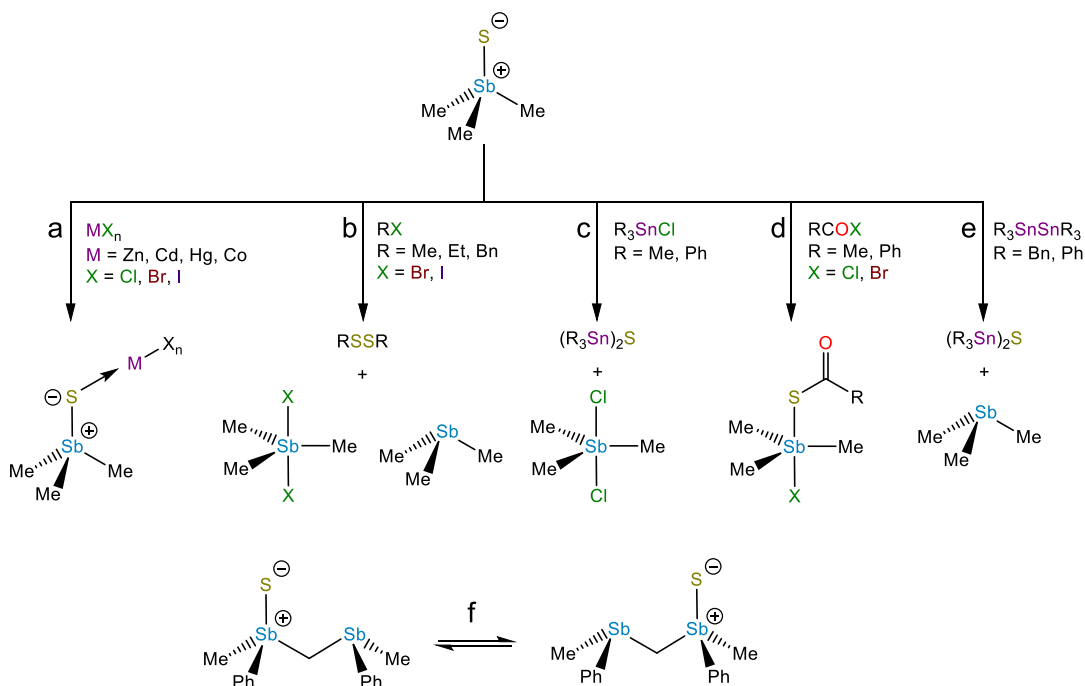


**Figure 1.9.** Reactivity of stibine sulfides.

Species with the empirical formula $R_3SbO$ were obtained via synthetic routes analogous to those for stibine sulfides and stibine selenides. Early investigators described these species as monomeric stibine oxides, but [121]Sb Mössbauer spectroscopy, EXAFS, and X-

18

ray diffraction experiments unambiguously determined stibine oxides such as "Me$_3$SbO" to feature trigonal bipyramidal geometries about the antimony center.[102] These experiments suggested the species had self-associated to form either cyclic or linear head-to-tail oligomers (Figure 1.7d).[120-123] Similarly, bismuthine oxides exist as dimers or oligomers.[124-125] Researchers have isolated disassociated stibine oxides by employing Lewis acids in a thermodynamic stabilization approach, but examples remain quite rare. (Ph$_3$SbO)$_2$ was treated with B(C$_6$F$_5$)$_3$ to isolate a Lewis adduct,[126] and treatment of 1,8-bis(diphenylstibino)napthalene with *o*-chloranil in the presence of adventitious water resulted in the formation of a stibine oxide engaged in an intramolecular dative interaction with an adjacent stiborane unit.[127] It has also been reported that a mixture of Et$_3$Sb and the tetrakis(3,5-difluorophenyl)stibonium tetrakis(pentafluorophenyl)borate resulted in the formation of a Lewis adduct between triethylstibine oxide and the Lewis acidic stibonium cation in the presence of oxygen.[128]

There have also been efforts to isolate monomeric stibine oxides with a kinetic stabilization approach. Prior to the work that is described in this thesis, these efforts were unsuccessful in the isolation of a genuine monomeric stibine oxide. A crystalline product that was described as a hydrogen-bonded adduct of Mes$_3$SbO and a sulfonic acid, Mes$_3$SbO···HO$_3$SR (R = Ph or CF$_3$) was formed by treatment of Mes$_3$Sb(OH)$_2$ with sulfonic acids.[129] A reinvestigation of these species and their ultimate recharacterization as hydroxystibonium salts, [Mes$_3$SbOH][O$_3$SR] (R = Ph or CF$_3$), is described in Chapter 2.

## 1.5 – Pnictoryl (Pn=O/Pn$^+$–O$^-$) bonding

It is initially surprising that despite the prevalence of phosphine oxides and arsine oxides in chemistry, genuine monomeric stibine oxides are an entirely undiscovered class of molecule. The lack of monomeric stibine oxides can be understood by understanding the pnictoryl bond of phosphine oxides and arsine oxides, and how it would be expected to vary for the heavier pnictogen atoms. Phosphine oxides are tetracoordinated monomers bearing a phosphoryl functional group that is commonly depicted with a formal double bond in Lewis diagrams. The nature of the bonding in phosphine oxides that gives rise to their remarkable stability has served as a fruitful topic of debate.[130] The unsaturated nature of the phosphoryl group was initially thought to arise from backdonation of O-centered lone pairs into d-orbitals centered on the phosphorous atom,[13,131] but these orbitals are now known to be too high in energy to participate in bonding. The enhanced agreement between theory and experiment observed upon inclusion of d-functions in theoretical calculations arises because they serve as polarization functions. We now understand that the P–C σ* orbitals are of appropriate energy and symmetry to accept electron density from the O-centered lone pairs (Figure 1.10).
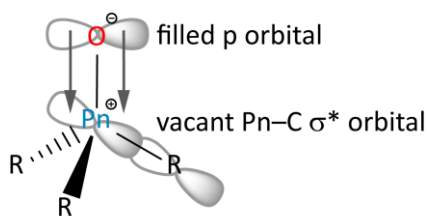


**Figure 1.10.** Accepted model for pnictoryl bonding featuring a polar covalent single bond between the Pn and O atoms and dative interactions between the O-centered, *p*-hybridized lone pairs and Pn–C σ* acceptor orbitals (Pn = P, As, Sb).

Topological analyses of the electron densities of amine, phosphine, and arsine oxides under the framework of Bader's Quantum Theory of Atoms in Molecules (QTAIM) revealed 0

ellipticity at the Pn–O bond critical point (bcp), indicating a cylindrically symmetrical bonding interaction that is reminiscent of single and triple bonds.[132-133] Further analysis of pnictine oxides found three valence shell charge concentrations (minima in the Laplacian) corresponding to three O-centered lone pairs that were staggered relative to the three Pn–X bonds. The extent of back-bonding to the P–C $\sigma$* orbitals was later quantified by analysis of the QTAIM delocalization index and ELF.[134-135] Recently, energy decomposition analysis provided extremely compelling evidence to further support the description of the pnictoryl bond as a polar covalent single-bond stabilized by backdonation from the O-centered lone pairs to the P–C $\sigma$* antibonding orbitals.[130]

Based on this description, certain periodic trends for pnictoryl bonds become evident.[54] As the pnictogen atom becomes heavier, Pn-centered valence orbitals increase in size and diffuseness and overlap between O-centered p and the vacant Pn–C $\sigma$* orbitals is diminished. A decrease in the efficiency of this back-bonding with the heavier pnictogens reduces the thermodynamic stability and increases the polarity of the pnictoryl bond. Furthermore, an increasing difference in electronegativity between the O and Pn atoms as the group is descended should favor a greater separation of charge across the Pn–O bond. The greater propensity of stibine oxides and bismuthine oxides to self-associate than maintain a monomeric form is rationalized by the greater separation of charge in $Sb^+$–$O^-$ and $Bi^+$–$O^-$ relative to $P^+$–$O^-$ and $As^+$–$O^-$, coupled with the greater propensity for the larger pnictogens to expand their coordination spheres. This model of the electron density is consistent with our theoretical analysis of the electron density topology of various species with varied Pn–O bonds.[54] The isolation of the first monomeric stibine oxide, $Dipp_3SbO$ is discussed in Chapter 3.

## 1.6 – References

1.      Melen, R. L., Frontiers in molecular p-block chemistry: From structure to reactivity. *Science* **2019,** *363*, 479-484.

2.      You, D.; Gabbaï, F. P., Tunable σ-Accepting, Z-Type Ligands for Organometallic Catalysis. *Trends Chem.* **2019,** *1*, 485-496.

3.      Bullock, R. M.; Chen, J. G.; Gagliardi, L.; Chirik, P. J.; Farha, O. K.; Hendon, C. H.; Jones, C. W.; Keith, J. A.; Klosin, J.; Minteer, S. D.; Morris, R. H.; Radosevich, A. T.; Rauchfuss, T. B.; Strotman, N. A.; Vojvodic, A.; Ward, T. R.; Yang, J. Y.; Surendranath, Y., Using nature's blueprint to expand catalysis with Earth-abundant metals. *Science* **2020,** *369*, eabc3183.

4.      Power, P. P., Main-group elements as transition metals. *Nature* **2010,** *463*, 171-177.

5.      Johnstone, T. C.; Wee, G. N. J. H.; Stephan, D. W., Accessing Frustrated Lewis Pair Chemistry from a Spectroscopically Stable and Classical Lewis Acid-Base Adduct. *Angew. Chem., Int. Ed.* **2018,** *57*, 5881-5884.

6.      Pang, Y.; Leutzsch, M.; Nöthling, N.; Cornella, J., Dihydrogen and Ethylene Activation by a Sterically Distorted Distibene. *Angew. Chem., Int. Ed.* **2023,** *62*, e202302071.

7.      Hino, S.; Olmstead, M.; Phillips, A. D.; Wright, R. J.; Power, P. P., Terphenyl Ligand Stabilized Lead(II) Derivatives:  Steric Effects and Lead–Lead Bonding in Diplumbenes. *Inorg. Chem.* **2004,** *43*, 7346-7352.

8.      Caputo, C. A.; Power, P. P., Heavier Main Group Dimetallene Reactivity: Effects of Frontier Orbital Symmetry. *Organometallics* **2013,** *32*, 2278-2286.

9.      Stephan, D. W., The broadening reach of frustrated Lewis pair chemistry. *Science* **2016,** *354*, aaf7229.

10.     Moon, H. W.; Cornella, J., Bismuth Redox Catalysis: An Emerging Main-Group Platform for Organic Synthesis. *ACS Catal.* **2022,** *12*, 1382-1393.

11.     Lipshultz, J. M.; Li, G.; Radosevich, A. T., Main Group Redox Catalysis of Organopnictogens: Vertical Periodic Trends and Emerging Opportunities in Group 15. *J. Am. Chem. Soc.* **2021,** *143*, 1699-1721.

12.     Loh, Y. K.; Aldridge, S., Acid–Base Free Main Group Carbonyl Analogues. *Angew. Chem., Int. Ed.* **2021,** *60*, 8626-8648.

13.     Zhao, L.; Pan, S.; Holzmann, N.; Schwerdtfeger, P.; Frenking, G., Chemical Bonding and Bonding Models of Main-Group Compounds. *Chem. Rev.* **2019,** *119*, 8781-8845.

14. Himmel, H.-J., Structural motifs and reactivity of small molecules containing subvalent Group 13 elements: matrix isolation and quantum chemical studies. *Dalton Trans.* **2003**, 3639-3649.

15. Fischer, R. C.; Power, P. P., π-Bonding and the Lone Pair Effect in Multiple Bonds Involving Heavier Main Group Elements: Developments in the New Millennium. *Chem. Rev.* **2010,** *110*, 3877-3923.

16. Nesterov, V.; Reiter, D.; Bag, P.; Frisch, P.; Holzner, R.; Porzelt, A.; Inoue, S., NHCs in Main Group Chemistry. *Chem. Rev.* **2018,** *118*, 9678-9842.

17. Hashimoto, H.; Nagata, K., Transition-metal Complexes with Triple Bonds to Si, Ge, Sn, and Pb and Relevant Complexes. *Chem. Lett.* **2021,** *50*, 778-787.

18. Rivard, E.; Power, P. P., Multiple Bonding in Heavier Element Compounds Stabilized by Bulky Terphenyl Ligands. *Inorg. Chem.* **2007,** *46*, 10047-10064.

19. Liptrot, D. J.; Power, P. P., London dispersion forces in sterically crowded inorganic and organometallic molecules. *Nat. Rev. Chem.* **2017,** *1*, 0004.

20. Lim, S.; Radosevich, A. T., Round-Trip Oxidative Addition, Ligand Metathesis, and Reductive Elimination in a $P^{III}/P^{V}$ Synthetic Cycle. *J. Am. Chem. Soc.* **2020,** *142*, 16188-16193.

21. Pang, Y.; Leutzsch, M.; Nöthling, N.; Katzenburg, F.; Cornella, J., Catalytic Hydrodefluorination via Oxidative Addition, Ligand Metathesis, and Reductive Elimination at Bi(I)/Bi(III) Centers. *J. Am. Chem. Soc.* **2021,** *143*, 12487-12493.

22. Chulsky, K.; Malahov, I.; Bawari, D.; Dobrovetsky, R., Metallomimetic Chemistry of a Cationic, Geometrically Constrained Phosphine in the Catalytic Hydrodefluorination and Amination of Ar–F Bonds. *J. Am. Chem. Soc.* **2023,** *145*, 3786-3794.

23. Bonfante, S.; Lorber, C.; Lynam, J. M.; Simonneau, A.; Slattery, J. M., Metallomimetic C–F Activation Catalysis by Simple Phosphines. *J. Am. Chem. Soc.* **2024,** *146*, 2005-2014.

24. Luh, T.-Y., Trimethylamine N-oxide—a versatile reagent for organometallic chemistry. *Coord. Chem. Rev.* **1984,** *60*, 255-276.

25. Wittig, G.; Schöllkopf, U., Über Triphenyl-phosphin-methylene als olefinbildende Reagenzien (I. Mitteil). *Chem. Ber.* **1954,** *87*, 1318-1330.

26. Mitsunobu, O.; Yamada, M., Preparation of Esters of Carboxylic and Phosphoric Acid via Quaternary Phosphonium Salts. *Bull. Chem. Soc. Jpn.* **1967,** *40*, 2380-2382.

27.   Appel, R., Tertiary Phosphane/Tetrachloromethane, a Versatile Reagent for Chlorination, Dehydration, and P–N Linkage. *Angew. Chem., Int. Ed.* **1975,** *14*, 801-811.

28.   Staudinger, H.; Meyer, J., Über neue organische Phosphorverbindungen III. Phosphinmethylenderivate und Phosphinimine. *Helv. Chim. Acta* **1919,** *2*, 635-646.

29.   Kotani, S.; Nakajima, M., Recent advances in asymmetric phosphine oxide catalysis. *Tetrahedron Lett.* **2020,** *61*.

30.   Morimoto, H.; Yoshino, T.; Yukawa, T.; Lu, G.; Matsunaga, S.; Shibasaki, M., Lewis Base Assisted Brønsted Base Catalysis: Bidentate Phosphine Oxides as Activators and Modulators of Brønsted Basic Lanthanum-Aryloxides. *Angew. Chem., Int. Ed.* **2008,** *47*, 9125-9129.

31.   Yazaki, R.; Kumagai, N.; Shibasaki, M., Direct Catalytic Asymmetric Addition of Allyl Cyanide to Ketones via Soft Lewis Acid/Hard Brønsted Base/Hard Lewis Base Catalysis. *J. Am. Chem. Soc.* **2010,** *132*, 5522-5531.

32.   Shankar, B.; Elumalai, P.; Shanmugam, R.; Singh, V.; Masram, D. T.; Sathiyendiran, M., New Class of Phosphine Oxide Donor-Based Supramolecular Coordination Complexes from an in Situ Phosphine Oxidation Reaction or Phosphine Oxide Ligands. *Inorg. Chem.* **2013,** *52*, 10217-10219.

33.   Keener, M.; Hunt, C.; Carroll, T. G.; Kampel, V.; Dobrovetsky, R.; Hayton, T. W.; Ménard, G., Redox-switchable carboranes for uranium capture and release. *Nature* **2020,** *577*, 652-655.

34.   Beckett, M. A.; Strickland, G. C.; Holland, J. R.; Sukumar Varma, K., A convenient n.m.r. method for the measurement of Lewis acidity at boron centres: correlation of reaction rates of Lewis acid initiated epoxide polymerizations with Lewis acidity. *Polymer* **1996,** *37*, 4629-4631.

35.   Nemoto, T.; Ohshima, T.; Yamaguchi, K.; Shibasaki, M., Catalytic Asymmetric Epoxidation of Enones Using La–BINOL–Triphenylarsine Oxide Complex: Structural Determination of the Asymmetric Catalyst. *J. Am. Chem. Soc.* **2001,** *123*, 2725-2732.

36.   Phillips, D.; Tyree Jr, S., The donor properties of triphenylarsine oxide. *J. Am. Chem. Soc.* **1961,** *83*, 1806-1810.

37.   Klofutar, C.; Krašovec, F.; Kušar, M., Base Strength of Various Organic Oxides. *Croat. Chem. Acta* **1968,** *40*, 23-28.

38.   Hollow, S. E.; Johnstone, T. C., Realgar and arsenene nanomaterials as arsenic-based anticancer agents. *Curr. Opin. Chem. Biol.* **2023,** *72*, 102229.

39. Lance-Byrne, A.; Lindquist-Kleissler, B.; Johnstone, T. C., Chemical Structure Elucidation in the Development of Inorganic Drugs: Evidence from Ru-, Au-, As-, and Sb-based Medicines. *Eur. J. Inorg. Chem.* **2024,** *27*.

40. Huang, W.-S.; Liu, S.; Zou, D.; Thomas, M.; Wang, Y.; Zhou, T.; Romero, J.; Kohlmann, A.; Li, F.; Qi, J.; Cai, L.; Dwight, T. A.; Xu, Y.; Xu, R.; Dodd, R.; Toms, A.; Parillon, L.; Lu, X.; Anjum, R.; Zhang, S.; Wang, F.; Keats, J.; Wardwell, S. D.; Ning, Y.; Xu, Q.; Moran, L. E.; Mohemmad, Q. K.; Jang, H. G.; Clackson, T.; Narasimhan, N. I.; Rivera, V. M.; Zhu, X.; Dalgarno, D.; Shakespeare, W. C., Discovery of Brigatinib (AP26113), a Phosphine Oxide-Containing, Potent, Orally Active Inhibitor of Anaplastic Lymphoma Kinase. *J. Med. Chem.* **2016,** *59*, 4948-4964.

41. Lindquist-Kleissler, B.; Johnstone, T. C., Models of the putative antimony(V)–diolate motifs in antileishmanial pentavalent antimonial drugs. *Dalton Trans.* **2023,** *52*, 9229-9237.

42. Griffith, D. M.; Li, H.; Werrett, M. V.; Andrews, P. C.; Sun, H., Medicinal chemistry and biomedical applications of bismuth-based compounds and nanoparticles. *Chem. Soc. Rev.* **2021,** *50*, 12037-12069.

43. Fiszbein, D. J.; Brown, V.; Thiele, N. A.; Woods, J. J.; Wharton, L.; Macmillan, S. N.; Radchenko, V.; Ramogida, C. F.; Wilson, J. J., Tuning the Kinetic Inertness of Bi[3+] Complexes: The Impact of Donor Atoms on Diaza-18-Crown-6 Ligands as Chelators for [213]Bi Targeted Alpha Therapy. *Inorg. Chem.* **2021,** *60*, 9199-9211.

44. Wilson, J. J.; Ferrier, M.; Radchenko, V.; Maassen, J. R.; Engle, J. W.; Batista, E. R.; Martin, R. L.; Nortier, F. M.; Fassbender, M. E.; John, K. D.; Birnbaum, E. R., Evaluation of nitrogen-rich macrocyclic ligands for the chelation of therapeutic bismuth radioisotopes. *Nuclear Medicine and Biology* **2015,** *42*, 428-438.

45. Maltz, L. T.; Gabbaï, F. P., Analyzing Fluoride Binding by Group 15 Lewis Acids: Pnictogen Bonding in the Pentavalent State. *Inorg. Chem.* **2023,** *62*, 13566-13572.

46. Sharma, D.; Balasubramaniam, S.; Kumar, S.; Jemmis, E. D.; Venugopal, A., Reversing Lewis acidity from bismuth to antimony. *Chem. Commun.* **2021,** *57*, 8889-8892.

47. Warring, L. S.; Walley, J. E.; Dickie, D. A.; Tiznado, W.; Pan, S.; Gilliard, R. J., Lewis Superacidic Heavy Pnictaalkene Cations: Comparative Assessment of Carbodicarbene-Stibenium and Carbodicarbene-Bismuthenium Ions. *Inorg. Chem.* **2022,** *61*, 18640-18652.

48. Yang, M.; Tofan, D.; Chen, C. H.; Jack, K. M.; Gabbaï, F. P., Digging the Sigma-Hole of Organoantimony Lewis Acids by Oxidation. *Angew. Chem., Int. Ed.* **2018,** *57*, 13868-13872.

49. Pan, B.; Gabbaï, F. P., [Sb(C$_6$F$_5$)$_4$][B(C$_6$F$_5$)$_4$]: An Air Stable, Lewis Acidic Stibonium Salt That Activates Strong Element-Fluorine Bonds. *J. Am. Chem. Soc.* **2014,** *136*, 9564-9567.

50. Hirai, M.; Gabbaï, F. P., Squeezing Fluoride out of Water with a Neutral Bidentate Antimony(V) Lewis Acid. *Angew. Chem., Int. Ed.* **2015,** *54*, 1205-1209.

51. Murphy, B. L.; Gabbaï, F. P., Binding, Sensing, And Transporting Anions with Pnictogen Bonds: The Case of Organoantimony Lewis Acids. *J. Am. Chem. Soc.* **2023,** *145*, 19458-19477.

52. Hirai, M.; Cho, J.; Gabbaï, F. P., Promoting the Hydrosilylation of Benzaldehyde by Using a Dicationic Antimony-Based Lewis Acid: Evidence for the Double Electrophilic Activation of the Carbonyl Substrate. *Chem.–Eur. J.* **2016,** *22*, 6537-6541.

53. Lance-Byrne, A.; Lindquist-Kleissler, B.; Johnstone, T. C., Chemical Structure Elucidation in the Development of Inorganic Drugs: Evidence from Ru-, Au-, As-, and Sb-based Medicines. *Eur. J. Inorg. Chem.* **2024**.

54. Lindquist-Kleissler, B.; Wenger, J. S.; Johnstone, T. C., Analysis of Oxygen–Pnictogen Bonding with Full Bond Path Topological Analysis of the Electron Density. *Inorg. Chem.* **2021,** *60*, 1846-1856.

55. Hedges, S. W.; Bowen, L. H., Antimony (III) orbital population analysis using antimony-121 Mössbauer data. *J. Chem. Phys.* **1977,** *67*, 4706-4710.

56. Jaffe, H.; Doak, G., Disproportionation of Aromatic Stiboso Compounds. I. Mechanism. *J. Am. Chem. Soc.* **1949,** *71*, 602-606.

57. Doak, G.; Jaffe, H., The Disproportionation of Aromatic Stiboso Compounds. II. Methods of Synthesis. *J. Am. Chem. Soc.* **1950,** *72*, 3025-3027.

58. Jaffe, H.; Doak, G., The Disproportionation of Aromatic Stiboso Compounds. III. Effect of Structure. *J. Am. Chem. Soc.* **1950,** *72*, 3027-3029.

59. Breunig, H. J.; Ebert, K. H.; Mohammed, M. A.; Pawlik, J.; Probst, J., Novel Organo Antimony Homo and Hetero Cycles. *Phosphorus, Sulfur Silicon Relat. Elem.* **1994,** *93*, 293-296.

60. Breunig, H. J.; Mohammed, M. A.; Ebert, K. H., Ein cyclisches Organoantimon(III)-oxid, (RSbO)$_4$ [R = (Me$_3$Si)$_2$CH] / A Cyclic Organoantimony(III) Oxide, (RSbO)$_4$ [R = (Me$_3$Si)$_2$CH]. *Z. Naturforsch., B: J. Chem. Sci.* **1994,** *49*, 877-880.

61. Mohammed, M. A.; Ebert, K. H.; Breunig, H. J., Zwischenmolekulare Wechselwirkungen bei RSbCl$_2$ und die Bildung cyclischer Organoantimon(III)-

chalkogenide, $(RSbE)_n$ [R = $(Me_3Si)_2CH$, E = S, Se, Te] / Intermolecular Interactions of $RSbCl_2$ and Formation. *Z. Naturforsch., B: J. Chem. Sci.* **1996,** *51*, 149-152.

62. Tokitoh, N.; Arai, Y.; Okazaki, R.; Nagase, S., Synthesis and Characterization of a Stable Dibismuthene: Evidence for a Bi-Bi Double Bond. *Science* **1997,** *277*, 78-80.

63. Tokitoh, N.; Arai, Y.; Sasamori, T.; Okazaki, R.; Nagase, S.; Uekusa, H.; Ohashi, Y., A Unique Crystalline-State Reaction of an Overcrowded Distibene with Molecular Oxygen: The First Example of a Single Crystal to a Single Crystal Reaction with an External Reagent. *J. Am. Chem. Soc.* **1998,** *120*, 433-434.

64. Tokitoh, N.; Arai, Y.; Harada, J.; Okazaki, R., Syntheses and Crystal Structures of Novel Antimony-Containing Cyclic Polysulfides. *Chem. Lett.* **1995,** *24*, 959-960.

65. Tokitoh, N.; Arai, Y.; Sasamori, T.; Takeda, N.; Okazaki, R., Formation of antimony–sulfur double-bond compounds and their trapping with nitrile oxides. *Heteroat. Chem.* **2001,** *12*, 244-249.

66. Sasamori, T.; Mieda, E.; Takeda, N.; Tokitoh, N., Reaction of an Overcrowded Distibene with Elemental Sulfur and Crystallographic Analysis of the Sulfurization Products. *Chem. Lett.* **2004,** *33*, 104-105.

67. Sasamori, T.; Mieda, E.; Takeda, N.; Tokitoh, N., Telluradistibirane and Telluradibismirane: Three-Membered Heterocycles of Heavier Main Group Elements. *Angew. Chem., Int. Ed.* **2005,** *44*, 3717-3720.

68. Sasamori, T.; Mieda, E.; Tokitoh, N., Chalcogenation Reactions of Overcrowded Doubly Bonded Systems between Heavier Group 15 Elements. *Bull. Chem. Soc. Jpn.* **2007,** *80*, 2425-2435.

69. Sasamori, T.; Mieda, E.; Tsurusaki, A.; Nagahora, N.; Tokitoh, N., Selenization and tellurization reactions of kinetically stabilized dipnictenes. *Phosphorus, Sulfur, and Silicon* **2008,** *183*, 998-1002.

70. Sasamori, T.; Tokitoh, N., Doubly bonded systems between heavier Group 15 elements. *Dalton Trans.* **2008**, 1395-1408.

71. Jambor, R.; Dostál, L., The Chemistry of Pincer Complexes of 13–15 Main Group Elements. In *Organometallic Pincer Chemistry*, Springer Berlin Heidelberg: 2013; pp 175-202.

72. Raţ, C. I.; Silvestru, C.; Breunig, H. J., Hypervalent organoantimony and -bismuth compounds with pendant arm ligands. *Coord. Chem. Rev.* **2013,** *257*, 818-879.

73. Breunig, H. J., The role of the substituents in the chemistry of organoantimony(I) compounds. *Rev. Roum. Chim.* **2020,** *65*, 635-646.

74. Dostál, L.; Jambor, R.; Růžička, A.; Holeček, J., Syntheses and Structures of $Ar_3Sb_5$ and $Ar_4Sb_4$ Compounds (Ar = $C_6H_3$-2,6-$(CH_2NMe_2)_2$). *Organometallics* **2008,** *27*, 2169-2171.

75. Dostál, L.; Jambor, R.; Růžička, A.; Lyčka, A.; Brus, J.; de Proft, F., Synthesis and Structure of Organoantimony(III) Compounds Containing Antimony–Selenium and –Tellurium Terminal Bonds. *Organometallics* **2008,** *27*, 6059-6062.

76. Sasamori, T.; Arai, Y.; Takeda, N.; Okazaki, R.; Furukawa, Y.; Kimura, M.; Nagase, S.; Tokitoh, N., Syntheses, Structures and Properties of Kinetically Stabilized Distibenes and Dibismuthenes, Novel Doubly Bonded Systems between Heavier Group 15 Elements. *Bull. Chem. Soc. Jpn.* **2002,** *75*, 661-675.

77. Dostál, L.; Jambor, R.; Růžička, A.; Jirásko, R.; Lochař, V.; Beneš, L.; de Proft, F., Nonconventional Behavior of NCN-Chelated Organoantimony(III) Sulfide and Isolation of Cyclic Organoantimony(III) Bis(pentasulfide). *Inorg. Chem.* **2009,** *48*, 10495-10497.

78. Dostál, L.; Jambor, R.; Růžička, A.; Jirásko, R.; Černošková, E.; Beneš, L.; de Proft, F., [2 + 2] Cycloaddition of Carbon Disulfide to NCN-Chelated Organoantimony(III) and Organobismuth(III) Sulfides: Evidence for Terminal Sb–S and Bi–S Bonds in Solution. *Organometallics* **2010,** *29*, 4486-4490.

79. Dostál, L.; Jambor, R.; Růžička, A.; Erben, M.; Jirásko, R.; Černošková, E.; Holeček, J., Efficient and Reversible Fixation of Carbon Dioxide by NCN-Chelated Organoantimony(III) Oxide. *Organometallics* **2009,** *28*, 2633-2636.

80. Fridrichová, A. l.; Svoboda, T.; Jambor, R.; Padělková, Z. k.; Růžička, A.; Erben, M.; Jirásko, R.; Dostál, L., Synthesis and Structural Study on Organoantimony(III) and Organobismuth(III) Hydroxides Containing an NCN Pincer Type Ligand†. *Organometallics* **2009,** *28*, 5522-5528.

81. Strîmb, G.; Pöllnitz, A.; Raţ, C. I.; Silvestru, C., A general route to monoorganopnicogen(III) (M = Sb, Bi) compounds with a pincer (N,C,N) group and oxo ligands. *Dalton Trans.* **2015,** *44*, 9927-9942.

82. Svoboda, T.; Jambor, R.; Růžička, A.; Padělková, Z.; Erben, M.; Jirásko, R.; Dostál, L., NCN-Chelated Organoantimony(III) and Organobismuth(III) Phosphonates: Syntheses and Structures. *Eur. J. Inorg. Chem.* **2010,** *2010*, 1663-1669.

83. Svoboda, T.; Dostál, L.; Jambor, R.; Růžička, A.; Jirásko, R.; Lyčka, A., NCN-Chelated Organoantimony(III) and Organobismuth(III) Phosphates: Synthesis and Solid-State and Solution Structures. *Inorg. Chem.* **2011,** *50*, 6411-6413.

84. Svoboda, T.; Jambor, R.; Růžička, A.; Jirásko, R.; Lyčka, A.; de Proft, F.; Dostál, L., Reactivity of NCN-Chelated (NCN = $C_6H_3$-2,6-$(CH_2NMe_2)_2$) Antimony(III) and Bismuth(III) Oxides toward Oxides of Arsenic. *Organometallics* **2012,** *31*, 1725-1729.

85.     Mairychová, B.; Svoboda, T.; Erben, M.; Růžička, A.; Dostál, L.; Jambor, R., Intramolecularly Coordinated Group 14 and 15 Chalcogenites. *Organometallics* **2013,** *32*, 157-163.

86.     Fridrichová, A.; Mairychová, B.; Padělková, Z.; Lyčka, A.; Jurkschat, K.; Jambor, R.; Dostál, L., Straightforward synthesis of novel cyclic metallasiloxanes supported by an N,C,N-chelating ligand. *Dalton Trans.* **2013,** *42*, 16403-16411.

87.     Mairychová, B.; Svoboda, T.; Štěpnička, P.; Růžička, A.; Havenith, R. W. A.; Alonso, M.; de Proft, F.; Jambor, R.; Dostál, L., Synthesis and Structural Characterization of Heteroboroxines with $MB_2O_3$ Core (M = Sb, Bi, Sn). *Inorg. Chem.* **2013,** *52*, 1424-1431.

88.     Svoboda, T.; Warneke, J.; Růžička, A.; Dostál, L.; Beckmann, J., Synthesis and structure of heavy group 15 metallastannoxanes $[2,6-(Me_2NCH_2)_2C_6H_3E](2,6-Mes_2C_6H_3Sn)_3O_3(OH)_5$ (E = Sb, Bi). *J. Organomet. Chem.* **2015,** *797*, 171-173.

89.     Chovancová, M.; Jambor, R.; Růžička, A.; Jirásko, R.; Císařová, I.; Dostál, L., Synthesis, Structure, and Reactivity of Intramolecularly Coordinated Organoantimony and Organobismuth Sulfides. *Organometallics* **2009,** *28*, 1934-1941.

90.     Vrána, J.; Jambor, R.; Růžička, A.; Lyčka, A.; Dostál, L., Organoantimony(III) and organobismuth(III) sulfides and selenide stabilized by NCO chelating pincer type ligand. *J. Organomet. Chem.* **2012,** *718*, 78-81.

91.     Opris, L. M.; Silvestru, A.; Silvestru, C.; Breunig, H. J.; Lork, E., Syntheses and chemistry of hypervalent cyclo-$R_4Sb_4$, cyclo-$(RSbE)_n$[R = 2-$(Me_2NCH_2)C_6H_4$, E = O, S] and precursors. *Dalton Trans.* **2004**, 3575-3585.

92.     Breunig, H. J.; Ghesner, I.; Lork, E., A complex with the *cyclo*-$R_2Sb_2S_2$ [R = $CH(SiMe_3)_2$] ligand. *Appl. Organomet. Chem.* **2002,** *16*, 547-549.

93.     Breunig, H. J.; Ghesner, I.; Lork, E., Syntheses and structures of $(R_2Bi)_2E$ (E=S, Te) and cyclo-$(RSbSe)_2[W(CO)_5]_2$ [R=$CH(SiMe_3)_2$]. *J. Organomet. Chem.* **2002,** *664*, 130-135.

94.     Preda, A. M.; Raţ, C. I.; Silvestru, C.; Breunig, H. J.; Lang, H.; Rüffer, T.; Mehring, M., Organoantimony(III) compounds containing (imino)aryl ligands of the type 2-$(RN=CH)C_6H_4$(R = 2′,4′,6′-$Me_3C_6H_2$, 2′,6′-$^iPr_2C_6H_3$): bromides and chalcogenides. *Dalton Trans.* **2013,** *42*, 1144-1158.

95.     Šimon, P.; Jambor, R.; Růžička, A.; Lyčka, A.; de Proft, F.; Dostál, L., Monomeric organoantimony(III) sulphide and selenide with terminal Sb–E bond (E = S, Se). Synthesis, structure and theoretical consideration. *Dalton Trans.* **2012,** *41*, 5140-5143.

96.     Šimon, P.; de Proft, F.; Jambor, R.; Růžička, A.; Dostál, L., Monomeric Organoantimony(I) and Organobismuth(I) Compounds Stabilized by an NCN Chelating Ligand: Syntheses and Structures. *Angew. Chem., Int. Ed.* **2010,** *49*, 5468-5471.

97.     Wu, M.; Li, H.; Chen, W.; Wang, D.; He, Y.; Xu, L.; Ye, S.; Tan, G., A triplet stibinidene. *Chem* **2023,** *9*, 2573-2584.

98.     Wu, M.; Chen, W.; Wang, D.; Chen, Y.; Ye, S.; Tan, G., Triplet Bismuthinidenes Featuring Unprecedented Giant and Positive Zero Field Splittings. *Natl. Sci. Rev.* **2023**, nwad169.

99.     Pang, Y.; Nöthling, N.; Leutzsch, M.; Kang, L.; Bill, E.; van Gastel, M.; Reijerse, E.; Goddard, R.; Wagner, L.; SantaLucia, D.; DeBeer, S.; Neese, F.; Cornella, J., Synthesis and isolation of a triplet bismuthinidene with a quenched magnetic response. *Science* **2023,** *380*, 1043-1048.

100.    Zechovský, J.; Kertész, E.; Kremláček, V.; Hejda, M.; Mikysek, T.; Erben, M.; Růžička, A.; Jambor, R.; Benkő, Z.; Dostál, L., Exploring Differences between Bis(aldimino)- and amino-aldimino-N,C,N-Pincer-Stabilized Pnictinidenes: Limits of Synthesis, Structure, and Reversible Tautomerization-Controlled Oxidation. *Organometallics* **2022,** *41*, 2535-2550.

101.    Kaufmann, L., Triphenylstibin-sulfid. *Ber. Dtsch. Chem. Ges.* **1908,** *41*, 2762-2766.

102.    Pebler, J.; Weller, F.; Dehnicke, K., Beiträge zum $^{121}$Sb-Mößbauer-Effekt. V. Triorganoantimon-Chalkogenderivate Die Kristallstruktur von $Ph_3SbS$. *Z. Anorg. Allg. Chem.* **1982,** *492*, 139-147.

103.    Shindo, M.; Matsumura, Y.; Okawara, R., Study on triorganostibine sulfide and its complexes. *J. Organomet. Chem.* **1968,** *11*, 299-305.

104.    Chremos, G. N.; Zingaro, R. A., The synthesis and infrared spectra of some group Va chalcogenides. *J. Organomet. Chem.* **1970,** *22*, 637-646.

105.    Zingaro, R. A.; Merijanian, A., Some stibine sulfides and stibine selenides. *J. Organomet. Chem.* **1964,** *1*, 369-372.

106.    Heimann, S.; Bläser, D.; Wölper, C.; Haack, R.; Jansen, G.; Schulz, S., The bonding situation in triethylchalcogenostiboranes – polarized single bonds vs. double bonds. *Dalton Trans.* **2014,** *43*, 14772-14777.

107.    Raj, P.; Saxena, A. K.; Singhal, K.; Ranjan, A., Synthesis and some reactions of tris (pentafluorophenyl) antimony compounds. *Polyhedron* **1985,** *4*, 251-258.

108.    Chremos, G. N.; Zingaro, R. A., Correlation of metal-chalcogen stretching frequencies of some trialkyl group Va chalcogenides. *J. Organomet. Chem.* **1970,** *22*, 647-651.

109.    Otera, J.; Okawara, R., Sb–S bond in trimethylstibine sulfide. *Inorg. Nucl. Chem. Lett.* **1970,** *6*, 855-857.

110. Maeda, T.; Yoshida, G.; Okawara, R., Reactions of indium compounds with trimethylstibine sulfide. *J. Organomet. Chem.* **1972,** *44*, 237-241.

111. Saito, T.; Otera, J.; Okawara, R., Metal Halide Complexes with Trimethylstibine Sulfide. *Bull. Chem. Soc. Jpn.* **1970,** *43*, 1733-1736.

112. Okawara, R.; Otera, J.; Osaki, T., Metal nitrate complexes with trimethylstibine sulfide. *Inorg. Chem.* **1971,** *10*, 402-404.

113. Kuhn, N.; Schumann, H., $C_5H_5Fe(CO)_2(Me_3Sb=Se)]BF_4$, ein stabiler selenostiborankomplex. *J. Organomet. Chem.* **1985,** *288*, c51-c52.

114. Kuhn, N.; Schumann, H., Chemische und spektroskopische untersuschungen an komplex-kationen des types $[C_5H_5Fe(CO)_2(R_3EX)]^+$. Ein beitrag zur diskussion der koordinationseigenschaften von phosphanchalkogeniden und deren höheren homologen. *J. Organomet. Chem.* **1986,** *304*, 181-193.

115. Otera, J.; Okawara, R., Reaction of trimethylstibine sulfide with alkyl halides. *J. Organomet. Chem.* **1969,** *16*, 335-338.

116. Shindo, M.; Matsumura, Y.; Okawara, R., On the Behavior of the Mixture of Trimethylstibine Sulfide and Tin (IV) Halides in Solution. *Bull. Chem. Soc. Jpn.* **1969,** *42*, 265-266.

117. Otera, J.; Okawara, R., Preparation and properties of trimethylantimony halide thiocarboxylates. *J. Organomet. Chem.* **1969,** *17*, 353-357.

118. Donahue, J. P., Thermodynamic Scales for Sulfur Atom Transfer and Oxo-for-Sulfido Exchange Reactions. *Chem. Rev.* **2006,** *106*, 4747-4783.

119. Sato, S.-I.; Matsumura, Y., Preparation and configurational isomerism of ditertiary stibine sulfides, $(C_6H_5)(CH_3)(S)SbCH_2Sb(CH_3)(C_6H_5)$ and $[(C_6H_5)(CH_3)(S)Sb]_2(CH_2)_3$. *J. Organomet. Chem.* **1975,** *96*, 57-61.

120. Bordner, J.; Doak, G. O.; Everett, T. S., Crystal structure of 2,2,4,4-tetrahydro-2,2,2,4,4,4-hexaphenyl-1,3,2,4-dioxadistibetane (triphenylstibene oxide dimer) and related compounds. *J. Am. Chem. Soc.* **1986,** *108*, 4206-4213.

121. Venezky, D. L.; Sink, C. W.; Nevett, B. A.; Fortescue, W. F., Preparation, properties and structure of poly(triphenylstibine oxide). *J. Organomet. Chem.* **1972,** *35*, 131-142.

122. Ferguson, G.; Glidewell, C.; Kaitner, B.; Lloyd, D.; Metcalfe, S., Second determination of the structure of dimeric triphenylstibine oxide. *Acta Crystallogr. Sect. C* **1987,** *43*, 824-826.

123.    Carmalt, C. J.; Crossley, J. G.; Norman, N. C.; Orpen, A. G., The structure of amorphous Ph$_3$SbO: information from EXAFS (extended X-ray absorption fine structure) spectroscopy. *Chem. Commun.* **1996**, 1675-1676.

124.    Suzuki, H.; Ikegami, T.; Matano, Y., Ultrasonic reaction of triarylbismuthines and triarylstibines with iodosylbenzene. Mild oxidizing ability of the organobismuth oxide function for organic substrates. *Tetrahedron Lett.* **1994,** *35*, 8197-8200.

125.    Matano, Y.; Nomura, H.; Hisanaga, T.; Nakano, H.; Shiro, M.; Imahori, H., Diverse Structures and Remarkable Oxidizing Ability of Triarylbismuthane Oxides. Comparative Study on the Structure and Reactivity of a Series of Triarylpnictogen Oxides. *Organometallics* **2004,** *23*, 5471-5480.

126.    Kather, R.; Svoboda, T.; Wehrhahn, M.; Rychagova, E.; Lork, E.; Dostál, L.; Ketkov, S.; Beckmann, J., Lewis-acid induced disaggregation of dimeric arylantimony oxides. *Chem. Commun.* **2015,** *51*, 5932-5935.

127.    Chen, C.-H.; Gabbaï, F. P., Coordination of a stibine oxide to a Lewis acidic stiborane at the upper rim of the biphenylene backbone. *Dalton Trans.* **2018,** *47*, 12075-12078.

128.    Coughlin, O. Structural manipulation of Organoantimony Cations for Tuneable Lewis Acidity and Reactivity of Palladium Organoantimony Complexes. Nottingham Trent University, 2021.

129.    Huber, F.; Westhoff, T.; Preut, H., Tris(2,4,6-trimethylphenyl)antimony dihydroxide; synthesis and reaction with sulfonic acids RSO$_3$H (R = C$_6$H$_5$, CF$_3$). Crystal structure of [2,4,6-(CH$_3$)$_3$C$_6$H$_2$]$_3$SbO · HO$_3$SC$_6$H$_5$. *J. Organomet. Chem.* **1987,** *323*, 173-180.

130.    Yang, T.; Andrada, D. M.; Frenking, G., Dative versus electron-sharing bonding in N-oxides and phosphane oxides R$_3$EO and relative energies of the R$_2$EOR isomers (E = N, P; R = H, F, Cl, Me, Ph). A theoretical study. *Phys. Chem. Chem. Phys.* **2018,** *20*, 11856-11866.

131.    Gilheany, D. G., No D-Orbitals but Walsh Diagrams and Maybe Banana Bonds - Chemical Bonding in Phosphines, Phosphine Oxides, and Phosphonium Ylides. *Chem. Rev.* **1994,** *94*, 1339-1374.

132.    Bader, R. F. W., A Quantum Theory of Molecular Structure and Its Applications. *Chem. Rev.* **1991,** *91*, 893-928.

133.    Dobado, J. A.; Martínez-García, H.; Jose Molina Molina; Sundberg, M. R., Chemical Bonding in Hypervalent Molecules Revised. Application of the Atoms in Molecules Theory to Y$_3$X and Y$_3$XZ (Y = H or CH$_3$; X = N, P or As; Z = O or S) Compounds. *J. Am. Chem. Soc.* **1998,** *120*, 8461-8471.

134. Chesnut, D. B.; Savin, A., The Electron Localization Function (ELF) Description of the PO Bond in Phosphine Oxide. *J. Am. Chem. Soc.* **1999,** *121*, 2335-2336.

135. Chesnut, D. B., Atoms-in-Molecules and Electron Localization Function Study of the Phosphoryl Bond. *J. Phys. Chem. A* **2003,** *107*, 4307-4313.

# Chapter 2

## A reinvestigation of previously reported monomeric stibine oxides

## 2.1 – Introduction

After an extensive literature search for an unperturbed monomeric stibine oxide of the form ($R_3Sb=O/R_3Sb^+–O$), I was able to find only a single well-characterized example of such a species. As mentioned in Chapter 1, Huber and co-workers reported the isolation of the hydrogen-bonded adduct $Mes_3SbO\cdots HO_3SR$.[1] This was the purported product of the reaction between *trans*-$Sb(OH)_2Mes_3$ and either benzenesulfonic acid or trifluoromethanesulfonic (triflic) acid, in which protonation of an apical hydroxide ligand from the *trans*-$Sb(OH)_2Mes_3$ resulted in the loss of a water molecule. The resulting sulfonate anion was then believed to abstract a proton from the remaining $Mes_3SbOH^+$ moiety, suggesting that $Mes_3SbO$ is a weaker Brønsted base than $PhSO_3^-$. Elemental analysis, conductivity, and $^1H$ NMR and IR spectroscopic data were consistent with the formation of $Mes_3SbO\cdots HO_3SR$, but the strongest evidence offered in support of the identity of the $Mes_3SbO\cdots HO_3SR$ species was the X-ray crystal structure of the benzenesulfonate adduct, the refined model of which featured a hydrogen bond between the acid and the stibine oxide.

In this chapter, I describe my reinvestigation of species that were previously reported as monomeric stibine oxides. A combined theoretical, spectroscopic, and crystallographic investigation unambiguously confirmed previous reports of stibine oxides to be hydroxystibonium salts. Furthermore, this chapter includes a discussion on the application of neutron diffraction, multipole modelling, and Hirschfeld atom refinement with *NoSpherA2* to elucidating the chemical structures of molecules that bear both heavy main-group elements and polar X–H bonds.

## 2.2 – Theoretical investigation of previously reported monomeric stibine oxides

We were excited to investigate the bonding and reactivity of the monomeric stibine oxide, Mes₃SbO, which could presumably be isolated by simple removal of PhSO₃H from Mes₃SbO···HO₃SPh. We conducted several theoretical analyses to gain preliminary insight into the nature of Mes₃SbO···HO₃SPh. We performed a geometry optimization (PBE0/def2-TZVPP) starting from the previously reported crystallographic coordinates (Figure 2.1a). In the optimized structure the Sb–O bond length of 1.887 Å was in excellent agreement with the experimental value of 1.894(5) Å. However, the H atom had migrated from PhSO₃⁻ to Mes₃SbO to form the hydroxystibonium benzenzenesulfonate salt [Mes₃Sb(OH)][PhSO₃] with an O–H bond length of 1.035 Å. A relaxed surface scan (BP86/def2-TZVP) in which the hydrogen atom is systematically moved from the Sb-bound O atom to the S-bound O atom revealed a single minimum along this internal coordinate that corresponds to the ionic formulation, [Mes₃Sb(OH)][PhSO₃] (Figure 2.1b). These results seemed to indicate that PhSO₃H is a stronger
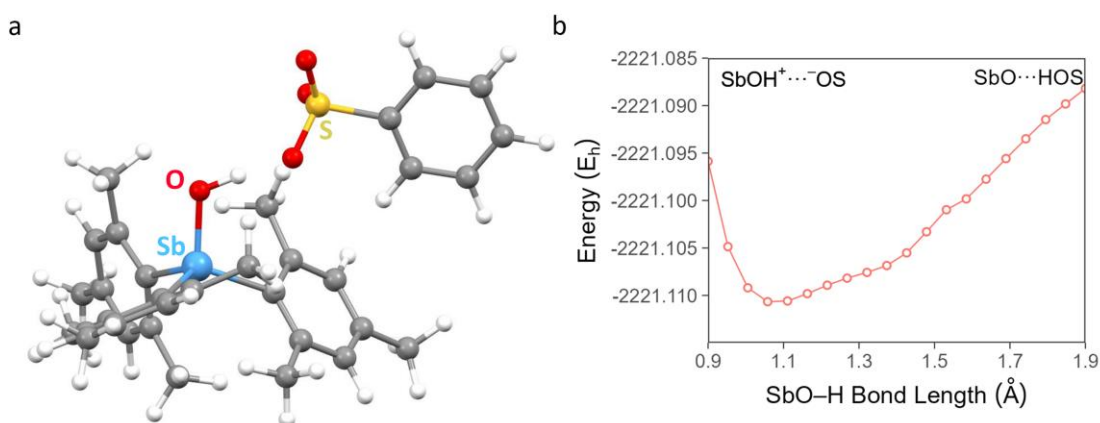


**Figure 2.1.** (a) Ball-and-stick representation of the optimized structure (PBE0/def2-TZVPP) of [Mes₃Sb(OH)][PhSO₃]. (b) Relaxed surface scan (BP86/def2-TZVP) of the [Mes₃Sb(OH)][PhSO₃] along the SbO–H bond length.

36

Brønsted acid than Mes$_3$SbOH$^+$, as reflected by the independently calculated proton affinities computed for PhSO$_3^-$ (270 kcal mol$^{-1}$) and Mes$_3$SbO (286 kcal mol$^{-1}$).

Upon close inspection of the crystallographic details previously reported for Mes$_3$SbO···HO$_3$SPh, we realized that there was no evidence to support the placement of the protic H atom at PhSO$_3^-$ rather than Mes$_3$SbO. Moreover, the previously reported elemental analysis and spectroscopic data do not provide useful information pertaining to the location of the protic H atom. To further elucidate differences between Mes$_3$SbO and [Mes$_3$SbOH]$^+$, the geometries of these isolated species were optimized computationally (PBE0/def2-TZVPP). The Sb–O bond lengths of Mes$_3$SbO and [Mes$_3$SbOH]$^+$ are quite different at 1.827 Å and 1.932 Å, respectively. The latter of which agrees better with the previously reported experimental Sb–O bond length of 1.894(5) Å.

## 2.3 – Synthesis and recharacterization of previously reported monomeric stibine oxides

To resolve the discrepancy between our computational analysis and the previous report, we resynthesized the species in question by adding a DCM solution of the sulfonic acid to a DCM suspension of 1 equiv of *trans*-Sb(OH)$_2$Mes$_3$ (Figure 2.2a). Large colorless crystals of [Mes$_3$SbOH][PhSO$_3$] and [Mes$_3$SbOH][CF$_3$SO$_3$] could be obtained by addition of hexanes to the reactions with PhSO$_3$H and CF$_3$SO$_3$H, respectively. These species feature identical analytical characteristics to those reported by Huber and co-workers.[1] The $^1$H and $^{13}$C NMR spectra of these species feature a single set of mesityl resonances, suggesting a 3-fold rotational symmetry, and a single set of *ortho* methyl resonances, indicating rapid rotation about the Sb–C$_{ipso}$ bond on the NMR time scale. A broad signal corresponding to the hydroxyl proton resonance appeared at 9.10 ppm for the benzenesulfonate salt and 7.51 ppm for the triflate
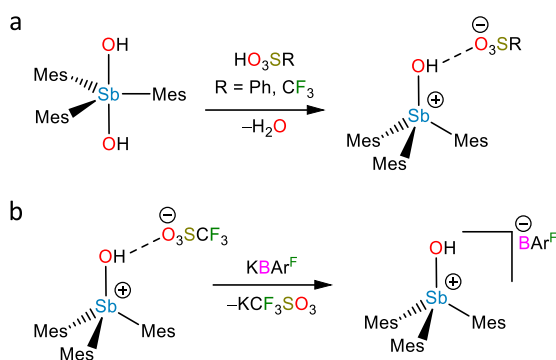
**Figure 2.2.** Synthesis of hydroxystibonium salts. BArF$_4$ is [B(C$_6$H$_3$(3,5-CF$_3$)$_2$)$_4$]$^-$.

salt. The NMR data, however, are not particularly useful in establishing the position of the protic H atom on the stiboryl group as opposed to the benzenesulfonate group.

By collecting IR spectra of the compounds in question and comparing that data with our simulated spectra for Mes$_3$SbO and Mes$_3$SbOH$^+$, we were able to gain more direct insight into the bonding between the Sb and O atoms. Frequency calculations on the optimized coordinates Mes$_3$SbO and [Mes$_3$SbOH]$^+$ returned $v_{SbO}$ values of 817 cm$^{-1}$ and 647 cm$^{-1}$, respectively (Figure 2.3a,b). These values are consistent with the greater Sb–O bond strength/stiffness expected for the stibine oxide. The IR spectra of [Mes$_3$SbOH][RSO$_3$] (R = Ph or CF$_3$) are broadly similar and feature strong signals at 612 cm$^{-1}$ and 637 cm$^{-1}$, respectively, which we assign as the $v_{SbO}$ stretching frequency (Figure 2.3c,d). These bands were previously interpreted as being indicative of a stiboryl given that they are higher in energy than the $v_{SbO}$ of Sb–O single bonded species like *trans*-Sb(OH)$_2$Mes$_3$ ($v_{SbO}$ = 520 cm$^{-1}$).[1-2] It should also be notated that, at that time, there were no $v_{SbO}$ of uncomplexed monomeric stibine oxides with which to compare. The significantly better agreement of the experimental $v_{SbO}$ with that calculated for [Mes$_3$SbOH]$^+$ provides a strong confirmation that the species reported by Huber and co-workers are in fact salts of hydroxystibonium cations.

A metathetical reaction between [Mes$_3$SbOH][CF$_3$SO$_3$] and K[B(C$_6$H$_3$(3,5-CF$_3$)$_2$)$_4$] to afford the salt [Mes$_3$SbOH][B(C$_6$H$_3$(3,5-CF$_3$)$_2$)$_4$] highlights the ionic nature of these species

(Figure 2.2b). In the case of [Mes$_3$SbOH][B(C$_6$H$_3$(3,5-CF$_3$)$_2$)$_4$], the lack of an alternative O-donor in this species renders its formulation as an H-bonded adduct implausible.

Ultimately, we redetermined the structures of [Mes$_3$SbOH][PhSO$_3$] and [Mes$_3$SbOH][CF$_3$SO$_3$] using X-ray diffraction experiments (Figure 2.4a,b). Solution and refinement of the structure of [Mes$_3$SbOH][PhSO$_3$] produced a non-H atom model essentially identical to that reported previously. We could clearly identify a maximum electron density signal along the Sb–O···O–S vector at distance of 0.72 Å from the Sb-bound O atom by
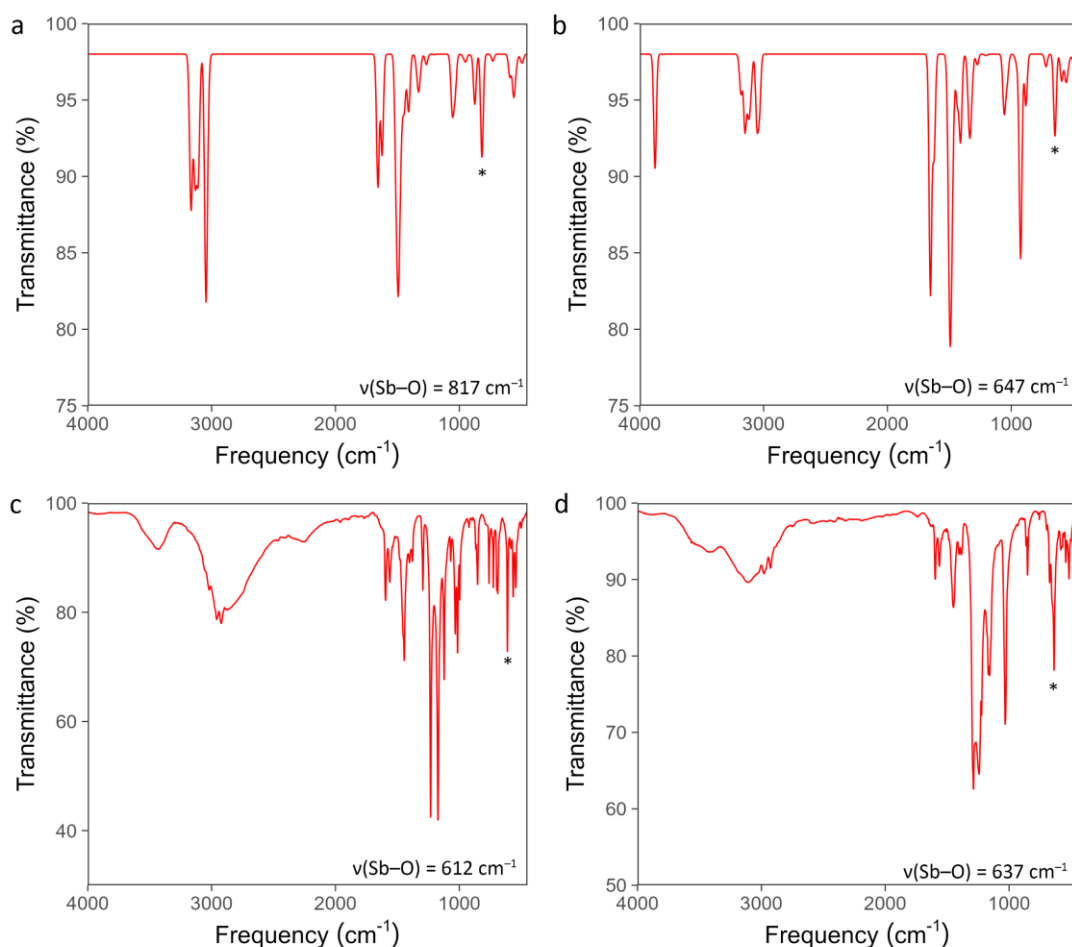


**Figure 2.3.** Calculated infrared spectra (PBE0/def2-TZVPP) of (a) Mes$_3$SbO (b) [Mes$_3$SbOH]$^+$. Experimental infrared spectra (KBr pellets) of (c) [Mes$_3$SbOH][PhSO$_3$] and (d) [Mes$_3$SbOH][CF$_3$SO$_3$].

inspection of the difference Fourier synthesis (Figure 2.4d). This maximum indicates that, in contrast to the previous report, the H atom resides on the Sb-bound O atom.

During refinement of the crystal structure of [Mes$_3$SbOH][CF$_3$SO$_3$], inspection of the difference Fourier synthesis reveals that it also contains the [Mes$_3$SbOH]$^+$ cation. The quality of the collected data provides a high degree of confidence in the locations of these H atoms
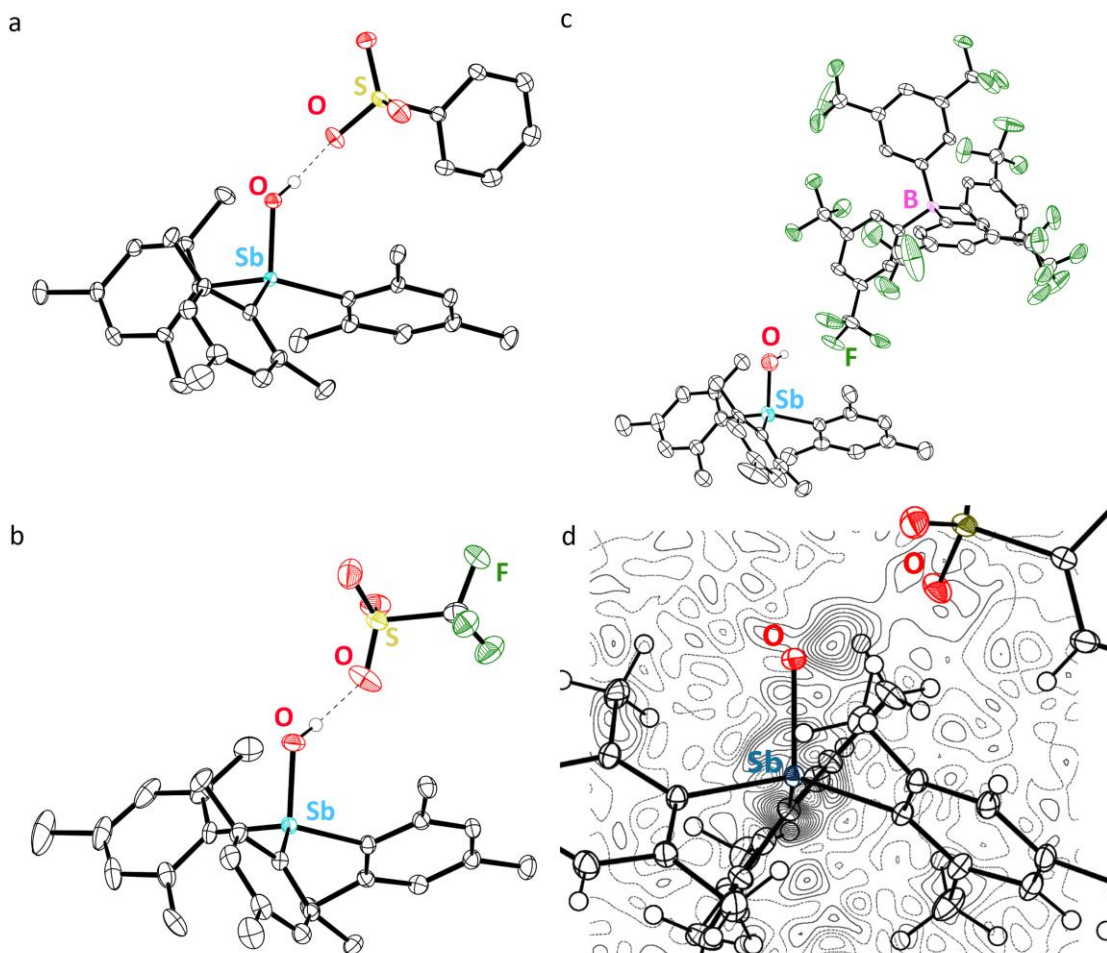


**Figure 2.4.** Thermal ellipsoid plots (50% probability) of (a) [Mes$_3$SbOH][PhSO$_3$] (b) [Mes$_3$SbOH][CF$_3$SO$_3$], and (c) [Mes$_3$SbOH][B(C$_6$H$_3$(3,5-CF$_3$)$_2$)$_4$]. H atoms are omitted for clarity with the exception of the protic H atom. (d) Thermal ellipsoid plot (50% probability, H atoms as spheres of arbitrary radius) of [Mes$_3$SbOH][PhSO$_3$] less the protic hydrogen atom expanded about the residual electron density maximum. Overlaid in grey contours (0.075 e$^-$Å$^{-3}$) is the F$_o$–F$_c$ map plotted in the plane defined by Sb1, O1, and O2. Color Code: Sb teal, O red, S yellow, C black, H white.

on the Sb-bound oxygen, despite the well-known difficulties associated with locating H atoms by X-ray crystallography.[3] Moreover, the influence of the H atoms on the Sb–O bond lengths is unmistakable. The Sb–O bond lengths in [Mes$_3$SbOH][PhSO$_3$] (1.9055(8) Å) and [Mes$_3$SbOH][CF$_3$SO$_3$] (1.910(1) Å) are in good agreement with the computationally optimized Sb–O bond length of [Mes$_3$SbOH]$^+$ (1.932 Å) and are significantly longer than the Sb–O bond length calculated for Mes$_3$SbO (1.827 Å).

The crystals of [Mes$_3$SbOH][B(C$_6$H$_3$(3,5-CF$_3$)$_2$)$_4$]·C$_5$H$_{12}$ (Figure 2.4c) were weakly diffracting, but we were able to determine the Sb–O bond length to be 1.932(3) Å. While there are no strong H-bonds between the cation and anion, an F atom of one CF$_3$ group is positioned 3.050(5) Å from the hydroxyl O atom and the O–H⋯F angle is 159(5)°. The lack of a stronger H-bond allows a sharp $v_{OH}$ IR band to be observed at 3601 cm$^{-1}$. In [Mes$_3$SbOH][PhSO$_3$] and [Mes$_3$SbOH][CF$_3$SO$_3$], a broad band is observed in this region.

We did find a second example of a monomeric stibine oxide, tris(2,6-dimethoxyphenyl)stibine oxide, (2,6-(OMe)$_2$C$_6$H$_3$)$_3$SbO.[4] However, (2,6-(OMe)$_2$C$_6$H$_3$)$_3$SbO was only characterized by a $v_{SbO}$ of 664 cm$^{-1}$ and a crystal structure. The $v_{SbO}$ was a strong indicator that the species was not actually a monomeric stibine oxide and featured an Sb–O bond similar to the species discussed herein. Very importantly, the deposited structure contains voids near the Sb-bound O atoms where a protic H atom might reside. The SQUEEZE algorithm had been employed to remove the contribution of the electron density within this region of space to the observed diffraction intensities.[4] Furthermore, the reported Sb–O bond length of 1.918(3) Å is consistent with the molecule being a hydroxystibonium cation. We computationally optimized (PBE0/def2-TVZPP) the structures of both the stibine oxide (2,6-(OMe)$_2$C$_6$H$_3$)$_3$SbO and the hydroxystibonium cation [(2,6-(OMe)$_2$C$_6$H$_3$)$_3$SbOH]$^+$ and performed

41

a similar analysis as with the mesityl-substituted species. The Sb–O bond length of the former

was 1.818 Å and that of the latter was 1.920 Å. We suggest that the voids in the crystal

structure contain either a neutral Lewis acid or both a charged Lewis acid (such as a proton)

and a charge-balancing counterion. The interaction of the acid with the Sb-bound O atom

would afford a lengthened Sb–O bond, as observed previously and in this work.


**2.4 – Background information on X-ray crystallography, neutron diffraction, Hirshfeld atom refinement and multipole modeling.**

In this section, I present the results of a single-crystal neutron diffraction experiment

that definitively confirms the assignment of [Mes$_3$SbOH][O$_3$SPh] on the basis of H-atom

location. The neutron-derived H-atom positions and ADPs were then used to conduct a MM

refinement of the structure against high-angle X-ray data. Analysis of the refined charge

density, particularly along the Sb–O bond and the Sb–O···O–S vector, allows us to further

corroborate our conclusion. I end with an assessment of whether a non-spherical atom

refinement of X-ray data (*NoSpherA2* refinement), without any input from the neutron

experiments, can recover the same H-atom parameters as single-crystal neutron diffraction

and the same electron density topological features as MM refinement. These analyses of

[Mes$_3$SbOH][O$_3$SPh] demonstrate not only that *NoSpherA2* can self-consistently describe polar

H atoms and disordered methyl groups in heavy-atom-containing structures, as well as the

electron density in polar-covalent heavy-element bonds, but that the results agree with those

obtained from neutron diffraction and multipole refinement.

X-ray crystallography remains one of the most powerful techniques used by

chemists to determine molecular structure. The scattering of X-rays from the regularly

arrayed electrons in a crystal produces observable reflections when Bragg's Law is satisfied. The intensities of these reflections are proportional to the squared structure factors of the crystal and Fourier transformation of the phased reciprocal-space structure factors produces a real-space image of the electron density of the crystal. Modern crystal structure refinement involves (i) constructing a model comprising non-interacting spherical atoms and (ii) allowing the parameters that describe the positions and harmonic (an)isotropic displacements of these atoms to refine such that the structure factors calculated for the model best agree with those observed experimentally.[5] Atomic form factors capture the contribution of each atom in the crystal to a given structure factor, and an independent atom model (IAM) of the type described above employs spherically symmetric atomic form factors that are the same for all atoms of a given element regardless of their environment in the crystal. The use of this IAM formalism has persisted for almost a century, in large part because it has been so successful in shedding light on molecular structure. Because the majority of the electron density in most molecules is locally centered about the atomic nuclei, graphs comprising linked electron-density maxima map well to the conventional notion of molecular structure. There are, however, features that are not well-captured by the IAM: most notably, H-atom positions and valence electron density.

As a result of the low concentration of electron density at H atoms, they scatter X-rays only weakly and variation in the parameters describing H atoms during refinement has a small impact on the calculated structure factors. Because of the instability in H-atom parameters during refinement, they are frequently heavily restrained or constrained.[6] A further consequence of the fact that H atoms have only a single, valence electron, is the lack of a core

of electrons centered on the nucleus. When engaged in bonding, particularly to an electronegative atom, the probability distribution of this electron distorts significantly. Compounded by an apparent shortening of X–H bond lengths due to libration, X–H bond lengths in an IAM are approximately 20% shorter than the X···H internuclear distance.[7-8] True internuclear distances can be established very accurately using gas-phase spectroscopic measurements but the currently accepted standard for determining accurate H-atom positions and displacement parameters for complex molecules is neutron diffraction.

Whereas X-rays scatter predominantly off of the electrons in the crystal, neutrons scatter predominantly off of the nuclei; the position of an H atom refined against neutron data thus better reflects the position of the H-atom nucleus. Furthermore, the atomic form factors for neutron scattering do not scale monotonically with atomic number and variation in H-atom parameters strongly influences the calculated neutron structure factors. It is therefore possible to freely refine H-atom positions and anisotropic displacement parameters (ADPs). Although neutron diffraction offers the possibility of significant chemical insight, these experiments require sophisticated technical facilities for the generation of the incident neutron beam, either via a nuclear reactor or a spallation source fed by a linear accelerator, and detection of the diffracted radiation. Even with access to such facilities, neutron diffraction experiments require crystals much larger than those needed for single-crystal X-ray diffraction and the quality of data can be diminished by strong H-atom background scattering. The H-atom background can be reduced by partial or complete deuteration of the molecule under investigation, but this substitution may be experimentally difficult or infeasible.

As noted above, a second shortcoming of the IAM is its inability to describe the deformation of valence electron density from spherical symmetry. Although isolated atoms

have spherically symmetric electron density, when atoms engage in bonding interactions, they donate and receive electron density and that electron density distorts from sphericity. This transfer of charge that occurs when atoms interact can be modeled by dividing the electron density of atoms into core portions and valence portions and allowing the populations of the valence portions to freely refine under the constraint that the total charge remain constant. Although such an approach captures the charge transfer that accompanies chemical bonding, it does not address the deformation of the electron density of each atom from sphericity. Indeed, difference density ($F_o - F_c$) maps for fully refined IAM structures routinely show residual electron density maxima on bonds and in regions presumed to be occupied by lone pairs.

The most widely-accepted method used to account for aspherical atomic shape is the multipole refinement formalism put forward by Hansen and Coppens.[9] In this method, the total electron density of the crystal is taken to be the sum of pseudo-atom electron densities, each of which is divided into three components: a spherical core density, a spherical valence density, and valence deformation density (Equation 1).

$$\rho(r) = P_{core}\rho_{core}(r) + P_{val}\kappa^3\rho_{val}(\kappa r) + \sum_{l=0}^{l_{max}} \kappa'^3 R_l(\kappa' r) \sum_{m=0}^{l} P_{lm\pm}Y_{lm\pm}(\Omega) \qquad (1)$$

The latter two terms contain refinable population ($P$) and scaling ($\kappa$ and $\kappa'$) parameters to allow expansion and contraction of the valence shell in a manner similar to that described above. In addition to this charge transfer, the valence deformation term also includes density-normalized spherical harmonics ($Y_{lm\pm}$), each with an associated population ($P_{lm\pm}$), that are uniquely chosen for each atom to allow for aspherical multipolar deformation of the valence electron density. A radial function ($R_l$), typically of a Gaussian or Slater type, specifies the

manner by which the deformation density expands into the valence region. Although the parameters for these radial functions could in principle be refined, they are generally fixed at element-specific values obtained from high-level *ab initio* atomic wavefunction calculations.

Successful refinement of a multipole model (MM) is significantly more involved than that of an IAM. Stable refinement of the large number of parameters in such a model requires the collection of a large number of unique X-ray reflections, typically requiring collection of weak, high-angle data. Although very high-angle data are required, the asphericity of the valence electron density most significantly impacts the intensities of the low-angle reflections, and proper care is required during data processing and absorption correction to ensure that these subtle variations are preserved. Aside from experimental considerations, the process of refining a MM also requires great attention: care must be taken in the implementation and systematic relaxation of restraints and constraints on multipole parameters, a logical local coordinate system must be explicitly defined for each atom, the local symmetry of each atom must be defined, and the crystallographer must choose multipoles of appropriate order for each atom. Moreover, minimization of residual values (e.g., $R_1$ and $wR_2$) cannot serve as the primary criterion of success; careful inspection of difference density maps and the values assumed by refined parameters is necessary to ensure that the improvements made to the structure by allowing aspherical refinement remain physically meaningful. Finally, because H atoms typically have large-amplitude ADPs that can be strongly coupled to their multipole parameters, these ADPs must either be constrained to values obtained from neutron diffraction or estimated using a rigid-body assumption and non-H ADPs from the other atoms in the crystal.

Despite these difficulties, multipole refinement has been invaluable in extending our understanding of molecular structure and bonding by providing access to experimental electron densities,[5] the topologies of which can be explored within a framework such as Bader's Quantum Theory of Atoms in Molecules (QTAIM).[10] Detailed descriptions of this framework are provided elsewhere,[11] but we mention briefly here that analysis of the gradient of the electron density provides a means of dividing a molecule into atoms and identifies paths in space that map to conventional notions of chemical bonds. By assessing the magnitude of real-space functions such as the electron density ($\rho$), the Laplacian of the electron density ($\nabla^2\rho$), and the ellipticity of the electron density ($\varepsilon$) at different locations within a molecule, insight into the nature of the bonds that hold the molecule together can be obtained. Finally, although we will not discuss it in greater detail here, we note that another approach to obtaining experimental charge densities from X-ray diffraction data is wavefunction refinement.[12-16] In this approach, the coefficients of the molecular orbitals of the molecules comprising the crystal are treated as refinable parameters and are allowed to take on values such that the difference between $F_c$ and $F_o$ is minimized.

As described earlier in this chapter, our investigation into the chemistry of stibine oxides uncovered only two well-characterized examples of putative monomeric stibine oxides: $Mes_3SbO\cdots HO_3SR$, where R = Ph and $CF_3$. A reanalysis of these substances revealed, however, that both in fact feature the hydroxytrimesitylstibonium cation.[1,17] To support this reassignment, we redetermined the crystal structures of both $Mes_3SbO\cdots HO_3SR$ compounds. The originally reported crystal structure of $Mes_3SbO\cdots HO_3SPh$ featured a H-bond between the stibine oxide and sulfonic acid, with the H atom residing on the S-bound O atom. In our conventional IAM refinement of this structure, we observed the electron density maximum

for the H-bonding H atom to be proximal to the Sb-bound O atom, which is more consistent with the $[Mes_3SbOH][O_3SPh]$ formulation. We observed the same in our structure of $[Mes_3SbOH][O_3SCF_3]$. We corroborated our conclusion by comparing other bond metrics, notably the Sb–O distance, from our models to those calculated for $Mes_3SbO$ and $[Mes_3SbOH]^+$. Comparison of the observed and calculated Sb–O stretching frequencies provided further support. Nevertheless, the assignment as $[Mes_3SbOH][O_3SR]$ or $Mes_3SbO···HO_3SR$ rests most heavily on the X-ray IAM position of an H atom, the refinement of which, as noted above, is fraught with complications.

During our investigation of the $[Mes_3SbOH][O_3SR]$ compounds, a new implementation of Hirshfeld Atom Refinement (HAR) in *Olex2*, *NoSpherA2* (non-spherical atom refinement in *Olex2*),[18] was released that boasts an ability to perform aspherical atom refinement on X-ray data of the resolution typically collected for IAM structures.[3] *NoSpherA2* builds upon a decade of successful development in the area of HAR.[7,19-21] In HAR, the electron density of the model is obtained from quantum-chemical calculations and divided into atoms according to the Hirshfeld stockholder scheme.[22] The aspherical atomic electron densities are then Fourier transformed to obtain aspherical form factors, which are used to generate calculated structure factors for comparison with observed structure factors.[20] The process can be iterated, with *ab initio* recalculation of the aspherical form factors using the newly refined atomic coordinates, until convergence is achieved. One significant advantage of this procedure is that the H atoms do not need to be placed at artificially short X–H distances. Indeed, extensive validation studies have demonstrated that HAR of H-atom positions and ADPs returned parameters comparable to those obtained from neutron diffraction, even with X-ray data of only 0.80 Å resolution.[7,21,23] *NoSpherA2* builds upon these earlier successes but adds the advantages of (i)

48

calling on one of a number of external programs to run the quantum mechanical (QM) calculation and (ii) performing the refinement in *Olex2* using the native *olex.refine*[24] engine. The freedom to choose from powerful, modern, and flexible computational chemistry programs permits a range of chemistries to be investigated, including those of heavy elements. The use of *olex.refine* permits the full suite of crystallographic capabilities implemented in *Olex2* (constraints, restraints, disorder modeling, etc.) to be utilized. Conveniently, a byproduct of performing *NoSpherA2* analysis is a QM-calculated electron density. The topology of this electron density could, in principle, be analyzed to extract bonding information, although we note that this electron density is *not* a refined charge density of the type generated from a multipole or X-ray wavefunction refinement.[25-26]

## 2.5 – H-Atom assignment of [Mes₃SbOH][O₃SPh] confirmed by neutron diffraction and Hirshfeld atom refinement

In the course of our earlier investigation into $[Mes_3SbOH]^+$ species, we came to appreciate that $[Mes_3SbOH][O_3SPh]$ not only afforded crystals of X-ray diffraction quality, but also produced crystals of sufficient size for neutron diffraction, raising the possibility of directly observing the H atom in the Sb–OH unit. Irradiation of a colorless prism of $[Mes_3SbOH][O_3SPh]$ measuring $1.08 \times 0.80 \times 0.35$ mm$^3$ using TOPAZ at the spallation neutron source of Oak Ridge National Laboratory did indeed produce observable neutron reflections. The high H-atom content of the crystal produces appreciable background scattering but using 5 h exposures, reflections could be observed out to a resolution of 0.79 Å. Our previously-reported X-ray IAM agreed reasonably with the neutron data, but the agreement increased significantly when the

positions and ADPs of the C-bound H atoms were allowed to refine freely while non-H-atom positions and ADPs were constrained to the X-ray IAM values (Table 2.1). The neutron data even revealed the presence of disorder in one of the methyl groups that had gone undetected in the IAM X-ray refinement (Figure 2.5a). The positions of the

**Table 2.1.** Crystallographic details for different refinement methods of [Mes$_3$SbOH][O$_3$SPh].[a]

|  | X-ray IAM | Neutron | X-ray HAR | X-ray Multipole |
|---|---|---|---|---|
| Wavelength (Å) | 0.71073 | 0.41-3.50 | 0.71073 | 0.71073 |
| Crystal size (mm$^3$) | 0.19×0.14×0.07 | 1.05×0.8×0.35 | 0.19×0.14×0.07 | 0.19×0.14×0.07 |
| θ range (°) | 1.967 to 38.084 | 7.36 to 78.50 | 1.97 to 38.08 | 1.97 to 38.08 |
| Total reflections | 129747 | 10216 | 129747 | 129747 |
| Unique reflections | 15556 | 1941 | 15556 | 13013 [c] |
| Parameters | 383 | 350 | 703 | 1472 |
| Completeness (%) | 100 | N/A[b] | 100 | 100 |
| $R_{int}$ | 0.0251 | 0.1235 | 0.0251 | 0.0251 |
| $R_1$ (I > 2σ) | 0.0209 | 0.0685 | 0.0157 | 0.0144 [d] |
| $R_1$ (all data) | 0.0268 | 0.0694 | 0.0216 | 0.0246 |
| $wR_2$ (all data) | 0.0590 | 0.1552 | 0.0372 | 0.0272 |
| Goodness of fit, S | 1.028 | 1.235 | 1.0317 | 1.873 |

[a] Empirical formula: C$_{33}$H$_{39}$O$_4$SSb; formula weight: 653.45; temperature: 100(2) K; crystal system: orthorhombic; space group: *Pbca*; *a* 16.62251(11) Å; *b* 16.92326(15) Å; *c* 21.21101(15) Å; volume 5966.81(8) Å$^3$; *Z* 8; ρ$_{calc}$ 1.455 Mg/m$^3$.

[b] Neutron data were collected with better than 99% coverage. Hydrogen is a negative scatterer for neutrons. The completeness appeared low due to the high hydrogen content in [Mes$_3$SbOH][O$_3$SPh], not all peaks had enough neutron counts to be considered as observed.

[c] Reflections with I < 0, I > 1×10$^{10}$, I/σ < 3, or I/σ > 1×10$^{10}$ were excluded from the refinement but the full 15556 reflections were included in the structure factor calculation.

[d] $R_1$ (I > 3σ)

two components of the disorder were freely refined and their motion was modeled anisotropically, albeit using rigid-bond and similarity restraints.

All of the methyl and aryl C–H bond lengths from the final neutron model agree with reported average distances found in neutron structures stored in the CSD (Tables A.4-5).[27] Inspection of the thermal ellipsoid plot reveals satisfactory modeling of the H-atom ADPs

a
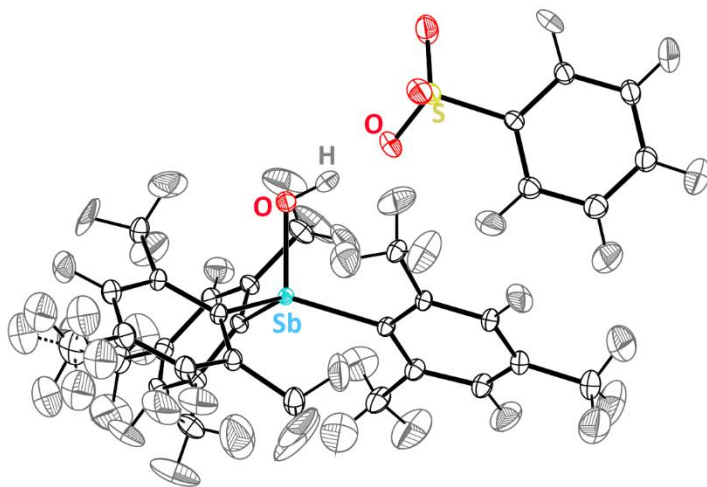


b
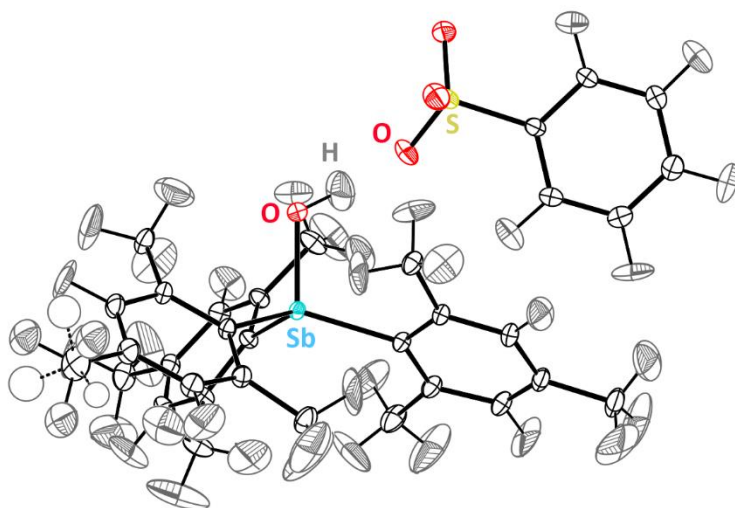


**Figure 2.5.** Thermal ellipsoid plots (50% probability level) of [Mes$_3$SbOH][O$_3$SPh] from the (a) neutron diffraction and (b) X-ray diffraction (HAR) crystal structures. In (B), the H atoms in the minor component of the disorder, which are refined with isotropic thermal parameters, are shown as spheres. Color code: Sb teal, O red, S yellow, C black, H grey.

(Figure 2.5a). The difference Fourier synthesis from the model containing all C-bound H atoms shows only one significant negative residual peak; it lies along the Sb–O···O–S vector and arises from the protic H atom. This atom was included in the model and with its position and ADPs refined freely, it was found to reside on the Sb-bound O atom with an O–H bond length of 0.979(15) Å. As expected, this length is longer than that from the X-ray IAM, 0.80(1) Å.[17] Observation and stable refinement of this H atom provides definitive confirmation of our earlier assignment of this species as a hydroxystibonium salt.

Although the neutron diffraction results were able to provide unambiguous confirmation of our assignment, it is not always possible to access this analytical method. We sought to determine whether *NoSpherA2* refinement of our X-ray data would return a similar conclusion. Our previously reported IAM[17] of [Mes$_3$SbOH][O$_3$SPh] was used as the starting point for the aspherical atom refinement. A density functional theory (DFT) wavefunction was calculated with tight SCF convergence criteria using the PBE0 hybrid functional and the x2c-TZVPP all-electron relativistically contracted basis set.[28-30] The effects of relativity were introduced using the second-order Douglas-Kroll-Hess formalism. Using the aspherical atomic form factors obtained from Hirshfeld stockholder partitioning of the computed wavefunction, the positions and ADPs of all atoms, including H atoms, were freely refined. The newly refined atomic coordinates were used as the input for a new DFT calculation, from which new aspherical form factors were obtained. This procedure was iterated until it had converged. The residual factors indicate an exceptional agreement between $F_o$ and $F_c$ with an R$_1$ value of 1.53%. The ADPs of the H atoms produce well-formed thermal ellipsoids with the exception of a single methyl group, where the H-atom ellipsoids are elongated and suggestive of rotational disorder. This methyl group is the same that was observed to be disordered in the

neutron diffraction data, indicating that *NoSpherA2* can allow H-atom disorder to be discerned from X-ray data in instances where it is not evident in IAM refinement. The HAR was therefore continued by including the methyl disorder in the model. Rigid bond and similarity restraints were applied to the disordered methyl group. The major component of the disorder was refined anisotropically, and the minor component was refined isotropically. The final disordered model features a slightly increased $R_1$ value of 1.57 % (Table 2.1).

The C–H bond lengths from the *NoSpherA2* refinement show excellent agreement with the model refined against the neutron data (RMSD = 0.036 Å). The H-atom ADPs were compared quantitatively through the calculation of correlation coefficients for each H atom (Figure A.16).[31] The average correlation coefficient value of 0.84 reflects the overall agreement between the models. Visual inspection of the ellipsoid plots highlights the exceptional agreement of not just the size and shape of the H-atom ellipsoids, but their orientation as well (Figure 2.5). Of particular interest to us, the SbO–H bond distance provided by the *NoSpherA2* analysis, 0.99(1) Å, is equal to that from the neutron refinement within experimental uncertainty. The correlation coefficient between the neutron and *NoSpherA2* ADPs for this atom was 0.83, comparable to that calculated for the other H atoms in the structure.

## 2.6 – Topological analysis of the electron density by multipole modelling and Hirschfeld atom refinement

In our original IAM of [Mes$_3$SbOH][O$_3$SPh], we corroborated our assignment of the antimony compound as a hydroxystibonium cation, as opposed to a stibine oxide, by comparing the experimentally observed Sb–O bond length to those calculated for

[Mes$_3$SbOH]$^+$ and Mes$_3$SbO. We have also previously shown that these bond types (Sb–OH vs Sb$^+$–O$^-$/Sb=O) can be distinguished by analyzing the topology of the electron density along the length of the Sb–O bond.[32] With a high-resolution X-ray data set and neutron-diffraction H-atom positions and ADPs, we were equipped to perform a multipole refinement of [Mes$_3$SbOH][O$_3$SPh] to obtain an experimental charge density for subsequent topological analysis.

Briefly, the atomic coordinates and ADPs from the X-ray IAM were used as a starting point for multipole refinement. Dipoles were introduced for all C*H* atoms and the Sb–O*H* was modelled with a quadrupole. The C, S, O, and Sb atoms were modelled with octupoles in the initial phase of refinement. The κ parameters were then refined, and the H-atom ADPs and bond distances were set to the neutron model values. The model was allowed to systematically increase in flexibility until all non-H atoms were modelled with hexadecapoles and all H atoms were refined as bond-directed quadrupoles. Site symmetry and chemical similarity constraints were only applied to H atoms in the final model. The full refinement strategy is described in Table A.11. In contrast to the difference Fourier synthesis of the IAM structure, which shows extensive residual electron density on bonds and at lone pairs (Figure 2.6a-c), the corresponding difference Fourier maps of the MM are much less featured (Figure 2.6d-f). We do note that there is unsurprisingly residual electron density proximal to the heavy Sb atom, highlighting that caution should be exercised in interpreting these results because of the possible influence of extinction effects or anharmonic thermal motion, which have not been refined in the present model.

54

A search of ρ for topologically critical points (Figure 2.7) revealed (3, −3) critical points at the locations of all nuclei and (3, −1) critical points between all pairs of atoms depicted as covalently bonded in Figure 2.5. These latter critical points are also called bond critical points (bcps) and unique trajectories in $\nabla\rho$ were found to link each bcp to the two (3, −3) critical points associated with nuclei of the bonded atoms. The union of the two $\nabla\rho$ trajectories emanating from a bcp comprises a bond path and bond paths mapping to all covalent bonds in the $Mes_3SbOH^+$ cation and the $PhSO_3^-$ anion were obtained. The magnitude of $\rho$ at a bcp ($\rho_b$) can be taken as a measure of the strength of the interaction and we do indeed see the
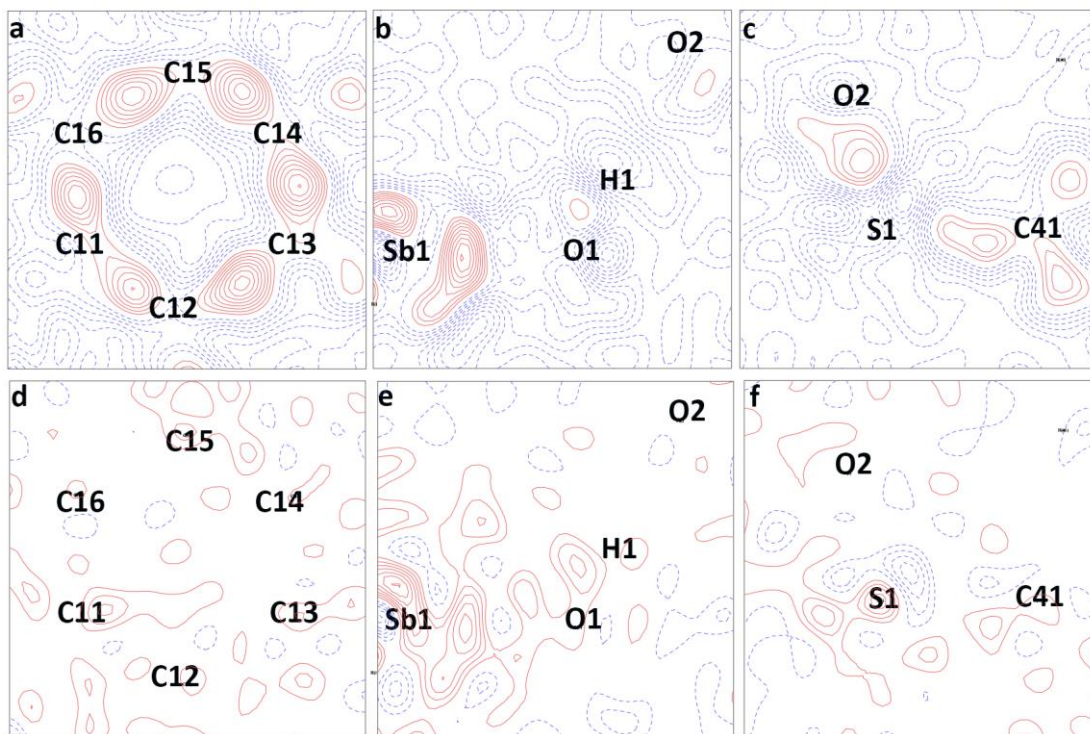


**Figure 2.6.** 2D contour plots of the IAM difference Fourier synthesis ($F_o − F_c$) of [$Mes_3SbOH$][$O_3SPh$] in the planes defined by (a) C11, C13, and C25, (b) Sb1, O1, and O2, and (c) S1, O2, and C41. 2D contour plots of the MM difference Fourier synthesis ($F_o − F_c$) of [$Mes_3SbOH$][$O_3SPh$] in the planes defined by (d) C11, C13, and C15, (e) Sb1, O1, and O2, and (f) S1, O2, and C41. Positive contours are shown as red solid lines. Negative contours are shown as blue dashed lines. Contours are drawn at intervals of 0.05 e$^−$ Å$^{-3}$.

expected greater value for the aromatic $C_{Ar}$–$C_{Ar}$ bonds as compared to the single $C_{Ar}$–$C_{Me}$ bonds of the mesityl rings (Table 2.2). The $\rho_b(C_{Ar}$–$C_{Ar})$ values of the benzenesulfonate compare favorably with those of the mesityl groups. Within the cation, $\rho_b(Sb$–$C) < \rho_b(Sb$–$O)$. We additionally identified a bcp between $Mes_3SbOH^+$ and $PhSO_3^-$, as well as an SbOH···OS bond path (Figure 2.7). The value of $\rho_b(SbO$–$H)$ was 0.31 $e^-$ $bohr^{-3}$, whereas $\rho_b(SbOH···OS)$ was 0.053 $e^-$ $bohr^{-3}$. These values are consistent with the former being a stronger covalent interaction and the latter being a weaker hydrogen bond.
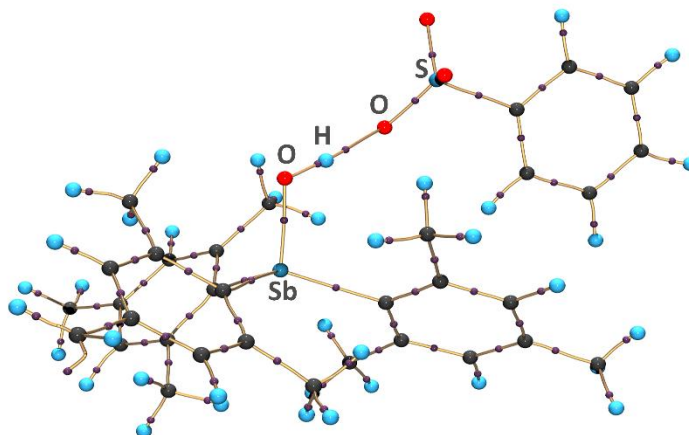


**Figure 2.7.** The molecular graph of $[Mes_3SbOH][O_3SPh]$ from the MM charge density. Color code: (3, −1) purple, Sb/S blue, C black, H teal. Bond paths are shown as tan lines. Ring critical points and critical points from crystal packing and intermolecular interactions other than the SbOH···OS H-bond are omitted for clarity.

Further insight into the nature of the different bonding interactions present in the structure can be obtained from an analysis of the Laplacian of the electron density ($\nabla^2\rho$), which is typically evaluated at a bcp. The Laplacian is negative at the bcps of all C–H, C–C, and S–C bonds, reflecting the local concentration of electronic charge that is characteristic of an open-shell, covalent interaction. As expected, $|\rho(C_{Ar}$–$C_{Ar})| > |\rho(C_{Ar}$–$C_{Me})|$, which is consistent

with the greater strength of the aromatic bond. Among the atoms involved in the H-bond, the

SbO–H bcp features a negative Laplacian, whereas the SbOH⋯OS bcp features a positive

Laplacian (Table 2.2). Consistent with the relative values of $\rho$ at the bcp, these Laplacian values

suggest that the SbO–H interaction is covalent and that the SO⋯H interaction is a non-covalent

H-bond.

Our initial analysis of the IAM suggested that the Sb was bound to a hydroxo, as

opposed to an oxo, substituent by comparison of the refined Sb⋯O distance to

computationally optimized Sb–OH and $Sb^+$–$O^-$/Sb=O bond lengths. Previous computational

experiments that we conducted highlighted the importance of evaluating the behavior of $\rho$

and $\nabla^2\rho$ along the length of the bond path.[32] The variations of the experimentally refined

charge density and its Laplacian along the length of the Sb–O bond (Figure 2.9) are consistent

with those obtained from DFT calculations of $Ph_3SbOH^+$. The Laplacian features a single,

moderate O-based charge concentration in the valence region, reflected in the local minimum

proximal to the O atom. The ellipticity of $\rho$ provides an unambiguous distinction between $Sb^+$–

**Table 2.2.** Average values of $\rho_b$ and $\nabla^2\rho_b$ derived from the MM with standard deviations provided for bond types occurring more than twice.

| Bond Type | $\rho_b$ ($e^-$ bohr$^{-3}$) | $\nabla^2\rho_b$ ($e^-$ bohr$^{-5}$) |
|---|---|---|
| $C_{Ar}$–$C_{Ar}$ | $0.32 \pm 0.01$ | $-0.79 \pm 0.09$ |
| $C_{Ar}$–$C_{Me}$ | $0.27 \pm 0.006$ | $-0.71 \pm 0.08$ |
| $C_{Ar}$–H | $0.27 \pm 0.014$ | $-0.71 \pm 0.11$ |
| $C_{Me}$–H | $0.28 \pm 0.015$ | $-0.96 \pm 0.13$ |
| S–O | $0.35 \pm 0.02$ | $-0.30 \pm 0.33$ |
| Sb–C | $0.10 \pm 0.01$ | $0.19 \pm 0.06$ |
| Sb–O | 0.17 | 0.49 |
| S–C | 0.22 | −0.37 |
| SbO–H | 0.31 | −1.54 |
| SbOH⋯OS | 0.053 | 0.10 |

O⁻/Sb=O and Sb–OH and topological analysis of the MM returned an $\varepsilon_b$ of 0.058 for the Sb–O bond. This value is in better agreement with that calculated for Sb–OH (0.081) than Sb⁺–O⁻/Sb=O (0.0003).[32]
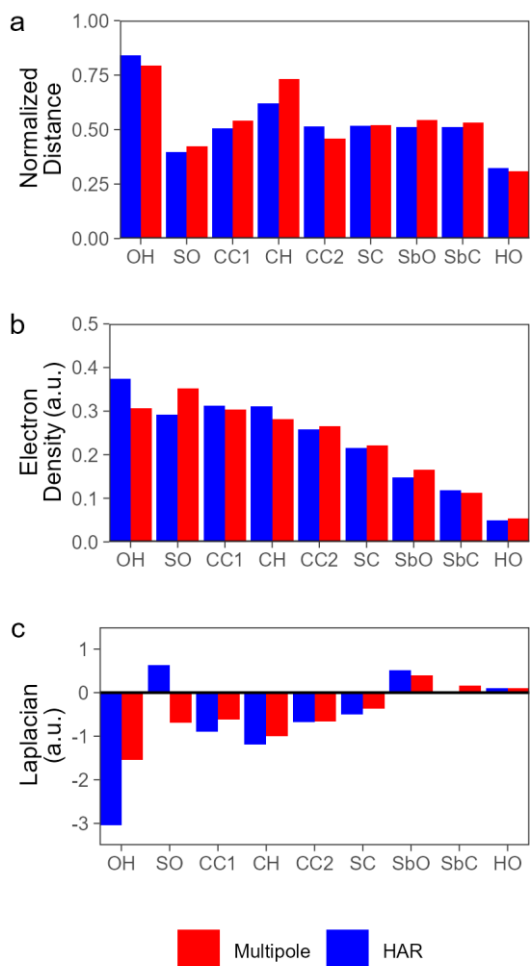


**Figure 2.8.** Values of (a) the normalized distances (e.g., from O to H for OH), (b) $\rho$, and (c) $\nabla^2\rho$ at the bcps derived from the MM (red) and HAR (blue). For (a) bond lengths are normalized to unit length; values reflect the fraction of the bond length along the bond at which the bcp occurs. CC1 = $C_{Ar}$–$C_{Ar}$, CC2 = $C_{Ar}$–$C_{Me}$, CH = $C_{Me}$–$H_{Me}$. For bond types that arise multiple times, a representative example was selected.

A by-product of the non-spherical atom refinement described above, whereby we were able to determine accurate H-atom parameters from X-ray data, is the DFT-calculated electron density of the contents of the asymmetric unit. Not only is the calculation of the electron density a necessary step in performing the Hirshfeld stockholder partitioning, the *NoSpherA2* analysis in *Olex2* stores this electron density in a *.wfn file of the type readily amenable for detailed topological analysis. We sought to determine whether an analysis of this readily produced electron density would return the same conclusions as our analysis of the refined charge density from the MM. The *NoSpherA2* electron density exhibited all of the same molecular critical points as the MM. The similarity in the

locations of the critical points is reflected in the agreement of the positions of the bcps along the bond paths (Figure 2.8a). The C–H bonds are the notable exception, with the MM bcps appearing closer to the H atoms. The $\rho_b$ values show only minor discrepancies in magnitude, the greatest of which are associated with the polar O–H, S–O, and Sb–C bond paths (Figure 2.8b). In each of these cases, the *NoSpherA2* model returns a greater $\rho_b$. Analysis of the Laplacian (Figure 2.8c) suggests that the *NoSpherA2* model favors charge concentration in bonding interactions: $\nabla^2\rho_b$ values are consistently lower (i.e., less positive or more negative). Nevertheless, both models generally track each other well and maintain the same sign. The greatest discrepancy lies in the O–H bond: $\nabla^2\rho_b$ was $-1.54$ e$^-$ bohr$^{-5}$ for the MM, but $-3.02$ e$^-$ bohr$^{-5}$ for the *NoSpherA2* model.

The similarities between the models are made more evident by comparing the behavior of $\rho$ and $\nabla^2\rho$ along the length of the bond path. The morphologies of $\rho$ calculated from the MM and *NoSpherA2* wavefunction exhibit remarkable agreement (representative bond paths in Figure 2.9; all bond paths in Figure A.17). As captured in Figure 2.9, the full bond path analyses recover the close positioning of the bcps. The large discrepancy noted for the C–H bonds can now be understood as arising from a relatively shallow well in $\rho$.

The similarity between the Sb–O bond paths was particularly satisfying given our special interest in the nature of Sb–O bonding interactions and pnictogen–oxygen bonds in general. As noted above, the values of $\rho_b$ for the S–O and O–H bond paths feature the greatest differences in magnitude between the two models. One possible origin for the discrepancy is the perturbation of the electron density by basis set superposition error (BSSE).[33] BSSE arises when the basis functions of atoms on different molecules overlap, as typically occurs with strong intermolecular interactions. The influence of this effect could in principle be minimized

by using the Chemical Hamiltonian Approach method[34] but it has also been observed that the effects of BSSE on $\rho$ obtained from DFT calculations are minimized by using diffuse basis sets.[35] The relatively diffuse nature of the basis sets used in this work are likely the reason why the effect is relatively minor.
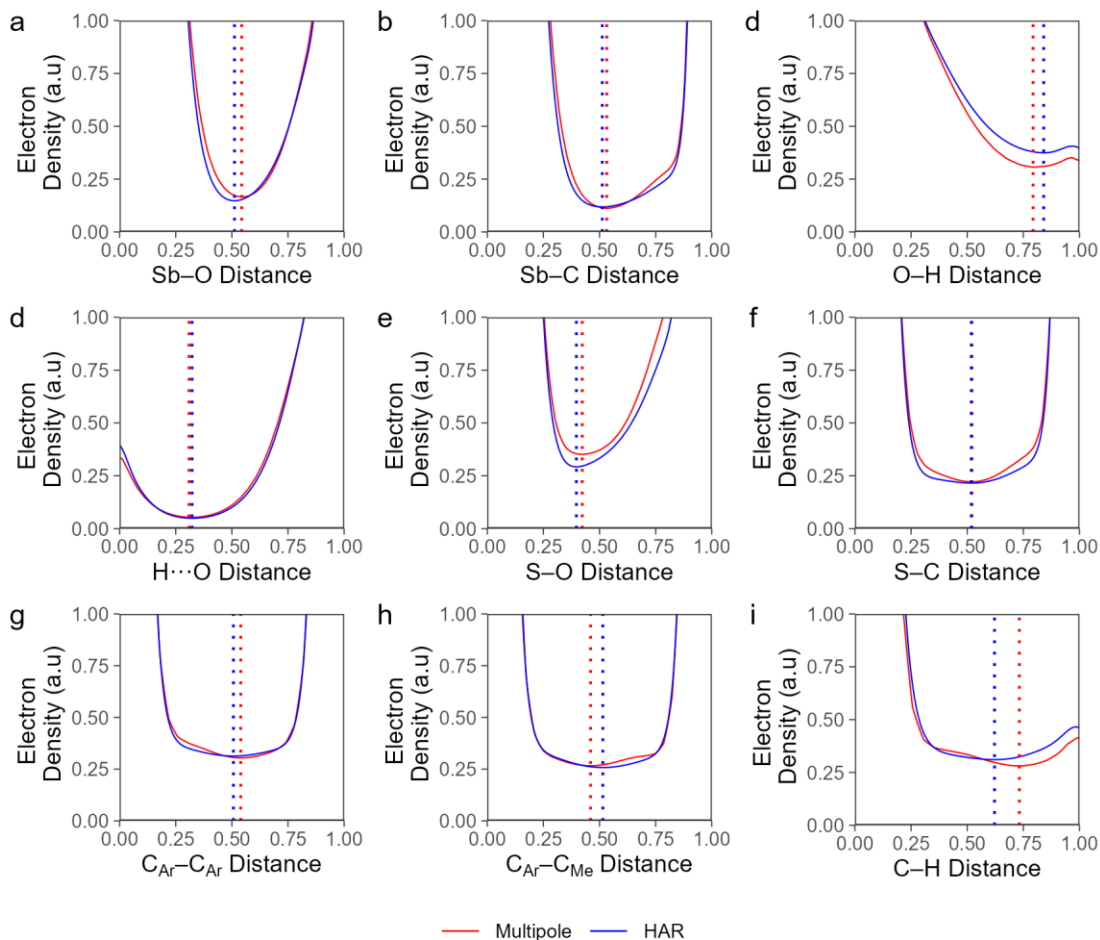


**Figure 2.9.** Evaluation of $\rho$ derived from the MM (red) and HAR (blue) along representative interatomic bond paths. Dashed vertical lines represent the bond critical point. Distances are normalized.

Comparison of $\nabla^2\rho$ along representative bond paths (Figure 2.10) recapitulates the results obtained from the analysis of $\rho$ discussed above (Figure 2.9). The curves exhibit similar local maxima and minima, including along the Sb–O bond path, indicating that the

*NoSpherA2* analysis can also reliably report on the nature of the Sb–OH bonding. As with $\rho$, the greatest discrepancy lies in the species involved in the H-bond. The O-proximal local minima for both the O–H and S–O assume less negative values in the *NoSpherA2* model, consistent with a dissipation of charge density concentration by BSSE. Overall, the full bond path topological analysis of $\rho$ and $\nabla^2\rho$ confirm the ability of the *NoSpherA2* wavefunction to reproduce electron density topologies derived from multipole refinement.
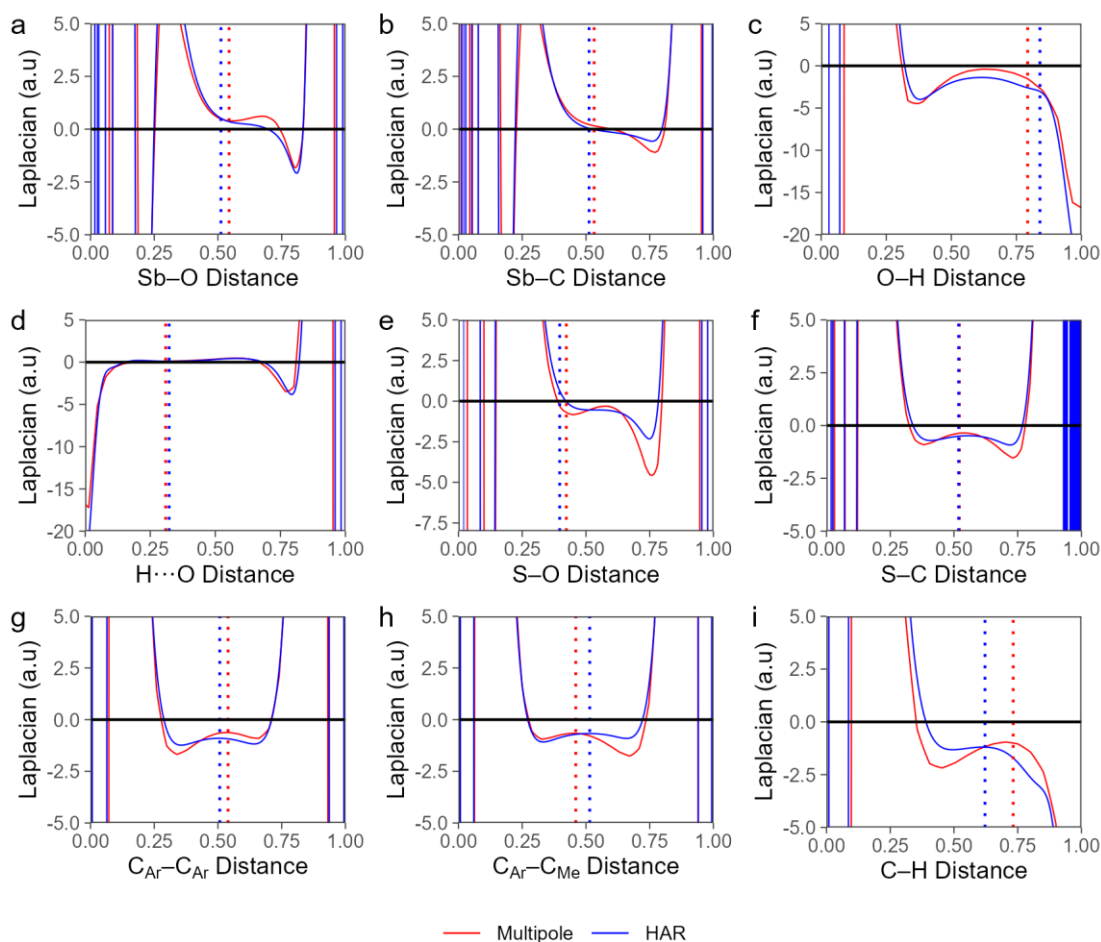


**Figure 2.10.** Evaluation of $\nabla^2\rho$ derived from the MM (red) and HAR (blue) along representative interatomic bond paths. Dashed vertical lines represent the bond critical point. Distances are normalized.
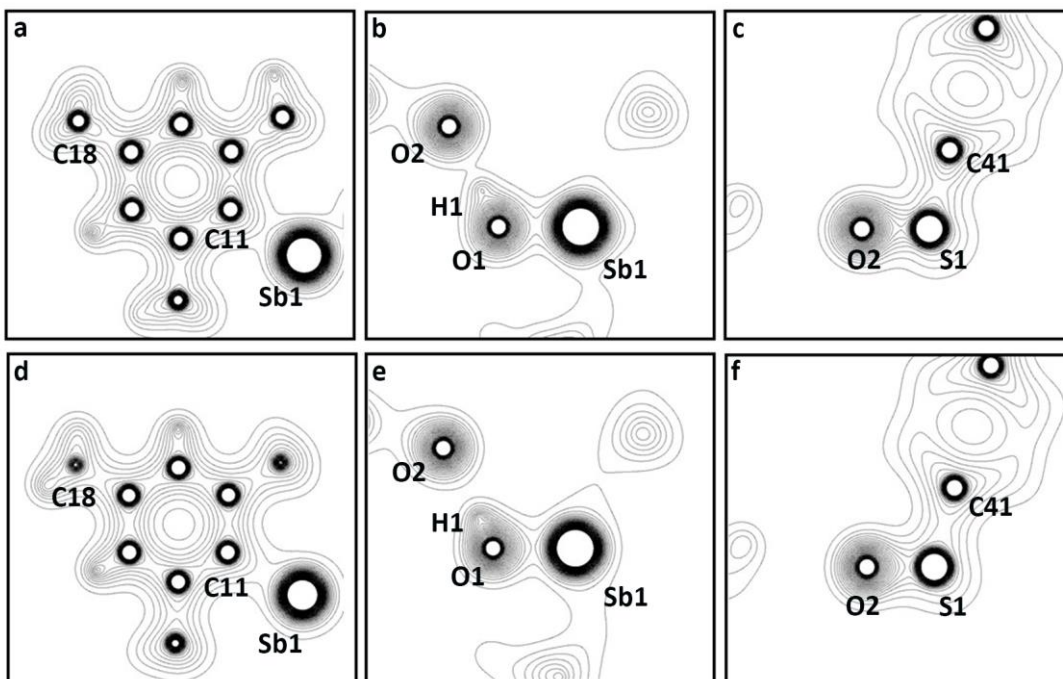
**Figure 2.11.** Contour plots of ρ depicting planes defined by the (a, d) C11, C13, and C15 atoms, (b, e) Sb1, O1, and O2 atoms, and (c, f) S1, O2, and C41 atoms derived from the (a-c) MM and (d-f) HAR model. Atom positions are labelled by element symbols. Contours are drawn at intervals of 0.05 e⁻ Å⁻³.

Finally, the overall similarity between the two models can be further appreciated by comparing 2D contour plots of the electron density (Figure 2.11). The electron density of mesityl groups highlights that the two models do not only agree along bond paths, but across and outside the ring. This agreement extends to planes containing the polar Sb–O, Sb–C, S–O, and S–C bonds.

The subtle differences present in ρ are, as expected, accentuated by double differentiation (Figure 2.12). The 2D plots of $\nabla^2\rho$ highlight that the *NoSpherA2* electron density exhibits the same regions of local charge concentration between pairs of C atoms and pairs of C and H atoms in the mesityl rings. The charge concentration extending from the ipso C to the Sb atom is present in both but is slightly more pronounced in the *NoSpherA2* data. The

topology of $\nabla^2\rho$ around the O atom of the S–O unit involved in H-bonding to the hydroxystibonium cation is markedly different, as expected from the 1D bond path plots. Interestingly, however, it is the Laplacian of the O atom from the *NoSpherA2* model that takes on the conventional morphology expected for a covalent bond. In contrast, the MM displays the overall morphology of a polar bond (cf. the Sb–O and Sb–C bonds). These minor discrepancies notwithstanding, the 2D plots of $\nabla^2\rho$ highlight the excellent degree to which the *NoSpherA2* data approximate the refined charge density.
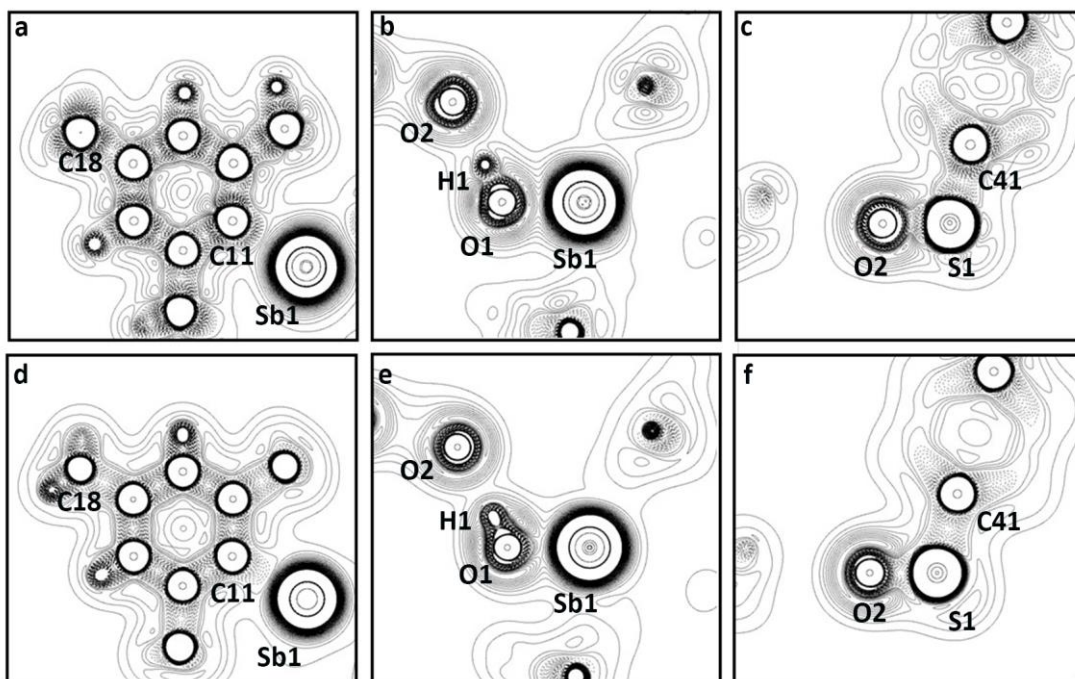


**Figure 2.12.** Contour plots of $\nabla^2\rho$ depicting planes defined by the (a, d) C11, C13, and C15 atoms, (B, E) Sb1, O1, and O2 atoms, and (c, f) S1, O2, and C41 atoms derived from the (a-c) MM and (d-f) HAR model. Atom positions are labelled by element symbols. Positive contours are shown as solid lines. Negative contours are shown as dashed lines. Contours are drawn at intervals of 0.05 e⁻ Å⁻⁵.

**2.7 – Conclusion**

Our attempts to investigate the properties and reactivity of the $Sb^+–O^-$ functional group in monomeric stibine oxides led to the discovery that the only previously reported examples are hydroxystibonium cations in which a Lewis acid interacts with the Sb-bound O atom. As such, this work demonstrates that monomeric stibine oxides unstabilized by interaction with a Lewis acid had still yet to be prepared. The lack of access to such molecules had greatly hampered any effort to observe and understand the systematic variation in the nature and reactivity of pnictogen–oxygen bonds.

Due to the challenging nature of H-atom position determination by the IAM, aspherical atom refinement by *NoSpherA2* was performed on [$Mes_3SbOH$][$O_3SPh$], a structure containing a heavy atom and a polar O-H bond. *NoSpherA2* reproduced H-atom positions and ADPs in exceptional agreement with those obtained from neutron diffraction. The wavefunction generated by *NoSpherA2* features a charge density topology that mimics the charge density refined experimentally from the multipole method. The *NoSpherA2* refinement also identified a H-atom disorder that could not be diagnosed in the IAM. Beyond highlighting the ability of *NoSpherA2* to handle further complications than previously reported, this work brings to light an entirely separate advantage that this method confers: a by-product of the HAR is an electron density, in a convenient file format, that can be readily subjected to topological analyses and gives results in agreement with the significantly more intensive charge density refinement.

**2.8 – Experimental methods**

**General methods.** Reagents and solvents were purchased from commercial vendors and used as received unless otherwise specified. All solvents were dried over 4-Å molecular sieves. The syntheses of trimesitylstibine, hydroxytrimesitylstibonium benzenesulfonate, and hydroxytrimesitylstibonium trifluoromethanesulfonate (triflate) were performed using flame-dried glassware under a nitrogen atmosphere. Other manipulations were performed under ambient conditions. NMR spectra were collected using a Bruker Avance III HD 500 spectrometer equipped with a multinuclear Smart Probe. Signals in the $^1$H and $^{13}$C NMR spectra are reported in ppm as chemical shifts from tetramethylsilane and were referenced using the CHCl$_3$ ($^1$H, 7.26 ppm) and CDCl$_3$ ($^{13}$C, 77.16 ppm) solvent signals. The frequencies of $^{11}$B NMR signals are reported in ppm as chemical shifts from BF$_3$·Et$_2$O and those of $^{19}$F NMR spectra as shifts from CFCl$_3$ (referenced to BF$_3$·Et$_2$O at −152.8 ppm). IR spectra were collected using a PerkinElmer Spectrum One FT-IR spectrometer. Mass spectrometry measurements were collected using an LTQ-Orbitrap Velos Pro MS instrument. Elemental analysis was performed by Midwest Microlabs (Indianapolis, IN) using an Exeter CE440 analyzer. Melting point data were collected with an electrothermal Mel-Temp apparatus and a partial-immersion thermometer; temperatures are uncorrected.

**Synthesis of trimesitylstibine (Mes$_3$Sb).** A dry 250 mL two-necked round bottom flask with a water-jacketted condenser was charged with a stir bar and magnesium turnings (1.451 g, 59.69 mmol). The magnesium turnings were suspended in 45 mL of dry tetrahydrofuran (THF) and activated with 1,2-dibromoethane (5.606 g, 29.84 mmol) at 0 °C for 3 h. 2-Bromomesitylene (5.942 g, 29.84 mmol) was then added dropwise and the reaction was

refluxed for 6 h. A solution of trichlorostibine (2.269 g, 9.947 mmol) in dry THF (5 mL) was then added dropwise into the yellow solution of mesitylmagnesium bromide, which became dark brown. The reaction mixture was refluxed for 14 h. The resulting mixture was cooled to room temperature, diluted with diethyl ether (200 mL), and washed with water (200 mL). The aqueous wash was back-extracted with diethyl ether (2 × 50 mL), and the organic phases were combined, washed with water (3 × 100 mL), and washed with brine (1 × 100 mL). The organic phase was dried over anhydrous sodium sulfate for 30 min and stripped of solvent under reduced pressure to yield a crude yellow oil. Cold ethanol was added dropwise with sonication to precipitate a white powder that was collected via vacuum filtration and dried in vacuo. Yield: 3.288 g, 69%. Analytical data match those previously reported for this compound.[36] M.p. 129 °C **IR (KBr, cm$^{-1}$)** v 1438 (s), 844 (s), 546 (s). **$^1$H (500 MHz, CDCl$_3$)** δ 6.83 (1 H, s, *m*-H), 2.29 (18 H, s, *o*-Me), 2.27 (9 H, s, *p*-Me). **$^{13}$C{$^1$H} (125 MHz, CDCl$_3$)** δ 144.90, 137.93, 136.80, 128.98, 25.46, (*o*-Me), 21.02 (*p*-Me).

**Synthesis of *trans*-dihydroxytrimesitylstiborane (*trans*-Sb(OH)$_2$Mes$_3$).** Trimesitylstibine (1.061 g, 2.213 mmol) was suspended in acetone (25 mL) and cooled to 0 °C. A solution of 50% hydrogen peroxide (0.828 mL, 12.17 mmol H$_2$O$_2$) in acetone (4 mL) was added dropwise to the suspension of trimesitylstibine. The white suspension was warmed to room temperature and stirred for 2 h. The volume of solvent was reduced by approximately 90% under reduced pressure and hexanes (30 mL) were added to precipitate a white powder that was collected via vacuum filtration and dried in vacuo. Yield: 856 mg, 75%. Analytical data match those previously reported for this compound.[1] M.p. 109 °C. **IR (KBr, cm$^{-1}$)** v$_{OH}$ 3642 (s), v$_{SbO}$ 517 (s).

**¹H (500 MHz, CDCl₃)** δ 6.97 (6 H, s, *m*-H), 2.57 (18 H, s, *o*-Me), 2.31 (9 H, s, *p*-Me). **¹³C{¹H} (125 MHz, CDCl₃)** δ 142.33, 142.19, 139.79, 130.18, 24.79 (*o*-Me), 21.08 (*p*-Me).

**Synthesis of hydroxytrimesitylstibonium benzenesulfonate ([Mes₃Sb(OH)][PhSO₃]).** *trans*-Dihydroxytrimesitylstiborane (94 mg, 0.18 mmol) was suspended in dichloromethane (DCM, 2 mL) and a solution of benzenesulfonic acid (29 mg, 0.184 mmol) in DCM (3 mL) was added dropwise into the reaction mixture. The reaction mixture clarified over the course of the addition and was stirred at room temperature for 30 min. Hexanes (30 mL) were added and the reaction mixture was cooled to −20 °C to yield a crop of colorless crystals. Yield: 70 mg, 58%. Diffraction-quality crystals of [Mes₃Sb(OH)][PhSO₃] were grown by layering hexanes over a CDCl₃ solution of the compound. M.p. 218 °C (decomp). **Found:** C, 60.32; H, 5.93. **Calc. for C₃₃H₃₉O₄SSb:** C, 60.65; H, 6.02 %. **ESI-MS (*m/z*)** M⁺ 495.34 (calc 495.16). **IR (KBr, cm⁻¹)** $\nu_{SbO}$ 612 (s). **¹H (500 MHz, CDCl₃)** δ 9.08 (1 H, s br, OH), 7.605 (2 H, d, *J* = 7.5 Hz, *o*-H), 7.24 (1 H, t, *J* = 7.5 Hz, *p*-H), 7.17 (2H, t, *J* = 7.5 Hz, *m*-H), 6.97 (6 H, s, *m*-H), 2.41 (18 H, s, *o*-Me), 2.31 (9 H, s, *p*-Me). **¹³C{¹H} (125 MHz, CDCl₃)** δ 146.09, 143.87, 143.47, 131.76, 131.34, 129.04, 127.64, 126.21, 24.04 (*o*-Me), 21.32 (*p*-Me).

**Synthesis of hydroxytrimesitylstibonium triflate ([Mes₃Sb(OH)][CF₃SO₃]).** Dihydroxytrimesitylstiborane (366 mg, 0.714 mmol) was suspended in DCM (2 mL) and a solution of triflic acid (63 mL, 0.714 mmol) in DCM (3 mL) was added dropwise into the cloudy mixture. The reaction mixture clarified over the course of the addition and was stirred at room temperature for 30 min. Hexanes (30 mL) were added and the reaction mixture was cooled to −20 °C to yield a crop of colorless crystals. Yield: 361 mg, 79%. Diffraction-quality crystals of

[Mes₃Sb(OH)]][CF₃SO₃] were grown by layering hexanes over a CDCl₃ solution of the compound. M.p. 252 °C (decomp). **Found:** C, 52.04; H, 5.20**. Calc. for C₂₈H₃₄F₃O₄SSb:** C, 52.11; H, 5.31 %. **ESI-MS (*m/z*)** M⁺ 495.32 (calc 495.16). **IR (KBr, cm⁻¹)** $v_{SbO}$ 637 (s). **¹H (500 MHz, CDCl₃)** δ 7.51 (1 H, s, OH),7.05 (6 H, s, *m*-H), 2.41 (18 H, s, *o*-Me), 2.35 (9 H, s, *p*-Me). **¹³C{¹H} (125 MHz, CDCl₃)** δ 144.59, 143.25, 131.54, 130.80, 120.46 (q, $J_{FC}$ = 319 Hz), 23.98 (*o*-Me), 21.30 (*p*-Me). **¹⁹F{¹H} (470 MHz, CDCl₃)** δ −78.28 (s).

**Synthesis of potassium tetrakis(3,5-bis(trifluoromethyl)phenyl)borate (KBArᶠ).** A dry 250 mL two-necked round bottom flask with a water-jacketted condenser was charged with a stir bar, magnesium turnings (2.015 g, 82.9 mmol), and sodium tetrafluoroborate (1.821 g, 16.6 mmol). The reagents were suspended in diethyl ether (100 mL). The magnesium turnings were activated with 1,2-dibromoethane (1.44 mL, 16.6 mmol), and the reaction mixture was brought to a reflux. 1,3-Bis(trifluoromethyl)-5-bromobenzene (11.44 mL, 66.3 mmol) was added dropwise to the suspension. The reaction mixture was refluxed for 18 h to produce a cloudy brown suspension. The contents were poured into a 2 L beaker and diluted with diethyl ether (90 mL). A solution of potassium carbonate (24 g, 0.17 mol) in water (240 mL) was added to the reaction mixture, and the contents were stirred vigorously for 1 h. The suspension was filtered to remove undissolved salts, and the filtrate was transferred to a separation funnel. The aqueous layer was extracted with diethyl ether (3 × 30 mL), and the combined organic layers were dried over Na₂SO₄. The organic layer was stripped of solvent to yield a yellow-brown oil. A mixture of DCM and hexanes was added to precipitate the product as a white powder. Yield: 2.290 g, 15.3%. Analytical data match those previously reported for this compound. **¹H (500 MHz, CDCl₃)** δ 7.72 (8H, br m, *o*-H), 7.69 (4H, s, *p*-H). **¹³C{¹H} (125 MHz,**

**CD$_3$CN)** δ 162.59 (q, $J_{BC}$ = 50 Hz, *ipso*-C), 135.64, 129.91 (qq, $J_{FC, 1}$ = 32.5 Hz, $J_{FC, 2}$ = 3.75 Hz), 125.45 (q, $J_{FC}$ = 271.25 Hz) **$^{19}$F{$^1$H} (470 MHz, CDCl$_3$)** δ -81.85 (s). **$^{11}$B{$^1$H} (160 MHz, CD$_3$CN)** δ −6.59 (s).

**Synthesis of hydroxytrimesitylstibonium tetrakis(3,5-bis(trifluoromethyl)phenyl)borate ([Mes$_3$Sb(OH)][BAr$^F$]).** A solution of [Mes$_3$Sb(OH)][CF$_3$SO$_3$] (201 mg, 0.311 mmol) in DCM (4 mL) was added dropwise to a cloudy suspension of potassium tetrakis(bis(3,5-trifluoromethyl)phenyl)borate (295 mg, 0.327 mmol) in DCM (20 mL). The cloudy suspension briefly became clear before potassium triflate precipitated from solution as a colorless solid. The suspension was vacuum filtered and the filtrate was stripped of solvent to yield a yellowish oil. The oil was taken up in CHCl$_3$ (3 mL) and passed through a pad of Celite to remove any excess KBAr$^F$. The solvent volume was reduced and pentane was added to precipitate the product as a white powder. The white powder was dried under vacuum for 72 h. Yield: 264 mg, 63%. Diffraction quality crystals of [Mes$_3$Sb(OH)][BAr$^F$] were grown from a mixture of CHCl$_3$ and pentane at −20 °C. **Found:** C, 52.28; H, 3.38**. Calc. for C$_{28}$H$_{34}$F$_3$O$_4$SSb:** C, 52.12; H, 3.41 %. **ESI-MS (*m/z*)** M$^+$ 495.54 (calc 495.16). **IR (KBr, cm$^{-1}$)** $v_{SbO}$ 683 (s). **$^1$H (500 MHz, CDCl$_3$)** δ 7.70 (8 H, s, *o*-H), 7.50 (4 H, s, *p*-H) 7.08 (6 H, s, *m*-H), 2.86 (1 H, s br, OH), 2.35 (18 H, s, *o*-Me), 2.32 (9 H, s, *p*-Me). **$^{13}$C{$^1$H}(125 MHz, CDCl$_3$)** δ 161.81 (q, $J_{BC}$ = 50 Hz, *ipso*-C), 146.20, 142.70, 134.95, 132.18, 130.14, 129.04 (qq, $J_{FC, 1}$ = 31.25 Hz, $J_{FC, 2}$ = 2.50 Hz) 120.46 (q, $J_{FC}$ = 271.25 Hz), 117.58, 23.86 (*o*-Me), 21.25 (*p*-Me). **$^{19}$F{$^1$H}(470 MHz, CDCl$_3$)** δ −62.30 (s). **$^{11}$B{$^1$H}(160 MHz, CD$_3$CN)** δ −6.72 (s).

**Computational experiments.** All density functional theory (DFT) calculations were carried out using ORCA 4.2.1.[37-38] Geometry optimizations and frequency calculations were performed at the PBE0/def2-TZVPP level of theory with the RIJCOSX approximation and def2/J auxiliary basis set.[28-29,39-41] A relaxed surface scan of a H atom across the Sb–O⋯O–S interatomic vector of [Mes$_3$Sb(OH)][PhSO$_3$] was carried out at BP86/def2-TZVP level of theory with the RI approximation and def2/J auxiliary basis set. Proton affinities were estimated by calculating the Gibbs free energy for the reaction of PhSO$_3^-$ or Mes$_3$SbO with H$^+$ with implicit DCM solvation provided by a conductor-like polarizable continuum model (CPCM).

**X-ray diffraction: Independent atom model (IAM).** Crystals were grown as described above, selected under a microscope, loaded onto a nylon fiber loop using Paratone-N, and mounted onto a Rigaku XtaLAB Synergy-S single crystal diffractometer. Each crystal was cooled to 100 K under a stream of nitrogen. Diffraction of Mo Kα radiation from a PhotonJet-S microfocus source was detected using a HyPix-6000HE hybrid photon counting detector. Screening, indexing, data collection, and data processing were performed with CrysAlis$^{Pro}$.[42] The structures were solved using SHELXT and refined using SHELXL following established strategies.[6,43-44] All non-H atoms were refined anisotropically. Carbon-bound H atoms were placed at calculated positions and refined with a riding model and coupled isotropic displacement parameters (1.2 × U$_{eq}$ for aryl groups and 1.5 × U$_{eq}$ for methyl groups). The oxygen-bound H atoms were located in the difference Fourier synthesis; their positional parameters were refined semi-freely and their isotropic displacement parameters were set equal to 1.5 × U$_{eq}$ of the oxygen atom. In the case of [Mes$_3$Sb(OH)][CF$_3$SO$_3$], the triflate counterion was disordered across two positions and was refined with similarity restrains on

bond lengths, bond angles, and displacement parameters. In the case of [Mes$_3$Sb(OH)][BAr$^F$], the two pentane molecules in the unit cell were each disordered across a distinct crystallographic inversion center and were modeled with similarity restraints on bond lengths, bond angles, and displacement parameters.

**Neutron diffraction**. A colorless prism measuring 1.08 × 0.80 × 0.35 mm$^3$ was cooled to 100 K and irradiated using TOPAZ at the Spallation Neutron Source (SNS) of Oak Ridge National Laboratory.[45] Data were collected using 17 crystal orientations optimized with CrystalPlan[46] software for better than 99% coverage of symmetry-equivalent reflections of the orthorhombic cell. Each orientation was measured for approximately 5 h with 25 C of proton charge at an SNS beam power of 1.4 MW. The integrated raw Bragg intensities were obtained using 3D ellipsoidal Q-space integration in accordance with previously reported methods.[47] The reflections could be observed out to a resolution of 0.79 Å. Data reduction, including neutron TOF spectrum, Lorentz, and detector efficiency corrections, was carried out with the ANVRED3 program.[48] Gaussian numerical absorption correction was applied with $\mu$ = 0.13489 + 0.10068$\lambda$ mm$^{-1}$. The reduced data were saved in SHELX HKLF2 format, in which the wavelength is recorded separately for each reflection, and data were not merged. The X-ray IAM was used as the starting point for refinement with SHELXL.[43] The positions and ADPs of the H atoms were allowed to refine freely while non-H-atom positions and ADPs were constrained to the IAM values. The neutron data revealed the presence of disorder in one of the methyl groups. The disordered methyl group was split into two parts related by rotational symmetry and refined anisotropically while employing rigid bond and similarity restraints.

**X-ray diffraction: Hirshfeld atom refinement.** The IAM of [Mes$_3$SbOH][O$_3$SPh] was refined using the *NoSpherA2* implementation of HAR in *Olex2* with the *olex2.refine* engine.[3] The quantum chemistry calculations were performed by ORCA (version 4.2.1).[37-38] A wavefunction was calculated with tight SCF convergence criteria using the PBE0 hybrid functional and the x2c-TZVPP all-electron relativistically contracted basis set.[28-30,39] The effects of relativity were introduced using the second-order Douglas-Kroll-Hess formalism.[49] The ADPs and positions of all atoms, including H atoms, were freely refined using the aspherical atomic form factors obtained from Hirshfeld stockholder partitioning of the computed wavefunction.[22] The newly refined atomic coordinates were used as the input for a new density functional theory (DFT) calculation, from which new aspherical form factors were obtained. This procedure was iterated until it had converged. The ADPs of the H atoms produce well-formed thermal ellipsoids with the exception of a single methyl group, where the H-atom ellipsoids are elongated and suggestive of rotational disorder. The HAR was repeated under the same conditions from the IAM after splitting the disordered methyl group into two parts related by rotational symmetry. The disordered H atoms were non-positive definite after refinement. Rigid bond and similarity restraints were applied to all disordered H atoms, and the minor component was refined isotropically without recalculating the wavefunctions and tabulated aspherical atomic form factors. Refinement parameters are collected in Table 2.1. H-atom ADPs from the neutron (Table A.6) and HAR (Table A.7) structures were compared quantitatively with correlation coefficients (Figure A.16 and Table A.9).[31]

**X-ray diffraction: Multipole refinement**. The full MM refinement strategy is described in Table A.11. The atomic coordinates and thermal parameters from the X-ray IAM were used as a

starting point for the multipole refinement, which was carried out under the Hansen-Coppens formalism[9] using the full-matrix-least-squares refinement program XDLSM within the *XD2016* suite. Form factors were derived from the STO wavefunctions of the Volkov-Macchi-ZORA databank within the *XD2016* suite. An initial site symmetry-restricted multipolar expansion was performed with the C, O, S, and Sb functions truncated at an octupolar level, the Sb–O*H* atom at a quadrupolar level, and the C*H* atoms at a dipolar level. Chemical similarity constraints were employed for the initial stages of refinement. The non-H-atom atomic coordinates and thermal parameters were allowed to refine again. At this stage, the κ parameters for non-H atoms (one for each element type) were then allowed to refine while κ and κ' for H atoms were set to 1.13 and 1.18, respectively. The H-atom coordinates were allowed to refine, while being reset to the neutron model bond lengths at each stage of refinement. The neutron model H-atom thermal parameters were then added to the model but not refined. A subsequent multipolar expansion was performed with all non-H atoms truncated at the hexadecapolar level and all H atoms truncated at the quadrupolar level. The number of κ parameters was allowed to increase (one for each chemically equivalent atom type) and the H-atom κ parameters were allowed to refine. Site symmetry and chemical similarity constraints were systematically relaxed until they were only applied to H atoms. Inspection of the difference Fourier synthesis revealed no clear peaks corresponding to unmodelled valence electron density (Figure 2.6). The final multipole model (MM) featured satisfactory residual factors (Table 2.1).

**Topological analysis.** The electron density and Laplacian of the MM were calculated using the *XDPROP* program within the *XD2016* suite. Topological analyses were performed with

*Multiwfn*[50] using the cube files for the MM and the wavefunction file from *NoSpherA2* HAR. The electron density and Laplacian values along interatomic vectors and 2D planes were calculated using *Multiwfn.* The values of these real-space functions along the chosen interatomic lines were visualized and the bond critical points were extracted using R (version 4.0.2) through RStudio (version 1.3.1073). The following R packages were used for analysis and visualization: ggplot2, tidyverse, gridExtra, ggtext, and grid.

## 2.9 – References

1.  Huber, F.; Westhoff, T.; Preut, H., Tris(2,4,6-trimethylphenyl)antimony dihydroxide; synthesis and reaction with sulfonic acids $RSO_3H$ (R = $C_6H_5$, $CF_3$). Crystal structure of $[2,4,6-(CH_3)_3C_6H_2]_3SbO \cdot HO_3SC_6H_5$. *J. Organomet. Chem.* **1987,** *323*, 173-180.

2.  Westhoff, T.; Huber, F.; Rüther, R.; Preut, H., Synthesis and structural characterization of some new triorganoantimony oxides. Molecular and crystal structure of tris(2,4,6-trimemethylphenyl)antimony dihydroxide. *J. Organomet. Chem.* **1988,** *352*, 107-113.

3.  Kleemiss, F.; Dolomanov, O. V.; Bodensteiner, M.; Peyerimhoff, N.; Midgley, L.; Bourhis, L. J.; Genoni, A.; Malaspina, L. A.; Jayatilaka, D.; Spencer, J. L.; White, F.; Grundkötter-Stock, B.; Steinhauer, S.; Lentz, D.; Puschmann, H.; Grabowsky, S., Accurate crystal structures and chemical properties from NoSpherA2. *Chem. Sci.* **2021,** *12*, 1675-1692.

4.  Egorova, I. V.; Zhidkov, V. V.; Grinishak, I. P.; Rodionova, N. A., Novel organoantimony compounds $[2,6-(OMe)_2C_6H_3]_3SbO$ and $[2,6-(OMe)_2C_6H_3]_3Sb(NCO)_2 \cdot 0.5(CH_3)_2CO$. Synthesis and structure. *Russ. J. Gen. Chem.* **2016,** *86*, 2484-2491.

5.  Koritsanszky, T. S.; Coppens, P., Chemical Applications of X-ray Charge-Density Analysis. *Chem. Rev.* **2001,** *101*, 1583-1628.

6.  Müller, P., Practical suggestions for better crystal structures. *Crystallogr. Rev.* **2009,** *15*, 57-83.

7.  Woińska, M.; Grabowsky, S.; Dominiak, P. M.; Woźniak, K.; Jayatilaka, D., Hydrogen atoms can be located accurately and precisely by x-ray crystallography. *Sci. Adv.* **2016,** *2*, e1600192.

8.  Madsen, A. Ø., Modeling and Analysis of Hydrogen Atoms. Springer Berlin Heidelberg: 2012; pp 21-52.

9.  Hansen, N. K.; Coppens, P., Testing aspherical atom refinements on small-molecule data sets. *Acta Crystallogr. Sect. A* **1978,** *34*, 909-921.

10. Bader, R. F. W., Atoms in Molecules. *Acc. Chem. Res.* **1985**, 9-15.

11. Bader, R. F. W., A Quantum Theory of Molecular Structure and Its Applications. *Chem. Rev.* **1991,** *91*, 893-928.

12. Bytheway, I.; Grimwood, D. J.; Figgis, B. N.; Chandler, G. S.; Jayatilaka, D., Wavefunctions derived from experiment. IV. Investigation of the crystal environment of ammonia. *Acta Crystallogr. Sect. A* **2002,** *58*, 244-251.

13. Grimwood, D. J.; Jayatilaka, D., Wavefunctions derived from experiment. II. A wavefunction for oxalic acid dihydrate. *Acta Crystallogr. Sect. A* **2001,** *57*, 87-100.

14.  Bytheway, I.; Grimwood, D. J.; Jayatilaka, D., Wavefunctions derived from experiment. III. Topological analysis of crystal fragments. *Acta Crystallogr. Sect. A* **2002,** *58*, 232-243.

15.  Grimwood, D. J.; Bytheway, I.; Jayatilaka, D., Wave functions derived from experiment. V. Investigation of electron densities, electrostatic potentials, and electron localization functions for noncentrosymmetric crystals. *J. Comput. Chem.* **2003,** *24*, 470-483.

16.  Woińska, M.; Jayatilaka, D.; Dittrich, B.; Flaig, R.; Luger, P.; Woźniak, K.; Dominiak, P. M.; Grabowsky, S., Validation of X-ray Wavefunction Refinement. *ChemPhysChem* **2017,** *18*, 3334-3351.

17.  Wenger, J. S.; Johnstone, T. C., Unsupported monomeric stibine oxides ($R_3SbO$) remain undiscovered. *Chem. Commun.* **2021,** *57*, 3484-3487.

18.  Dolomanov, O. V.; Bourhis, L. J.; Gildea, R. J.; Howard, J. A. K.; Puschmann, H., OLEX2: a complete structure solution, refinement and analysis program. *J. Appl. Crystallogr.* **2009,** *42*, 339-341.

19.  Jayatilaka, D.; Dittrich, B., X-ray structure refinement using aspherical atomic density functions obtained from quantum-mechanical calculations. *Acta Crystallogr. Sect. A* **2008,** *64*, 383-393.

20.  Capelli, S. C.; Bürgi, H.-B.; Dittrich, B.; Grabowsky, S.; Jayatilaka, D., Hirshfeld atom refinement. *IUCrJ* **2014,** *1*, 361-379.

21.  Fugel, M.; Jayatilaka, D.; Hupf, E.; Overgaard, J.; Hathwar, V. R.; Macchi, P.; Turner, M. J.; Howard, J. A. K.; Dolomanov, O. V.; Puschmann, H.; Iversen, B. B.; Bürgi, H.-B.; Grabowsky, S., Probing the accuracy and precision of Hirshfeld atom refinement with HARt interfaced with Olex2. *IUCrJ* **2018,** *5*, 32-44.

22.  Hirshfeld, F. L., Bonded-atom fragments for describing molecular charge densities. *Theor. Chim. Acta* **1977,** *44*, 129-138.

23.  Jayatilaka, D.; Grimwood, D. J., Tonto: A Fortran Based Object-Oriented System for Quantum Chemistry and Crystallography. In *Computational Science — ICCS 2003*, Sloot, P. M. A.; Abramson, D.; Bogdanov, A. V.; Gorbachev, Y. E.; Dongarra, J. J.; Zomaya, A. Y., Eds. Springer Berlin Heidelberg: Berlin, Heidelberg, 2003; pp 142-151.

24.  Bourhis, L. J.; Dolomanov, O. V.; Gildea, R. J.; Howard, J. A. K.; Puschmann, H., The anatomy of a comprehensive constrained, restrained refinement program for the modern computing environment –Olex2dissected. *Acta Crystallogr. Sect. A* **2015,** *71*, 59-75.

25. Grabowsky, S.; Luger, P.; Buschmann, J.; Schneider, T.; Schirmeister, T.; Sobolev, A. N.; Jayatilaka, D., The Significance of Ionic Bonding in Sulfur Dioxide: Bond Orders from X-ray Diffraction Data. *Angew. Chem., Int. Ed.* **2012,** *51*, 6776-6779.

26. Jayatilaka, D., Wave Function for Beryllium from X-Ray Diffraction Data. *Phys. Rev. Lett.* **1998,** *80*, 798-801.

27. Allen, F. H.; Bruno, I. J., Bond lengths in organic and metal-organic compounds revisited: X—H bond lengths from neutron diffraction data. *Acta Crystallogr. Sect. B* **2010,** *66*, 380-386.

28. Perdew, J. P.; Ernzerhof, M.; Burke, K., Rationale for mixing exact exchange with density functional approximations. *J. Chem. Phys.* **1996,** *105*, 9982-9985.

29. Perdew, J. P.; Burke, K.; Ernzerhof, M., Generalized Gradient Approximation Made Simple. *Phys. Rev. Lett.* **1996,** *77*, 3865-3868.

30. Pollak, P.; Weigend, F., Segmented Contracted Error-Consistent Basis Sets of Double- and Triple-ζ Valence Quality for One- and Two-Component Relativistic All-Electron Calculations. *J. Chem. Theory Comput.* **2017,** *13*, 3696-3705.

31. Merritt, E. A., Comparing anisotropic displacement parameters in protein structures. *Acta Crystallographica Section D Biological Crystallography* **1999,** *55*, 1997-2004.

32. Lindquist-Kleissler, B.; Wenger, J. S.; Johnstone, T. C., Analysis of Oxygen–Pnictogen Bonding with Full Bond Path Topological Analysis of the Electron Density. *Inorg. Chem.* **2021,** *60*, 1846-1856.

33. Salvador, P.; Fradera, X.; Duran, M., Effect of basis set superposition error on the electron density of molecular complexes. *J. Chem. Phys.* **2000,** *112*, 10106-10115.

34. Salvador, P.; Duran, M.; Fradera, X., A chemical Hamiltonian approach study of the basis set superposition error changes on electron densities and one- and two-center energy components. *J. Chem. Phys.* **2002,** *116*, 6443-6457.

35. Salvador, P.; Fradera, X.; Duran, M., Quantitative assessment of the effect of basis set superposition error on the electron density of molecular complexes by means of quantum molecular similarity measures. *Int. J. Quantum Chem.* **2009,** *109*, 2572-2580.

36. Chalmers, B. A.; Bühl, M.; Athukorala Arachchige, K. S.; Slawin, A. M. Z.; Kilian, P., Structural, Spectroscopic and Computational Examination of the Dative Interaction in Constrained Phosphine-Stibines and Phosphine-Stiboranes. *Chem.–Eur. J.* **2015,** *21*, 7520-7531.

37. Neese, F., The ORCA program package. *Wiley Interdiscip. Rev.-Comput. Mol. Sci* **2012,** *2*, 73-78.

38. Neese, F., *WIREs Comput. Mol. Sci* **2018,** *8*, e1327.

39. Weigend, F.; Ahlrichs, R., Balanced basis sets of split valence, triple zeta valence and quadruple zeta valence quality for H to Rn: Design and assessment of accuracy. *Phys. Chem. Chem. Phys.* **2005,** *7*, 3297-3305.

40. Weigend, F., Accurate Coulomb-fitting basis sets for H to Rn. *Phys. Chem. Chem. Phys.* **2006,** *8*, 1057-1065.

41. Neese, F.; Wennmohs, F.; Hansen, A.; Becker, U., Efficient, approximate and parallel Hartree–Fock and hybrid DFT calculations. A 'chain-of-spheres' algorithm for the Hartree–Fock exchange. *Chem. Phys.* **2009,** *356*, 98-109.

42. Rigaku Oxford Diffraction, *CrysAlis^{Pro}* **2020**.

43. Sheldrick, G. M., SHELXT– Integrated space-group and crystal-structure determination. *Acta Crystallogr. Sect. A* **2015,** *71*, 3-8.

44. Sheldrick, G. M., Crystal structure refinement with SHELXL. *Acta Crystallogr. Sect. C* **2015,** *71*, 3-8.

45. Coates, L.; Cao, H.; Chakoumakos, B.; Frontzek, M.; Hoffmann, C.; Kovalevsky, A.; Liu, Y.; Meilleur, F.; dos Santos, A.; Myles, D.; Wang, X.; Ye, F., A suite-level review of the neutron single-crystal diffraction instruments at Oak Ridge National Laboratory. *Rev. Sci. Instrum.* **2018,** *89*, 092802.

46. Zikovsky, J.; Peterson, P.; Wang, X.; Frost, M.; Hoffmann, C., CrystalPlan: An experiment-planning tool for crystallography. *J. Appl. Crystallogr.* **2011,** *44*, 418-423.

47. Schultz, A. J.; Jorgensen, M.; Wang, X.; Mikkelson, R.; Mikkelson, D.; Lynch, V.; Peterson, P.; Green, M.; Hoffmann, C., Integration of neutron time-of-flight single-crystal Bragg peaks in reciprocal space. *J. Appl. Crystallogr.* **2014,** *47*, 915-921.

48. Schultz, A. J.; Srinivasan, K.; Teller, R. G.; Williams, J. M.; Lukehart, C. M., Single-Crystal Time-of-Flight Neutron-Diffraction Structure of Hydrogen cis-Diacetyltetracarbonylrhenate, [cis-(Oc)$_4$Re(CH$_3$CO)$_2$]H - a Metallaacetylacetone Molecule. *J. Am. Chem. Soc.* **1984,** *106*, 999-1003.

49. Wolf, A.; Reiher, M.; Hess, B. A., The generalized Douglas–Kroll transformation. *J. Chem. Phys.* **2002,** *117*, 9215-9226.

50. Lu, T.; Chen, F., Multiwfn: A multifunctional wavefunction analyzer. *J. Comput. Chem.* **2012,** *33*, 580-592.

# Chapter 3

## Isolation, bonding, and reactivity of a monomeric stibine oxide

**3.1 – Introduction**

With the realization that all previous reports of unsupported monomeric stibine oxides were in fact hydroxystibonium salts (see Chapter 2), we sought to isolate a monomeric stibine oxide with an unperturbed stiboryl bond for the first time. We understood that oxidation of triphenylstibine resulted in self-associated dimers or oligomers. By increasing the steric bulk around the antimony center with mesityl substituents, self-association could be prevented, but the antimony center could still expand its coordination sphere to form the *trans*-dihydroxystiborane. Thus, we hypothesized that by increasing the steric bulk further, we could prevent the self-association and the expansion of the coordination sphere that typically occurs upon oxidation of the stibine.

In this chapter, I discuss the isolation and initial investigation of $Dipp_3SbO$ (Dipp = 2,6-diisopropylphenyl), the first unsupported monomeric stibine oxide. $Dipp_3PO$ and $Dipp_3AsO$ were also prepared, allowing for trends in bonding and reactivity across a directly comparable series of pnictine oxides to be observed. This work includes a rigorous theoretical investigation into the electronic structures of these species, with a focus on the pnictoryl bond ($Pn=O/Pn^+-O^-$). A series of reactivity studies were also performed on $Dipp_3PnO$. $Dipp_3SbO$ was found to have the most highly polarized pnictoryl bond of the series. $Dipp_3SbO$ was also the most highly reactive species in response to all substrates employed in these reactivity studies.

**3.2 – Synthesis of sterically encumbered pnictines, $Dipp_3Pn$ (Pn = P, As, Sb)**

Attempts to isolate the stibine $Dipp_3Sb$ by treating $SbCl_3$ and either DippMgBr or DippLi were unsuccessful. The reason this common synthetic route does not afford Dipp-substituted pnictines is due to the formation of undesirable reduction products $(Dipp_2Pn)_2$.

Sasaki and co-workers had previously reported the synthesis of Tipp₃Sb (Tipp = 2,4,6-triisopropylphenyl), in which the Tipp substituent is installed on the Sb center with a less-reducing organocopper(I) species that is, in turn, produced from a Grignard reagent.[2-3] We followed a similar protocol and isolated Dipp₃Sb as a crystalline solid (Figure 3.1). The yield is moderate relative to the more facile synthesis of less encumbered stibines, such as Ph₃Sb and Mes₃Sb. The $^1$H NMR spectrum Dipp₃Sb indicates that rotation about the Sb–C and $C_{Ar}$–$C_{iPr}$ bonds is rapid on the NMR time scale at room temperature, and features the expected diastereotopic splitting of the isopropyl substituents.
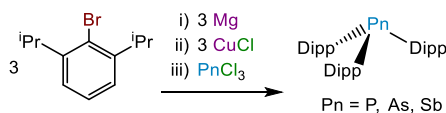


**Figure 3.1.** Synthesis of sterically crowded pnictines Dipp₃Pn (Pn = P, As, Sb; Dipp = 2,6-diisopropylphenyl).

Dipp₃As and Dipp₃P were prepared following a similar synthetic route (Figure 3.1). The isolation of the lighter pnictines would ultimately allow us to form lighter analogues of the desired monomeric stibine oxide. We note that the yields are increased significantly if freshly purified CuCl, colorless and free of green impurities, is used. After reaction with either PCl₃ or AsCl₃, the product is purified by column chromatography and recrystallized from a mixture of ether/acetonitrile to yield well-formed crystals in good yield (Dipp₃P: 53%; Dipp₃As: 56%). The $^{31}$P NMR spectrum of Dipp₃P displays a single resonance at –50.41 ppm, which agrees well with the similarly encumbered Tipp₃P (–52.4 ppm). The substantial upfield shift relative to triphenylphosphine (–5.35 ppm) can be attributed to the inductive effect of the electron-donating isopropyl groups on the aryl substituents and perhaps more importantly to the shielding by the six isopropyl groups above and below the pnictogen center. The $^{13}$C and $^1$H

NMR spectra of Dipp$_3$P and Dipp$_3$As are consistent with the proposed structures of the pnictines and exhibit the effects of hindered rotation about the Pn–C$_{ipso}$ bonds. Remarkably, Dipp$_3$P exists as a pale green solid. Initially, the color was thought to arise from a cupric impurity, but elemental analysis and spectral data confirm the purity of Dipp$_3$P. The green color is evident upon inspection of single crystals under a microscope but its origin remains to be explored.

The structures of Dipp$_3$P and Dipp$_3$As were unambiguously determined by X-ray crystallography (Figure 3.2a,b,d,e). Crystals of Dipp$_3$P and Dipp$_3$As were found to be isomorphous; each species crystallizes in the trigonal space group $R$3 with the C$_3$-symmetrical molecules residing on a crystallographic 3-fold rotation axis. Although grown under similar conditions, crystals of Dipp$_3$Sb are not isomorphous with Dipp$_3$P and Dipp$_3$As; Dipp$_3$Sb also crystalized on a 3-fold rotation axis, but in the cubic space group $I\overline{4}3m$ (Figure 3.2c,f). The canting of the aryl groups imparts chirality on the species, and both structures were best
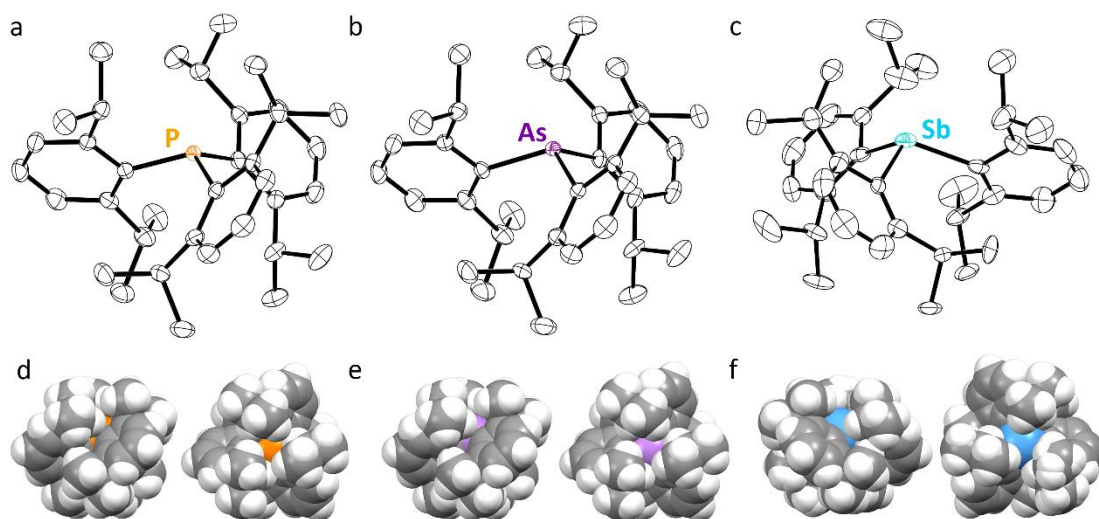


**Figure 3.2.** Thermal ellipsoid plots (50% probability level) of (a) Dipp$_3$P, (b) Dipp$_3$As, and (c) Dipp$_3$Sb. H atoms are omitted for clarity. Space-fill diagrams of (d) Dipp$_3$P, (e) Dipp$_3$As, and (f) Dipp$_3$Sb. Color code: P orange, As purple, Sb teal, C grey, H white.

refined as inversion twins. Space-filling diagrams show the extremely crowded environment around the pnictogen centers (Figure 3.2d-f). For the different $Dipp_3Pn$ species, the P–C bond length is 1.8547(21) Å, the As–C bond length is 1.9964(33) Å, and the Sb–C bond length is 2.176(7) Å. The C–Pn–C bond angles systematically decrease as the period is descended in accordance with the Pn-centered hybrid orbitals engaged in Pn–C bonding becoming increasingly enriched in p-character (C–P–C = 111.67(7)°, C–As–C = 109.61(11)°, C–Sb–C = 106.96(18)°).

### 3.3 – Oxidation of $Dipp_3Pn$ (Pn = P, As, Sb)

Treatment of a suspension of PhIO in DCM with $Dipp_3Sb$ resulted in the consumption of the solid PhIO. Solvent was stripped from the reaction mixture and the residue was washed with pentane to yield a colorless solid, $Dipp_3SbO$ (Figure 3.3a). The IR spectrum of $Dipp_3SbO$ shows a single new signal, $v_{SbO}$, at 779 $cm^{-1}$. This value is greater than any of the $v_{SbO}$ values of $(Ph_3SbO)_2$ (643/651 $cm^{-1}$),[4] $trans$-$Sb(OH)_2Mes_3$ (520 $cm^{-1}$),[5-6] or $[Mes_3SbOH][O_3SPh]$ (612 $cm^{-1}$),[7] as we would expect for the higher-bond-order stiboryl group. The ^{1}H NMR spectrum of $Dipp_3SbO$ varies from that of $Dipp_3Sb$ in that it is consistent with a single Dipp environment that is restricted about the Sb–C bonds on the NMR time scale. Exchange spectroscopy (EXSY) and variable temperature (VT) NMR experiments demonstrated chemical exchange and reversible coalescence of the desymmetrized Dipp groups (Figures B.17, B.18).

We performed Sb X-ray absorption spectroscopy experiments, which we have found to be useful in elucidating the structures of Sb-containing compounds.[8] The K edge provides information about the oxidation state, while EXAFS data provides information about the coordination environment of the Sb center. $Dipp_3SbO$ exhibits an Sb K edge that is 2 eV higher

in energy than that of Dipp₃Sb (Figure 3.3c). The Sb K edge of Dipp₃SbO is consistent with a series of Sb(V) compounds, including the dimeric stibine oxide (Ph₃SbO)₂ (**A**), the dihydroxystiborane *trans*-Sb(OH)₂Mes₃ (**B**), and the hydroxystibonium salt [Dipp₃SbOH][O₃SPh] (**C**, *vide infra*), confirming the presence of an Sb(V) center in Dipp₃SbO (Figure 3.3c). High-resolution K-edge EXAFS data were collected for Dipp₃SbO as well as Dipp₃Sb, **A**, **B**, and **C** for comparison (Figure 3.3d). The Fourier transform of the data from **A** reveals a prominent signal corresponding Sb···Sb scattering at 3.148(3) Å that is superimposed upon outer-shell carbon backscattering. Such intense scattering at this distance is absent for Dipp₃Sb, **B**, **C**, and Dipp₃SbO, suggesting Dipp₃SbO does not feature a dioxadistibetane. The fit from the data of **B** features two O-atom scatters at 2.128(3) Å, and the best model for **C**
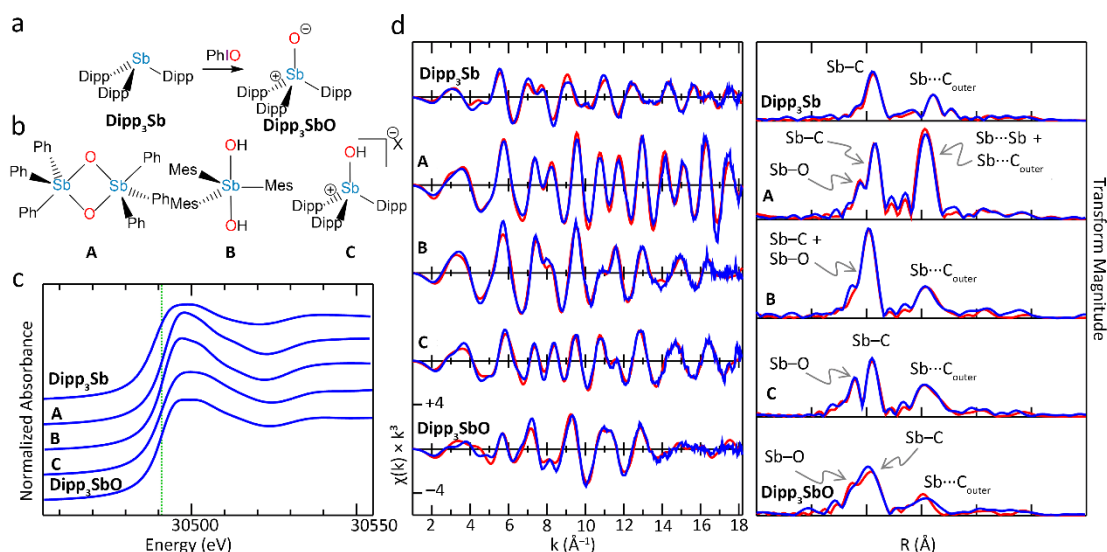


**Figure 3.3.** Oxidation of sterically crowded stibine Dipp₃Sb. (a) Oxidation of Dipp₃Sb with PhIO to give Dipp₃SbO. (b) Model compounds featuring different Sb–O bonding motifs. **A** = a dimeric stibine oxide, **B** = a dihydroxystiborane, **C** = a hydroxystibonium salt with X = O₃SPh. (c) Sb K-edge XAS spectra with green dotted line where the derivative is maximal for Dipp₃SbO. Full normalized Sb K-edge XAS spectra are provided in the Figure B.102. (d) Sb K-edge EXAFS (*left*) and Sb–C phase-corrected Fourier transforms (*right*). Experimental data are shown in blue and fits in red. Relevant EXAFS parameters are provided in Table B.7. A breakdown of the contributions of the different scatterers to the EXAFS and Sb–C phase-corrected Fourier transforms of **A** and Dipp₃SbO are shown in the Figure B.103.

contains only a single O-atom scatterer at 1.905(1) Å. The crystal structures of these compounds are in excellent agreement with these spectral results. The best model to fit the data collected on Dipp$_3$SbO features a single O-atom scatterer at a distance of 1.837(2) Å, indicating Dipp$_3$SbO contains the shortest Sb–O bond ever characterized. If we attempt to fit a C atom in the place of the O atom, we observe a worse goodness-of-fit index ($F$ = 0.335 for Sb–C vs. 0.319 for Sb–O) and an unreasonable Debye-Waller factor ($\sigma^2$ = 0.0010 Å$^2$ for Sb–C vs. 0.0021 Å$^2$ for Sb–O).

Unexpectedly, Dipp$_3$P and Dipp$_3$As do not react with iodosobenzene. We attribute this difference in reactivity to the smaller size of the central pnictogen atom, which enhances the effective steric shielding of the bulky Dipp groups; these groups create a greater kinetic barrier for oxidants to approach the smaller pnictogen centers. We turned, therefore, to *m*CPBA, which has been previously reported to successfully oxidize bulky phosphines and arsines.[9] Dissolution of Dipp$_3$P and *m*CPBA in DCM yields a red solution whose color fades away as the starting materials are consumed. The crude product obtained following an aqueous workup was purified by column chromatography and recrystallized from a mixture of ether/acetonitrile. Dipp$_3$AsO was synthesized similarly.

We were able to obtain single crystals of Dipp$_3$SbO that were suitable for an X-ray diffraction experiment, as well as Dipp$_3$AsO and Dipp$_3$PO (Figure 3.4). The diffraction data for Dipp$_3$SbO were of sufficient quality to perform Hirshfeld Atom Refinement (HAR) with *NoSpherA2* to elucidate structural information of Dipp$_3$SbO, including H-atom positional and thermal parameters, with extreme precision. The HAR model exhibits an Sb–O bond length of 1.8372(5) Å, consistent with the distance obtained from the EXAFS data. The next-nearest Sb⋯O distance is 9.0791(4) Å, confirming the monomeric nature of the species. Space-filling

diagrams conveniently show the extremely encumbered steric environment produced by the Dipp substituents (Figure B.92). One of the $^i$Pr benzylic C–H groups is positioned such that an H-bonding interaction is formed with the stiboryl group at an O···H distance of 2.132(9) Å.[10] The structural data indicate that this H-bonding interaction is of moderate strength, with a C–H···O bond angle of 148.1(8)° suggesting a strong electrostatic contribution to the interaction relative to C–H···O H-bonds that are supported by weaker isotropic van der Waals forces.[11] We believe that, while interesting, steric shielding provided by the Dipp groups, not thermodynamic stabilization by serendipitous intramolecular H-bonds, enables the isolation of Dipp$_3$SbO as a bench-stable solid.
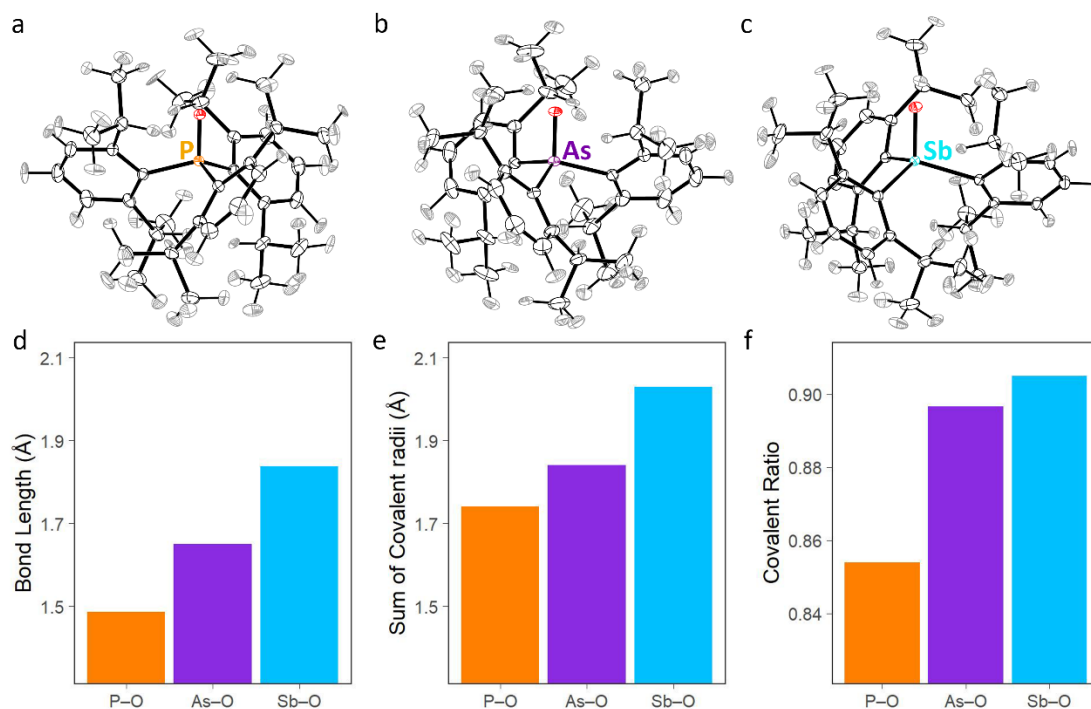


**Figure 3.4.** Thermal ellipsoid plots (50% probability level) of (a) Dipp$_3$PO, (b) Dipp$_3$AsO, and (c) Dipp$_3$SbO (monoclinic). (d) Pn–O bond lengths, (e) sum of Pn and O covalent radii,[1] and (f) covalent ratios. Color code: P orange, As purple, Sb teal, C black, H grey.

X-ray diffraction experiments revealed $Dipp_3PO$ and $Dipp_3AsO$ to crystallize as isomorphs of both each other and the parent pnictines, with the Pn–O bond coincident with the 3-fold rotation axis. The isomorphism of $Dipp_3P$, $Dipp_3PO$, $Dipp_3As$, and $Dipp_3AsO$ highlights that, for each oxide, the O atom resides within a sterically protected pocket created by the Dipp substituents; the addition of the O atom does not sufficiently perturb the envelope the pnictine to change its crystal packing. $Dipp_3SbO$ does not share this isomorphism and crystalizes on a general position in the space group $P2_1/c$. The final structures of $Dipp_3AsO$ and $Dipp_3PO$ obtained by HAR, allowing for accurate refinement of H atom positional and thermal parameters and direct comparison with the HAR model of $Dipp_3SbO$ (Figure 3.4a,b,c). As expected, the $Pn^+$–$O^-$ bond distance systematically increases as the group is descended. The $P^+$–$O^-$ and $As^+$–$O^-$ bond distances are 1.4857(8) and 1.650(2) Å, respectively, as compared to the $Sb^+$–$O^-$ bond length of 1.8372(5) Å reported above. The covalent ratio is a useful parameter for comparing bond lengths across congeners featuring bonded atoms of different sizes.[1] The $P^+$–$O^-$ bond features the greatest discrepancy between the bond length and the expected single covalent bond length with a covalent ratio of 0.854, indicating that it has the highest bond order of the series. The covalent ratio of the $As^+$–$O^-$ bond fell only slightly under that $Sb^+$–$O^-$ bond with values of 0.897 and 0.905 respectively. The O atoms in the three species vary in their proximity to benzylic H atoms with the stiboryl oxygen in the closest contact with a neighboring H atom at 2.132(9) Å. The increased capacity of the stiboryl oxygen to engage in this H-bonding interaction could be responsible for the desymmetrization of $Dipp_3SbO$ from 3-fold rotational symmetry in the solid state.

A theoretical geometry optimization (PBE0/def2-TZVPP) was performed starting from the crystallographic coordinates of $Dipp_3SbO$. The theoretical model agreed with experiment,

with an Sb–O distance of 1.827 Å and a scaled theoretical $\nu_{SbO}$ of 781 cm$^{-1}$. We obtained theoretical models for Dipp$_3$PO and Dipp$_3$AsO at the same level of theory.

As expected, the calculated Pn$^+$–O$^-$ bond stretching frequency decreases dramatically as the period is descended (Figure 3.5d). Although consistent with a weakening of the Pn$^+$–O$^-$ bond across the series, the trend is confounded by the concomitant variation in reduced mass. Moreover, the vibrations nominally assigned as the Pn$^+$–O$^-$ stretching modes also involve variable contributions from displacement along other internal coordinates. To better
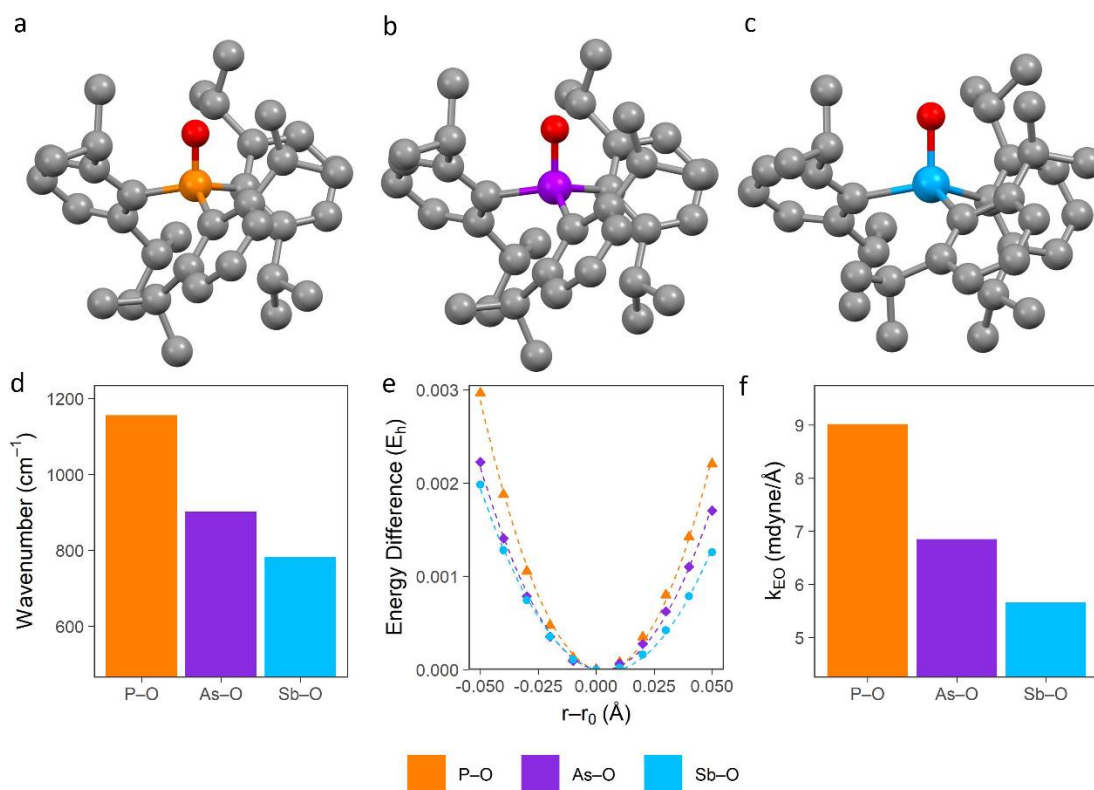


**Figure 3.5.** Geometry-optimized (PBE0/def2-TZVPP) structures of (a) Dipp$_3$PO, (b) Dipp$_3$AsO, and (c) Dipp$_3$SbO (H atoms are omitted for clarity). (d) Calculated vibrational frequency for the nominal Pn$^+$–O$^-$ stretching mode. (e) Unrelaxed surface scan (DKH-PBE0/old-DKH-TZVPP) energies plotted as a function of Pn$^+$–O$^-$ bond contraction/elongation from the equilibrium bond length ($r_0$). Dashed lines represent the best quadratic fit to the points. Force constants for the Pn$^+$–O$^-$ stretching modes obtained from the quadratic fit are shown in panel (f). Force constants shown here and those obtained from diagonalization of the Hessian matrix with respect to potential energy are tabulated in Table B.17.

understand the variation in the strengths of the $Pn^+–O^-$ bonds, we estimated the $Pn^+–O^-$ stretching force constants by performing an unrelaxed surface scan (DKH-PBE0/old-DKH-TZVPP). Plots of the change in energy as a function of deviation from equilibrium reveal that the potential energy well becomes shallower as the family is descended (Figure 3.5e). These potential energy surfaces are modeled well by a simple quadratic harmonic oscillator and the extracted force constants systematically decrease with increasing pnictogen size (Figure 3.5f) ($Dipp_3PO$: 9.01; $Dipp_3AsO$: 6.85; $Dipp_3SbO$: 5.66 mdyne $Å^{-1}$). The same trend is seen in the elements of the diagonalized Hessian matrices that correspond to the nominal $Pn^+–O^-$ stretching modes: $k_{(P–O)}$ = 8.29, $k_{(As–O)}$ = 6.34, $k_{(Sb–O)}$ = 5.36 mdyne $Å^{-1}$. This correspondence highlights that the Pn–O stretch is relatively decoupled from other vibrations.

## 3.4 – Electronic structure of $Dipp_3PnO$

A single-point energy calculation (DKH-PBE0/old-DKH-TZVPP) was performed on each optimized structure. Topological analysis of the theoretical electron density along the Pn–O interatomic vector revealed that $\rho_{bcp}$ systematically shifts toward the O atom and decreases in magnitude as the period is descended, indicative of a weakening bonding interaction ($Dipp_3PO$: 0.2317; $Dipp_3AsO$: 0.2156; $Dipp_3SbO$: 0.1735 $e^-$ $Å^{-3}$) (Figure 3.6e). The Laplacian features a single minimum in the valence region that decreases and biases towards the pnictogen as the group is descended (Figure 3.6e). In addition to the value at the local minimum, there is a decrease in the negative character of $\nabla^2\rho$ across the entire valence region as the family is descended, which is indicative of a lesser concentration of charge between the atoms and a weaker bonding interaction. The results of $\rho$ and $\nabla^2\rho$ agree with our earlier topological analysis of simpler compounds.[12] The bond path topologies approximate
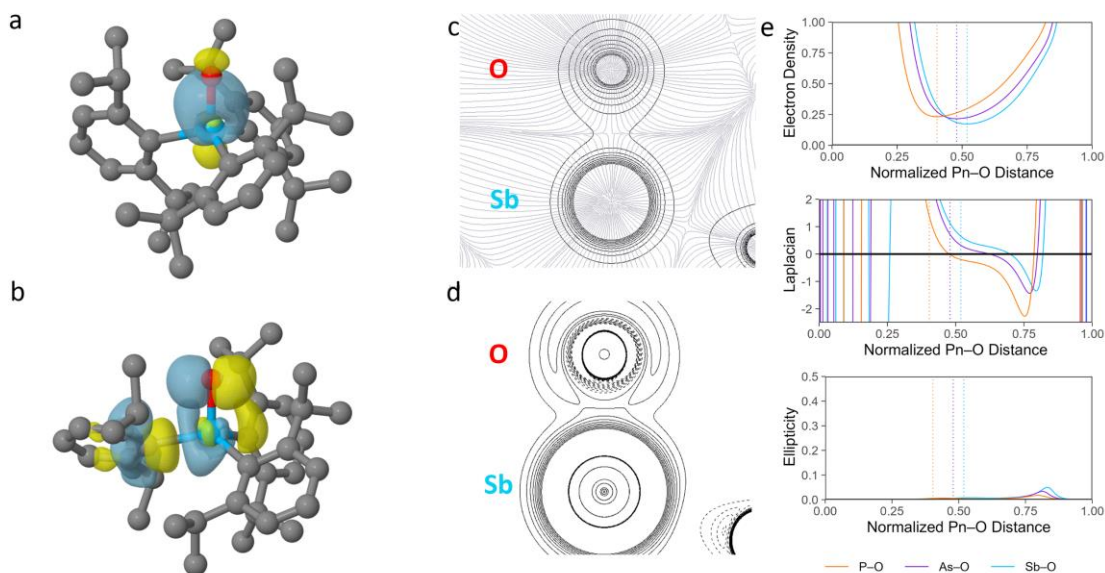
**Figure 3.6.** The structure and bonding of Dipp$_3$SbO, a monomeric stibine oxide. Surface plots (isovalue = 0.05) depicting the Sb–O bonding natural localized molecular orbital (NLMO, a) and overlap of O lone pair and Sb–C antibonding pre-orthogonalized NLMOs (b). Color code: Sb teal, O red, C grey, H white (c) Contour plot of ρ overlaid with the gradient field lines of ρ for the Sb–O bond. (d) Contour plot of $\nabla^2\rho$ for the Sb–O bond with positive values contoured with solid lines and negative values contoured with dashed lines. (e) Values of ρ (e$^{-}$Å$^{-3}$), $\nabla^2\rho$ (e$^{-}$Å$^{-5}$), and ε for Dipp$_3$Pn (Pn = P, As, Sb) along the Pn–O bond paths, with Pn at left and O at right along the horizontal axis. The bond length is normalized to 1.00. The location of the (3, −1) critical point is shown with a dashed vertical line.

cylindrical symmetry with low ε values along the entire bond path. There is a small maximum that biases towards the O atom and increases in magnitude as the group is descended, which we suspect arises from interaction with the isopropyl substituents.[13] For all three compounds, analysis of the topology of ρ identified bond paths between the O atom and proximal benzylic H atoms (Figures B.78-80).

We next turned to information-rich molecular orbital-based methods. Each pnictine oxide under study features nearly degenerate HOMO and HOMO–1 orbitals with large contribution from the O-atom lone pairs (Figure 3.7). The energy of the HOMO increases systematically as the family is descended. This trend is expected because the reduced capacity

to delocalize into the larger, more diffuse Pn–C σ* orbitals destabilizes the O-atom lone pairs. The higher energy of the HOMO suggests that Dipp₃SbO should be the strongest Lewis base of the series. Although there is significant Sb–O σ* antibonding orbital contribution to the
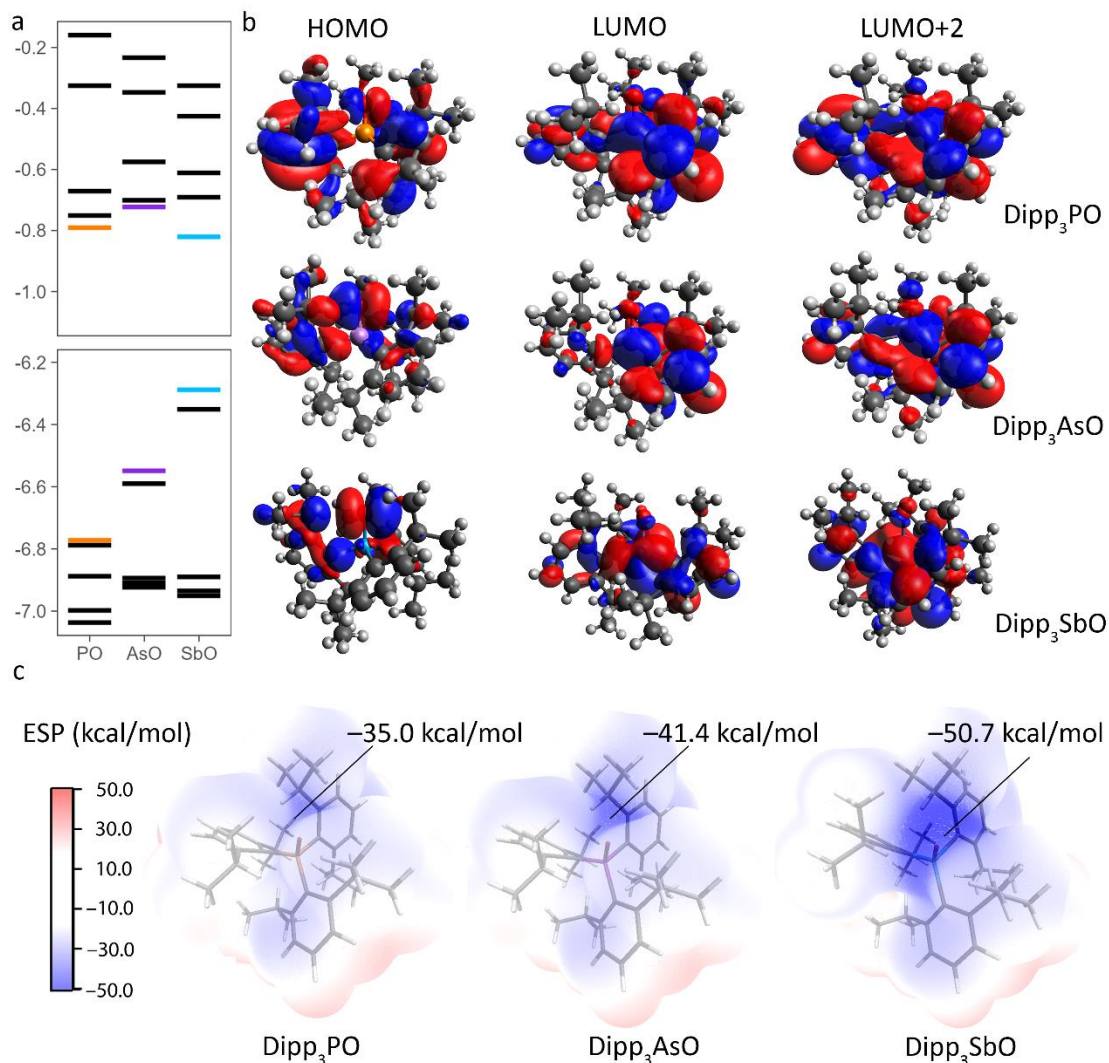


**Figure 3.7.** Variation in the electronic structure of the pnictine oxides Dipp₃Pn (Pn = P, As, Sb). (a) Calculated orbital energies (DKH-PBE0/old-DKH-TZVPP//PBE0/def2-TZVPP) in eV with frontier molecular orbitals shown in color (P orange, As purple, Sb teal). (b) Canonical molecular orbital diagrams of Dipp₃PO, Dipp₃AsO, and Dipp₃SbO. Color code surfaces: red positive, blue negative (isovalue = 0.02). (c) Electrostatic surface potential (ESP)-mapped van der Waals surfaces of Dipp₃Pn (Pn = P, As, Sb), values in kcal mol⁻¹. The value of the surface minimum is displayed. Color code: C grey, H white, O red, P orange, As purple, Sb teal.

LUMO of Dipp$_3$SbO, the LUMOs of Dipp$_3$PO and Dipp$_3$AsO are substantially more delocalized and feature significant $\pi$ and $\pi^*$ contributions from the aryl substituents. The LUMO+2 features appreciable Pn–O $\sigma^*$ character for the lighter species, but there is again a significant amount of delocalization and contribution from the aryl rings. Although the delocalization in the unoccupied orbital complicates direct comparison, the LUMO of Dipp$_3$SbO is the lowest in energy, which is consistent with trends observed for other classes of pnictogen compounds.[14] This trend has been exploited to develop extremely Lewis acidic tetrasubstituted antimony(V) compounds.[15] Finally, we note that the HOMO-LUMO gap systematically decreases as the group is descended, a feature that provides a foreshadowing of the biphilicity of the stiboryl group, described in depth in Chapter 6 for Mes$_3$SbO.

The complications introduced into the analysis above by the extensive delocalization of canonical molecular orbital can be addressed using Natural Bond Orbital (NBO) analysis, which transforms the canonical orbitals into NBOs that are more readily interpreted according to standard Lewis models of chemical structure and bonding. All three pnictine oxides each have NBOs that correspond well to a Pn–O $\sigma$ bonding orbital (Figure 3.6a), a Pn–O $\sigma^*$ antibonding orbital, two O-centered lone pairs, and three Pn–C $\sigma^*$ antibonding orbitals. Second order perturbation theory analysis identified donor–acceptor interactions between the O-centered lone pairs and the Pn–C $\sigma^*$ orbitals in all Dipp$_3$PnO species (Figure 3.6b). The energy of stabilization afforded by this delocalization of electron density systematically decreases with increasing size of the pnictogen (Table B.15). The extent to which deletion of all dative interactions between the O atom and the Dipp$_3$Pn fragment destabilizes the molecule follows a similar descending trend. Consequently, the natural charge on the O atom becomes increasingly negative as the series is descended. The increased separation of charge

for the heavier pnictogens is expected as backdonation from the O-centered lone pairs is disrupted and the electronegativity difference between the Pn and O atoms increases. The impact of these electronic effects on bonding are reflected in the Wiberg bond index (WBI), which decreases systematically as the pnictogen becomes heavier (Table B.15).

Natural localized molecular orbital (NLMO) analysis was performed on each pnictine oxide to evaluate variation in the Pn–O σ-bond composition across the series (Table B.15). Each Pn–O bonding NLMO is polarized towards the oxygen, but the hybridization of the contributing Pn and O-centered orbitals varies systematically. The contribution from the pnictogen increases in s-character and decreases in p-character as the series is descended, whereas the O-atom contribution increases in p-character and decreases in s-character. In the pnictines, enrichment of the Pn-based atomic orbital that contributes to the Pn–C bonding orbital in p-character is expected as heavier atoms have a lower propensity for s,p-orbital hybridization. This variation is in agreement with the observation of narrowing C–Pn–C angles with increasing Pn atomic number. Consequently, the lone pair of pnictines is enriched in s-character and the O atom thus engages with an increasingly s-enriched pnictogen-based orbital to form the Pn–O bond as the series is descended.

The accumulation of electron density on the O atom is reflected in the magnitude of the electrostatic surface potential minimum (Figure 3.7c). $Dipp_3SbO$ also clearly maintains more steric access to the region of maximum negative surface potential of the series. An energy decomposition analysis of O and $Dipp_3Pn$ fragments also highlights the diminishing stability of the pnictoryl bonds as the Pn atom becomes heavier, as reflected in the ratio $DE_{orb}/DE_{total}$ (Tables B.8–10). A redistribution of charge density between a $Dipp_3Pn$ fragment

to the O atom also demonstrates the enhanced polarity of Dipp$_3$SbO relative to the lighter congeners (Figure B.85).

As noted above, intramolecular H-bonding interactions are present in all cases. Donor-acceptor interactions between O-centered lone pairs to the $^i$Pr C–H antibonding orbitals for Dipp$_3$Pn appear in the second-order perturbation analysis and are visualized in Figure B.88. Such interactions also manifest in the electron density topology; non-covalent interaction analysis of Dipp$_3$SbO (Figure B.84) reveals negative sign($\lambda_2$)$\rho$ in the space between the O and $^i$Pr C–H. The H-bonds are stronger in the case of Dipp$_3$SbO, highlighting the enhanced basicity of the group.

### 3.5 – Reactivity of Dipp$_3$PnO

With a genuine monomeric stibine oxide in hand for the first time, we explored its reactivity in response to a variety of substrates (Figure 3.8). We began by exploring its capacity to H-bond with external reagents. A cooled solution of Dipp$_3$SbO in neat 4-fluoroaniline (Figure 3.8a) resulted in crystal growth of an H-bonded adduct Dipp$_3$SbO·H$_2$NPhF (Figure 3.9a). HAR found the H-bonding H atom of Dipp$_3$SbO·H$_2$NPhF to reside on the N atom with an N–H distance of 1.04(2) Å. The H-bonding interaction is of moderate strength, with an N···O
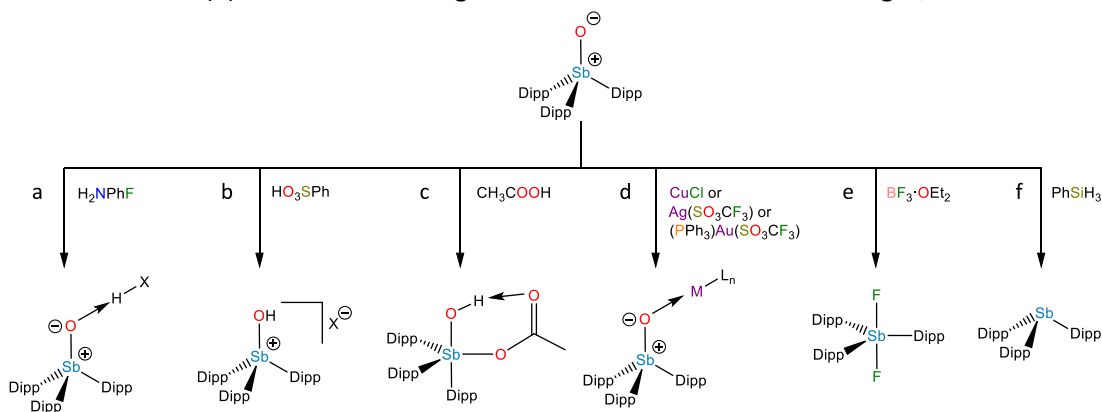


**Figure 3.8.** Reactivity of Dipp$_3$SbO.

distance of 2.858(1) Å. The Sb–O bond lengthens slightly to 1.8421(7) Å and the Sb–O IR
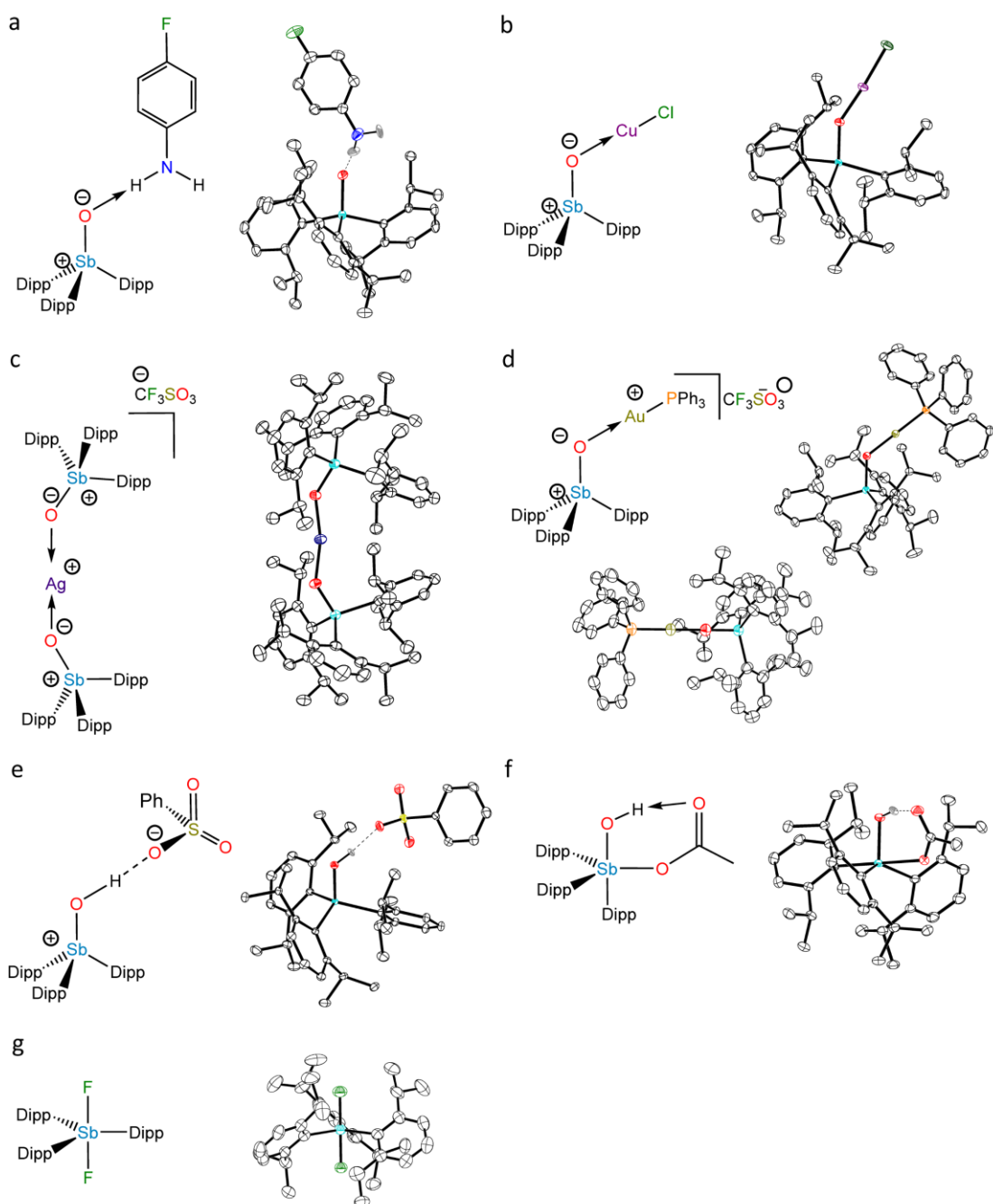


**Figure 3.9.** Molecular diagrams and thermal ellipsoid plots (50% probability) of (a) $Dipp_3SbO·H_2NPhF$ (b) $Dipp_3SbOCuCl·(CHCl_3)_2$ (c) $[Ag(Dipp_3SbO)_2](CF_3SO_3)·OEt_2$ (d) $[Dipp_3SbOAuPPh_3][CF_3SO_3]$ (e) $[Dipp_3SbOH][O_3SPh]$ (f) *cis*-$Sb(OH)(OAc)Dipp_3$ (g) *trans*-$Dipp_3SbF_2$. Color code: Sb teal, O red, C black, H grey, N blue, Ag purple, F green, S yellow, Au gold, P orange, Cu mauve.

stretching frequency decreases from 779 cm$^{-1}$ for Dipp$_3$SbO to 762 cm$^{-1}$ for Dipp$_3$SbO·H$_2$NPhF. Under similar conditions, neither Dipp$_3$AsO nor Dipp$_3$PO result in a similar product, likely due to their lower Brønsted basicity.

We next explored the capacity of Dipp$_3$SbO to act as a Lewis base and ligand in coordination chemistry (Figure 3.8d). Treatment of Dipp$_3$SbO with a single equivalent of CuCl resulted in the formation of (Dipp$_3$SbO)CuCl (Figure 3.9b). Treatment of Dipp$_3$SbO half an equivalent of AgOTf resulted in the bis-coordinated silver complex [(Dipp$_3$SbO)$_2$Ag][OTf] (Figure 3.9c). ClAu(PPh$_3$) was treated with AgOTf to replace the chloride ion with a weakly coordinating and readily displaceable triflate ion. Subsequent treatment of the solution with Dipp$_3$SbO yielded the gold complex [(Dipp$_3$SbO)Au(PPh$_3$)][OTf] (Figure 3.9d). All three of the coinage metal stibine oxide complexes exhibit significantly non-linear Sb–O–M angles in the solid state (Table B.18). However, a second polymorph of [(Dipp$_3$SbO)Au(PPh$_3$)][OTf] exhibits a rigorously linear configuration. No evidence of complex formation between these metal salts and Dipp$_3$AsO nor Dipp$_3$PO was observed in spectral data (Figures B.49-51).

Dipp$_3$SbO was protonated by the strong Brønsted acid, PhSO$_3$H, (Figure 3.8b) to afford the hydroxystibonium salt [Dipp$_3$Sb(OH)][O$_3$SPh] (Figure 3.9e). This species had structural and spectral features comparable to the hydroxystibonium salts discussed in Chapter 2, with an Sb–O bond length of 1.9119(7) Å and a $v_{SbO}$ of 611 cm$^{-1}$. Dipp$_3$AsO also accepts a proton from PhSO$_3$H to form [Dipp$_3$As(OH)][O$_3$SPh] under similar conditions (Figure B.99). In contrast, it was necessary to titrate a solution of Dipp$_3$PO with up to 10 equivalents of PhSO$_3$H to observe an equilibrium with the hydroxyphosphonium species by $^1$H NMR (Figures B.59–60).

Dipp$_3$SbO was treated with iodobenzene in an attempt to isolate a halogen-bonded product. However, such a product was not observed, but crystals of *cis*-Sb(OH)(OAc)Dipp$_3$ had

formed in quite a welcomed surprise. The commercial iodobenzene must have contained trace amounts of acetic acid but the reaction could be repeated by intentional combination of stoichiometric amounts of AcOH and $Dipp_3SbO$. Acetic acid not only protonates the O atom of $Dipp_3SbO$, but adds across the Sb–O bond (Figure 3.8c, 3.9f), highlighting the unsaturated nature and biphilicity of the stiboryl group. This reaction was the first in which we observed the Sb atom of $Dipp_3SbO$ expand its coordination sphere. The unexpected *cis* configuration occurs despite expectations that the more apicophilic hydroxy and acetoxy groups would reside in the axial positions and that the more sterically demanding Dipp substituents would assume equatorial positions. The stability of the *cis* configuration may be in part attributed to an intramolecular H-bonding interaction between the hydroxy and acetoxy groups (O···O = 2.630(2) Å). No reaction was observed between $Dipp_3AsO$ or $Dipp_3PO$ and acetic acid (Figures B.64–66). Attempts to observe other addition reactions were unsuccessful (Figure B.74). In Chapter 6, I describe a strategy to access enhanced reactivity at the stiboryl unit and I anticipate that this strategy will ultimately permit a range of addition reactions.

Reaction between $Dipp_3SbO$ and $BF_3 \cdot OEt_2$ did not form the expected Lewis adduct, but at −78 °C the reagents cleanly form *trans*-$SbF_2Dipp_3$, which features a $^{19}F$ resonance at −74.35 ppm (Figure 3.8e, 3.9g). This reaction was the first in which we observed cleavage of the Sb–O bond. The Sb center maintains its +5 oxidation state in an oxide-for-two-fluorides group exchange; the fluorophilicity of organoantimony(V) Lewis acids is well documented.[15] The B-containing by-product(s) is(are) likely boroxine species.[16] $Dipp_3AsO$ or $Dipp_3PO$ did not react similarly with $BF_3 \cdot OEt_2$.

Our initial reactivity screening concluded with the result that PhSiH$_3$ cleanly reduces Dipp$_3$SbO to form its parent stibine Dipp$_3$Sb within 1 h at 50 °C (Figure 3.8f). Neither Dipp$_3$AsO nor Dipp$_3$PO reacts with PhSiH$_3$ under similar mild conditions (Figure B.72–73).

## 3.6 – Conclusion

The isolation of Dipp$_3$SbO allowed for the direct investigation of an unperturbed stiboryl group within a tractable material for the first time. We have also isolated and characterized the lighter congeners of the first isolated stibine oxide, allowing us to directly compare the molecular and electronic structure of the new Sb$^+$–O$^-$ bond with the lighter pnictoryl congeners. Several distinct classes of reactivity that arise from this incredibly interesting bonding situation were characterized and the enhanced reactivity of Dipp$_3$SbO relative to Dipp$_3$PnO (Pn = P, As) was evident in these studies.

**3.7 – Experimental methods**

**General methods.** Reagents and solvents were purchased from commercial vendors and used as received unless otherwise specified. Commercially purchased CuCl was purified by dissolution in concentrated HCl followed by dilution with $H_2O$ to precipitate colorless crystals that were washed with ethanol and diethyl ether before being dried *in vacuo*. The dry, colorless crystals of CuCl were ground into a fine powder immediately before use. Tetrahydrofuran (THF), dichloromethane (DCM), and acetonitrile (MeCN) were purified using an Innovative Technology PURE-SOLV solvent purification system. All solvents were dried over 3-Å molecular sieves. All syntheses were performed using flame-dried glassware under a nitrogen atmosphere. NMR spectra were collected using a Bruker Avance III HD 500 spectrometer equipped with a multinuclear Smart Probe. HSQC and HMBC NMR data were collected using a Bruker Avance III HD 800 MHz spectrometer equipped with a TCI cryoprobe. Signals in the $^1H$ and $^{13}C$ NMR spectra are reported in ppm as chemical shifts from tetramethylsilane and were referenced using the $CHCl_3$ ($^1H$, 7.26 ppm), $CHD_2CN$ ($^1H$, 1.94 ppm), $CHD_2C_6D_5$ ($^1H$, 2.08 ppm), $CDCl_3$ ($^{13}C$, 77.16 ppm), and $CD_3CN$ ($^{13}C$, 118.26 ppm) solvent signals. The frequencies of $^{19}F$ NMR signals are reported in ppm as chemical shifts from $CFCl_3$ ($Dipp_3SbO \cdot H_2NPhF$, $[Ag(Dipp_3SbO)_2](CF_3SO_3) \cdot OEt_2$, and $Dipp_3SbOAuPPh_3CF_3SO_3$ referenced to $BF_3 \cdot OEt_2$ at $-152.8$ ppm and *trans*-$Dipp_3SbF_2$ referenced to 4-fluoroaniline at $-126.88$ ppm). $^{31}P$ NMR signals are reported as chemical shifts from 85% $H_3PO_4$ and were referenced using triphenylphosphine ($-5.35$ ppm). Infrared (IR) spectra were collected on KBr pellets using a PerkinElmer Spectrum One FT-IR spectrometer. Mass spectrometry measurements were collected using an LTQ-Orbitrap Velos Pro MS instrument. Elemental analyses were performed by Midwest Microlabs (Indianapolis, IN) using an Exeter CE440 analyzer or by NuMega

Resonance Labs using a Perkin Elmer PE2400-Series II, CHNS/O analyzer. Melting point data were collected with an electrothermal Mel-Temp apparatus and a partial-immersion thermometer; temperatures are uncorrected.

**Synthesis of 1-bromo-2,6-diisopropylbenzene.** 1-Bromo-2,6-diisopropylbenzene was synthesized following a literature procedure.[17] In brief, 2,6-diisopropylaniline (22.5 mL, 119 mmol) was added dropwise to rapidly stirring conc. HBr (100 mL) to form a colorless suspension. The reaction mixture was cooled to –50 °C and $NaNO_2$ (13.24 g, 192 mmol) was added in portions to form a viscous brown suspension. Reddish brown gas evolved from the mixture. The reaction mixture was diluted with conc. HBr (33 mL) and water (33 mL) and held at –50 °C for 1 h. The reaction mixture was then diluted with $OEt_2$ (100 mL) and allowed to warm to –15 °C. The mixture was again cooled to –50 °C and $Na_2CO_3$ (24.5 g, 231 mmol) was added in portions. The mixture was allowed to stir at room temperature overnight. The following day, the solid was removed by vacuum filtration and the filtrate was extracted with $OEt_2$ (150 mL). The aqueous phase was then back-extracted with $OEt_2$ (2 × 50 mL). The combined organic phases were washed with water (2 × 150 mL) and brine (100 mL) before being dried over $Na_2SO_4$ for 15 min. The solvent was stripped to yield a crude red oil that was purified by flash chromatography ($SiO_2$/hexanes) to yield the product as a colorless oil. Yield: 9.10 g (32%). ^{1}H NMR spectroscopic data collected from the product agree with those previously reported.[17] **^{1}H NMR (500 MHz, CDCl$_3$)** $\delta$ 7.24 (d, $J$ = 7.7 Hz, 1H), 7.13 (d, $J$ = 7.6 Hz, 2H), 3.51 (hept, $J$ = 6.9 Hz, 2H), 1.25 (d, $J$ = 6.9 Hz, 12H).

**Synthesis of iodosobenzene.** Iodosobenzene was synthesized following a literature procedure.[18] In brief, iodobenzene diacetate (2.004 g, 6.22 mmol) was suspended in water (75 mL). A solution of NaOH (1.453 g, 36.4 mmol) in water (75 mL) was added dropwise to form a yellow suspension. The reaction mixture was allowed to stir at room temperature for 2 h. The mixture was decanted and diluted with water (100 mL) three times before the solid was collected by vacuum filtration. The yellow powder was washed with water (3 × 10 mL) and chloroform (2 × 5 mL) and dried in vacuo. Yield: 598 mg (44%). No further characterization data were collected.

**Synthesis of triphenylsibine oxide dimer (($Ph_3SbO)_2$) (A).** Triphenylstibine oxide was synthesized according to a literature reference.[4] In brief, triphenylstibine (1.003 g, 2.84 mmol) was dissolved in acetone (27 mL) and 50% $H_2O_2$ in water (140 μL) was added to the colorless solution. An amorphous precipitate formed and the supernatant was decanted. Colorless crystals grew from the supernatant. The mother liquor was decanted and the crystals were washed with hexanes before being collected by vacuum filtration. Yield: 35 mg (3.5%). ^{1}H NMR spectroscopic data collected from the product agree with those previously reported.[4] **^{1}H NMR (500 MHz, CDCl₃)** $\delta$ 8.26 − 8.17 (m, 6H), 7.75 (d, $J$ = 7.0 Hz, 6H), 7.57 − 7.43 (m, 9H), 7.42 − 7.31 (m, 9H).

**Synthesis of trimesitylstibine.** Trimesitylstibine was synthesized following a reported protocol.[19] In brief, a dry 250 mL two-necked round bottom flask fitted with a water-jacketed Liebig condenser was charged with a stir bar and magnesium turnings (693 mg, 28.5 mmol). The magnesium turnings were suspended in dry THF (80 mL) and activated with 1,2-

dibromoethane (618 mL, 7.2 mmol). 2-Bromomesitylene (3.22 mL, 21.3 mmol) was added dropwise to the mixture and the reaction was refluxed for 3 h. The reaction mixture was cooled to room temperature and a solution of $SbCl_3$ (1.619 g, 7.1 mmol) in THF (18 mL) was added dropwise. The reaction mixture was refluxed overnight. The reaction mixture was cooled to room temperature and diluted with $OEt_2$ (150 mL) and water (150 mL). The aqueous layer was back-extracted with $OEt_2$ (2 × 50 mL). The combined organic phases were then washed with water (2 × 150 mL) and with brine (100 mL). The organic layer was dried over $Na_2SO_4$. The solvent was removed under reduced pressure to yield a crude yellow oil. Ethanol was added dropwise with sonication to precipitate a white powder that was collected via vacuum filtration. The product was washed with ethanol (3 × 5 mL) and dried under vacuum. $^1$H NMR spectroscopic data collected from the product agree with those previously reported.[19] **$^1$H NMR (500 MHz, CDCl$_3$)** δ 6.83 (6 H, s), 2.29 (18 H, s), 2.27 (9 H, s).

**Synthesis of *trans*-dihydroxytrimesitylstibine (Mes₃Sb(OH)₂) (B).** *trans*-Dihydroxytrimesitystiborane was synthesized following a reported protocol.[20] 50% $H_2O_2$ in water (200 μL) was added to a solution of trimesitylstibine (274 mg, 576 μmol) in acetone (40 mL). The reaction mixture was allowed to stir at room temperature for 1 h. The solvent was stripped to yield a white powder. The product was suspended in hexanes and collected by vacuum filtration. Yield: 240 mg (81%). $^1$H NMR spectroscopic data collected from the product agree with those previously reported.[20] **$^1$H NMR (500 MHz, CDCl₃)** δ 6.97 (6 H, s), 2.57 (18 H, s), 2.31 (9 H, s).

**Synthesis of tris(2,6-diisopropylphenyl)stibine (Dipp₃Sb).** A dry 250 mL two-necked round bottom flask fitted with a water-jacketed Liebig condenser was charged with a stir bar and magnesium turnings (405 mg, 16.6 mmol). The magnesium turnings were suspended in dry THF (30 mL) and activated with 1,2-dibromoethane (360 mL, 4.2 mmol). 1-Bromo-2,6-diisopropylbenzene (2.6 mL, 12.5 mmol) was then added dropwise and the reaction was refluxed for 3 h. After the magnesium turnings had been consumed, the colorless solution was cooled to –78 °C and CuCl (1.244 g, 12.5 mmol) was added against a backflow of $N_2$. The reaction mixture was allowed to warm to room temperature and stir overnight. The resulting suspension was cooled to –78 °C and a solution of trichlorostibine (0.950 g, 4.2 mmol) in THF (10 mL) was then added dropwise to the reaction mixture. The reaction mixture was stirred at room temperature for 4 h before being refluxed for 20 h. The reaction mixture was cooled to room temperature and diluted with $OEt_2$ (150 mL) and water (150 mL). The aqueous layer was back-extracted with $OEt_2$ (2 × 50 mL). The combined organic phases were then washed with water (2 × 150 mL) and with brine (150 mL). The organic layer was dried over $Na_2SO_4$. The solvent was removed under reduced pressure. The resulting yellow oil was diluted with hexanes and purified by flash chromatography ($SiO_2$/hexanes). The collected fractions were stripped of solvent to obtain a white powder. This crude product was of sufficient purity for the routine synthesis of Dipp₃SbO. Yield: 1.464 g (58%). To obtain analytically pure material, 684 mg of crude product was recrystallized from a mixture of MeCN/$OEt_2$ to yield 410 mg (60%) of colorless crystals. Crystals suitable for X-ray diffraction were obtained similarly. M.p. 210 °C. **Found:** C, 71.83; H, 8.70%. **Calc. for C₃₆H₅₁Sb:** C, 71.40; H, 8.49%. **ESI-MS (*m/z*) [M+H]⁺** 605.26 (calc 605.3). **¹H NMR (500 MHz, CDCl₃)** δ 7.27 (t, *J* = 7.5 Hz, 3H), 7.13 (d, *J* = 8.1 Hz, 6H), 3.34 (hept, *J* = 6.6 Hz, 6H), 1.35 (d, *J* = 6.5 Hz, 9H), 1.14 (d, *J* = 6.1, 9H), 1.13 (d, *J* = 6.1, 9H),

0.55 (d, *J* = 6.5 Hz, 9H). $^{13}$**C{$^1$H} NMR (125 MHz, CDCl$_3$)** δ 155.35, 155.08, 140.95, 129.14, 124.86, 122.99, 37.33, 36.28, 26.08, 25.01, 24.58, 23.32.

**Synthesis of tris(2,6-diisopropylphenyl)arsine (Dipp$_3$As).** A dry 100 mL two-necked round bottom flask fitted with a water-jacketed Liebig condenser was charged with a stir bar and magnesium turnings (0.3096 mg, 12.7 mmol). The magnesium turnings were suspended in dry THF (30 mL) and activated with 1,2-dibromoethane (275 mL, 3.2 mmol). 1-Bromo-2,6-diisopropylbenzene (1.97 mL, 9.6 mmol) was then added dropwise and the reaction was refluxed for 3 h. After the magnesium turnings had been consumed, the colorless solution was cooled to −78 °C and CuCl (0.946 g, 9.6 mmol) was added against a backflow of N$_2$. The reaction mixture was allowed to warm to room temperature and stir overnight. The resulting suspension was cooled to −78 °C and a solution of trichloroarsine (577 mg, 3.2 mmol) in THF (8 mL) was then added dropwise to the reaction mixture. The reaction mixture was allowed to warm to room temperature and then stirred for 30 min before being refluxed for 24 h. The reaction mixture was cooled to room temperature and diluted with OEt$_2$ (150 mL) and water (150 mL). The aqueous layer was back-extracted with OEt$_2$ (2 × 50 mL). The combined organic phases were then washed with water (2 × 150 mL) and with brine (150 mL). The organic layer was dried over Na$_2$SO$_4$. The solvent was removed under reduced pressure to yield a white solid coated in oil. The residue was suspended in MeCN and collected by vacuum filtration. The powder was recrystallized from a mixture of MeCN and OEt$_2$ to yield 1.001 g (56%) of colorless crystals. Crystals suitable for X-ray diffraction were obtained similarly. M.p. 220 °C (decomp). **Found:** C, 77.17; H, 9.29%. **Calc. for C$_{36}$H$_{51}$As:** C, 77.39; H, 9.20%. **ESI-MS (*m/z*) [M+H]$^+$** 558.2 (calc 558.3). $^1$**H NMR (500 MHz, CDCl$_3$)** δ 7.26 (t, *J* = 7.7 Hz, 3H), 7.09 (d, *J* = 7.7

Hz, 6H), 3.43 (hept, $J$ = 6.6 Hz, 3H), 3.29 (hept, $J$ = 6.6 Hz, 3H), 1.28 (d, $J$ = 6.6 Hz, 9H), 1.10 (d, $J$ = 6.8 Hz, 9H), 1.04 (d, $J$ = 6.7 Hz, 9H), 0.50 (d, $J$ = 6.6 Hz, 9H). $^{13}$C{$^1$H} NMR (125 MHz, CDCl$_3$) δ 153.63, 153.20, 139.44, 128.95, 125.24, 122.97, 33.83, 32.95, 25.50, 24.38, 24.15, 22.86.

**Synthesis of tris(2,6-diisopropylphenyl)phosphine (Dipp$_3$P).** A dry 100 mL two-necked round bottom flask fitted with a water-jacketed Liebig condenser was charged with a stir bar and magnesium turnings (0.5103 g, 20.9 mmol). The magnesium turnings were suspended in dry THF (30 mL) and activated with 1,2-dibromoethane (0.45 mL, 5.2 mmol). 1-Bromo-2,6-diisopropylbenzene (3.31 mL, 15.7 mmol) was then added dropwise and the reaction was refluxed for 3 h. After the magnesium turnings had been consumed, the colorless solution was cooled to −78 °C and CuCl (1.559 g, 15.7 mmol) was added against a backflow of N$_2$. The reaction mixture was allowed to warm to room temperature and stir overnight. The resulting suspension was cooled to −78 °C and a solution of trichlorophosphine (0.711 g, 5.2 mmol) in THF (10 mL) was added dropwise to the reaction mixture. The reaction mixture was warmed to room temperature and stirred for 30 min before being refluxed for an additional 24 h. The reaction mixture was cooled to room temperature and diluted with OEt$_2$ (150 mL) and water (150 mL). The aqueous layer was back-extracted with OEt$_2$ (2 × 50 mL). The combined organic phases were then washed with water (2 × 150 mL) and with brine (150 mL). The organic layer was dried over Na$_2$SO$_4$. The solvent was removed under reduced pressure to yield a pale green solid coated in oil. The residue was suspended in MeCN and collected by vacuum filtration. The solid was recrystallized from a mixture of MeCN and OEt$_2$ to yield 1.445 g (53%) of pale yellow-green crystals. Crystals suitable for X-ray diffraction were obtained similarly. M.p. 313 °C (decomp). **Found:** C, 83.98; H, 10.01%. **Calc. for C$_{36}$H$_{51}$P:** C, 84.00; H, 9.99%. **ESI-MS (*m/z*)**

[M+H]$^+$ 515.4 (calc 515.4). **$^1$H NMR (500 MHz, CDCl$_3$)** δ 7.27 (t, *J* = 7.7 Hz, 3H), 7.08 (dd, *J* = 7.7, 3.3 Hz, 6H), 3.49 (hept, *J* = 6.5 Hz, 3H), 3.48 (hept, *J* = 6.5 Hz, 3H), 1.16 (d, *J* = 6.7 Hz, 18H), 0.71 (d, *J* = 6.7 Hz, 18H). **$^{13}$C{$^1$H} NMR (125 MHz, CDCl$_3$)** δ 153.38 (d, *J* = 8.75 Hz), 135.13 (d, *J* = 25.6 Hz), 129.18, 124.20 (d, *J* = 4.3 Hz), 32.23 (d, *J* = 17.6 Hz), 24.69, 23.12. **$^{31}$P{$^1$H} NMR (202 MHz, CDCl$_3$)** δ −50.41.

**Synthesis of tris(2,6-diisopropylphenyl)stibine oxide (Dipp$_3$SbO).** Dipp$_3$Sb (1.35 g, 2.2 mmol) was added to a suspension of iodosobenzene (502 mg, 2.3 mmol) in DCM (20 mL). The solid was rapidly consumed to produce a faintly yellow hazy solution. The reaction mixture was passed through a Celite pad to remove excess iodosobenzene and the filtrate was stripped of its solvent to yield a white powder coated with a pale yellow oil. The crude product was washed with cold pentane to yield Dipp$_3$SbO as an analytically pure colorless solid. Yield: 862 mg (62%). Crystals (monoclinic polymorph) suitable for X-ray diffraction were grown from pentane. Dipp$_3$SbO (492 mg) was recrystallized from hot MeCN to obtain large colorless block crystals (398 mg, 81%). Crystals (orthorhombic polymorph) suitable for X-ray diffraction were grown similarly. M.p. 181 °C. **Found:** C, 69.22; H, 8.33% **Calc. for C$_{36}$H$_{51}$OSb:** C, 69.57; H, 8.27%. **ESI-MS (*m/z*) [M+H]$^+$** 621.27 (calc 621.3). **IR (KBr, cm$^{-1}$)** $v_{SbO}$ 779 (s). **$^1$H NMR (500 MHz, CDCl$_3$)** δ 7.41 (t, *J* = 7.7 Hz, 3H), 7.32 (d, *J* = 6.9 Hz, 3H), 7.17 (d, *J* = 6.8 Hz, 3H), 4.41 (br s, 3H), 3.01 (br s, 3H), 1.45 (br s, 9H), 1.17 (br s, 9H), 0.99 (br s, 9H), 0.71 (br s, 9H**). $^1$H NMR (500 MHz, CD$_3$CN)** δ 7.47 (t, *J* = 7.7 Hz, 3H), 7.37 (d, *J* = 7.5 Hz, 3H), 7.30 (d, *J* = 7.6 Hz, 3H), 4.22 (hept, *J* = 6.3 Hz, 3H), 3.01 (hept, *J* = 6.2 Hz, 3H), 1.36 (d, *J* = 5.4 Hz, 9H), 1.19 (d, *J* = 5.8 Hz, 9H), 0.97 (d, *J* = 6.0 Hz, 9H), 0.71 (d, *J* = 5.6 Hz, 9H). **$^{13}$C{$^1$H} NMR**

**(125 MHz, CDCl$_3$)** δ 157.28, 152.01, 142.03, 131.46, 126.72, 125.08, 36.93, 33.90, 27.39 (br s), 24.83 (br s, 2C), 24.42 (br s).

**Synthesis of tris(2,6-diisopropylphenyl)arsine oxide (Dipp$_3$AsO).** Dipp$_3$As (511 mg, 0.9 mmol) and *m*CPBA (238 mg, 1.4 mmol) were dissolved in DCM (25 mL) to form a colorless solution that was allowed to stir at room temperature. The reaction was monitored by TLC (hexanes/SiO$_2$). After 2 h, no starting material was detectable by TLC, and the reaction mixture was diluted with 50 mL DCM and washed with a saturated aqueous solution of NaHCO$_3$ (50 mL) and brine (50 mL). The organic phase was dried over Na$_2$SO$_4$ before being stripped of solvent under reduced pressure to yield a white powder. The crude product was dissolved in ethyl acetate and purified by flash chromatography (1:4 ethyl acetate:hexanes/SiO$_2$). Crystals suitable for X-ray diffraction were grown in bulk from a mixture of OEt$_2$ and MeCN. The solvent was decanted, and the colorless crystals were washed with MeCN and dried *in vacuo*. Yield: 274 mg (54%) M.p. 298 °C (decomp). **Found:** C, 75.23; H, 8.91%. **Calc. for C$_{36}$H$_{51}$AsO:** C, 75.24; H, 8.94 %. **ESI-MS (*m/z*) [M+H]$^+$** 575.3 (calc 575.3). **$^1$H NMR (500 MHz, CDCl$_3$)** δ 7.38 (t, *J* = 7.6 Hz, 3H), 7.30 (d, *J* = 7.5 Hz, 3H), 7.14 (d, *J* = 7.5 Hz, 3H), 3.97 (hept, *J* = 6.4 Hz, 3H), 3.25 (hept, *J* = 9.5 Hz, 3H), 1.41 (d, *J* = 6.2 Hz, 9H), 1.11 (d, *J* = 6.5 Hz, 9H), 0.94 (d, *J* = 6.7 Hz, 9H), 0.70 (d, *J* = 6.3 Hz, 9H). **$^{13}$C{$^1$H} NMR (125 MHz, CDCl$_3$)** δ 155.73, 149.57, 142.76, 130.92, 126.87, 124.96, 33.38, 32.02, 27.54, 25.20, 24.08.

**Synthesis of tris(2,6-diisopropylphenyl)phosphine oxide (Dipp$_3$PO).** Dipp$_3$P (91 mg, 0.17 mmol) and *m*CPBA (124 mg, 0.71 mmol) were dissolved in DCM (25 mL) to form a pink solution that was allowed to stir at room temperature. The reaction was monitored by TLC

(hexanes/SiO$_2$). After 2 h, no starting material was detectable by TLC, and the reaction mixture was diluted with DCM (40 mL) and washed with a saturated aqueous solution of NaHCO$_3$ (40 mL) and brine (40 mL). During the washes, the pink color was discharged from the organic phase, which was dried over Na$_2$SO$_4$ before being stripped of solvent under reduced pressure to yield a white powder. The crude product was dissolved in ethyl acetate and purified by flash chromatography (1:5 ethyl acetate:hexanes/SiO$_2$). Crystals suitable for X-ray diffraction were grown in bulk from a mixture of OEt$_2$ and MeCN. The solvent was decanted, and the colorless crystals were washed with MeCN and dried *in vacuo*. Yield: 51.2 mg (55%) M.p. 228 °C (decomp). **Found:** C, 80.92; H, 9.87%. **Calc. for C$_{36}$H$_{51}$PO:** C, 81.46; H, 9.69 %. **ESI-MS (*m/z*) [M+H]$^+$** 531.3751 (calc 531.3750). **$^1$H NMR (500 MHz, CDCl$_3$)** δ 7.37 (t, *J* = 7.7 Hz, 3H), 7.27 (dd, *J* = 4.5, 3.5 Hz, 3H), 7.12 (dd, *J* = 7.6, 4.4 Hz, 3H), 3.37 (hept, *J* = 6.6 Hz, 3H), 3.31 (hept, *J* = 6.6 Hz, 3H), 1.32 (d, *J* = 6.4 Hz, 9H), 1.07 (d, *J* = 6.7 Hz, 9H), 0.94 (d, *J* = 6.8 Hz, 9H), 0.66 (d, *J* = 6.5 Hz, 9H). **$^{13}$C{$^1$H} NMR (125 MHz, CDCl$_3$)** δ 156.73 (d, *J* = 8.8 Hz), 149.36 (d, *J* = 11.4 Hz), 139.04 (d, *J* = 91.3 Hz), 130.695 (d, *J* = 3.8 Hz), 126.08 (d, *J* = 10 Hz), 124.31 (d, *J* = 10 Hz), 32.34, 32.29, 32.25, 26.86, 24.81, 23.76. **$^{31}$P{$^1$H} NMR (202 MHz, CDCl$_3$)** δ 25.33. The elemental composition of Dipp$_3$PO found from elemental analysis was consistently outside of the acceptable deviation from the theoretical value. In addition to the NMR spectra, we also obtained PXRD data from freshly prepared bulk solid; these powder data agreed with the simulated powder diffractogram generated from the crystal structure of Dipp$_3$PO (Figure B.27). Furthermore, high-resolution mass spectrometry data were collected to corroborate the proposed elemental composition.

**Synthesis of tris(2,6-diisopropylphenyl)stibine oxide 4-fluoroaniline (Dipp₃SbO·H₂NPhF).** A solution of Dipp₃SbO (76 mg, 0.12 mmol) in neat 4-fluoroaniline (200 mL) was cooled to 4 °C to grow colorless crystals suitable for X-ray diffraction. The crystals were collected by vacuum filtration and dried under vacuum. Yield: 4 mg (4%). **IR (KBr, cm⁻¹)** $v_{SbO}$ 762 (s). **¹H NMR (500 MHz, CDCl₃)** δ 7.41 (t, $J$ = 7.6 Hz, 3H), 7.33 (br s, 3H), 7.18 (br s, 3H), 6.85 (t, $J$ = 8.6 Hz, 2H), 6.66-6.58 (m, 2H), 4.42 (br s, 3H), 3.52 (br s, 2H), 3.02 (br s, 3H), 1.44 (br s, 9H), 1.17 (br s, 9H), 1.00 (br s, 9H), 0.72 (br s, 9H). **¹³C{¹H} NMR (125 MHz, CDCl₃)** δ 157.40 (br s), 156.67 (d, $J$ = 235 Hz), 152.08, 142.58, 142.16, 131.48, 126.76, 125.10, 116.23 (d, $J$ = 7.5 Hz), 115.83 (d, $J$ = 22.5 Hz), 36.94, 33.91, 27.38, 24.86 (br s, 2C), 24.46. **¹⁹F{¹H} NMR (470 MHz, CDCl₃)** δ −126.88. Compound Dipp₃SbO·H₂NPhF is thermally unstable and elemental analyses were consistently unsuccessful. In addition to the NMR spectra, we also obtained PXRD data from freshly prepared bulk solid; these powder data agreed with the simulated powder diffractogram generated from the crystal structure of Dipp₃SbO·H₂NPhF (Figure B.33).

**Synthesis of (tris(2,6-diisopropylphenyl)stibine oxide)chlorocopper(I) chloroform disolvate (Dipp₃SbOCuCl·(CHCl₃)₂).** Dipp₃SbO (48.5 mg, 0.07 mmol) and CuCl (7.7 mg, 0.07 mmol) were dissolved in MeCN (8 mL) and stirred for 15 min at room temperature. OEt₂ (30 mL) was added to the colorless solution and the reaction mixture was stripped of solvent under reduced pressure. The resulting colorless solid was suspended in pentane and collected by vacuum filtration. The white solid was recrystallized by vapor diffusion of pentane into chloroform. Crystals suitable for X-ray diffraction were grown similarly. Yield: 16 mg (21%). M.p. 202 °C (decomp). **IR (KBr, cm⁻¹)** $v_{SbO}$ 732. **ESI-MS (*m/z*) [M−Cl]⁺** 683.2253 (calc. 683.2268); **[M−Cl+Dipp₃SbO]⁺** 1303.5243 (calc. 1303.5246). **¹H NMR (500 MHz, CDCl₃)** δ 7.49 (t, $J$ = 7.6 Hz,

3H), 7.38 (d, *J* = 7.4 Hz, 3H), 7.24 (d, *J* = 7.5 Hz, 3H), 3.80 (br hept, 3H), 2.88 (br hept, 3H), 1.61 (br s, 9H), 1.17 (br s, 9H), 0.99 (br s, 9H), 0.77 (br s, 9H). **$^{13}$C{$^1$H} NMR (125 MHz, CDCl₃)** δ 156.46, 152.10, 140.49, 132.71, 127.85, 126.00, 37.56, 35.35, 28.26 (br s), 25.17 (br s, 2C), 24.59 (br s). Compound Dipp₃SbOCuCl·(CHCl₃)₂ is unstable in air and combustion microanalyses were consistently unsuccessful. In addition to the NMR spectra, we also obtained PXRD data from freshly prepared bulk solid; these powder data agreed with the simulated powder diffractogram generated from the crystal structure of Dipp₃SbOCuCl·(CHCl₃)₂ (Figure B.37). Furthermore, high-resolution mass spectrometry data were collected to corroborate the proposed elemental composition.

**Synthesis of bis(tris(2,6-diisopropylphenyl)stibine oxide)silver(I) trifluoromethanesulfonate diethyl ether solvate ([Ag(Dipp₃SbO)₂](CF₃SO₃)·OEt₂).** In the absence of light, Dipp₃SbO (75 mg, 0.12 mmol) and silver triflate (11 mg, 0.060 mmol) were dissolved in MeCN (3 mL) and stirred for 30 min at room temperature. OEt₂ (30 mL) was added to the colorless solution and the mixture was placed in a –20 °C freezer overnight to grow colorless crystals that were suitable for X-ray diffraction. The solid was collected by vacuum filtration and washed with OEt₂. Yield: 30 mg (33%). **IR (KBr, cm⁻¹)** ν_SbO 637. **ESI-MS (*m/z*) [M–Dipp₃SbO–CF₃SO₃]⁺** 727.45 (calc 727.2). **$^1$H NMR (500 MHz, CD₃CN)** δ 7.51 (t, *J* = 7.7 Hz, 6H), 7.37 (d, *J* = 7.6 Hz, 6H), 7.33 (d, *J* = 7.7 Hz, 6H), 4.01 (hept, *J* = 6.1 Hz, 6H), 3.42 (quart, *J* = 7.0 Hz, 4H), 2.95 (hept, *J* = 6.5 Hz, 6H), 1.33 (d, *J* = 5.6 Hz, 18H), 1.19 (d, *J* = 5.9 Hz, 18H), 1.12 (t, *J* = 7.0 Hz, 6H), 0.93 (d, *J* = 6.1 Hz, 18H), 0.72 (d, *J* = 5.7 Hz, 18H). **$^{13}$C{$^1$H} NMR (125 MHz, CD₃CN)** δ 156.93, 153.24, 142.32, 133.05, 128.01, 126.83, 66.24, 38.19, 35.31, 27.43, 25.09, 24.80, 24.49, 15.59. **$^{19}$F{$^1$H} NMR (470 MHz, CD₃CN)** δ –79.33. The crystals of [Ag(Dipp₃SbO)₂](CF₃SO₃)·OEt₂ are both thermally

and photolytically sensitive and combustion microanalyses were consistently unsuccessful. In addition to the NMR spectra, we also obtained PXRD data from freshly prepared bulk solid; these powder data agreed with the simulated powder diffractogram generated from the crystal structure of [Ag(Dipp$_3$SbO)$_2$](CF$_3$SO$_3$)·OEt$_2$ (Figure B.42).

**Synthesis of (tris(2,6-diisopropylphenyl)stibine oxide)(triphenylphosphine)gold(I) trifluoromethanesulfonate ([Dipp$_3$SbOAuPPh$_3$][CF$_3$SO$_3$]).** In the absence of light, Dipp$_3$SbO (48.5 mg, 0.07 mmol), PPh$_3$AuCl (48.5 mg, 0.07 mmol), and silver triflate (7.7 mg, 0.07 mmol) were suspended in DCM, sonicated, and stirred at room temperature for 1 h. The reaction mixture was filtered through a plug of laboratory tissue and hexanes were layered on top of the filtrate to grow colorless crystals overnight. The crystals were collected by vacuum filtration, washed with pentane (3 × 3 mL), and dried *in vacuo*. Crystals suitable for X-ray diffraction were grown similarly. Yield: 65 mg (64 %). M.p. 149 °C (decomp). **IR (KBr, cm$^{-1}$)** $v_{SbO}$ 638. **ESI-MS (*m/z*) [M–CF$_3$SO$_3$]$^+$** 1079.3549 (calc 1079.3549). **$^1$H NMR (500 MHz, CDCl$_3$)** δ 7.61-7.50 (br m, 6H), 7.49-7.41 (br m, 7H), 7.35 (d, *J* = 6.0 Hz, 7H), 7.31-7.27 (m, 4H), 3.67 (br s, 3H), 2.87 (br s, 3H), 1.51-0.70 (m, 36H). **$^{13}$C{$^1$H} NMR (125 MHz, CDCl$_3$)** δ 140.77, 134.03 (d, *J* = 13.75 Hz), 133.80 (d, *J* = 12.5 Hz), 133.60, 132.65 (d, *J* = 2.5 Hz), 132.46, 129.62 (d, *J* = 11.25 Hz), 129.49, 128.18, 127.66, 37.98 (br s, 1C), 35.73 (br s, 1C), 24.75 (br s, 4C). **$^{19}$F{$^1$H} NMR (470 MHz, CD$_3$CN)** δ −77.97. **$^{31}$P{$^1$H} NMR (202 MHz, CDCl$_3$)** δ 25.92, 23.84. [Dipp$_3$SbOAuPPh$_3$][CF$_3$SO$_3$] is unstable and combustion microanalyses were consistently unsuccessful. In addition to the NMR spectra, we also obtained PXRD data from freshly prepared bulk solid; these powder data agreed with the simulated powder diffractogram generated from the crystal structure of the linear (rhombohedral) polymorph (Figure B.48).

Furthermore, high-resolution mass spectrometry data were collected to corroborate the proposed elemental composition.

**Synthesis of tris(2,6-diisopropylphenyl)hydroxystibonium benzenesulfonate ([Dipp₃SbOH][O₃SPh]).** A solution of benzenesulfonic acid (18 mg, 0.12 mmol) in DCM (4 mL) was added dropwise to a solution of Dipp₃SbO (72 mg, 0.12 mmol) in DCM (3 mL). The colorless solution was stirred at room temperature for 30 min. The solvent level was reduced to 2 mL under reduced pressure and hexanes (15 mL) were added to precipitate a white powder. Yield: 69 mg (76%). Diffraction-quality crystals were grown from layering hexanes over a DCM solution of the compound. M.p. 230 °C. **Found:** C 64.57; H 7.53%, **Calc. for C₄₂H₅₇O₄SSb:** C, 64.70; H, 7.37%. **ESI-MS (*m/z*) [M–O₃SPh]⁺** 621.27 (calc 621.3). **IR (KBr, cm⁻¹)** $v_{SbO}$ 611 (s). **¹H NMR (500 MHz, CDCl₃)** δ 8.22 (br s, 1H), 7.56 (t, *J* = 7.7 Hz, 3H), 7.49 (d, *J* = 7.0 Hz, 2H), 7.40 (dd, *J* = 7.7, 1.1 Hz, 3H), 7.30 (dd, *J* = 7.7, 1.1 Hz, 3H), 7.22 (t, *J* = 7.2 Hz, 1H), 7.19-7.14 (m, 2H), 3.17 (hept, *J* = 6.4 Hz, 3H), 2.82 (hept, *J* = 6.4 Hz, 3H), 1.43 (d, *J* = 6.3 Hz, 9H), 1.21 (d, *J* = 6.6 Hz, 9H), 0.97 (d, *J* = 6.5 Hz, 9H), 0.86 (d, *J* = 6.4 Hz, 9H). **¹³C{¹H} NMR (125 MHz, CDCl₃)** δ 156.30, 152.25, 146.71, 137.93, 133.79, 128.70, 128.62, 127.47, 126.49, 126.47, 38.92, 36.96, 26.41, 25.29, 24.83, 24.30.

**Synthesis of tris(2,6-diisopropylphenyl)hydroxyarsonium benzenesulfonate ([Dipp₃AsOH][O₃SPh]).** Benzenesulfonic acid (15 mg, 0.092 mmol) and Dipp₃AsO (53 mg, 0.092 mmol) were dissolved in DCM (3 mL). The colorless solution was transferred under a layer of hexanes to grow colorless crystals. The product was washed with pentane (3 × 3 mL) and dried *in vacuo*. Yield: 44 mg (66%). Crystals suitable for X-ray diffraction were grown

similarly. M.p. 221 °C (decomp). **ESI-MS (*m/z*) [M−O₃SPh]⁺** 575.3228 (calc 575.3228). **¹H NMR (500 MHz, CDCl₃)** δ 7.56-7.49 (m, *J* = 7.5 Hz, 5H), 7.38 (d, *J* = 7.7 Hz, 3H), 7.29 (d, *J* = 7.6 Hz, 3H), 7.25-7.18 (m, 3H), 3.10 (hept, 3H, *J* = 6.4 Hz), 3.09 (hept, 3H, *J* = 6.4 Hz), 1.62 (br s), 1.41 (d, *J* = 6.2 Hz, 9H), 1.17 (d, *J* = 6.4 Hz, 9H), 0.90 (d, *J* = 6.3 Hz, 9H), 0.81 (d, *J* = 6.1 Hz, 9H). **¹³C{¹H} NMR (125 MHz, CDCl₃)** δ 154.73, 150.67, 136.27, 133.88, 129.31, 128.88, 127.61, 126.68, 126.60, 35.19, 33.76, 26.18, 25.36, 24.96, 23.94. The elemental composition of [Dipp₃AsOH][O₃SPh] found from combustion microanalyses was outside of the acceptable deviation from the theoretical value. In addition to the NMR spectra, we also obtained PXRD data from freshly prepared bulk solid; these powder data agreed with the simulated powder diffractogram generated from the crystal structure of [Dipp₃AsOH][O₃SPh] (Figure B.58). Furthermore, high-resolution mass spectrometry data were collected to corroborate the proposed elemental composition.

**Synthesis of *cis*-hydroxyacetatotris(2,6-diisopropylphenyl)stiborane (*cis*-Sb(OH)(OAc)Dipp₃).** Glacial acetic acid (8.5 mL, 0.15 mmol) was added to a solution of Dipp₃SbO (93 mg, 0.14 mmol) in DCM (4 mL). The colorless solution was stirred for 10 min at room temperature before being stripped of solvent under reduced pressure to yield the crude product as a white powder. The product was recrystallized from DCM/pentane at −20 °C. The solvent was then decanted and the crystals were washed with cold pentane and dried under vacuum. Yield: 62 mg (61%). M.p. 188 °C (decomp). **Found:** C, 67.02; H, 7.97%, **Calc. for C₃₉H₅₈O₃Sb:** C, 67.24; H, 8.39%. **ESI-MS (*m/z*) [M−OAc]⁺** 621.27 (calc 621.3). **IR (KBr, cm⁻¹)** ν$_{SbO}$ 649 (s). **¹H NMR (500 MHz, CDCl₃)** δ 7.44 (t, *J* = 7.7 Hz, 3H), 7.34 (d, *J* = 7.4 Hz, 3H), 7.20 (d, *J* = 7.4 Hz, 3H), 5.73 (br s, 3H), 3.97 (br sept, *J* = 6.05 Hz, 3H), 2.94 (br sept, *J* = 5.8 Hz, 3H), 1.95

(s, 3H), 1.40 (br s, 9H), 1.19 (br s, 9H), 0.96 (br s, 9H), 0.76 (br s, 9H).**$^{13}$C{$^1$H} NMR (125 MHz, CDCl$_3$)** δ 175.04, 156.67, 152.03, 141.32, 132.10, 127.36, 125.62, 37.59, 34.45, 26.78, 25.11, 24.73, 24.62, 22.80.

**Synthesis of *trans*-difluorotris(2,6-diisopropylphenyl)stiborane (*trans*-Dipp$_3$SbF$_2$).** BF$_3$·OEt$_2$ (19 mL, 0.15 mmol) was added to a solution of Dipp$_3$SbO (95 mg, 0.15 mmol) in DCM (2 mL) at −78 °C resulting in rapid precipitation of a white solid. The reaction mixture was allowed to warm to room temperature before being filtered through a Celite pad. The solvent was removed to yield a white powder. The crude product was recrystallized from OEt$_2$/MeCN. Yield: 57 mg, 59%. Crystals suitable for X-ray diffraction were grown by slow evaporation of MeCN. M.p. 279 °C. **Found:** C, 67.07; H, 8.49%, **Calc. for C$_{36}$H$_{51}$F$_2$Sb:** C, 67.19; H, 7.99%. **IR (KBr, cm$^{−1}$)** n$_{SbF}$ 528 (s). **$^1$H NMR (500 MHz, CDCl$_3$)** δ 7.42 (t, *J* = 7.6 Hz, 3H), 7.30 (d, *J* = 7.6 Hz, 6H), 3.16 (hept, *J* = 6.3 Hz, 6H), 1.18 (d, *J* = 6.1 Hz, 18H), 1.09 (d, *J* = 6.5 Hz, 18H). **$^{13}$C{$^1$H} NMR (125 MHz, CDCl$_3$)** δ 154.56, 130.93, 125.52, 35.48, 27.13, 24.53. **$^{19}$F{$^1$H} NMR (470 MHz, CDCl$_3$)** δ − 74.35 (s).

**Conversion of Dipp$_3$SbO to Dipp$_3$Sb by phenylsilane.** Phenylsilane (20 mL, 0.16 mmol) was added to a solution of Dipp$_3$SbO (98 mg, 0.16 mmol) in toluene (5 mL). The colorless solution was heated to 50 °C for 1.5 h. The reaction mixture was then stripped of solvent to yield a white solid. The crude product was dissolved in hexanes and purified by column chromatography to obtain Dipp$_3$Sb. Yield: 76 mg (80%). NMR spectra of the product match those reported above for Dipp$_3$Sb. An NMR-scale reaction was also performed to demonstrate > 93% conversion of Dipp$_3$SbO to Dipp$_3$Sb by one equivalent of phenylsilane at 50 °C for 1 h in

d$_8$-toluene (Figure B.71). No reaction was observed when Dipp$_3$AsO or Dipp$_3$PO were mixed with phenylsilane under similar conditions (Figures B.72 and B.73).

**X-ray absorption spectroscopy.** The Sb K-edge XAS data were collected at beamline 7-3 at the Stanford Synchrotron Radiation Lightsource (SSRL) using a Si(220) double crystal monochromator. Solid samples were placed into aluminum sample holders sealed with Kapton adhesive tape. Samples were flash frozen in liquid nitrogen and maintained at 10 K using a He-flow cryostat (Oxford instruments, Abingdon, UK). To gain access to the high energies of the Sb K edge, the beamline was operated in mirrorless mode, employing a 0.25 mm vertical aperture so as to give adequate energy resolution. The X-ray absorption spectrum was measured using N$_2$-filled gas-ionization chambers employing a sweeping voltage of 1.8 kV and operating above the recombination region. The incident beam energy was calibrated to the lowest-energy K-edge inflection from Sb foil (assumed to be 30488.0 eV) with a photoionization threshold (at which $k = 0.0$ Å$^{-1}$) assumed to be 30510 eV. XAS data reduction and analysis were performed using the EXAFSPAK suite of programs[21] and employing the program FEFF (v8.5)[22] for ab-initio phase and amplitude functions to fit the EXAFS. All fitting was performed in $k$-space using the data as shown in Figure 3.3. The goodness of fit parameter $F$ is defined as $F = [\Sigma k^6(\chi_{calc}(k) - \chi_{exp}(k))^2 / \Sigma k^6(\chi_{exp}(k))^2]^{0.5}$ in which $\chi_{exp}(k)$ and $\chi_{calc}(k)$ are the experimental and calculated EXAFS, respectively, and the summations are over all points included within the fitted $k$-range, which in all cases was 1-18.1 Å$^{-1}$. Values of $F$ close to 0.3 are typically considered adequate fits, while 0.4 and above are poor fits. Only the first-shell or Sb$\cdots$Sb contributions (in the case of **A**) to the EXAFS discussed are shown in the Table B.7 but, in all cases, the outer C shells were approximated in a similar manner to that reported by

Ferreira *et al.* using a rigid benzene ring, assuming a C–C bond-length of 1.381 Å, with multiple scattering included, which was found to be significant (>2% of total amplitude) only for third- and fourth-shell C atoms. Pendant groups on the phenyl rings were approximated using single scattering analysis with interatomic distances grouped into clusters when Sb⋯C distances were less than the EXAFS resolution of $\pi/2k_{max}$.[23] We note that for the EXAFS fitting of Dipp$_3$SbO, fitting a C atom in the place O gave a worse goodness-of-fit index ($F$ = 0.335 for Sb–C vs. 0.319 for Sb–O) and a physically unreasonable Debye-Waller factor ($\sigma^2$ of 0.0010 Å$^2$ for Sb–C vs. 0.0021 Å$^2$ for Sb–O).

**Computational experiments.** Geometry optimization and frequency DFT calculations were performed using ORCA 4.2.1 or ORCA 5.0.1.[24] Geometry optimization and frequency calculations were performed on Dipp$_3$PO, Dipp$_3$AsO, Dipp$_3$SbO, **A**, **B**, and *cis*-Sb(OH)(OAc)Dipp$_3$ at the PBE0/def2-TZVPP level of theory with the RIJCOSX approximation and def2/J auxiliary basis set.[25-29] The TIGHTOPT keyword was used to tighten the optimization convergence criteria for Dipp$_3$PO, Dipp$_3$AsO, **A**, and the VERYTIGHTOPT keyword was used for **B**. Geometry optimization and frequency calculations were performed on (Dipp$_3$SbO)$_2$Ag$^+$ at the BP86/def2-SVP level of theory with the RI approximation and def2/J auxiliary basis set. Frequency calculations on Dipp$_3$PO, Dipp$_3$AsO, and Dipp$_3$SbO found small imaginary modes at –13.97 cm$^{-1}$, –11.37 cm$^{-1}$, and –11.38 cm$^{-1}$ respectively that arise from an aryl substituent vibration. The frequency calculation of **B** found an imaginary mode at –30.07 cm$^{-1}$ that arises from a rotating *para*-methyl group. The calculated IR vibrational frequencies of Dipp$_3$PO, Dipp$_3$AsO, and Dipp$_3$SbO were corrected with a 0.96 scalar factor.[30] Single point energy calculations were performed using ORCA 5.0.0 or ORCA 5.0.1 on the optimized structures using the PBE0 hybrid

functional and old-DKH-TZVPP all-electron basis set using the RIJCOSX approximation and SARC/J auxiliary basis set.[31-34] Single point energy calculations on [Dipp₃AsOH][O₃SPh], [Dipp₃SbOH][O₃SPh], and Dipp₃SbOH₂NPhF were performed on the coordinates obtained from Hirschfeld atom refinement at the same level of theory. Single point energy calculations on Dipp₃SbOCuCl, [Dipp₃SbOAuPPh₃][CF₃SO₃]-bent, and [Dipp₃SbOAuPPh₃][CF₃SO₃]-linear were performed on the crystallographic coordinates after normalizing C–H bond distances to 1.089 Å at the same level of theory. Gold atoms were treated with the ANO-RCC-TZP basis set. The effects of relativity were introduced using the second order Douglas-Kroll-Hess formalism (DKH).[35] Single point energy calculations generated wavefunctions that were subject to topological and Natural Bond Orbital (NBO) analyses. In the case of (Dipp₃SbO)₂Ag⁺, NBO analysis was performed using the BP86 pure functional and def2-SVP basis set. Canonical molecular orbitals were visualized using Avogadro.[36] Topological analysis of the electron density was performed in MultiWFN (version 3.7).[37] Bond paths were visualized in MultiWFN (version 3.7). The values of the real space functions $\rho$, $\nabla^2\rho$, and $\varepsilon$ along interatomic vectors were visualized using R (version 4.0.2) through RStudio (version 1.3.1073). The following R packages were used for analysis and visualization: ggplot2, tidyverse, gridExtra, ggtext, scales, ggbreak, and grid.[38] NBO analysis was performed using the NBO program (version 7.0.7).[39] For Dipp₃PnO, the $DEL keylist was used to calculate the energy of deletion by eliminating all non-Lewis delocalizations of electron density from the oxo unit to the rest of the molecule and vice versa. The energy of deletion of the strongest H-bond in Dipp₃SbO was calculated by eliminating all delocalizations from the O atom to the C–H fragment and vice versa to be 7.427 kcal/mol. Pre-orthogonalized natural bond orbitals were visualized in JMOL (version 14.31.18). Electrostatic surface potentials, deformation densities, and non-covalent interactions (NCI)

117

were calculated using MultiWFN and the results were visualized in VMD.[40] Energy decomposition analysis was performed using Gaussian 09[41] to perform single point energy calculations on the O atom and $Dipp_3Pn$ fragments using coordinates from the optimized $Dipp_3PnO$ structures (Pn = P, As, Sb). $\Delta E_{tot}$ was then obtained by subtracting the energies of the $Dipp_3Pn$ and O fragments from that of the parent $Dipp_3PnO$ molecule. MultiWFN was then used to generate an input file for $Dipp_3PnO$ with an initial guess for the combined O and $Dipp_3Pn$ fragments with no orbital interaction. The energy of the initial guess wavefunction was then subtracted from the final converged energy to obtain $\Delta E_{orb}$. Force constants for the pnictoryl bonds were obtained by diagonalization of the Hessian matrix using ORCA 5.0.1 and by fitting a quadratic equation to the energies obtained from a rigid surface scan of the potential energy surface of the Pn–O stretch/contraction, which was also performed with ORCA 5.0.1.

**X-ray crystallography: Independent Atom Model (IAM).** Crystals of $Dipp_3Sb$, $Dipp_3As$, $Dipp_3P$, $Dipp_3SbO$, $Dipp_3AsO$, $Dipp_3PO$, $Dipp_3SbO·H_2NPhF$, $Dipp_3SbOCuCl·(CHCl_3)_2$, $[Ag(Dipp_3SbO)_2](CF_3SO_3)·OEt_2$, $[Dipp_3SbOAuPPh_3][CF_3SO_3]$, $[Dipp_3SbOH][O_3SPh]$, $[Dipp_3AsOH][O_3SPh]$, cis-Sb(OH)(OAc)$Dipp_3$, and trans-$Dipp_3SbF_2$ were grown as described above, selected under a microscope, loaded onto a MiTeGen polyimide sample loop using Paratone-N, and mounted onto a Rigaku XtaLAB Synergy-S single crystal diffractometer. Each crystal was cooled to 100 K under a stream of nitrogen. Diffraction of Mo Kα or Cu Kα radiation from a PhotonJet-S microfocus source was detected using a HyPix6000HE hybrid photon counting detector. Screening, indexing, data collection, and data processing were performed with CrysAlisPro.[42] The structures were solved using SHELXT and refined using SHELXL

following established strategies.[43-45] All non-H atoms were refined anisotropically. Carbon-bound H atoms were placed at calculated positions and refined with a riding model and coupled isotropic displacement parameters ($1.2 \times U_{eq}$ for aryl groups and $1.5 \times U_{eq}$ for methyl groups). In the cases of [Dipp$_3$AsOH][O$_3$SPh] and *cis*-Sb(OH)(OAc)Dipp$_3$, oxygen-bound H atoms were located in the difference Fourier synthesis; their positional and isotropic displacement parameters were refined freely. In the case of Dipp$_3$SbO, the isopropyl groups are disordered across two positions. The extensive disorder and high symmetry of the Laue group lowered the data-to-parameter ratio to 5.99 (B-level CheckCIF alert), which was addressed using similarity, distance, and rigid bond restraints. The $F_o$–$F_c$ map featured a residual electron density maximum of 2.98 e Å$^{-3}$ located 1.51 Å from the Sb center (B-level CheckCIF alert). This maximum is interpreted as artefactual, consistent with its location on a special position, the presence of the heavy Sb atom on a special position, and the extensive disorder in the structure. In the case of Dipp$_3$As, there is a similar electron density maximum (B-level CheckCIF alert) near the heaviest atom which is believed to arise for the same reason. In the case of Dipp$_3$P, which crystallizes in the Sohncke space group $R$3, there is low coverage of Friedel pairs (B-level CheckCIF alert). The high symmetry of the Laue group and long wavelength (Cu) used for collection decreased the coverage of Friedel pairs. We note that the crystal is a racemic twin of the two different conformations of the compound, which simply arise from the differential canting of the aryl rings; these conformations rapidly convert in solution and the molecule does not feature fixed molecular chirality. In the case of [Ag(Dipp$_3$SbO)$_2$](CF$_3$SO$_3$)·OEt$_2$, the ether molecule was disordered across two positions and was modelled using similarity, distance, and rigid bond restraints. In the case of the

rhombohedral polymorph of [Dipp₃SbOAuPPh₃][CF₃SO₃], the triflate counterion was disordered across two general positions and the $\overline{3}$ special position.

**X-ray crystallography: Hirshfeld atom refinement (HAR).** The IAM results for Dipp₃SbO, Dipp₃AsO, Dipp₃PO, Dipp₃SbO·H₂NPhF, [Dipp₃SbOH][O₃SPh], [Dipp₃AsOH][O₃SPh], and *cis*-Sb(OH)(OAc)Dipp₃ were used as input for the *NoSpherA2* implementation of HAR in *Olex2* (version 1.3 for Dipp₃SbO and Dipp₃SbO·H₂NPhF, and version 1.5 for Dipp₃AsO, Dipp₃PO, [Dipp₃SbOH][O₃SPh], [Dipp₃AsOH][O₃SPh], and *cis*-Sb(OH)(OAc)Dipp₃).[46] The quantum chemistry calculations were performed by ORCA (version 4.2.1 for Dipp₃SbO, version 5.0.0 for Dipp₃SbOH₂NPhF, and version 5.0.1 for Dipp₃AsO, Dipp₃PO, [Dipp₃SbOH][O₃SPh], [Dipp₃AsOH][O₃SPh], and *cis*-Sb(OH)(OAc)Dipp₃).[24,47] A wavefunction was calculated with high integration accuracy and tight SCF convergence criteria using the PBE0 hybrid functional and the x2c-TZVPP all-electron relativistically contracted basis set.[25-27,48] The effects of relativity were introduced using the second-order Douglas-Kroll-Hess formalism.[35] Least-squares crystallographic refinement was carried out with the *olex2.refine* engine.[49] The ADPs and positions of all atoms, including H atoms, were freely refined using the aspherical atomic form factors obtained from Hirshfeld stockholder partitioning of the theoretical electron density obtained from the computed wavefunction.[50] The newly refined atomic coordinates were used as the input for a new density functional theory (DFT) calculation, from which new aspherical form factors were obtained. This procedure was iterated until it had converged. In the cases of Dipp₃AsO, Dipp₃PO, [Dipp₃SbOH][O₃SPh], and *cis*-Sb(OH)(OAc)Dipp₃, a preliminary round of HAR was performed on the IAMs using the PBE functional and x2c-SVP basis set with low integration accuracy and sloppy SCF convergence criteria. The resulting

120

preliminary model contained non-positive definite H-atom ADPs. Similarity and rigid bond restraints were applied to H-atom ADPs and the preliminary HAR model was used as an input for the higher-level iterative HAR described above. In the case of [Dipp$_3$AsOH][O$_3$SPh], H atoms were refined freely and isotropically. The structure of Dipp$_3$PO featured a low data-to-parameter ratio (A-level CheckCIF alert), the effects of which were mitigated by introducing extensive distance similarity restraints between the two components of the disorder as describe above for Dipp$_3$P.

**Powder X-ray diffraction (PXRD).** Bulk samples of Dipp$_3$P, Dipp$_3$SbO·H$_2$NPhF, Dipp$_3$SbOCuCl·(CHCl$_3$)$_2$, [Ag(Dipp$_3$SbO)$_2$](CF$_3$SO$_3$)·OEt$_2$, [Dipp$_3$SbOAuPPh$_3$][CF$_3$SO$_3$], and [Dipp$_3$AsOH][O$_3$SPh] were ground using an agate mortar and pestle. The fine white powders were each loaded onto a MiTeGen polyimide sample loop using Paratone-N, and mounted onto a Rigaku XtaLAB Synergy-S single-crystal diffractometer. The powder was cooled to 100 K under a stream of nitrogen. The diffraction of Cu Kα radiation was collected while the sample underwent a Gandolfi scan. Data collection and processing were performed using CrysAlisPro. Simulated PXRD diffractograms were generated from the crystal structures of Dipp$_3$P, Dipp$_3$SbO·H$_2$NPhF, Dipp$_3$SbOCuCl·(CHCl$_3$)$_2$, [Ag(Dipp$_3$SbO)$_2$](CF$_3$SO$_3$)·OEt$_2$, [Dipp$_3$SbOAuPPh$_3$][CF$_3$SO$_3$]-linear (rhombohedral polymorph), and [Dipp$_3$AsOH][O$_3$SPh] using Mercury and compared to the experimentally determined diffractograms.

## 3.8 – References

1. Pyykkö, P., Additive Covalent Radii for Single-, Double-, and Triple-Bonded Molecules and Tetrahedrally Bonded Crystals: A Summary. *J. Phys. Chem. A* **2015,** *119*, 2326-2337.

2. Sasaki, S.; Sutoh, K.; Murakami, F.; Yoshifuji, M., Synthesis, Structure, and Redox Properties of the Extremely Crowded Triarylpnictogens: Tris(2,4,6-triisopropylphenyl)phosphine, Arsine, Stibine, and Bismuthine. *J. Am. Chem. Soc.* **2002,** *124*, 14830-14831.

3. Sasaki, S.; Sutoh, K.; Shimizu, Y.; Kato, K.; Yoshifuji, M., Oxidation of tris(2,4,6-triisopropylphenyl)phosphine and arsine. *Tetrahedron Lett.* **2014,** *55*, 322-325.

4. Bordner, J.; Doak, G. O.; Everett, T. S., Crystal structure of 2,2,4,4-tetrahydro-2,2,2,4,4,4-hexaphenyl-1,3,2,4-dioxadistibetane (triphenylstibene oxide dimer) and related compounds. *J. Am. Chem. Soc.* **1986,** *108*, 4206-4213.

5. Huber, F.; Westhoff, T.; Preut, H., Tris(2,4,6-trimethylphenyl)antimony dihydroxide; synthesis and reaction with sulfonic acids $RSO_3H$ (R = $C_6H_5$, $CF_3$). Crystal structure of $[2,4,6-(CH_3)_3C_6H_2]_3SbO \cdot HO_3SC_6H_5$. *J. Organomet. Chem.* **1987,** *323*, 173-180.

6. Westhoff, T.; Huber, F.; Rüther, R.; Preut, H., Synthesis and structural characterization of some new triorganoantimony oxides. Molecular and crystal structure of tris(2,4,6-trimemethylphenyl)antimony dihydroxide. *J. Organomet. Chem.* **1988,** *352*, 107-113.

7. Wenger, J. S.; Johnstone, T. C., Unsupported monomeric stibine oxides ($R_3SbO$) remain undiscovered. *Chem. Commun.* **2021,** *57*, 3484-3487.

8. Lindquist-Kleissler, B.; Weng, M.; Le Magueres, P.; George, G. N.; Johnstone, T. C., Geometry of Pentaphenylantimony in Solution: Support for a Trigonal Bipyramidal Assignment from X-ray Absorption Spectroscopy and Vibrational Spectroscopic Data. *Inorg. Chem.* **2021,** *60*, 8566–8574.

9. Sasaki, S.; Sutoh, K.; Shimizu, Y.; Kato, K.; Yoshifuji, M., Oxidation of tris(2,4,6-triisopropylphenyl)phosphine and arsine. **2014,** *55*, 322-325.

10. Kleemiss, F.; Dolomanov, O. V.; Bodensteiner, M.; Peyerimhoff, N.; Midgley, L.; Bourhis, L. J.; Genoni, A.; Malaspina, L. A.; Jayatilaka, D.; Spencer, J. L.; White, F.; Grundkötter-Stock, B.; Steinhauer, S.; Lentz, D.; Puschmann, H.; Grabowsky, S., Accurate crystal structures and chemical properties from NoSpherA2. *Chem. Sci.* **2021,** *12*, 1675-1692.

11. Desiraju, G. R., Hydrogen Bridges in Crystal Engineering: Interactions without Borders. *Acc. Chem. Res.* **2002,** *35*, 565-573.

12.  Lindquist-Kleissler, B.; Wenger, J. S.; Johnstone, T. C., Analysis of Oxygen–Pnictogen Bonding with Full Bond Path Topological Analysis of the Electron Density. *Inorg. Chem.* **2021,** *60*, 1846-1856.

13.  Dobado, J. A.; Martínez-García, H.; Jose Molina Molina; Sundberg, M. R., Chemical Bonding in Hypervalent Molecules Revised. Application of the Atoms in Molecules Theory to $Y_3X$ and $Y_3XZ$ (Y = H or $CH_3$; X = N, P or As; Z = O or S) Compounds. *J. Am. Chem. Soc.* **1998,** *120*, 8461-8471.

14.  You, D.; Gabbaï, F. P., Tunable σ-Accepting, Z-Type Ligands for Organometallic Catalysis. *Trends Chem.* **2019,** *1*, 485-496.

15.  Pan, B.; Gabbaï, F. P., $[Sb(C_6F_5)_4][B(C_6F_5)_4]$: An Air Stable, Lewis Acidic Stibonium Salt That Activates Strong Element-Fluorine Bonds. *J. Am. Chem. Soc.* **2014,** *136*, 9564-9567.

16.  Bhat, K. L.; Markham, G. D.; Larkin, J. D.; Bock, C. W., Thermodynamics of Boroxine Formation from the Aliphatic Boronic Acid Monomers $R–B(OH)_2$ (R = H, $H_3C$, $H_2N$, HO, and F): A Computational Investigation. *J. Phys. Chem. A* **2011,** *115*, 7785-7793.

17.  Warsitz, M.; Doye, S., Linear Hydroaminoalkylation Products from Alkyl-Substituted Alkenes. *Chem.–Eur. J.* **2020,** *26*, 15121-15125.

18.  Li, K.; Weber, A. E.; Tseng, L.; Malcolmson, S. J., Diastereoselective and Enantiospecific Synthesis of 1,3-Diamines via 2-Azaallyl Anion Benzylic Ring-Opening of Aziridines. *Org. Lett.* **2017,** *19*, 4239-4242.

19.  Wenger, J. S.; Johnstone, T. C., Unsupported monomeric stibine oxides ($R_3SbO$) remain undiscovered. *Chem. Commun.* **2021,** *57*, 3484-3487.

20.  Huber, F.; Westhoff, T.; Preut, H., Tris(2,4,6-trimethylphenyl)antimony dihydroxide; synthesis and reaction with sulfonic acids $RSO_3H$ (R = $C_6H_5$, $CF_3$). Crystal structure of $[2,4,6-(CH_3)_3C_6H_2]_3SbO \cdot HO_3SC_6H_5$. *J. Organomet. Chem.* **1987,** *323*, 173-180.

21.  George, G. N.; Pickering, I. J., EXAFSPAK: A suite of computer programs for analysis of X-ray absorption spectra. Stanford Synchrotron Radiation Laboratory, Stanford, CA, USA: 1995.

22.  Rehr, J. J.; Albers, R. C., Theoretical approaches to x-ray absorption fine structure. *Rev. Mod. Phys.* **2000,** *72*, 621-654.

23.  Ferreira, G. C.; Franco, R.; Mangravita, A.; George, G. N., Unraveling the Substrate–Metal Binding Site of Ferrochelatase: An X-ray Absorption Spectroscopic Study. *Biochemistry* **2002,** *41*, 4809-4818.

24.     Neese, F., The ORCA program package. *Wiley Interdiscip. Rev.-Comput. Mol. Sci* **2012,** *2*, 73-78.

25.     Perdew, J. P.; Burke, K.; Ernzerhof, M., Generalized Gradient Approximation Made Simple. *Phys. Rev. Lett.* **1996,** *77*, 3865-3868.

26.     Perdew, J. P.; Ernzerhof, M.; Burke, K., Rationale for mixing exact exchange with density functional approximations. *J. Chem. Phys.* **1996,** *105*, 9982-9985.

27.     Weigend, F.; Ahlrichs, R., Balanced basis sets of split valence, triple zeta valence and quadruple zeta valence quality for H to Rn: Design and assessment of accuracy. *Phys. Chem. Chem. Phys.* **2005,** *7*, 3297-3305.

28.     Weigend, F., Accurate Coulomb-fitting basis sets for H to Rn. *Phys. Chem. Chem. Phys.* **2006,** *8*, 1057-1065.

29.     Neese, F.; Wennmohs, F.; Hansen, A.; Becker, U., Efficient, approximate and parallel Hartree–Fock and hybrid DFT calculations. A 'chain-of-spheres' algorithm for the Hartree–Fock exchange. *Chem. Phys.* **2009,** *356*, 98-109.

30.     NIST, NIST Computational Chemistry Comparison and Benchmark Database; NIST Standard Reference Database Number 101, Release 21 (August 2020). <http://cccbdb.nist.gov/>.

31.     Pantazis, D. A.; Chen, X.-Y.; Landis, C. R.; Neese, F., All-Electron Scalar Relativistic Basis Sets for Third-Row Transition Metal Atoms. *J. Chem. Theory Comput.* **2008,** *4*, 908-919.

32.     Pantazis, D. A.; Neese, F., All-Electron Scalar Relativistic Basis Sets for the Lanthanides. *J. Chem. Theory Comput.* **2009,** *5*, 2229-2238.

33.     Pantazis, D. A.; Neese, F., All-Electron Scalar Relativistic Basis Sets for the Actinides. *J. Chem. Theory Comput.* **2011,** *7*, 677-684.

34.     Pantazis, D. A.; Neese, F., All-electron scalar relativistic basis sets for the 6p elements. *Theor. Chem. Acc.* **2012,** *131*, 1292.

35.     Wolf, A.; Reiher, M.; Hess, B. A., The generalized Douglas–Kroll transformation. *J. Chem. Phys.* **2002,** *117*, 9215-9226.

36.     Hanwell, M. D.; Curtis, D. E.; Lonie, D. C.; Vandermeersch, T.; Zurek, E.; Hutchison, G. R., Avogadro: an advanced semantic chemical editor, visualization, and analysis platform. *J. Cheminformatics* **2012,** *4*, 17.

37.     Lu, T.; Chen, F., Multiwfn: A multifunctional wavefunction analyzer. *J. Comput. Chem.* **2012,** *33*, 580-592.

38. Xu, S.; Chen, M.; Feng, T.; Zhan, L.; Zhou, L.; Yu, G., Use ggbreak to Effectively Utilize Plotting Space to Deal With Large Datasets and Outliers. *Front. Genet.* **2021,** *12*, 774846.

39. Glendening, E. D.; Landis, C. R.; Weinhold, F., NBO 7.0 : New vistas in localized and delocalized chemical bonding theory. *J. Comput. Chem.* **2019,** *40*, 2234-2241.

40. Humphrey, W.; Dalke, A.; Schulten, K., VMD: Visual molecular dynamics. *J. Mol. Graph.* **1996,** *14*, 33-38.

41. M. J. Frisch, G. W. T., H. B. Schlegel, G. E. Scuseria, M. A. Robb, J. R. Cheeseman, G. Scalmani, V. Barone, G. A. Petersson, H. Nakatsuji, X. Li, M. Caricato, A. Marenich, J. Bloino, B. G. Janesko, R. Gomperts, B. Mennucci, H. P. Hratchian, J. V. Ortiz, A. F. Izmaylov, J. L. Sonnenberg, D. Williams-Young, F. Ding, F. Lipparini, F. Egidi, J. Goings, B. Peng, A. Petrone, T. Henderson, D. Ranasinghe, V. G. Zakrzewski, J. Gao, N. Rega, G. Zheng, W. Liang, M. Hada, M. Ehara, K. Toyota, R. Fukuda, J. Hasegawa, M. Ishida, T. Nakajima, Y. Honda, O. Kitao, H. Nakai, T. Vreven, K. Throssell, J. A. Montgomery, Jr., J. E. Peralta, F. Ogliaro, M. Bearpark, J. J. Heyd, E. Brothers, K. N. Kudin, V. N. Staroverov, T. Keith, R. Kobayashi, J. Normand, K. Raghavachari, A. Rendell, J. C. Burant, S. S. Iyengar, J. Tomasi, M. Cossi, J. M. Millam, M. Klene, C. Adamo, R. Cammi, J. W. Ochterski, R. L. Martin, K. Morokuma, O. Farkas, J. B. Foresman, and D. J. Fox *Gaussian 09, Revision A.02*, Gaussian Inc: Wallingford CT, 2016.

42. Rigaku Oxford Diffraction, *CrysAlis^Pro* **2020**.

43. Sheldrick, G. M., SHELXT– Integrated space-group and crystal-structure determination. *Acta Crystallogr. Sect. A* **2015,** *71*, 3-8.

44. Sheldrick, G. M., Crystal structure refinement with SHELXL. *Acta Crystallogr. Sect. C* **2015,** *71*, 3-8.

45. Müller, P., Practical suggestions for better crystal structures. *Crystallogr. Rev.* **2009,** *15*, 57-83.

46. Kleemiss, F.; Dolomanov, O. V.; Bodensteiner, M.; Peyerimhoff, N.; Midgley, L.; Bourhis, L. J.; Genoni, A.; Malaspina, L. A.; Jayatilaka, D.; Spencer, J. L.; White, F.; Grundkötter-Stock, B.; Steinhauer, S.; Lentz, D.; Puschmann, H.; Grabowsky, S., Accurate crystal structures and chemical properties from NoSpherA2. *Chem. Sci.* **2021,** *12*, 1675-1692.

47. Neese, F., *WIREs Comput. Mol. Sci* **2018,** *8*, e1327.

48. Pollak, P.; Weigend, F., Segmented Contracted Error-Consistent Basis Sets of Double- and Triple-ζ Valence Quality for One- and Two-Component Relativistic All-Electron Calculations. *J. Chem. Theory Comput.* **2017,** *13*, 3696-3705.

49.    Dolomanov, O. V.; Bourhis, L. J.; Gildea, R. J.; Howard, J. A. K.; Puschmann, H., OLEX2: a complete structure solution, refinement and analysis program. *J. Appl. Crystallogr.* **2009,** *42*, 339-341.

50.    Hirshfeld, F. L., Bonded-atom fragments for describing molecular charge densities. *Theor. Chim. Acta* **1977,** *44*, 129-138.

**Chapter 4**

**Variation in pnictogen–oxygen bonding unlocks greatly enhanced Brønsted basicity for the monomeric stibine oxide**

**4.1 – Introduction**

Following our discovery of Dipp₃SbO (discussed in Chapter 3), we wanted to quantify the relative basicity of Dipp₃PnO (Pn = P, As, Sb). Already, we had strong indications that Dipp₃SbO was the most potent Brønsted base of the series based on our quantum chemical calculations and its relatively enhanced reactivity with PhSO₃H and acetic acid. We looked in the literature to find p$K_{aH}$ values for pnictine oxides. Triphenylphosphine oxide and triphenylarsine oxide in water have been reported to have p$K_{aH}$ values of −2.10 and 0.99, respectively.[1] Trimethylphosphine oxide, trimethylarsine oxide, and trimethylstibine oxide were reported to have p$K_{aH}$ values 0, 3.75, and 5.36, respectively.[1-2] This work represented the only p$K_{aH}$ determination of a series of pnictine oxides that include the Sb-containing analogue. However, our results discussed in earlier chapters suggest that trimethylstibine oxide should exist as a multimeric species; head-to-tail association of the Me₃SbO units would dramatically attenuate the basicity of the stiboryl group.[3-4]

Phosphine oxides can complex with phenols to form isolable H-bonded adducts, and these adducts have been explored as a means of measuring the Brønsted basicity of phosphine oxides.[5-9] Solution and solid-state NMR spectroscopy have been employed to inform on the extent of proton transfer from substituted phenols to triphenylphosphine oxide.[7] Generally, as the phenol becomes more acidic, the extent of proton transfer to the phosphine oxide increased. However, in certain cases, intramolecular H-bonding and steric effects caused species to deviate from the expect trends. While these studies only yielded H-bonded adducts (O–H···O), the phosphoryl group can be protonated by stronger acids to yield hydroxyphosphonium salts (X⁻···⁺H–O) in the solid state.[10] As discussed in Chapter 2, the

characterization of a species on the salt–co-crystal continuum can be a non-trivial endeavor and is relevant to appropriately identify a chemical species.[11-12]
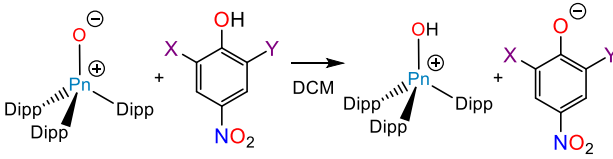
In this chapter, I describe results that unambiguously confirm that Brønsted basicity increases for a series of monomeric pnictine oxides $Dipp_3PnO$ (Pn = P, As, Sb) from $Dipp_3PO$ < $Dipp_3AsO$ < $Dipp_3SbO$. This work includes a theoretical investigation that rationalizes the enhanced basicity of $Dipp_3SbO$ based on variation in the electronic structure of the pnictoryl bond across the series. Solution- and solid-state investigations of the stoichiometric reactivity of $Dipp_3PnO$ with a series of acids that systematically vary in $pK_a$ inform on the $pK_{aH}$ values of the pnictine oxides. [1]H spectrometric titration experiments quantitatively determined the $pK_{aH}$ values of $Dipp_3AsO$ and $Dipp_3SbO$ to be 13.89(13) and 19.81(5), respectively. The approximately one million-fold increase in Brønsted basicity enjoyed by the stibine oxide enables it to catalyze a transesterification reaction, where the lighter congeners are not.

**4.2 – Theoretical investigation of basicity**

In Chapter 3, I described several computational experiments that are all consistent with increased relative basicity of the stibine oxide. Additionally, theoretical gas-phase proton affinities (PBE0/def2-TZVPP) of $Dipp_3PnO$ follow the same trend and increase from $Dipp_3PO$ < $Dipp_3AsO$ < $Dipp_3SbO$ (Table 4.1). We also calculated isodesmic reaction free energies for the protonation of $Dipp_3PnO$ with substituted phenols before embarking on the reactivity studies described below (Table 4.1). From these calculations, we predicted that $Dipp_3SbO$ or $Dipp_3AsO$ would react with picric acid to form the corresponding hydroxypnictonium salts, while

Dipp₃PO would not. We also predicted that 2,4-dinitrophenol would fully protonate only

Dipp₃SbO and that protonation of Dipp₃SbO by *p*-nitrophenol would be only slightly favorable.


**Table 4.1.** Calculated proton affinities of Dipp₃PnO.[a,b]



| | PA | $\Delta G$ (i) | $\Delta G$ (ii) | $\Delta G$ (iii) |
|---|---|---|---|---|
| Dipp₃SbO | 266 | −16.9 | −7.9 | −3.4 |
| Dipp₃AsO | 253 | −5.45 | 4.0 | 8.0 |
| Dipp₃PO | 239 | 7.7 | 16.7 | 21.2 |

[a] Proton affinities (PA) and isodesmic reaction free energies calculated at the PBE0/def2-TZVPP level of theory. Units are kcal/mol.
[b] i) X = Y = NO₂, ii) X = H, Y = NO₂, iii) X = Y = H


**4.3 – Stoichiometric reactivity between Dipp₃PnO and Brønsted acids**

We combined Dipp₃PnO with acids of varying strengths to evaluate their relative

Brønsted basicities experimentally (Figure 4.1). ¹H NMR spectral features of Dipp₃PnO are very

informative on the extent of proton transfer from an acid. Two distinct benzylic proton

resonances are observed in the pnictines due to restricted rotation about the Sb–$C_{ipso}$ bond.

There is a relatively deshielded Pn-proximal proton and a relatively shielded O-proximal

benzylic proton resonance. Chemical manipulation results in dramatic shifts of these signals,

and they appear in a spectral region that is unobscured by other resonances in these systems,

so we employed these benzylic resonances as convenient reporters for the extent of H-

bonding between Dipp₃PnO and Brønsted acids.

Dipp$_3$PnO were treated with triflic acid (Figure 4.1), resulting in dramatic shifts of the benzylic proton resonances (Figure C.15) suggesting that, in each case, hydroxypnictonium triflate salts had formed.[13] The chemical change to [Dipp$_3$POH][CF$_3$SO$_3$] is reflected in the $^{31}$P{$^1$H} NMR spectrum of a mixture of Dipp$_3$PO and triflic acid, a single broad signal is observed at 50.60 ppm, which is shifted significantly downfield from that of free Dipp$_3$PO (25.33 ppm). The signal breadth may arise because of a significant equilibrium with disassociated phosphine oxide and triflic acid. Crystals of the hydroxystibonium triflate [Dipp$_3$SbOH][CF$_3$SO$_3$] grew from a mixture of DCM and hexanes. These crystals belong to space group $P\overline{1}$ (Figure 4.2a). The Sb–O bond length was 1.9198(12) Å, which agrees with the hydroxystibonium salts
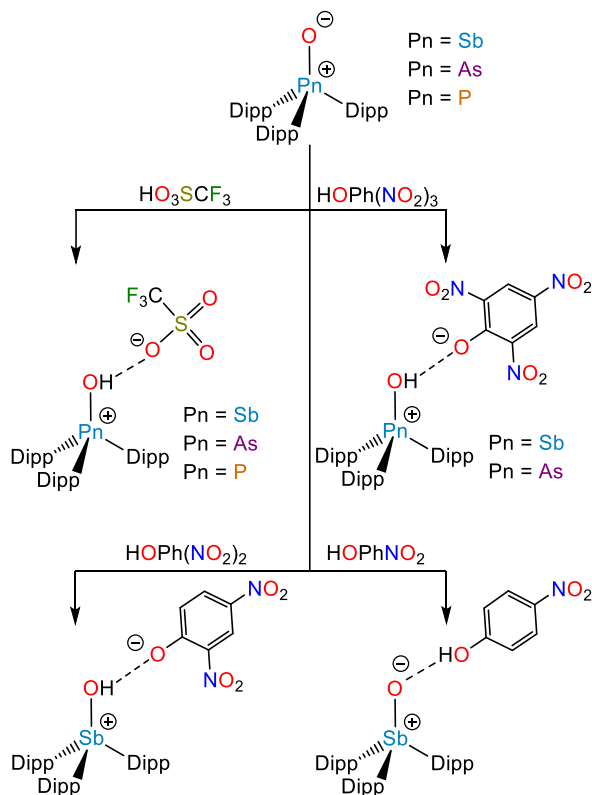


**Figure 4.1.** Reactions between Dipp$_3$PnO and acids.

131

described in Chapter 2 and not Dipp$_3$SbO.[11-14] The triflate counteranion engages the hydroxystibonium cation as an H-bond acceptor in the solid state.

Two polymorphs of [Dipp$_3$AsOH][CF$_3$SO$_3$]·CHCl$_3$ were obtained by vapor diffusion of pentane into a chloroform solution of Dipp$_3$AsO and triflic acid, as determined by single crystal X-ray diffraction. The two polymorphs exhibit visibly different crystal habits: blocks and needles. The blocks were of the triclinic crystal family, while the needles were monoclinic. Notably, the position of the triflate counteranion is variable across the polymorphs; it is free in the triclinic polymorph (Figure 4.2b) but engaged in an H-bonding interaction in the monoclinic polymorph.

Slow evaporation of a DCM/pentane solution of Dipp$_3$PO and triflic acid afforded colorless crystals of the hydroxyphosphonium triflate [Dipp$_3$POH][CF$_3$SO$_3$]. However, the crystals were unstable and rapidly decomposed in Paratone oil, presumably due to a deprotonation reaction. We were able to perform an X-ray diffraction experiment by rapidly manipulating the crystals and immersing one into a stream of 100 K N$_2$. Interestingly, the triflate anion does not hydrogen bond with the hydroxyl group (Figure 4.2c). The X-ray structures reveal a trend whereby the triflate anion acts as an H-bond acceptor in [Dipp$_3$SbOH][CF$_3$SO$_3$], is variable in [Dipp$_3$AsOH][CF$_3$SO$_3$], and is disassociated in [Dipp$_3$POH][CF$_3$SO$_3$]. This is likely due to variation in the steric environment; the hydroxy group in the phosphonium is too buried within the hydrophobic pocket to engage the triflate. Electronic arguments favor the opposite trend as there is enhanced positive charge on the protic H atom of the phosphonium relative to the protic H atom of the stibonium (see Appendix C).
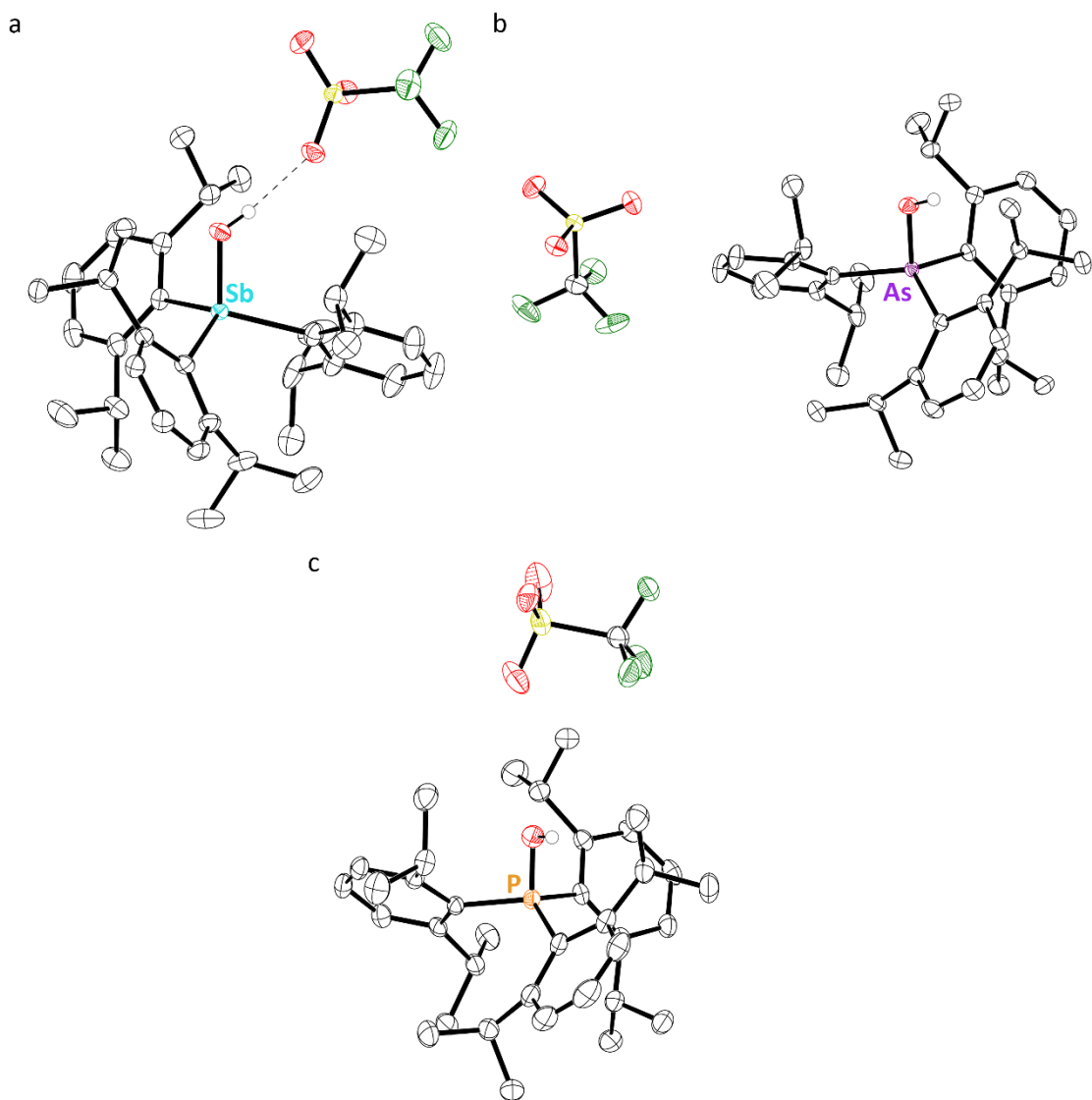
**Figure 4.2.** Thermal ellipsoid plots (50% probability) of (a) Dipp₃SbO, (b) Dipp₃AsO triclinic, and (c) Dipp₃PO. Color code: Sb teal, As purple, P orange, O red, C black, S yellow, F green, and H grey spheres of arbitrary radius. C-bound H atoms and solvent molecules are omitted for clarity.

In one instance, a small portion of crystals grown from a mixture of Dipp₃PO and triflic acid was shown by X-ray crystallography to be composed not of [Dipp₃POH][CF₃SO₃], but rather a cyclized alkoxyphosphonium triflate salt **1** (Figure 4.3). Presumably, this species forms through the formal elimination of H₂ from [Dipp₃POH][CF₃SO₃]. The formation of this species
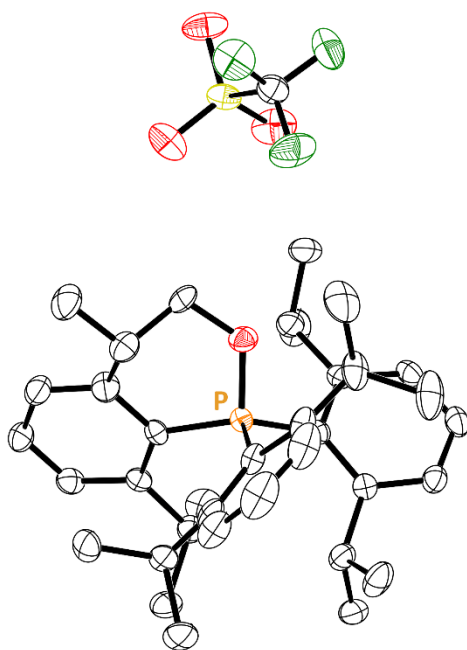
**Figure 4.3.** Thermal ellipsoid plot (50% probability) of **1**. Color code: P orange, O red, C black, S yellow, F green. H atoms are omitted for clarity.

prompted a further investigation of the computationally optimized structures Dipp$_3$PnOH$^+$. As noted above, the hydroxy groups of Dipp$_3$PnOH$^+$ are buried to a greater or lesser extent within the pocket created by the Dipp groups. A close inspection of the intramolecular interactions in which these hydroxyl groups engage revealed that a dihydrogen bond between the protic H atom and a methyl H atom is present in each case; Dipp$_3$POH$^+$ features the shortest computed OH···HC distance at 1.786 Å, suggesting a bond strength comparable to conventional hydrogen bonds.[15] Although the heavier congeners engage in similar hydroxy-methyl interactions, the OH group of Dipp$_3$POH$^+$ uniquely features a bifurcated dihydrogen bonding interaction in which the benzylic H atom appears at 1.833 Å. Topological analysis of the theoretical electron density (DKH-PBE0/old-DKH-TZVPP) of the isolated Dipp$_3$PnOH$^+$ cations confirms the presence of a bond critical point between the dihydrogen-bonding H atoms in each case. The magnitude of $\rho$ at the bond critical point becomes smaller as the pnictogen becomes heavier. Furthermore, non-covalent interaction analysis[16] of Dipp$_3$PnOH$^+$ reveals singularities in the reduced density gradient between the dihydrogen-bonding H atoms, but only in Dipp$_3$POH$^+$ do the dihydrogen bonds appear at a negative sign($\lambda_2$)$\rho$, indicating the strongest dihydrogen-bonding interaction in the series

(Figure C.59). As noted above, natural population analysis reveals a systematic increase in the charge of the protic H atom from $Dipp_3SbOH^+ < Dipp_3AsOH^+ < Dipp_3POH^+$. The increasing trend in dihydrogen bond strength from $Dipp_3SbOH^+ < Dipp_3AsOH^+ < Dipp_3POH^+$ can be rationalized by multiple factors that were noted above with regards to H-bonding to triflate in the crystal structures. First, the lower Brønsted basicity of the O atom in $Dipp_3PO$ attenuates charge transfer to the proton, thus the corresponding O–H group of $Dipp_3POH^+$ is a more polarized, potent H-bond donor. Second, as the pnictogen becomes smaller, the Dipp groups impose greater steric pressure on the hydroxyl group, shielding the hydroxyl group from intermolecular, stabilizing H-bonding interactions and positioning the isopropyl substituents in close contact with the protic H atom. Importantly, we verified that the dihydrogen bonding is not only present in the computed structures, but in the experimental crystal structures as well. Specifically, in the structure of $[Dipp_3POH][CF_3SO_3]$, the triflate anion cannot donate to the extremely protic H atom because of the steric shielding from the Dipp groups, but an isopropyl substituent is poised to act as an H-bond acceptor. It is noteworthy that this arrangement is observed in both of the crystallographically independent units of the hydroxyphosphonium cation present in the crystal structure.

The dihydrogen bond can be thought of as a pre-arrangement necessary for the reaction whereby $[Dipp_3POH][CF_3SO_3]$ produces **1** and $H_2$. Energetic analysis of the elimination of $H_2$ from cations $Dipp_3PnOH^+$ to form cyclized alkoxypnictonium cations **1$^+$**(Sb), **1$^+$**(As), and **1$^+$**, respectively, was performed computationally (Table 4.2). In all cases, $\Delta G_{rxn} > 0$, but the lowest positive number was obtained in the case of $Dipp_3POH^+$, consistent with the crystallographic observation of **1** but not the As or Sb analogs. Although the variations in Brønsted basicity/acidity that are the focus of this chapter have informed our initial

interpretation of this result as arising from a closed-shell process, we highlight that the final

product could also be obtained via an open-shell mechanism. We have tried repeatedly to

effect this transformation on a preparative scale without success, but efforts in this direction

are ongoing.

**Table 4.2.** Calculated reaction enthalpies and Gibbs free energies of elimination of $H_2$ from hydroxypnictonium cations $Dipp_3PnOH^+$ to form cyclized alkoxypnictonium cations $\mathbf{1}^+$(Sb), $\mathbf{1}^+$(As), and $\mathbf{1}^+$, respectively.



| Compound | $\Delta H$ (kcal/mol) | $\Delta G$ (kcal/mol) |
|---|---|---|
| $Dipp_3SbOH^+$ | 16.3 | 9.6 |
| $Dipp_3AsOH^+$ | 13.5 | 6.6 |
| $Dipp_3POH^+$ | 12.4 | 5.3 |

Returning to the reactions computationally investigated in Table 4.1, we explored

nitro-substituted phenols as less acidic proton donors. Addition of picric acid to solutions of

$Dipp_3PnO$ resulted in the diagnostic shifts in the benzylic proton resonances of $Dipp_3SbO$ and

$Dipp_3AsO$, but not $Dipp_3PO$. Yellow crystals of $[Dipp_3SbOH][OPh(NO_2)_3]$ grew from a

chloroform/pentane mixture (Figure 4.4a). The hydroxyarsonium picrate cyclohexane solvate

$[Dipp_3AsOH][Oph(NO_2)_3]\cdot\frac{3}{4}(C_6H_{12})$ could also be isolated in good yield (Figure 4.4b). We were

unable to isolate an H-bonded adduct between picric acid and $Dipp_3PO$, likely due to steric

shielding. We note that an H-bonded adduct between triphenylphosphine oxide and *p*-

a



b



c
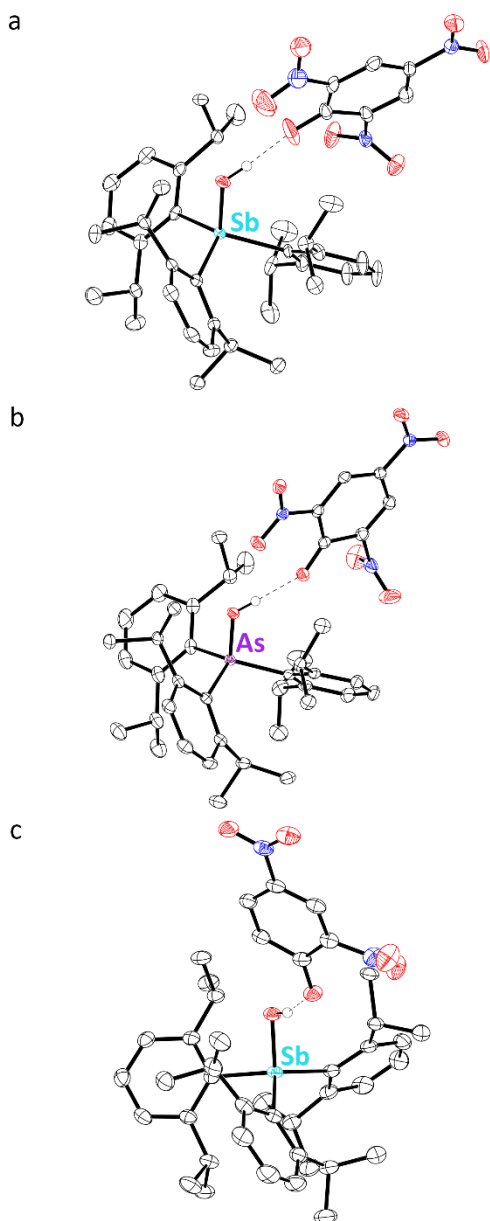


**Figure 4.4.** Thermal ellipsoid plots (50% probability) of (a) [Dipp$_3$SbOH][OPh(NO$_2$)$_3$], (b) [Dipp$_3$AsOH][OPh(NO$_2$)$_3$], (c) [Dipp$_3$SbOH][OPh(NO$_2$)$_2$]. Color code: Sb teal, As purple O red, N blue, C black, H grey spheres of arbitrary radius. C-bound H atoms and solvent molecules are omitted for clarity.

nitrophenol has been isolated, so an electronic argument for the lack of engagement is unlikely.[5,7]

Bright yellow crystals of [Dipp$_3$SbOH][Oph(NO$_2$)$_2$]·2(CHCl$_3$) could be grown by layering a chloroform solution of Dipp$_3$SbO and 2,4-dinitrophenol under cyclohexane (Figure 4.4c). Dissolution of these crystals in CDCl$_3$ again reveals the diagnostic signals for the hydroxystibonium cation. We did not observe any reaction between Dipp$_3$AsO or Dipp$_3$PO with 2,4-dinitrophenol, as we had predicted (Table 4.1).

Strikingly, treatment of Dipp$_3$SbO with one equivalent of p-nitrophenol did not result in an expected large shift of the benzylic resonances. However, yellow crystals were grown by vapor diffusion of pentane into a 1:1 mixture of *p*-nitrophenol and Dipp$_3$SbO in chloroform. In NMR spectra of solutions of these crystals, the benzylic resonances of Dipp$_3$SbO appeared only slightly shifted and sharpened, consistent with a weak interaction

137

between the two species. X-ray diffraction data ultimately revealed this species to be Dipp$_3$SbO·HOPhNO$_2$ where the stiboryl and phenolic O atoms are positioned to engage in an H-bond at a distance of 2.449(1) Å (Figure 4.5a). The Sb–O bond of 1.8627(9) Å is significantly shorter than a hydroxystibonium and is reminiscent of Lewis acid-stibine oxide adducts.[11-13] We performed a Hirschfeld atom refinement to freely refine the position and isotropic thermal parameters of the protic H atom between the two O atoms. The O$_{phenol}$–H and O$_{stiboryl}$···H distances are 1.14(3) and 1.32(3) Å, respectively, suggesting that Dipp$_3$SbO·HOPhNO$_2$ is an H-bonded adduct between Dipp$_3$SbO and $p$-nitrophenol. Interestingly, when crystals were grown from a 2:1 mixture of $p$-nitrophenol and Dipp$_3$SbO, a second equivalent of $p$-nitrophenol crystallizes in the asymmetric unit. We employed HAR to determine the nature of this species in solid state. The compound features a phenoxide anion that forms two H-bonding interactions, one with a hydroxystibonium cation and another with the second equivalent of
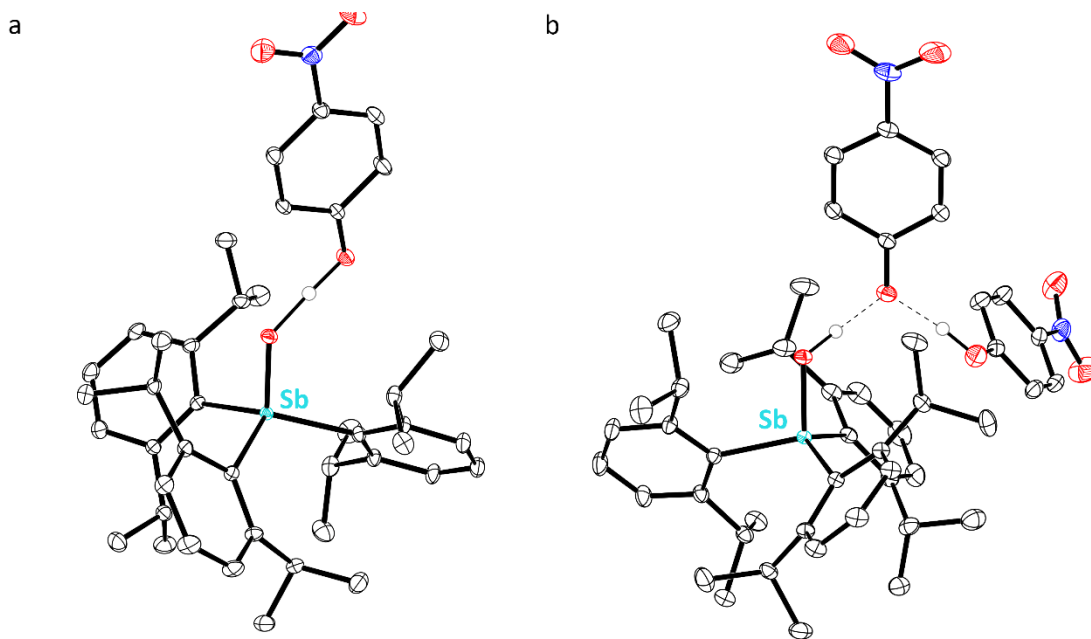


**Figure 4.5.** Thermal ellipsoid plots (50% probability) of (a) Dipp$_3$SbO·HOPhNO$_2$, (b) Dipp$_3$SbO·HOPhNO$_2$·$p$-nitrophenol. Color code: Sb teal, O red, N blue, C black, H grey spheres of arbitrary radius. C-bound H atoms are omitted for clarity.

*p*-nitrophenol (Figure 4.5b). We rationalize this result as follows: the second equivalent of *p*-nitrophenol stabilizes the phenoxide O-atom and diminishes its basicity such that the stiboryl O atom is the stronger O donor of the two; thus, the proton migrates to the stiboryl O atom to form a hydroxystibonium salt. The Sb–O bond length in this compound is 1.9026(7) Å. The $O_{phenoxide}\cdots H$ and $O_{stiboryl}–H$ distances are 1.53(2) and 1.03(2) Å, respectively. These results ultimately reveal that $Dipp_3SbO$ approximates the Brønsted basicity of *p*-nitrophenoxide.

## 4.4 – Determination of stibine oxide p$K_{aH}$

The reactivity observed for $Dipp_3SbO$ in Chapter 3 and earlier in this chapter confirms the expectation of enhanced basicity at $Dipp_3SbO$ relative to $Dipp_3AsO$ and $Dipp_3PO$. p$K_{aH}$ values of triphenyl- and trimethyl-substituted arsine oxides are typically 3-4 units greater than their respective corresponding phosphine oxides.[1] With a stibine oxide in hand for the first time, we wanted to extend this trend quantitatively. The stoichiometric reactivity presented here provided boundaries for the possible p$K_{aH,MeCN}$ value of $Dipp_3SbO$. The p$K_{aH,MeCN}$ of the stibine oxide would lie between that of 2,4-dinitrophenol (p$K_{a,MeCN}$ = 16.66) and *p*-nitrophenol (p$K_{a,MeCN}$ = 20.7).[17] We designed an NMR spectrometric titration experiment in which we titrated a solution of $[Dipp_3SbOH][CF_3SO_3]$ in acetonitrile-$d_3$ with a base to systematically generate increasing populations of $Dipp_3SbO$ in solution. The benzylic proton resonances serve as a convenient spectroscopic handle to assess the relative populations of stibine oxide and hydroxystibonium in solution as the chemical shift is a result of the weighted average of the relative populations of the protonated and deprotonated species. We chose the sterically bulky base $Et_3N$ (p$K_{aH.MeCN}$ = 18.83)[18] as its p$K_{a,MeCN}$ lies within the boundaries set by the stoichiometric reactions. Furthermore, the steric bulk may prevent additional reactivity that

may disrupt the equilibrium, and [Dipp₃SbOH][CF₃SO₃] was chosen because the weakly coordinating triflate anion should not strongly engage other species in the solution. Systematic conversion of [Dipp₃SbOH][CF₃SO₃] into Dipp₃SbO was observed upon titration with triethylamine in a smooth and controlled manner (Figure 4.6a). With the concentrations of each species in solution known based on the chemical shift and the amount of titrant added
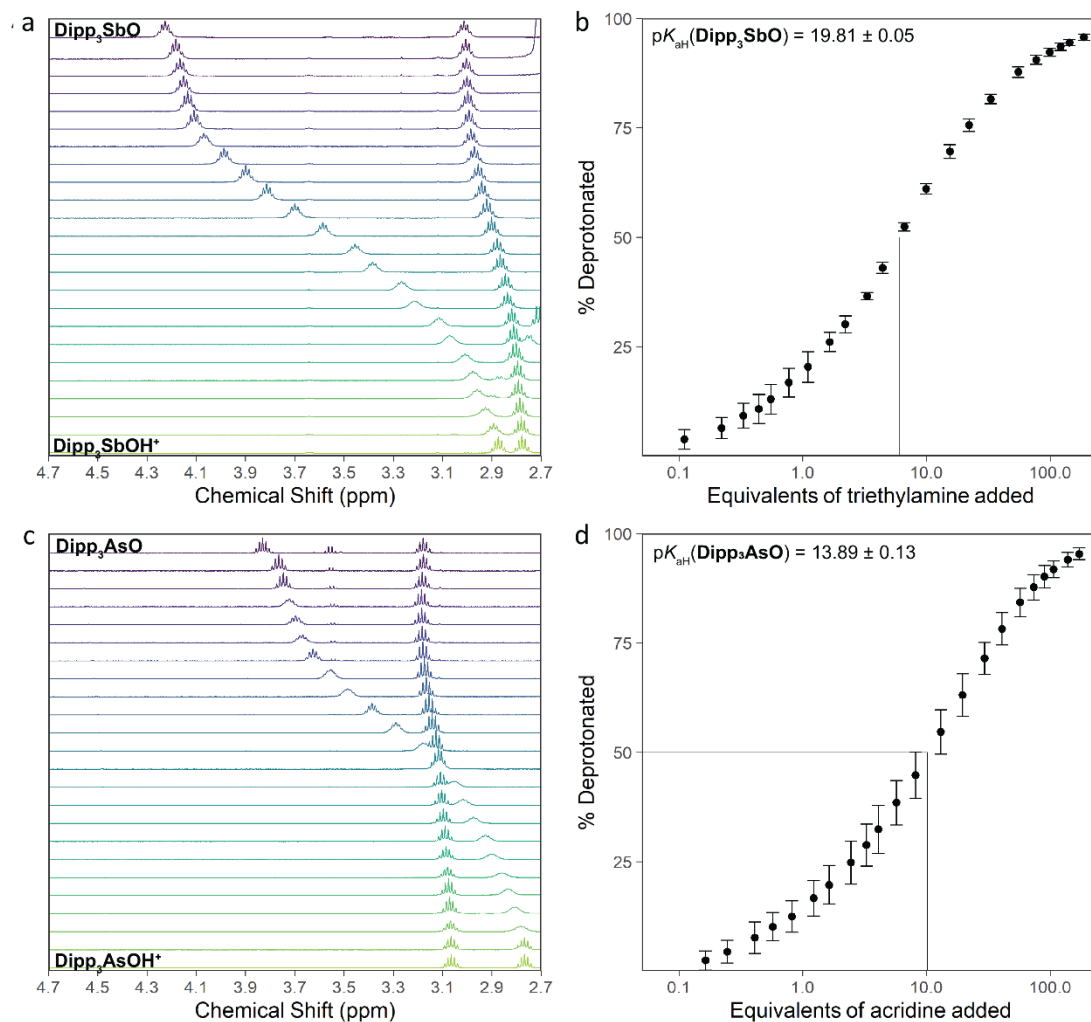


**Figure 4.6.** *Left*: Stacked $^1$H NMR spectra used to determine p$K_{aH}$ of (a) Dipp₃SbO and (c) Dipp₃AsO. The bottom spectrum is of a solution of only hydroxypnictonium triflate and the top spectrum is of a solution of only pnictine oxide. Intervening spectra are of samples with increasing concentration of titrant from bottom to top (see Appendix C for numerical data). *Right*: Averaged data that were fit to determine the p$K_{aH}$ of (b) Dipp₃SbO and (d) Dipp₃AsO. Error bars reflect the standard deviation of three independent replicates.

140

the $pK_{aH,MeCN}$ of Dipp$_3$SbO was found to be 19.81(5), in which the error is the standard deviation of the $pK_{aH,MeCN}$ values from three independently performed titrations (Figure 4.6b).
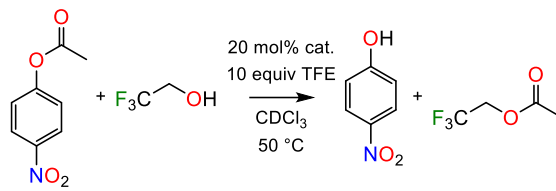
The $pK_{aH,MeCN}$ of Dipp$_3$AsO was determined by a similar methodology to be 13.89(13) (Figure 4.6c). We employed acridine as the basic titrant for its steric bulk and because its $pK_{a,MeCN}$ of 12.16[18] lies between the boundaries set by picric acid ($pK_{a,MeCN}$ = 11.00) and 2,4-dinitrophenol ($pK_{a,MeCN}$ = 16.66). With the $pK_{aH}$ values in hand, we could finally quantitatively compare the pnictine oxide basicities. The increase of basicity from Dipp$_3$AsO to Dipp$_3$SbO is orders of magnitude greater than the usual increase from phosphine oxide to arsine oxide. Arsine oxides are typically 1000-fold stronger bases than phosphine oxides,[1-2] but Dipp$_3$SbO is $10^6$-fold more basic than the arsine oxide Dipp$_3$AsO.

## 4.5 – Brønsted base catalysis

One application of pnictine oxides is as Brønsted bases in organic catalysis. We reasoned that Dipp$_3$SbO could act as a more potent Brønsted base catalyst relative to Dipp$_3$AsO or Dipp$_3$PO. We sought to test Dipp$_3$SbO as a catalyst for the synthesis of 2,2,2-trifluoroethyl acetate. Such 2,2,2-trifluoroethyl esters are useful because they are moderately activated and can react with primary amines to form amides without the need for a coupling reagent.[19-20] In the presence of 20 mol% of Dipp$_3$SbO, transesterification between *p*-nitrophenyl acetate and 2,2,2-trifluoroethanol to form *p*-nitrophenol and 2,2,2-trifluoroethyl acetate reached 97% completeness within 26 h at 50 °C in chloroform-*d*. In the presence of Dipp$_3$AsO, the reaction only reached 13% completion and Dipp$_3$PO showed no catalytic activity under similar conditions. In monitoring the reactions by $^1$H NMR, the reaction with Dipp$_3$SbO showed only signals for the [Dipp$_3$Sb(OH)]$^+$ cation (Figure C.35); the reaction with Dipp$_3$AsO

showed a mixture of [Dipp₃As(OH)]⁺ and Dipp₃AsO (Figure C.37); and the reaction performed with Dipp₃PO showed only Dipp₃PO (Figure C.39). We note that this reactivity assay serves to probe the reactivity of Dipp₃SbO, not to demonstrate that this new compound can out-compete current state-of-the-art transesterification catalysts.

**Table 4.3.** Transesterification between *p*-nitrophenyl acetate and 2,2,2-trifluoroethanol (TFE).



| Catalyst | % Conversion |
| --- | --- |
| Dipp₃SbO | 97 |
| Dipp₃AsO | 13 |
| Dipp₃PO | 0 |
| None | 0 |

**4.6 – Conclusion**

As described in earlier chapters, altering the Pn center of a pnictine oxide causes systematic and predictable variations in the electronic structure of the pnictoryl bond and directly impacts the Brønsted basicities of these species. Notably, the decrease in donation from the oxygen lone pairs into Pn–C σ* orbitals as the pnictogen becomes heavier results a dramatic increase in basicity for the stibine oxide. In this work, stoichiometric reactivity provided p$K_{aH}$ limits for the pnictine oxides and agreed with our theoretical results. This reactivity guided the design of a ¹H NMR spectrometric titration, which permitted the first determination of the p$K_{aH,MeCN}$ of a monomeric stibine oxide. We were ultimately able to utilize the dramatically enhance Brønsted basicity of Dipp₃SbO to catalyze a transesterification reaction.

**4.7 – Experimental methods**

**General methods.** Reagents and solvents were purchased from commercial vendors and used as received unless otherwise specified. 1-Bromo-2,6-diisopropylbenzene, *p*-nitrophenyl acetate, iodosobenzene, $Dipp_3SbO$, $Dipp_3AsO$, and $Dipp_3PO$ were prepared using established procedures.[21-23] **Picric acid is explosive and should be handled with caution**. Triethylamine was freshly distilled before use. Dichloromethane (DCM) was purified using an Innovative Technology PURE-SOLV solvent purification system. All solvents were dried over 3-Å molecular sieves. NMR spectra were collected using a Bruker Avance III HD 500 spectrometer equipped with a multinuclear Smart Probe. Signals in the $^1H$ and $^{13}C$ NMR spectra are reported in ppm as chemical shifts from tetramethylsilane and were referenced using the $CHCl_3$ ($^1H$, 7.26 ppm), $CHD_2CN$ ($^1H$, 1.94 ppm), $CDCl_3$ ($^{13}C$, 77.16 ppm), and $CD_3CN$ ($^{13}C$, 118.26 ppm) solvent signals. The frequencies of $^{19}F$ NMR signals are reported in ppm as chemical shifts from $CFCl_3$ (referenced to $BF_3 \cdot Et_2O$ at −152.8 ppm). $^{31}P$ NMR spectra were reported as chemical shifts from 85% $H_3PO_4$ and were referenced using triphenylphosphine (−5.35 ppm). Infrared (IR) spectra were collected on KBr pellets using a PerkinElmer Spectrum One FT-IR spectrometer. Mass spectrometry measurements were collected using an LTQ-Orbitrap Velos Pro MS instrument.

**Synthesis of tris(2,6-diisopropylphenyl)hydroxystibonium trifluoromethanesulfonate ([Dipp₃SbOH][O₃SCF₃]).** Triflic acid (9.3 μL, 0.11 mmol) was added to a solution of $Dipp_3SbO$ (66 mg, 0.11 mmol) in DCM (2 mL). The reaction mixture was transferred under a layer of hexanes. Colorless crystals suitable for X-ray diffraction formed overnight, and the mixture was cooled to −20 °C for 1 h to drive crystallization. The mother liquor was decanted and the

product was washed with pentane (3 x 5 mL). Yield: 69 mg (85%). M.p. 308 °C (decomposed).

**MS (*m/z*) [M–O₃SCF₃]⁺** 621.305 (calc 621.305). **¹H NMR (500 MHz, CD₃CN)** $\delta$ 7.72 (t, *J* = 7.7 Hz, 3H), 7.59 (dd, *J* = 7.7, 1.1 Hz, 3H), 7.53 (dd, *J* = 7.7, 1.1 Hz, 3H), 4.71 (br s, 1H), 2.87 (sept, *J* = 6.4 Hz, 3H), 2.78 (sept, *J* = 6.3 Hz, 3H), 1.37 (d, *J* = 6.4 Hz, 9H), 1.25 (d, *J* = 6.5 Hz, 9H), 1.03 (d, *J* = 6.5 Hz, 9H), 0.90 (d, *J* = 6.4 Hz, 9H). **¹³C{¹H} NMR (125 MHz, CD₃CN)** $\delta$ 155.76, 153.75, 137.78, 135.49, 129.58, 128.43, 40.56, 37.81, 26.21, 25.26, 24.73, 24.22. **¹⁹F NMR (470 MHz, CDCl₃)** $\delta$ −77.88.

**Synthesis of tris(2,6-diisopropylphenyl)hydroxyarsonium trifluoromethanesulfonate chloroform solvate ([Dipp₃AsOH][O₃SCF₃]·CHCl₃).** Triflic acid (8.3 μL, 0.093 mmol) was added to a solution of Dipp₃AsO (53.7 mg, 0.093 mmol) in CHCl₃ (1 mL). Pentane was allowed to transfer into the reaction mixture by vapor diffusion. Colorless crystals suitable for X-ray diffraction formed overnight. The mother liquor was decanted and the product was washed with pentane (3 x 3 mL). Yield: 44 mg (56%). M.p. 249 °C (decomposed). **MS (*m/z*) [M–O₃SCF₃]⁺** 575.323 (calc 575.323). **¹H NMR (500 MHz, CDCl₃)** $\delta$ 7.63 (t, *J* = 7.8 Hz, 3H), 7.48 (d, *J* = 7.8 Hz, 3H), 7.34 (d, *J* = 7.7 Hz, 3H), 7.01 (s, 1H), 3.09 (sept, *J* = 6.3 Hz, 3H), 2.90 (sept, *J* = 6.4 Hz, 3H), 1.41 (d, *J* = 6.4 Hz, 9H), 1.19 (d, *J* = 6.6 Hz, 9H), 0.97 (d, *J* = 6.5 Hz, 9H), 0.83 (d, *J* = 6.4 Hz, 9H). **¹³C{¹H} NMR (125 MHz, CDCl₃)** $\delta$ 154.26, 150.80, 135.69, 134.33, 129.06, 126.99, 35.42, 33.88, 26.07, 25.32, 24.88, 23.82. **¹⁹F NMR (470 MHz, CDCl₃)** $\delta$ −77.80.

**Crystal growth of tris(2,6-diisopropylphenyl)hydroxyphosphonium trifluoromethanesulfonate ([Dipp₃POH][O₃SCF₃]).** Triflic acid (8 μL, 0.09 mmol) was added to a solution of Dipp₃PO (49.2 mg, 0.09 mmol) in DCM (0.7 mL). Colorless crystals of

[Dipp₃POH][O₃SCF₃] were grown by allowing the solution to slowly concentrate by evaporation, but not to dryness. The product was characterized by single-crystal X-ray diffraction. A portion of the crystals of [Dipp₃POH][O₃SCF₃] grown in this manner were dissolved in CDCl₃ and characterized by NMR spectroscopy. **$^1$H NMR (500 MHz, CDCl₃)** $\delta$ 7.61 (td, $J$ = 7.8, 1.6 Hz, 3H), 7.46 (ddd, $J$ = 7.8, 4.5, 1.1 Hz, 3H), 7.37 − 7.30 (m, 3H), 5.12 (s, 4H), 3.26 (sept, $J$ = 6.4 Hz, 3H), 2.82 (sept, $J$ = 6.4 Hz, 3H), 1.36 (d, $J$ = 6.5 Hz, 9H), 1.14 (d, $J$ = 6.6 Hz, 9H), 0.96 (d, $J$ = 6.5 Hz, 9H), 0.75 (d, $J$ = 6.4 Hz, 9H). **$^{13}$C{$^1$H} NMR (125 MHz, CDCl₃)** $\delta$ 156.26 (d, $J$ = 9.0 Hz), 152.23 (d, $J$ = 15.5 Hz), 134.35 (d, $J$ = 2.6 Hz), 130.52 (d, $J$ = 95.5 Hz), 128.30 (d, $J$ = 11.2 Hz), 126.52 (d, $J$ = 12.2 Hz), 33.85 (d, $J$ = 7.6 Hz), 33.16 (d, $J$ = 4.3 Hz), 26.08, 25.19, 24.85, 23.91. **$^{19}$F NMR (470 MHz, CDCl₃)** $\delta$ −78.09. **$^{31}$P{$^1$H} NMR (470 MHz, CDCl₃)** $\delta$ 52.15. NMR spectra were also collected on a mixture of Dipp₃PO (5 mg, 9 µmol) and triflic acid (0.8 µL, 9 µmol) in CDCl₃ (550 µL) and are consistent with the formation of [Dipp₃POH][O₃SCF₃] in solution. When pentane was allowed to diffuse into a solution of triflic acid (7.8 µL, 0.089 µmol) and Dipp₃PO (47 mg, 0.089 mmol) in chloroform (1 mL), an oil was produced. The oil was redissolved in DCM and addition of hexanes produced a small batch of crystals of **1**, which were characterized by single-crystal X-ray diffraction.

**Synthesis of tris(2,6-diisopropylphenyl)hydroxystibonium 2,4,6-trinitrophenoxide ([Dipp₃SbOH][OPh(NO₂)₃]).** Picric acid (20 mg, 0.088 mmol) was added to a solution of Dipp₃SbO (55 mg, 0.088 mmol) in CHCl₃ (1 mL) to form a bright yellow solution. Pentane was allowed to transfer into the reaction mixture by vapor diffusion. Yellow crystals suitable for X-ray diffraction formed overnight. The mother liquor was decanted and the product was washed with pentane (3 x 3 mL). Yield: 51 mg (71%). The melting point was not measured

because of the known exothermic reactivity of picric acid and picrate salts. **MS (*m/z*) [M–**

**(O₂N)₃PhO]⁺** 621.305 (calc 621.305). **¹H NMR (500 MHz, CDCl₃)** δ 8.75 (s, 2H), 7.59 (t, *J* = 7.7

Hz, 3H), 7.39 (dd, *J* = 7.7, 1.2 Hz, 3H), 7.35 (dd, *J* = 7.7, 1.2 Hz, 3H), 3.19 (sept, *J* = 6.3 Hz, 3H),

2.86 (sept, *J* = 6.4 Hz, 3H), 1.31 (d, *J* = 6.3 Hz, 9H), 1.24 (d, *J* = 6.6 Hz, 9H), 0.96 (d, *J* = 6.5 Hz,

9H), 0.91 (d, *J* = 6.4 Hz, 9H). **¹³C{¹H} NMR (125 MHz, CDCl₃)** δ 161.04, 155.98, 152.35, 141.71,

137.67, 133.93, 128.33, 126.89, 126.75, 126.42, 39.05, 36.65, 26.27, 25.29, 24.94, 24.23.

**Synthesis of tris(2,6-diisopropylphenyl)hydroxyarsonium 2,4,6-trinitrophenoxide**

**cyclohexane solvate ([Dipp₃AsOH][OPh(NO₂)₃]·¾(C₆H₁₂)).** Picric acid (24 mg, 0.11 mmol) was

added a solution of Dipp₃AsO (60 mg, 0.11 mmol) in DCM (2 mL) to form a bright yellow

solution. The reaction mixture was transferred under a layer of cyclohexane. Yellow crystals

suitable for X-ray diffraction formed overnight. The mother liquor was decanted and the

product was washed with pentane (3 x 3 mL). Yield: 45 mg (50%). The melting point was not

measured because of the known exothermic reactivity of picric acid and picrate salts. **MS**

**(*m/z*) [M–(O₂N)₃PhO]⁺** 575.323 (calc 575.323). **¹H NMR (500 MHz, CDCl₃)** δ 8.76 (s, 2H), 7.57

(t, *J* = 7.7 Hz, 3H), 7.38 (d, *J* = 7.2 Hz, 3H), 7.34 (d, *J* = 7.7 Hz, 3H), 3.15 (sept, *J* = 6.3 Hz, 3H),

3.12 (sept, *J* = 6.3 Hz, 3H), 1.42 (s, 8H), 1.27 (d, *J* = 6.4 Hz, 9H), 1.19 (d, *J* = 6.6 Hz, 9H), 0.89 (d,

*J* = 6.5 Hz, 9H), 0.85 (d, *J* = 6.4 Hz, 9H). **¹³C{¹H} NMR (125 MHz, CDCl₃)** δ 160.23, 154.67, 150.77,

141.55, 136.35, 133.82, 128.45, 127.51, 126.83, 126.36, 35.09, 33.44, 27.06, 26.05, 25.41,

25.16, 23.84.

**Synthesis of tris(2,6-diisopropylphenyl)hydroxystibonium 2,4-dinitrophenoxide chloroform**

**disolvate ([Dipp₃SbOH][OPh(NO₂)₂]·2(CHCl₃)).** 2,4-Dinitrophenol (14.8 mg, 0.080 mmol) and

146

Dipp$_3$SbO (50 mg, 0.080 mmol) were dissolved in CHCl$_3$ (1.5 mL). The bright yellow solution was transferred under a layer of cyclohexane (18 mL). Yellow crystals suitable for X-ray diffraction grew overnight. The solvent was decanted and the crystals were washed with pentane (5 mL). Yield: 41 mg (49%). M.p. 186 °C (decomposed). **MS ($m/z$) [M–(O$_2$N)$_2$PhO]$^+$** 621.305 (calc 621.305). **$^1$H NMR (500 MHz, CDCl$_3$)** δ 8.80 (d, $J$ = 3.0 Hz, 1H), 7.86 (dd, $J$ = 9.6, 3.0 Hz, 1H), 7.57 (t, $J$ = 7.7 Hz, 3H), 7.40 (d, $J$ = 6.9 Hz, 3H), 7.32 (d, $J$ = 7.6 Hz, 3H), 6.30 (d, $J$ = 9.6 Hz, 1H), 3.40 (sept, $J$ = 5.9 Hz, 3H), 2.88 (sept, $J$ = 6.3 Hz, 3H), 1.34 (d, $J$ = 6.3 Hz, 9H), 1.23 (d, $J$ = 6.5 Hz, 9H), 0.96 (d, $J$ = 6.5 Hz, 9H), 0.86 (d, $J$ = 6.4 Hz, 9H). **$^{13}$C{$^1$H} NMR (125 MHz, CDCl$_3$)** δ 156.25, 152.32, 138.28, 136.55, 133.57, 128.41, 128.26, 126.51, 124.92, 124.35, 38.51, 36.28, 27.06, 26.52, 25.17, 24.73, 24.48.

**Synthesis of tris(2,6-diisopropylphenyl)stibine oxide 4-nitrophenol adduct (Dipp$_3$SbO·HOPhNO$_2$).** 4-Nitrophenol (3.3 mg, 0.024 mmol) and Dipp$_3$SbO (15 mg, 0.024 mmol) were dissolved in CHCl$_3$ (1 mL). The bright yellow solution was transferred under a layer of cyclohexane (18 mL). Yellow crystals suitable for X-ray diffraction grew overnight. The solvent was decanted and the crystals were washed with pentane (5 mL). Yield: 6 mg (32%). M.p. 224 °C (decomposed). **MS ($m/z$) [M–O$_2$NPhO]$^+$** 621.305 (calc 621.305). **$^1$H NMR (500 MHz, CDCl$_3$)** δ 8.00 (d, $J$ = 9.2 Hz, 2H), 7.48 (t, $J$ = 7.7 Hz, 3H), 7.36 (d, $J$ = 7.5 Hz, 3H), 7.23 (d, $J$ = 7.6 Hz, 3H), 6.90 (d, $J$ = 9.2 Hz, 2H), 3.99 (br sept, $J$ = 6.3 Hz, 3H), 2.95 (sept, $J$ = 6.3 Hz, 3H), 1.35 (d, $J$ = 5.7 Hz, 9H), 1.19 (d, $J$ = 6.1 Hz, 9H), 0.96 (d, $J$ = 6.3 Hz, 9H), 0.77 (d, $J$ = 6.0 Hz, 9H). **$^{13}$C{$^1$H} NMR (125 MHz, CDCl$_3$)** δ 156.69, 152.21, 140.38, 138.32, 132.43, 128.23, 127.52, 126.22, 125.82, 116.58, 37.48, 34.77, 26.78, 25.07, 24.69.

**Titration of [Dipp₃SbOH][CF₃SO₃] with triethylamine.** A solution of [Dipp₃SbOH][CF₃SO₃] (2.5 mg, 4.0 µmol) in d₃-MeCN (600 µL) was prepared. Triethylamine (100 µL) was diluted in d₃-MeCN (900 µL). NMR spectra were collected after addition of aliquots of the triethylamine solution or pure triethylamine (Tables C.5-7). The experiment was performed in triplicate.

**Titration of [Dipp₃AsOH][CF₃SO₃] with acridine.** A solution of [Dipp₃AsOH][CF₃SO₃] (1.5 mg, 2.6 µmol) in d₃-MeCN (500 µL) was prepared. A separate solution of acridine (37.1 mg, 0.2 mmol) in d₃-MeCN (750 µL) was prepared. NMR spectra were collected after addition of aliquots of the acridine solution (Table C.8-10). For the final data points, solid acridine was added to the sample. The experiment was performed in triplicate.

**General transesterification reaction.** A solution of *p*-nitrophenyl acetate (13.4 mg, 0.074 mmol), 2,2,2-trifluoroethanol (10 equiv, 53.2 µL, 0.74 mmol), and catalyst (0.2 equiv, 0.015 mmol) in CDCl₃ (500 µL) was prepared and transferred to an NMR tube. The NMR tube was heated to 50 °C in an oil bath. ¹H and ¹⁹F NMR spectra were collected on the samples to monitor the reaction after 26 h (Figures C.35 - C.42).

**X-ray crystallography: Independent Atom Model (IAM).** Crystals of [Dipp₃SbOH][CF₃SO₃], [Dipp₃AsOH][CF₃SO₃]·CHCl₃, [Dipp₃POH][O₃SCF₃], **1**, [Dipp₃SbOH][OPh(NO₂)₃], [Dipp₃AsOH][OPh(NO₂)₃]·¾(C₆H₁₂), [Dipp₃SbOH][OPh(NO₂)₂]·2(CHCl₃), Dipp₃SbO·HOPhNO₂, and [Dipp₃SbOH][OPhNO₂]·*p*-nitrophenol were grown as described above, selected under a microscope, loaded onto a MiTeGen polyimide sample loop using Paratone-N, and mounted onto a Rigaku XtaLAB Synergy-S single-crystal diffractometer. Each crystal was cooled to 100

K under a stream of nitrogen. Diffraction of Mo K$\alpha$ or Cu K$\alpha$ radiation from a PhotonJet-S microfocus source was detected using a HyPix6000HE hybrid photon counting detector. Screening, indexing, data collection, and data processing were performed with CrysAlisPro.[24] The structures were solved using SHELXT and refined using SHELXL following established strategies.[25-27] All non-H atoms were refined anisotropically. C-bound H atoms were placed at calculated positions and refined with a riding model and coupled isotropic displacement parameters (1.2 × $U_{eq}$ for aryl and methylene groups and 1.5 × $U_{eq}$ for methyl groups). O-bound H atoms were located in the Fourier difference map and refined semi-freely, employing distance restraints. Disordered atoms were treated with distance, similarity, and rigid-bond restraints.

**X-ray crystallography: Hirshfeld atom refinement (HAR).** The IAM results for $Dipp_3SbO \cdot HOPhNO_2$ and $[Dipp_3SbOH][OPhNO_2] \cdot p$-nitrophenol were used as input for the *NoSpherA2* implementation of HAR in *Olex2* (version 1.5).[28] The quantum chemistry calculations were performed by ORCA (version 5.0.1).[29-30] A wavefunction was calculated with high integration accuracy and tight SCF convergence criteria using the PBE0 hybrid functional and the x2c-TZVPP all-electron relativistically contracted basis set.[31-34] The effects of relativity were introduced using the second-order Douglas-Kroll-Hess formalism.[35] Least-squares crystallographic refinement was carried out with the *olex2.refine* engine.[36] The ADPs and positions of non-H atoms were freely refined using the aspherical atomic form factors obtained from Hirshfeld stockholder partitioning of the theoretical electron density obtained from the computed wavefunction.[37] C-bound H-atom positions were refined semi-freely; distance restraints were applied to chemically similar C–H bond lengths. H-atom isotropic

thermal parameters were refined freely. The positional and isotropic thermal parameters of O-bound H atoms were refined freely. The newly refined atomic coordinates were used as the input for a new density functional theory (DFT) calculation, from which new aspherical form factors were obtained. This procedure was iterated until it had converged.

**Powder X-ray diffraction (PXRD).** Bulk samples of were ground using an agate mortar and pestle. The fine white powders were each loaded onto a MiTeGen polyimide sample loop using Paratone-N and mounted onto a Rigaku XtaLAB Synergy-S single-crystal diffractometer. The powder was cooled to 100 K under a stream of nitrogen. The diffraction of Cu K$\alpha$ radiation was collected while the sample underwent a Gandolfi scan. Data collection and processing were performed using CrysAlisPro. Simulated PXRD diffractograms were generated from the crystal structures of [Dipp$_3$SbOH][CF$_3$SO$_3$], [Dipp$_3$AsOH][CF$_3$SO$_3$]·CHCl$_3$ triclinic, [Dipp$_3$POH][O$_3$SCF$_3$], **1**, [Dipp$_3$SbOH][OPh(NO$_2$)$_3$], [Dipp$_3$AsOH][OPh(NO$_2$)$_3$]·¾(C$_6$H$_{12}$), [Dipp$_3$SbOH][OPh(NO$_2$)$_2$]·2(CHCl$_3$), and Dipp$_3$SbO·HOPhNO$_2$ using Mercury and compared to the experimentally determined diffractograms.

**Computational experiments.** Geometry optimizations were performed on Dipp$_3$PnO, Dipp$_3$PnOH$^+$, *p*-nitrophenol, *p*-nitrophenoxide, 2,4-dintrophenol, 2,4-dinitrophenoxide, picric acid, picrate, **1**$^+$, **1**$^+$(As), and **1**$^+$(Sb) at the PBE0/def2-TZVPP level of theory with the RIJCOSX approximation and def2/J auxiliary basis set in the gas phase.[31-33,38-39] Frequency calculations were performed at the same level of theory for Dipp$_3$PnO, Dipp$_3$PnOH$^+$, **1**$^+$, **1**$^+$(As), and **1**$^+$(Sb) in the gas phase. Proton affinities of Dipp$_3$PnO were calculated by subtracting the enthalpy of the deprotonated species from that of the protonated species. Frequency calculations were

then performed on Dipp$_3$PnO, Dipp$_3$PnO H$^+$, *p*-nitrophenol, *p*-nitrophenoxide, 2,4-dintrophenol, 2,4-dinitrophenoxide, picric acid, and picrate at the same level of theory including the dielectric constant for DCM. Isodesmic reaction free energies in DCM were calculated by subtracting the sum of the free energies of the products from that of the reactants. Energetic analysis of the elimination of H$_2$ from cations Dipp$_3$PnO H$^+$ to form cyclized alkoxypnictonium cations **1**$^+$(Sb), **1**$^+$(As), and **1**$^+$, respectively, were performed by subtracting the sum of the Gibbs free energies of the cyclized alkoxyphosphonium and H$_2$ from that of the corresponding hydroxypnictonium cation. Single point energy calculations were performed using ORCA 5.0.0 or ORCA 5.0.1 on the optimized structures using the PBE0 hybrid functional and the old-DKH-TZVPP all-electron basis set using the RIJCOSX approximation and the SARC/J auxiliary basis set.[40-43] The effects of relativity were introduced using the second-order Douglas-Kroll-Hess formalism (DKH).[35] Single point energy calculations were used to generate wavefunctions that were subject to topological and Natural Bond Orbital (NBO) analyses. Topological analysis of the electron density was performed in MultiWFN (version 3.7).[44] Bond paths were visualized in MultiWFN (version 3.7). The values of the real space functions $\rho$, $\nabla^2\rho$, and $\varepsilon$ along interatomic vectors were visualized using R (version 4.0.2) through RStudio (version 1.3.1073). The following R packages were used for analysis and visualization: ggplot2, tidyverse, gridExtra, ggtext, scales, ggbreak, and grid.[45] NBO analysis was performed using the NBO program (version 7.0.7).[46] Non-covalent interactions (NCI) were calculated using MultiWFN and the results were visualized in VMD.[16,47]

**p*K*$_a$ determination from titration data.** The observed chemical shift of the Pn-proximal benzylic proton resonance (the benzylic proton resonance that appears most downfield in

pure pnictine oxide) was used to determine the percentage of deprotonated pnictine oxide in solution according to Equation 1. The percentage of pnictine oxide in solution, the initial moles of hydroxypnictonium in the sample, and the total volume can be used to determine the concentrations of pnictine oxide, hydroxypnictonium, free base titrant, and protonated titrant in the sample according to Equations 2-7. The equilibrium constant of Equations 8 and 9 ($K_8$) was obtained by non-linear regression of the data by the nls function in R of Equation 10. The known $pK_a$ value of the titrant was then used to determine the $pK_a$ of hydroxypnictonium, following equations 11-20.

1. $\dfrac{[\text{PnO}]}{[\text{PnO}]+[\text{PnOH}^+]} = \dfrac{\delta(\text{observed})-\delta(\text{PnOH}^+)}{\delta(\text{PnO})-\delta(\text{PnOH}^+)}$

2. $\text{Base} + \text{PnOH}^+ \rightleftharpoons \text{PnO} + \text{BaseH}^+$

3. $\text{mole PnO} = \text{mole PnOH}^+{}_0 * \dfrac{[\text{PnO}]}{[\text{PnO}]+[\text{PnOH}^+]}$

4. $[\text{PnO}] = \dfrac{\text{mole PnO}}{\text{Total Volume}}$

5. $[\text{PnOH}^+] = \dfrac{\text{mole PnOH}^+{}_0-\text{mole PnO}}{\text{Total Volume}}$

6. $[\text{Base}] = \dfrac{\text{mole Based added}-\text{mole PnO}}{\text{Total Volume}}$

7. $[\text{BaseH}^+] = [\text{PnO}]$

8. $K_8 = \dfrac{[\text{PnO}]\,[\text{BaseH}^+]}{[\text{Base}][\text{PnOH}^+]}$

9. $K_8 = \dfrac{[\text{PnO}]^2}{[\text{Base}][\text{PnOH}^+]}$

10. $[\text{PnO}] = \sqrt{K_8[\text{Base}][\text{PnOH}^+]}$

11. $\text{PnOH}^+ \rightleftharpoons \text{PnO} + \text{H}^+$

12. $\text{Base} + \text{H}^+ \rightleftharpoons \text{BaseH}^+$

13. $\Delta G_8 = \Delta G_{11} + \Delta G_{12}$

14. $-RT\ln K_8 = -RT\ln K_{11} + (-RT\ln K_{12})$

15. $\ln K_8 = \ln(K_{11}K_{12})$

16. $K_8 = K_{11}K_{12}$

17. $\dfrac{K_8}{K_{12}} = K_{11}$

18. $K_a = 10^{-pK_a}$

19. $K_{12} = \dfrac{1}{10^{-pK_a \text{ of base}}}$

20. $pK_a$ of PnO $= -\log(K_{11})$

## 4.8 – References

1.	Klofutar, C.; Krašovec, F.; Kušar, M., Base Strength of Various Organic Oxides. *Croat. Chem. Acta* **1968,** *40*, 23-28.

2.	Nylén, P., Die Basenstärke der Arsinoxyde und analoger Verbindungen aus der Stickstoff- und Schwefelgruppe. *Z. Anorg. Allg. Chem.* **1941,** *246*, 227-242.

3.	Bordner, J.; Doak, G. O.; Everett, T. S., Crystal structure of 2,2,4,4-tetrahydro-2,2,2,4,4,4-hexaphenyl-1,3,2,4-dioxadistibetane (triphenylstibene oxide dimer) and related compounds. *J. Am. Chem. Soc.* **1986,** *108*, 4206-4213.

4.	Carmalt, C. J.; Crossley, J. G.; Norman, N. C.; Orpen, A. G., The structure of amorphous $Ph_3SbO$: information from EXAFS (extended X-ray absorption fine structure) spectroscopy. *Chem. Commun.* **1996**, 1675-1676.

5.	Fuquen, R. M.; Lechat, J. R., Structure of the 1:1 complex formed by triphenylphosphine oxide and 4-nitrophenol. *Acta Crystallogr. Sect. C* **1992,** *48*, 1690-1692.

6.	Cuypers, R.; Burghoff, B.; Marcelis, A. T. M.; Sudhölter, E. J. R.; De Haan, A. B.; Zuilhof, H., Complexation of Phenols and Thiophenol by Phosphine Oxides and Phosphates. Extraction, Isothermal Titration Calorimetry, and ab Initio Calculations. *J. Phys. Chem. A* **2008,** *112*, 11714-11723.

7.	Lagier, C. M.; Scheler, U.; McGeorge, G.; Sierra, M. G.; Olivieri, A. C.; Harris, R. K., Solution and solid state proton transfer from phenols to triphenylphosphine oxide studied by 1H, 13C and 31P NMR spectroscopy. *J. Chem. Soc., Perkin Trans. 2* **1996**, 1325-1329.

8.	Lagier, C. M.; Olivieri, A. C.; Harris, R. K., NMR studies of proton transfer in 1:1 tris(trimethoxyphenyl)phosphine oxide–phenol complexes. *J. Chem. Soc., Perkin Trans. 2* **1998**, 1791-1796.

9.	Apperley, D. C.; Chaloner, P. A.; Crowe, L. A.; Harris, R. K.; Harrison, R. M.; Hitchcock, P. B.; Lagier, C. M., X-ray diffraction and phosphorus-31 NMR studies of the dynamically disordered 3:2 phenol–triphenylphosphine oxide complex. *Phys. Chem. Chem. Phys.* **2000,** *2*, 3511-3518.

10.	Krachko, T.; Lyaskovskyy, V.; Lutz, M.; Lammertsma, K.; Slootweg, J. C., Brønsted Acid Promoted Reduction of Tertiary Phosphine Oxides. *Z. Anorg. Allg. Chem.* **2017,** *643*, 916-921.

11.	Wenger, J. S.; Johnstone, T. C., Unsupported monomeric stibine oxides ($R_3SbO$) remain undiscovered. *Chem. Commun.* **2021,** *57*, 3484-3487.

12. Wenger, J. S.; Wang, X.; Johnstone, T. C., H-Atom Assignment and Sb–O Bonding of [Mes₃SbOH][O₃SPh] Confirmed by Neutron Diffraction, Multipole Modeling, and Hirshfeld Atom Refinement. *Inorg. Chem.* **2021,** *60*, 16048-16052.

13. Wenger, J. S.; Weng, M.; George, G. N.; Johnstone, T. C., Isolation, bonding, and reactivity of a monomeric stibine oxide. *Nat. Chem.* **2023,** *15*, 633-640.

14. Lindquist-Kleissler, B.; Wenger, J. S.; Johnstone, T. C., Analysis of Oxygen–Pnictogen Bonding with Full Bond Path Topological Analysis of the Electron Density. *Inorg. Chem.* **2021,** *60*, 1846-1856.

15. Cybulski, H.; Tymińska, E.; Sadlej, J., The Properties of Weak and Strong Dihydrogen-Bonded D−H···H−A Complexes. *ChemPhysChem* **2006,** *7*, 629-639.

16. Johnson, E. R.; Keinan, S.; Mori-Sánchez, P.; Contreras-García, J.; Cohen, A. J.; Yang, W., Revealing Noncovalent Interactions. *J. Am. Chem. Soc.* **2010,** *132*, 6498-6506.

17. Eckert, F.; Leito, I.; Kaljurand, I.; Kütt, A.; Klamt, A.; Diedenhofen, M., Prediction of acidity in acetonitrile solution with COSMO-RS. *J. Comput. Chem.* **2009,** *30*, 799-810.

18. Tshepelevitsh, S.; Kütt, A.; Lõkov, M.; Kaljurand, I.; Saame, J.; Heering, A.; Plieger, P. G.; Vianello, R.; Leito, I., On the Basicity of Organic Bases in Different Media. *Eur. J. Org. Chem.* **2019,** *2019*, 6735-6748.

19. Latham, A. H.; Williams, M. E., Versatile Routes toward Functional, Water-Soluble Nanoparticles via Trifluoroethylester–PEG–Thiol Ligands. *Langmuir* **2006,** *22*, 4319-4326.

20. Biesta, W.; van Lagen, B.; Gevaert, V. S.; Marcelis, A. T. M.; Paulusse, J. M. J.; Nielen, M. W. F.; Zuilhof, H., Preparation, Characterization, and Surface Modification of Trifluoroethyl Ester-Terminated Silicon Nanoparticles. *Chem. Mater.* **2012,** *24*, 4311-4318.

21. Warsitz, M.; Doye, S., Linear Hydroaminoalkylation Products from Alkyl-Substituted Alkenes. *Chem.–Eur. J.* **2020,** *26*, 15121-15125.

22. Li, K.; Weber, A. E.; Tseng, L.; Malcolmson, S. J., Diastereoselective and Enantiospecific Synthesis of 1,3-Diamines via 2-Azaallyl Anion Benzylic Ring-Opening of Aziridines. *Org. Lett.* **2017,** *19*, 4239-4242.

23. Chakraborty, D.; Das, R., Silver Triflate Catalyzed Acetylation of Alcohols, Thiols, Phenols, and Amines. *Synthesis* **2011,** *2011*, 1621-1625.

24. Rigaku Oxford Diffraction, *CrysAlis^{Pro}* **2020**.

25.     Sheldrick, G. M., SHELXT– Integrated space-group and crystal-structure determination. *Acta Crystallogr. Sect. A* **2015,** *71*, 3-8.

26.     Sheldrick, G. M., Crystal structure refinement with SHELXL. *Acta Crystallogr. Sect. C* **2015,** *71*, 3-8.

27.     Müller, P., Practical suggestions for better crystal structures. *Crystallogr. Rev.* **2009,** *15*, 57-83.

28.     Kleemiss, F.; Dolomanov, O. V.; Bodensteiner, M.; Peyerimhoff, N.; Midgley, L.; Bourhis, L. J.; Genoni, A.; Malaspina, L. A.; Jayatilaka, D.; Spencer, J. L.; White, F.; Grundkötter-Stock, B.; Steinhauer, S.; Lentz, D.; Puschmann, H.; Grabowsky, S., Accurate crystal structures and chemical properties from NoSpherA2. *Chem. Sci.* **2021,** *12*, 1675-1692.

29.     Neese, F., The ORCA program package. *Wiley Interdiscip. Rev.-Comput. Mol. Sci* **2012,** *2*, 73-78.

30.     Neese, F., *WIREs Comput. Mol. Sci* **2018,** *8*, e1327.

31.     Weigend, F.; Ahlrichs, R., Balanced basis sets of split valence, triple zeta valence and quadruple zeta valence quality for H to Rn: Design and assessment of accuracy. *Phys. Chem. Chem. Phys.* **2005,** *7*, 3297-3305.

32.     Perdew, J. P.; Ernzerhof, M.; Burke, K., Rationale for mixing exact exchange with density functional approximations. *J. Chem. Phys.* **1996,** *105*, 9982-9985.

33.     Perdew, J. P.; Burke, K.; Ernzerhof, M., Generalized Gradient Approximation Made Simple. *Phys. Rev. Lett.* **1996,** *77*, 3865-3868.

34.     Pollak, P.; Weigend, F., Segmented Contracted Error-Consistent Basis Sets of Double- and Triple-ζ Valence Quality for One- and Two-Component Relativistic All-Electron Calculations. *J. Chem. Theory Comput.* **2017,** *13*, 3696-3705.

35.     Wolf, A.; Reiher, M.; Hess, B. A., The generalized Douglas–Kroll transformation. *J. Chem. Phys.* **2002,** *117*, 9215-9226.

36.     Dolomanov, O. V.; Bourhis, L. J.; Gildea, R. J.; Howard, J. A. K.; Puschmann, H., OLEX2: a complete structure solution, refinement and analysis program. *J. Appl. Crystallogr.* **2009,** *42*, 339-341.

37.     Hirshfeld, F. L., Bonded-atom fragments for describing molecular charge densities. *Theor. Chim. Acta* **1977,** *44*, 129-138.

38.     Weigend, F., Accurate Coulomb-fitting basis sets for H to Rn. *Phys. Chem. Chem. Phys.* **2006,** *8*, 1057-1065.

39.     Neese, F.; Wennmohs, F.; Hansen, A.; Becker, U., Efficient, approximate and parallel Hartree–Fock and hybrid DFT calculations. A 'chain-of-spheres' algorithm for the Hartree–Fock exchange. *Chem. Phys.* **2009,** *356*, 98-109.

40.     Pantazis, D. A.; Chen, X.-Y.; Landis, C. R.; Neese, F., All-Electron Scalar Relativistic Basis Sets for Third-Row Transition Metal Atoms. *J. Chem. Theory Comput.* **2008,** *4*, 908-919.

41.     Pantazis, D. A.; Neese, F., All-Electron Scalar Relativistic Basis Sets for the Lanthanides. *J. Chem. Theory Comput.* **2009,** *5*, 2229-2238.

42.     Pantazis, D. A.; Neese, F., All-Electron Scalar Relativistic Basis Sets for the Actinides. *J. Chem. Theory Comput.* **2011,** *7*, 677-684.

43.     Pantazis, D. A.; Neese, F., All-electron scalar relativistic basis sets for the 6p elements. *Theor. Chem. Acc.* **2012,** *131*, 1292.

44.     Lu, T.; Chen, F., Multiwfn: A multifunctional wavefunction analyzer. *J. Comput. Chem.* **2012,** *33*, 580-592.

45.     Xu, S.; Chen, M.; Feng, T.; Zhan, L.; Zhou, L.; Yu, G., Use ggbreak to Effectively Utilize Plotting Space to Deal With Large Datasets and Outliers. *Front. Genet.* **2021,** *12*, 774846.

46.     Glendening, E. D.; Landis, C. R.; Weinhold, F., NBO 7.0 : New vistas in localized and delocalized chemical bonding theory. *J. Comput. Chem.* **2019,** *40*, 2234-2241.

47.     Humphrey, W.; Dalke, A.; Schulten, K., VMD: Visual molecular dynamics. *J. Mol. Graph.* **1996,** *14*, 33-38.

**Chapter 5**

**Steric congestion in heavy pnictines alters oxidative halogenation pathways**

**5.1 – Introduction**

As discussed in earlier chapters, heavy pnictines and pnictinidenes that feature bulky aryl substituents have been very useful as precursors in the isolation of interesting chemical motifs, and oxidative halogenation is often a key step in these synthetic efforts.[1-7] There has been significant interest in the design of stibonium and bismuthonium species with tunable Lewis acidity that can be leveraged for applications in ion sensing and catalysis.[4,8-11] Such $\sigma^4,\lambda^5$ pnictonium species can be isolated via the oxidative halogenation of a $\sigma^3,\lambda^3$ triarylpnictine to form the corresponding $\sigma^5,\lambda^5$ pnictorane, followed by the replacement of one of the axial halides with weakly a coordinating anion by a metathesis reaction. This procedure can generate pnictonium species of the form, $\sigma^4,\lambda^5$ [Ar$_3$PnX]$^+$, in which a low-lying Pn–X $\sigma^*$ orbital can be accessed by nucleophiles at the open coordination site of the pnictogen cation.[4] For this synthetic route to achieve desirable results, however, the steric environment about the antimony center must be designed appropriately by the choice of the installed aryl substituents. The species may undergo polymerization or engage in other undesirable reactivity if the pnictogen center is insufficiently shielded by the aryl groups. Alternatively, desirable Lewis acidity at the Pn center may be precluded if access to the $\sigma^*$ orbital is blocked.[13] These principles are demonstrated well by a recent study in which a series of mono-, di-, and trinuclear fluorobismuthonium cations were able to be isolated by careful ligand design.[10] In this report, Mes$_3$Bi underwent an oxidative fluorination followed by a salt metathesis reaction to abstract an equivalent of fluoride to form the monomeric fluorobismuthonium cation. In a different study, the oxidation of Mes$_3$Bi with PhIO was explored. In dichloromethane (DCM), this reaction yielded an unexpected oxidation product, Mes$_3$BiCl$_2$. Under different conditions and with different aryl groups, unexpected

159

tetraarylbismuthonium salts were isolated, rather than a desirable bismuthine oxide.[14] Bi(V) species can indeed be difficult to isolate in a similar manner to lighter pnictogen analogues, and great attention must be paid to the choice of ligand.

In this chapter, I will discuss the isolation of $Dipp_3Bi$, a sterically encumbered bismuthine, and its reactivity with oxidative halogenating agents. In my work, I was unsuccessful in isolating a bismuthine oxide with this platform, but the isolation of $Dipp_3Bi$ did lead to some interesting discoveries on how the steric environment of heavy pnictines can alter oxidative halogenation reactions. With $Dipp_3Bi$ in hand, we were able to investigate how the oxidative halogenation of Bi(III) varies in comparison to less encumbered species and Sb-containing analogues. $Dipp_3Bi$ reacted with the oxidative halogenation reagents $XeF_2$ to form the difluorobismuthorane $Dipp_3BiF_2$. In contrast, oxidation of $Dipp_3Bi$ with iodobenzene dichloride ($PhICl_2$) resulted in the decomposition of the bismuthine to intractable materials with the generation of 1-chloro-2,6-diisopropylbenzene, which presumably forms through a reductive elimination pathway. The reactivity of $Dipp_3Bi$ was varied relative to the less sterically encumbered bismuthine, $Mes_3Bi$, as well as the antimony-containing analogues $Dipp_3Sb$ and $Mes_3Sb$. In contrast to $Dipp_3Bi$, $Dipp_3Sb$ could be oxidized to form $Dipp_3SbCl_2$. $Dipp_3SbCl_2$ exhibits a highly unusual square pyramidal geometry in the solid state, and our theoretical results suggest that this geometry is also more thermodynamically stable than the usual trigonal bipyramidal geometry in the gas phase. The discovery of these unique oxidative halogenation pathways of sterically encumbered pnictines will hopefully guide researchers who continue to pursue the interesting and useful chemistry of heavy pnictogens.

## 5.2 – Synthesis and fluorination of Dipp₃Bi

Dipp₃Bi was isolated in a similar manner as Dipp₃Pn (Pn = P, As, Sb), as described in Chapter 3 (Figure 5.1).[12,15] BiCl₃ was treated with the organocopper(I) reagent in THF and refluxed to form a dark green suspension. The suspension was then extracted with ether and purified by flash chromatography (SiO₂/hexanes) to yield a yellow oil. Crystals rapidly grew from the oil and, after washing with MeCN, Dipp₃Bi was isolated in 11% yield. The yield was significantly lower than that of the lighter pnictine analogues, which agrees with the yields reported for the series Tipp₃Pn (Pn = P, As, Sb, Bi).[15] The $^1$H and $^{13}$C NMR spectra of Dipp₃Bi are reminiscent of Tipp₃Bi, with very broadened signals, due to partially restricted rotation about the $C_{ipso}$–Bi bond (Figure D.1, D.2). The NMR spectra of other Dipp₃Pn (Pn = P, As, Sb) feature sharp, decoalesced signals suggesting that, in these cases, rotation about the $C_{ipso}$–Pn bond is slow on the NMR time scale. The increased rate of rotation for the bismuthine can be attributed to a longer Pn–$C_{ipso}$ bond for the bismuthine such that the energetic barrier of rotation is reduced, and the signals broaden and coalesce.
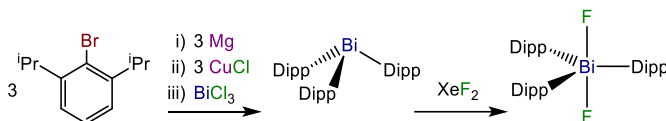


**Figure 5.1.** Synthesis of Dipp₃Bi and oxidative fluorination to form Dipp₃BiF₂.

We performed a single-crystal X-ray diffraction experiment on crystals of Dipp₃Bi (Figure 5.2a). The crystals Dipp₃Bi were found to be isomorphous with Dipp₃Sb; the compound had crystallized in the space group $I\bar{4}3d$ on a 3-fold rotation axis (Figure 5.2a).[12] The Bi–C bond lengths are 2.302(5) Å and the C–Bi–C bond angles are 106.16(12)°. Due to the utility of difluorobismuthoranes as synthetic precursors, and our lack of success in forming a

bismuthine oxide, we sought to subject Dipp$_3$Bi to an oxidative fluorination to explore the reactive landscape of the novel sterically encumbered bismuthine.[10]
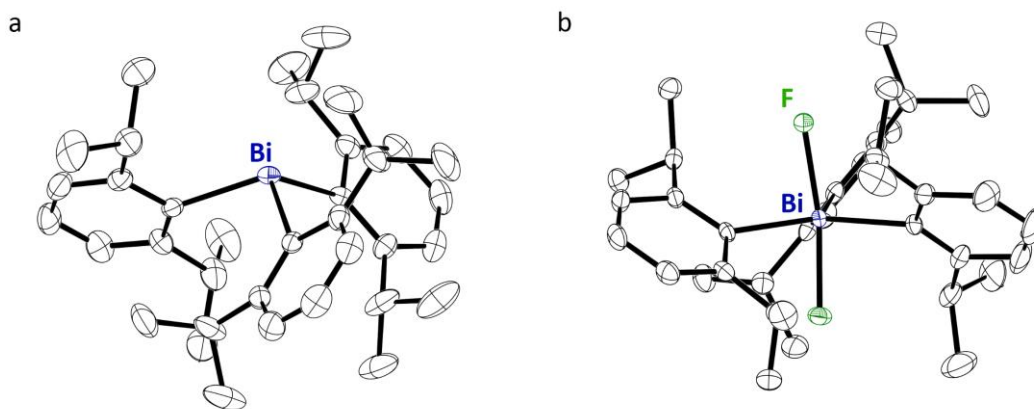


**Figure 5.2.** Thermal ellipsoid plots (50% probability) of (a) Dipp$_3$Bi and (b) Dipp$_3$BiF$_2$. Color code: Bi navy, F light-green, and C black. Hydrogen atoms are omitted for clarity and only one of the crystallographically inequivalent molecules of Dipp$_3$BiF$_2$ is depicted.

Because we had previously isolated Dipp$_3$SbF$_2$ (Chapter 3), we believed that the steric environment imposed by the Dipp groups would not be too encumbering for the oxidation to occur smoothly.[12] Indeed, dropwise addition of a yellow DCM solution of Dipp$_3$Bi to a DCM solution of XeF$_2$ resulted in immediate effervescence and discharge of color from the solution. Crystals of Dipp$_3$BiF$_2$ could be isolated in a 50% yield by addition of hexamethyldisiloxane to the reaction mixture followed by slow evaporation of the DCM. $^1$H and $^{13}$C NMR spectroscopic analyses of the product were consistent with the formation of a *trans*-dihalotriarylpnictorane with D$_3$ symmetry (Figure D.5, D.6). A single signal at −65.85 ppm was observed in the $^{19}$F NMR. This signal was comparable to, but significantly upfield of, the $^{19}$F resonances of both Mes$_3$BiF$_2$ (−100.41 ppm) and Dipp$_3$SbF$_2$ (−74.35 ppm).[10]

A diffraction experiment on Dipp$_3$BiF$_2$ found the compound to crystallize in space group $P\overline{1}$ with $Z'$ = 2 (Figure 5.21b). The solid-state structure of Dipp$_3$BiF$_2$ features an unusual

bent F–Bi–F bond angle of 169.68(6)°/169.82(6)° (values are provided for both of the crystallographically independent molecules in the asymmetric unit). $Ph_3BiF_2$ and $Mes_3BiF_2$ both crystallize with almost perfectly linear F–Bi–F bond angles.[10] The τ parameter of $Dipp_3BiF_2$ was found to be 0.716(2)/0.723(2), highlighting the distortion from an ideal trigonal bipyramidal geometry (Table 5.1). The Bi–F bond lengths of $Dipp_3BiF_2$ are 2.1265(14)/2.1265(14) and 2.1132(14)/2.1099(14) Å. The Bi–F bond lengths of $Mes_3BiF_2$ are similar to that of $Dipp_3BiF_2$, bond lengths but $Mes_3BiF_2$ exhibits a much more ideal trigonal bipyramidal geometry with a τ parameter of 0.954(1).

## 5.3 – Crystallographic characterization of dihalotrimesitylpnictoranes

The oxidation products of $Mes_3Bi$, $Mes_3BiCl_2$ or $Mes_3BiBr_2$, have been reported, but their solid-state structures had not been solved. It was thus necessary for us to resynthesize these species and elucidate their solid-state structures to draw comparisons with the oxidation products of $Dipp_3Bi$. We reprepared $Mes_3BiCl_2$ and $Mes_3BiBr_2$ following modified literature procedures and determined their crystal structures using single-crystal X-ray diffraction methods (Figure 5.3a,b).[16] $Mes_3SbCl_2$ and $Mes_3SbBr_2$ were also structurally characterized for comparison (Figure 5.3c,d) [4,17].

From a mixture of DCM and cyclohexane, $Mes_3BiCl_2$ crystallized as a cyclohexane solvate in space group $P31c$; the molecule resides on a crystallographic 3-fold rotation axis that imposes rigorous linearity on the Cl–Bi–Cl angle. The Bi–Cl bond lengths of the dichlorobismuthorane are 2.645(6) and 2.582(6) Å. Yellow crystals of $Mes_3BiBr_2$ grew as a chloroform solvate from a mixture of chloroform and pentane in space group $P2_1/n$. In alignment with a previous report, $Mes_3BiBr_2$ was found to rapidly decompose when dried.[16]

The Br–Bi–Br bond angle is relatively linear 178.326(13)° and the Bi–Br bond lengths are 2.8109(4) and 2.7643(4) Å.

While not isomorphous, the antimony compounds $Mes_3SbCl_2$ and $Mes_3SbBr_2$ both crystallized from hot hexanes in space group $P\bar{1}$ with two molecules in the asymmetric unit. $Mes_3SbCl_2$ features an almost linear Cl–Sb–Cl bond angle of 177.29(2)/178.55(3)° and the Sb–Cl bond lengths are 2.4976(7)/2.4810(8) and 2.4790(7)/2.4748(8) Å. Although the difference is subtle, $Mes_3SbBr_2$ features a more bent X–Sb–X bond angle of 173.724(9)/177.953(9)° with Sb–Br bond lengths of 2.6730(3)/2.6829(3) and 2.6694(3)/2.6427(3) Å. The distortion from linearity may arise by steric repulsion between the bromide substituents and the Mes groups.
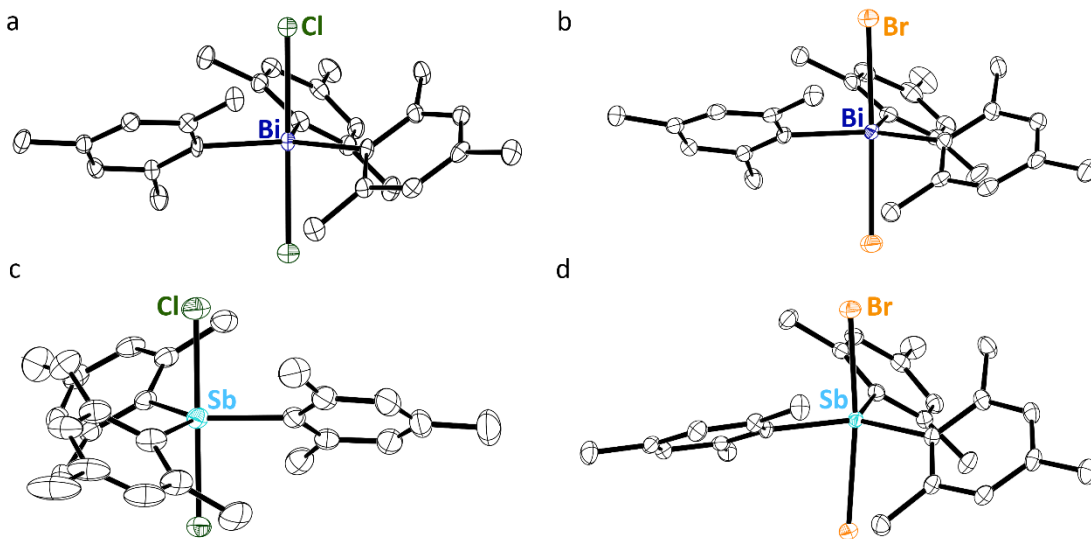


**Figure 5.3.** Thermal ellipsoid plots (50% probability) of (a) $Mes_3BiCl_2$, (b) $Mes_3BiBr_2$, (c) $Mes_3SbCl_2$, and (d) $Mes_3SbBr_2$. Color code: Bi navy, Sb teal, Cl dark-green, Br orange, and C black. Hydrogen atoms are omitted for clarity. For c and d, only one of the crystallographically independent molecules is depicted.

### 5.4 – Oxidative chlorination of $Dipp_3Bi$ and $Dipp_3Sb$

We next attempted to isolate the dichlorobismuthorane, $Dipp_3BiCl_2$, and were curious to see if there would be structural variation with the less encumbered congeners. Treatment

of Dipp$_3$Bi and PhICl$_2$ in CDCl$_3$ under inert atmosphere resulted in the formation of a yellow suspension with a rapidly forming colorless amorphous precipitate that is likely comprised of polymeric Bi-containing species.[13-14] $^1$H and $^{13}$C NMR spectra of the supernatant reveal the presence of 1-chloro-2,6-diisopropylbenzene (Figure D.14, D.15). We tentatively suggest that DippCl is generated by reductive elimination from a transient Bi(V) species (e.g., Dipp$_3$BiCl$_2$), but it could also arise via ligand exchange between Dipp$_3$Bi and PhICl$_2$ that installs a Dipp group on the iodine center, and subsequent reductive elimination from the resulting I(III) species. Other unidentified decomposition products were present in the supernatant (Figure D.14, D.15). While Bi(III) species are relatively stable, electronegative substituents are often needed to stabilize Bi(V) species. The stability of Mes$_3$BiCl$_2$ in the solid state and solution indicates that axial chloride substituents are sufficiently electronegative to stabilize a dichlorotriarylbismuthorane. Thus, we suggest that increased steric pressure imposed by the Dipp substituents destabilizes the 5-coordinate Dipp$_3$BiCl$_2$ in favor of decomposition through a reductive elimination process. Reductive elimination from Bi(V) species has been reported.[18] The formation of the organic reductive elimination product indicates that the oxidation did indeed occur. Low-temperature experiments or otherwise altered reaction conditions may one day permit the isolation of the target bismuthorane.

Sb(V) species are often less prone to reductive elimination than Bi(V) species,[19] and we investigated the oxidation of Dipp$_3$Sb with PhICl$_2$. Addition of a colorless DCM solution of Dipp$_3$Sb to a yellow DCM solution of PhICl$_2$ resulted in the immediate loss of color. Addition of pentane to the reaction mixture, followed by slow evaporation of the DCM resulted in the formation of colorless crystals of Dipp$_3$SbCl$_2$ in 50% yield. The $^1$H and $^{13}$C NMR spectra of the product are consistent with other symmetric dihalotriarylstiboranes (Figure 5.4, 5.5).
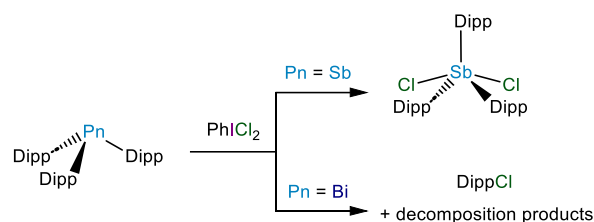
**Figure 5.4.** Oxidative chlorination of $Dipp_3Sb$ and $Dipp_3Bi$ with $PhICl_2$.

We collected X-ray diffraction data on the isolated crystals. $Dipp_3SbCl_2$ crystallized in space group $C2/c$, and the molecule resides on a 2-fold rotation axis. In a stark contrast to $Mes_3SbCl_2$, which features a Cl–Sb–Cl bond angle of 177.29(2)°, $Dipp_3SbCl_2$ features a Cl–Sb–Cl bond angle of 154.89(2)° in the solid state. The remarkably low τ parameter of 0.087(2) indicates that $Dipp_3SbCl_2$ is appropriately characterized as square pyramidal, in which the crystallographic 2-fold rotation axis bisects the apical Dipp group. To the best of our knowledge, this is the only dihalotriarylpnictorane that has crystallized with a square pyramidal geometry. In typical cases, such as $Dipp_3SbF_2$, the apicophillic halide ions occupy the axial positions of a trigonal bipyramid and the bulkier aryl substituents reside in the equatorial positions. We suggest that the square pyramidal geometry of $Dipp_3SbCl_2$ arises from a combination of the extreme steric crowding of the Dipp groups, the larger size of the chloride ligands (as compared to fluoride), and the lower apicophillicity of chloride than fluoride. The decreased steric pressure exerted by mesityl substituents rationalizes the trigonal bipyramidal structures of $Mes_3SbCl_2$ and $Mes_3SbBr_2$.



**Figure 5.5.** Thermal ellipsoid plot (50% probability) of $Dipp_3SbCl_2$. Color code: Sb teal, Cl dark-green, and C black. Hydrogen atoms are omitted for clarity.

**5.5 – Theoretical investigation of dihalopnictoranes**

We next asked the question: does the square pyramidal geometry assumed by Dipp$_3$SbCl$_2$ simply arise from crystal packing forces? We turned to quantum chemical calculations. A gas-phase geometry optimization (PBE0/def2-TZVPP) of Dipp$_3$SbCl$_2$ starting from the crystallographic coordinates converged upon a square pyramidal geometry ($\tau$ = 0.10), very similar to that in the crystal structure, confirming that the square pyramidal geometry resides on a local minimum on the potential energy surface (PES) of the compound. This result, however, does not necessarily indicate that it is the most stable geometry. We performed a separate geometry optimization starting from a linear input structure and found that the linear structure (Cl–Sb–Cl angle of 179.62°) is also a local minimum on the PES. The square pyramidal geometry features a ΔH that is 9.3 kcal/mol lower than that of the trigonal bipyramidal geometry, confirming the unusual square pyramidal is the most stable molecular geometry for Dipp$_3$SbCl$_2$ in gas phase (Table D.3).

In the crystal structure of Dipp$_3$BiF$_2$, the crystallographically independent molecules exhibit slightly bent F–Bi–F angles of 169.68(6)° and 169.82(6)°. The geometry optimized structure converged starting from the crystallographic coordinates to a distorted trigonal bipyramidal structure; the F–Bi–F bond angle of 173.04° was even more linear than in the crystal, but bent, nonetheless. Following a similar methodology as was employed for Dipp$_3$SbCl$_2$, we also optimized the structure of Dipp$_3$BiF$_2$ starting from a linear input geometry. This structure converged upon a structure with a linear F–Bi–F angle of 180.00°. The linear geometry Dipp$_3$BiF$_2$ was slightly more thermodynamically stable, with a ΔH that is 1.1 kcal/mol more stable than that of the distorted geometry (Table D.3). These results highlight the shallow nature of the PES.

We performed an energy decomposition analysis (EDA) of each geometry (PBE0/QZVP) to rationalize the thermodynamic favorability of the unusual structure of $Dipp_3SbCl_2$. The ratio $\Delta E_{orb}/\Delta E_{total}$ was slightly greater in the square pyramidal geometry relative to the trigonal bipyramidal structure suggesting that the driving force could be the formation of more favorable bonding interactions, rather than attenuation of steric repulsion (Table D.4).

In Chapters 3 and 4, we found that the Dipp groups could engage in stabilizing intramolecular hydrogen bonding interactions in pnictine oxide and hydroxypnictonium species.[12,20] The EDA results above suggested that the geometries of $Dipp_3SbCl_2$ and $Dipp_3BiF_2$ that deviate from trigonal bipyramidal might also be stabilized by such intramolecular secondary interactions. We employed non-covalent interaction (NCI) analysis to search for secondary interactions between the halides and the Dipp substituents.[21] NCI analysis

**Table 5.1.** Selected crystallographic metrics.[a]

| Compound | X–Pn–X bond angle (°) | Pn–X bond length (Å) | τ parameter |
|---|---|---|---|
| $Dipp_3BiF_2$ | 169.68(6)/169.82(6) | 2.1265(14)/2.1265(14), 2.1132(14)/2.1099(14) | 0.716(2)/0.723(2) |
| $Dipp_3SbF_2$ [b] | 180.00(7) | 1.971(3), 1.967(3) | 1.00(2) |
| $Dipp_3SbCl_2$ | 154.89(2) | 2.4864(4) | 0.087(2) |
| $Mes_3BiF_2$ [c] | 179.00(4) | 2.1222(10), 2.1223(10) | 0.954(1) |
| $Mes_3SbF_2$ [d] | 179.53(5) | 1.9821(10) | 0.972(1) |
| $Mes_3BiCl_2$ | 180 | 2.645(6), 2.582(6) | 1.00(2) |
| $Mes_3SbCl_2$ | 177.29(2)/178.55(3) | 2.4976(7)/2.4810(8), 2.4790(7)/2.4748(8) | 0.920(2)/0.929(2) |
| $Mes_3BiBr_2$ | 178.326(13) | 2.8109(4), 2.7643(4) | 0.913(3) |
| $Mes_3SbBr_2$ | 173.724(9)/177.953(9) | 2.6730(3)/2.6829(3), 2.6694(3)/2.6427(3) | 0.839(2)/0.943(2) |

[a] Values for crystallographically independent molecules are separated by slashes. [b] Crystallographic data of $Dipp_3SbF_2$ were obtained from a prior report.[12] [c] Crystallographic data of $Mes_3BiF_2$ were obtained from a prior report.[10] [d] Crystallographic data of $Mes_3SbF_2$ were obtained from a prior report.[4]

identifies regions of space between atoms where singularities in the reduced gradient of the electron density are present; these results are typically depicted using isosurface plots. The isosurfaces are color-mapped with the function $\text{sign}(\lambda_2)\rho$, where $\lambda_2$ is the second largest eigenvalue of the Hessian matrix, or Laplacian, and $\rho$ is the electron density. Regions where $\text{sign}(\lambda_2)\rho$ is close to 0 or negative represent attractive forces of strength comparable to hydrogen bonding interactions. Using this method, we found attractive interactions between the benzylic protons of the apical Dipp substituent and the chloride substituents of $Dipp_3SbCl_2$ (Figure 5.6). $Dipp_3BiF_2$ exhibited similar, albeit significantly weaker, attractive interactions
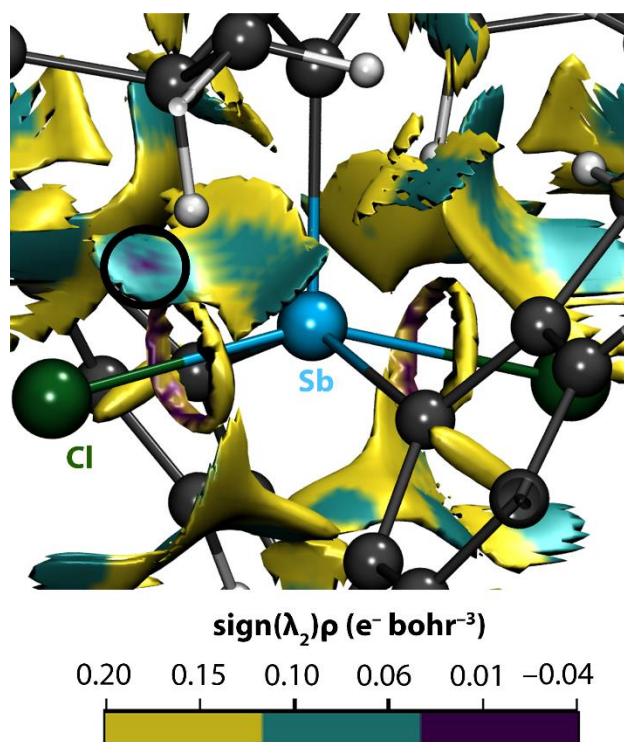


**Figure 5.6.** NCI analysis of $Dipp_3SbCl_2$ depicting reduced gradient surfaces (isovalue = 0.45 a.u.) with the function $\text{sign}(\lambda_2)\rho$ (where $\lambda_2$ is the second-largest eigenvalue of the Laplacian) color-mapped on the surface. Purple is indicative of H-bonding interactions, aqua is indicative of van der Waals interactions, and yellow is indicative of steric repulsions. H-bonding interactions are highlighted with a black circle for clarity. Color code: Sb teal, Cl dark green, C black, H grey.

between Dipp and fluoride substituents (Figure D.23). NCI analysis of $Dipp_3SbF_2$ and the trigonal bipyramidal geometries of $Dipp_3SbCl_2$ and $Dipp_3BiF_2$ revealed the presence of van der Waals interactions between the Dipp and halide substituents rather than stronger H-bonding interactions.

**5.6 – Conclusion**

Following our isolation of $Dipp_3SbO$, we were curious about the reactivity of $Dipp_3Bi$ in response to oxidants. In my work, I was unsuccessful in isolating $Dipp_3BiO$, but we did subject $Dipp_3Bi$ to oxidative halogenation reactions and found the species to have remarkably different reactivity from that of $Mes_3Bi$ and $Dipp_3Sb$. The reaction between $Dipp_3Bi$ and $XeF_2$ afforded $Dipp_3BiF_2$, which features a bent F–Bi–F bond angle. $Dipp_3BiCl_2$ was not similarly isolated; rather, the reaction between $Dipp_3Bi$ and $PhICl_2$ resulted in decomposition and the generation of products including 1-chloro-2,6-diisopropylbenzene. $Dipp_3SbCl_2$ was isolated by reaction between $Dipp_3Sb$ and $PhICl_2$ and features a highly unusual distorted square pyramidal geometry in the solid state. The square pyramidal geometry of $Dipp_3SbCl_2$ was calculated to be more thermodynamically stable than the more common trigonal bipyramidal geometry. Our results collectively highlight the utility in employing bulky aryl substituents to modulate the reactivity of heavy pnictines.

### 5.7 – Experimental methods

**General methods.** Reagents and solvents were purchased from commercial vendors and used as received unless otherwise specified. $Mes_3Sb$, $Mes_3Bi$, and $Dipp_3Sb$ were synthesized following literature protocols.[10,12,17] DCM and tetrahydrofuran (THF) were purified using an Innovative Technology PURE-SOLV solvent purification system. All solvents were dried over 3-Å molecular sieves. NMR spectra were collected using a Bruker Avance III HD 500 spectrometer equipped with a multinuclear Smart Probe. Signals in the ^{1}H and ^{13}C NMR spectra are reported in ppm as chemical shifts from tetramethylsilane and were referenced using the $CHCl_3$ (^{1}H, 7.26 ppm) and $CDCl_3$ (^{13}C, 77.16 ppm) solvent signals. The frequencies of ^{19}F NMR signals are reported in ppm as chemical shifts from $CFCl_3$ (referenced to 4-fluoroaniline at −126.88 ppm). The 4-fluoroaniline reference was an 87 µM solution in $CDCl_3$, collected at 298 K. Infrared (IR) spectra were collected on KBr pellets using a Thermo Nicolet Nexus 870 FT-IR spectrometer. Mass spectrometry measurements were collected using an LTQ-Orbitrap Velos Pro MS instrument. In addition to NMR analyses, the purity of novel materials was confirmed by observing agreement between experimental PXRD data of freshly prepared bulk solid and simulated powder diffraction patterns from single-crystal structures.

**Synthesis of tris(2,6-diisopropylphenyl)bismuthine ($Dipp_3Bi$).** A dry 250 mL two-necked round bottom flask fitted with a water-jacketed Liebig condenser was charged with a stir bar and magnesium turnings (771 mg, 31.7 mmol). Under an atmosphere of $N_2$, the magnesium turnings were suspended in dry THF (40 mL) and activated with 1,2-dibromoethane (690 µL, 8.0 mmol). 1-Bromo-2,6-diisopropylbenzene (4.8 mL, 23 mmol) was added dropwise and the reaction was refluxed for 3 h. After the magnesium turnings had been consumed, the colorless

solution was cooled to −78 °C and CuCl (2.36 g, 23.8 mmol) was added against a backflow of N$_2$ with an additional 15 mL of THF. The reaction mixture was allowed to warm to room temperature and stir overnight to form a pale white suspension. The resulting suspension was cooled to −78 °C and a suspension of trichlorobismuthine (2.490 g, 7.900 mmol) in THF (10 mL) was then added dropwise to the reaction mixture. The reaction mixture was stirred at room temperature for 30 min before being refluxed for 19 h. The resulting dark green suspension was cooled to room temperature, opened to air, and diluted with OEt$_2$ (150 mL) and water (200 mL). The aqueous layer was back-extracted with OEt$_2$ (2 × 50 mL). The combined organic phases were then washed with water (2 × 200 mL) and with brine (250 mL). The organic layer was dried over Na$_2$SO$_4$. The solvent was removed under reduced pressure. The resulting yellow oil was diluted with hexanes, filtered through Celite, and purified by flash chromatography (SiO$_2$, 1:20 ethyl acetate : hexanes). The collected fractions were stripped of solvent to obtain a yellow oil. Yellow crystals grew from the oil and were washed with acetonitrile and collected by vacuum filtration. Yield: 0.587 g (11%). Crystals suitable for X-ray diffraction were obtained similarly. M.p. 208 °C (decomp.). **ESI-MS (*m/z*) [M−Dipp]$^+$** 531.246 (calc 531.246). **$^1$H NMR (500 MHz, CDCl$_3$)** δ 7.28 (br s, 9H), 3.14 (br s, 6H), 1.5–0.25 (br m, 36 H). **$^{13}$C{$^1$H} NMR (125 MHz, CDCl$_3$)** δ 162.68, 156.68, 155.17, 128.37, 125.25, 123.65, 41.86, 37.63, 26.76, 24.93, 24.48, 23.52. In addition to NMR data, purity was confirmed by PXRD data from freshly prepared bulk solid; these powder data agreed with the simulated powder diffractogram generated from the crystal structure of Dipp$_3$Bi (Figure D.4).

**Synthesis of difluorotris(2,6-diisopropylphenyl)bismuthorane (Dipp$_3$BiF$_2$).** A solution of XeF$_2$ (13.1 mg, 0.0774 mmol) in DCM (0.6 mL) was added dropwise to a yellow solution of Dipp$_3$Bi

(51.5 mg, 0.0743 mmol) in DCM (0.6 mL). Bubbling occurred and the yellow color subsided. After 5 min, hexamethyldisiloxane (5 mL) was added and the solvent level was reduced to induce crystallization. Colorless crystals grew overnight. The solvent was decanted and the crystals were washed with 1 mL hexamethyldisiloxane before being dried under vacuum. Yield: 27 mg (50%). Crystals suitable for X-ray diffraction were obtained similarly. M.p. 178 °C. **ESI-MS ($m/z$) [M–F]$^+$** 711.377 (calc 711.377). **$^1$H NMR (500 MHz, CDCl$_3$)** δ 7.42 (s, 9H), 3.37 (br hept, $J$ = 7.0 Hz, 6H), 1.26 (d, $J$ = 5.9 Hz, 18H), 1.09 (d, $J$ = 6.4 Hz, 18H). **$^{13}$C{$^1$H} NMR (125 MHz, CDCl$_3$)** δ 167.38, 153.73, 130.72, 127.56, 36.06, 27.18, 24.51. **$^{19}$F{$^1$H} NMR (470 MHz, CDCl$_3$)** δ –65.85. In addition to NMR data, purity was confirmed by PXRD data from freshly prepared bulk solid; these powder data agreed with the simulated powder diffractogram generated from the crystal structure of Dipp$_3$BiF$_2$ (Figure D.9).

**Synthesis of dichlorotris(2,6-diisopropylphenyl)stiborane (Dipp$_3$SbCl$_2$).** A solution of Dipp$_3$Sb (49 mg, 0.081 mmol) in DCM (0.6 mL) was added dropwise to a solution of PhICl$_2$ (24 mg, 0.088 mmol) in DCM (0.6 mL). The yellow iodobenzene dichloride solution immediately became colorless and the solution was passed through Celite with an additional 1 mL of DCM for quantitative transfer. Pentane (10 mL) was added and the solvent was stripped to yield a colorless crystalline solid. The product was washed with pentane (2 x 1 mL) and dried under vacuum. Crystals suitable for X-ray diffraction were grown by slow evaporation of a mixture of DCM/pentane. Yield: 30 mg, 58%. M.p. 167 °C. **ESI-MS ($m/z$) [M–2Cl+OH]$^+$** 621.305 (calc 621.305) (HR-MS experiment only detected hydrolysis product Dipp$_3$SbOH$^+$, highlighting the instability of this species). **$^1$H NMR (500 MHz, CDCl$_3$)** δ 7.38 (s, 3H), 7.28 (d, $J$ = 5.7 Hz, 6H), 3.58 (br s, 6H), 1.24 (d, $J$ = 5.6 Hz, 18H), 0.99 (d, $J$ = 6.1 Hz, 18H). **$^{13}$C{$^1$H} NMR (125 MHz, CDCl$_3$)**

δ 152.06, 130.92, 126.62, 36.47, 26.68, 24.17. In addition to NMR data, purity was confirmed by PXRD data from freshly prepared bulk solid; these powder data agreed with the simulated powder diffractogram generated from the crystal structure of $Dipp_3SbCl_2$ (Figure D.13).

**Reaction between $Dipp_3Bi$ and iodobenzene dichloride ($PhICl_2$).** $Dipp_3Bi$ (8.2 mg, 0.011 mmol) and $PhICl_2$ (3.4 mg, 0.012 mmol) were dissolved in $CDCl_3$ (0.6 mL) to form a yellow solution. A colorless solid precipitated rapidly. After 2 h, $^1H$ and $^{13}C\{^1H\}$ NMR analyses revealed the generation of 1-chloro-2,6-diisopropylbenzene,[22] along with other unknown decomposition products (Figures D.14, D.15).

**Crystal growth of dichlorotrimesitylbismuthorane cyclohexane solvate [$Mes_3BiCl_2 \cdot (C_6H_{12})$].** $Mes_3BiCl_2$ was synthesized according to a modified literature protocol.[16] Briefly, $Mes_3Bi$ (55 mg, 0.079 mmol) and $PhICl_2$ (24 mg, 0.087 mmol) were dissolved in DCM (3 mL) to form a colorless solution. After 5 min, cyclohexane (20 mL) was added, and the reaction mixture was filtered through a Celite pad. The solvent level was reduced under reduced pressure to induce crystallization of pale-yellow crystals that were suitable for X-ray diffraction. NMR analysis of the crystals match literature reported values for $Mes_3BiCl_2$.[23] **$^1H$ NMR (500 MHz, $CDCl_3$)** δ 7.15 (s, 6H), 2.73 (s, 18H), 2.32 (s, 9H). **$^{13}C\{^1H\}$ NMR (125 MHz, $CDCl_3$)** δ 168.17, 141.98, 141.08, 132.24, 25.61, 20.94.

**Crystal growth of dibromotrimesitylbismuthorane chloroform solvate [$Mes_3BiBr_2 \cdot (CHCl_3)$].** $Mes_3BiBr_2$ was synthesized according to a modified literature protocol.[16] $Mes_3Bi$ (50 mg, 0.088 mmol) was dissolved in $CHCl_3$ (0.6 mL) and added to liquid $Br_2$ (15 mg, 0.095 mmol), resulting

in a yellow solution. Vapor diffusion of pentane into the reaction mixture resulted in the precipitation of yellow crystals suitable for X-ray diffraction. $Mes_3BiBr_2$ has been reported and described as thermally unstable when dried, preventing many characterization techniques. **$^1$H NMR (500 MHz, CDCl$_3$)** δ 7.13 (s, 6H), 2.75 (s, 18H), 2.33 (s, 9H).

**Crystal growth of dichlorotrimesitylstiborane (Mes$_3$SbCl$_2$).** A solution of $Mes_3Sb$ (198 mg, 0.413 mmol) in DCM (2 mL) was added dropwise to a yellow solution of $PhICl_2$ (114 mg, 0.414 mmol) in DCM (1 mL). The colorless reaction mixture was passed through a Celite pad. The solvent was stripped to form a colorless solid. Recrystallization from hot hexanes afforded crystals suitable for X-ray diffraction. NMR analysis of the crystals match literature reported values for $Mes_3SbCl_2$.[17] **$^1$H NMR (500 MHz, CDCl$_3$)** δ 7.00 (s, 6H), 2.66 (s, 18H), 2.31 (s, 9H). **$^{13}$C{$^1$H} NMR (125 MHz, CDCl$_3$)** δ 145.50, 142.34, 140.87, 131.09, 25.51, 21.01.

**Crystal growth of dibromotrimesitylstiborane (Mes$_3$SbBr$_2$).** A solution of $Mes_3Sb$ (192 mg, 0.400 mmol) in DCM (2 mL) was added dropwise to a solution of $Br_2$ (64.1 mg, 0.406 mmol) in DCM (1 mL). The yellow reaction mixture was stirred for 5 min before hexanes were added resulting in white precipitate that was collected via vacuum filtration. Recrystallization from hot hexanes afforded crystals suitable for X-ray diffraction. NMR analysis of the crystals match literature reported values for $Mes_3SbBr_2$.[17] **$^1$H NMR (500 MHz, CDCl$_3$)** δ 6.98 (s, 6H), 2.70 (s, 18H), 2.32 (s, 9H). **$^{13}$C{$^1$H} NMR (125 MHz, CDCl$_3$)** δ 145.65, 142.12, 140.87, 131.16, 26.20, 20.97.

**X-ray crystallography.** Crystals of $Dipp_3Bi$, $Dipp_3BiF_2$, $Mes_3BiCl_2 \cdot$cyclohexane, $Mes_3BiBr_2 \cdot CHCl_3$, $Mes_3SbCl_2$, $Mes_3SbBr_2$, and $Dipp_3SbCl_2$ were grown as described above, selected under a microscope, loaded onto a MiTeGen polyimide sample loop using Paratone-N, and mounted onto a Rigaku XtaLAB Synergy-S single-crystal diffractometer. Each crystal was cooled to 100 K under a stream of nitrogen. Diffraction of Cu K$\alpha$ radiation from a PhotonJet-S microfocus source was detected using a HyPix6000HE hybrid photon counting detector. Screening, indexing, data collection, and data processing were performed with CrysAlisPro.[24] The structures were solved using SHELXT and refined using SHELXL following established strategies.[25-27] All non-H atoms were refined anisotropically. C-bound H atoms were placed at calculated positions and refined with a riding model and coupled isotropic displacement parameters ($1.2 \times U_{eq}$ for non-methyl C-H atoms and $1.5 \times U_{eq}$ for methyl groups).

**Powder X-ray diffraction (PXRD).** Bulk samples of $Dipp_3Bi$, $Dipp_3BiF_2$, and $Dipp_3SbCl_2$ were ground using an agate mortar and pestle. The fine white powders were each loaded onto a MiTeGen polyimide sample loop using Paratone-N and mounted onto a Rigaku XtaLAB Synergy-S single-crystal diffractometer. The powder was cooled to 100 K under a stream of nitrogen. The diffraction of Cu K$\alpha$ radiation was collected while the sample underwent a Gandolfi scan. Data collection and processing were performed using CrysAlisPro. Simulated PXRD diffractograms were generated from the crystal structures of $Dipp_3Bi$, $Dipp_3BiF_2$, and $Dipp_3SbCl_2$ using Mercury and compared to the experimentally determined diffractograms.

**Computational experiments.** All geometry optimizations and frequency calculations were performed using ORCA 5.0.1.[28] Geometry optimizations were performed on $Dipp_3BiF_2$,

$Dipp_3SbF_2$, and $Dipp_3SbCl_2$ starting from crystallographic coordinates employing the BP86 pure functional and def2-SVP basis set, with the RI approximation and def2/J auxiliary basis set.[29] The optimized coordinates were then used as a starting point for a subsequent geometry optimization using the PBE0 hybrid functional and def2-TZVPP basis set, with the RIJCOSX approximation and def2/J auxiliary basis set.[30-34] Frequency calculations were then performed at the same level of theory in the gas phase. We then optimized structures of $Dipp_3BiF_2$(linear) and $Dipp_3SbCl_2$(linear) starting from the coordinates of $Dipp_3SbF_2$, where the antimony or fluorine atoms were replaced by bismuth or chlorine, respectively, in order to find a minimum on the potential energy surface where the X–Pn–X bond angle approximates 180°. EDA was performed using Gaussian 09.[35] Single point energy calculations (PBE0/QZVP) were performed on the 2Cl and $Dipp_3Sb$ fragments using coordinates from the optimized trigonal bipyramidal and square pyramidal structures. $\Delta E_{tot}$ was obtained by subtracting the energies of the 2Cl and $Dipp_3Sb$ fragments from that of the $Dipp_3SbCl_2$ molecule. MultiWFN (Version 3.7) was used to generate an input file for $Dipp_3SbCl_2$ with an initial guess for the combined 2Cl and $Dipp_3Sb$ fragments with no orbital interaction.[36] The energy of the initial guess wavefunction was subtracted from the final converged energy to obtain $\Delta E_{orb}$. For the NCI analysis, single point energy calculations were performed using ORCA 5.0.1 on the optimized coordinates using the PBE0 hybrid functional and old-DKH-TZVPP all-electron, relativistically contracted basis set following the Douglas-Kroll-Hess formalism, with the RIJCOSX approximation and SARC/J auxiliary basis set.[37-40] Non-covalent interactions were calculated using MultiWFN and the results were visualized in VMD.[41]

## 5.8 – References

1.    Pang, Y.; Nöthling, N.; Leutzsch, M.; Kang, L.; Bill, E.; van Gastel, M.; Reijerse, E.; Goddard, R.; Wagner, L.; SantaLucia, D.; DeBeer, S.; Neese, F.; Cornella, J., Synthesis and isolation of a triplet bismuthinidene with a quenched magnetic response. *Science* **2023,** *380*, 1043-1048.

2.    Wu, M.; Chen, W.; Wang, D.; Chen, Y.; Ye, S.; Tan, G., Triplet Bismuthinidenes Featuring Unprecedented Giant and Positive Zero Field Splittings. *Natl. Sci. Rev.* **2023**, nwad169.

3.    Lindquist-Kleissler, B.; Johnstone, T. C., Models of the putative antimony(V)–diolate motifs in antileishmanial pentavalent antimonial drugs. *Dalton Trans.* **2023,** *52*, 9229-9237.

4.    Yang, M.; Gabbaï, F. P., Synthesis and Properties of Triarylhalostibonium Cations. *Inorg. Chem.* **2017,** *56*, 8644-8650.

5.    Šimon, P.; de Proft, F.; Jambor, R.; Růžička, A.; Dostál, L., Monomeric Organoantimony(I) and Organobismuth(I) Compounds Stabilized by an NCN Chelating Ligand: Syntheses and Structures. *Angew. Chem., Int. Ed.* **2010,** *49*, 5468-5471.

6.    Šimon, P.; Jambor, R.; Růžička, A.; Lyčka, A.; de Proft, F.; Dostál, L., Monomeric organoantimony(III) sulphide and selenide with terminal Sb–E bond (E = S, Se). Synthesis, structure and theoretical consideration. *Dalton Trans.* **2012,** *41*, 5140-5143.

7.    Planas, O.; Wang, F.; Leutzsch, M.; Cornella, J., Fluorination of arylboronic esters enabled by bismuth redox catalysis. *Science* **2020,** *367*, 313-317.

8.    Pan, B.; Gabbaï, F. P., [Sb(C$_6$F$_5$)$_4$][B(C$_6$F$_5$)$_4$]: An Air Stable, Lewis Acidic Stibonium Salt That Activates Strong Element-Fluorine Bonds. *J. Am. Chem. Soc.* **2014,** *136*, 9564-9567.

9.    Hirai, M.; Myahkostupov, M.; Castellano, F. N.; Gabbaï, F. P., 1-Pyrenyl- and 3-Perylenyl-antimony(V) Derivatives for the Fluorescence Turn-On Sensing of Fluoride Ions in Water at Sub-ppm Concentrations. *Organometallics* **2016**, *35*, 1854-1860.

10.   Kuziola, J.; Magre, M.; Nöthling, N.; Cornella, J., Synthesis and Structure of Mono-, Di-, and Trinuclear Fluorotriarylbismuthonium Cations. *Organometallics* **2022,** *41*, 1754-1762.

11.   Matano, Y.; Begum, S. A.; Miyamatsu, T.; Suzuki, H., A New and Efficient Method for the Preparation of Bismuthonium and Telluronium Salts Using Aryl- and Alkenylboronic Acids. First Observation of the Chirality at Bismuth in an Asymmetrical Bismuthonium Salt. *Organometallics* **1998,** *17*, 4332-4334.

12.  Wenger, J. S.; Weng, M.; George, G. N.; Johnstone, T. C., Isolation, bonding, and reactivity of a monomeric stibine oxide. *Nat. Chem.* **2023,** *15*, 633-640.

13.  Solyntjes, S.; Neumann, B.; Stammler, H.-G.; Ignat'ev, N.; Hoge, B., Difluorotriorganylphosphoranes for the Synthesis of Fluorophosphonium and Bismuthonium Salts. *Eur. J. Inorg. Chem.* **2016,** *2016*, 3999-4010.

14.  Suzuki, H.; Ikegami, T.; Azuma, N., Unexpected formation of highly stabilized tetrakis-(2-alkoxyphenyl)bismuthonium salts in the oxidation of tris-(2-alkoxyphenyl)bismuthanes with iodosylbenzene. *J. Chem. Soc., Perkin Trans. 1* **1997**, 1609-1616.

15.  Sasaki, S.; Sutoh, K.; Murakami, F.; Yoshifuji, M., Synthesis, Structure, and Redox Properties of the Extremely Crowded Triarylpnictogens: Tris(2,4,6-triisopropylphenyl)phosphine, Arsine, Stibine, and Bismuthine. *J. Am. Chem. Soc.* **2002,** *124*, 14830-14831.

16.  Gilman, H.; Yablunky, H., Unsymmetrical Organobismuth Compounds. *J. Am. Chem. Soc.* **1941,** *63*, 207-211.

17.  Ates, M.; Breunig, H. J.; Soltani-Neshan, A.; Tegeler, M., Synthese von Mesitylstibanen / Synthesis of Mesitylstibanes. *Z. Naturforsch., B: J. Chem. Sci.* **1986,** *41*, 321-326.

18.  Moon, H. W.; Cornella, J., Bismuth Redox Catalysis: An Emerging Main-Group Platform for Organic Synthesis. *ACS Catal.* **2022,** *12*, 1382-1393.

19.  Lipshultz, J. M.; Li, G.; Radosevich, A. T., Main Group Redox Catalysis of Organopnictogens: Vertical Periodic Trends and Emerging Opportunities in Group 15. *J. Am. Chem. Soc.* **2021,** *143*, 1699-1721.

20.  Wenger, J. S.; Getahun, A.; Johnstone, T. C., Variation in pnictogen–oxygen bonding unlocks greatly enhanced Brønsted basicity for the monomeric stibine oxide. *Dalton Trans.* **2023,** *52*, 11325-11334.

21.  Johnson, E. R.; Keinan, S.; Mori-Sánchez, P.; Contreras-García, J.; Cohen, A. J.; Yang, W., Revealing Noncovalent Interactions. *J. Am. Chem. Soc.* **2010,** *132*, 6498-6506.

22.  Hoshi, T.; Honma, T.; Mori, A.; Konishi, M.; Sato, T.; Hagiwara, H.; Suzuki, T., An Active, General, and Long-Lived Palladium Catalyst for Cross-Couplings of Deactivated (Hetero)aryl Chlorides and Bromides with Arylboronic Acids. *J. Org. Chem.* **2013,** *78*, 11513-11524.

23.  Matano, Y.; Nomura, H.; Suzuki, H.; Shiro, M.; Nakano, H., Synthesis, Structure, and Reactions of (Acylimino)triaryl-$\lambda^5$-bismuthanes: First Comparative Study of the (Acylimino)pnictorane Series. *J. Am. Chem. Soc.* **2001,** *123*, 10954-10965.

24.     Rigaku Oxford Diffraction, *CrysAlis^{Pro}* **2020**.

25.     Sheldrick, G. M., SHELXT– Integrated space-group and crystal-structure determination. *Acta Crystallogr. Sect. A* **2015,** *71*, 3-8.

26.     Sheldrick, G. M., Crystal structure refinement with SHELXL. *Acta Crystallogr. Sect. C* **2015,** *71*, 3-8.

27.     Müller, P., Practical suggestions for better crystal structures. *Crystallogr. Rev.* **2009,** *15*, 57-83.

28.     Neese, F., The ORCA program package. *Wiley Interdiscip. Rev.-Comput. Mol. Sci* **2012,** *2*, 73-78.

29.     Becke, A. D., Density-functional exchange-energy approximation with correct asymptotic behavior. *Phys. Rev. A* **1988,** *38*, 3098-3100.

30.     Perdew, J. P.; Burke, K.; Ernzerhof, M., Generalized Gradient Approximation Made Simple. *Phys. Rev. Lett.* **1996,** *77*, 3865-3868.

31.     Perdew, J. P.; Ernzerhof, M.; Burke, K., Rationale for mixing exact exchange with density functional approximations. *J. Chem. Phys.* **1996,** *105*, 9982-9985.

32.     Weigend, F.; Ahlrichs, R., Balanced basis sets of split valence, triple zeta valence and quadruple zeta valence quality for H to Rn: Design and assessment of accuracy. *Phys. Chem. Chem. Phys.* **2005,** *7*, 3297-3305.

33.     Weigend, F., Accurate Coulomb-fitting basis sets for H to Rn. *Phys. Chem. Chem. Phys.* **2006,** *8*, 1057-1065.

34.     Neese, F.; Wennmohs, F.; Hansen, A.; Becker, U., Efficient, approximate and parallel Hartree–Fock and hybrid DFT calculations. A 'chain-of-spheres' algorithm for the Hartree–Fock exchange. *Chem. Phys.* **2009,** *356*, 98-109.

35.     Frisch, M. J.; Trucks, G. W.; Schlegel, H. B.; Scuseria, G. E.; Robb, M. A.; Cheeseman, J. R.; Scalmani, G.; Barone, V.; Petersson, G. A.; Nakatsuji, H.; Li, X.; Caricato, M.; Marenich, A. V.; Bloino, J.; Janesko, B. G.; Gomperts, R.; Mennucci, B.; Hratchian, H. P.; Ortiz, J. V.; Izmaylov, A. F.; Sonnenberg, J. L.; Williams; Ding, F.; Lipparini, F.; Egidi, F.; Goings, J.; Peng, B.; Petrone, A.; Henderson, T.; Ranasinghe, D.; Zakrzewski, V. G.; Gao, J.; Rega, N.; Zheng, G.; Liang, W.; Hada, M.; Ehara, M.; Toyota, K.; Fukuda, R.; Hasegawa, J.; Ishida, M.; Nakajima, T.; Honda, Y.; Kitao, O.; Nakai, H.; Vreven, T.; Throssell, K.; Montgomery Jr., J. A.; Peralta, J. E.; Ogliaro, F.; Bearpark, M. J.; Heyd, J. J.; Brothers, E. N.; Kudin, K. N.; Staroverov, V. N.; Keith, T. A.; Kobayashi, R.; Normand, J.; Raghavachari, K.; Rendell, A. P.; Burant, J. C.; Iyengar, S. S.; Tomasi, J.; Cossi, M.; Millam, J. M.; Klene, M.; Adamo, C.; Cammi, R.; Ochterski, J. W.; Martin, R. L.;

Morokuma, K.; Farkas, O.; Foresman, J. B.; Fox, D. J. *Gaussian 16 Rev. D.01*, Wallingford, CT, 2016.

36.     Lu, T.; Chen, F., Multiwfn: A multifunctional wavefunction analyzer. *J. Comput. Chem.* **2012,** *33*, 580-592.

37.     Pantazis, D. A.; Chen, X.-Y.; Landis, C. R.; Neese, F., All-Electron Scalar Relativistic Basis Sets for Third-Row Transition Metal Atoms. *J. Chem. Theory Comput.* **2008,** *4*, 908-919.

38.     Pantazis, D. A.; Neese, F., All-Electron Scalar Relativistic Basis Sets for the Lanthanides. *J. Chem. Theory Comput.* **2009,** *5*, 2229-2238.

39.     Pantazis, D. A.; Neese, F., All-Electron Scalar Relativistic Basis Sets for the Actinides. *J. Chem. Theory Comput.* **2011,** *7*, 677-684.

40.     Pantazis, D. A.; Neese, F., All-electron scalar relativistic basis sets for the 6p elements. *Theor. Chem. Acc.* **2012,** *131*, 1292.

41.     Humphrey, W.; Dalke, A.; Schulten, K., VMD: Visual molecular dynamics. *J. Mol. Graph.* **1996,** *14*, 33-38.

# Chapter 6

# A sterically accessible monomeric stibine oxide activates organotetrel(IV) halides, including C–F and Si–F bonds

**6.1 – Introduction**

There is growing interest in the design of main-group systems that can engage in the types of reactivity that are typically mediated by transition metals to provide sustainable alternatives comprised of cheap, Earth-abundant elements.[1-2] Transition metal complexes are often employed to activate strong σ bonds, utilizing their ability to cycle between oxidation states and coordination numbers to oxidatively add and reductively eliminate substrates. Redox-active pnictogen compounds have recently been identified as particularly suitable to mediate similar reaction pathways with main-group elements.[3-4] Beyond metallomimetic chemistry, the unique properties of p-block elements can be exploited to unlock reaction pathways and synthetic strategies that are entirely unprecedented or serve a complementary role to d-block elements. A notable example is the activation of $C(sp^3)$–F bonds, which can be achieved by potent main-group Lewis acids such as silylium cations.[5-6] The related Si–F bonds are among the strongest covalent single bonds and their functionalization often poses an even more formidable challenge, as reflected in the bond dissociation energies of $H_3C$–F ($D°_{298}$ = 460.2 ± 8.4 kJ mol$^{-1}$) and $H_3Si$–F ($D°_{298}$ = 638 ± 5 kJ mol$^{-1}$).[7] Because of their stability, the formation of fluorosilanes such as $SiEt_3F$ often serves as the thermodynamic driving force for catalytic defluorination reactions. The activation of Si–F bonds by transition metals is rare and examples are limited to fluorosilanes with pendent phosphine groups that direct the active metal center to engage in the bond activation.[8-9] Recently, neutral Lewis superacids[10] competent in the abstraction of fluoride from $SiEt_3F$ have been developed and show promise in overcoming issues with solubility and functional group tolerance associated with silylium salts.[11-12]

In this chapter, I discuss the isolation of a novel monomeric stibine oxide, Mes$_3$SbO. The use of less sterically demanding Mes substituents enables Mes$_3$SbO to engage in a more extended range of reactions than Dipp$_3$SbO. A theoretical investigation of Mes$_3$SbO was conducted and we found a negligible degree of variation in the electronic structure of the stiboryl bond relative to that of Dipp$_3$SbO, suggesting that differences in reactivity between these two species are likely to arise primarily from steric factors. We describe here that Mes$_3$SbO forms stable Lewis adducts with the main-group Lewis acids PbMe$_3$Cl and SnMe$_3$Cl. In contrast, treatment of Mes$_3$SbO with either GeMe$_3$Cl, SiMe$_3$Cl, or CPh$_3$Cl results in addition products of the general form, Mes$_3$Sb(OER$_3$)Cl (ER$_3$ = GeMe$_3$, SiMe$_3$, CPh$_3$). The ability of Mes$_3$SbO to access the biphilicity of the stiboryl group in addition chemistry prompted us to pursue more challenging C–F and Si–F bond activations. Treatment of Mes$_3$SbO with C($p$-MeOPh)$_3$F resulted in the formation of the expected C–F activation product, Mes$_3$Sb(OC($p$-MeOPh)$_3$)F. Most remarkably, treatment of Mes$_3$SbO with SiEt$_3$F results in the clean formation of Mes$_3$Sb(OSiEt$_3$)F within minutes at room temperature. More broadly, the ability of the stiboryl group to activate C(sp$^3$)–F and Si–F bonds marks a significant contribution to an increasingly rich literature on bond activation by polar, unsaturated main-group motifs.

## 6.2 – Synthesis and characterization of Mes$_3$SbO

Phosphine oxides and arsine oxides are commonly used as Lewis bases, and in Chapter 3, I described the interaction between Dipp$_3$SbO and transition-metal centers.[13] This coordination chemistry, in combination with the dramatically enhanced Brønsted basicity of Dipp$_3$SbO relative to its lighter congeners (Chapter 4),[14] led us to anticipate that the stibine oxide would readily form stable Lewis adducts with a wide variety of main-group Lewis acids.

As an initial test of this capability, we investigated its reaction with PbMe$_3$Cl, which features a sterically unencumbered Pb atom capable of expanding its coordination sphere and a low-lying Pb–Cl σ* orbital into which it can accept electron donation. Despite these favorable characteristics, ^{1}H NMR analysis of a CDCl$_3$ solution of Dipp$_3$SbO and excess PbMe$_3$Cl revealed no significant interactions between the two (Figure E.1). We suspect that this lack of reactivity results from the steric shielding of the bulky Dipp substituents. Although the Dipp substituents prevent self-association and hydrolysis, this stability comes at the cost of attenuated reactivity with substrates that could otherwise engage with the stiboryl group. Decreasing the bulk of pnictine substituents can indeed have a drastic impact on their reactivity, as demonstrated in Chapter 5 by comparing the oxidative halogenation of Mes$_3$Pn and Dipp$_3$Pn (Pn = Sb, Bi).[15]

Prior studies with Mes-substituted Sb compounds suggested that a Mes$_3$Sb framework, although more open, is still sufficiently encumbered to prevent deactivating self-association upon oxidation. Specifically, treatment of Mes$_3$Sb with H$_2$O$_2$ yields Mes$_3$Sb(OH)$_2$, the monomeric structure of which was confirmed with X-ray crystallography and EXAFS.[13,16] Decreasing the steric bulk further to simple Ph groups results in polymerization upon oxidation, although we note that monomeric Ph$_3$Sb(OH)$_2$ has been isolated via the oxidative hydrolysis of [Et$_4$N][PhSbCl$_2$Br] in methanol.[17-21] We interpret a prior report that treatment of Mes$_3$Sb with iodosobenzene affords Mes$_3$Sb(OH)$_2$ as confirmation that the Mes$_3$Sb framework is not only capable of supporting a monomeric stibine oxide, but that the resulting stiboryl unit is sufficiently accessible that it rapidly hydrolyzes in the presence of adventitious water.[22] Such facile hydrolytic behavior of the putative Mes$_3$SbO stands in stark contrast to the relative

stability of Dipp$_3$SbO, which can be heated in the presence of excess water with no effect. Thus, we sought to isolate Mes$_3$SbO to more deeply probe the reactivity of the stiboryl group.

Under rigorously dry conditions, treatment of Mes$_3$Sb with a suspension of PhIO in DCM resulted in the rapid consumption of the solid oxidant to produce Mes$_3$SbO (Figure 6.1), which could be isolated as a colorless crystalline solid on a multi-gram scale. The $^1$H and $^{13}$C NMR spectra of the product reveal a single mesityl environment averaged by rapid rotation about the Sb–C$_{ipso}$ bond. In contrast, the $^1$H and $^{13}$C NMR spectra of Dipp$_3$SbO display a single Dipp environment that is desymmetrized by restricted rotation about the Sb–C$_{ipso}$ axis.[13] This observation provides preliminary insight into the difference in the steric environment about the stiboryl groups of the two compounds. In Mes$_3$SbO, the *ortho*-methyl protons of the mesityl groups are deshielded as compared to Mes$_3$Sb, consistent with other oxidation products of this stibine. The IR spectrum of Mes$_3$SbO is in excellent agreement with the calculated (PBE0/def2-TZVPP) spectrum for monomeric Mes$_3$SbO (Figure E.4). The correspondence of the Mes$_3$SbO stiboryl stretching frequency, $\nu$(Sb–O) 778 cm$^{-1}$, with that of Dipp$_3$SbO (779 cm$^{-1}$) suggests that despite the significant change in sterics between the two species, there is little variation in the electronic structure of the stiboryl group.
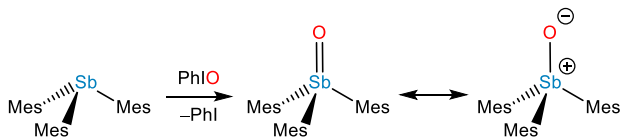


**Figure 6.1.** Synthesis of Mes$_3$SbO.

The solid-state structure of Mes$_3$SbO was determined by single crystal X-ray diffraction (SC-XRD) (Figure 6.2). Mes$_3$SbO crystallizes as a tetrahedral monomer in space group $P2_1/c$. The stiboryl Sb–O bond length is 1.848(2) Å, in agreement with that of Dipp$_3$SbO (1.8371(4) Å), and signif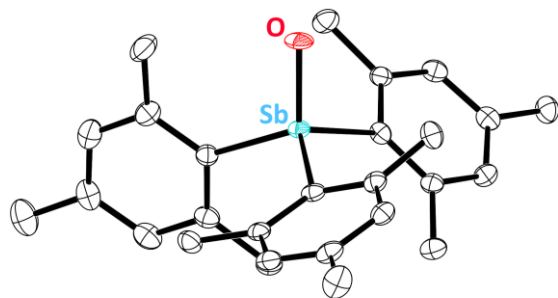icantly shorter than the Sb–O bond lengths of 1.9055(8) Å in [Mes$_3$SbOH][PhSO$_3$],[23] 2.027(2) Å in Mes$_3$Sb(OH)$_2$,[16] and 1.934(2) Å in (Ph$_3$SbO)$_2$.[19] The next shortest Sb⋯O distance in the crystal structure of Mes$_3$SbO is 6.980(2) Å, confirming that there are no interactions between stiboryl groups of adjacent monomers.



**Figure 6.2.** Thermal ellipsoid plot (50% probability) of Mes$_3$SbO. Color code: Sb teal, O red, and C black. Hydrogen atoms are omitted for clarity.

We were curious if Mes$_3$SbO would exhibit more ideal geometric features relative to Dipp$_3$SbO due to the less encumbered steric environment. The sum of the C$_{ipso}$–Sb–C$_{ipso}$ bond angles is 333.1(2)° in Mes$_3$SbO and 338.73(3)° in the monoclinic structure of Dipp$_3$SbO from Chapter 3. Furthermore, the average Sb–C$_{ipso}$–C$_{para}$ bond angles are 173.06(7)° in Mes$_3$SbO and 169.46(2)° in Dipp$_3$SbO. These variations suggest that Mes$_3$SbO more closely approximates an ideal tetrahedral geometry at the Sb center, and that the Sb center resides more closely to the planes defined by the aryl substituents. However, an orthorhombic polymorph of of Dipp$_3$SbO was also reported in Chapter 3. In this polymorph, Dipp$_3$SbO is even further distorted from an ideal structure relative to Mes$_3$SbO (Table E.3). Evidently, these variations may arise from intermolecular packing forces within the crystal and complicate a direct comparison of the molecular geometries. Comparison of the calculated geometries (PBE0/def2-TZVPP) of Mes$_3$SbO and

Dipp$_3$SbO in the gas phase reveals that Dipp$_3$SbO is indeed significantly more distorted from an ideal VSEPR geometry than Mes$_3$SbO and to a greater extent than observed in the crystallographic data. The sum of the C$_{ipso}$–Sb–C$_{ipso}$ bond angles is 332.01° in Mes$_3$SbO and 339.62° in Dipp$_3$SbO, and the average Sb–C$_{ipso}$–C$_{para}$ bond angles are 174.26° in Mes$_3$SbO and 169.16° in Dipp$_3$SbO (PBE0/def2-TZVPP).

## 6.3 – Electronic structure of Mes$_3$PnO (Pn = P, As, Sb)

To gain deeper insight into the electronic structure of the novel monomeric stibine oxide, we subjected Mes$_3$SbO to a number of theoretical analyses; computational data for Mes$_3$PnO and Dipp$_3$PnO (Pn = P, As, Sb) are collected in Table E.4. Topological analysis (PBE0-DKH/old-DKH-TZVPP) of the electron density (ρ) found a (3,–1) critical point (bcp) along the Sb–O interatomic vector, confirming the presence of a bond (Figure 6.3a). The value of ρ at the Sb–O bcp of Mes$_3$SbO is almost identical to that of Dipp$_3$SbO. As with Dipp$_3$PnO (Pn = P, As, Sb), comparing Mes$_3$PnO (Pn = P, As, Sb) in the Pn–O bonding region finds the lowest value of ρ for the stibine oxide. Assessment of the Laplacian of ρ ($\nabla^2\rho$) reveals a minimum that is the lowest in magnitude for the stibine oxide, consistent with the weakest bond and the lowest local concentration of charge in the bonding region across the series (Figure 6.3a). The low ellipticity (ε) of ρ along the pnictoryl Pn–O bond relative to other types of Pn–O bonds results from the cylindrically symmetrical back-donation from O-centered lone pairs to Pn–C σ* orbitals.[24] As with Dipp$_3$SbO, the HOMO and HOMO–1 of Mes$_3$SbO feature strong contributions from the two O-centered p-orbitals and are significantly destabilized relative to the corresponding orbitals for its lighter congeners (Figure 6.3b). In Chapter 3, I described how, for the Dipp$_3$PnO series, this variation in electronic structure manifests as comparatively

enhanced basicity for the stibine oxide. The LUMO of Mes$_3$SbO, although delocalized across the stiboryl unit and the aryl groups, nonetheless exhibits significant Sb–O σ* character with a pronounced lobe opposite the Sb–O bond (Figure 6.3c). The low-lying LUMO of Mes$_3$SbO relative to its lighter congeners suggests that there will be enhanced Lewis acidity at the Sb center as well as enhanced biphilic reactivity across the polar unsaturated stiboryl group. Natural population analysis is consistent with a highly polarized stiboryl bond with significant positive charge on the Sb atom (+2.22) and significant negative charge on the O atom (−1.23).

Further detailed information was obtained by analysis of the natural bond orbitals (NBOs) and natural localized molecular orbitals (NLMOs). An approximately cylindrically symmetrical Sb–O bonding NLMO is polarized towards the oxygen with a 26% contribution from an Sb-centered orbital (s: 41%, p: 59%) and a 73% contribution from an O-centered orbital (s: 19%, p: 80%) (Figure 6.3f). The corresponding Sb–O σ* NLMO closely resembles the LUMO; we expect that increased steric access to the lobe of this orbital, as compared to Dipp$_3$SbO, will unlock enhanced Lewis acidity for Mes$_3$SbO (Figure 6.3e). Two O-centered p-hybridized NLMOs recapitulate the two nearly degenerate highest occupied canonical MOs (Figure 6.3d). The two corresponding parent lone pair NBOs are each populated with 1.89 electrons, suggesting appreciable non-Lewis character in the electronic structure. Second-order perturbation theory analysis finds significant delocalizations of electron density from these O-centered lone pairs into Sb–C σ* orbitals (Figure 6.3g). Deletion calculations suggest that these back-bonding interactions are of similar strength to those present in Dipp$_3$SbO, and much weaker than those present in arsine and phosphine oxides (Table E.4). Our experimental and theoretical data suggest that electronic variations between the stiboryl groups of Mes$_3$SbO and Dipp$_3$SbO are quite subtle, and that differences in the reactivity of these two

species are more likely to result from the distinctly different steric environments of the two species imparted by the aryl substituents.
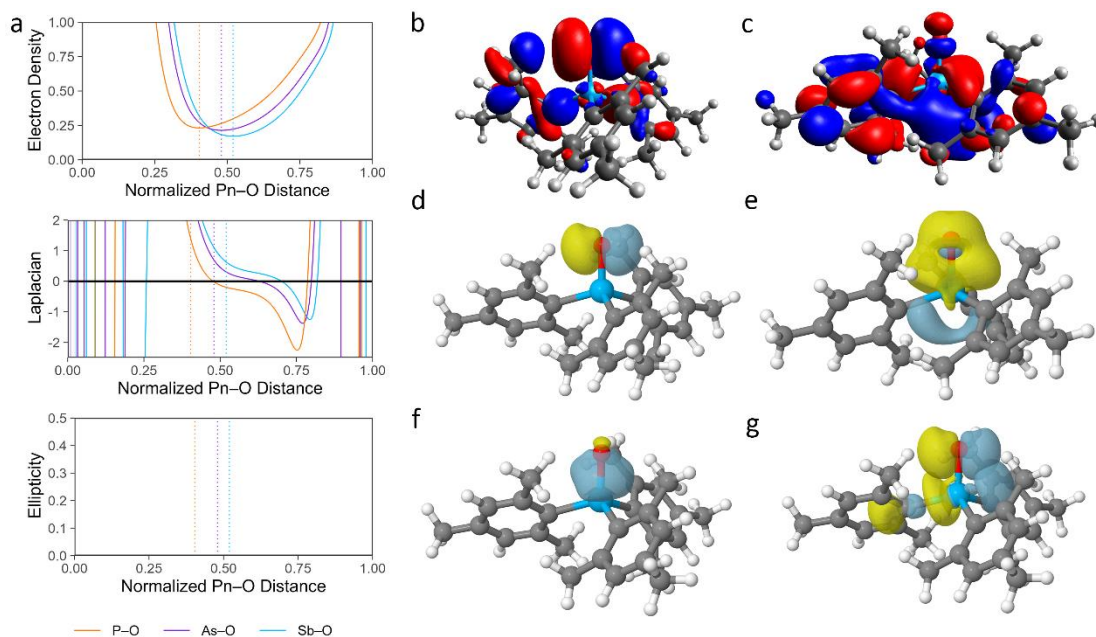


**Figure 6.3.** (a) Values of $\rho$ ($e^-\text{Å}^{-3}$), $\nabla^2\rho$ ($e^-\text{Å}^{-5}$), and $\varepsilon$ for Mes$_3$PnO (Pn = P, As, Sb) along the Pn–O bond paths, with Pn at 0.00 and O at 1.00 along the horizontal axis. The bond length is normalized to 1.00. The location of the (3, –1) critical point is shown with a dashed vertical line. Canonical molecular orbital diagrams of the (b) HOMO and (c) LUMO of Mes$_3$SbO (isovalue = 0.02). Surface plots (isovalue = 0.05) depicting an (d) O-centered lone pair NLMO, (e) the Sb–O $\sigma^*$ antibonding NLMO, (f) the Sb–O $\sigma$ bonding NLMO, and (g) overlap of an O-centered lone pair and an Sb–C $\sigma^*$ antibonding NLMOs. Color code: Sb teal, O red, C grey, H white.

## 6.4 – Reactivity between organotetrel(IV) chlorides and Mes$_3$SbO

With the more sterically accessible stibine oxide in hand, we reinvestigated PbMe$_3$Cl as a Lewis acidic substrate. Treatment of a suspension of PbMe$_3$Cl with Mes$_3$SbO in DCM resulted in the rapid consumption of the solid (Figure 6.4a). Addition of pentane to the mixture led to the growth of colorless crystals. [207]Pb NMR analysis of the product found a
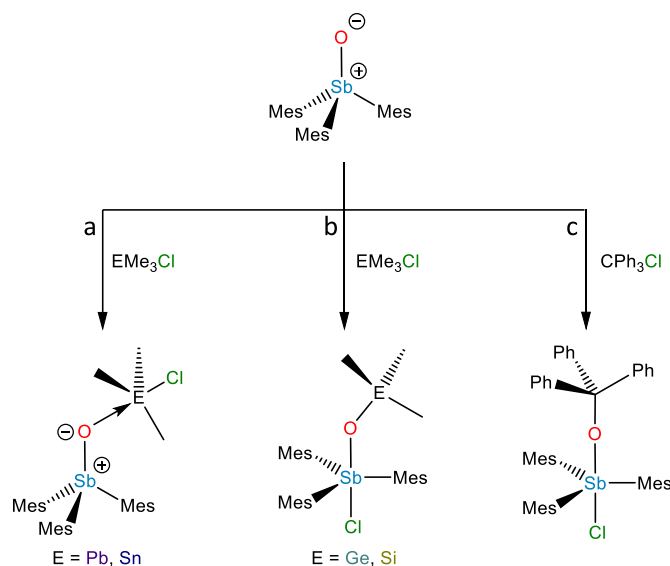
**Figure 6.4.** Synthesis of (a) Mes₃SbO→PbMe₃Cl and Mes₃SbO→SnMe₃Cl, (b) Mes₃Sb(OGeMe₃)Cl and Mes₃Sb(OSiMe₃)Cl, and (c) Mes₃Sb(OCPh₃)Cl.

single resonance at 207.6 ppm, significantly shielded relative to PbMe₃Cl (413.2 ppm), consistent with the expansion of the Pb coordination sphere.[25] The $^1$H NMR spectrum was consistent with the formation of Mes₃SbO→PbMe₃Cl; the equimolar Sb-bound mesityl substituents and Pb-bound methyl substituents each exhibited significantly shifted proton resonances relative to the corresponding precursors. The *ortho*-methyl mesityl protons remained symmetrized by rapid rotation about the Sb–C$_{ipso}$ bond. The Pb-bound methyl protons feature a strengthened $^2J_{PbH}$ coupling constant of 85.1 Hz relative to that of PbMe₃Cl (65.5 Hz). The increase in $^2J_{PbH}$ would be consistent with the enrichment expected in the s-character of the Pb-based orbitals used to make the equatorial Pb–C bonds if the Pb atom moves to a trigonal bipyramidal geometry with three equatorial methyl substituents and axial chloride and Mes₃SbO ligands. This geometry was subsequently confirmed crystallographically.

Mes$_3$SbO→PbMe$_3$Cl crystallized as the DCM solvate in space group $P2_1/c$ (Figure 6.5a). The Sb atom maintains a tetrahedral coordination sphere and, as predicted spectroscopically, the Pb atom features a trigonal bipyramidal geometry (τ = 0.958(4)). Mes$_3$SbO coordinates the Pb atom through the stiboryl oxygen with an O–Pb distance of 2.351(3) Å. Coordination to the Lewis acid lengthens the Sb–O bond to 1.860(3) Å, consistent with other Lewis adducts of stibine oxides and with the notion that donation of O-based lone-pair electron density to the Pb center reduces the strength of backbonding and weakens the Sb–O bond.

Treatment of Mes$_3$SbO with SnMe$_3$Cl afforded similar results (Figure 6.4a). The [119]Sn nucleus in the product resonates at –36.38 ppm in CDCl$_3$, significantly upfield of Me$_3$SnCl (169.1 ppm), and the $^2J_{SnH}$ coupling (69.0 Hz) is stronger in the product.[26-27] These NMR data are consistent with the formation of a 5-coordinate Sn center in solution. Crystals of Mes$_3$SbO→SnMe$_3$Cl·(C$_7$H$_8$) were grown from a concentrated toluene solution and the solid-state structure was determined by SC-XRD. Mes$_3$SbO→SnMe$_3$Cl·(C$_7$H$_8$) crystallized in space group $P2_1/n$ (Figure 6.5b). As with the Pb-containing analogue, the tetrahedral geometry is
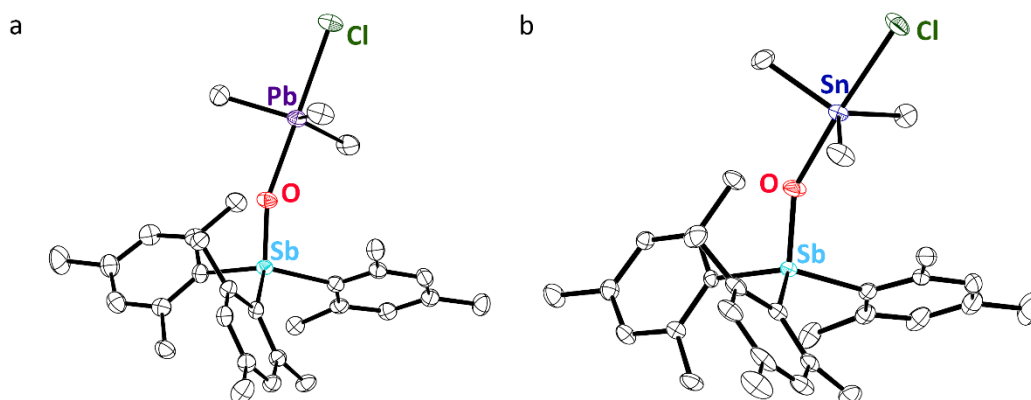


**Figure 6.5.** Thermal ellipsoid plots (50% probability) of (a) Mes$_3$SbO→PbMe$_3$Cl and (b) Mes$_3$SbO→SnMe$_3$Cl. Color code: Sb teal, Pb purple, Sn blue, Cl dark-green, O red, and C black. Hydrogen atoms and solvent molecules are omitted for clarity.

maintained about the Sb center and the stiboryl O atom coordinates to the Sn, affording a trigonal bipyramidal geometry about the Sn atom ($\tau$ = 0.84). The O–Sn interatomic distance is 2.180(2) Å and the Sb–O bond length is 1.865(2) Å.

We expanded our investigation of Mes$_3$SbO toward reactivity with lighter organotetrel(IV) chlorides. A toluene solution of Mes$_3$SbO was treated with GeMe$_3$Cl (Figure 6.4b). Evaporation of the solvent resulted in the growth of colorless crystals. These crystals were determined to be the toluene hemisolvate of Mes$_3$Sb(OGeMe$_3$)Cl using SC-XRD (Figure 6.6a). In contrast to the Pb- and Sn-containing analogues, the Sb atom expands its coordination sphere to a trigonal bipyramid ($\tau$ = 0.917(2)) to incorporate the chloride ion in the axial position opposite the trimethylgermyloxide ligand. Mes$_3$Sb(OGeMe$_3$)Cl can be viewed as the formal addition product of GeMe$_3$Cl across the unsaturated stiboryl bond. This addition demonstrates the capability of Mes$_3$SbO to engage substrates in a biphilic manner with both the Lewis basic O atom and the Lewis acidic Sb atom. The Sb–O bond distance of 1.970(2) Å is significantly longer than that of Lewis acid-coordinated monomeric stibine oxides described above. The longer Sb–O bond length in the stiborane is expected due to the even stronger interaction between the O and Ge atoms and because of the 3-center-4-electron bonding along the Cl–Sb–O axis (which can alternatively be described as donation from the axial chloride substituent into the Sb–O $\sigma^*$ orbital).

PXRD and elemental analysis confirm that bulk samples of the Ge-containing product match the identity of the crystal analyzed by SC-XRD in high purity. NMR analyses of this compound are, however, complicated by apparent isomerization in solution. In toluene-$d_8$, the ^{1}H and ^{13}C NMR spectra each reveal the presence of two sets of sharp signals in approximately an 8 : 1 ratio. Each set of signals in the ^{1}H and ^{13}C NMR spectra in toluene-$d_8$
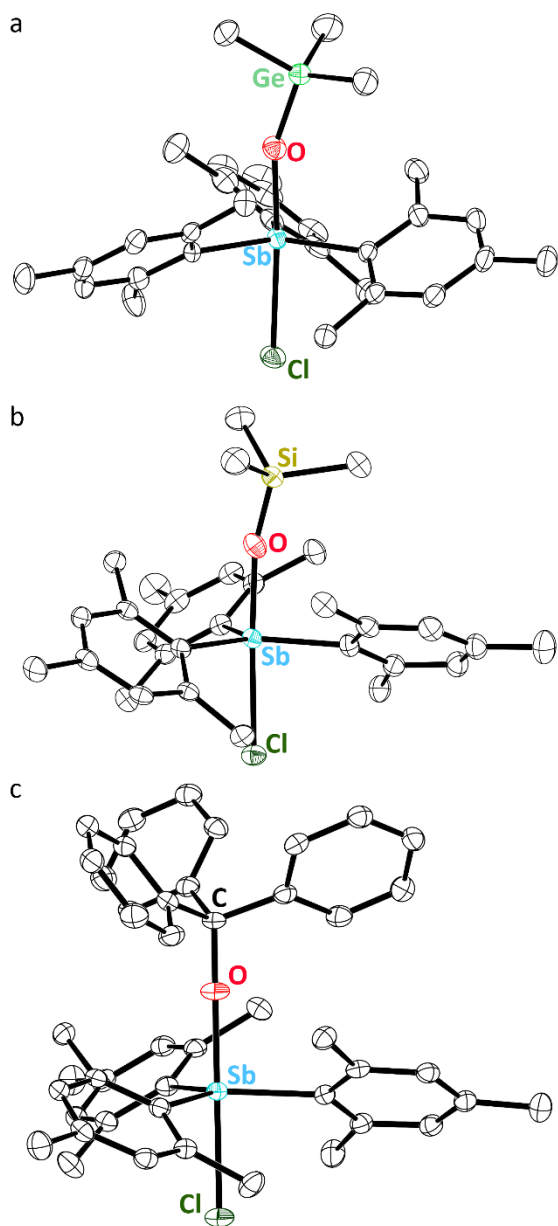
**Figure 6.6.** Thermal ellipsoid plots (50% probability) of (a) Mes$_3$Sb(OGeMe$_3$)Cl, (b) Mes$_3$Sb(OSiMe$_3$)Cl, and (c) Mes$_3$Sb(OCPh$_3$)Cl. Color code: Sb teal, Ge light-green, Si yellow, Cl dark-green, O red, and C black. Hydrogen atoms and solvent molecules are omitted for clarity.

shows a single mesityl environment desymmetrized by restricted rotation about the Sb–C$_{ipso}$ bond axis. The restricted rotation in each species is consistent with an increase in steric congestion at the stiboryl group caused by the trimethylgermanium motif. Initially, we suspected that one species was the addition product, as observed in the solid state, and that the other species was a Lewis adduct of the type observed for the Pb- and Sn-containing products. We note, however, that attempts to computationally optimize the geometry of such a Lewis adduct (PBE0/def2-TZVPP) only resulted in the dissociation of the GeMe$_3$Cl group from the stibine oxide, suggesting that the Lewis adduct with a 5-coordinate Ge atom does not exist at a minimum on the potential energy surface of the molecule. The two species present in solution could alternatively be Mes$_3$Sb(OGeMe$_3$)Cl and

[Mes$_3$Sb(OGeMe$_3$)]Cl. The latter is simply the trimesitylgermyloxystibonium chloride salt that

would form if the chloride dissociated from the neutral trimesitylgermyloxychlorostiborane. To date, our attempts to observe exchange between these species by VT-NMR and EXSY experiments have been unsuccessful.

Treatment of $Mes_3SbO$ with $SiMe_3Cl$ in DCM resulted in the formation of $Mes_3Sb(OSiMe_3)Cl$ (Figure 6.4b). The $^1H$ and $^{13}C$ NMR spectra in $CDCl_3$ reveal a single species in solution with a single mesityl environment. The breadth of the *ortho*-methyl and aryl proton resonances are indicative of restricted rotation about the $Sb-C_{ipso}$ bond axis that is consistent with the more sterically encumbered addition product relative to $Mes_3SbO$. Crystals of $Mes_3Sb(OSiMe_3)Cl$ were grown from a mixture of DCM/pentane and analyzed by SC-XRD. Similar to the Ge-containing analogue, the solid-state structure features the 5-coordinate stiborane (Figure 6.6b). Interestingly, if $Mes_3SbO$ is treated with two equivalents of $SiMe_3Cl$ in $CDCl_3$ and heated to 50 °C, the initially formed $Mes_3Sb(OSiMe_3)Cl$ converts to the deoxygenation product, $Mes_3SbCl_2$, with the generation of $(Me_3Si)_2O$ (Figure E.24).

The series was completed with trityl chloride. Upon combination of DCM solutions of $Mes_3SbO$ and $Ph_3CCl$, the reaction mixture quickly became cloudy before ultimately precipitating large colorless crystals (Figure 6.4c). SC-XRD analysis determined the identity of the product to be $Mes_3Sb(OCPh_3)Cl \cdot (CH_2Cl_2)_{1.5}$ (Figure 6.6c). $Mes_3Sb(OCPh_3)Cl \cdot (CH_2Cl_2)_{1.5}$ crystallizes in space group $R\overline{3}$ on a crystallographic 3-fold rotation axis. The steric bulk of the triphenylmethoxide ligand could favor a linear Sb–O–C bond angle, as compared to the bent Sb–O–E angles observed for $Mes_3Sb(OGeMe_3)Cl$ and $Mes_3Sb(OSiMe_3)Cl$, but we anticipate that the potential energy surface is rather shallow along the Sb–O–E internal coordinate.

### 6.5 – Activation of C–F and Si–F bonds

The capacity of Mes$_3$SbO to access biphilic reactivity and add substrates across the polar, unsaturated stiboryl group encouraged us to pursue more challenging bond activations. Main-group compounds with sufficiently potent Lewis acidity can abstract fluoride from C(sp$^3$)–F bonds, and so we next investigated whether Mes$_3$SbO could engage in C–F activation through a biphilic mechanism. Mes$_3$SbO and C($p$-MeOPh)$_3$F were combined in a Teflon vessel and dissolved in DCM. After 5 d, a crystalline precipitate had deposited beneath an intense yellow-orange supernatant. The yellow-tinged precipitate was collected, washed, and recrystallized to yield a colorless powder. The $^{19}$F NMR spectrum of the product revealed a single signal at –89.47 ppm, indicating the presence of an $^{19}$F nucleus that is significantly deshielded relative to either Mes$_3$SbF$_2$ (–100.72 ppm, CDCl$_3$) or Mes$_3$SbF(O$_3$SCF$_3$) (–144.66 ppm, CD$_2$Cl$_2$).[28] This relative deshielding is consistent with the formation of a stiborane that bears a fluoride trans to a strongly donating alkoxide ligand. The $^{13}$C NMR spectrum reveals $J_{CF}$ coupling with mesityl C atoms and one of the two magnetically distinct *ortho*-methyl C atoms of the mesityl substituents but not with any of the triarlylmethyl C atoms, providing unambiguous evidence for the fluoride abstraction (Figure 6.7). The desymmetrization of the mesityl resonances in the $^1$H and $^{13}$C NMR spectra provides further evidence for the existence of an asymmetrically substituted 5-coordinate stiborane in
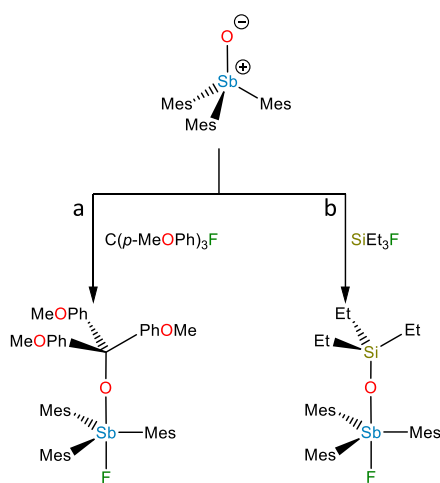


**Figure 6.7.** Synthesis of (a) Mes$_3$Sb(OC($p$-MeOPh)$_3$)F and (b) Mes$_3$Sb(OSiEt$_3$)F.
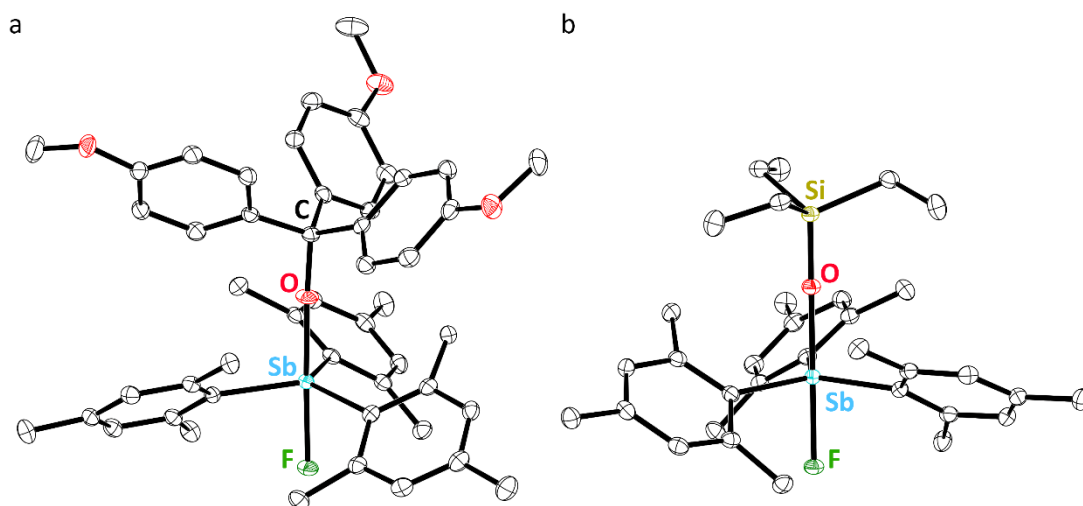
**Figure 6.8.** Thermal ellipsoid plots (50% probability) of (a) Mes$_3$Sb(OC($p$-MeOPh)$_3$)F and (b) Mes$_3$Sb(OSiEt$_3$)F. Color code: Sb teal, Si yellow, F green, O red, and C black. Hydrogen atoms and solvent molecules are omitted for clarity.

solution. SC-XRD of crystals of the C–F activation product obtained from a mixture of DCM and pentane afforded a structure of Mes$_3$Sb(OC($p$-MeOPh)$_3$)F·(DCM)$_2$ in space group $P\bar{1}$ (Figure 6.8a). As expected from the spectral data, the C–F bond of C($p$-MeOPh)$_3$F had been cleaved by the stiboryl group, with the formation of new O–C and Sb–F bonds, with interatomic distances of 1.428(2) Å and 2.0238(10) Å, respectively.

This collection of promising results finally led us to test whether a stibine oxide would be able to activate an Si–F bond, such as that in an SiR$_3$F fluorosilane. Although competing with silylium cations for binding to fluoride requires extremely high Lewis acidity, the activation of fluorosilanes by more modest Lewis acids has previously been facilitated by Lewis basic solvents that bind to and stabilize the resulting silylium cation.[11-12] We hypothesized the biphilic reactivity of the stiboryl group would be sufficiently potent to cleave the Si–F bond of a fluorosilane and generate the product of 1,2-addition across the unsaturated Sb–O bond. Addition of SiEt$_3$F to a solution of Mes$_3$SbO in toluene followed

immediately by concentration of the reaction mixture resulted in the growth of colorless crystals. ^{19}F NMR analysis of the product in toluene-$d_8$ revealed a new signal at −82.34 ppm, relatively close to the signal observed for $Mes_3Sb(OC(p\text{-}MeOPh)_3)F$, suggesting the reaction had proceeded cleanly within minutes at room temperature. The ^{13}C NMR spectrum of the new product also featured a $J_{CF}$ coupling pattern similar to that of $Mes_3Sb(OC(p\text{-}MeOPh)_3)F$, with coupling apparent to the aryl C atoms and one of the *ortho*-methyl C atoms of the mesityl groups. An SC-XRD experiment confirmed the identity of the product to be $Mes_3Sb(OSiEt_3)F$ (Figure 6.8b), which crystallized in space group $R\overline{3}$ with the molecule residing on a crystallographic three-fold rotation axis.

The activation of Si–F bonds is most commonly achieved by extremely potent Lewis acids, so we were curious to calculate the fluoride ion affinity (FIA) of $Mes_3SbO$ to interrogate its Lewis acidity.[29] $Mes_3SbO$ exhibits a modest gas-phase FIA of 216 kJ/mol relative to the extreme FIA of 910 kJ/mol calculated for $Et_3Si^+$ at the same level of theory (PBE0/def2-TZVPP). It can thus be concluded that the Lewis acidity of the Sb atom in $Mes_3SbO$ is insufficient to abstract fluoride from $Et_3SiF$ and the activation of the Si–F bond must largely be driven by stabilization of the silylium cation by the Lewis basic stiboryl O atom.


## 6.6 – Conclusion

In conclusion, we report the isolation and biphilic reactivity of a novel monomeric stibine oxide, $Mes_3SbO$. Although electronically similar to $Dipp_3SbO$, the less encumbered steric environment about the stiboryl group unlocks a greater scope of reactivity for $Mes_3SbO$. We have characterized the ability of $Mes_3SbO$ to act as both a Lewis base and a biphilic reagent in its reactivity with organotetrel(IV) halides. Remarkably, the biphilicity of $Mes_3SbO$

is sufficiently potent to cleave the C–F and Si–F bonds and stoichiometrically form 1,2-addition products. The activation of C–F and Si–F bonds poses a formidable challenge, and the results presented herein are an unprecedented display of how unquenched reactivity at a polar, unsaturated main-group bond can be utilized in small-molecule activation. We are continuing to explore the exciting chemistry of monomeric stibine oxides; efforts to expand the reactivity of $Mes_3SbO$ toward more practical applications in catalysis and to elucidate the reactivity of other Pn–Ch bonding motifs are currently underway.

## 6.7 – Experimental methods

**General methods.** Reagents and solvents were purchased from commercial vendors and used as received unless otherwise specified. Tris(*p*-methoxyphenyl)methyl tetrafluoroborate and tris(*p*-methoxyphenyl)methyl fluoride were synthesized according to literature protocols.[30-32] All reactions were performed in an OMNI-lab glove box under a $N_2$ atmosphere unless otherwise stated. Dry KF was obtained by recrystallization from water at 100 °C. The KF was then oven-dried at 140 °C in a ceramic dish before being brought into a glove box, where the KF was finally stored in polypropylene tubes under a dry, $N_2$ atmosphere. Dichloromethane (DCM), acetonitrile (MeCN), and toluene were purified using an Innovative Technology PURE-SOLV solvent purification system. All solvents were dried over 3-Å molecular sieves. NMR spectra were collected using a Bruker Avance III HD 500 spectrometer equipped with a multinuclear Smart Probe. Signals in the $^1$H and $^{13}$C NMR spectra are reported in ppm as chemical shifts from tetramethylsilane and were referenced using the $CHCl_3$ ($^1$H, 7.26 ppm) and $CDCl_3$ ($^{13}$C, 77.16 ppm) solvent signals for samples analyzed in $CDCl_3$ and the $CHD_2C_6D_5$ ($^1$H, 2.08 ppm) and $CD_3C_6D_5$ ($^{13}$C, 20.43 ppm) solvent signals for samples analyzed in toluene-*d*$_8$. The frequencies of $^{19}$F NMR signals are reported in ppm as chemical shifts from $CFCl_3$ (referenced to $BF_3$-etherate at −152.8 ppm). Signals in $^{207}$Pb NMR spectra are reported as chemical shifts from $Me_4Pb$ (referenced to $Ph_4Pb$ at −177.4 ppm). Signals in $^{119}$Sn NMR spectra are reported in ppm as chemical shifts from $Me_4Sn$ (referenced to $Bu_3SnCl$ at 153 ppm). Infrared (IR) spectra were collected on KBr pellets using a Thermo Nicolet Nexus 870 FT-IR spectrometer. Mass spectrometry measurements were collected using an LTQ-Orbitrap Velos Pro MS instrument. Elemental analysis was performed at the UC Berkeley College of Chemistry

Microanalytical Facility. Unless otherwise stated, all NMR data were processed by apodization along t1 by an exponential function at 0.30 Hz in Mestrenova (version 12.0.2).

**Synthesis of trimesitylstibine oxide (Mes₃SbO).** A solution of $Mes_3Sb$ (2.595 g, 5.420 mmol) in DCM (5 mL) was added to a suspension of iodosobenzene (1.192 g, 5.420 mmol) in DCM (1 mL). Additional aliquots of DCM (3 × 1 mL) were used for quantitative transfer of the stibine solution. The resulting yellow suspension was allowed to stir at room temperature. After 1.5 h, the iodosobenzene had been consumed and the reaction mixture was dark yellow. The reaction mixture was passed through a Celite pad with additional aliquots of DCM (3 × 1 mL) for quantitative transfer. The solvent level was reduced and cyclohexane (3 mL) was added. Continued removal of solvent resulted in the precipitation of colorless, crystalline solid. The supernatant was decanted and the product was washed with cyclohexane (3 × 1.5 mL) and pentane (3 × 1.5 mL) before being dried under vacuum. Crystals suitable for X-ray diffraction were grown similarly. Yield: 2.347 g, 88%. M.p. 170 °C. **ESI-MS (*m/z*) [M+H]⁺** 495.164 (calc 495.164). **IR ν(Sb–O)** 778 cm⁻¹. **¹H NMR (500 MHz, CDCl₃)** δ 6.89 (s, 6H), 2.49 (s, 18 H), 2.27 (s, 9H). **¹³C{¹H} NMR (125 MHz, CDCl₃)** δ 143.47, 141.22, 136.31, 130.36, 23.84, 21.19. $Mes_3SbO$ rapidly decomposes to $Mes_3Sb(OH)_2$ in the presence of trace moisture. In addition to ¹H and ¹³C NMR analyses, purity of bulk material was confirmed by PXRD.

**Synthesis of tetramethylplumbane (PbMe₄).** $PbMe_4$ was prepared using a variation of a previously reported procedure.[33] Under inert atmosphere provided via Schlenk technique, methyl iodide (2.4 mL, 38.6 mmol) was added to a suspension of Mg turnings (938 mg, 38.6 mmol) in diethyl ether (50 mL). The magnesium turnings were fully consumed. The mixture

was brought to −78 °C and PbBr$_2$ (4.721 g, 12.9 mmol) was added against a back-flow of N$_2$. An additional aliquot of methyl iodide (0.8 mL, 12.9 mmol) was added, and the mixture was allowed to warm to room temperature before being refluxed overnight. The reaction mixture, a black suspension, was diluted with ether (100 mL) and washed with water (100 mL). The aqueous layer was back-extracted with ether (3 × 50 mL). The combined organic phases were washed with water (2 × 100 mL) and brine (50 mL) before being dried over anhydrous Na$_2$SO$_4$. The organic layer was stripped of solvent to produce a yellow oil. Yield: 879 mg (51%). The $^1$H NMR data match those previously reported for this compound.[34] **$^1$H NMR (500 MHz, CDCl$_3$)** δ 0.73 (s, satellite d, $J_{PbH}$ = 61.9 Hz, 9H).

**Synthesis of chlorotrimethylplumbane (PbMe$_3$Cl).** PbMe$_3$Cl was prepared using a variation of a previously reported procedure.[35] Under ambient conditions, Me$_4$Pb (879 mg, 3.3 mmol) was dissolved in pentane (4 mL). Dry HCl gas was generated by slow addition of conc. H$_2$SO$_4$ to dry NaCl. This dry HCl gas was bubbled through the pentane solution to precipitate an off-white solid. The product was washed with pentane (3 × 3 mL) before being dried under vacuum. Yield: 95 mg (10%). The $^1$H NMR data match those previously reported for this compound.[25] **$^1$H NMR (500 MHz, CDCl$_3$)** δ 1.59 (s, satellite d, $J_{PbH}$ = 63.3 Hz, 9H).

**Synthesis of (trimesitylstibine oxide)·chlorotrimethylplumbane adduct DCM hemisolvate (Mes$_3$SbO→PbMe$_3$Cl·(CH$_2$Cl$_2$)$_{0.5}$).** A solution of Mes$_3$SbO (55 mg, 0.11 mmol) in DCM (0.6 mL) was added to a suspension of Me$_3$PbCl (32 mg, 0.11 mmol) in DCM (0.6 mL). The resulting hazy yellow mixture was passed through a Celite pad into a pre-weighed scintillation vial with an additional aliquot of DCM (1 mL) used for quantitative transfer. The clarified filtrate was

stripped of solvent to yield an oily residue. The residue was redissolved in DCM (0.5 mL) and pentane was added until the mixture was cloudy (3 mL). Over the course of 30 min, off-white crystalline material formed. The mixture was decanted, and the crystals were washed with pentane (2 × 0.6 mL) before being dried under vacuum. Yield: 72 mg (80%). Crystals suitable for X-ray diffraction were grown similarly. M.p. 201 °C. **Found:** C, 44.49; H, 5.21%. **Calc. for C$_{61}$H$_{86}$Cl$_4$O$_2$Pb$_2$Sb$_2$:** C, 44.38; H, 5.25%. **ESI-MS (*m/z*) [M–OPbMe$_3$]$^+$** 513.29 (calc 513.130). **$^1$H NMR (500 MHz, CDCl$_3$)** δ 6.93 (s, 6H), 2.38 (s, 18H), 2.30 (s, 9H), 1.39 (s, satellite d, $J_{PbH}$ = 84.9 Hz, 9H). **$^{13}$C{$^1$H} NMR (125 MHz, CDCl$_3$)** δ 142.95, 142.31, 135.21, 130.80, 23.77, 21.22, 21.14 (s, satellite d, $J_{PbC}$ = 406.8 Hz). **$^{207}$Pb{$^1$H} NMR (105 MHz, CDCl$_3$)** δ 207.55.

**Synthesis of (trimesitylstibine oxide)·chlorotrimethylstannane adduct toluene solvate (Mes$_3$SbO→SnMe$_3$Cl·(C$_7$H$_8$)).** A solution of Mes$_3$SbO (46 mg, 0.093 mmol) in toluene (1 mL) was added to a solution of Me$_3$SnCl (19 mg, 0.095 mmol) in toluene (0.5 mL). A solid began precipitating, and DCM (1 mL) was added to redissolve the reagents. The solvent level was reduced to 0.5 mL to produce colorless crystals. The remaining solvent was decanted, and the crystals were washed with pentane (2 × 0.6 mL) before being dried under vacuum. Yield: 57 mg (78%). Crystals suitable for X-ray diffraction were grown similarly. M.p. 209 °C. **Found:** C, 56.18; H, 6.35%. **Calc. for C$_{37}$H$_{50}$ClOSbSn:** C, 56.49; H, 6.41%. **ESI-MS (*m/z*) [M–OSnMe$_3$]$^+$** 513.29 (calc 513.130). **$^1$H NMR (500 MHz, CDCl$_3$)** δ 7.25 (t, toluene, $J_{HH}$ = 7.26 Hz, 1H), 7.20–7.10 (m, toluene, 2H), 6.96 (s, 6H), 2.35 (s, toluene, 2H), 2.35 (s, 18H), 2.31 (s, 9H), 0.55 (s, satellite d, $J_{SnH}$ = 69.0 Hz, 9H). **$^{13}$C{$^1$H} NMR (125 MHz, CDCl$_3$)** δ 142.89, 142.78, 137.98 (toluene), 134.67, 130.97, 129.15 (toluene), 128.34 (toluene), 125.41 (toluene), 23.90, 21.57 (toluene), 21.24, 6.09 (s, satellite d, $J_{SnC}$ = 546.4 Hz). **$^{119}$Sn{$^1$H} NMR (186 MHz, CDCl$_3$)** δ −36.38.

We note that we consistently observed only a partial molar equivalent (~70%) of toluene by NMR spectroscopy, presumably due to partial evaporation of solvate toluene during drying. In addition to $^1$H and $^{13}$C NMR analyses, purity of the material was confirmed by elemental analysis and PXRD.

**Synthesis of *trans*-chloro(trimethylgermyloxy)trimesitylstiborane toluene hemisolvate (Mes$_3$Sb(OGeMe$_3$)Cl·(C$_7$H$_8$)$_{0.5}$).** Me$_3$GeCl (10 μL, 0.082 mmol) was added to a solution of Mes$_3$SbO (40.5 mg, 0.082 mmol) in toluene (1.5 mL). The mixture was allowed to stand for 4 h at room temperature before the solvent level was reduced to form colorless crystals. The crystals were washed with pentane (2 × 0.5 mL). Yield: 33 mg (59%). M.p. 191 °C. **Found:** C, 57.68; H, 6.52%. **Calc. for C$_{67}$H$_{92}$Cl$_2$Ge$_2$O$_2$Sb$_2$:** C, 57.93; H, 6.68%. **ESI-MS (*m/z*) [M–OGeMe$_3$]$^+$** 513.29 (calc 513.130). **$^1$H NMR (500 MHz, toluene-*d*$_8$)** δ 7.09–6.97 (toluene, m), 6.75 (major, s, 3 H), 6.73 (major, s 3H), 6.68 (minor, s, 0.5 H), 2.84 (major, s, 8H), 2.80 (minor, s, 1 H), 2.63 (major, s, 8 H), 2.55 (minor, s, 1 H), 2.11 (toluene), 2.03 (minor, s, 1 H), 2.02 (major, s, 8H), 0.06 (major/minor, s, 9H). **$^{13}$C{$^1$H} NMR (125 MHz, toluene-*d*$_8$)** δ 147.48 (major), 144.85 (minor), 143.55 (minor), 143.18 (major), 141.84 (minor), 141.41 (major), 140.01 (minor), 139.57 (major), 137.58 (toluene), 131.18 (major), 131.15 (minor), 130.24 (minor), 129.84 (minor), 129.31 (major), 128.50 (toluene), 125.43 (toluene), 26.04 (major), 25.93 (minor), 24.75 (major), 24.52 (minor), 21.37 (toluene), 20.89 (minor), 20.79 (major), 4.18 (major), 3.43 (minor). Due to the apparent presence of distinct species in solution in approximately an 8:1 ratio, the signals are assigned as major or minor based on the relative intensities of the signals.

**Synthesis of *trans*-chloro(trimethylsiloxy)trimesitylstiborane (Mes₃Sb(OSiMe₃)Cl).** Me₃SiCl

(15 μL, 0.12 mmol) was added to a solution of Mes₃SbO (55 mg, 0.11 mmol) in DCM (0.8 mL).

Cyclohexane (5 mL) was added. The mixture was allowed to stand for 15 min before the

solvent was stripped under reduced pressure to produce a colorless solid. The solid was

washed with cyclohexane (2 × 1 mL), dried under vacuum, redissolved in DCM (2 mL), and

passed through Celite into a pre-weighed vial. The DCM level was reduced to 0.5 mL under

vacuum and cyclohexane (1 mL) was added. The solvent level was reduced to induce formation

of colorless crystals. The solvent was decanted, and the crystals were washed with pentane (3

× 1 mL). Yield: 23 mg (36%). M.p. 210 °C. **Found:** C, 59.49; H, 7.07%. **Calc. for C₃₀H₄₂ClOSbSi:**

C, 59.66; H, 7.01%. **ESI-MS (*m/z*) [M−Cl]⁺** 567.204 (calc 567.204). **¹H NMR (500 MHz, CDCl₃)** δ

6.96 (s, 6H), 2.61 (br s, 18H), 2.30 (s, 9H), −0.24 (s, 9H). **¹³C{¹H} NMR (125 MHz, CDCl₃)** δ

145.21, 140.17, 131.13, 130.02, 25.51, 24.53, 21.06, 3.07.


**Synthesis of *trans*-chloro(triphenylmethoxy)trimesitylstiborane DCM solvate**

**(Mes₃Sb(OCPh₃)Cl·(CH₂Cl₂)₁.₅).** A solution of Mes₃SbO (57 mg, 0.12 mmol) in DCM (1 mL) was

added to a solution of Ph₃CCl (32 mg, 0.12 mmol) in DCM (0.5 mL). An additional 0.5 mL of

DCM was used for quantitative transfer. The reaction mixture rapidly became cloudy. After 4

h, a large crop of crystals had deposited from the reaction mixture and the supernatant was

slightly yellow. The solvent was decanted, and the crystals were washed with pentane (3 ×

0.6 mL). Yield: 70 mg (67%). M.p. 176 °C. **Found:** C, 63.59; H, 5.75%. **Calc. for C₉₅H₁₀₂Cl₈O₂Sb₂:**

C, 63.29; H, 5.70%. **ESI-MS (*m/z*) [M−CPh₃Cl+H]⁺** 495.164 (calc 495.164). **¹H NMR (500 MHz,**

**toluene-*d*₈)** δ 6.96 (t, $J_{HH}$= 6.5 Hz, 3H), 6.84 (d, $J_{HH}$= 7.3 Hz, 6H), 6.80 (t, $J_{HH}$= 7.3 Hz, 6H), 6.76

(s, 3H), 6.54 (s, 3H), 4.30 (DCM, s, 2H), 2.79 (s, 9H), 2.19 (s, 9H), 2.08 (s, 9H). **¹³C{¹H} NMR (125**

**MHz, toluene-$d_8$)** δ 150.41, 148.61, 143.36, 142.74, 139.71, 131.51, 130.34, 129.96, 127.16, 126.52, 93.17, 53.27 (DCM), 26.31, 25.58, 20.70.

**Synthesis of *trans*-fluoro(tris-*p*-methoxyphenylmethoxy)trimesitylstiborane (Mes₃Sb(OC(*p*-MeOPh)₃)F).** A batch of Mes₃SbO (182 mg, 0.368 mmol) and tris(*p*-methoxyphenyl)methyl fluoride (131 mg, 0.371 mmol) were added to a poly(tetrafluoroethylene) vessel and dissolved in DCM (2 mL). After 5 d, colorless crystals had formed and the supernatant was an intense yellow-orange color. The supernatant was decanted, and the solid was washed with DCM (1 × 0.6 mL) and pentane (3 × 0.6 mL). The solid was then recrystallized from a mixture of DCM and pentane. The resulting colorless powder was washed with pentane (3 × 0.6 mL) before being dried under vacuum. Crystals suitable for X-ray diffraction were grown from a mixture of DCM and pentane. Yield: 111 mg (36%). M.p. 189 °C (decomp). **Found:** C, 68.99; H, 6.34%. **Calc. for C₄₉H₅₄FO₄Sb:** C, 69.43; H, 6.42%. **ESI-MS (*m/z*) [M–(OC(*p*-MeOPh)₃)]⁺** 497.159 (calc 497.159). **¹H NMR (500 MHz, CDCl₃)** δ 6.95 (s, 3H), 6.71 (s, 3H), 6.51 (d, $J_{HH}$= 8.8 Hz, 6H), 6.35 (d, $J_{HH}$= 8.8 Hz, 6H), 3.73 (s, 9H), 2.50 (s, 9H), 2.32 (s, 9H), 2.03 (s, 9H). **¹³C{¹H} NMR (125 MHz, CDCl₃)** δ 157.80, 143.99 (d, $J_{CF}$ = 15.4 Hz), 143.32, 143.30, 142.97, 142.91, 139.57, 130.79, 130.35, 129.68, 111.91, 55.24, 25.21, 23.74 (d, $J_{CF}$ = 7.3 Hz), 21.06. **¹⁹F{¹H} NMR (470 MHz, CDCl₃)** δ –89.47.

**Synthesis of *trans*-fluoro(triethylsiloxy)trimesitylstiborane (Mes₃Sb(OSiEt₃)F).** Et₃SiF (20 μL, 0.12 mmol) was added to a solution of Mes₃SbO (52 mg, 0.11 mmol) in toluene (1 mL). The solvent level was reduced under reduced pressure to grow well-formed colorless crystals. The

toluene was decanted, and the crystals were washed with pentane (3 × 0.6 mL) before being dried under vacuum. Yield: 59 mg (79%). M.p. 213 °C (decomp). **Found:** C, 63.07; H, 7.61%. **Calc. for C$_{33}$H$_{48}$FOSbSi:** C, 62.96; H, 7.69%. **ESI-MS (*m/z*) [M–F]$^+$** 609.250 (calc 609.250). **$^1$H NMR (500 MHz, toluene-*d$_8$*)** δ 6.79 (s, 3H), 6.72 (s, 3H), 2.66 (s, 18H), 2.04 (s, 9H), 0.81 (t, $J_{HH}$= 8.1 Hz, 9H), 0.53 (q, $J_{HH}$= 8.1 Hz, 6H). **$^{13}$C{$^1$H} NMR (125 MHz, toluene-*d$_8$*)** δ 143.65, 142.49 (d, $J_{CF}$ = 3.0 Hz), 142.19 (d, $J_{CF}$ = 16.9 Hz), 139.97, 130.51, 129.77, 25.11, 24.21 (d, $J_{CF}$ = 7.9 Hz), 20.87, 8.82, 8.15. **$^{19}$F{$^1$H} NMR (470 MHz, toluene-*d$_8$*)** δ −82.34.

**X-ray crystallography.** Crystals of Mes$_3$SbO, Mes$_3$SbO→PbMe$_3$Cl·(CH$_2$Cl$_2$), Mes$_3$SbO→SnMe$_3$Cl·(C$_7$H$_8$), Mes$_3$Sb(OGeMe$_3$)Cl·(C$_7$H$_8$)$_{0.5}$, Mes$_3$Sb(OSiMe$_3$)Cl, Mes$_3$Sb(OCPh$_3$)Cl·(CH$_2$Cl$_2$)$_{1.5}$, Mes$_3$Sb(OSiEt$_3$)F, and Mes$_3$Sb(OC(*p*-MeOPh)$_3$)F·(CH$_2$Cl$_2$)$_2$ were grown as described above, selected under a microscope, loaded onto a MiTeGen polyimide sample loop using Type NVH Cargille Immersion Oil, and mounted onto a Rigaku XtaLAB Synergy-S single-crystal diffractometer. Each crystal was cooled to 100 K under a stream of nitrogen. Diffraction of Cu Kα radiation from a PhotonJet-S microfocus source was detected using a HyPix6000HE hybrid photon counting detector. Screening, indexing, data collection, and data processing were performed with CrysAlisPro.[36] The structures were solved using SHELXT and refined using SHELXL following established strategies.[37-39] All non-H atoms were refined anisotropically. C-bound H atoms were placed at calculated positions and refined with a riding model and coupled isotropic displacement parameters (1.2 × U$_{eq}$ for non-methyl C-H atoms and 1.5 × U$_{eq}$ for methyl groups).

**Powder X-ray diffraction.** Bulk samples of $Mes_3SbO$, $Mes_3SbO \rightarrow PbMe_3Cl \cdot (CH_2Cl_2)$, $Mes_3SbO \rightarrow SnMe_3Cl \cdot (C_7H_8)$, $Mes_3Sb(OGeMe_3)Cl \cdot (C_7H_8)_{0.5}$, $Mes_3Sb(OSiMe_3)Cl$, $Mes_3Sb(OCPh_3)Cl \cdot (CH_2Cl_2)_{1.5}$, and $Mes_3Sb(OSiEt_3)F$ were ground using an agate mortar and pestle. The fine powders were each loaded onto a MiTeGen polyimide sample loop using Type NVH Cargille Immersion Oil and mounted onto a Rigaku XtaLAB Synergy-S single-crystal diffractometer. The powder was cooled to 100 K under a stream of nitrogen. The diffraction of Cu K$\alpha$ radiation was collected while the sample underwent a Gandolfi scan. Data collection and processing were performed using CrysAlisPro. Simulated PXRD diffractograms were generated by Mercury using the crystal structures of $Mes_3SbO$, $Mes_3SbOSnMe_3Cl \cdot (C_7H_8)$, $Mes_3SbOGeMe_3Cl \cdot (C_7H_8)_{0.5}$, $Mes_3SbOSiMe_3Cl$, $Mes_3SbOCPh_3Cl \cdot (CH_2Cl_2)_{1.5}$, and $Mes_3SbOSiEt_3F$. These simulated diffractograms were compared to the experimentally determined PXRD diffractograms. A similar PXRD analysis was not performed on $Mes_3Sb(OC(p\text{-}MeOPh)_3)F$ because crystals of $Mes_3Sb(OC(p\text{-}MeOPh)_3)F \cdot (CH_2Cl_2)_2$ suitable for X-ray diffraction were of different chemical and structural composition to the solid obtained from the bulk synthesis (i.e., non-solvate vs DCM solvate).

**Computational experiments.** All geometry optimizations and frequency calculations were performed using ORCA 5.0.1.[40] Geometry optimizations were performed on $Mes_3PnO$ (Pn = P, As, Sb) employing the BP86 pure functional and def2-SVP basis set, with the RI approximation and def2/J auxiliary basis set,[41] starting from the previously reported coordinates for $Mes_3SbO$ (PBE0/def2-TZVPP).[23] The optimized coordinates (BP86/def2-SVP) were then used as a starting point for a subsequent geometry optimization using the PBE0 hybrid functional and def2-TZVPP basis set, with the RIJCOSX approximation and def2/J auxiliary basis set.[42-46] In the

case of Mes$_3$SbO, the TIGHTOPT key word was employed to tighten the optimization convergence criteria. Frequency calculations were then performed at the same level of theory in the gas phase. Frequency calculations for all Mes$_3$PnO (Pn = Sb, As, P) found a small number of low-frequency imaginary modes that correspond to the rotation of methyl groups, but all structures were deemed to have converged to effective local minima on the potential energy surface. Single point energy calculations were performed using ORCA 5.0.1 on the optimized coordinates using the PBE0 hybrid functional and old-DKH-TZVPP all-electron, relativistically contracted basis set following the Douglas-Kroll-Hess formalism, with the RIJCOSX approximation and SARC/J auxiliary basis set.[47-50] The wavefunctions generated from the single point energy calculations were subject to topological, canonical molecular orbital, and Natural Bond Orbital (NBO) analyses. Topological analysis of the electron density was performed in MultiWFN (version 3.7).[51] The values of the real space functions $\rho$, $\nabla^2\rho$, and $\varepsilon$ along interatomic vectors were visualized using R (version 4.0.2) through Rstudio (version 1.3.1073). The following R packages were used for analysis and visualization: ggplot2, tidyverse, gridExtra, ggtext, scales, and grid. Canonical molecular orbitals were visualized using Avogadro.[52] NBO analysis was performed using the NBO program (version 7.0.7).[53] The $DEL keylist was used to calculate the energy of deletion by eliminating all non-Lewis delocalizations of electron density from the O-atom to the rest of the molecule and vice versa. Pre-orthogonalized NBOs and NLMOs were visualized in JMOL (version 16.2.1).[54] The gas-phase fluoride ion affinities (FIAs) of Mes$_3$SbO and Et$_3$Si$^+$ were calculated following a literature protocol.[29] In brief, the geometry and total enthalpy of Mes$_3$SbO, Mes$_3$SbOF$^-$, COF$_3^-$, and COF$_2$ were each calculated (PBE0/def2-TZVPP). The $\Delta$H of eq 3 was determined by subtracting the known experimental value for the $\Delta$H of eq 2 (208.8 kJ/mol) from the calculated value of $\Delta$H

for eq 1. The FIA of Mes$_3$SbO is the −ΔH of eq 3. The process was repeated to determine the

FIA of Et$_3$Si$^+$.

$$\text{Mes}_3\text{SbO} + \text{COF}_3^- \rightarrow \text{Mes}_3\text{SbOF}^- + \text{COF}_2 \qquad (1)$$

$$\text{COF}_3^- \rightarrow \text{F}^- + \text{COF}_2 \qquad (2)$$

$$\text{Mes}_3\text{SbO} + \text{F}^- \rightarrow \text{Mes}_3\text{SbOF}^- \qquad (3)$$
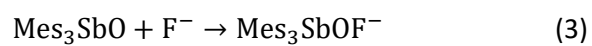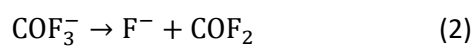
## 6.8 – References

1. Weetman, C.; Inoue, S., The Road Travelled: After Main-Group Elements as Transition Metals. *ChemCatChem* **2018,** *10*, 4213-4228.

2. Power, P. P., Main-group elements as transition metals. *Nature* **2010,** *463*, 171-177.

3. Lipshultz, J. M.; Li, G.; Radosevich, A. T., Main Group Redox Catalysis of Organopnictogens: Vertical Periodic Trends and Emerging Opportunities in Group 15. *J. Am. Chem. Soc.* **2021,** *143*, 1699-1721.

4. Moon, H. W.; Cornella, J., Bismuth Redox Catalysis: An Emerging Main-Group Platform for Organic Synthesis. *ACS Catal.* **2022,** *12*, 1382-1393.

5. Stahl, T.; Klare, H. F. T.; Oestreich, M., Main-Group Lewis Acids for C–F Bond Activation. *ACS Catal.* **2013,** *3*, 1578-1587.

6. Klare, H. F. T.; Albers, L.; Süsse, L.; Keess, S.; Müller, T.; Oestreich, M., Silylium Ions: From Elusive Reactive Intermediates to Potent Catalysts. *Chem. Rev.* **2021,** *121*, 5889-5985.

7. Luo, Y.-R.; Kerr, J. A., Bond dissociation energies. *CRC handbook of chemistry and physics* **2012,** *89*, 65-98.

8. Kameo, H.; Kawamoto, T.; Sakaki, S.; Bourissou, D.; Nakazawa, H., Transition-Metal-Mediated Cleavage of Fluoro-Silanes under Mild Conditions. *Chem.–Eur. J.* **2016,** *22*, 2370-2375.

9. Kameo, H.; Yamamoto, H.; Ikeda, K.; Isasa, T.; Sakaki, S.; Matsuzaka, H.; García-Rodeja, Y.; Miqueu, K.; Bourissou, D., Fluorosilane Activation by Pd/Ni→Si–F→Lewis Acid Interaction: An Entry to Catalytic Sila-Negishi Coupling. *J. Am. Chem. Soc.* **2020,** *142*, 14039-14044.

10. Greb, L., Lewis Superacids: Classifications, Candidates, and Applications. *Chem.–Eur. J.* **2018,** *24*, 17881-17896.

11. Tschernuth, F. S.; Thorwart, T.; Greb, L.; Hanusch, F.; Inoue, S., Bis(perfluoropinacolato)silane: A Neutral Silane Lewis Superacid Activates Si–F Bonds. *Angew. Chem., Int. Ed.* **2021,** *60*, 25799-25803.

12. Tschernuth, F. S.; Kostenko, A.; Stigler, S.; Gradenegger, A.; Inoue, S., A neutral germanium-centred hard and soft lewis superacid and its unique reactivity towards hydrosilanes. *Dalton Trans.* **2024,** *53*, 74-81.

13. Wenger, J. S.; Weng, M.; George, G. N.; Johnstone, T. C., Isolation, bonding, and reactivity of a monomeric stibine oxide. *Nat. Chem.* **2023,** *15*, 633-640.

14. Wenger, J. S.; Getahun, A.; Johnstone, T. C., Variation in pnictogen–oxygen bonding unlocks greatly enhanced Brønsted basicity for the monomeric stibine oxide. *Dalton Trans.* **2023,** *52*, 11325-11334.

15. Wenger, J. S.; Getahun, A.; Johnstone, T. C., Steric congestion in heavy pnictines alters oxidative halogenation pathways. *Polyhedron* **2024,** *247*, 116730.

16. Westhoff, T.; Huber, F.; Rüther, R.; Preut, H., Synthesis and structural characterization of some new triorganoantimony oxides. Molecular and crystal structure of tris(2,4,6-trimemethylphenyl)antimony dihydroxide. *J. Organomet. Chem.* **1988,** *352*, 107-113.

17. Venezky, D. L.; Sink, C. W.; Nevett, B. A.; Fortescue, W. F., Preparation, properties and structure of poly(triphenylstibine oxide). *J. Organomet. Chem.* **1972,** *35*, 131-142.

18. Bordner, J.; Doak, G. O.; Everett, T. S., Crystal structure of 2,2,4,4-tetrahydro-2,2,2,4,4,4-hexaphenyl-1,3,2,4-dioxadistibetane (triphenylstibene oxide dimer) and related compounds. *J. Am. Chem. Soc.* **1986,** *108*, 4206-4213.

19. Ferguson, G.; Glidewell, C.; Kaitner, B.; Lloyd, D.; Metcalfe, S., Second determination of the structure of dimeric triphenylstibine oxide. *Acta Crystallogr. Sect. C* **1987,** *43*, 824-826.

20. Carmalt, C. J.; Crossley, J. G.; Norman, N. C.; Orpen, A. G., The structure of amorphous $Ph_3SbO$: information from EXAFS (extended X-ray absorption fine structure) spectroscopy. *Chem. Commun.* **1996**, 1675-1676.

21. Pankaj, S.; Rosas, N.; Espinosa-Pérez, G.; Cabrera, A., Triphenylstibine Dihydroxide. *Acta Crystallogr. Sect. C* **1996,** *52*, 889-891.

22. Suzuki, H.; Ikegami, T.; Matano, Y., Ultrasonic reaction of triarylbismuthines and triarylstibines with iodosylbenzene. Mild oxidizing ability of the organobismuth oxide function for organic substrates. *Tetrahedron Lett.* **1994,** *35*, 8197-8200.

23. Wenger, J. S.; Johnstone, T. C., Unsupported monomeric stibine oxides ($R_3SbO$) remain undiscovered. *Chem. Commun.* **2021,** *57*, 3484-3487.

24. Lindquist-Kleissler, B.; Wenger, J. S.; Johnstone, T. C., Analysis of Oxygen–Pnictogen Bonding with Full Bond Path Topological Analysis of the Electron Density. *Inorg. Chem.* **2021,** *60*, 1846-1856.

25. Berger, S.; Bock, W.; Frenking, G.; Jonas, V.; Mueller, F., NMR Data of Methyltitanium Trichloride and Related Organometallic Compounds. A Combined Experimental and Theoretical Study of $Me_nXCl_{4-n}$ (n= 0-4; X= C, Si, Sn, Pb, Ti). *J. Am. Chem. Soc.* **1995,** *117*, 3820-3829.

26. López-Cardoso, M.; Vargas-Pineda, G.; Román-Bravo, P. P.; Rodríguez-Narváez, C.; Rosas-Valdez, E.; Cea-Olivares, R., Synthesis, crystal structures and coordination modes of some triorganotin(IV) complexes with 2-N-propyl and 2-N-benzyl-amino-1-cyclopentene-1-dithiocarboxylates. *J. Mol. Struct.* **2016,** *1116*, 116-121.

27. Lichtscheidl, A. G.; Janicke, M. T.; Scott, B. L.; Nelson, A. T.; Kiplinger, J. L., Syntheses, structures, and $^1H$, $^{13}C\{^1H\}$ and $^{119}Sn\{^1H\}$ NMR chemical shifts of a family of trimethyltin alkoxide, amide, halide and cyclopentadienyl compounds. *Dalton Trans.* **2015,** *44*, 16156-16163.

28. Yang, M.; Gabbaï, F. P., Synthesis and Properties of Triarylhalostibonium Cations. *Inorg. Chem.* **2017,** *56*, 8644-8650.

29. Erdmann, P.; Leitner, J.; Schwarz, J.; Greb, L., An Extensive Set of Accurate Fluoride Ion Affinities for p-Block Element Lewis Acids and Basic Design Principles for Strong Fluoride Ion Acceptors. *ChemPhysChem* **2020,** *21*, 987-994.

30. Horn, M.; Mayr, H., Stabilities of Trityl-Protected Substrates: The Wide Mechanistic Spectrum of Trityl Ester Hydrolyses. *Chem.–Eur. J.* **2010,** *16*, 7469-7477.

31. Farley, G. W.; Siegler, M. A.; Goldberg, D. P., Halogen Transfer to Carbon Radicals by High-Valent Iron Chloride and Iron Fluoride Corroles. *Inorg. Chem.* **2021,** *60*, 17288-17302.

32. Horn, M.; Mayr, H., Electrophilicity versus Electrofugality of Tritylium Ions in Aqueous Acetonitrile. *Chem.–Eur. J.* **2010,** *16*, 7478-7487.

33. Gilman, H.; Jones, R. G., Reactions of metallic thallium and metallic lead with organic halides. *J. Am. Chem. Soc.* **1950,** *72*, 1760-1761.

34. Varga, R. A.; Silvestru, C.; Haiduc, I., Synthesis and Spectroscopic Characterization of New Organolead(IV) Complexes Containing Organophosphorus Ligands. *Synth. React. Inorg. Met.-Org. Chem.* **2000,** *30*, 485-498.

35. Calingaert, G.; Dykstra, F. J.; Shapiro, H., The Preparation of Alkyllead Salts. *J. Am. Chem. Soc.* **1945,** *67*, 190-192.

36. Rigaku Oxford Diffraction, *CrysAlis^{Pro}* **2020**.

37. Sheldrick, G. M., SHELXT– Integrated space-group and crystal-structure determination. *Acta Crystallogr. Sect. A* **2015,** *71*, 3-8.

38. Sheldrick, G. M., Crystal structure refinement with SHELXL. *Acta Crystallogr. Sect. C* **2015,** *71*, 3-8.

39.    Müller, P., Practical suggestions for better crystal structures. *Crystallogr. Rev.* **2009,** *15*, 57-83.

40.    Neese, F., The ORCA program package. *Wiley Interdiscip. Rev.-Comput. Mol. Sci* **2012,** *2*, 73-78.

41.    Becke, A. D., Density-functional exchange-energy approximation with correct asymptotic behavior. *Phys. Rev. A* **1988,** *38*, 3098-3100.

42.    Perdew, J. P.; Burke, K.; Ernzerhof, M., Generalized Gradient Approximation Made Simple. *Phys. Rev. Lett.* **1996,** *77*, 3865-3868.

43.    Perdew, J. P.; Ernzerhof, M.; Burke, K., Rationale for mixing exact exchange with density functional approximations. *J. Chem. Phys.* **1996,** *105*, 9982-9985.

44.    Weigend, F.; Ahlrichs, R., Balanced basis sets of split valence, triple zeta valence and quadruple zeta valence quality for H to Rn: Design and assessment of accuracy. *Phys. Chem. Chem. Phys.* **2005,** *7*, 3297-3305.

45.    Weigend, F., Accurate Coulomb-fitting basis sets for H to Rn. *Phys. Chem. Chem. Phys.* **2006,** *8*, 1057-1065.

46.    Neese, F.; Wennmohs, F.; Hansen, A.; Becker, U., Efficient, approximate and parallel Hartree–Fock and hybrid DFT calculations. A 'chain-of-spheres' algorithm for the Hartree–Fock exchange. *Chem. Phys.* **2009,** *356*, 98-109.

47.    Pantazis, D. A.; Chen, X.-Y.; Landis, C. R.; Neese, F., All-Electron Scalar Relativistic Basis Sets for Third-Row Transition Metal Atoms. *J. Chem. Theory Comput.* **2008,** *4*, 908-919.

48.    Pantazis, D. A.; Neese, F., All-Electron Scalar Relativistic Basis Sets for the Lanthanides. *J. Chem. Theory Comput.* **2009,** *5*, 2229-2238.

49.    Pantazis, D. A.; Neese, F., All-Electron Scalar Relativistic Basis Sets for the Actinides. *J. Chem. Theory Comput.* **2011,** *7*, 677-684.

50.    Pantazis, D. A.; Neese, F., All-electron scalar relativistic basis sets for the 6p elements. *Theor. Chem. Acc.* **2012,** *131*, 1292.

51.    Lu, T.; Chen, F., Multiwfn: A multifunctional wavefunction analyzer. *J. Comput. Chem.* **2012,** *33*, 580-592.

52.    Hanwell, M. D.; Curtis, D. E.; Lonie, D. C.; Vandermeersch, T.; Zurek, E.; Hutchison, G. R., Avogadro: an advanced semantic chemical editor, visualization, and analysis platform. *J. Cheminformatics* **2012,** *4*, 17.

53.    Glendening, E. D.; Landis, C. R.; Weinhold, F., NBO 7.0 : New vistas in localized and delocalized chemical bonding theory. *J. Comput. Chem.* **2019,** *40*, 2234-2241.

54.     *Jmol: an open-source Java viewer for chemical structures in 3D.*, 16.2.1; http://www.jmol.org/, 2024.

**Appendix A**

**Supplementary data for**

**Chapter 2: A reinvestigation of previously reported monomeric stibine oxides**

**Published in part in:**

1.    Wenger, J. S.; Johnstone, T. C., Unsupported monomeric stibine oxides (R$_3$SbO) remain undiscovered. *Chem. Commun.* **2021,** *57*, 3484-3487.

2.    Wenger, J. S.; Wang, X.; Johnstone, T. C., H-Atom Assignment and Sb–O Bonding of [Mes$_3$SbOH][O$_3$SPh] Confirmed by Neutron Diffraction, Multipole Modeling, and Hirshfeld Atom Refinement. *Inorg. Chem.* **2021,** *60*, 16048-16052.
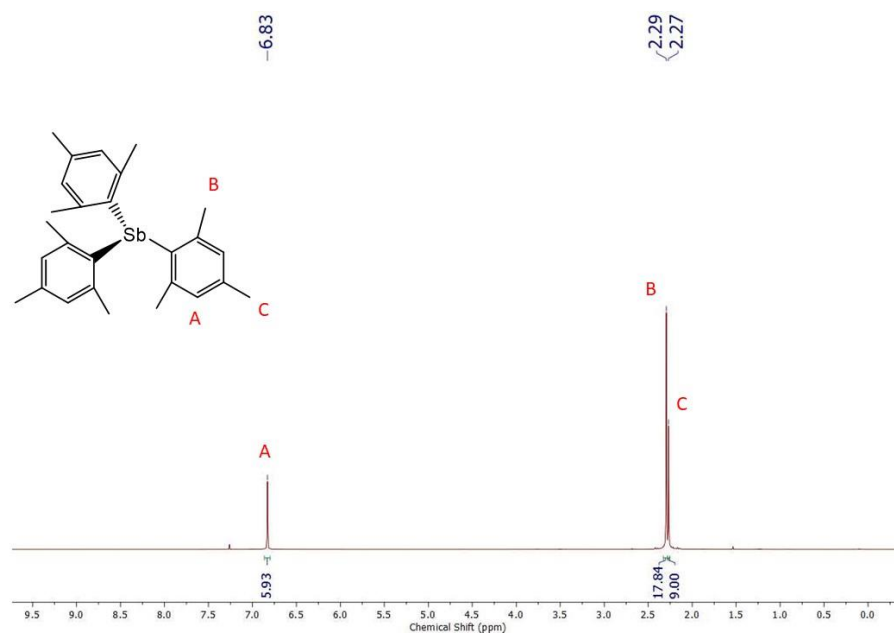
**Figure A.1.** $^1$H NMR spectrum (CDCl$_3$, 500 MHz) of trimesitylstibine at room temperature.
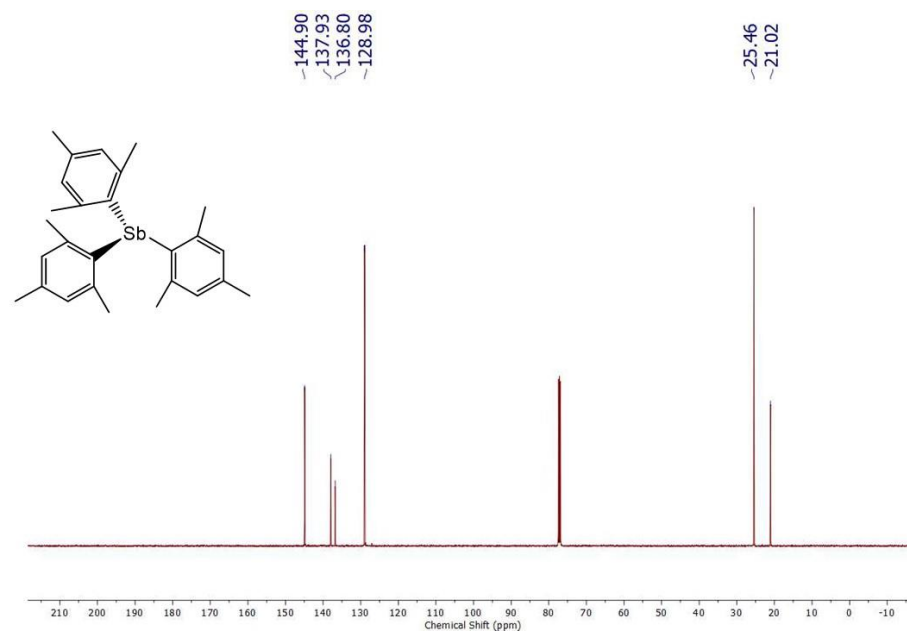


**Figure A.2.** $^{13}$C{$^1$H} NMR spectrum (CDCl$_3$, 125 MHz) of trimesitylstibine at room temperature.
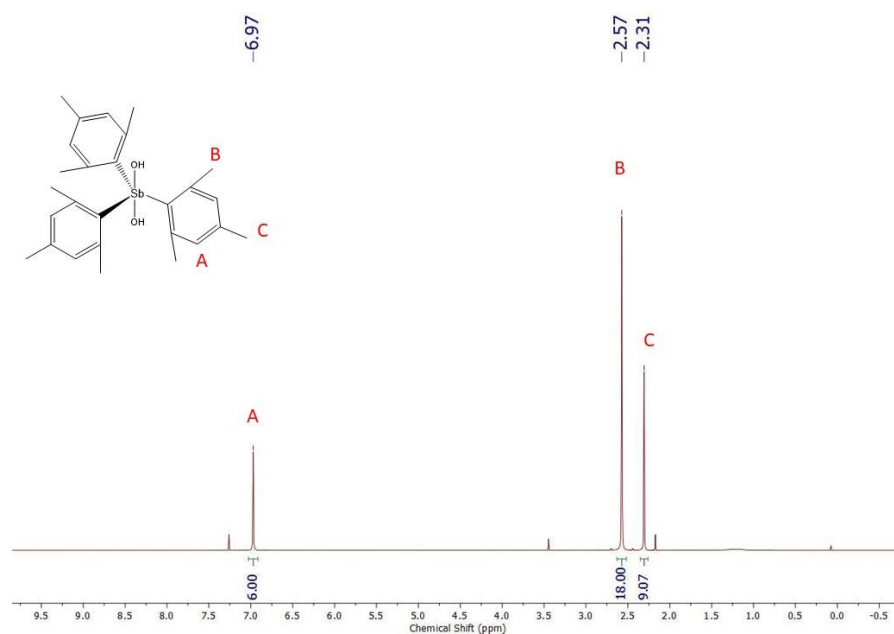
**Figure A.3.** ^{1}H NMR spectrum (CDCl$_3$, 500 MHz) of dihydroxytrimesitylstiborane at room temperature.
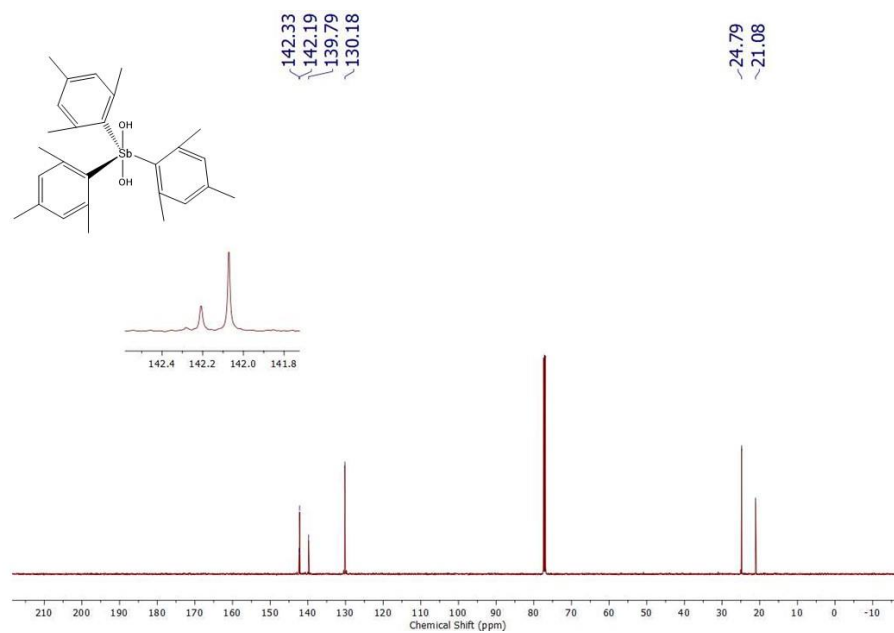


**Figure A.4.** ^{13}C{^{1}H} NMR spectrum (CDCl$_3$, 125 MHz) of dihydroxytrimesitylstiborane at room temperature.
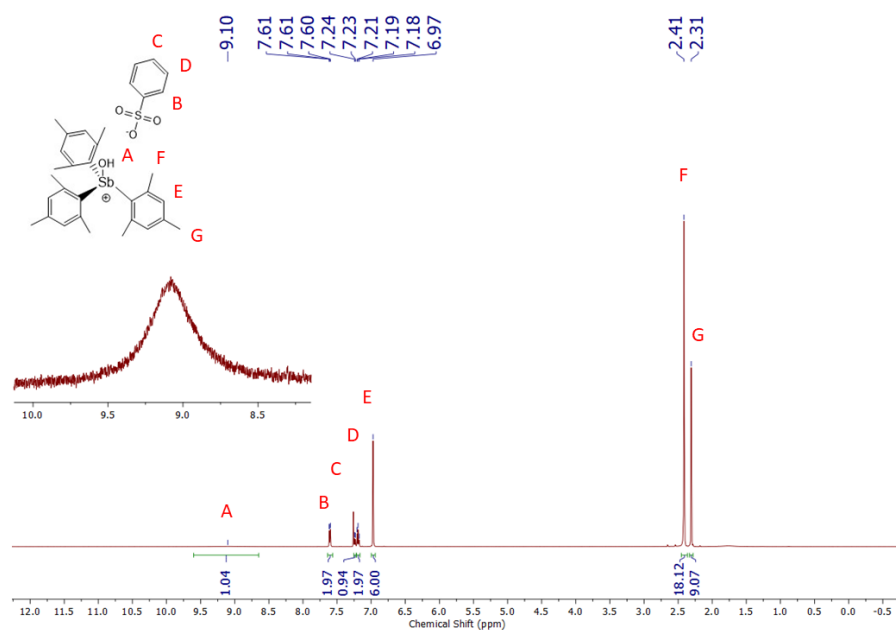
**Figure A.5.** $^1$H NMR spectrum (CDCl$_3$, 500 MHz) of [Mes$_3$Sb(OH)][PhSO$_3$] at room temperature.
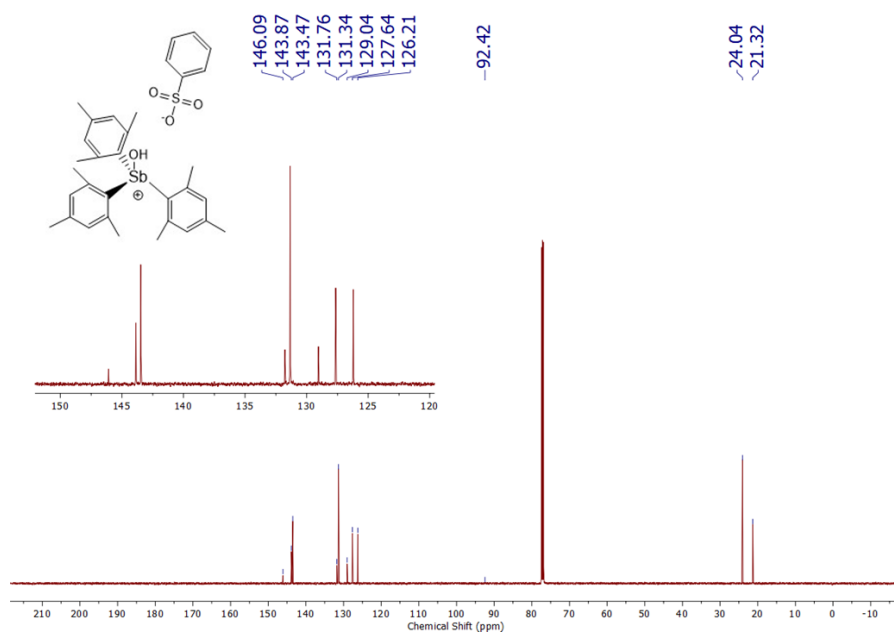


**Figure A.6.** $^{13}$C{$^1$H} NMR (CDCl$_3$, 125 MHz) spectrum of [Mes$_3$Sb(OH)][PhSO$_3$] at room temperature.
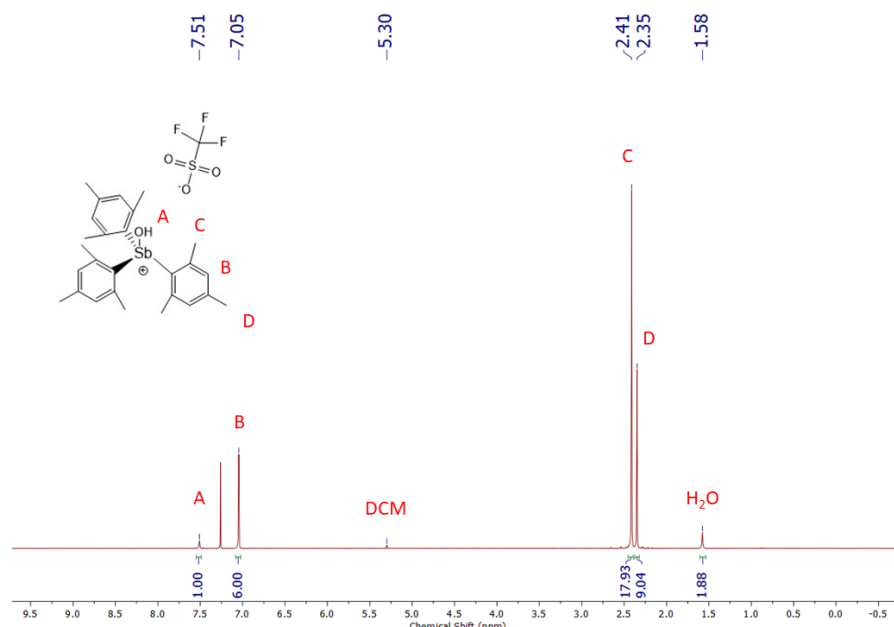
**Figure A.7.** $^1$H NMR spectrum (CDCl$_3$, 500 MHz) of [Mes$_3$Sb(OH)][CF$_3$SO$_3$] at room temperature.
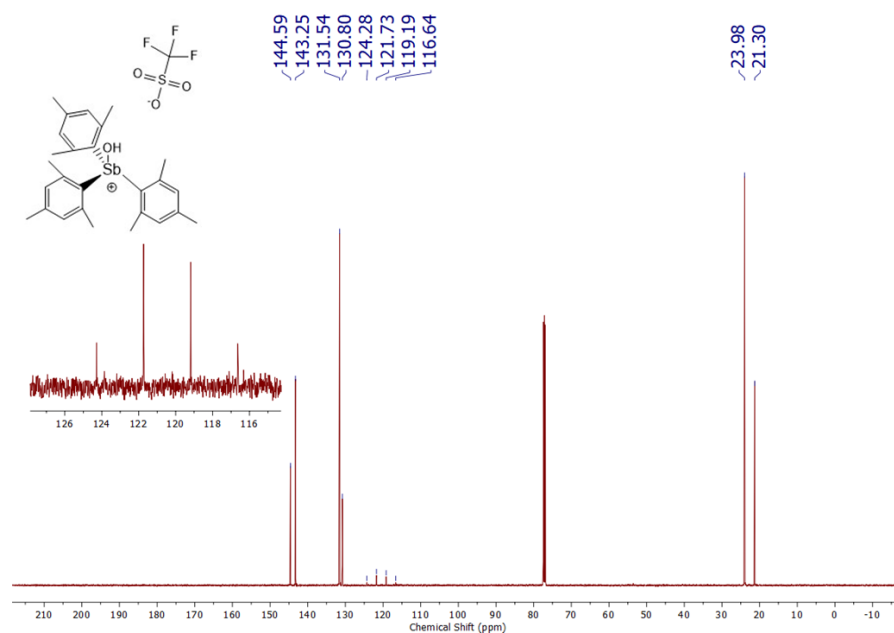


**Figure A.8.** $^{13}$C{$^1$H} NMR spectrum (CDCl$_3$, 125 MHz) of [Mes$_3$Sb(OH)][CF$_3$SO$_3$]) at room temperature.
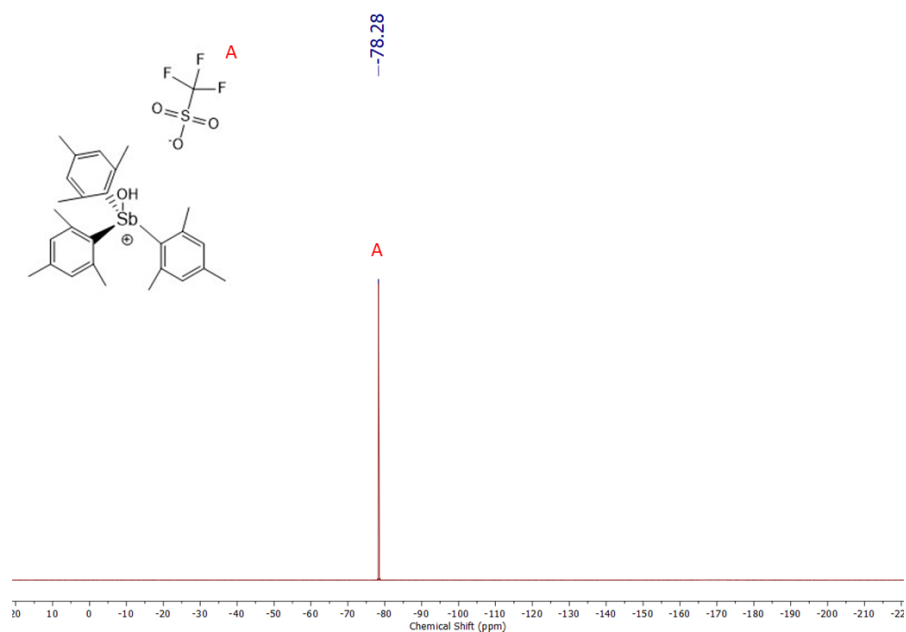
**Figure A.9.** $^{19}$F NMR spectrum (CDCl$_3$, 470 MHz) of [Mes$_3$Sb(OH)][CF$_3$SO$_3$] at room temperature.
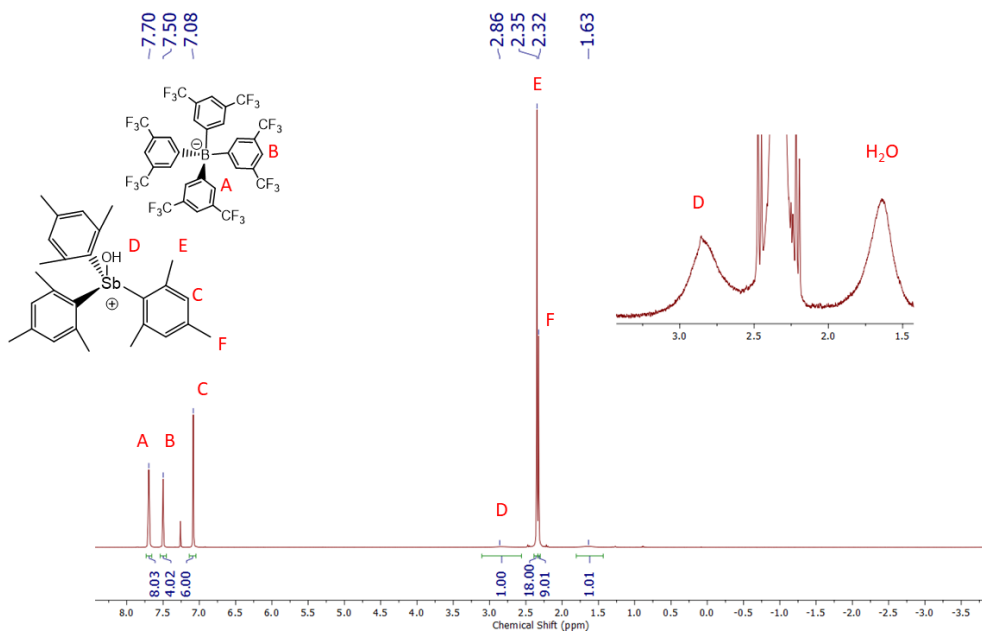


**Figure A.10.** $^1$H NMR spectrum (CDCl$_3$, 500 MHz) of [Mes$_3$Sb(OH)][BAr$^F$] at room temperature.
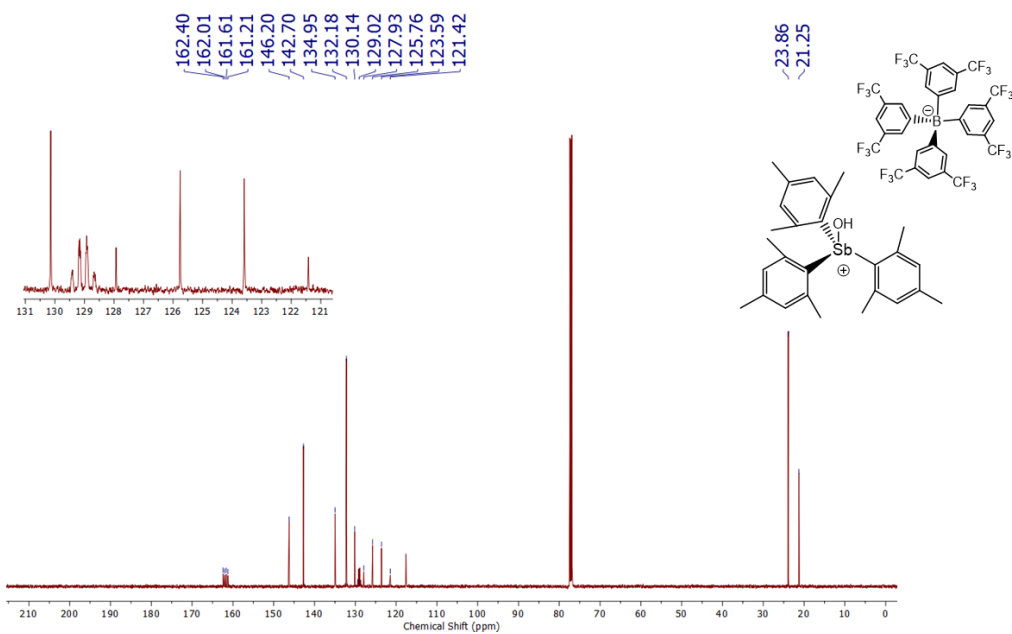
**Figure A.11.** $^{13}C\{^{1}H\}$ NMR spectrum (CDCl$_3$, 125 MHz) of [Mes$_3$Sb(OH)][BAr$^F$] at room temperature.
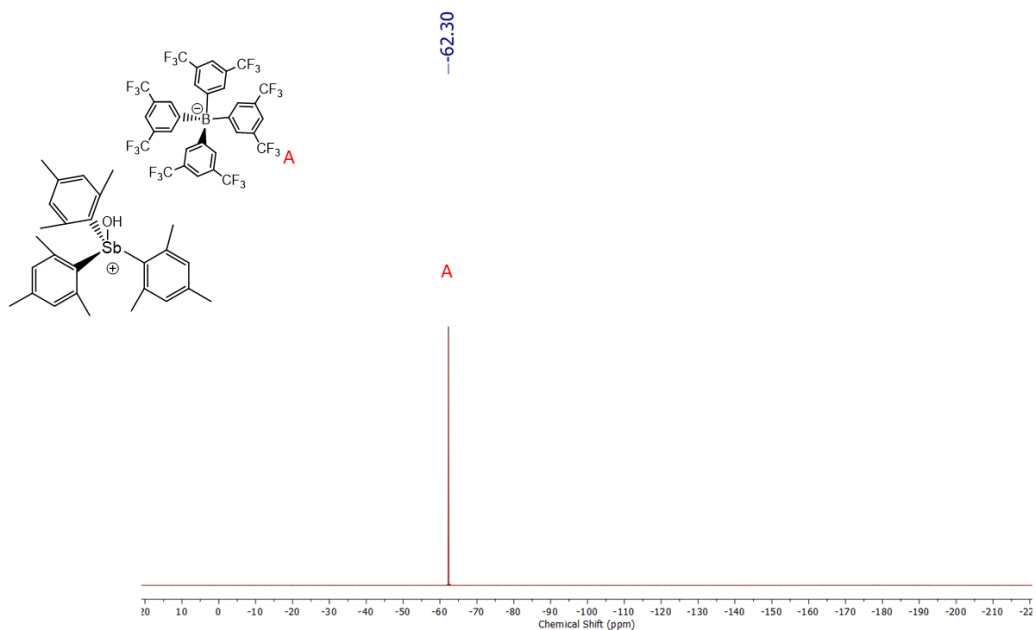


**Figure A.12.** $^{19}$F NMR spectrum (CDCl$_3$, 470 MHz) of [Mes$_3$Sb(OH)][BAr$^F$] at room temperature.
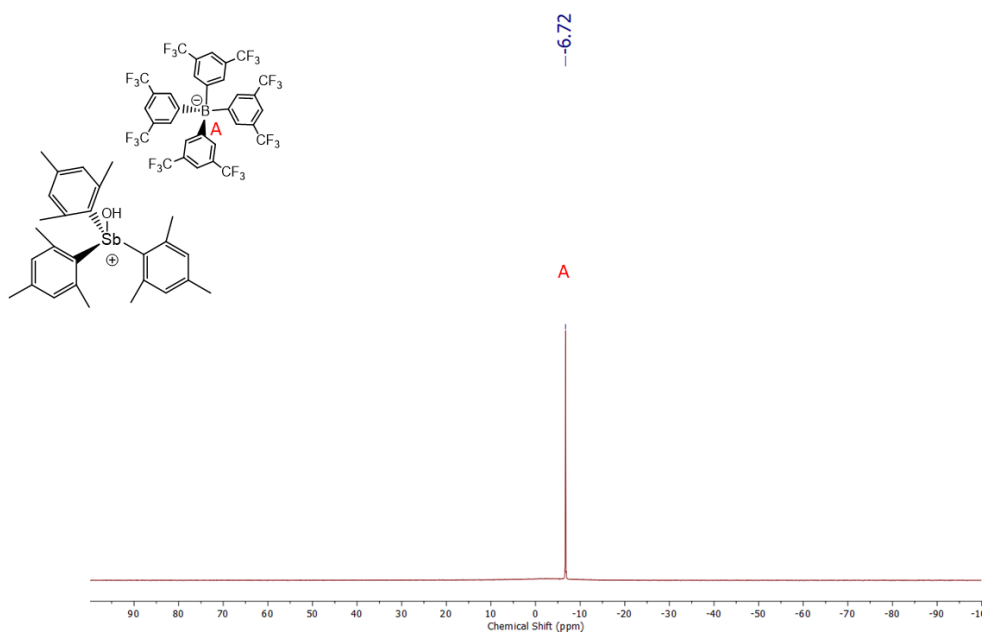
**Figure A.13.** $^{11}$B NMR spectrum (CDCl$_3$, 160 MHz) of [Mes$_3$Sb(OH)][BAr$^F$] at room temperature.
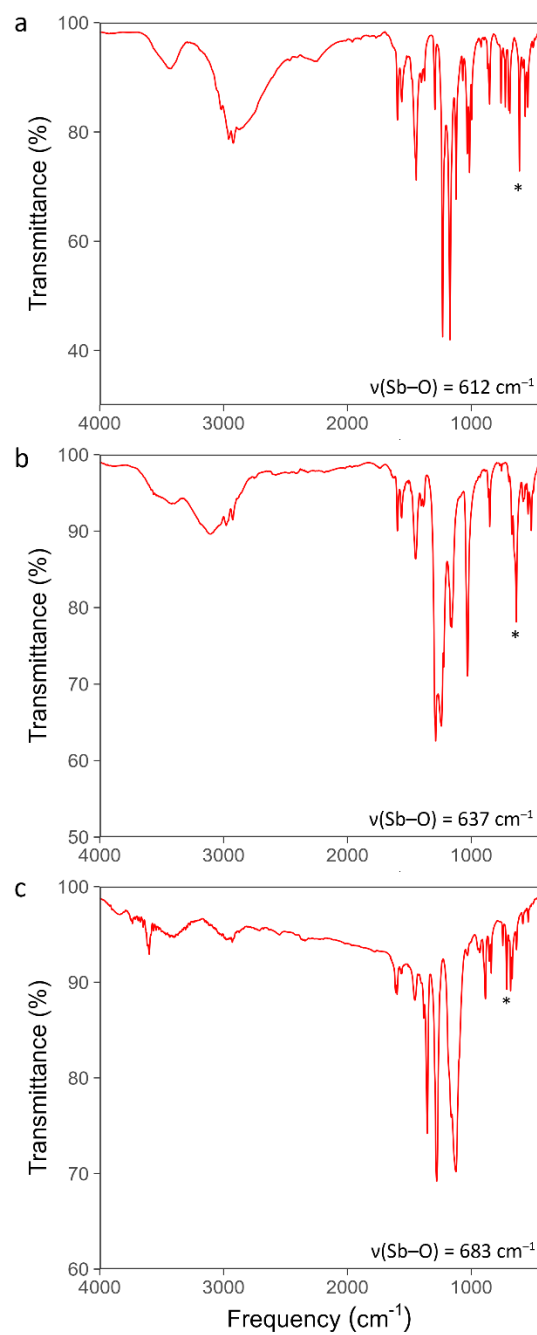
**Figure A.14.** Experimental infrared spectra (KBr pellets) of (a) hydroxytrimesitylstibonium benzenesulfonate, (b) hydroxytrimesitylstibonium triflate, and (c) hydroxytrimesitylstibonium tetrakis(3,5-bis(trifluoromethyl)phenyl)borate ($v_{OH}$ 3601 cm$^{-1}$ (s)).
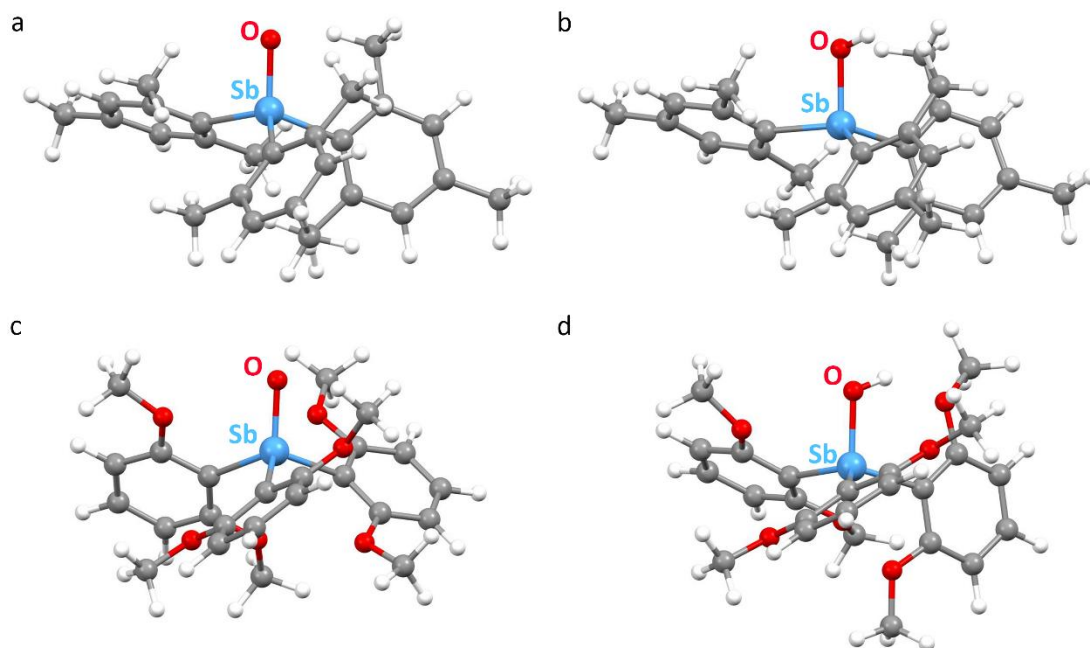
**Figure A.15.** Ball-and-stick representation of the optimized structures (PBE0/def2-TZVPP) of (a) hydroxytrimesitylstibonium benzenesulfonate**,** (b) hydroxytris(2,6-dimethoxyphenyl)stibonium cation, (c) tris(2,6-dimethoxyphenyl)stibine oxide, and (d) tris(2,6-dimethoxyphenyl)hydroxystibonium cation. Color code: O red, Sb purple, C grey, H white, S yellow.
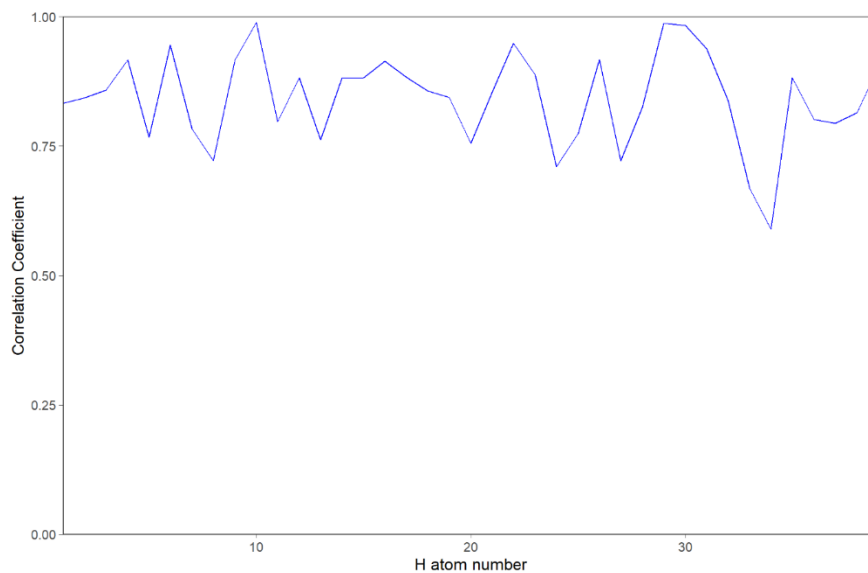


**Figure A.16.** Correlation coefficients between ADPs of H atoms in the neutron diffraction model and the HAR model.
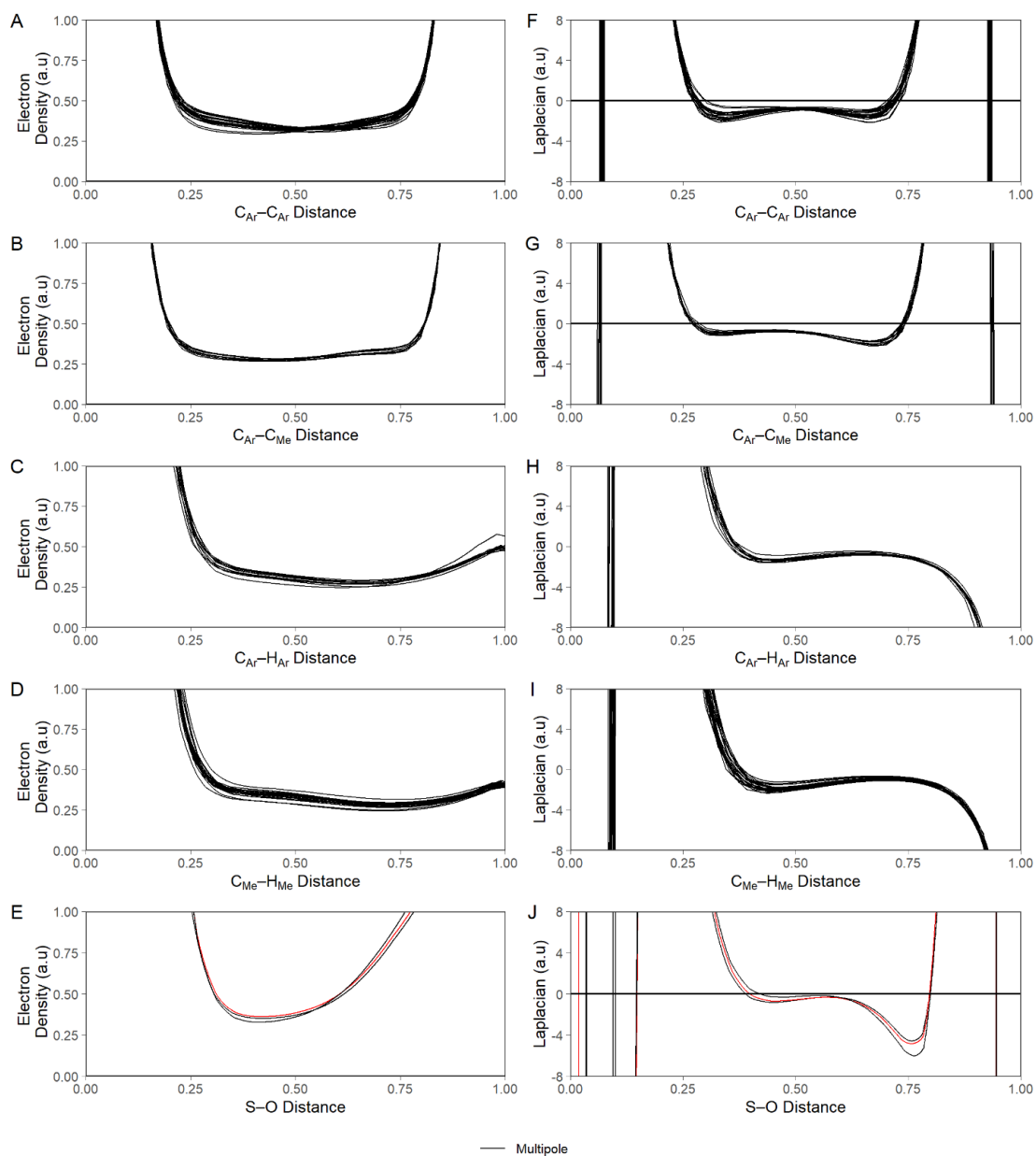
**Figure A.17.** Evaluation of $\rho$ for (A) aryl C–C bonds, (B) methyl C–C bonds, (C) aryl C–H bonds, (D) methyl C–H bonds, and (E) S–O bonds derived from the MM. Evaluation of $\nabla^2\rho$ for (F) aryl C–C bonds, (G) methyl C–C bonds, (H) aryl C–H bonds, (I) methyl C–H bonds, and (J) S–O bonds derived from the MM. Real space functions corresponding to the hydrogen bonding oxygen are shown in red.

**Supplementary Tables**

**Table A.1.** Crystallographic details for [Mes$_3$Sb(OH)][Ph$_3$SO$_3$], [Mes$_3$Sb(OH)][CF$_3$SO$_3$], and [Mes$_3$Sb(OH)][BAr$^F$] .

| Compound | [Mes$_3$Sb(OH)][Ph$_3$SO$_3$] | [Mes$_3$Sb(OH)][CF$_3$SO$_3$] | [Mes$_3$Sb(OH)][BAr$^F$]·C$_5$H$_{12}$ |
|---|---|---|---|
| Empirical formula | C$_{33}$H$_{39}$O$_4$SSb | C$_{28}$H$_{34}$F$_3$O$_4$SSb | C$_{64}$H$_{58}$BF$_{24}$OSb |
| Formula weight | 653.45 | 645.36 | 1431.66 |
| Temperature (K) | 100(2) | 100(2) | 100(2) |
| Wavelength (Å) | 0.71073 | 0.71073 | 0.71073 |
| Crystal system | Orthorhombic | Monoclinic | Triclinic |
| Space group | *Pbca* | *P*2$_1$/*n* | *P*$\bar{1}$ |
| *a* (Å) | 16.62251(11) | 10.4609(2) | 12.7443(4) |
| *b* (Å) | 16.92326(15) | 22.0134(4) | 13.0965(4) |
| *c* (Å) | 21.21101(15) | 12.4071(2) | 20.1296(7) |
| α (°) | | | 76.697(3) |
| β (°) | | 95.2150(10) | 79.142(3) |
| γ (°) | | | 78.266(3) |
| Volume (Å$^3$) | 5966.81(8) | 2845.28(9) | 3165.73(19) |
| *Z* | 8 | 4 | 2 |
| ρ$_{calc}$ (Mg/m$^3$) | 1.455 | 1.507 | 1.502 |
| Crystal size (mm$^3$) | 0.19 × 0.14 × 0.07 | 0.10 × 0.07 × 0.06 | 0.40 × 0.14 × 0.08 |
| θ range (°) | 1.967 to 38.084 | 2.163 to 31.113 | 2.385 to 25.027 |
| Reflections collected | 129747 | 67191 | 70027 |
| Independent reflections | 15556 | 7972 | 11179 |
| Parameters | 383 | 383 | 956 |
| Completeness | 100 | 100 | 99.9 |
| *R*$_{int}$ | 0.0251 | 0.0429 | 0.0799 |
| *R*$_1$ (I > 2σ) | 0.0209 | 0.0291 | 0.0517 |
| *R*$_1$ (all data) | 0.0268 | 0.0377 | 0.0600 |
| *wR*$_2$ (I > 2σ) | 0.0563 | 0.0709 | 0.1342 |
| *wR*$_2$ (all data) | 0.0590 | 0.0734 | 0.1399 |
| Goodness of fit, *S* | 1.028 | 1.068 | 1.022 |

**Table A.2.** Energies along the relaxed surface scan of SbO–H bond length of hydroxytrimesitylstibonium benzenesulfonate.

| SbO–H Bond Length (Å) | Energy ($E_h$) |
|---|---|
| 0.9 | -2221.095869 |
| 0.952632 | -2221.104861 |
| 1.005263 | -2221.109199 |
| 1.057895 | -2221.110664 |
| 1.110526 | -2221.110588 |
| 1.163158 | -2221.109817 |
| 1.215789 | -2221.108928 |
| 1.268421 | -2221.108183 |
| 1.321053 | -2221.107578 |
| 1.373684 | -2221.106854 |
| 1.426316 | -2221.105519 |
| 1.478947 | -2221.103297 |
| 1.531579 | -2221.100973 |
| 1.584211 | -2221.09983 |
| 1.636842 | -2221.097751 |
| 1.689474 | -2221.095581 |
| 1.742105 | -2221.093497 |
| 1.794737 | -2221.091467 |
| 1.847368 | -2221.089824 |
| 1.9 | -2221.088198 |

**Table A.3.** Estimated proton affinities.

| | |
|---|---|
| $PhSO_3^-$ | 270 kcal mol$^{-1}$ |
| $Mes_3SbO$ | 286 kcal mol$^{-1}$ |

**Table A.4.** Hydrogen bond lengths (Å) found from neutron diffraction data and HAR crystal structures.

| | Neutron | HAR |
|---|---|---|
| O(1)-H(1) | 0.979(15) | 0.99(1) |
| C(13)-H(13) | 1.097(15) | 1.10(1) |
| C(15)-H(15) | 1.090(16) | 1.09(1) |
| C(17)-H(17A) | 1.08(2) | 1.09(1) |
| C(17)-H(17B) | 1.03(2) | 1.13(1) |
| C(17)-H(17C) | 1.04(2) | 1.07(1) |
| C(18)-H(18A) | 1.09(2) | 1.08(1) |
| C(18)-H(18B) | 1.07(2) | 1.07(1) |

| | | |
|---|---|---|
| C(18)-H(18C) | 1.07(2) | 1.12(1) |
| C(19)-H(19A) | 1.09(2) | 1.10(1) |
| C(19)-H(19B) | 1.076(18) | 1.08(1) |
| C(19)-H(19C) | 1.090(18) | 1.11(1) |
| C(23)-H(23) | 1.061(17) | 1.095(9) |
| C(25)-H(25) | 1.130(15) | 1.089(9) |
| C(27)-H(27A) | 1.07(2) | 1.09(1) |
| C(27)-H(27B) | 1.058(19) | 1.09(1) |
| C(27)-H(27C) | 1.051(19) | 1.09(1) |
| C(28)-H(28A) | 1.11(2) | 1.09(1) |
| C(28)-H(28B) | 1.02(2) | 1.09(1) |
| C(28)-H(28C) | 1.053(19) | 1.10(1) |
| C(29)-H(29A) | 1.077(19) | 1.10(1) |
| C(29)-H(29B) | 1.075(16) | 1.10(1) |
| C(29)-H(29C) | 1.087(18) | 1.08(1) |
| C(33)-H(33) | 1.080(16) | 1.104(9) |
| C(35)-H(35) | 1.073(16) | 1.11(1) |
| C(37)-H(37A) | 1.084(19) | 1.07(1) |
| C(37)-H(37B) | 1.077(15) | 1.11(1) |
| C(37)-H(37C) | 1.08(2) | 1.08(1) |
| C(38)-H(38A) | 1.13(5) | 1.14(3) |
| C(38)-H(38B) | 1.16(5) | 1.14(4) |
| C(38)-H(38C) | 0.99(5) | 1.04(1) |
| C(38)-H(38D) | 1.12(4) | 1.13(2) |
| C(38)-H(38E) | 0.97(4) | 1.07(2) |
| C(38)-H(38F) | 1.11(4) | 1.13(2) |
| C(39)-H(39A) | 1.07(2) | 1.04(1) |
| C(39)-H(39B) | 1.032(18) | 1.05(1) |
| C(39)-H(39C) | 1.07(2) | 1.04(1) |
| C(42)-H(42) | 1.095(18) | 1.11(1) |
| C(43)-H(43) | 1.083(18) | 1.12(1) |
| C(44)-H(44) | 1.088(17) | 1.11(1) |
| C(45)-H(45) | 1.058(19) | 1.12(1) |
| C(46)-H(46) | 1.062(17) | 1.08(1) |

**Table A.5.** Literature values for averaged bond lengths found from neutron diffraction data.[1]

| Bond | Value | σ |
|---|---|---|
| Z—Csp$^3$—H$_3$ | 1.077 | 0.026 |
| C(ar)—H | 1.083 | 0.017 |
| Z—O—H | 0.983 | 0.025 |
| C(any)—O—H | 0.980 | 0.021 |

**Table A.6.** $U_{eq}$ ($Å^2 \times 10^3$) of H atoms from neutron diffraction and HAR X-ray crystal structures.

|          | $U_{eq}$ (Neutron) | $U_{eq}$ (HAR) |
|----------|-----------|-----------|
| H(1)     | 28(4)     | 48(4)     |
| H(13)    | 40(4)     | 52(3)     |
| H(15)    | 34(4)     | 40(3)     |
| H(17A)   | 82(8)     | 59(3)     |
| H(17B)   | 62(6)     | 70(4)     |
| H(17C)   | 60(6)     | 81(5)     |
| H(18A)   | 74(7)     | 73(5)     |
| H(18B)   | 69(7)     | 81(5)     |
| H(18C)   | 62(6)     | 73(5)     |
| H(19A)   | 63(6)     | 47(3)     |
| H(19B)   | 59(6)     | 57(4)     |
| H(19C)   | 49(5)     | 60(4)     |
| H(23)    | 45(5)     | 51(3)     |
| H(25)    | 32(4)     | 42(3)     |
| H(27A)   | 68(7)     | 52(3)     |
| H(27B)   | 62(6)     | 48(3)     |
| H(27C)   | 52(5)     | 46(3)     |
| H(28A)   | 64(6)     | 85(5)     |
| H(28B)   | 66(6)     | 68(4)     |
| H(28C)   | 72(7)     | 76(5)     |
| H(29A)   | 47(5)     | 77(5)     |
| H(29B)   | 50(5)     | 59(4)     |
| H(29C)   | 48(5)     | 64(4)     |
| H(33)    | 36(4)     | 51(3)     |
| H(35)    | 41(4)     | 58(3)     |
| H(37A)   | 52(5)     | 57(4)     |
| H(37B)   | 49(5)     | 60(4)     |
| H(37C)   | 50(5)     | 58(4)     |
| H(38A)   | 48(5)     | 42(7)     |
| H(38B)   | 47(5)     | 47(8)     |
| H(38C)   | 48(5)     | 25(6)     |
| H(38D)   | 49(5)     | 45(2)     |
| H(38E)   | 51(5)     | 48(2)     |
| H(38F)   | 46(5)     | 46(2)     |
| H(39A)   | 93(10)    | 101(6)    |
| H(39B)   | 69(7)     | 107(7)    |
| H(39C)   | 91(10)    | 73(4)     |
| H(42)    | 47(5)     | 49(3)     |
| H(43)    | 53(5)     | 58(3)     |
| H(44)    | 53(5)     | 58(4)     |
| H(45)    | 52(5)     | 62(4)     |
| H(46)    | 48(5)     | 55(3)     |

**Table A.7.** Anisotropic displacement parameters ($\text{Å}^2 \times 10^3$) for the neutron model.

| | $U_{11}$ | $U_{22}$ | $U_{33}$ | $U_{23}$ | $U_{13}$ | $U_{12}$ |
|---|---|---|---|---|---|---|
| H(1) | 31(10) | 32(8) | 21(7) | 0(6) | -10(7) | -9(8) |
| H(13) | 32(10) | 23(8) | 66(11) | 4(8) | 18(9) | -9(8) |
| H(15) | 37(11) | 35(9) | 29(8) | -5(7) | 8(8) | -9(8) |
| H(17A) | 140(20) | 58(13) | 45(11) | 1(11) | 3(14) | -11(16) |
| H(17B) | 67(15) | 15(8) | 105(17) | -21(10) | 21(13) | -12(9) |
| H(17C) | 60(14) | 16(9) | 104(17) | 5(10) | -10(12) | 10(9) |
| H(18A) | 53(14) | 120(20) | 50(11) | -1(12) | 33(11) | -36(13) |
| H(18B) | 61(15) | 76(15) | 69(14) | 9(11) | 31(12) | 32(13) |
| H(18C) | 51(14) | 98(17) | 36(9) | 16(11) | 16(10) | 13(12) |
| H(19A) | 53(15) | 56(13) | 80(14) | -4(11) | 16(12) | -25(11) |
| H(19B) | 73(15) | 11(8) | 91(15) | 2(9) | 35(13) | 0(10) |
| H(19C) | 63(14) | 38(11) | 47(10) | 17(8) | 12(10) | -16(9) |
| H(23) | 24(10) | 73(13) | 38(9) | 5(9) | -7(8) | -7(9) |
| H(25) | 23(9) | 40(9) | 33(8) | 10(7) | 10(7) | -3(7) |
| H(27A) | 26(12) | 110(20) | 67(14) | 25(13) | 10(10) | -4(11) |
| H(27B) | 17(10) | 120(20) | 51(11) | -2(12) | 3(9) | 10(11) |
| H(27C) | 36(12) | 69(13) | 50(11) | -15(10) | 10(9) | 0(10) |
| H(28A) | 66(15) | 77(15) | 49(11) | 26(11) | -4(12) | -23(13) |
| H(28B) | 47(14) | 102(17) | 48(11) | 19(12) | -10(11) | 22(13) |
| H(28C) | 130(20) | 34(11) | 53(12) | -5(9) | -39(14) | -3(13) |
| H(29A) | 21(10) | 59(12) | 61(12) | -8(9) | -12(9) | 2(9) |
| H(29B) | 26(10) | 94(16) | 30(8) | -6(10) | 5(8) | 24(10) |
| H(29C) | 33(11) | 53(12) | 57(11) | 15(10) | -4(9) | 9(9) |
| H(33) | 53(12) | 21(9) | 36(9) | 5(7) | -12(8) | 9(8) |
| H(35) | 44(12) | 16(8) | 63(11) | -18(8) | 6(10) | 5(8) |
| H(37A) | 67(15) | 48(11) | 41(9) | -23(9) | 0(10) | -19(10) |
| H(37B) | 82(16) | 48(11) | 15(7) | -11(7) | -26(9) | 14(10) |
| H(37C) | 45(13) | 52(11) | 52(11) | -21(9) | -11(9) | 14(9) |
| H(38A) | 51(10) | 37(10) | 57(8) | -2(8) | 3(8) | 23(9) |
| H(38B) | 51(9) | 31(9) | 60(10) | 8(9) | 4(8) | 24(8) |
| H(38C) | 51(8) | 33(9) | 59(8) | -1(8) | 0(9) | 24(7) |
| H(38D) | 47(9) | 42(9) | 59(9) | 3(9) | 4(8) | 23(6) |
| H(38E) | 52(9) | 40(8) | 61(9) | 0(8) | 0(8) | 22(7) |
| H(38F) | 50(10) | 31(9) | 57(9) | 6(7) | 4(6) | 27(9) |
| H(39A) | 49(15) | 190(30) | 41(11) | -22(15) | -24(11) | 10(17) |
| H(39B) | 97(19) | 56(13) | 54(11) | -37(10) | -52(13) | 29(12) |
| H(39C) | 170(30) | 51(13) | 56(12) | 33(11) | -57(17) | -38(16) |
| H(42) | 58(13) | 34(9) | 49(10) | 19(9) | -11(10) | -29(9) |
| H(43) | 62(14) | 61(13) | 37(10) | 28(10) | -13(10) | -14(11) |

| | | | | | | |
|---|---|---|---|---|---|---|
| H(44) | 60(13) | 57(12) | 41(10) | 13(9) | -20(10) | 1(10) |
| H(45) | 37(12) | 67(13) | 52(11) | 15(10) | -16(10) | -9(10) |
| H(46) | 54(12) | 53(11) | 36(9) | 6(8) | -2(9) | -30(10) |

**Table A.8.** Anisotropic displacement parameters ($Å^2 \times 10^3$) for the HAR model.

| | $U_{11}$ | $U_{22}$ | $U_{33}$ | $U_{23}$ | $U_{13}$ | $U_{12}$ |
|---|---|---|---|---|---|---|
| H(1) | 58(9) | 33(8) | 53(9) | -12(6) | 5(7) | 14(7) |
| H(13) | 57(8) | 35(7) | 64(8) | -7(5) | -24(6) | -20(5) |
| H(15) | 55(6) | 21(5) | 45(7) | 12(5) | -11(5) | 8(5) |
| H(17A) | 43(7) | 35(7) | 98(10) | -4(7) | -5(7) | 13(6) |
| H(17B) | 114(12) | 57(10) | 40(8) | 30(7) | -3(8) | -22(10) |
| H(17C) | 56(8) | 51(9) | 136(14) | 28(9) | -46(9) | -34(7) |
| H(18A) | 54(9) | 136(15) | 29(7) | -24(7) | 13(6) | 23(8) |
| H(18B) | 118(12) | 57(9) | 69(9) | -7(8) | -52(9) | 61(9) |
| H(18C) | 55(9) | 100(12) | 65(9) | 7(9) | -27(7) | -36(9) |
| H(19A) | 71(9) | 38(7) | 31(6) | -5(5) | -13(6) | -4(6) |
| H(19B) | 53(7) | 58(9) | 61(9) | -3(7) | 17(7) | -32(7) |
| H(19C) | 54(7) | 32(7) | 96(10) | -15(7) | -36(7) | 23(6) |
| H(23) | 21(5) | 81(9) | 52(7) | -16(6) | 18(5) | 18(5) |
| H(25) | 38(6) | 62(8) | 24(5) | -9(5) | -6(4) | -9(5) |
| H(27A) | 28(6) | 86(9) | 41(7) | 12(7) | -16(5) | 6(6) |
| H(27B) | 42(7) | 54(8) | 49(7) | -33(6) | 5(6) | 19(5) |
| H(27C) | 40(6) | 42(7) | 56(8) | 25(6) | 13(6) | -9(5) |
| H(28A) | 139(14) | 71(11) | 46(8) | 32(8) | 39(9) | -4(10) |
| H(28B) | 60(9) | 98(12) | 46(8) | -37(7) | -1(6) | -24(9) |
| H(28C) | 44(7) | 136(15) | 48(8) | -26(8) | 9(6) | 46(9) |
| H(29A) | 22(6) | 166(15) | 44(7) | -4(9) | 7(5) | 16(8) |
| H(29B) | 54(8) | 99(11) | 24(6) | 23(7) | 3(6) | 2(8) |
| H(29C) | 54(8) | 41(7) | 98(11) | -37(8) | -21(8) | -9(6) |
| H(33) | 65(7) | 63(8) | 25(5) | -7(5) | 30(5) | 5(6) |
| H(35) | 78(9) | 34(6) | 60(8) | 27(6) | 21(7) | 18(6) |
| H(37A) | 47(7) | 62(8) | 62(8) | 28(7) | -1(6) | 36(7) |
| H(37B) | 85(11) | 39(8) | 57(9) | 4(6) | -2(7) | -31(7) |
| H(37C) | 95(10) | 54(8) | 24(6) | 0(6) | 25(6) | 21(7) |
| H(38D) | 48(4) | 36(5) | 50(1) | -1(1) | 13(1) | 12(2) |
| H(38E) | 48(2) | 42(5) | 53(2) | 1(2) | 10(1) | 14(1) |
| H(38F) | 50(4) | 30(3) | 57(3) | 1(1) | 14(1) | 13(2) |
| H(39A) | 50(9) | 200(20) | 49(9) | 23(11) | 23(7) | 4(11) |
| H(39B) | 210(20) | 33(8) | 79(12) | -35(8) | 78(14) | -13(10) |
| H(39C) | 100(11) | 77(10) | 42(8) | 33(7) | 27(8) | 42(9) |
| H(42) | 41(7) | 54(8) | 53(8) | -13(6) | 16(6) | -29(5) |
| H(43) | 79(9) | 42(7) | 54(8) | -23(6) | 8(6) | -28(7) |
| H(44) | 72(9) | 69(10) | 33(7) | -22(6) | 27(6) | -7(8) |
| H(45) | 45(7) | 69(9) | 72(9) | 0(7) | 24(6) | -39(7) |
| H(46) | 71(8) | 36(7) | 56(8) | -24(6) | 13(6) | -21(6) |

**Table A.9.** Correlation coefficients (cc) of H-atom ADPs.

|         | cc       |
|---------|----------|
| H(1)    | 0.832696 |
| H(13)   | 0.843385 |
| H(15)   | 0.857652 |
| H(17A)  | 0.916581 |
| H(17B)  | 0.766857 |
| H(17C)  | 0.945588 |
| H(18A)  | 0.78299  |
| H(18B)  | 0.721625 |
| H(18C)  | 0.916156 |
| H(19A)  | 0.988597 |
| H(19B)  | 0.796888 |
| H(19C)  | 0.881696 |
| H(23)   | 0.761786 |
| H(25)   | 0.881206 |
| H(27A)  | 0.882148 |
| H(27B)  | 0.913866 |
| H(27C)  | 0.882691 |
| H(28A)  | 0.85669  |
| H(28B)  | 0.844364 |
| H(28C)  | 0.755422 |
| H(29A)  | 0.854291 |
| H(29B)  | 0.948834 |
| H(29C)  | 0.888005 |
| H(33)   | 0.709793 |
| H(35)   | 0.774052 |
| H(37A)  | 0.916926 |
| H(37B)  | 0.721733 |
| H(37C)  | 0.825541 |
| H(38D)  | 0.987215 |
| H(38E)  | 0.982857 |
| H(38F)  | 0.938197 |
| H(39A)  | 0.838086 |
| H(39B)  | 0.668517 |
| H(39C)  | 0.588946 |
| H(42)   | 0.882288 |
| H(43)   | 0.801182 |
| H(44)   | 0.794034 |
| H(45)   | 0.814204 |
| H(46)   | 0.901416 |

**Table A.10.** Average values of $\rho_b$ and $\nabla^2\rho_b$ derived from the MM with standard deviations provided for bond types occurring more than twice.

| Bond Type | $\rho_b$ (e⁻ bohr⁻³) | $\nabla^2\rho_b$ (e⁻ bohr⁻⁵) |
|---|---|---|
| $C_{Ar}$–$C_{Ar}$ | $0.32 \pm 0.01$ | $-0.79 \pm 0.09$ |
| $C_{Ar}$–$C_{Me}$ | $0.27 \pm 0.006$ | $-0.71 \pm 0.08$ |
| $C_{Ar}$–H | $0.27 \pm 0.014$ | $-0.71 \pm 0.11$ |
| $C_{Me}$–H | $0.28 \pm 0.015$ | $-0.96 \pm 0.13$ |
| S–O | $0.35 \pm 0.02$ | $-0.30 \pm 0.33$ |
| Sb–C | $0.10 \pm 0.01$ | $0.19 \pm 0.06$ |
| Sb–O | 0.17 | 0.49 |
| S–C | 0.22 | −0.37 |
| SbO–H | 0.31 | −1.54 |
| SbOH⋯OS | 0.053 | 0.10 |

**Table A.11.** Multipole modeling refinement strategy[a]

| Step | Parameter | #p | d/p | $R_1(F)$ | $R_1(F^2)$ | $R_1$(all) | GOF |
|---|---|---|---|---|---|---|---|
| 1 | IAM | 469 | 27.74 | 0.0227 | 0.0350 | 0.0329 | 4.1046 |
| 2 | Heteroatoms: D Q O<br>C11-C39: D Q O<br>C41-C46: D Q O<br>Hatoms: HD H1D H1Q | 189 | 68.84 | 0.0188 | 0.0264 | 0.0290 | 2.7086 |
| 3 | Heteroatoms: M D Q O<br>C11-C39: M D Q O<br>C41-C46: M D Q O<br>Hatoms: M HD H1D H1Q | 213 | 61.08 | 0.0178 | 0.0250 | 0.0280 | 2.4564 |
| 4 | Heteroatoms: Uij M D Q O<br>C11-C39: Uij M D Q O<br>C41-C46: Uij M D Q O<br>Hatoms: M HD H1D H1Q | 447 | 29.10 | 0.0176 | 0.0242 | 0.0278 | 2.3686 |
| 5 | Heteroatoms: XYZ Uij M D Q O<br>C11-C39: XYZ Uij M D Q O<br>C41-C46: XYZ Uij M D Q O<br>Hatoms: M HD H1D H1Q | 564 | 23.07 | 0.0175 | 0.0241 | 0.0277 | 2.3325 |

| 6 | Heteroatoms: k XYZ Uij M D Q O<br>C11-C39: k XYZ Uij M D Q O<br>C41-C46: k XYZ Uij M D Q O<br>Hatoms: M HD H1D H1Q | 568 | 22.90 | 0.0166 | 0.0221 | 0.0268 | 2.2226 |
|---|---|---|---|---|---|---|---|
| 7 | HXYZ Neutron Values | 122 | 106.65 | 0.0177 | 0.0245 | 0.0280 | 2.5611 |
| 8 | HUij added/HXYZ Neutron Values | 122 | 106.65 | 0.0180 | 0.0259 | 0.0282 | 2.8848 |
| 9 | Heteroatoms: k XYZ Uij M D Q O<br>C11-C39: k XYZ Uij M D Q O<br>C41-C46: k XYZ Uij M D Q O<br>Hatoms: M HD H1D H1Q | 568 | 22.90 | 0.0172 | 0.0237 | 0.0274 | 2.3837 |
| 10 | H | 108 | 120.48 | 0.0171 | 0.0235 | 0.0273 | 2.3023 |
| 11 | H k+ | 120 | 108.43 | 0.0172 | 0.0234 | 0.0274 | 2.3047 |
| 12 | Hk H k+ | 121 | 107.5 | 0.0171 | 0.0234 | 0.0273 | 2.2889 |
| 13 | Heteroatoms: NOSITESYMM D Q O H<br>Hatoms: HD HQ | 195 | 66.72 | 0.0168 | 0.0218 | 0.0270 | 2.2299 |
| 14 | C11-C39: NOSITESYMM | 265 | 49.10 | 0.0164 | 0.0210 | 0.0266 | 2.1173 |
| 15 | C41-C46: NOSITESYMM NOCHEMCON | 195 | 66.72 | 0.0160 | 0.0206 | 0.0262 | 2.0109 |
| 16 | Heteroatoms: XYZ Uij M D Q O H<br>C11-C39: XYZ Uij M D Q O  H<br>C41-C46: XYZ Uij M D Q O H<br>Hatoms: M HD H1D H1Q | 616 | 21.12 | 0.0153 | 0.0201 | 0.0256 | 1.9588 |
| 17 | Heteroatoms: NOSITESYMM XYZ Uij M D<br>      Q O H<br>C11-C39: NOSITESYMM XYZ Uij M D Q<br>    O H<br>C41-C46: XYZ Uij M D Q O H<br>Hatoms:  M HD H1D H1Q | 880 | 14.78 | 0.0152 | 0.0199 | 0.0254 | 1.9458 |
| 18 | Heteroatoms: XYZ NOSITESYMM Uij M D<br>      Q O H<br>C11-C39: XYZ NOCHEMCON<br>    NOSITESYMM Uij M D Q O H<br>C41-C46: XYZ Uij M D Q O H<br>Hatoms:  HXYZ M HD H1D H1Q | 1470 | 8.851 | 0.0146 | 0.0193 | 0.0249 | 1.9947 |

| 19 | Heteroatoms: NOSITESYMM k XYZ Uij M D     Q O H  C11-C39:                NOCHEMCON NOSITESYMM k      XYZ Uij M D Q O H  C41-C46: k XYZ Uij M D Q O H  Hatoms: Hk HXYZ HQ M HD H1D H1Q | 1472 | 8.83 | 0.0144 | 0.0181 | 0.0246 | 1.8703 |

**Abbreviations: #p:** number of parameters; **d/p:** data to parameter ratio; **GOF:** goodness of fit; **IAM:** the independent atom model was refined using XDLSM; **D:** dipoles, **Q:** quadrupoles, **O:** octupoles; **HD:** H-atom dipoles; **H1D:** H1 dipoles; **H1Q:** H1 quadrupoles; **M:** monopoles; **Uij:** anisotropic thermal parameters; **XYZ:** non-H-atom coordinates; **k:** kappa parameters allowed to refine for non-H atoms (1 per element type); **HXYZ Neutron Values:** H-atom coordinates refined and reset to neutron model bond lengths after each stage of refinement; **HUij added:** neutron derived H-atom thermal parameters added but not refined (disordered H atoms left anisotropic); **H:** hexadecapoles; **k+:** Additional kappa parameters allowed to refine based on chemical differences; **Hk:** H atom kappa parameters allowed to refine; **NOSITESYMM:** site symmetry restrictions on multipolar expansion are removed; **NOCHEMCON:** chemical similarity constraints between atoms are removed

[a] Refinement was performed using established strategies.[2]

**References**

1.      Allen, F. H.; Bruno, I. J., Bond lengths in organic and metal-organic compounds revisited: X—H bond lengths from neutron diffraction data. *Acta Crystallogr. Sect. B* **2010,** *66*, 380-386.

2.      Münch, A.; Knauer, L.; Ott, H.; Sindlinger, C.; Herbst-Irmer, R.; Strohmann, C.; Stalke, D., Insight into the Bonding and Aggregation of Alkyllithiums by Experimental Charge Density Studies and Energy Decomposition Analyses. *J. Am. Chem. Soc.* **2020,** *142*, 15897-15906.

**Appendix B**


**Supplementary data for**


**Chapter 3: Isolation, bonding, and reactivity of a monomeric stibine oxide**
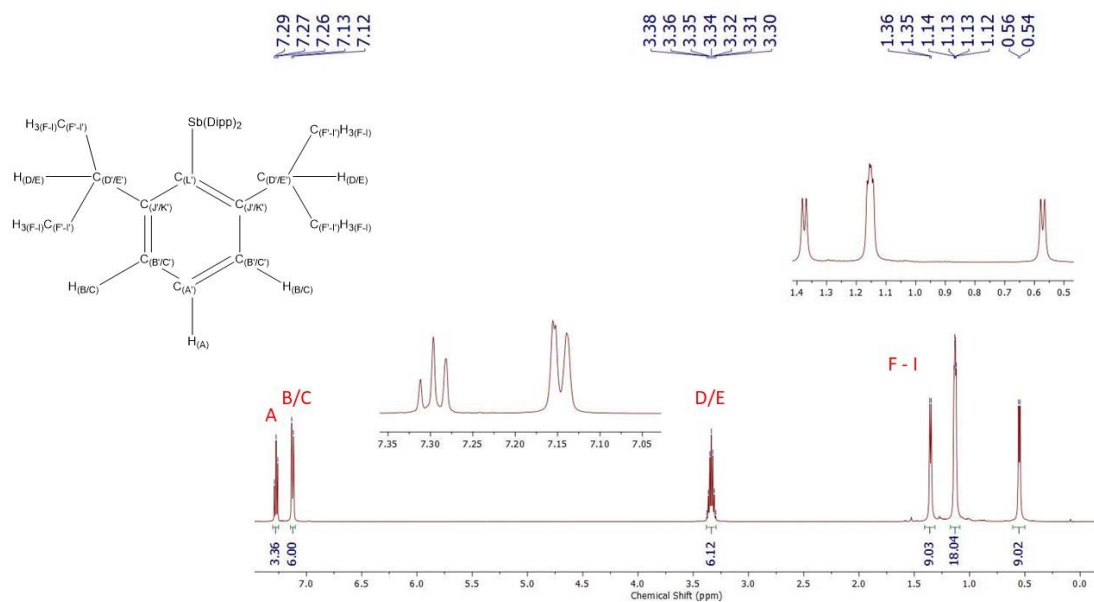
**Figure B.1.** $^1$H NMR spectrum (CDCl$_3$, 500 MHz) of Dipp$_3$Sb at room temperature.
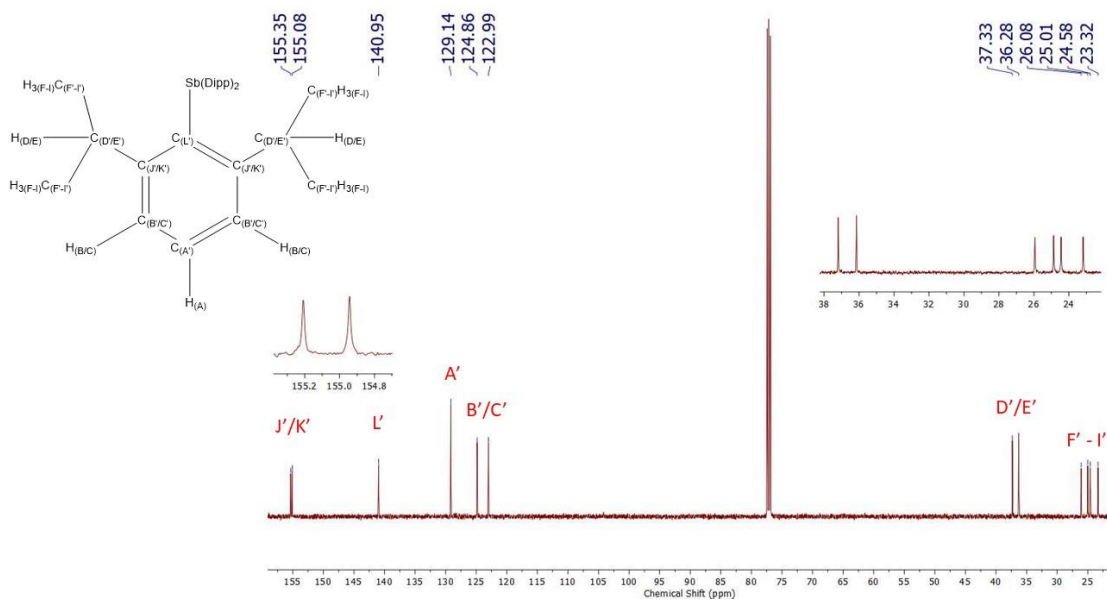


**Figure B.2.** $^{13}$C{$^1$H} NMR spectrum (CDCl$_3$, 125 MHz) of Dipp$_3$Sb at room temperature. Peaks are assigned based on HSQC and HMBC experiments (*vide infra*).
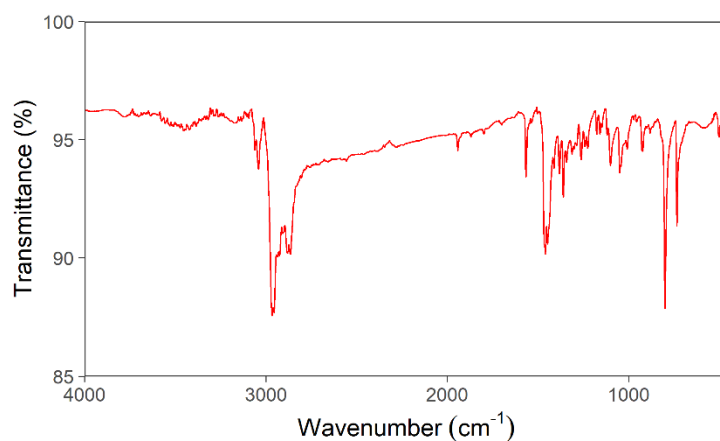
**Figure B.3.** Experimental IR spectrum (KBr pellet) of Dipp$_3$Sb.
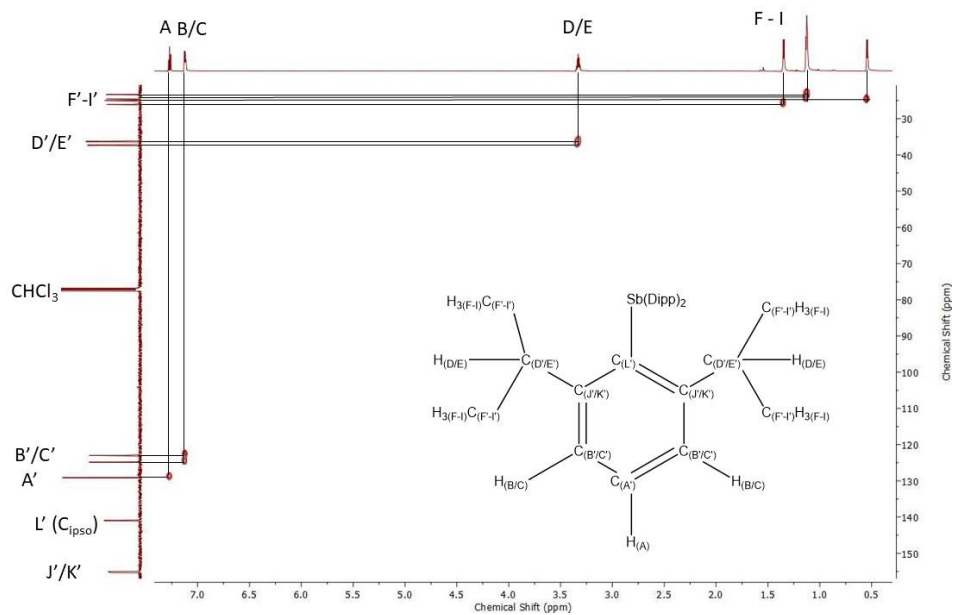


**Figure B.4.** $^1$H-$^{13}$C HSQC (800 MHz, CDCl$_3$) spectrum of Dipp$_3$Sb at room temperature.

239
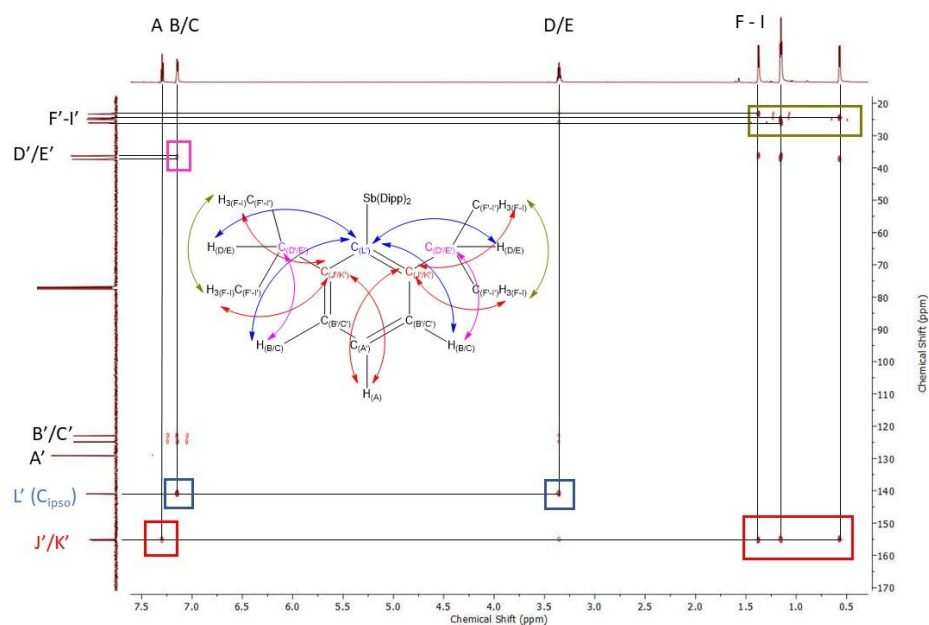
**Figure B.5.** $^1$H-$^{13}$C HMBC (800 MHz, CDCl$_3$) spectrum of Dipp$_3$Sb at room temperature.
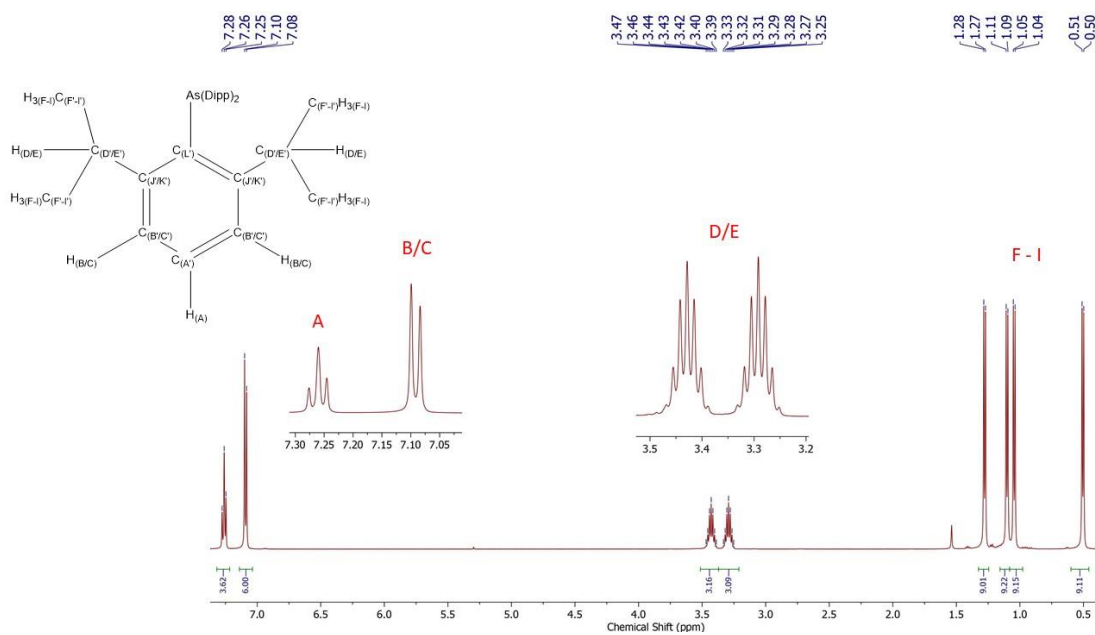


**Figure B.6.** $^1$H NMR spectrum (CDCl$_3$, 500 MHz) of Dipp$_3$As at room temperature.
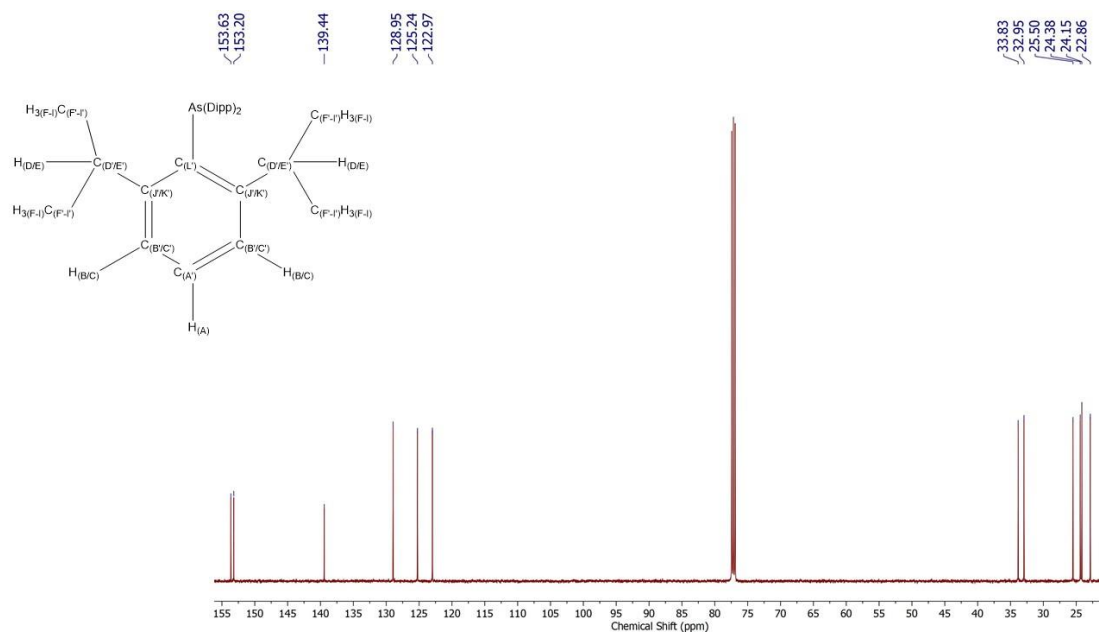
**Figure B.7.** $^{13}C\{^1H\}$ NMR spectrum (CDCl$_3$, 125 MHz) of Dipp$_3$As at room temperature.
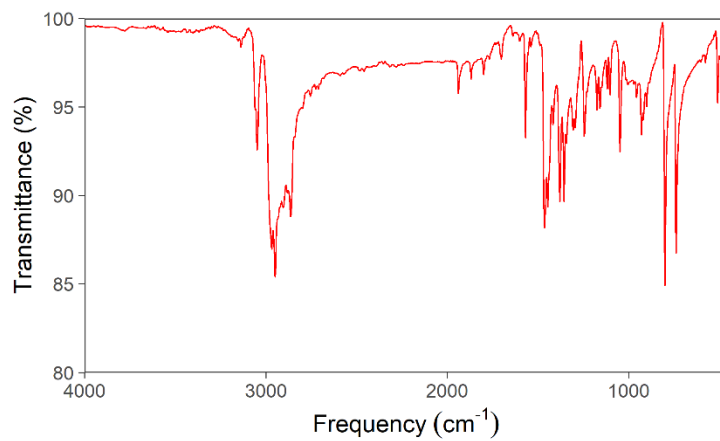


**Figure B.8.** Experimental IR spectrum (KBr pellet) of Dipp$_3$As.
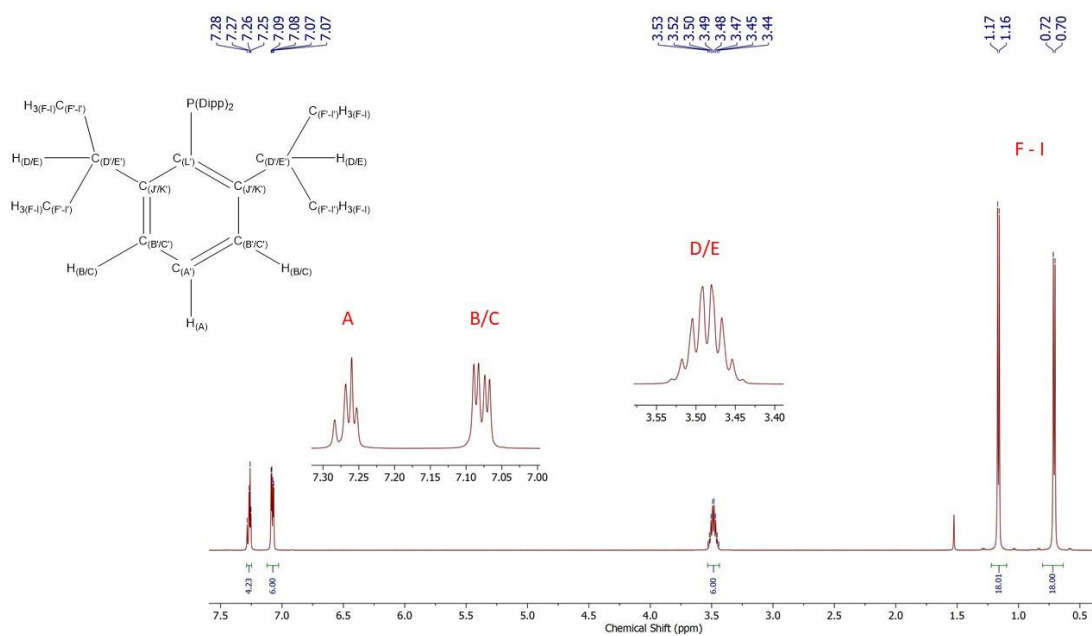
**Figure B.9.** $^{1}$H NMR spectrum (CDCl$_3$, 500 MHz) of Dipp$_3$P at room temperature.
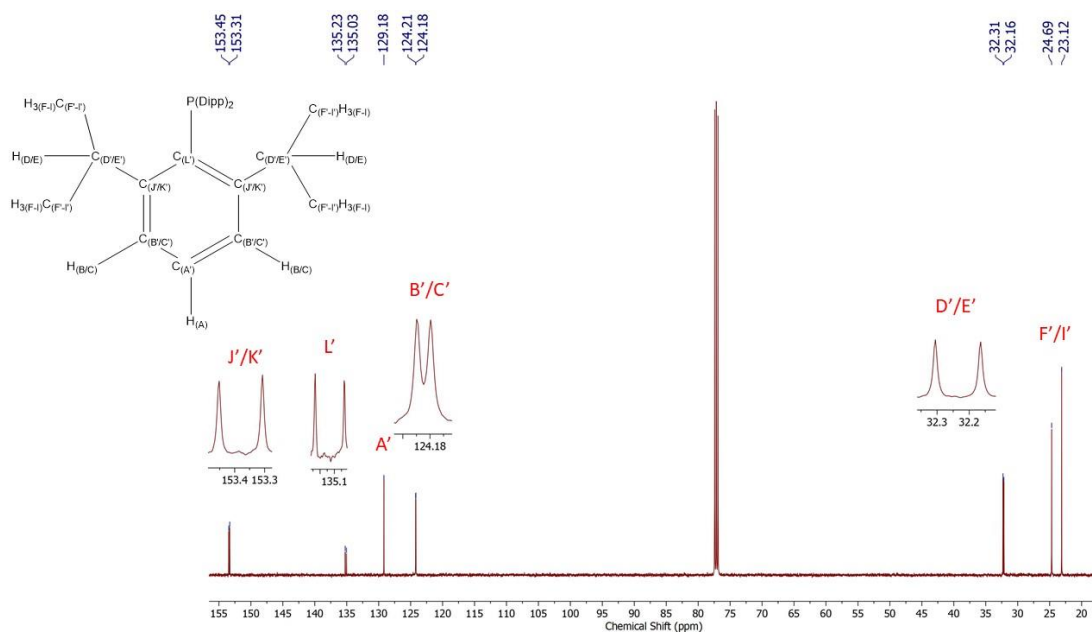


**Figure B.10.** $^{13}$C{$^{1}$H} NMR spectrum (CDCl$_3$, 125 MHz) of Dipp$_3$P at room temperature.
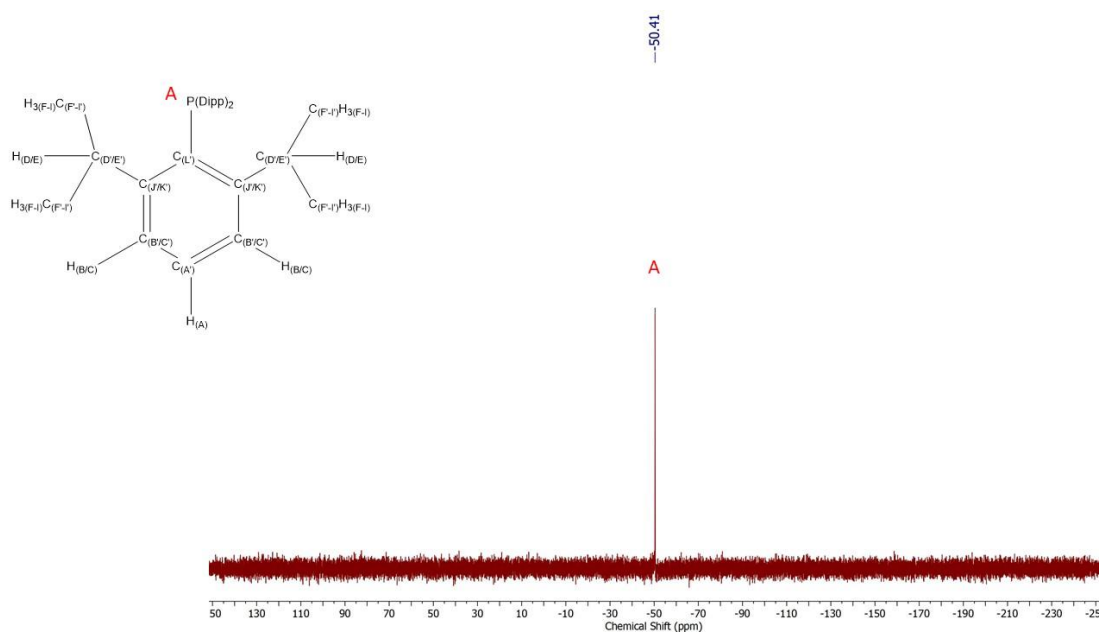
**Figure B.11.** $^{31}P\{^{1}H\}$ NMR spectrum (CDCl$_3$, 202 MHz) of Dipp$_3$P at room temperature.
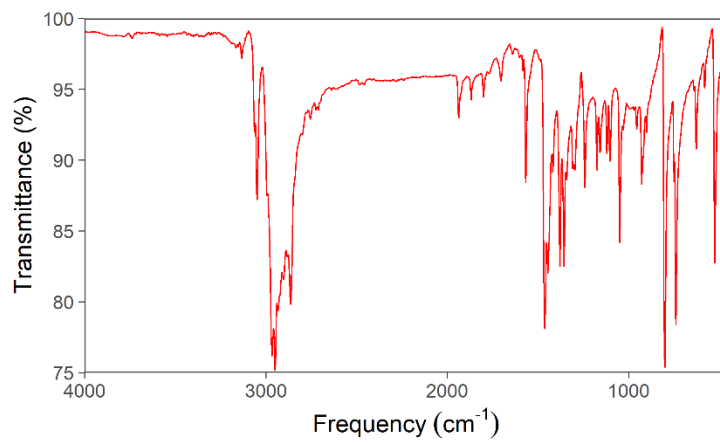


**Figure B.12.** Experimental IR spectrum (KBr pellet) of Dipp$_3$P.
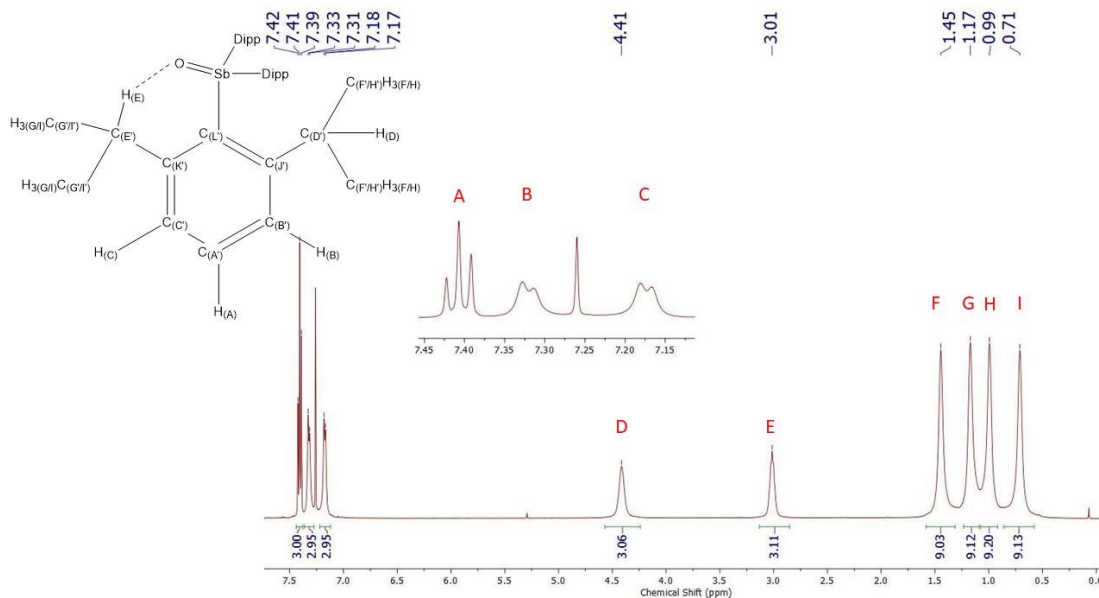
**Figure B.13.** $^1H$ NMR spectrum (CDCl$_3$, 500 MHz) of Dipp$_3$SbO at room temperature. Peaks are assigned based on HSQC and HMBC experiments (*vide infra*).
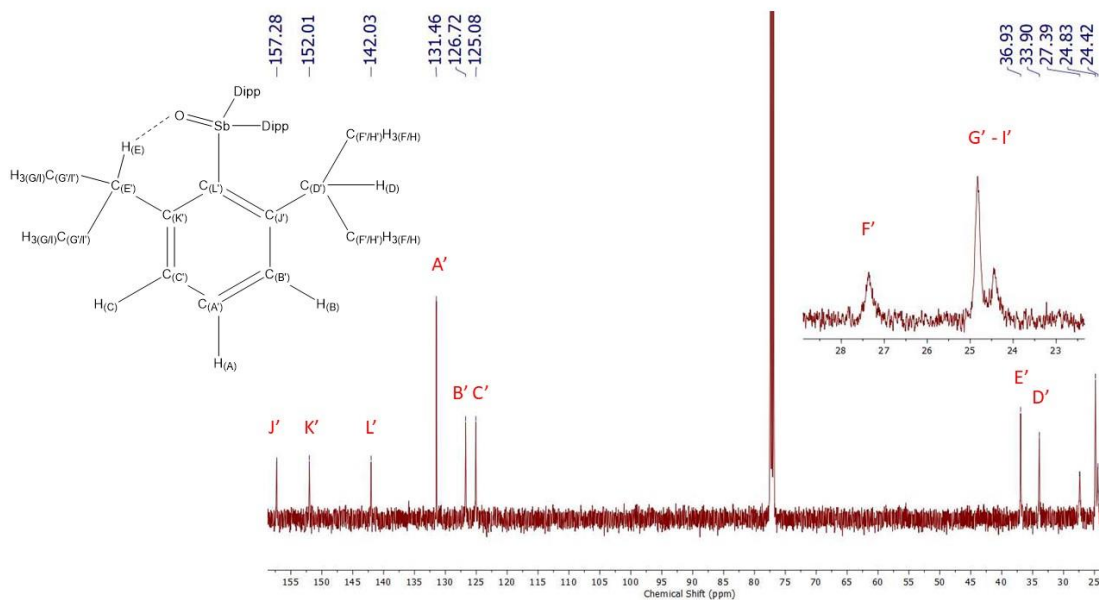


**Figure B.14.** $^{13}C\{^1H\}$ NMR spectrum (CDCl$_3$, 125 MHz) of Dipp$_3$SbO at room temperature. Peaks are assigned based on HSQC and HMBC experiments (*vide infra*).
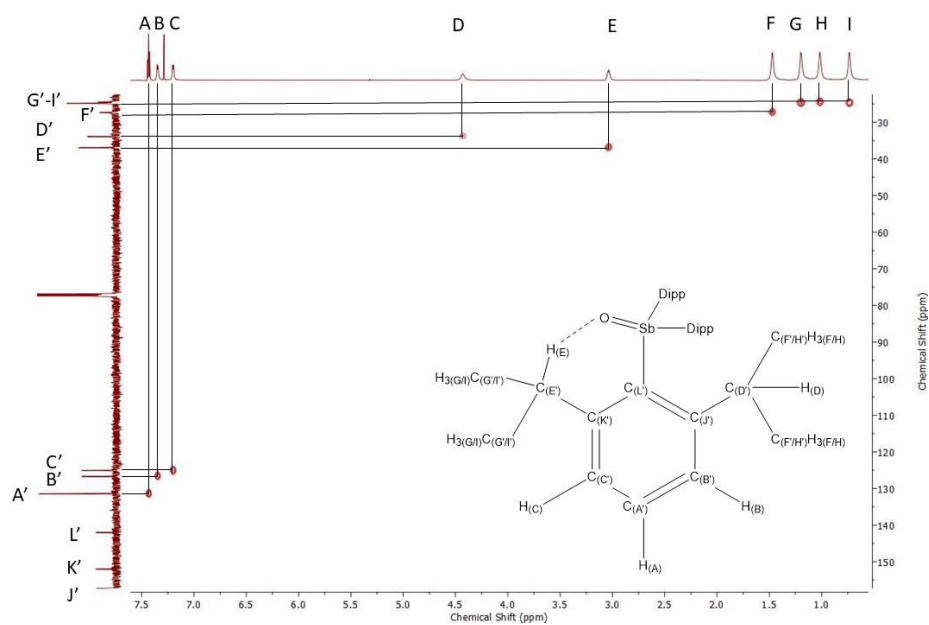
**Figure B.15.** $^1H$-$^{13}C$ HSQC (800 MHz, CDCl$_3$) spectrum of Dipp$_3$SbO at room temperature.
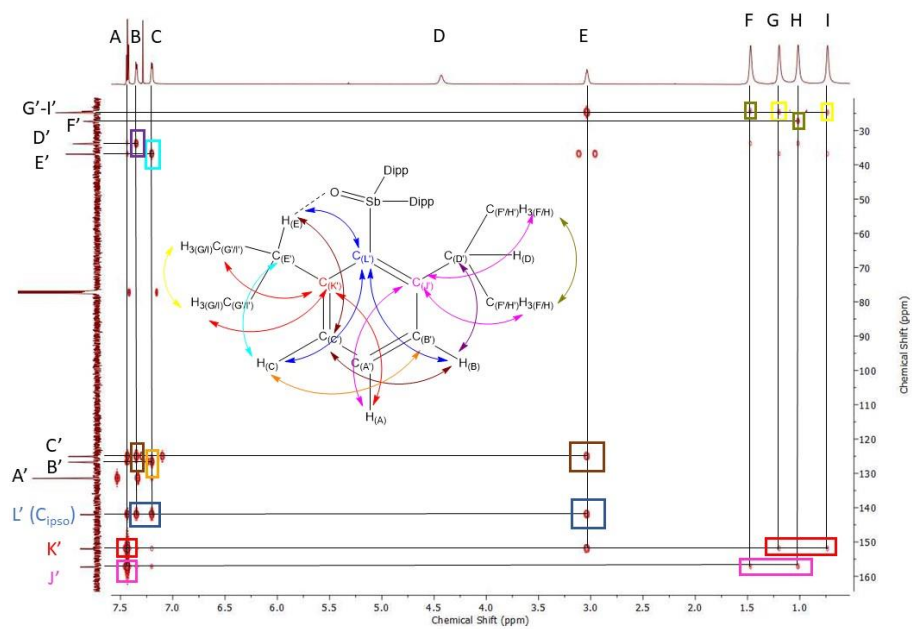


**Figure B.16.** $^1H$-$^{13}C$ HMBC (800 MHz, CDCl$_3$) spectrum of Dipp$_3$SbO at room temperature.
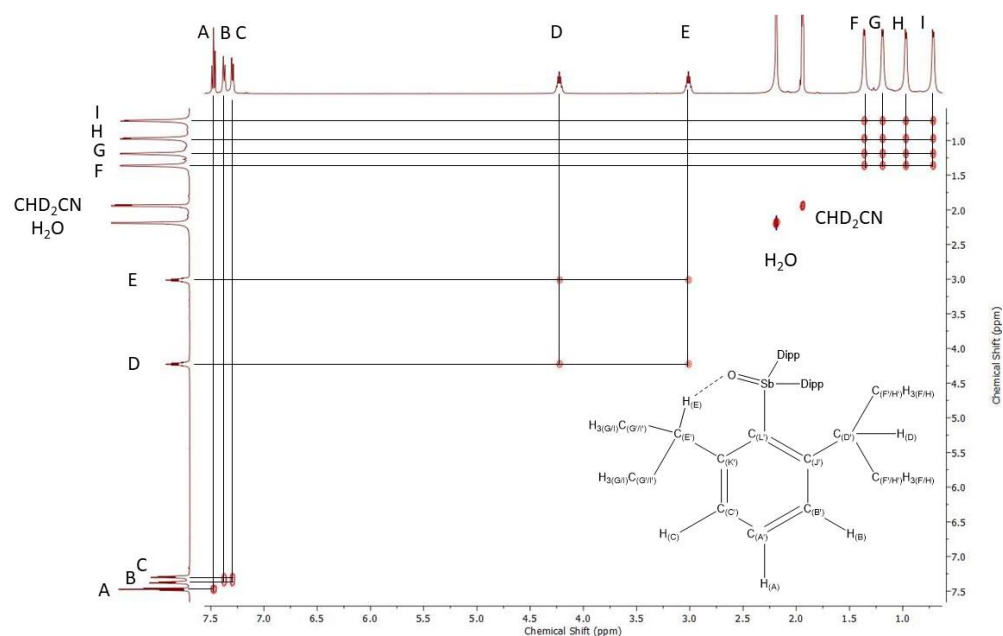
**Figure B.17.** $^1$H 2D EXSY (500 MHz, CD$_3$CN) of Dipp$_3$SbO at room temperature.
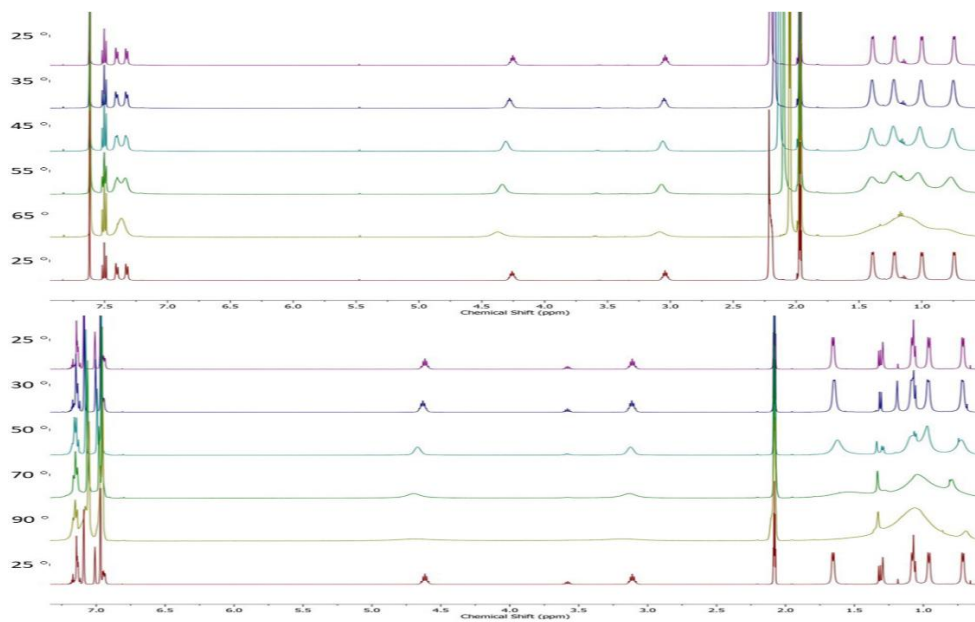


**Figure B.18**. (Top) Variable temperature $^1$H NMR (500 MHz, CD$_3$CN) spectra of Dipp$_3$SbO from 25 °C to 65 °C, followed by cooling back to 25 °C in 10 °C increments. (Bottom) Variable temperature $^1$H NMR (500 MHz, toluene-$d_8$) spectra of Dipp$_3$SbO from 30 °C to 90 °C in 20 °C increments followed by cooling back to 25 °C. Intensities are scaled arbitrarily for viewing.
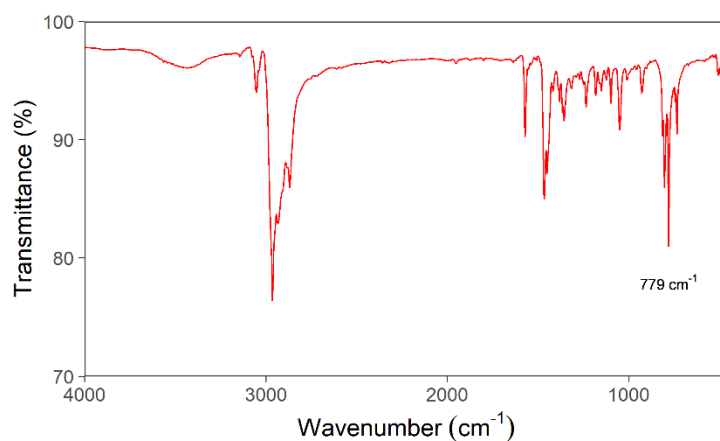
**Figure B.19.** Experimental IR spectrum (KBr pellet) of Dipp$_3$SbO ($v_{SbO}$ = 779 cm$^{-1}$).
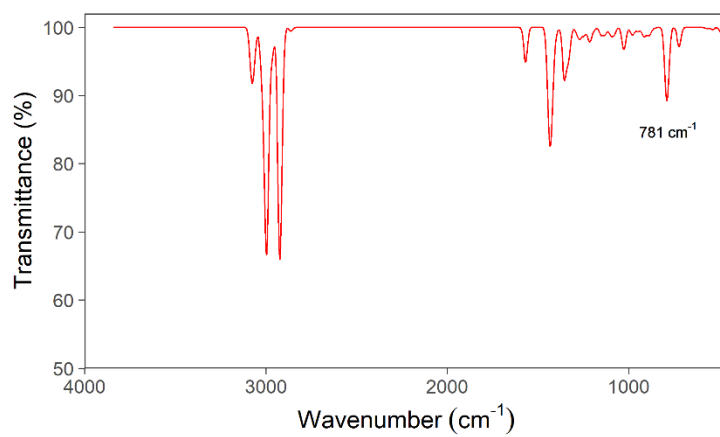


**Figure B.20.** Calculated IR spectrum (PBE0/def2-TZVPP) of Dipp$_3$SbO ($n_{SbO}$ = 781 cm$^{-1}$). The calculated IR vibrational frequencies were corrected with a 0.96 scalar factor.[1]
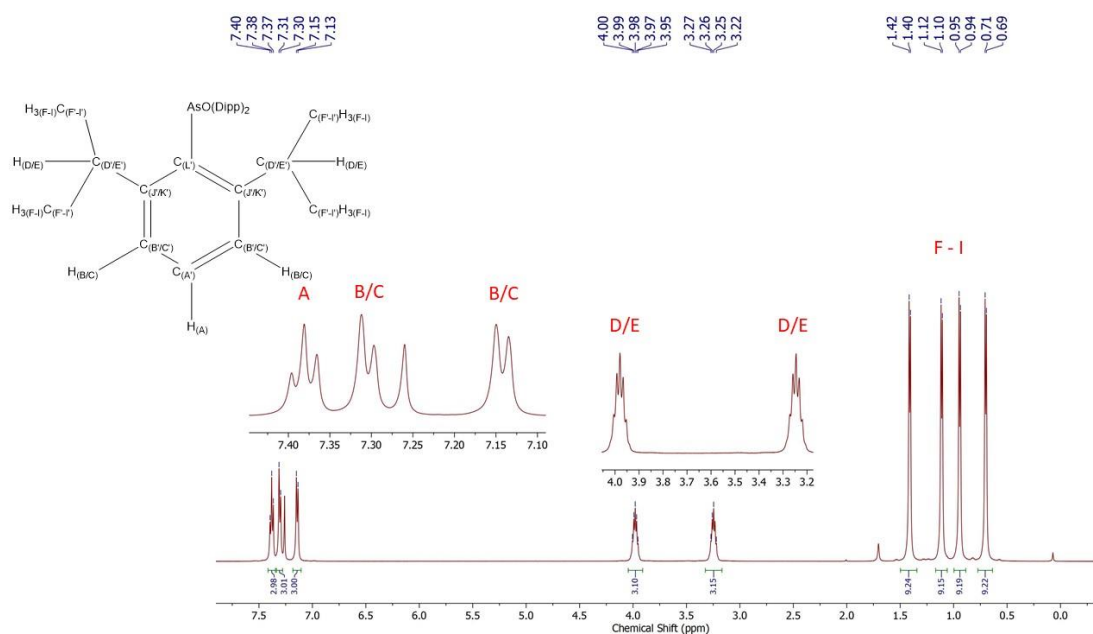
**Figure B.21.** $^1$H NMR spectrum (CDCl$_3$, 500 MHz) of Dipp$_3$AsO at room temperature.
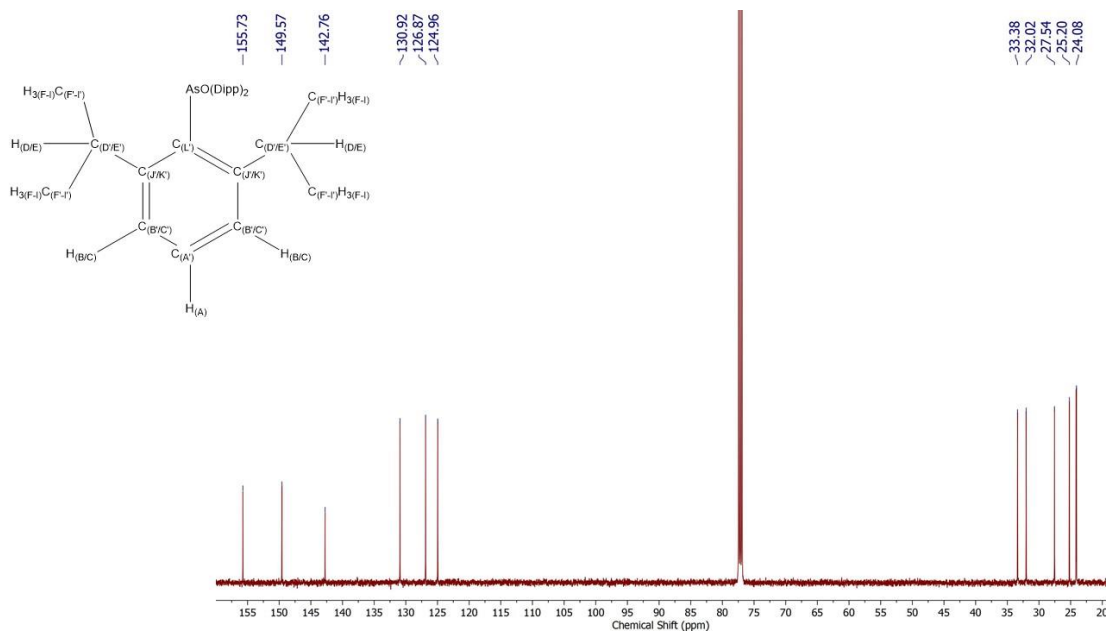


**Figure B.22.** $^{13}$C{$^1$H} NMR spectrum (CDCl$_3$, 125 MHz) of Dipp$_3$AsO at room temperature.
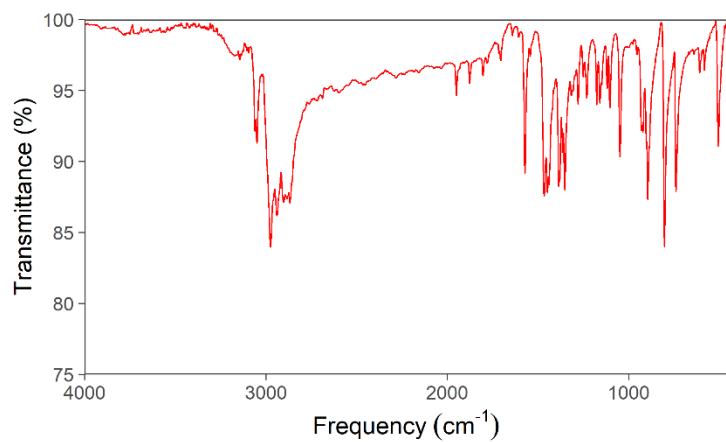
**Figure B.23.** Experimental IR spectrum (KBr pellet) of Dipp₃AsO.
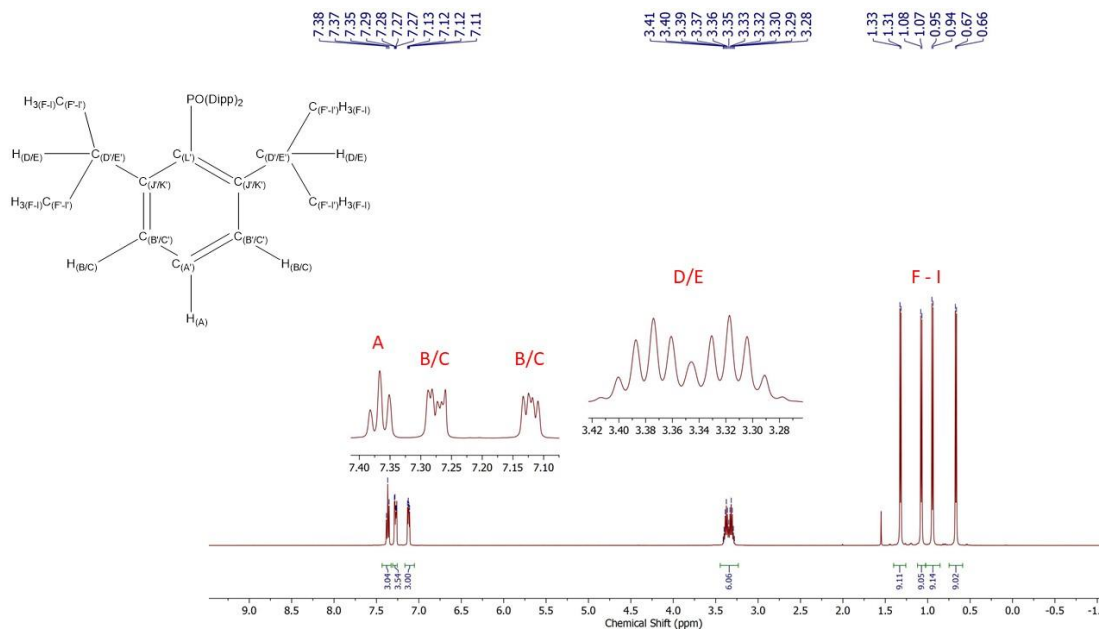


**Figure B.24.** ¹H NMR spectrum (CDCl₃, 500 MHz) of Dipp₃PO at room temperature.
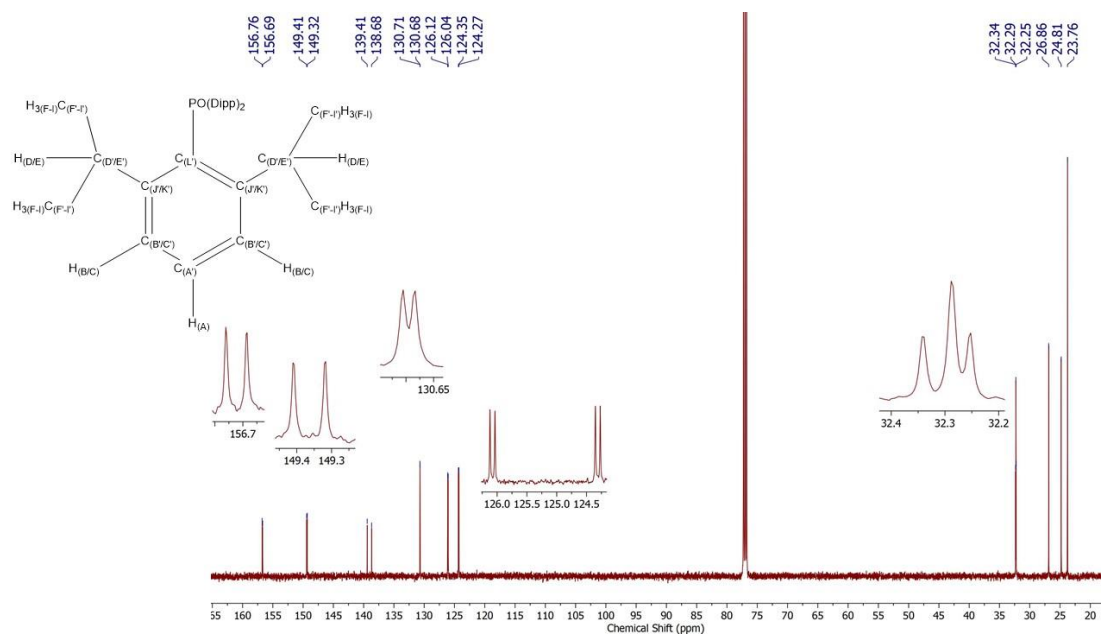
**Figure B.25.** $^{13}C\{^1H\}$ NMR spectrum (CDCl$_3$, 125 MHz) of Dipp$_3$PO at room temperature.
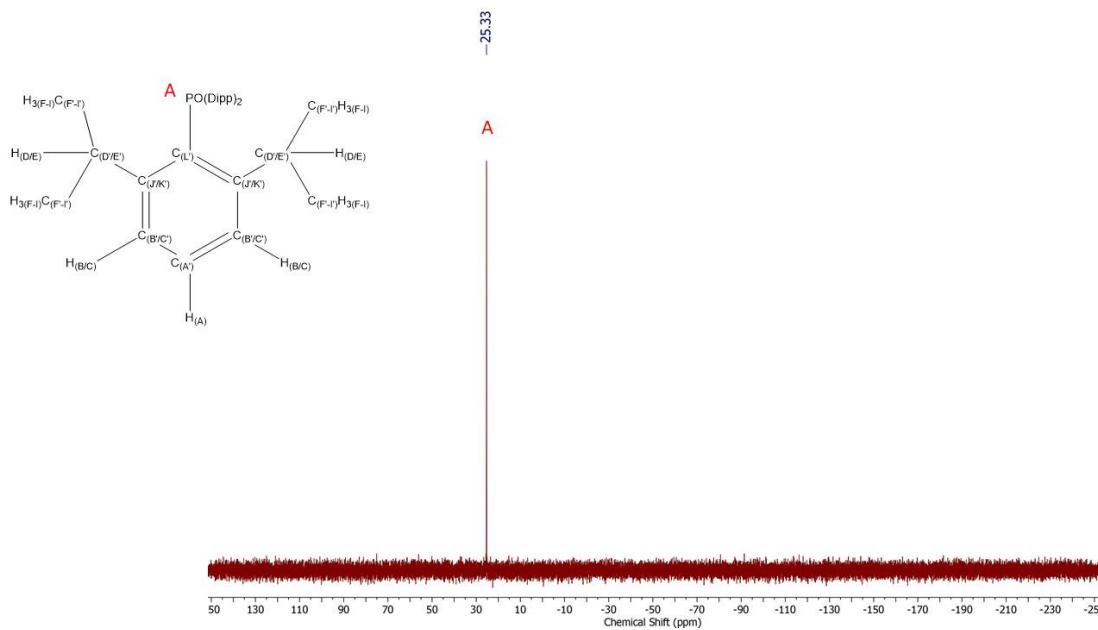


**Figure B.26.** $^{31}P\{^1H\}$ NMR spectrum (CDCl$_3$, 202 MHz) of Dipp$_3$PO at room temperature.
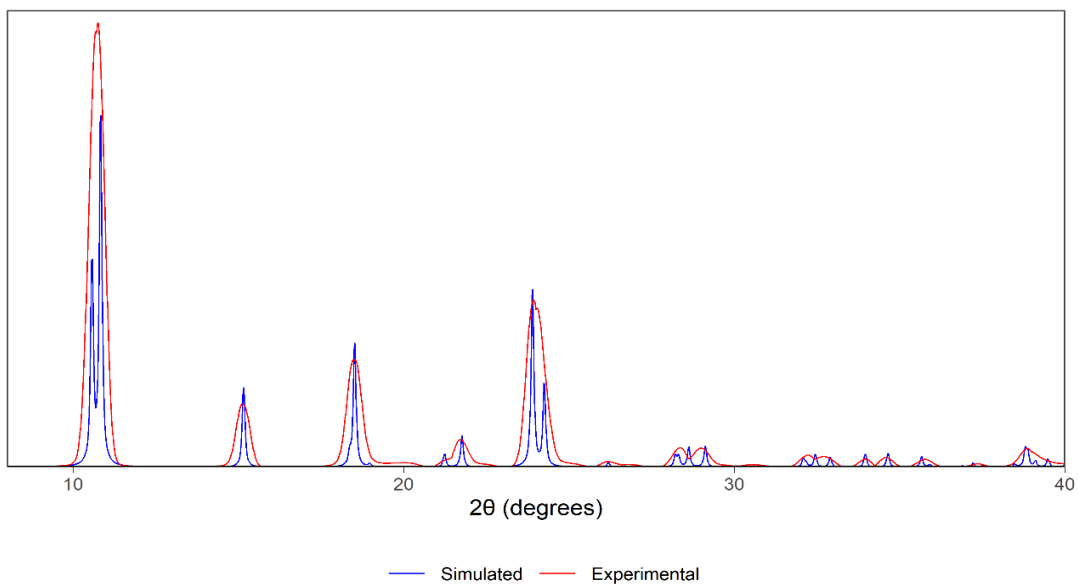
**Figure B.27.** Simulated and experimental PXRD diffractogram of Dipp$_3$PO.
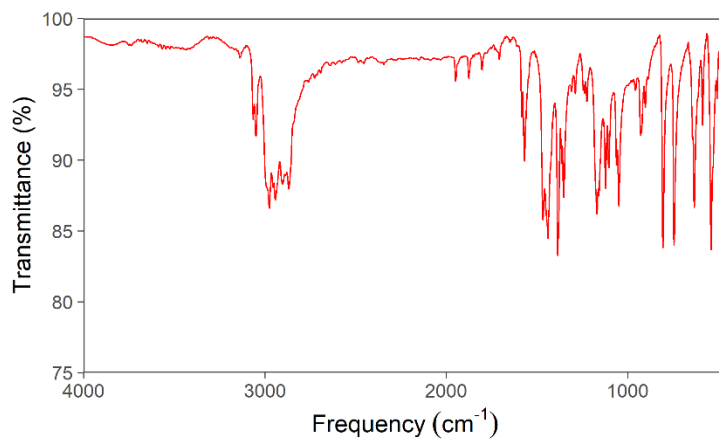


**Figure B.28.** Experimental IR spectrum (KBr pellet) of Dipp$_3$PO.
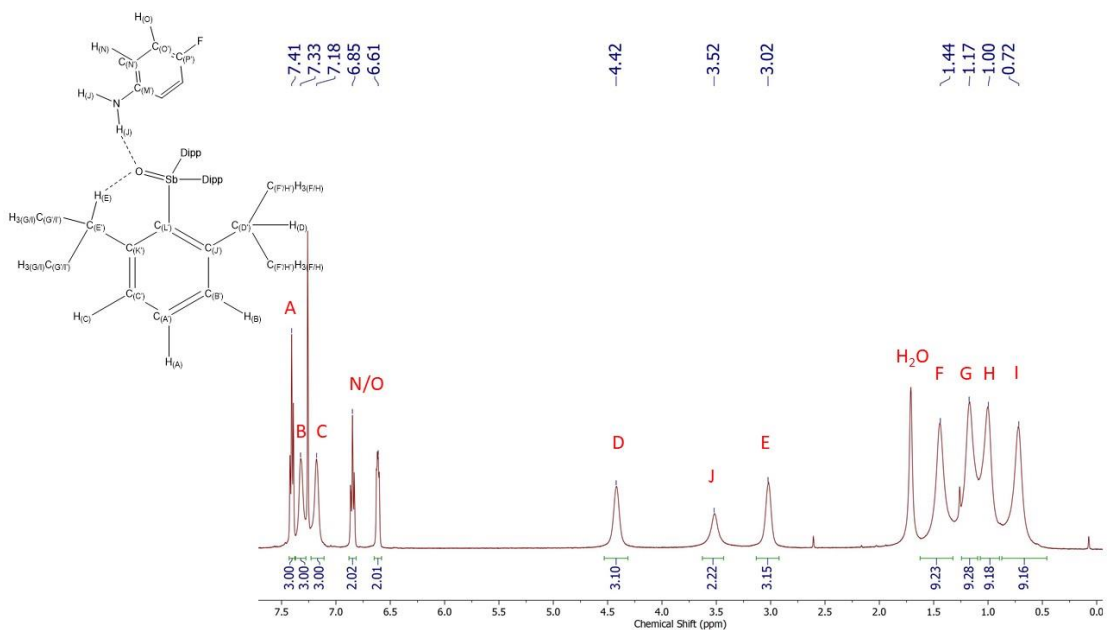
**Figure B.29.** $^1$H NMR spectrum (CDCl$_3$, 500 MHz) of Dipp$_3$SbO·H$_2$NPhF at room temperature.
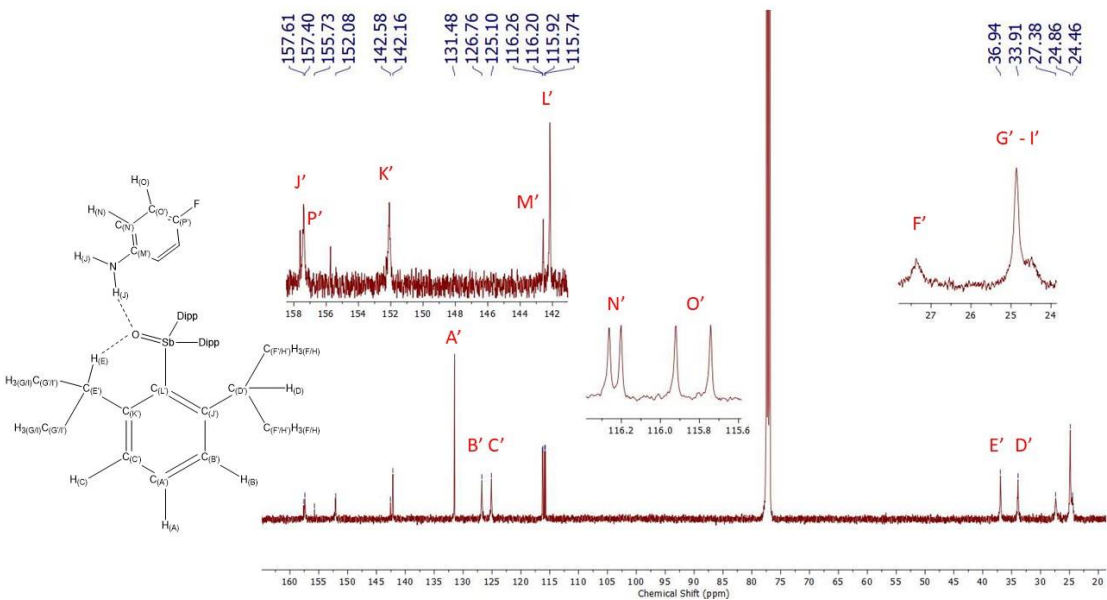


**Figure B.30.** $^{13}$C{$^1$H} NMR spectrum (CDCl$_3$, 125 MHz) of Dipp$_3$SbO·H$_2$NPhF at room temperature.
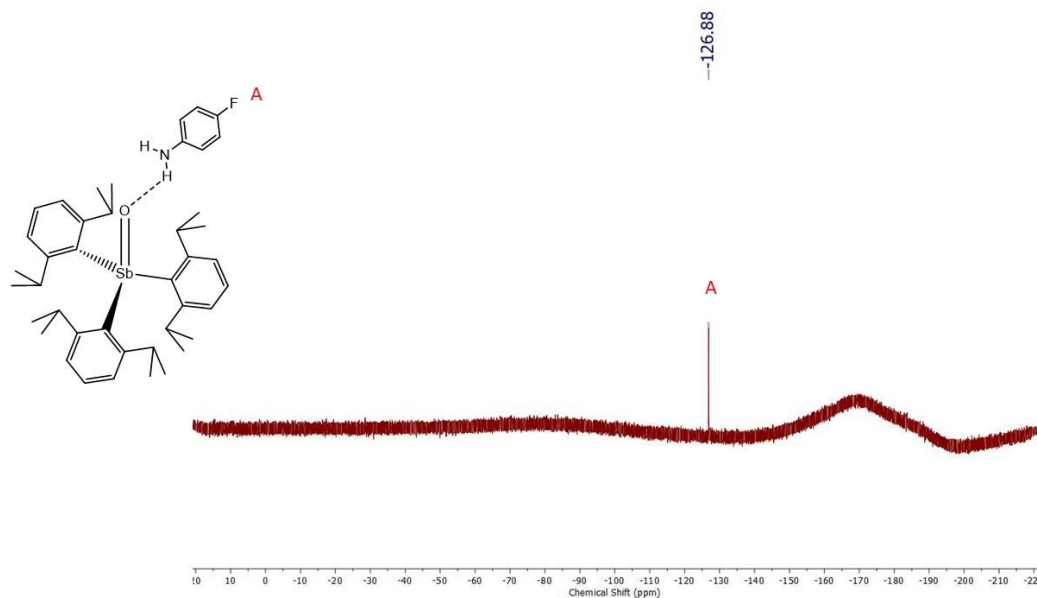
**Figure B.31.** $^{19}F$ NMR spectrum (CDCl$_3$, 470 MHz) of Dipp$_3$SbO·H$_2$NPhF at room temperature.
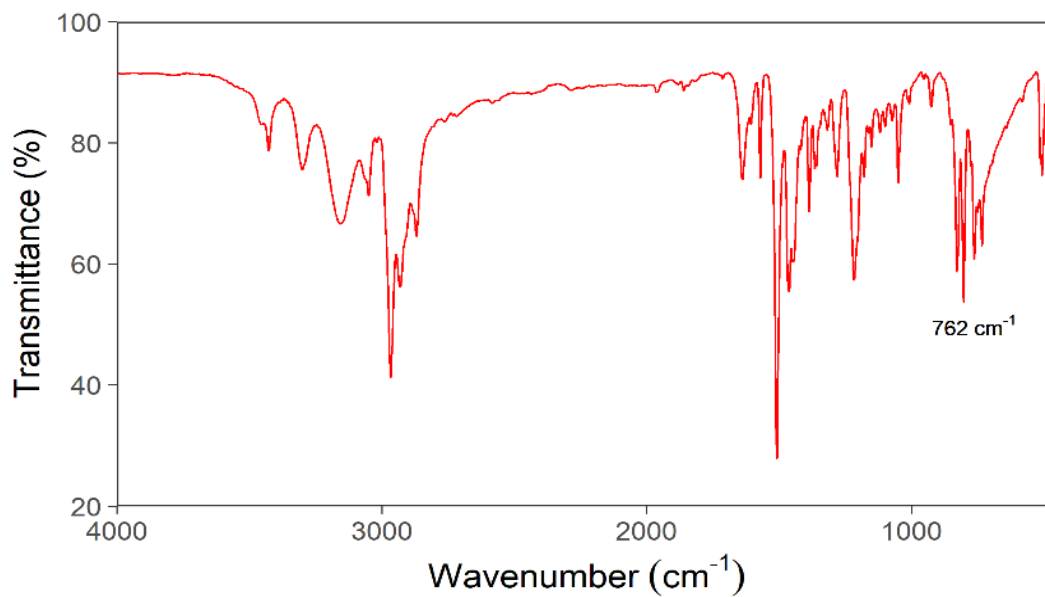


**Figure B.32.** Experimental IR spectrum (KBr pellet) of Dipp$_3$SbO·H$_2$NPhF ($\nu_{SbO}$ = 762 cm$^{-1}$).
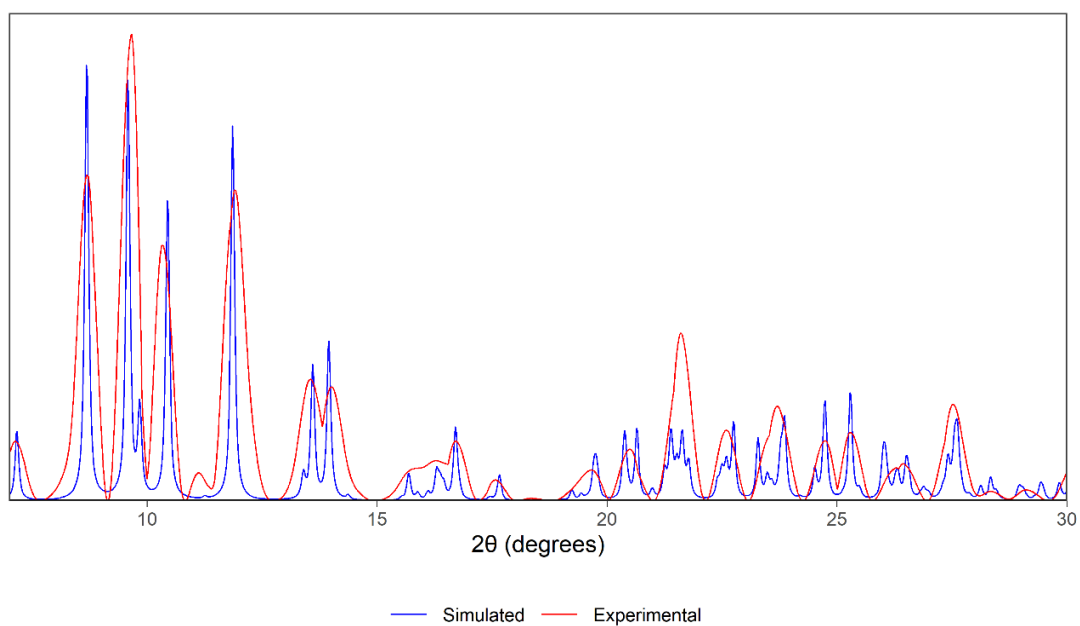
**Figure B.33.** Simulated and experimental PXRD diffractogram of Dipp₃SbO·H₂NPhF.
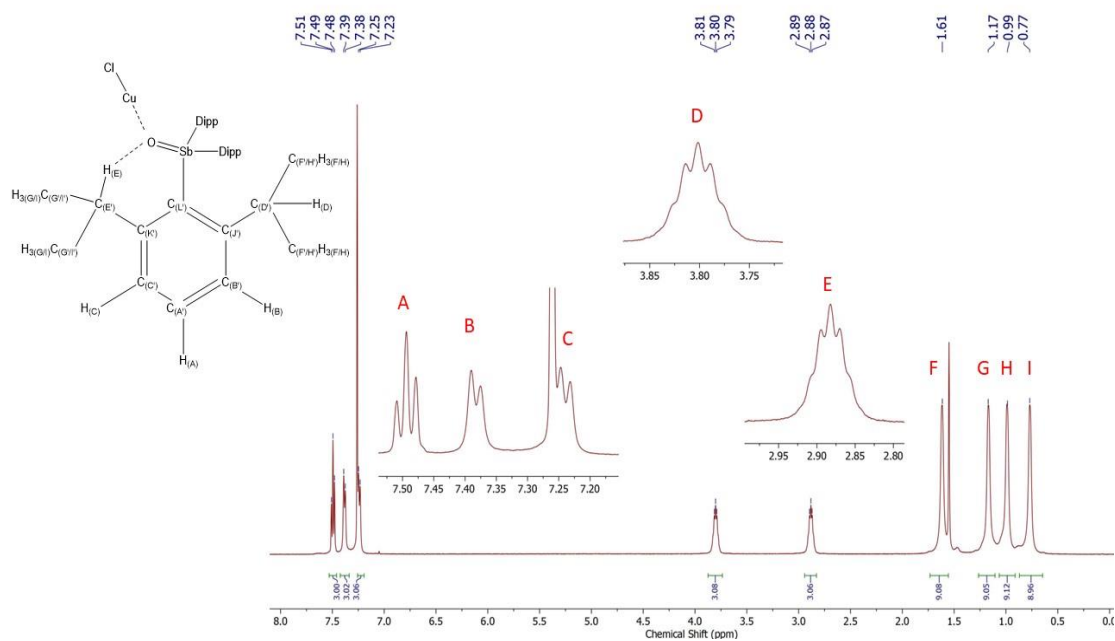


**Figure B.34.** ¹H NMR spectrum (CDCl₃, 500 MHz) of Dipp₃SbOCuCl·(CHCl₃)₂ at room temperature.
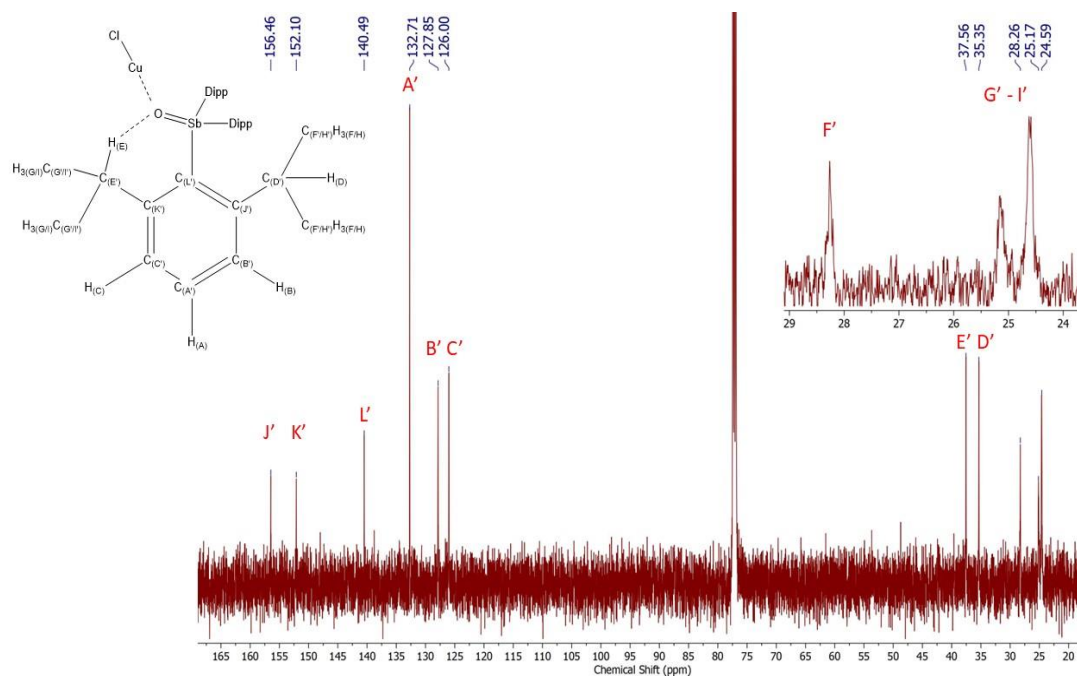
**Figure B.35.** $^{13}C\{^1H\}$ NMR spectrum (CDCl$_3$, 125 MHz) of Dipp$_3$SbOCuCl·(CHCl$_3$)$_2$ at room temperature.
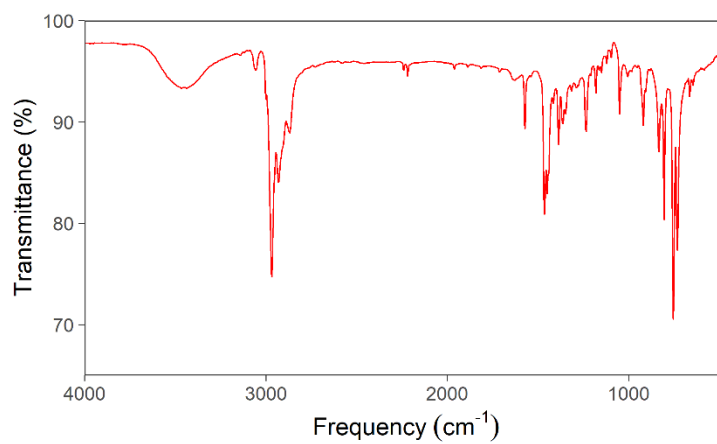


**Figure B.36.** Experimental IR spectrum (KBr pellet) of Dipp$_3$SbOCuCl·(CHCl$_3$)$_2$.
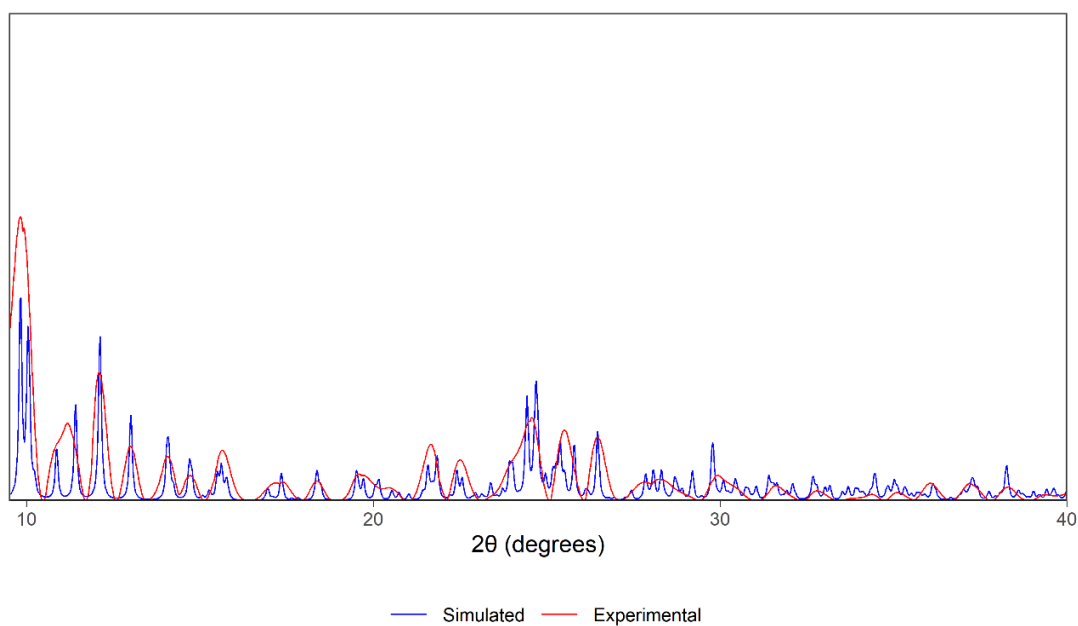
**Figure B.37.** Simulated and experimental PXRD diffractogram of Dipp$_3$SbOCuCl·(CHCl$_3$)$_2$.
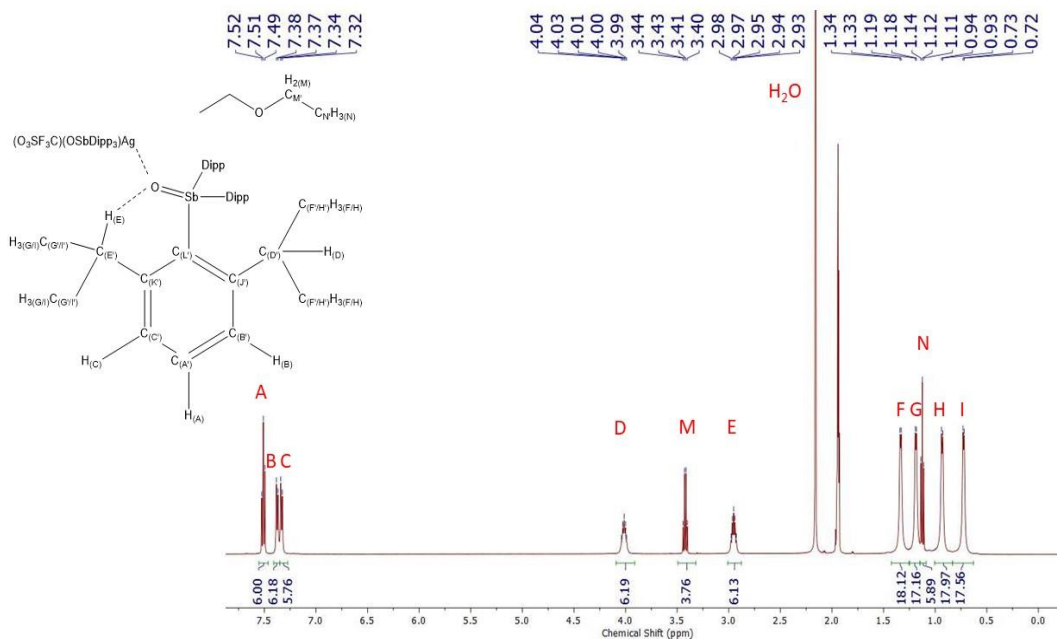


**Figure B.38.** $^1$H NMR spectrum (CD$_3$CN, 500 MHz) of [Ag(Dipp$_3$SbO)$_2$](CF$_3$SO$_3$)·OEt$_2$ at room temperature.
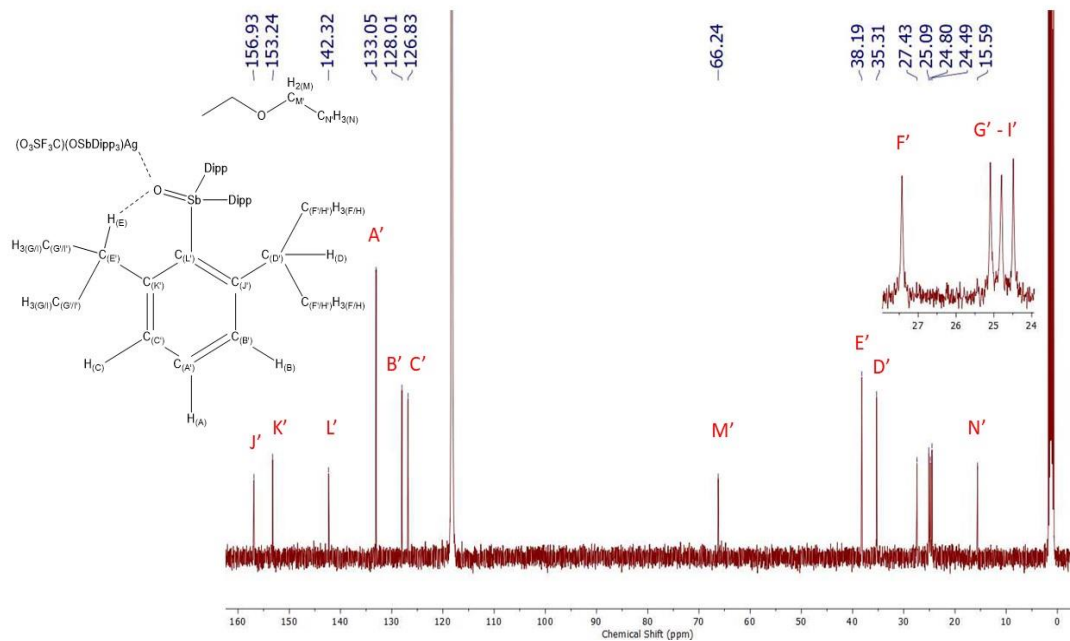
**Figure B.39.** $^{13}C\{^1H\}$ NMR spectrum (CD$_3$CN, 125 MHz) of [Ag(Dipp$_3$SbO)$_2$](CF$_3$SO$_3$)·OEt$_2$ at room temperature.
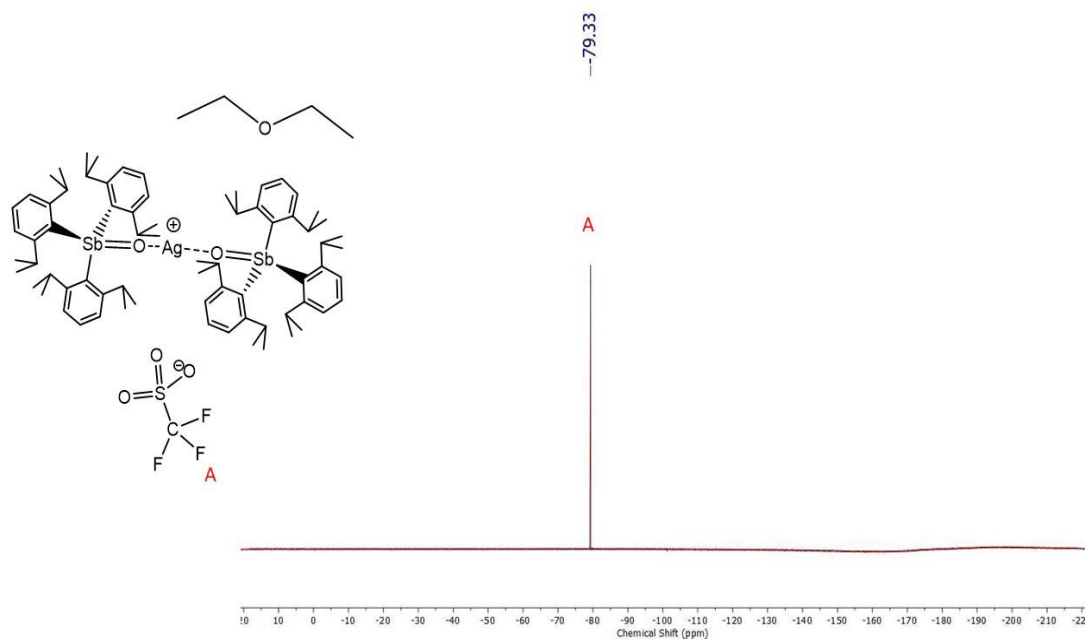


**Figure B.40.** $^{19}F$ NMR spectrum (CDCl$_3$, 470 MHz) of [Ag(Dipp$_3$SbO)$_2$](CF$_3$SO$_3$)·OEt$_2$ at room temperature.

257
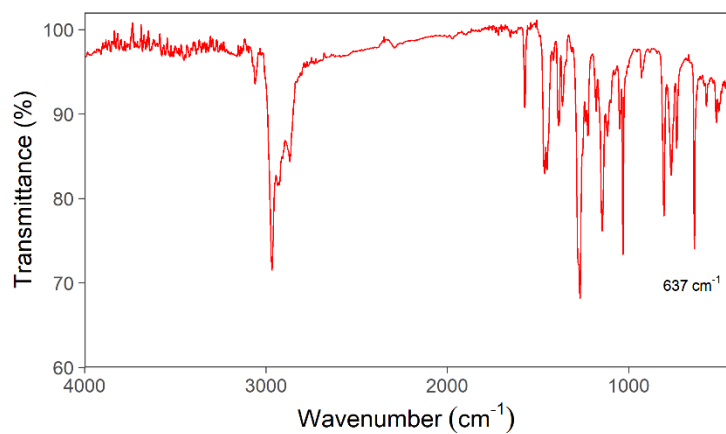
**Figure B.41.** Experimental IR spectrum (KBr pellets) of [Ag(Dipp$_3$SbO)$_2$](CF$_3$SO$_3$)·OEt$_2$ ($\nu_{SbO}$ = 637 cm$^{-1}$).
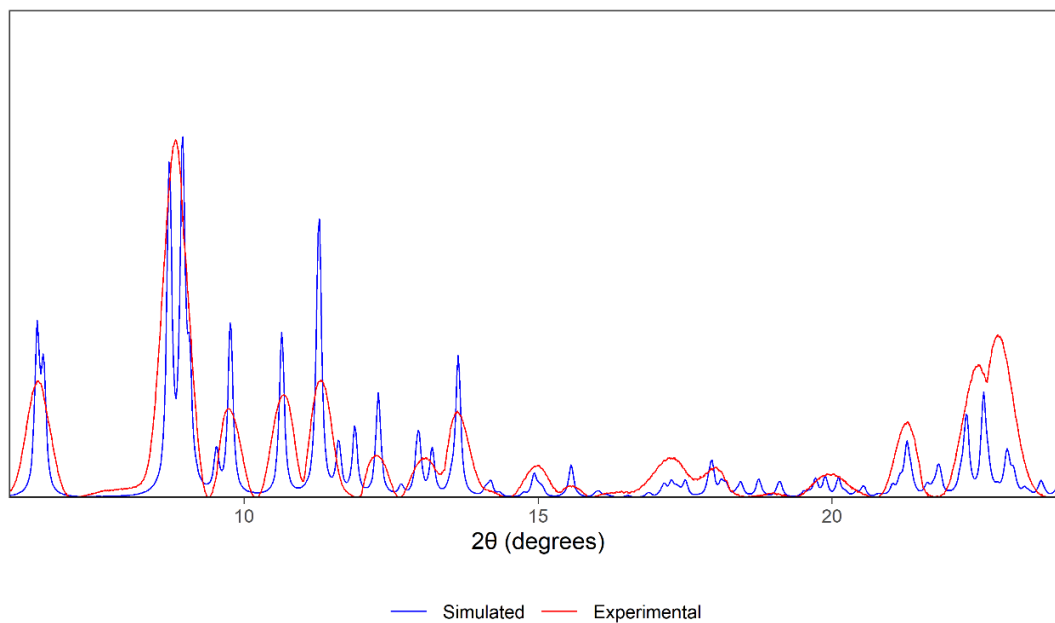


**Figure B.42.** Simulated and experimental PXRD diffractogram of [Ag(Dipp$_3$SbO)$_2$](CF$_3$SO$_3$)·OEt$_2$.
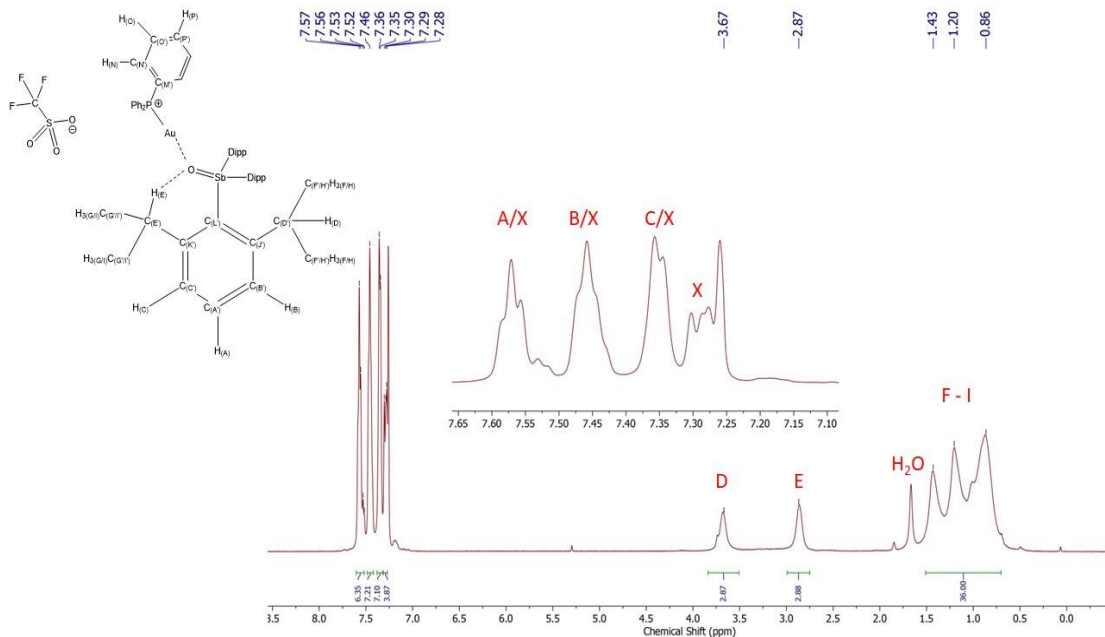
**Figure B.43.** $^1$H NMR spectrum (CDCl$_3$, 500 MHz) of [Dipp$_3$SbOAuPPh$_3$][CF$_3$SO$_3$] at room temperature. Peaks that correspond to [Dipp$_3$SbOAuPPh$_3$][CF$_3$SO$_3$] but that cannot be unambiguously assigned are labelled with an "X".
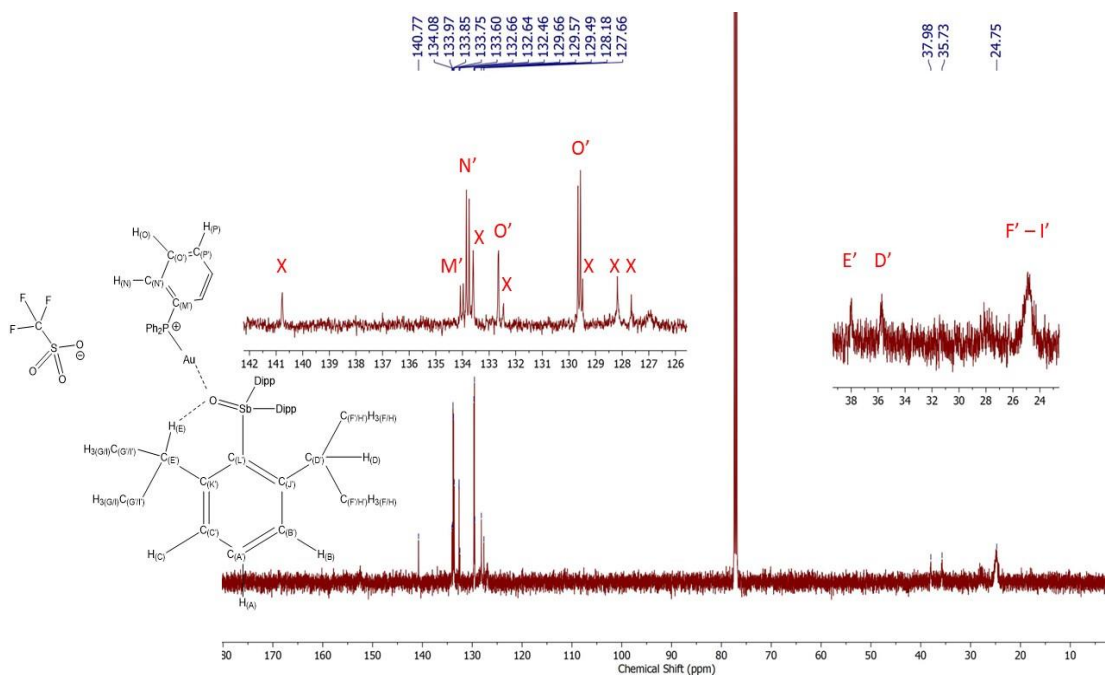


**Figure B.44.** $^{13}$C{$^1$H} NMR spectrum (CDCl$_3$, 125 MHz) of [Dipp$_3$SbOAuPPh$_3$][CF$_3$SO$_3$] at room temperature. Peaks that correspond to [Dipp$_3$SbOAuPPh$_3$][CF$_3$SO$_3$] but that cannot be unambiguously assigned are labelled with an "X".
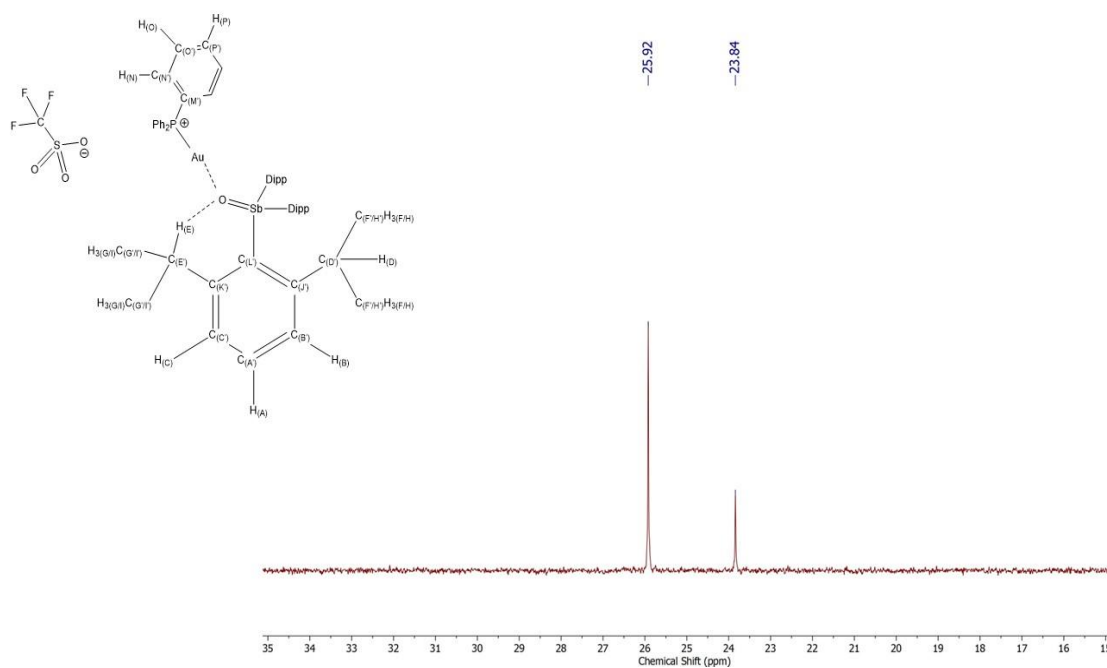
**Figure B.45.** $^{31}P\{^1H\}$ NMR spectrum (CDCl$_3$, 202 MHz) of [Dipp$_3$SbOAuPPh$_3$][CF$_3$SO$_3$] at room temperature.
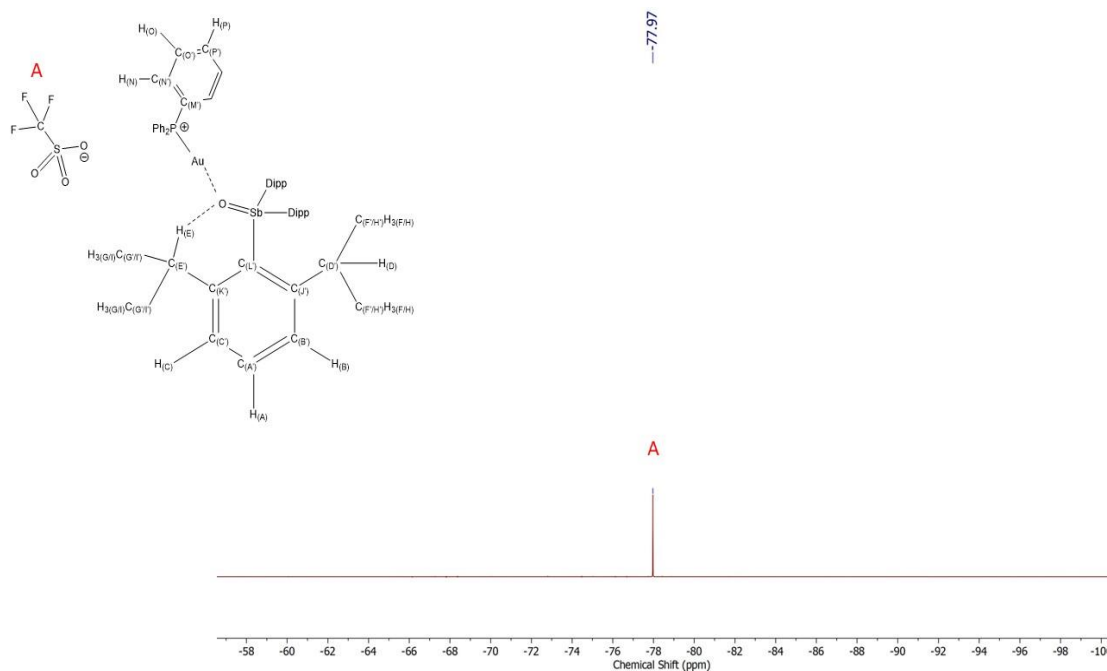


**Figure B.46.** $^{19}F$ NMR spectrum (CDCl$_3$, 470 MHz) of [Dipp$_3$SbOAuPPh$_3$][CF$_3$SO$_3$] at room temperature.
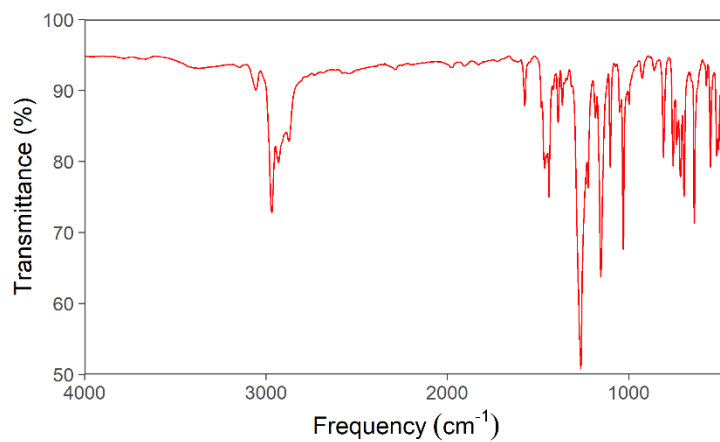
**Figure B.47.** Experimental IR spectrum (KBr pellet) of [Dipp$_3$SbOAuPPh$_3$][CF$_3$SO$_3$].
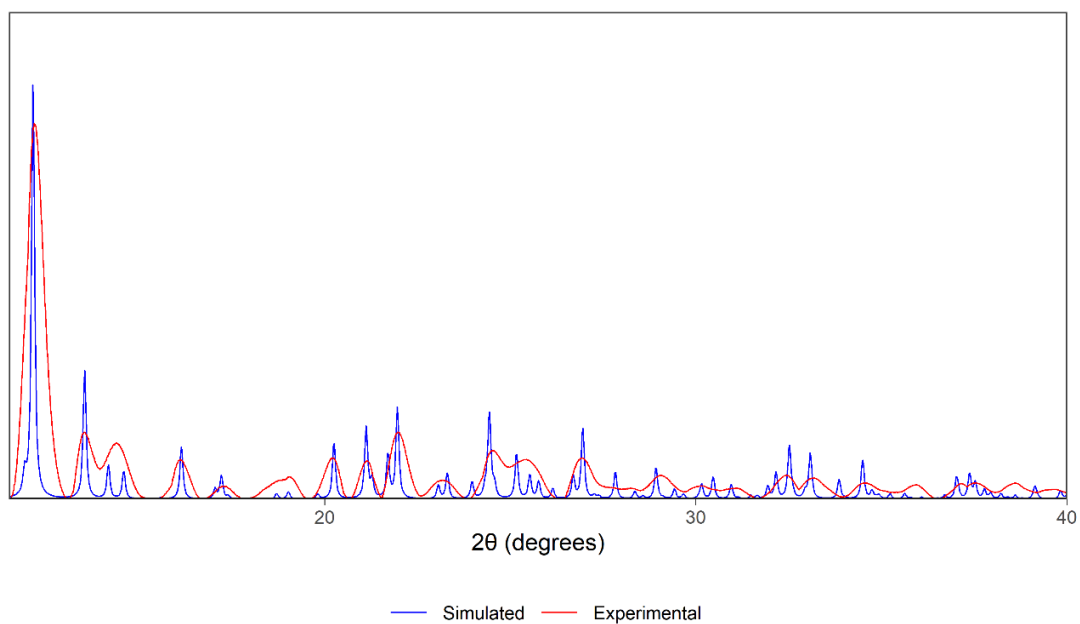


**Figure B.48.** Simulated and experimental PXRD diffractogram of [Dipp$_3$SbOAuPPh$_3$][CF$_3$SO$_3$]. The simulated diffractogram was simulated from the linear polymorph.
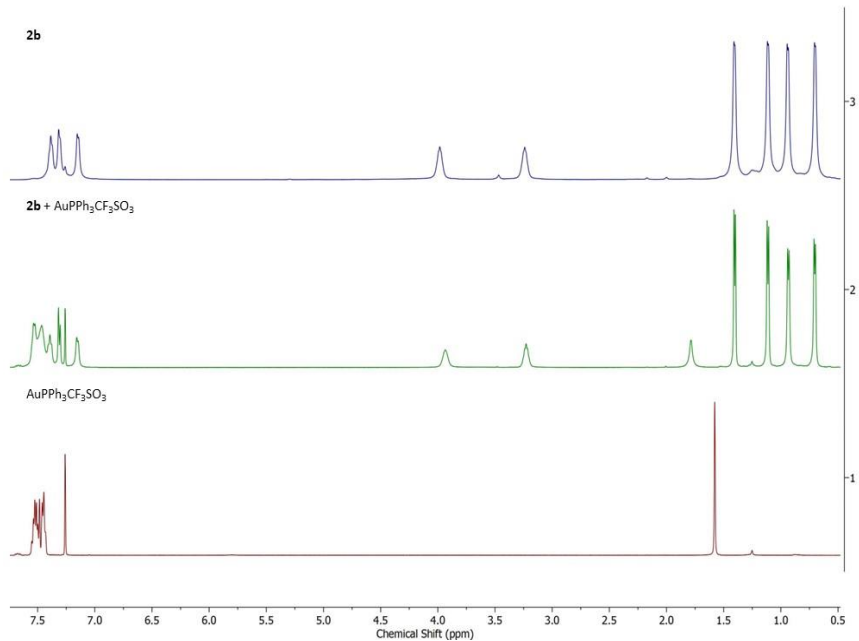
**Figure B.49.** $^1$H NMR spectra (CDCl$_3$, 500 MHz) of Dipp$_3$AsO (*top*), a 1:1 mixture of Dipp$_3$AsO and AuPPh$_3$CF$_3$SO$_3$ (*middle*), and AuPPh$_3$CF$_3$SO$_3$ (*bottom*) at room temperature.
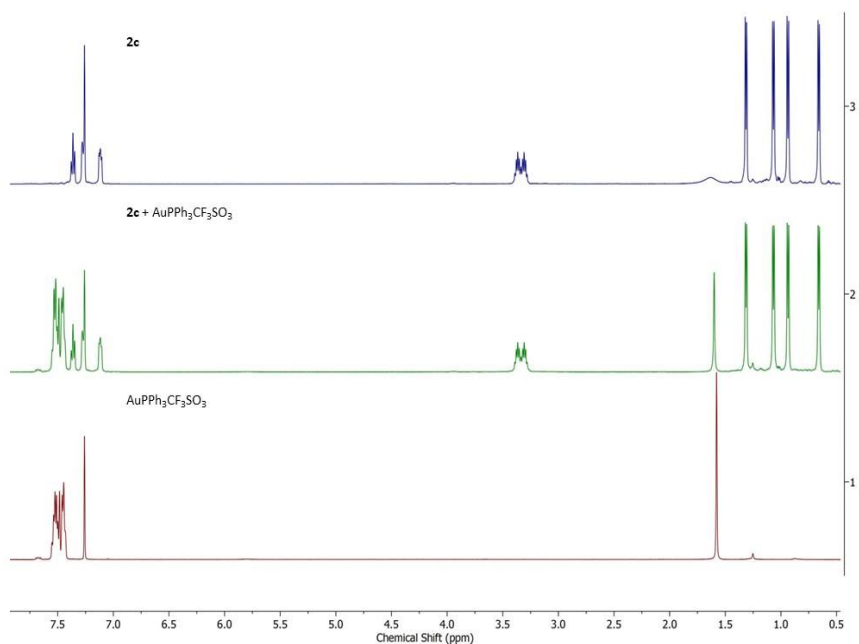


**Figure B.50.** $^1$H NMR spectra (CDCl$_3$, 500 MHz) of Dipp$_3$PO (*top*), a 1:1 mixture of Dipp$_3$PO and AuPPh$_3$CF$_3$SO$_3$ (*middle*), and AuPPh$_3$CF$_3$SO$_3$ (*bottom*) at room temperature.
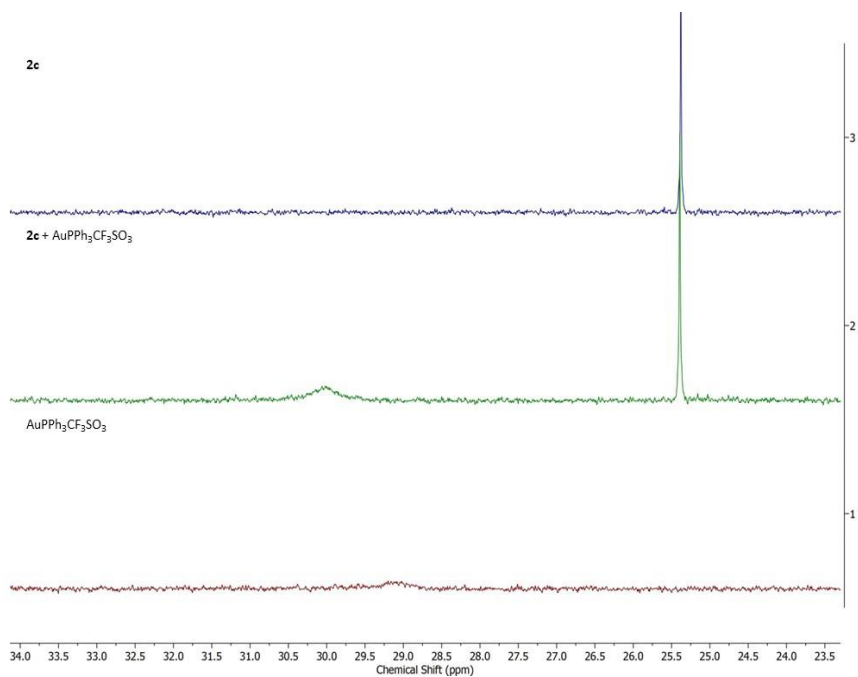
**Figure B.51.** $^{31}P\{^{1}H\}$ NMR spectrum (CDCl$_3$, 202 MHz) of Dipp$_3$PO (*top*), a 1:1 mixture of Dipp$_3$PO and AuPPh$_3$CF$_3$SO$_3$ (*middle*), and AuPPh$_3$CF$_3$SO$_3$ (*bottom*) at room temperature.
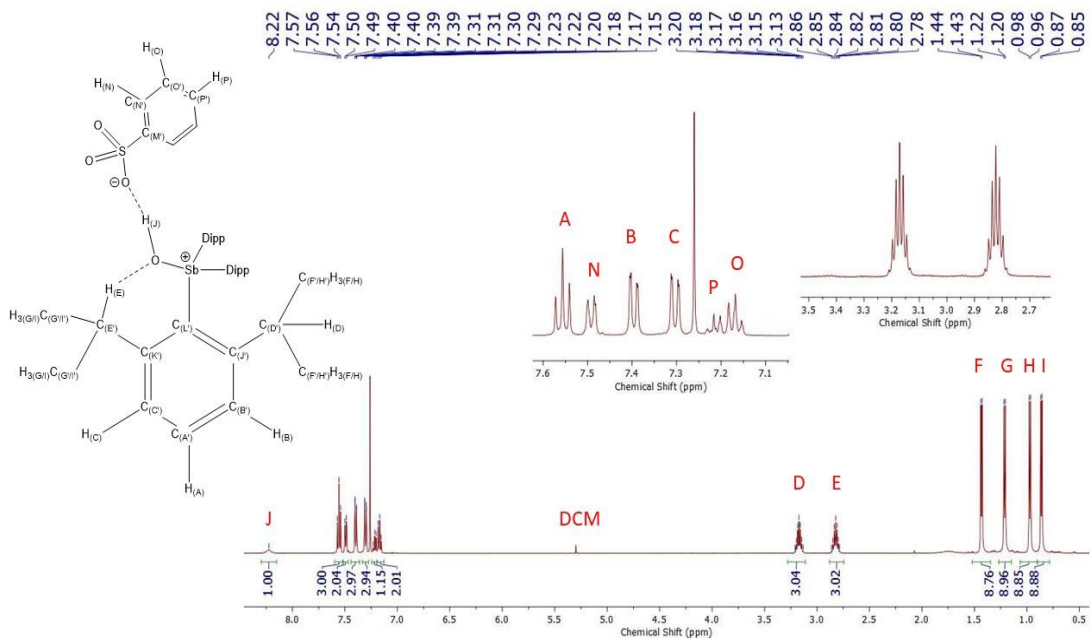


**Figure B.52.** $^1H$ NMR spectrum (CDCl$_3$, 500 MHz) of [Dipp$_3$SbOH][O$_3$SPh] at room temperature.
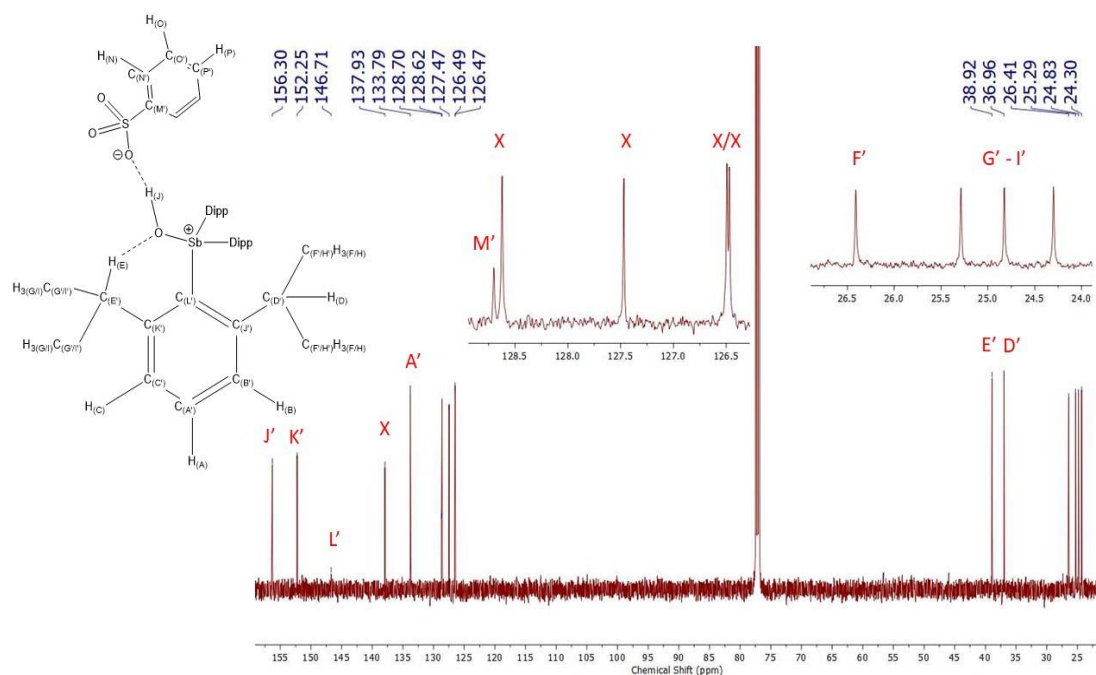
**Figure B.53.** $^{13}C\{^1H\}$ NMR spectrum (CDCl$_3$, 125 MHz) of [Dipp$_3$SbOH][O$_3$SPh] at room temperature. Peaks that correspond to [Dipp$_3$SbOH][O$_3$SPh] but that cannot be unambiguously assigned are labelled with an "X".
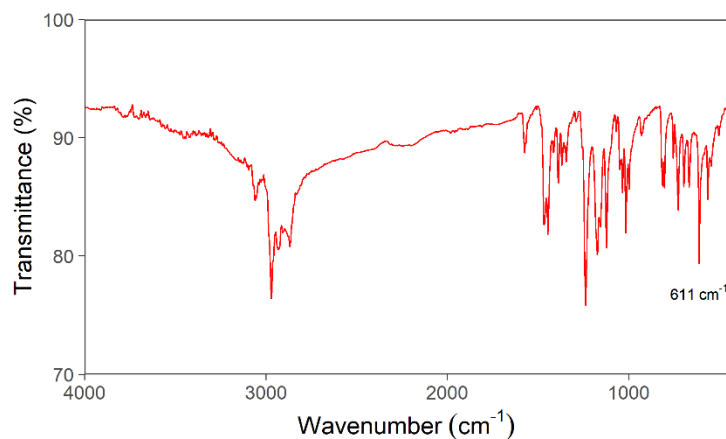


**Figure B.54.** Experimental IR spectrum (KBr pellet) of [Dipp$_3$SbOH][O$_3$SPh] ($\nu_{SbO}$ = 611 cm$^{-1}$).
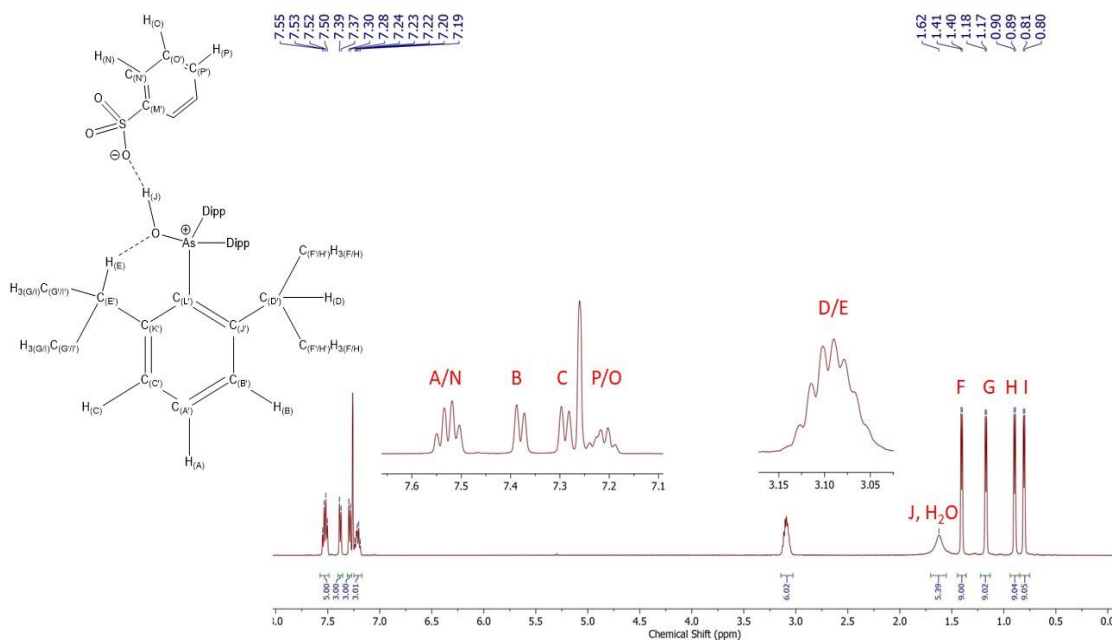
**Figure B.55.** $^1$H NMR spectrum (CDCl$_3$, 500 MHz) of [Dipp$_3$AsOH][O$_3$SPh] at room temperature.
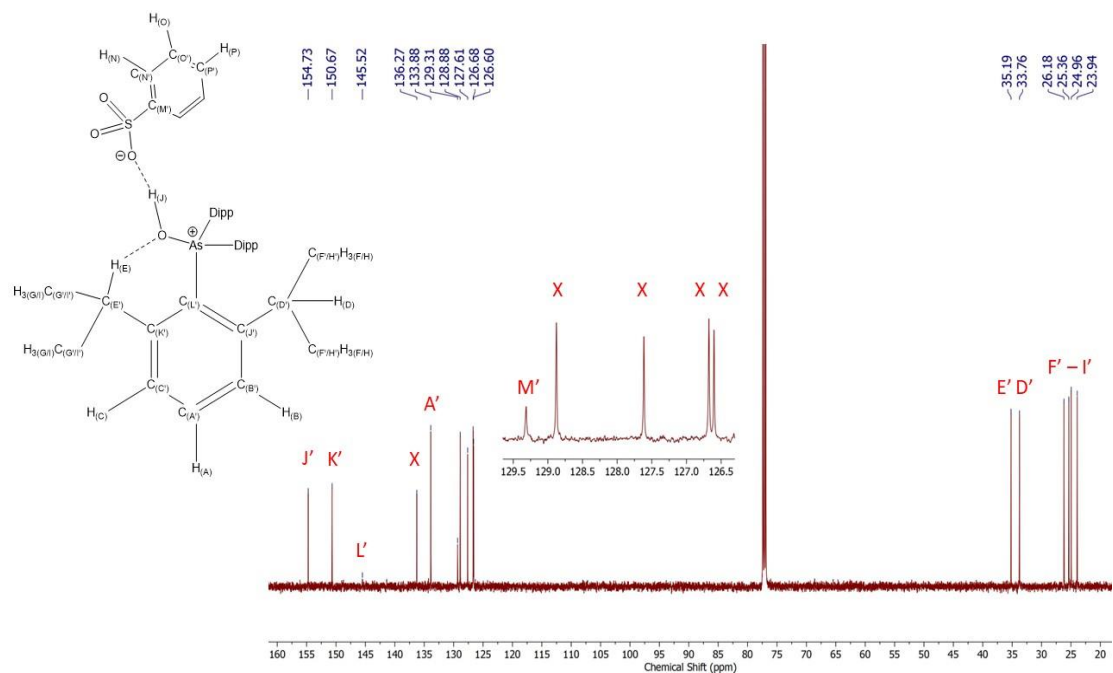


**Figure B.56.** $^{13}$C{$^1$H} NMR spectrum (CDCl$_3$, 125 MHz) of [Dipp$_3$AsOH][O$_3$SPh] at room temperature. Peaks that correspond to [Dipp$_3$AsOH][O$_3$SPh] but that cannot be unambiguously assigned are labelled with an "X".
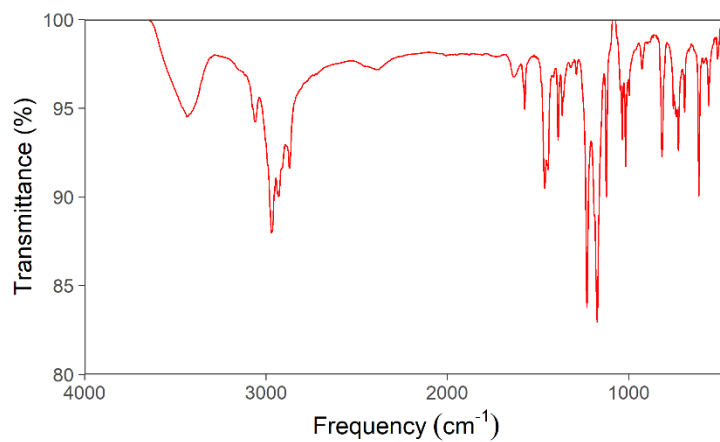
**Figure B.57.** Experimental IR spectrum (KBr pellet) of [Dipp₃AsOH][O₃SPh].



Simulated — Experimental —
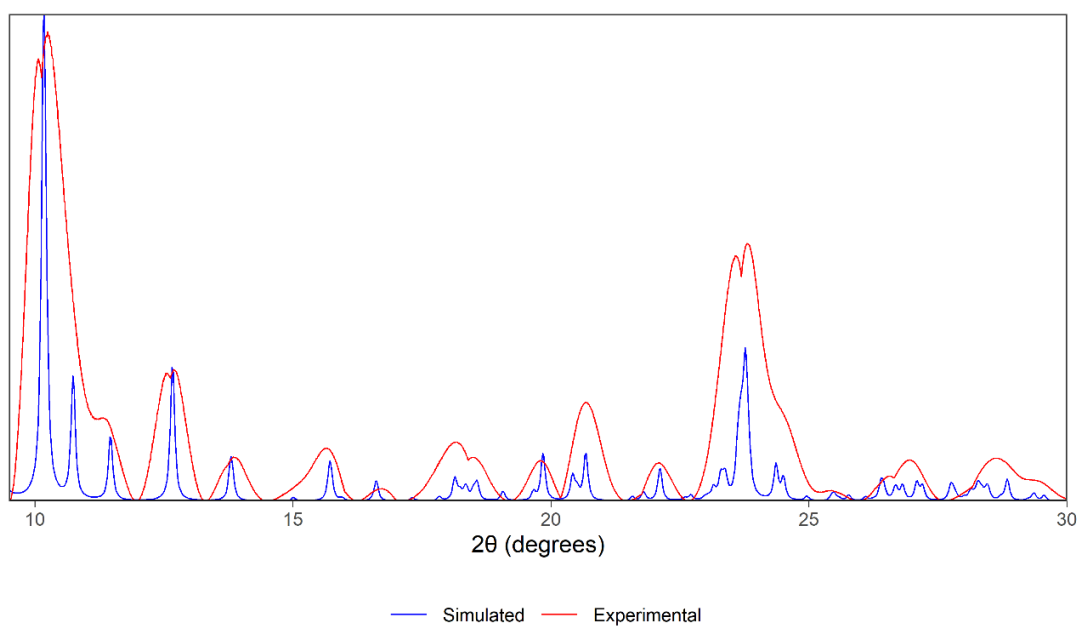
**Figure B.58.** Simulated and experimental PXRD diffractogram of [Dipp₃AsOH][O₃SPh].
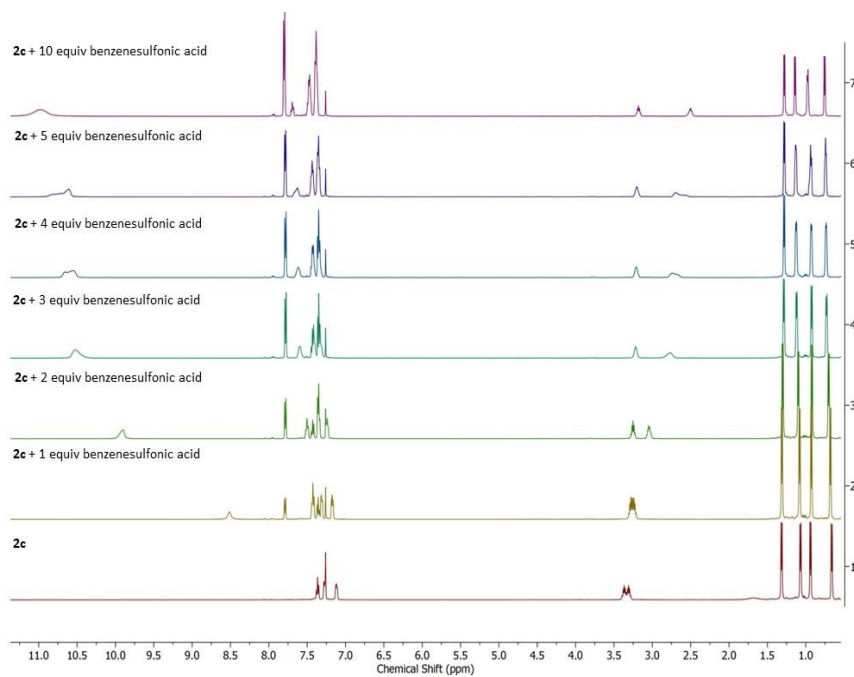
**Figure B.59.** Stacked plots of $^1$H NMR spectra (CDCl$_3$, 500 MHz) of Dipp$_3$PO with 0, 1, 2, 3, 4, 5, and 10 equivalents of benzenesulfonic acid (*bottom* to *top*).
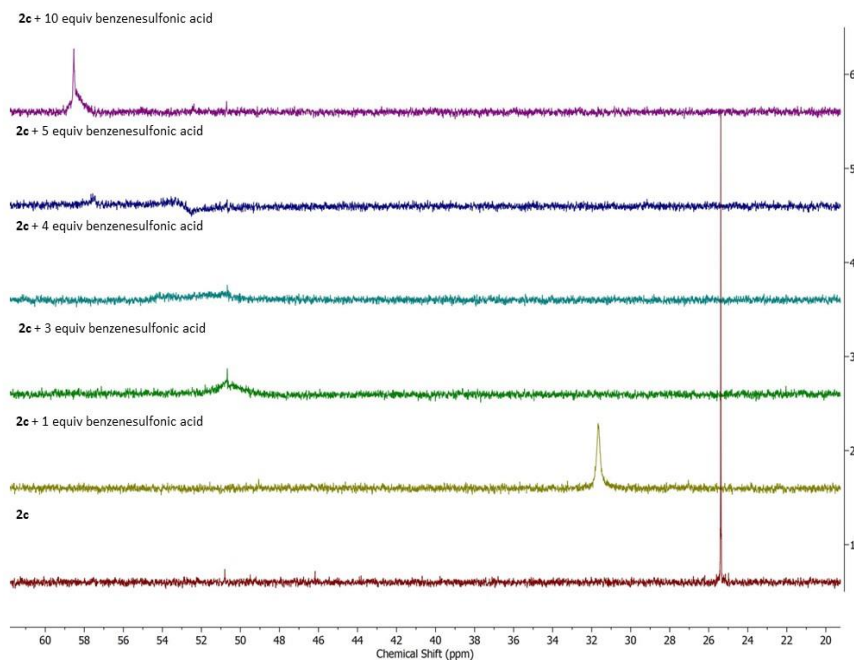


**Figure B.60.** Stacked plots of $^{31}$P{$^1$H} NMR spectra (CDCl$_3$, 202 MHz) of Dipp$_3$PO with 0, 1, 3, 4, 5, and 10 equivalents of benzenesulfonic acid (*bottom* to *top*).

267
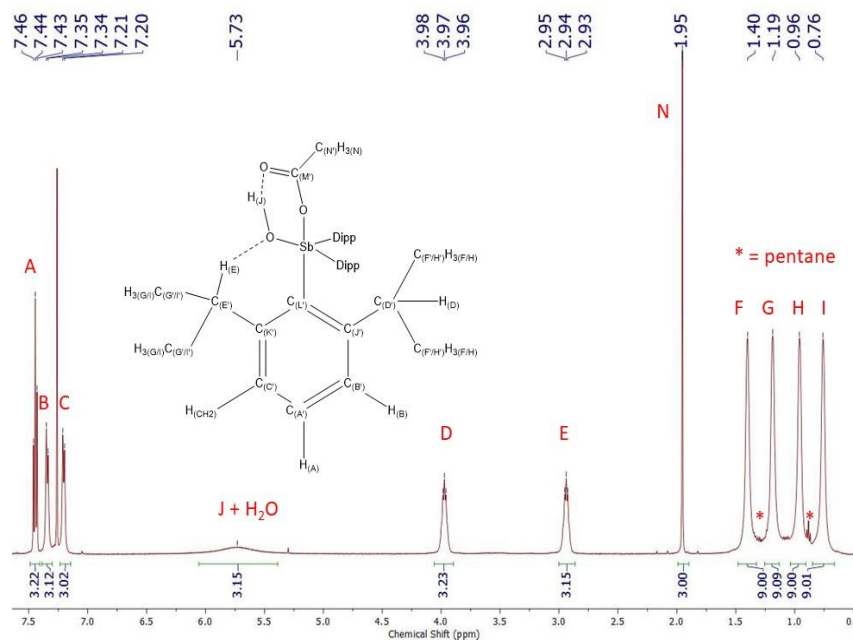
**Figure B.61.** ^{1}H NMR spectrum (CDCl$_3$, 500 MHz) of *cis*-Sb(OH)(OAc)Dipp$_3$ at room temperature.
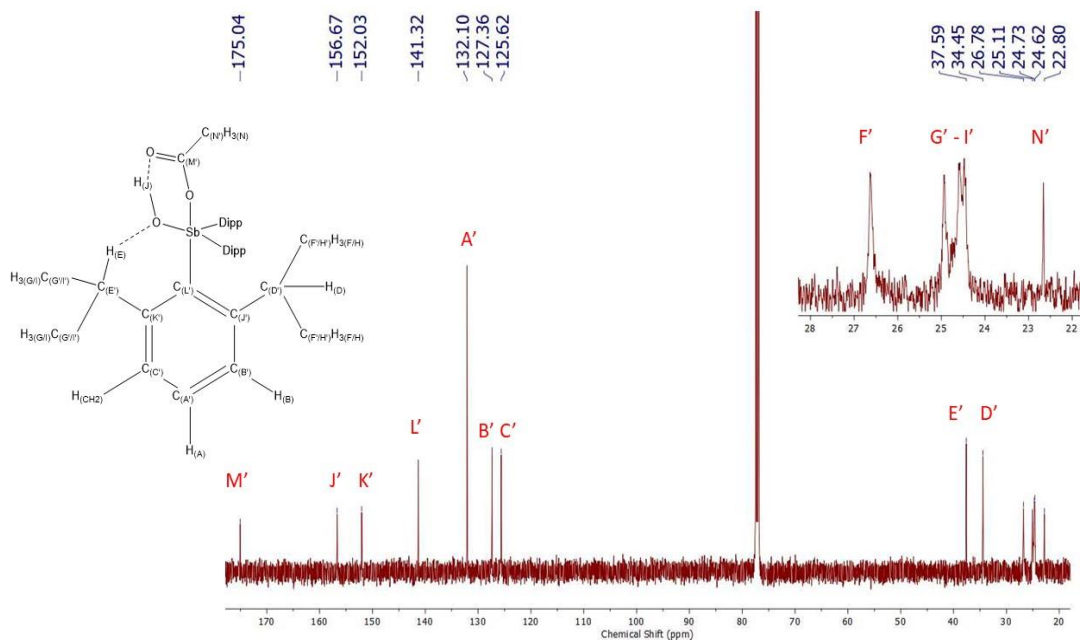


**Figure B.62.** ^{13}C{^{1}H} NMR spectrum (CDCl$_3$, 125 MHz) of *cis*-Sb(OH)(OAc)Dipp$_3$ at room temperature.
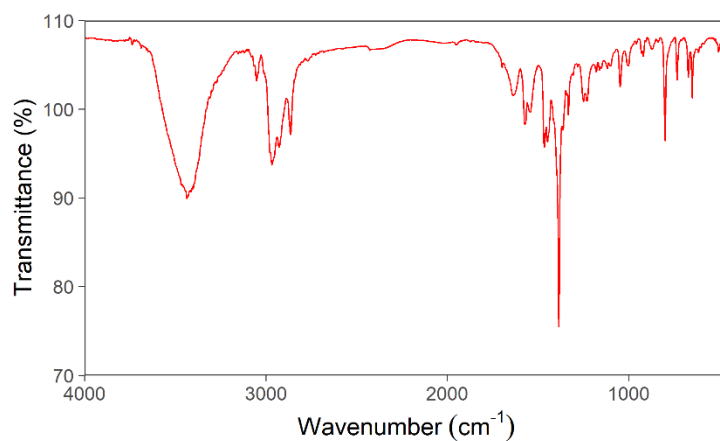
**Figure B.63.** Experimental IR spectrum (KBr pellet) of *cis*-Sb(OH)(OAc)Dipp$_3$ ($\nu_{SbO}$ = 649 cm$^{-1}$).
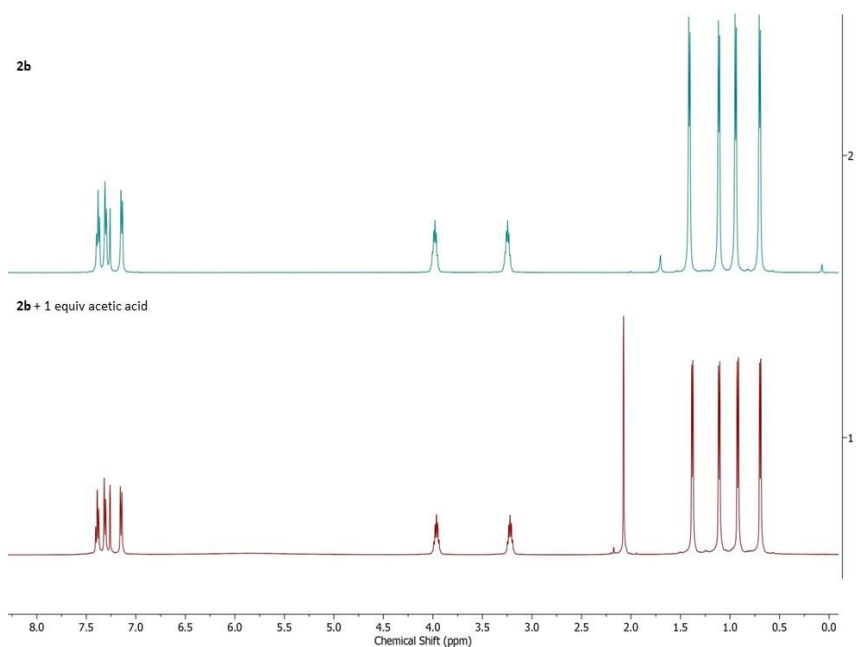


**Figure B.64.** $^1$H NMR spectra (CDCl$_3$, 500 MHz) of Dipp$_3$AsO (*top*) and a 1:1 mixture of Dipp$_3$AsO and acetic acid (*bottom*) at room temperature.
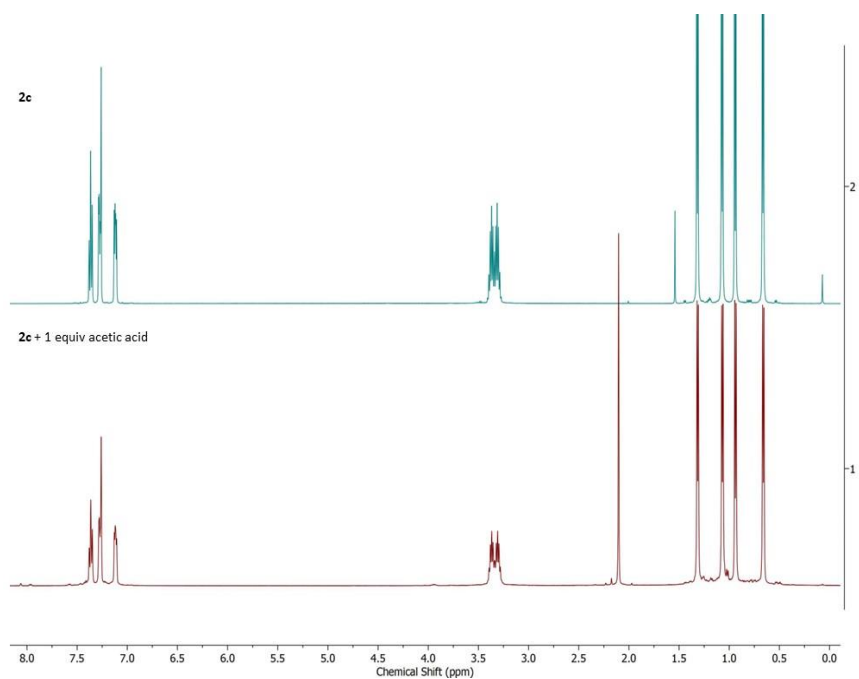
**Figure B.65.** $^1$H NMR spectra (CDCl$_3$, 500 MHz) of Dipp$_3$PO (*top*) and a 1:1 mixture of Dipp$_3$PO and acetic acid (*bottom*) at room temperature.
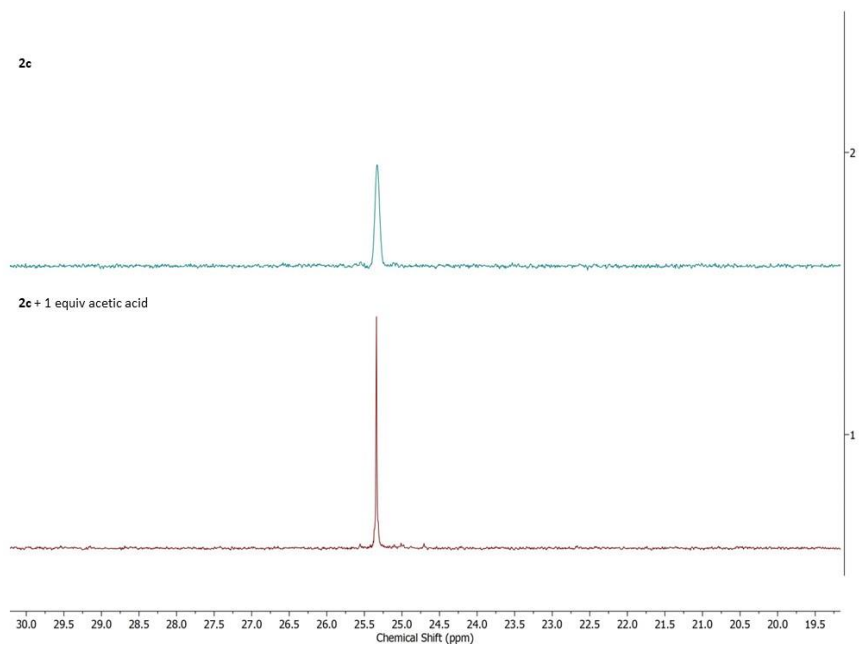


**Figure B.66.** $^{31}$P{$^1$H} NMR spectra (CDCl$_3$, 202 MHz) of Dipp$_3$PO (*top*) and a 1:1 mixture of Dipp$_3$PO and acetic acid (*bottom*) at room temperature.
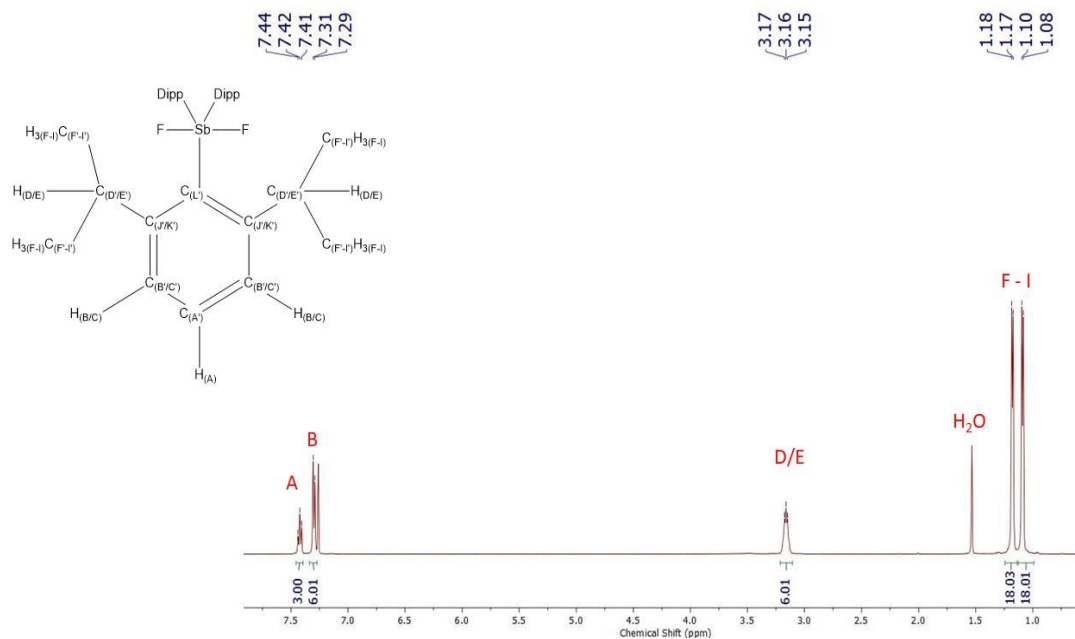
**Figure B.67.** $^1$H NMR spectrum (CDCl$_3$, 500 MHz) of *trans*-Dipp$_3$SbF$_2$ at room temperature.
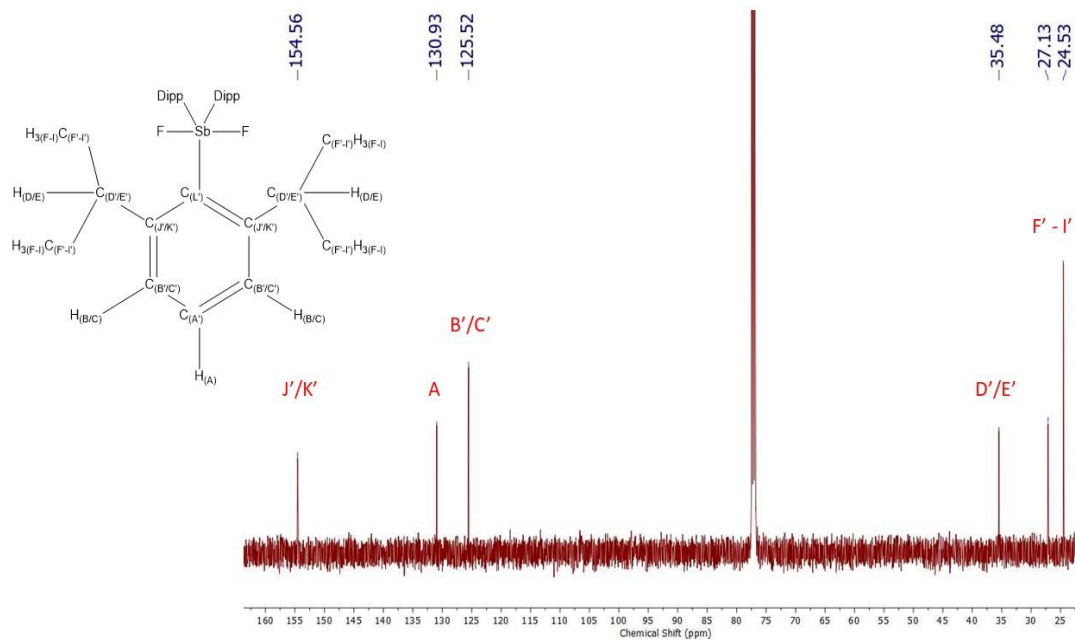


**Figure B.68.** $^{13}$C{$^1$H} NMR spectrum (CDCl$_3$, 125 MHz) of *trans*-Dipp$_3$SbF$_2$ at room temperature.
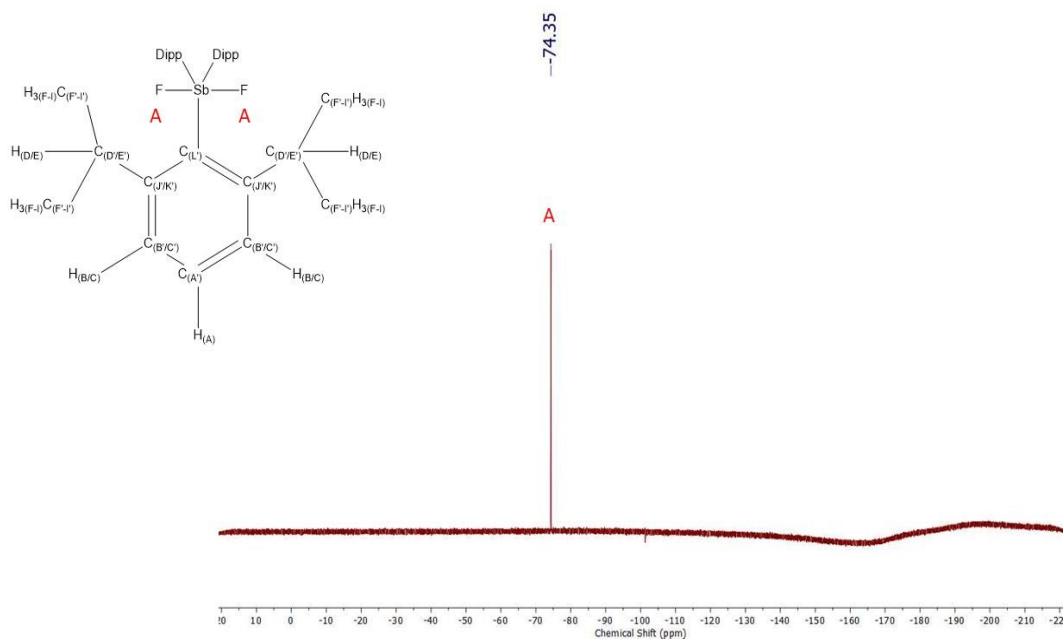
**Figure B.69.** $^{19}F$ NMR spectrum (CDCl$_3$, 470 MHz) of *trans*-Dipp$_3$SbF$_2$ at room temperature.
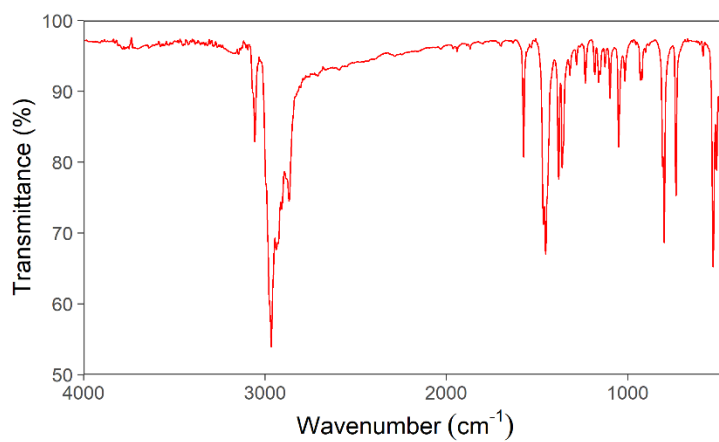


**Figure B.70.** Experimental IR spectrum (KBr pellet) of *trans*-Dipp$_3$SbF$_2$ ($\nu_{SbF}$ = 528 cm$^{-1}$).
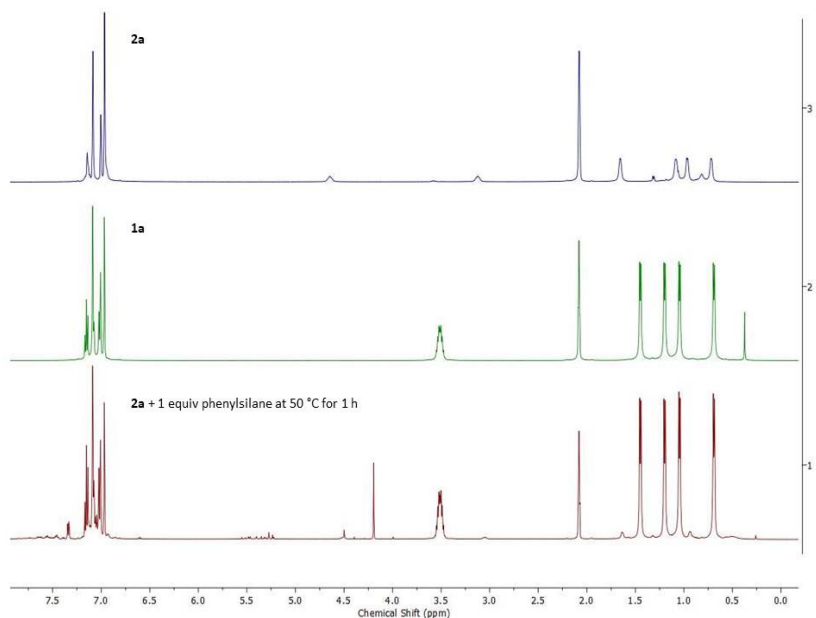
**Figure B.71.** ^{1}H NMR spectra (toluene-$d_8$, 500 MHz) of Dipp$_3$SbO (*top*), Dipp$_3$Sb (*middle*), and a reaction mixture of phenylsilane and Dipp$_3$SbO (1:1 mixture) after 1 h at 50 °C (*bottom*), collected at room temperature.
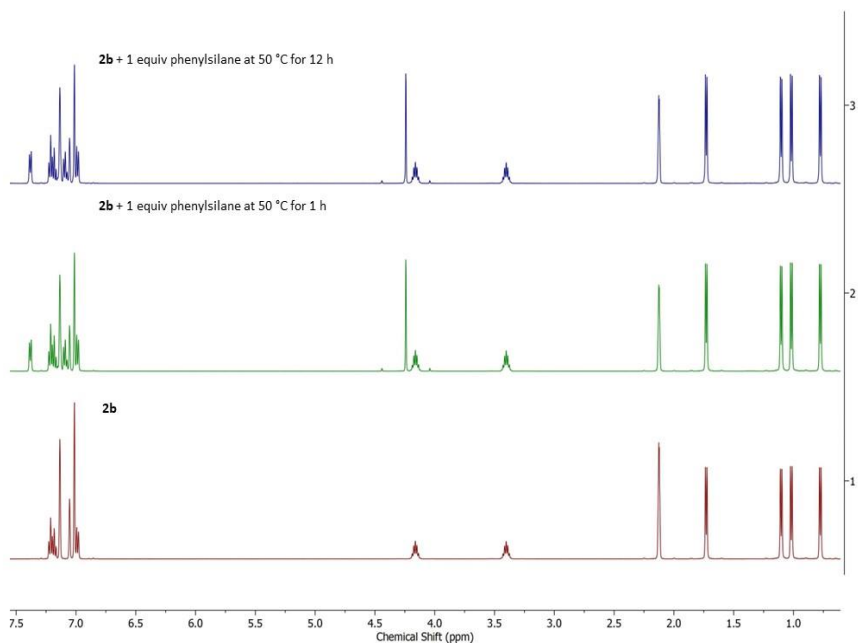


**Figure B.72.** ^{1}H NMR spectra (toluene-$d_8$, 500 MHz) of Dipp$_3$AsO (*bottom*), and a mixture of phenylsilane and Dipp$_3$AsO (1:1 mixture) after 1 h (*middle*) and 12 h (*top*) at 50 °C, collected at room temperature.
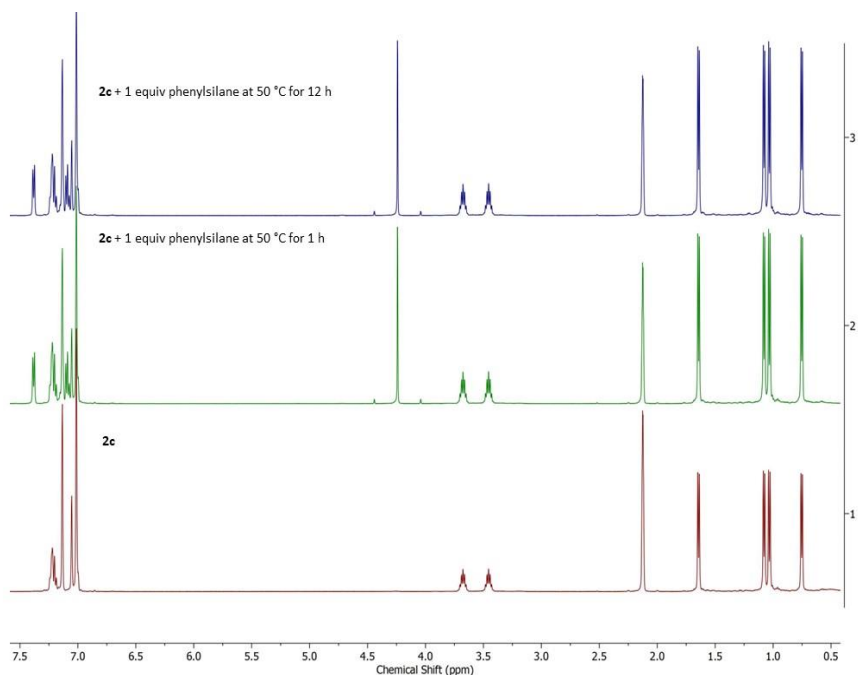
**Figure B.73.** ^{1}H NMR spectra (toluene-$d_8$, 500 MHz) of Dipp$_3$PO (*bottom*), and a mixture of phenylsilane and Dipp$_3$PO (1:1 mixture) after 1 h (*middle*) and 12 h (*top*) at 50 °C, collected at room temperature.
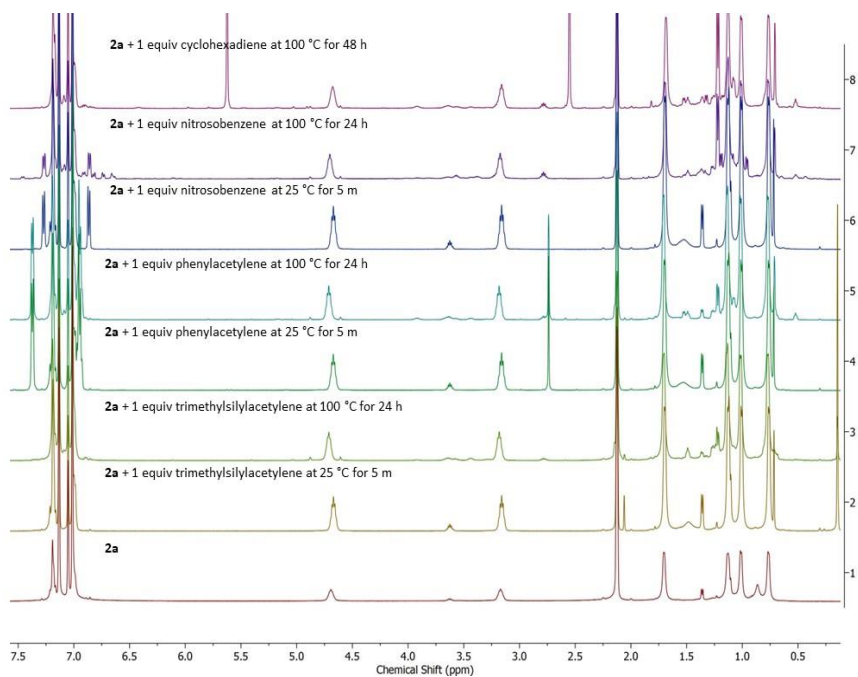


**Figure B.74.** ^{1}H NMR spectra (toluene-$d_8$, 500 MHz) of Dipp$_3$SbO and mixtures of 1 equivalent trimethylsilylacetylene, phenylacetylene, nitrosobenzene, and cyclohexadiene (*bottom* to *top*) at different time points.
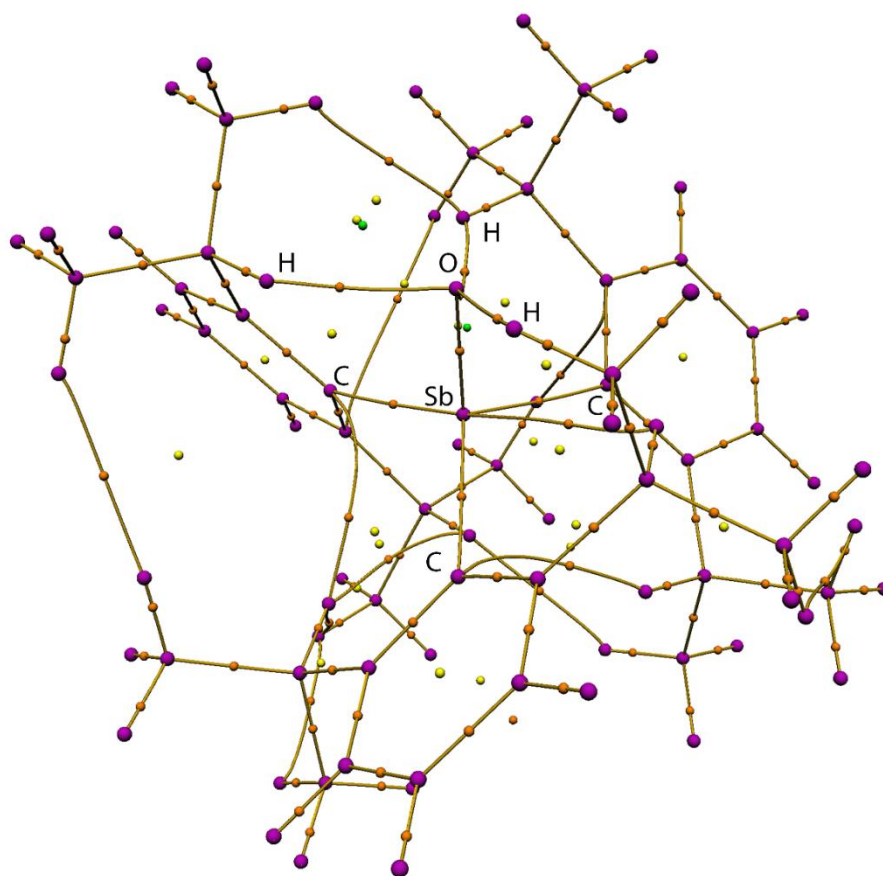
**Figure B.75.** Molecular graph of Dipp₃SbO derived from theoretical electron density (DKH-PBE0/old-DKH-TZVPP//PBE0/def2-TZVPP) depicting critical points and bond paths between (3, −3) and (3, −1) critical points. Color code: (3, −3) purple, (3, −1) orange, (3, +1) yellow, (3, +3) green.
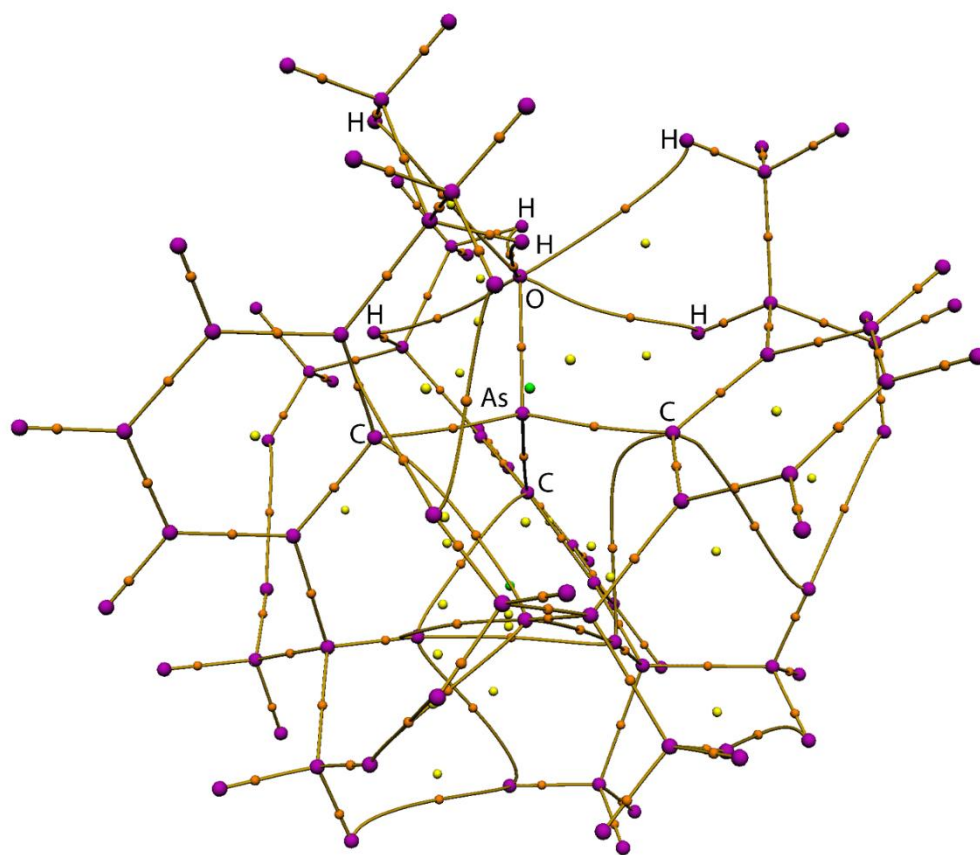
**Figure B.76.** Molecular graph of Dipp₃AsO derived from theoretical electron density (DKH-PBE0/old-DKH-TZVPP//PBE0/def2-TZVPP) depicting critical points and bond paths between (3, −3) and (3, −1) critical points. Color code: (3, −3) purple, (3, −1) orange, (3, +1) yellow, (3, +3) green.
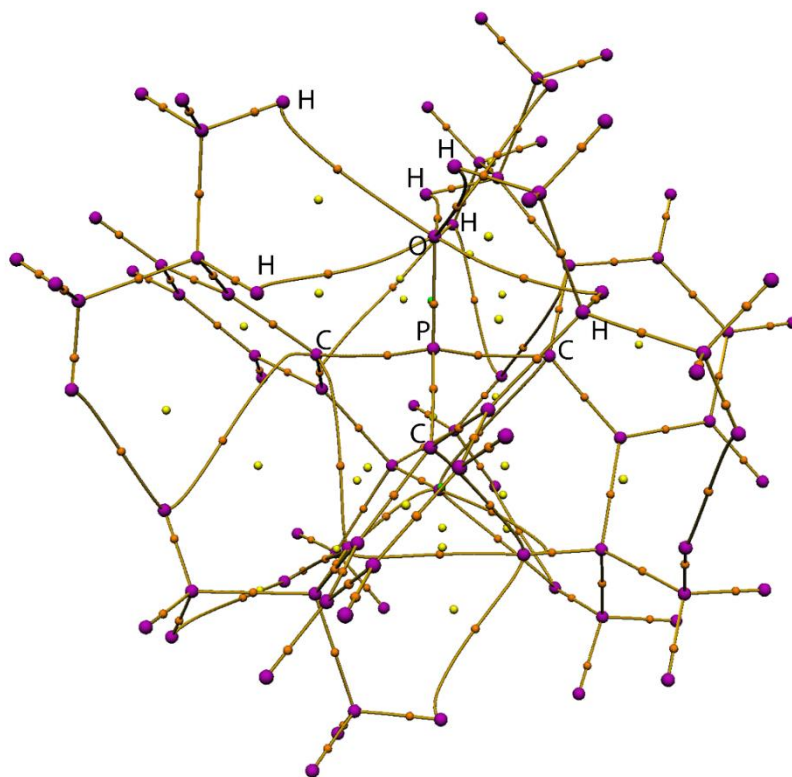
**Figure B.77.** Molecular graph of Dipp$_3$PO derived from theoretical electron density (DKH-PBE0/old-DKH-TZVPP//PBE0/def2-TZVPP) depicting critical points and bond paths between (3, −3) and (3, −1) critical points. Color code: (3, −3) purple, (3, −1) orange, (3, +1) yellow, (3, +3) green.
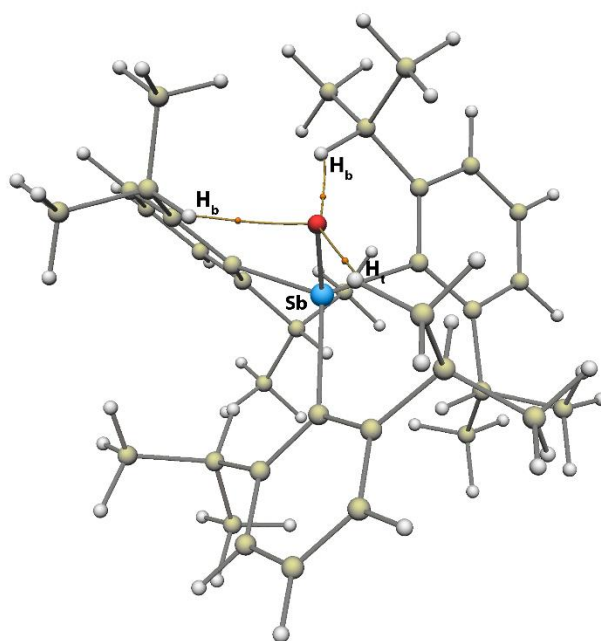
**Figure B.78.** Intramolecular O···H bond paths and bond critical points in Dipp₃SbO derived from theoretical electron density (DKH-PBE0/old-DKH-TZVPP//PBE0/def2-TZVPP) overlaid on the optimized molecular structure of Dipp₃SbO. Color code: O red, C tan, H white, Sb teal, bond grey, bond path yellow, (3, −1) critical point orange. Benzylic H atoms are denoted "H$_b$" and terminal H atoms are denoted "H$_t$."
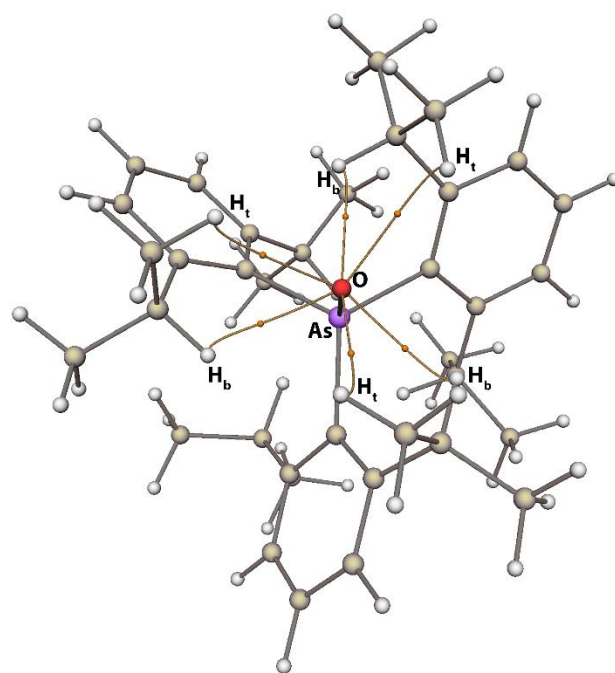
**Figure B.79.** Intramolecular O···H bond paths and bond critical points in Dipp$_3$AsO derived from theoretical electron density (DKH-PBE0/old-DKH-TZVPP//PBE0/def2-TZVPP) overlaid on the optimized molecular structure of Dipp$_3$AsO. Color code: O red, C tan, H white, As violet, bond grey, bond path yellow, (3, −1) critical point orange. Benzylic H atoms are denoted "H$_b$" and terminal H atoms are denoted "H$_t$."
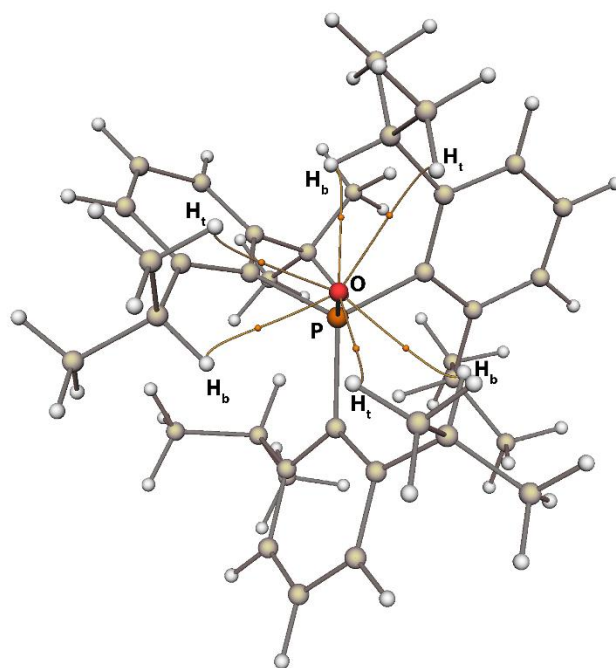
**Figure B.80.** Intramolecular O···H bond paths and bond critical points in Dipp$_3$PO derived from theoretical electron density (DKH-PBE0/old-DKH-TZVPP//PBE0/def2-TZVPP) overlaid on the optimized molecular structure of Dipp$_3$PO. Color code: O red, C tan, H white, P orange, bond grey, bond path yellow, (3, −1) critical point orange. Benzylic H atoms are denoted "H$_b$" and terminal H atoms are denoted "H$_t$."
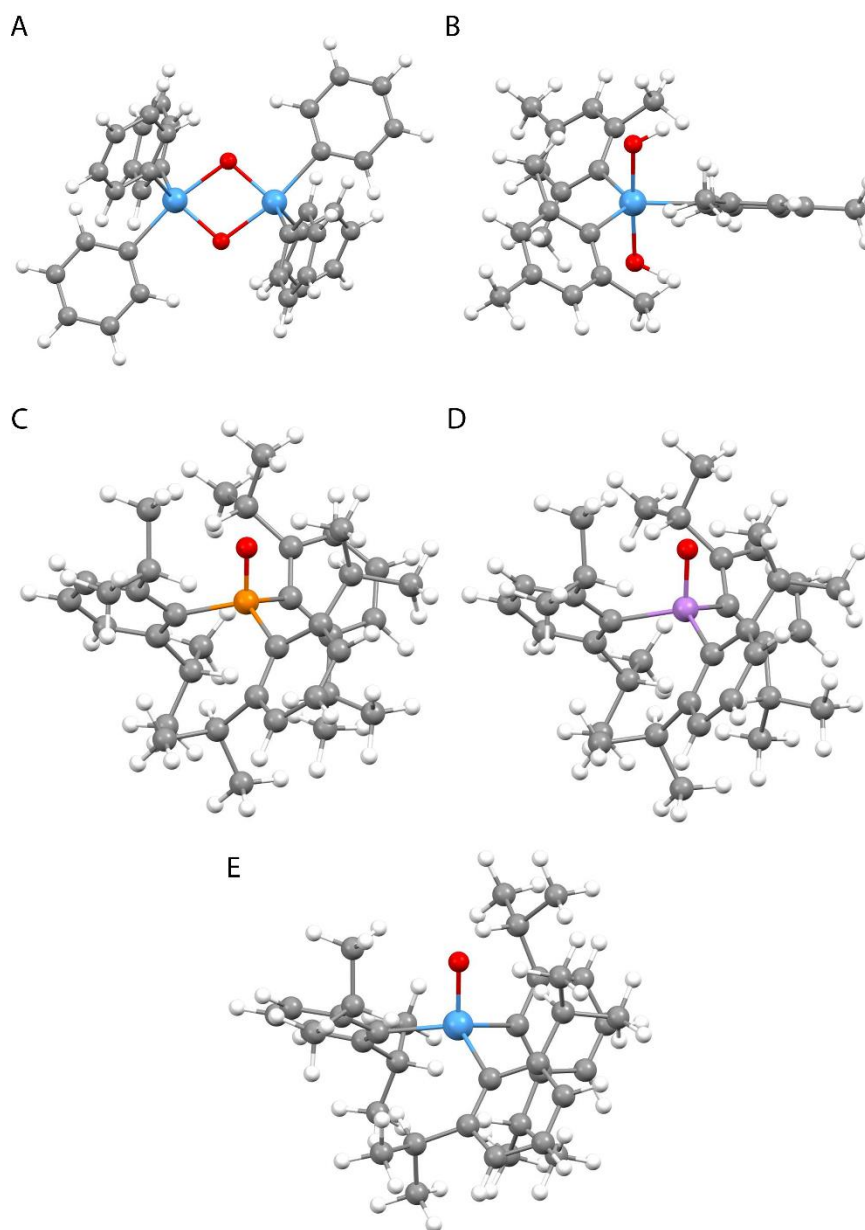
**Figure B.81.** Ball-and-stick representations of atomic coordinates of molecules used in theoretical studies. Geometry optimized (PBE0/def2-TZVPP) structure of (A) **A**, (B) **B**, (C) Dipp₃PO, (D) Dipp₃AsO, (E) Dipp₃SbO. Color code: C grey, H white, O red, Sb teal, As violet, P orange.
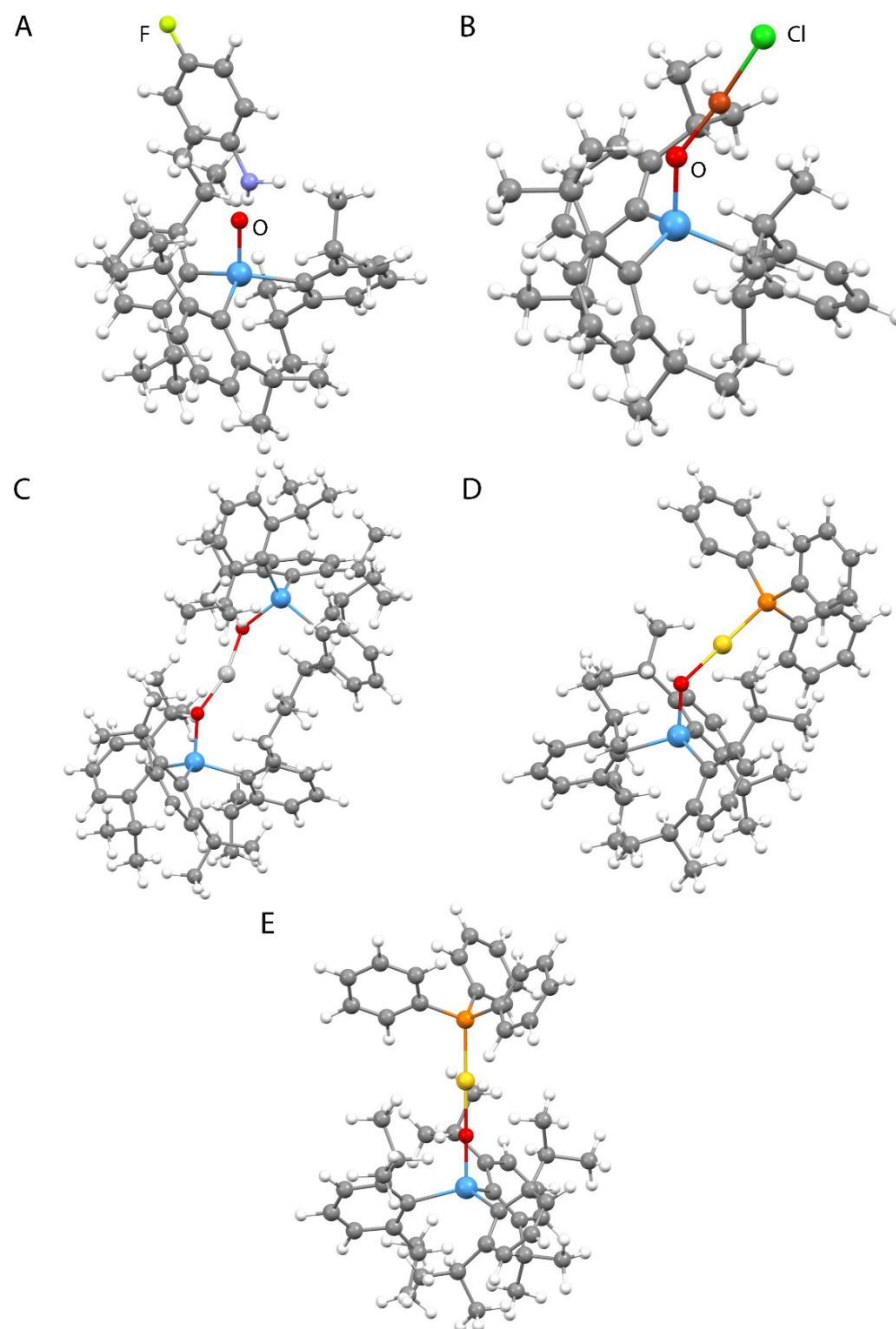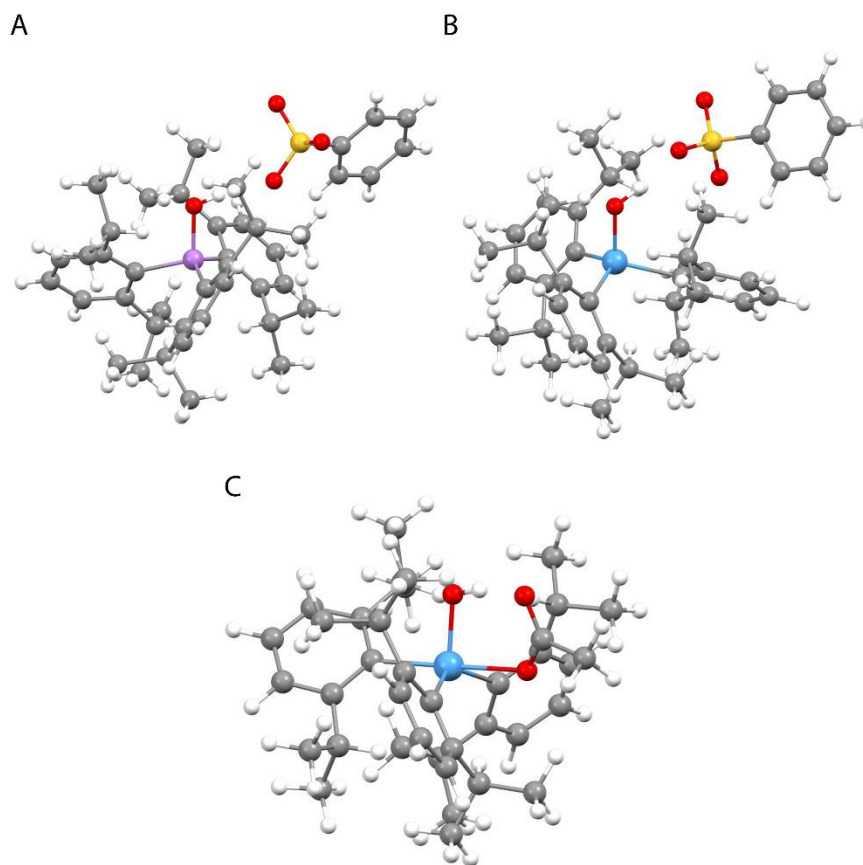
**Figure B.82.** Ball-and-stick representations of atomic coordinates of molecules used in theoretical studies. (A) HAR model of Dipp$_3$SbO·H$_2$NPhF. (B) IAM model of Dipp$_3$SbOCuCl with H-bond lengths normalized to 1.089 Å. (C) Geometry optimized (BP86/def2-SVP) structure of (Dipp$_3$SbO)$_2$Ag$^+$. IAM model of Dipp$_3$SbOAuPPh$_3$$^+$ in either the (D) triclinic polymorph (E) rhombohedral polymorph with C–H-bond lengths normalized to 1.089 Å (triflate counteranion is omitted). Color code: C grey, H white, O red, Sb teal, P orange, Au gold, Ag silver, Cu brown, F yellow-green, Cl green, N light-purple.

**Figure B.83.** Ball-and-stick representations of atomic coordinates of molecules used in theoretical studies. HAR model of (A) [Dipp$_3$AsOH][O$_3$SPh]and (B) [Dipp$_3$SbOH][O$_3$SPh]. (C) Geometry optimized (PBE0/def2-TVPPP) structure of *cis*-Sb(OH)(OAc)Dipp$_3$. Color code: C grey, H white, O red, Sb teal, As violet, S yellow.
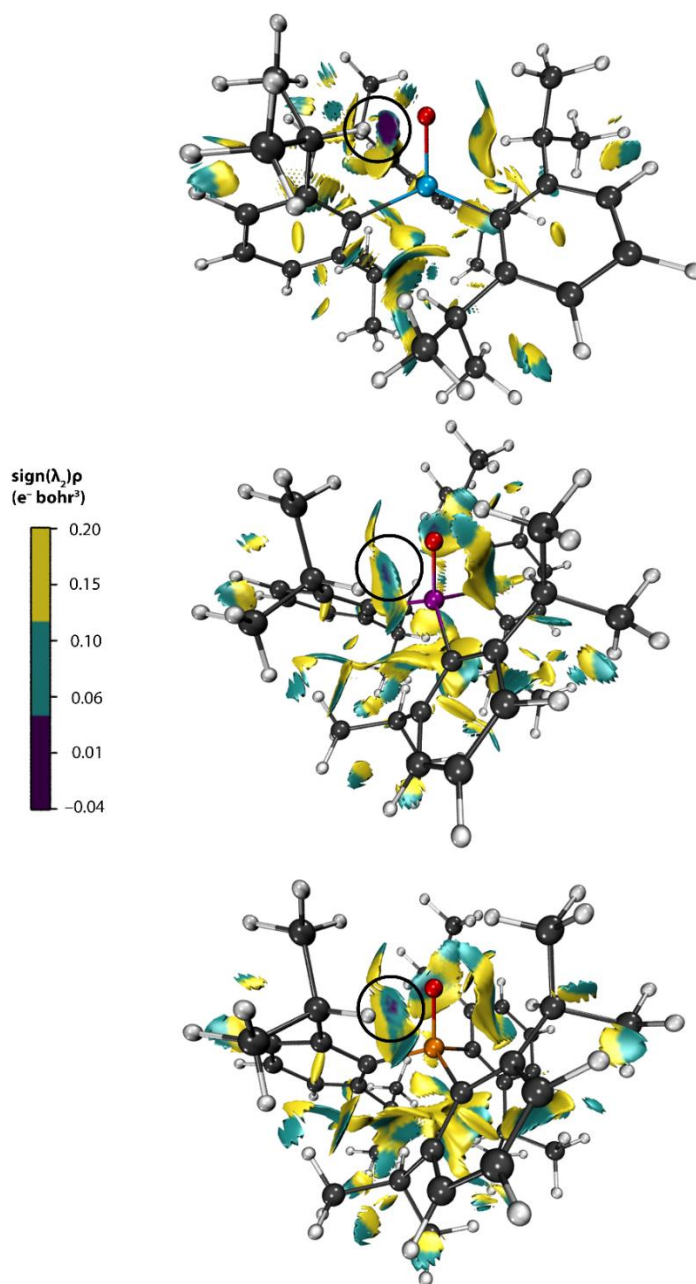
**Figure B.84.** NCI analysis of Dipp$_3$SbO (*top*), Dipp$_3$AsO (*middle*), and Dipp$_3$PO (*bottom*) depicting reduced gradient surfaces (isovalue = 0.45 a.u.) with the function sign($\lambda_2$)r, where $\lambda_2$ is the second-largest eigenvalue of the Laplacian, color-mapped on the surface. Purple is indicative of H-bonding interactions, aqua is indicative of van der Waals interactions, and yellow is indicative of steric repulsions.
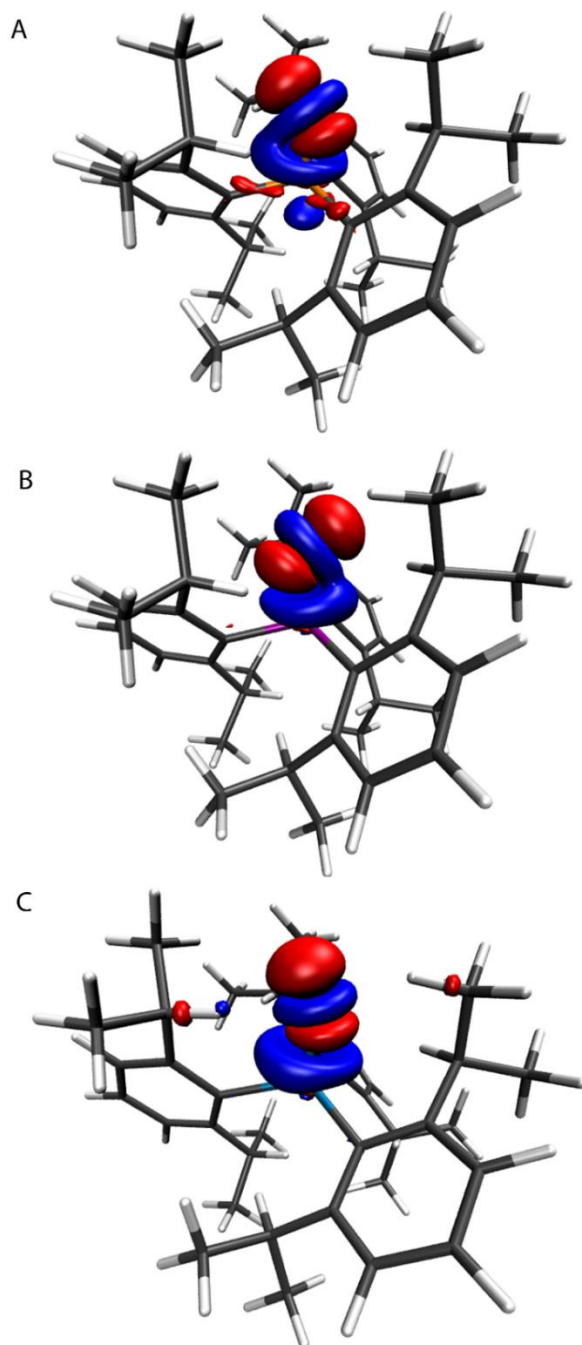
**Figure B.85.** Deformation density (DKH-PBE0/old-DKH-TZVPP) obtained by subtracting non-interacting pnictine and O atom wavefunctions from the corresponding pnictine oxide wavefunction at the optimized geometry of the pnictine oxide (PBE0/def2-TZVPP) in (A) Dipp₃PO, (B) Dipp₃AsO, (C) Dipp₃SbO (isovalue = –0.006 blue, 0.006 red e⁻ Å³). Color code: C grey, H white, O red, P orange, As purple, Sb teal.

BD ( 1) Sb 1- O 2

BD*( 1) Sb 1- O 2

LP ( 1) O 2

LP ( 2) O 2
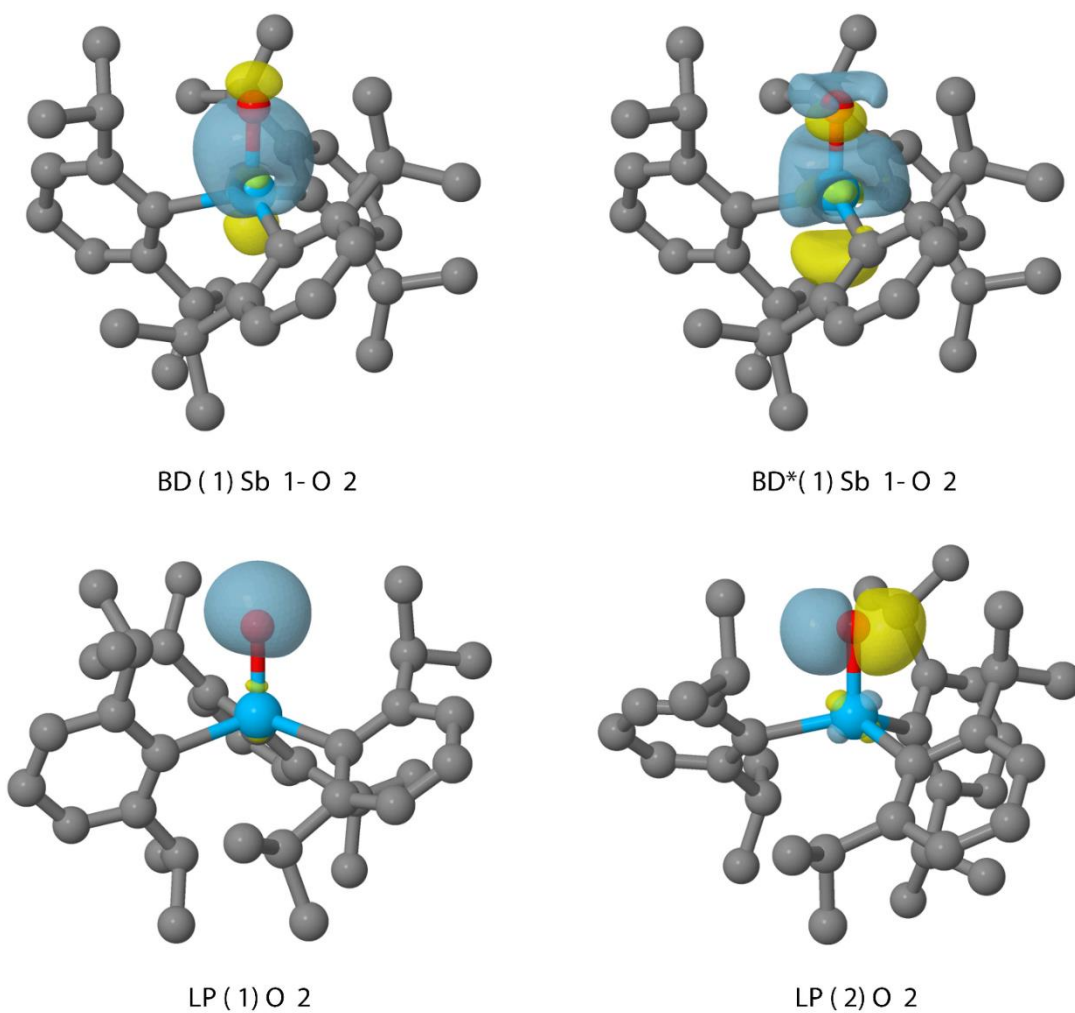
**Figure B.86.** NLMO plots for Dipp₃SbO (DKH-PBE0/old-DKH-TZVPP//PBE0/def2-TZVPP) of Sb–O bonding and antibonding orbitals and O-centered lone pairs (isosurface = 0.05).

LP ( 2) O 2  ->  BD*( 1)Sb  1- C 15
11.30 kcal/mol

LP ( 2) O  2 -> BD*( 1)Sb  1- C  3
4.04 kcal/mol

LP ( 3) O  2  ->  BD*( 1)Sb  1- C 27
9.45 kcal/mol

LP ( 3) O  2  ->  BD*( 1)Sb  1- C 3
8.46 kcal/mol
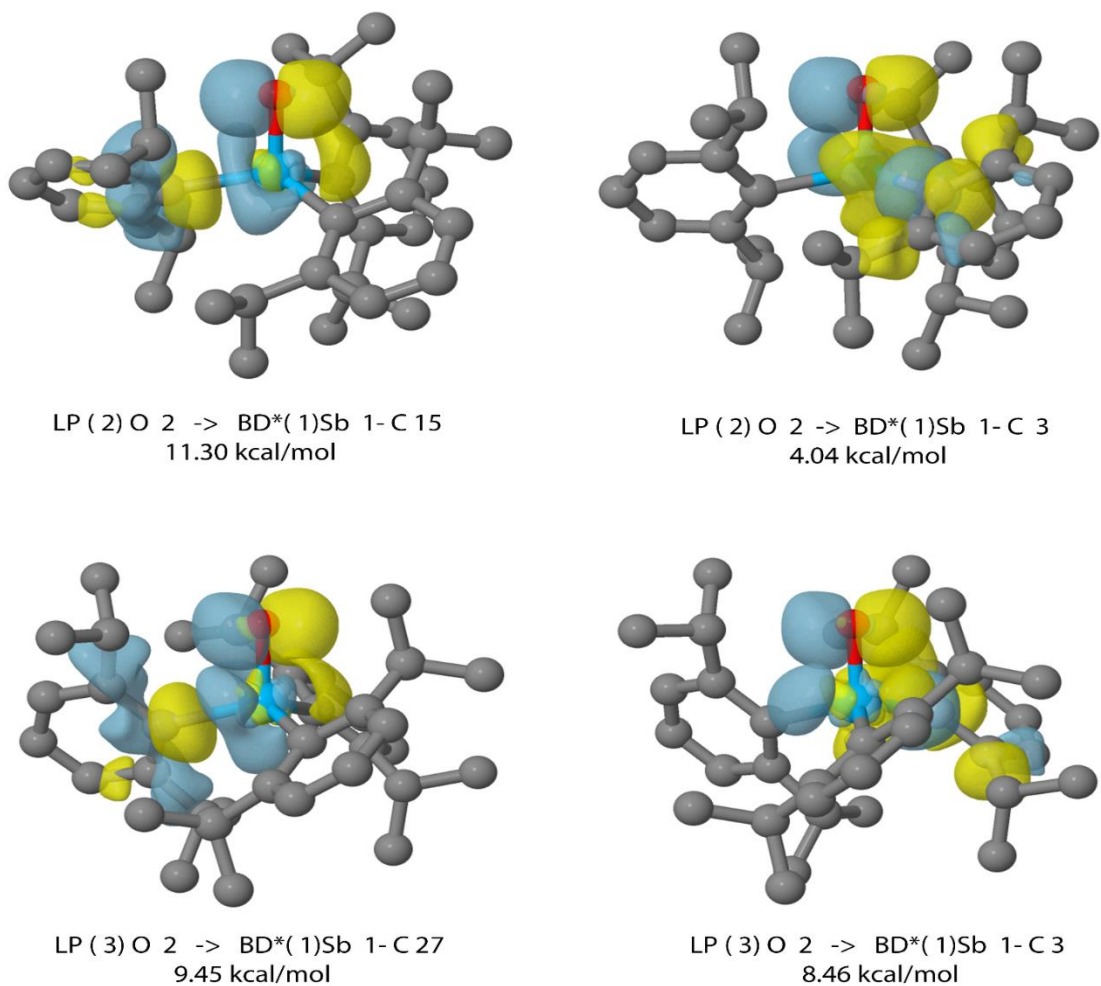
**Figure B.87.** Pre-orthogonalized NLMO plots for Dipp₃SbO (DKH-PBE0/old-DKH-TZVPP//PBE0/def2-TZVPP) of select O-centered lone pairs and Sb–C antibonding orbitals involved in donor-acceptor interactions (isosurface = 0.05). The energy of stabilization afforded by the interaction is displayed. H atoms are omitted for clarity.

LP ( 3) O 2  ->  BD*( 1) C 33- H 73
3.38 kcal/mol
(side view)

LP ( 3) O 2  ->  BD*( 1) C 33- H 73
3.38 kcal/mo
(top view)

LP ( 2) O 2  ->  BD*( 1) C 9- H 41
1.46 kcal/mol

LP ( 2) O 2  ->  BD*( 1) C 23- H 61
0.68 kcal/mol
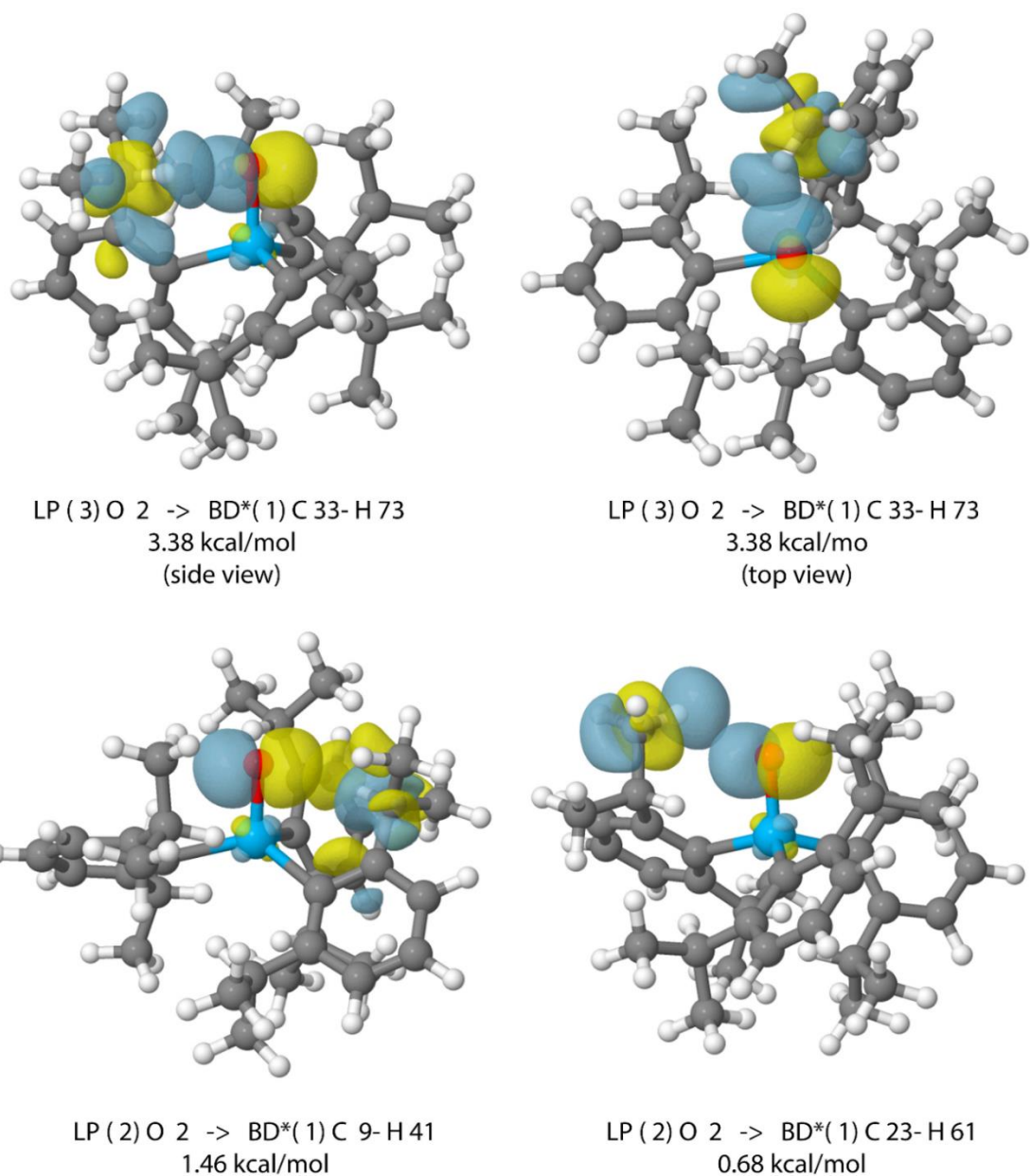
**Figure B.88.** Pre-orthogonalized NLMO plots for Dipp₃SbO (DKH-PBE0/old-DKH-TZVPP//PBE0/def2-TZVPP) of select O-centered lone pairs and C–H antibonding orbitals involved in donor-acceptor interactions (isosurface = 0.05). The energy of stabilization afforded by the interaction is displayed. An NBO deletion calculation for the strength the interaction between O2 and the C33–H73 unit affords an energy of 7.427 kcal/mol.
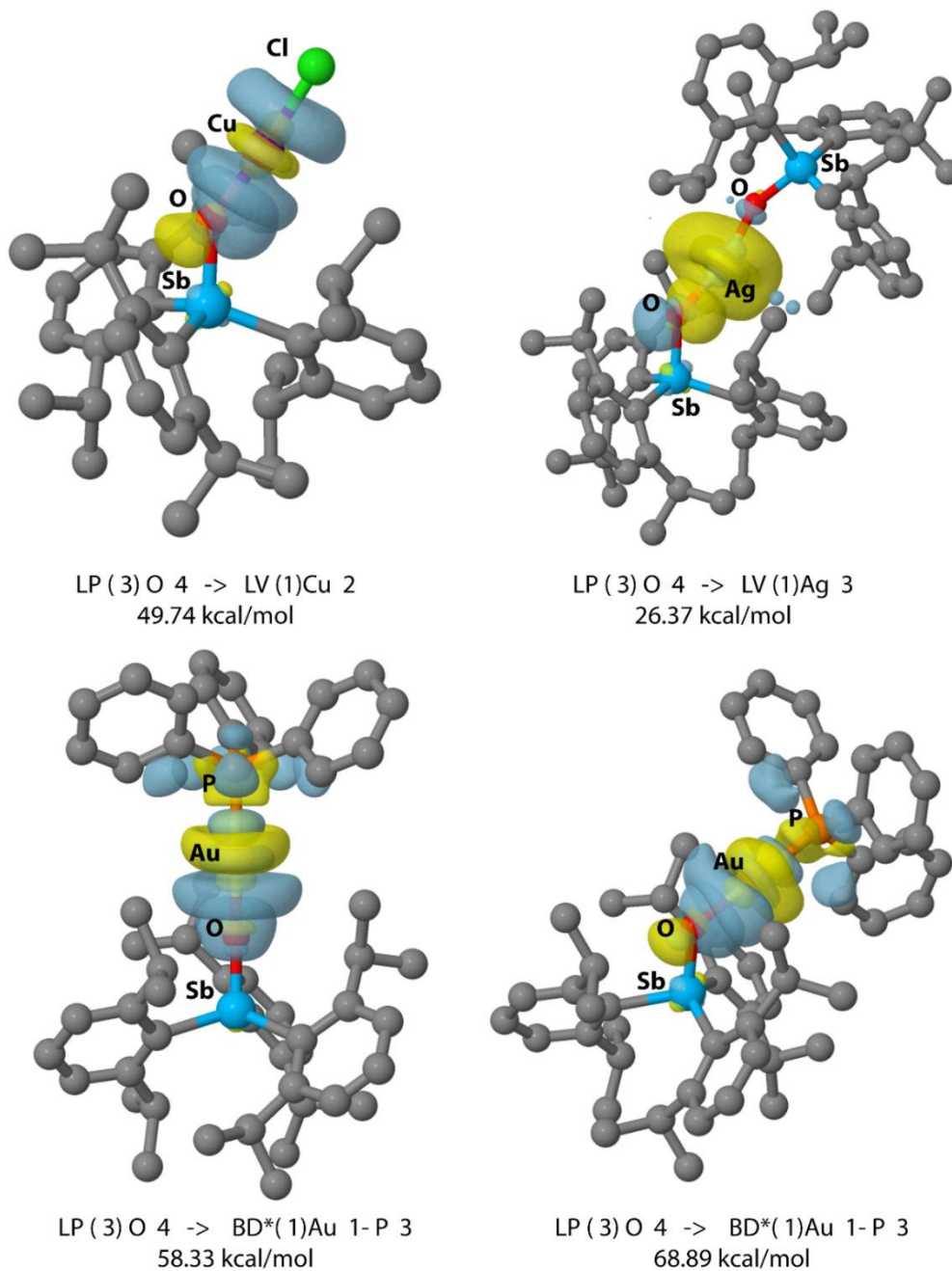
**Figure B.89.** Pre-orthogonalized NBO plots for Dipp₃SbOH₂NPhF (*top left*), (Dipp₃SbO)₂Ag⁺ (*top right*)**,** Dipp₃SbOAuPPh₃⁺-linear (*bottom left*), and Dipp₃SbOAuPPh₃⁺-bent (*bottom right*) (DKH-PBE0/old-DKH-TZVPP//PBE0/def2-TZVPP) of the O-centered lone pairs and metal-centered orbitals involved in donor-acceptor interactions (isosurface = 0.05). The energy of stabilization afforded by the interaction is displayed.
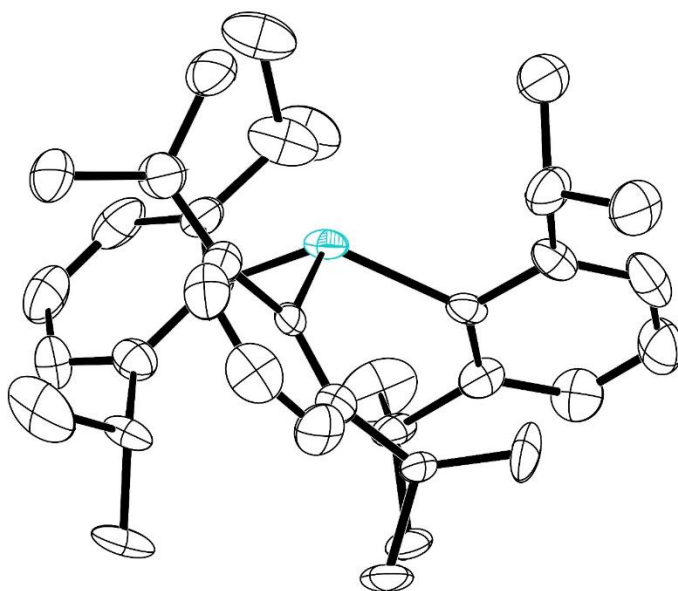
**Figure B.90.** Thermal ellipsoid plot (50% probability) of Dipp₃Sb. H atoms and disordered components are omitted for clarity. Color code: Sb teal, C black. CCDC 2133036.
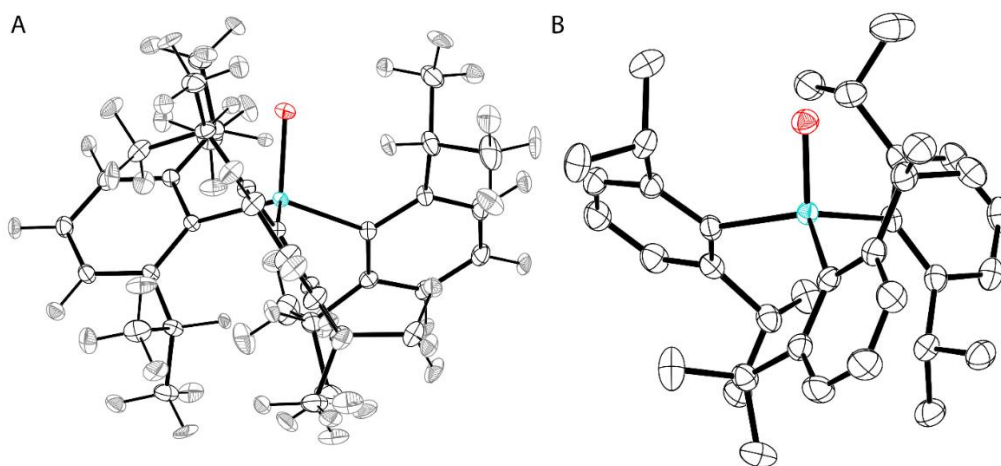


**Figure B.91.** Thermal ellipsoid plot (50% probability) of (A) Dipp₃SbO (monoclinic) and (B) Dipp₃SbO (orthorhombic). Dipp₃SbO (monoclinic) was refined using the HAR method, and Dipp₃SbO (orthorhombic) was refined using the IAM method. In panel B, H atoms are omitted for clarity. Color code: Sb teal, O red, C black, H grey. The Sb–O bond length in Dipp₃SbO (monoclinic) is 1.8372(5) Å and the Sb–O bond length in Dipp₃SbO (orthorhombic) is 1.8428(14) Å. CCDC 2133037 (A) and 2182474 (B).
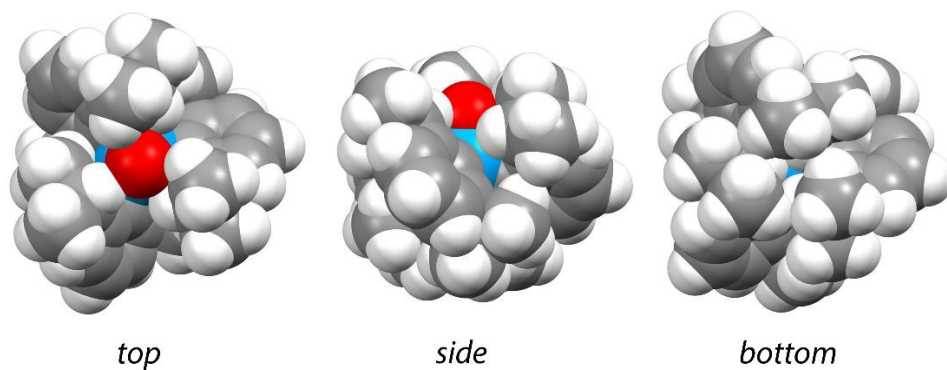
**Figure B.92.** Space-filling diagrams of Dipp₃SbO from views rotated successively by 90° about the horizontal axis. Color code: Sb teal, O red, C grey, H white.
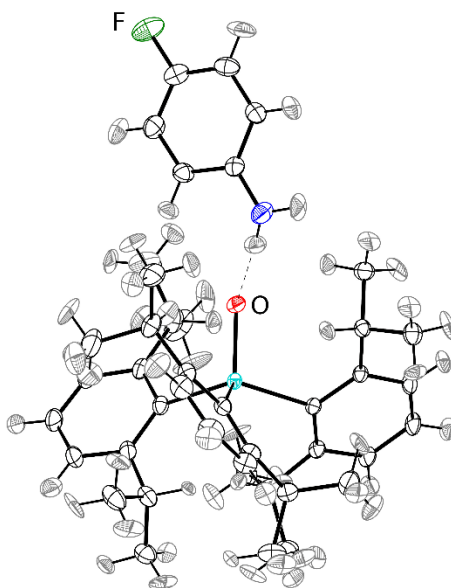


**Figure B.93.** Thermal ellipsoid plot (50% probability) of Dipp₃SbO·H₂NPhF. Color code: Sb teal, O red, C black, H grey, F green, N blue. The Sb–O bond length in Dipp₃SbO·H₂NPhF is 1.8421(7) Å. CCDC 2133038.
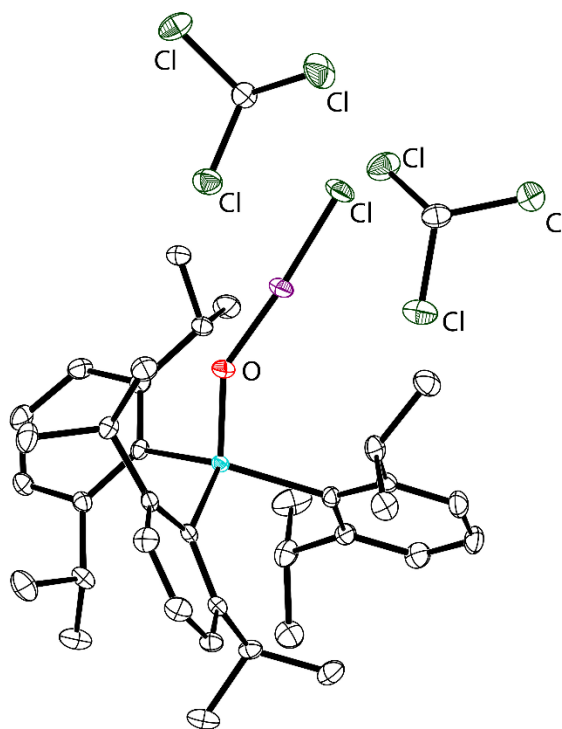
**Figure B.94.** Thermal ellipsoid plot (50% probability) of Dipp₃SbOCuCl·(CHCl₃)₂. H atoms are omitted for clarity. Color code: Sb teal, O red, C black, Cl dark green, Cu mauve. The Sb–O bond length in Dipp₃SbOCuCl·(CHCl₃)₂ is 1.8591(14) Å. CCDC 2182479.

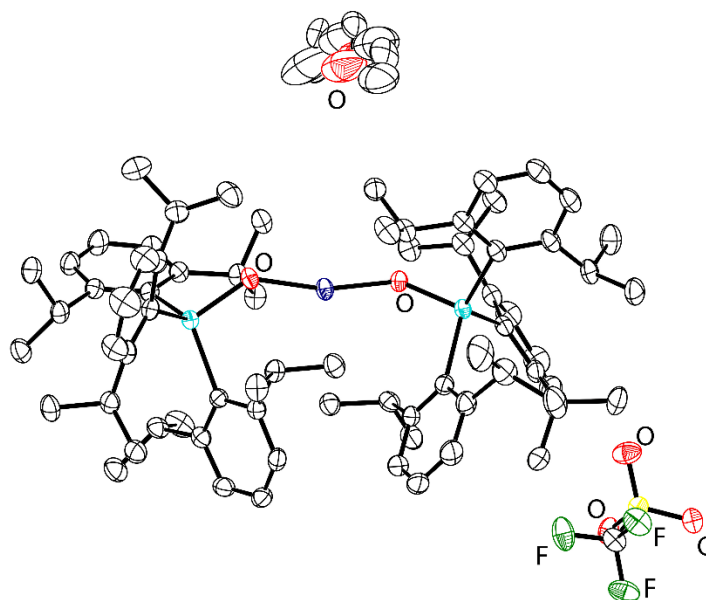**Figure B.95.** Thermal ellipsoid plot (50% probability) of $[Ag(Dipp_3SbO)_2](CF_3SO_3)\cdot OEt_2$. H atoms and disordered components are omitted for clarity. Color code: Sb teal, O red, C black, F green, S yellow, Ag blue. The Sb–O bond lengths in $[Ag(Dipp_3SbO)_2](CF_3SO_3)\cdot OEt_2$ are 1.8716(17) and 1.8670(17) Å. CCDC 2133039.
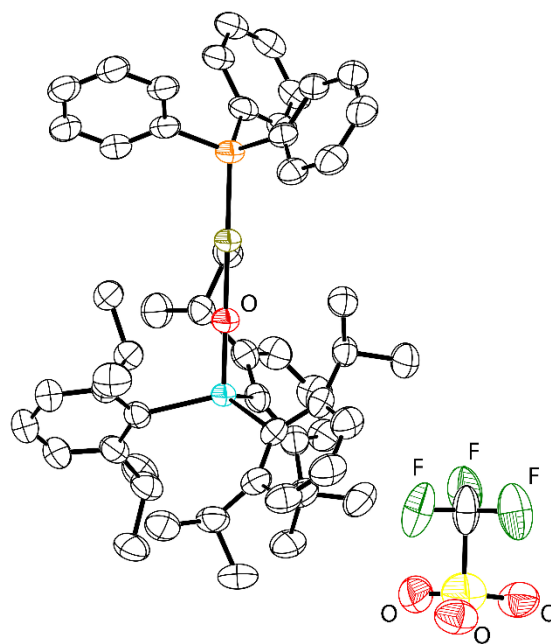
**Figure B.96.** Thermal ellipsoid plot (50% probability) of Dipp$_3$SbOAuPPh$_3$CF$_3$SO$_3$-linear (rhombohedral polymorph). H atoms are omitted for clarity. Color code: Sb teal, O red, C black, H grey, P orange, Au gold, S yellow, F green. The Sb–O bond length in Dipp$_3$SbOAuPPh$_3$CF$_3$SO$_3$-linear is 1.850(7) Å. The O–Au bond length in Dipp$_3$SbOAuPPh$_3$CF$_3$SO$_3$-linear is 1.982(7) Å. CCDC 2182481.
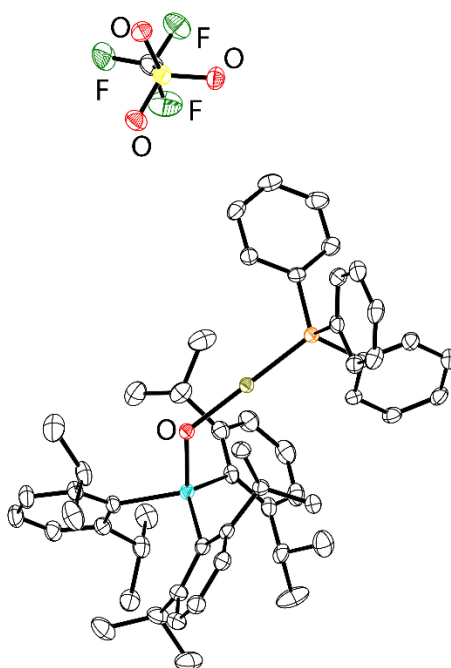
**Figure B.97.** Thermal ellipsoid plot (50% probability) of [Dipp₃SbOAuPPh₃][CF₃SO₃]-bent (triclinic polymorph). H atoms are omitted for clarity. Color code: Sb teal, O red, C black, H grey, P orange, Au gold, S yellow, F green. The Sb–O bond length in [Dipp₃SbOAuPPh₃][CF₃SO₃]-bent 1.8932(17) Å. The O–Au bond length in [Dipp₃SbOAuPPh₃][CF₃SO₃]-bent is 2.0582(16) Å. CCDC 2182480.
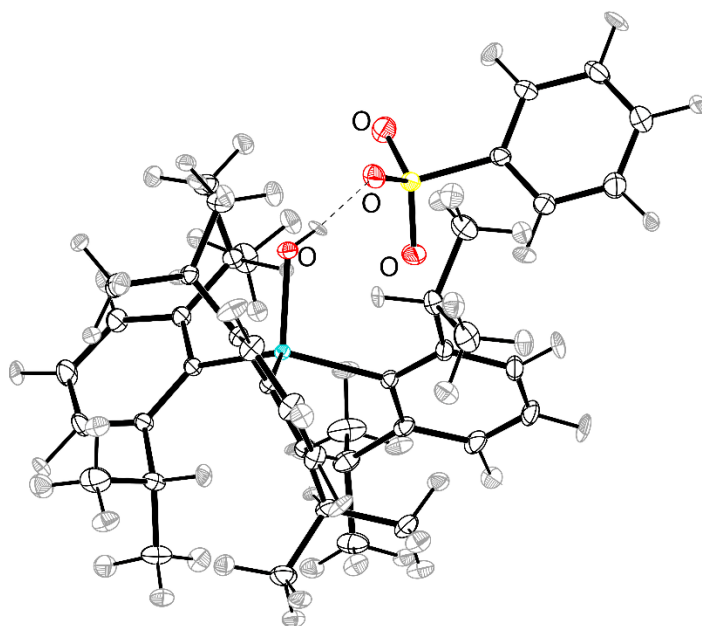
**Figure B.98.** Thermal ellipsoid plot (50% probability) of [Dipp₃SbOH][O₃SPh]. Color code: Sb teal, O red, C black, H grey, S yellow. The Sb–O bond length in [Dipp₃SbOH][O₃SPh] is 1.9119(7) Å. CCDC 2133040.
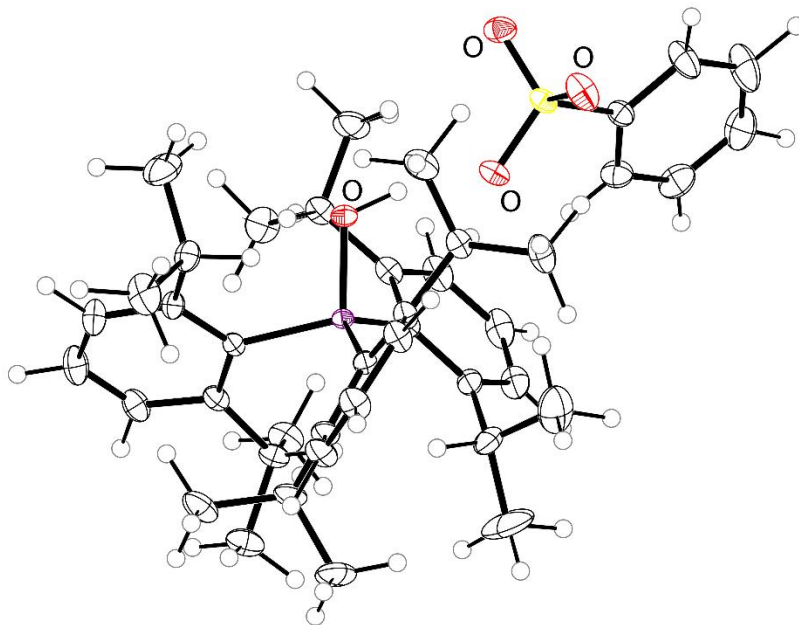
**Figure B.99.** Thermal ellipsoid plot (50% probability) of [Dipp$_3$AsOH][O$_3$SPh]. Color code: As purple, O red, C black, H grey, S yellow. The As–O bond length in [Dipp$_3$AsOH][O$_3$SPh] is 1.7386(19) Å. CCDC 2182482.
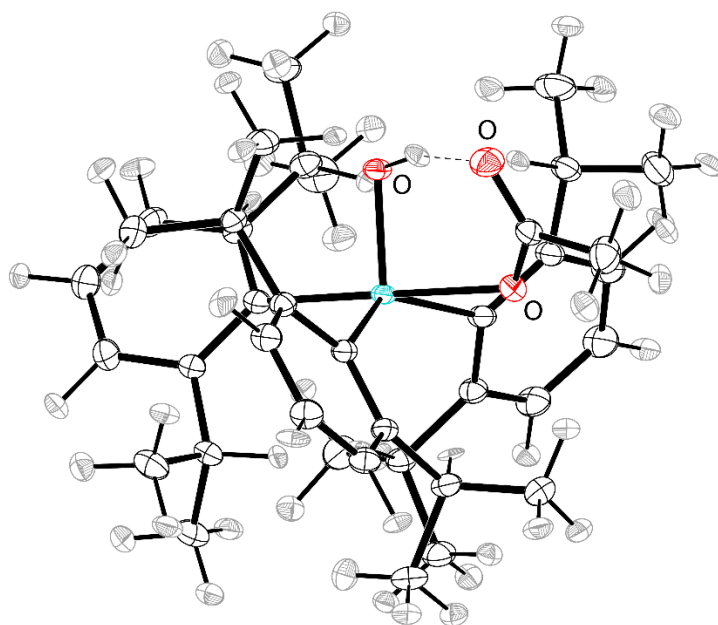
**Figure B.100.** Thermal ellipsoid plot (50% probability) of *cis*-Sb(OH)(OAc)Dipp$_3$. Color code: Sb teal, O red, C black, H grey. The Sb–O bond lengths in *cis*-Sb(OH)(OAc)Dipp$_3$ are 1.916(1) Å (equatorial hydroxo) and 2.320(1) Å (axial acetato). CCDC 2133041.
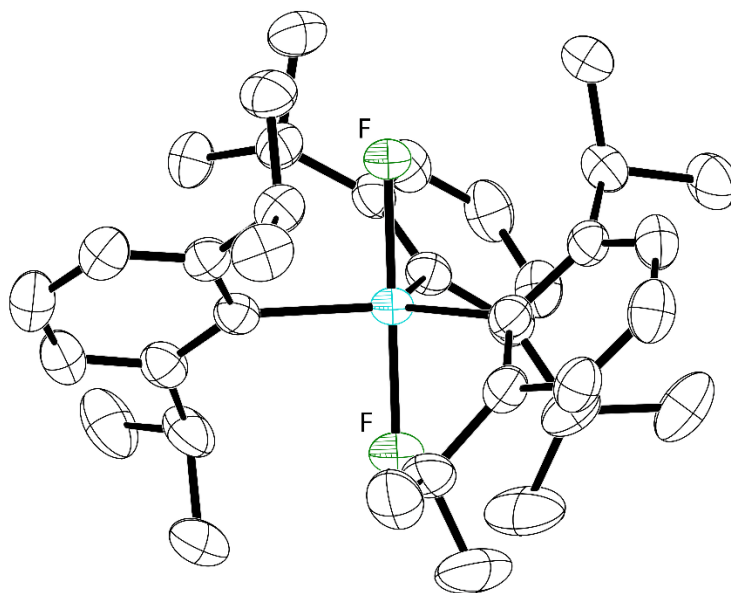


**Figure B.101.** Thermal ellipsoid plot (50% probability) of Dipp$_3$SbF$_2$. H atoms omitted for clarity. Color code: Sb teal, C black, F green. CCDC 2133042.
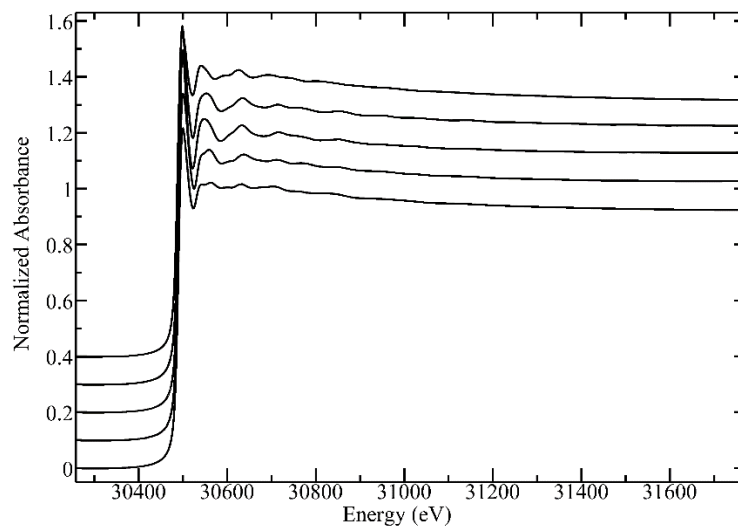
**Figure B.102.** Full normalized Sb K-edge XAS spectra for (*top to bottom*) Dipp₃Sb, **A**, **B**, **C**, Dipp₃SbO.
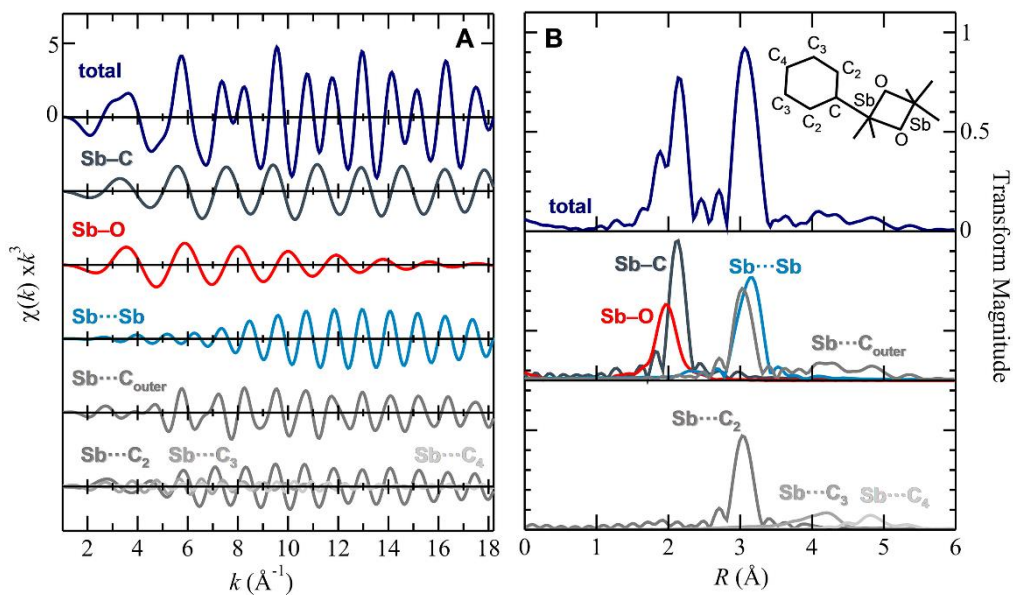


**Figure B.103.** Breakdown of EXAFS curve-fitting components (A) and corresponding Sb–C phase-corrected Fourier transforms (B) for compound **A**, showing major components and summed outer-shell C components; the inset in B shows the core used to model the spectra. The overlap of the Sb⋯Sb interaction and the Sb⋯C₂ gives rise to the intense Fourier transform peak at 3.1 Å.
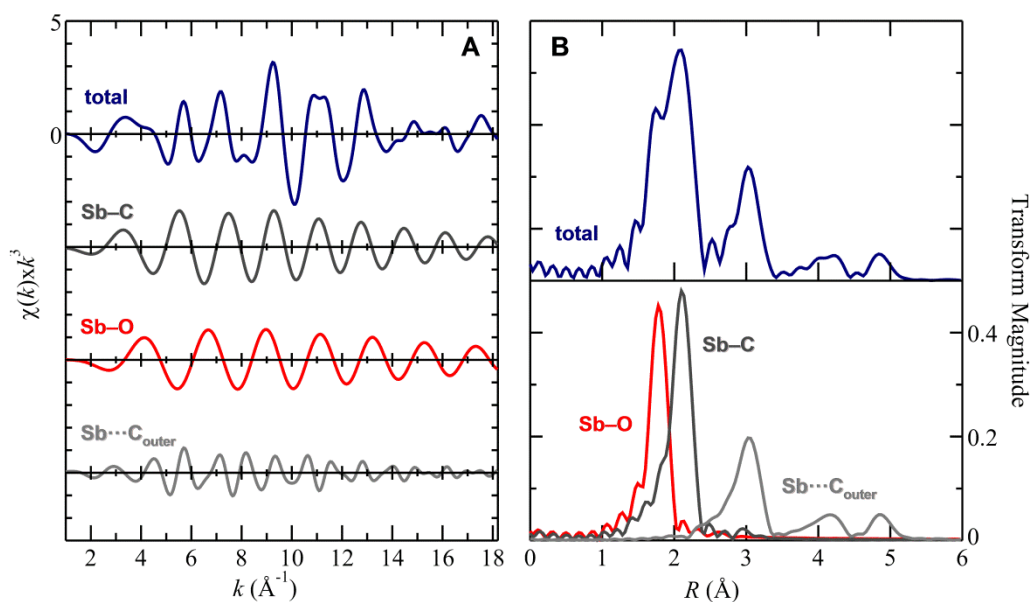
**Figure B.104.** Breakdown of EXAFS curve-fitting components (A) and corresponding Sb–C phase-corrected Fourier transforms (B) for compound Dipp$_3$SbO, showing major components and summed outer-shell C components.

**Table B.1.** Crystallographic details for Dipp$_3$Sb, Dipp$_3$As, Dipp$_3$P, and Dipp$_3$SbO(orthorhombic).

| Compound | Dipp$_3$Sb | Dipp$_3$As | Dipp$_3$P | Dipp$_3$SbO(orthorhombic) |
|---|---|---|---|---|
| Empirical formula | C$_{36}$H$_{51}$Sb | C$_{36}$H$_{51}$As | c$_{36}$H$_{51}$P | C$_{36}$H$_{51}$OSb |
| Formula weight | 605.51 | 558.68 | 514.73 | 621.51 |
| Temperature (K) | 100.0(1) | 100.0(1) | 100.0(1) | 100.0(1) |
| Wavelength (Å) | 1.54184 | 1.54184 | 1.54184 | 1.54184 |
| Crystal system | Cubic | Trigonal | Trigonal | Orthorhombic |
| Space group | $I\bar{4}3d$ | $R3$ | $R3$ | $Pbca$ |
| $a$ (Å) | 23.57660(10) | 16.5325(3) | 16.4276(3) | 17.4672(2) |
| $b$ (Å) | | | | 17.2872(1) |
| $c$ (Å) | | 10.1989(2) | 10.2126(2) | 21.0673(2) |
| Volume (Å$^3$) | 13105.20(17) | 2414.13(10) | 2386.79(10) | 21.0673(2) |
| $Z$ | 16 | 3 | 3 | 8 |
| $\rho_{calc}$ (Mg/m$^3$) | 1.228 | 1.153 | 1.074 | 1.298 |
| Crystal size (mm$^3$) | 0.1×0.09×0.07 | 0.09×0.06×0.0 | 0.1×0.07×0.05 | 0.15×0.11×0.0 |
| θ range (°) | 4.594 to 66.958 | 5.325 to | 5.332 to | 4.165 to |
| Total reflections | 43467 | 9258 | 5257 | 43495 |
| Unique | 1955 | 1908 | 1267 | 6653 |
| Method | IAM | IAM | IAM | IAM |
| Parameters | 176 | 117 | 117 | 355 |
| Completeness | 100 | 100.0 | 99.7 | 100.0 |
| R$_{int}$ | 0.0499 | 0.0438 | 0.0265 | 0.0368 |
| R$_1$ (I > 2σ) | 0.0403 | 0.0301 | 0.0277 | 0.0250 |
| R$_1$ (all data) | 0.0404 | 0.0302 | 0.0281 | 0.0287 |
| wR$_2$ (I > 2σ) | 0.1038 | 0.0768 | 0.0725 | 0.0620 |
| wR$_2$ (all data) | 0.1039 | 0.0768 | 0.0727 | 0.0640 |
| Goodness of fit, $S$ | 1.159 | 1.055 | 1.115 | 1.082 |

**Table B.2.** Crystallographic details for Dipp$_3$SbO(monoclinic) and Dipp$_3$AsO.

| Compound | Dipp$_3$SbO(monoclinic) | | Dipp$_3$AsO | |
|---|---|---|---|---|
| Empirical formula | C$_{36}$H$_{51}$OSb | | C$_{36}$H$_{51}$AsO | |
| Formula weight | 621.51 | | 574.68 | |
| Temperature (K) | 100.0(1) | | 100.0(1) | |
| Wavelength (Å) | 0.71073 | | 1.54184 | |
| Crystal system | Monoclinic | | Trigonal | |
| Space group | *P2$_1$/c* | | *R*3 | |
| *a* (Å) | 9.8768(1) | | 16.7925(3) | |
| *b* (Å) | 16.3435(2) | | | |
| *c* (Å) | 20.0481(3) | | 9.8907(3) | |
| β (°) | 101.240(1) | | | |
| Volume (Å$^3$) | 3174.12(7) | | 2415.40(11) | |
| *Z* | 4 | | 3 | |
| ρ$_{calc}$ (Mg/m$^3$) | 1.301 | | 1.185 | |
| Crystal size (mm$^3$) | 0.59×0.39×0.23 | | 0.13×0.07×0.05 | |
| θ range (°) | 2.417 to 30.033 | | 5.268 to 66.963 | |
| Total reflections | 93669 | | 7302 | |
| Unique reflections | 9259 | | 1848 | |
| Method | IAM | HAR | IAM | HAR |
| Parameters | 355 | 802 | 120 | 269 |
| Completeness | 99.9 | 99.9 | 100.0 | 100.0 |
| R$_{int}$ | 0.0385 | 0.0385 | 0.0402 | 0.0402 |
| R$_1$ (I > 2σ) | 0.0185 | 0.0124 | 0.0251 | 0.0233 |
| R$_1$ (all data) | 0.0196 | 0.0135 | 0.0252 | 0.0233 |
| wR$_2$ (I > 2σ) | 0.0446 | 0.0244 | 0.0611 | 0.0534 |
| wR$_2$ (all data) | 0.0451 | 0.0246 | 0.0611 | 0.0534 |
| Goodness of fit, *S* | 1.054 | 1.0903 | 1.046 | 1.0810 |

**Table B.3.** Crystallographic details for $Dipp_3PO$ and $Dipp_3SbO·H_2NPhF$.

| Compound | $Dipp_3PO$ | | $Dipp_3SbO·H_2NPhF$ | |
|---|---|---|---|---|
| Empirical formula | $C_{36}H_{51}PO$ | | $C_{42}H_{57}FNOSb$ | |
| Formula weight | 530.73 | | 732.63 | |
| Temperature (K) | 100.0(1) | | 100.0(1) | |
| Wavelength (Å) | 1.54184 | | 0.71073 | |
| Crystal system | Trigonal | | Monoclinic | |
| Space group | $R3$ | | $C2/c$ | |
| $a$ (Å) | 16.7252(3) | | 21.5840(4) | |
| $b$ (Å) | | | 16.9212(2) | |
| $c$ (Å) | 9.8790(2) | | 22.4080(4) | |
| $β$ (°) | | | 109.562(2) | |
| Volume (Å$^3$) | 2393.24(10) | | 7711.6(2) | |
| $Z$ | 3 | | 8 | |
| $ρ_{calc}$ (Mg/m$^3$) | 1.105 | | 1.262 | |
| Crystal size (mm$^3$) | 0.1×0.06×0.04 | | 0.37×0.10×0.05 | |
| θ range (°) | 5.289 to 66.828 | | 2.209 to 30.508 | |
| Total reflections | 7135 | | 81207 | |
| Unique reflections | 1894 | | 11781 | |
| Method | IAM | HAR | IAM | HAR |
| Parameters | 120 | 269 | 435 | 928 |
| Completeness | 100.0 | 100.0 | 99.9 | 99.9 |
| $R_{int}$ | 0.0253 | 0.0253 | 0.0439 | 0.0439 |
| $R_1$ (I > 2σ) | 0.0231 | 0.0133 | 0.0240 | 0.0189 |
| $R_1$ (all data) | 0.0233 | 0.0136 | 0.0293 | 0.0240 |
| $wR_2$ (I > 2σ) | 0.0591 | 0.0290 | 0.0599 | 0.0407 |
| $wR_2$ (all data) | 0.0592 | 0.0291 | 0.0620 | 0.0422 |
| Goodness of fit, $S$ | 1.067 | 1.0849 | 1.047 | 1.0253 |

**Table B.4.** Crystallographic details for $Dipp_3SbOCuCl·(CHCl_3)_2$, $[Ag(Dipp_3SbO)_2](CF_3SO_3)·OEt_2$, $[Dipp_3SbOAuPPh_3][CF_3SO_3]$-bent, and $[Dipp_3SbOAuPPh_3][CF_3SO_3]$-linear.

| Compound | $Dipp_3SbOCuCl·(CHCl_3)_2$ | $[Ag(Dipp_3SbO)_2](CF_3SO_3)·OEt_2$ | $[Dipp_3SbOAuPPh_3][CF_3SO_3]$-bent | $[Dipp_3SbOAuPPh_3][CF_3SO_3]$-linear |
|---|---|---|---|---|
| Empirical formula | $C_{38}H_{53}Cl_7CuOSb$ | $C_{77}H_{112}AgF_3O_6SSb_2$ | $C_{55}H_{66}AuF_3O_4PSSb$ | $C_{55}H_{66}AuF_3O_4PSSb$ |
| Formula weight | 959.24 | 1574.09 | 1229.82 | 1229.82 |
| Temperature (K) | 100.0(1) | 100.0(1) | 100.0(1) | 100.0(1) |
| Wavelength (Å) | 1.54184 | 1.54184 | 1.54184 | 1.54184 |
| Crystal system | Triclinic | Triclinic | Triclinic | Trigonal |
| Space group | $P\bar{1}$ | $P\bar{1}$ | $P\bar{1}$ | $R\bar{3}$ |
| $a$ (Å) | 10.4183(3) | 13.9579(2) | 11.91490(1) | 14.5599(2) |
| $b$ (Å) | 12.3198(2) | 16.4020(2) | 14.9286(2) | |
| $c$ (Å) | 18.2971(4) | 17.5587(2) | 15.2073(2) | 44.5120(8) |
| $\alpha$ (°) | 75.022(2) | 104.8710(10) | 99.7460(1) | |
| $\beta$ (°) | 79.759(2) | 100.3270(10) | 90.0020(10) | |
| $\gamma$ (°) | 67.747(2) | 93.9180(10) | 96.7000(1) | |
| Volume (Å$^3$) | 2091.30(9) | 3794.53(9) | 2647.18(6) | 8171.9(3) |
| $Z$ | 2 | 2 | 2 | 6 |
| $\rho_{calc}$ (Mg/m$^3$) | 1.523 | 1.378 | 1.543 | 1.499 |
| Crystal size (mm$^3$) | 0.09×0.07×0.05 | 0.22×0.09×0.07 | 0.17×0.06×0.05 | 0.22×0.17×0.09 |
| $\theta$ range (°) | 2.510 to 67.074 | 2.660 to 70.074 | 2.949 to 67.076 | 2.978 to 67.075 |
| Total reflections | 27551 | 93501 | 79065 | 23949 |
| Unique reflections | 7464 | 14385 | 9456 | 3258 |
| Method | IAM | IAM | IAM | IAM |
| Parameters | 445 | 881 | 607 | 227 |
| Completeness | 99.9 | 99.9 | 100.0 | 99.9 |
| $R_{int}$ | 0.0422 | 0.0623 | 0.0468 | 0.0609 |
| $R_1$ ($I > 2\sigma$) | 0.0236 | 0.0324 | 0.0206 | 0.0466 |
| $R_1$ (all data) | 0.0253 | 0.0351 | 0.0218 | 0.0586 |
| $wR_2$ ($I > 2\sigma$) | 0.0562 | 0.0841 | 0.0504 | 0.1167 |
| $wR_2$ (all data) | 0.0570 | 0.0863 | 0.0511 | 0.1330 |
| Goodness of fit, $S$ | 1.054 | 1.030 | 1.033 | 1.076 |

**Table B.5.** Crystallographic details for [Dipp$_3$SbOH][O$_3$SPh] and [Dipp$_3$AsOH][O$_3$SPh].

| Compound | [Dipp$_3$SbOH][O$_3$SPh] | | [Dipp$_3$AsOH][O$_3$SPh] | |
|---|---|---|---|---|
| Empirical formula | C$_{42}$H$_{57}$O$_4$SSb | | C$_{42}$H$_{57}$AsO$_4$S | |
| Formula weight | 779.68 | | 732.85 | |
| Temperature (K) | 100.0(1) | | 100.0(1) | |
| Wavelength (Å) | 0.71073 | | 0.71073 | |
| Crystal system | Monoclinic | | Orthorhombic | |
| Space group | *P*2$_1$/*n* | | *Pna*2$_1$ | |
| *a* (Å) | 10.5230(2) | | 20.4704(6) | |
| *b* (Å) | 17.9547(4) | | 11.7243(3) | |
| *c* (Å) | 20.0882(4) | | 16.4581(5) | |
| α (°) | | | | |
| β (°) | 92.246(2) | | | |
| γ (°) | | | | |
| Volume (Å$^3$) | 3792.49(13) | | 3949.96 | |
| *Z* | 4 | | 4 | |
| ρ$_{calc}$ (Mg/m$^3$) | 1.366 | | 1.232 | |
| Crystal size (mm$^3$) | 0.24×.2×0.13 | | 0.44×0.24×0.1 | |
| θ range (°) | 2.43 to 29.57 | | 2.343 to 29.57 | |
| Total reflections | 49940 | | 51691 | |
| Unique reflections | 10627 | | 12957 | |
| Method | IAM | HAR | IAM | HAR |
| Parameters | 449 | 946 | 450 | 606 |
| Completeness | 99.9 | 99.9 | 99.9 | 99.9 |
| R$_{int}$ | 0.0462 | 0.0462 | 0.0504 | 0.0527 |
| R$_1$ (I > 2σ) | 0.0264 | 0.0217 | 0.0517 | 0.0456 |
| R$_1$ (all data) | 0.0320 | 0.0272 | 0.0665 | 0.0520 |
| wR$_2$ (I > 2σ) | 0.0588 | 0.0414 | 0.1218 | 0.1117 |
| wR$_2$ (all data) | 0.0611 | 0.0432 | 0.13 | 0.1170 |
| Goodness of fit, *S* | 1.060 | 1.0263 | 1.031 | 1.0054 |

**Table B.6.** Crystallographic details for *cis*-Sb(OH)(OAc)Dipp$_3$ and Dipp$_3$SbF$_2$.

| Compound | *cis*-Sb(OH)(OAc)Dipp$_3$ | | Dipp$_3$SbF$_2$ |
|---|---|---|---|
| Empirical formula | C$_{38}$H$_{55}$O$_3$Sb | | C$_{36}$H$_{51}$F$_2$Sb |
| Formula weight | 681.57 | | 643.51 |
| Temperature (K) | 100.0(1) | | 100.0(1) |
| Wavelength (Å) | 0.71073 | | 1.54184 |
| Crystal system | Monoclinic | | Cubic |
| Space group | *P*2$_1$/*c* | | *I*$\bar{4}$3*d* |
| *a* (Å) | 10.1367(3) | | 23.7603(2) |
| *b* (Å) | 18.3322(4) | | |
| *c* (Å) | 19.0827(5) | | |
| β (°) | 102.117(3) | | |
| Volume (Å$^3$) | 3467.09(15) | | 13413.9(3) |
| *Z* | 4 | | 16 |
| ρ$_{calc}$ (Mg/m$^3$) | 1.306 | | 1.275 |
| Crystal size (mm$^3$) | 0.171×0.087×0.074 | | 0.21×0.14×0.13 |
| θ range (°) | 2.183 to 33.142 | | 4.558 to 66.925 |
| Total reflections | 51848 | | 16123 |
| Unique reflections | 13207 | | 1998 |
| Method | IAM | HAR | IAM |
| Parameters | 396 | 874 | 123 |
| Completeness | 99.9 | 99.9 | 100.0 |
| R$_{int}$ | 0.0529 | 0.0529 | 0.0239 |
| R$_1$ (I > 2σ) | 0.0355 | 0.0324 | 0.0222 |
| R$_1$ (all data) | 0.0578 | 0.0547 | 0.0229 |
| wR$_2$ (I > 2σ) | 0.0747 | 0.0609 | 0.0561 |
| wR$_2$ (all data) | 0.0820 | 0.0675 | 0.0565 |
| Goodness of fit, *S* | 1.024 | 1.0457 | 1.121 |

**Table B.7.** EXAFS parameters for Dipp$_3$Sb, **A**, **B**, **C**, and Dipp$_3$SbO.[a]

| Sample | Backscatterer[b] | $N$ | $R$ (Å) | $\sigma^2$ (Å$^2$) | $\Delta E_0$ (eV) | $F$ [c] |
|---|---|---|---|---|---|---|
| Dipp$_3$Sb | C | 3 | 2.200(2) | 0.0026(1) | −13.3(6) | 0.316 |
| **A** | O | 1 | 1.967(4) | 0.0025(2) | −15.8(4) | 0.221 |
| | O | 1 | 2.049(5) | 0.0028(2) | | |
| | C | 3 | 2.150(1) | 0.0022(1) | | |
| | Sb | 1 | 3.148(3) | 0.0025(3) | | |
| **B** | O | 2 | 2.128(3) | 0.0019(2) | −13.5(5) | 0.222 |
| | C | 3 | 2.077(4) | 0.0052(3) | | |
| **C** | O | 1 | 1.905(1) | 0.0019(1) | −16.5(4) | 0.249 |
| | C | 3 | 2.136(1) | 0.0024(1) | | |
| Dipp$_3$SbO | O | 1 | 1.837(2) | 0.0021(1) | −15.7(6) | 0.319 |
| | C | 3 | 2.165(2) | 0.0031(1) | | |

[a] $N$, coordination number; $R$, interatomic distance; $\sigma^2$, mean-square deviation in $R$ (Debye-Waller factor); $\Delta E_0$, threshold energy shift. Values in parentheses are estimated standard deviations. [b] Only the first-shell or Sb-Sb contributions (in the case of **A**) are shown in the table. Outer C shells were as described in the experimental section. [c] $F = [\Sigma k^6(\chi_{calc}(k) - \chi_{exp}(k))^2 / \Sigma k^6(\chi_{exp}(k))^2]^{0.5}$ in which $\chi_{exp}(k)$ and $\chi_{calc}(k)$ are the experimental and calculated EXAFS, respectively, and the summations are over all points included within the fitted $k$-range, which in all cases was 1-18.1 Å$^{-1}$.

**Table B.8.** Energy Decomposition Analysis (PBE0/QZVP) of Dipp$_3$SbO.[h]

| | $E_{SCF}$(first, Dipp$_3$SbO)[a] | $E_{SCF}$(last, Dipp$_3$SbO)[b] | $E_{SCF}$(Dipp$_3$Sb)[c] | $E_{SCF}$(O)[d] | $\Delta E_{tot}$[e] | $\Delta E_{orb}$[f] | $\Delta E_{steric}$[g] |
|---|---|---|---|---|---|---|---|
| Energy (a.u) | -3550.882 | -3552.812 | -3476.568 | -74.910 | -1.333 | -1.930 | 0.597 |
| Energy (kJ/mol) | -9322688 | -9327755 | -9127580 | -196674 | -3501 | -5068 | 1567 |

[a] Energy of Dipp$_3$SbO with no orbital interaction between O atom and Dipp$_3$Sb fragments. [b] Energy of Dipp$_3$SbO. [c] Energy of Dipp$_3$Sb at optimized coordinates for Dipp$_3$SbO. [d] Energy of O atom. [e] Difference in energy of Dipp$_3$SbO and the sum of the O and Dipp$_3$Sb fragments; the total energy afforded by interaction of the fragments. [f] Difference in energy between **$E_{SCF}$(last, Dipp$_3$SbO)** and **$E_{SCF}$(first, Dipp$_3$SbO)**; the energy of stabilization afforded by orbital interaction between the Dipp$_3$Sb and O atom fragments. [g] Difference between $\Delta E_{tot}$ and $\Delta E_{orb}$. [h] $\Delta E_{orb}/\Delta E_{tot}$ = 1.45.

**Table B.9.** Energy Decomposition Analysis (PBE0/TZVP) of $Dipp_3AsO$.[h]

| | $E_{SCF}$(first, $Dipp_3AsO$)[a] | $E_{SCF}$(last, $Dipp_3AsO$)[b] | $E_{SCF}$($Dipp_3As$)[c] | $E_{SCF}$(O)[d] | $\Delta E_{tot}$[e] | $\Delta E_{orb}$[f] | $\Delta E_{steric}$[g] |
|---|---|---|---|---|---|---|---|
| Energy (a.u) | -3711.344 | -3712.025 | -3636.863 | -74.908 | -0.255 | -0.681 | 0.427 |
| Energy (kJ/mol) | -9743974 | -9745763 | -9548428 | -196666 | -669 | -1789 | 1120 |

[a] Energy of $Dipp_3AsO$ with no orbital interaction between O atom and $Dipp_3As$ fragments. [b] Energy of $Dipp_3AsO$. [c] Energy of $Dipp_3As$ at optimized coordinates for $Dipp_3AsO$. [d] Energy of O atom. [e] Difference in energy of $Dipp_3AsO$ and the sum of the O and $Dipp_3As$ fragments; the total energy afforded by interaction of the fragments. [f] Difference in energy between $E_{SCF}$**(last, $Dipp_3AsO$)** and $E_{SCF}$**(first, $Dipp_3AsO$)**; the energy of stabilization afforded by orbital interaction between the $Dipp_3As$ and O atom fragments. [g] Difference between $\Delta E_{tot}$ and $\Delta E_{orb}$. [h] $\Delta E_{orb}/\Delta E_{tot}$ = 2.67.

**Table B.10.** Energy Decomposition Analysis (PBE0/TZVP) of $Dipp_3PO$.[h]

| | $E_{SCF}$(first, $Dipp_3PO$)[a] | $E_{SCF}$(last, $Dipp_3PO$)[b] | $E_{SCF}$($Dipp_3P$)[c] | $E_{SCF}$(O)[d] | $\Delta E_{tot}$[e] | $\Delta E_{orb}$[f] | $\Delta E_{steric}$[g] |
|---|---|---|---|---|---|---|---|
| Energy (a.u) | -1816.690 | -1817.690 | -1742.494 | -74.908 | -0.289 | -1.000 | 0.711 |
| Energy (kJ/mol) | -4769642 | -4772268 | -4574843 | -196667 | -759 | -2626 | 1867 |

[a] Energy of $Dipp_3PO$ with no orbital interaction between O atom and $Dipp_3P$ fragments. [b] Energy of $Dipp_3PO$. [c] Energy of $Dipp_3P$ at optimized coordinates for $Dipp_3PO$. [d] Energy of O atom. [e] Difference in energy of $Dipp_3PO$ and the sum of the O and $Dipp_3P$ fragments; the total energy afforded by interaction of the fragments. [f] Difference in energy between $E_{SCF}$**(last, $Dipp_3PO$)** and $E_{SCF}$**(first, $Dipp_3PO$)**; the energy of stabilization afforded by orbital interaction between the $Dipp_3P$ and O atom fragments. [g] Difference between $\Delta E_{tot}$ and $\Delta E_{orb}$. [h] $\Delta E_{orb}/\Delta E_{tot}$ = 3.46.

**Table B.11.** Values of ρ (e⁻ Å⁻³), $\nabla^2\rho$ (e⁻ Å⁻⁵), ε, and normalized distance at the Pn–O and O–A bond critical points for compounds.

| Compound | Bond | Density | Laplacian | Ellipticity | Distance |
|---|---|---|---|---|---|
| Dipp₃PO | P–O | 0.231744 | 1.386415 | 0.005527 | 0.403333 |
| Dipp₃AsO | As–O | 0.215627 | 0.718006 | 0.003327 | 0.479333 |
| Dipp₃SbO | Sb–O | 0.173485 | 0.649753 | 0.007443 | 0.519 |
| Dipp₃SbO·H₂NPhF | Sb–O | 0.167596 | 0.618702 | 0.002694 | 0.518 |
| Dipp₃SbO·H₂NPhF | O–H | 0.033441 | 0.094247 | 0.014997 | 0.651333 |
| Dipp₃SbOCuCl | Sb–O | 0.159136 | 0.613314 | 0.017536 | 0.516 |
| Dipp₃SbOCuCl | O–Cu | 0.111688 | 0.617602 | 0.001759 | 0.506667 |
| (Dipp₃SbO)₂Ag⁺ | Sb–O | 0.138281 | 0.444832 | 0.026744 | 0.513667 |
| (Dipp₃SbO)₂Ag⁺ | Sb–O | 0.138001 | 0.441971 | 0.027642 | 0.513667 |
| (Dipp₃SbO)₂Ag⁺ | O–Ag | 0.082517 | 0.404382 | 0.006623 | 0.472667 |
| (Dipp₃SbO)₂Ag⁺ | O–Ag | 0.082408 | 0.403461 | 0.00692 | 0.472667 |
| Dipp₃SbOAuPPh₃⁺-linear | Sb–O | 0.151297 | 0.624267 | 1.96E-05 | 0.515 |
| Dipp₃SbOAuPPh₃⁺-linear | O–Au | 0.129511 | 0.581037 | 3.71E-05 | 0.463 |
| Dipp₃SbOAuPPh₃⁺-bent | Sb–O | 0.149506 | 0.536553 | 0.041721 | 0.513667 |
| Dipp₃SbOAuPPh₃⁺-bent | O–Au | 0.108848 | 0.417859 | 0.011227 | 0.469 |
| [Dipp₃AsOH][O₃SPh] | O–H | 0.499385 | -4.89632 | 0.008756 | 0.846666 |
| [Dipp₃AsOH][O₃SPh] | As–O | 0.174469 | 0.473733 | 0.071716 | 0.471 |
| [Dipp₃SbOH][O₃SPh] | Sb–O | 0.144227 | 0.508145 | 0.075903 | 0.511333 |
| [Dipp₃SbOH][O₃SPh] | O–H | 0.346279 | -2.67294 | 0.005965 | 0.832334 |
| *cis*-Sb(OH)(OAc)Dipp₃ | Sb–O | 0.14362 | 0.497205 | 0.086585 | 0.510667 |
| *cis*-Sb(OH)(OAc)Dipp₃ | O–H | 0.318796 | -2.30282 | 0.006293 | 0.823333 |
| **A** | Sb–O | 0.136971 | 0.48016 | 0.088189 | 0.510667 |
| **A** | Sb–O | 0.136974 | 0.480125 | 0.088186 | 0.510667 |
| **A** | O–Sb | 0.100908 | 0.300082 | 0.043538 | 0.495667 |
| **A** | O–Sb | 0.100914 | 0.300104 | 0.043552 | 0.495667 |
| **B** | Sb–O | 0.10889 | 0.344495 | 0.080336 | 0.506667 |
| **B** | Sb–O | 0.110226 | 0.354613 | 0.082158 | 0.506667 |
| **B** | O–H | 0.374205 | -2.72717 | 0.007813 | 0.806333 |
| **B** | O–H | 0.374768 | -2.72953 | 0.007735 | 0.806001 |

**Table B.12.** Values of $\rho$ (e$^-$ Å$^{-3}$), $\nabla^2\rho$ (e$^-$ Å$^{-5}$), $\varepsilon$ and normalized distance at the O$\cdots$H bond critical points for compounds Dipp$_3$PnO. Benzylic H atoms are denoted "H$_b$" and terminal H atoms are denoted "H$_t$."

| Compound | Bond | Density | Laplacian | Ellipticity | Distance |
|---|---|---|---|---|---|
| Dipp$_3$SbO | O–H$_b$ | 0.018671 | 0.061694 | 0.63093 | 0.613 |
| Dipp$_3$SbO | O–H$_t$ | 0.012762 | 0.047758 | 0.161681 | 0.599667 |
| Dipp$_3$SbO | O–H$_b$ | 0.023615 | 0.081046 | 0.057021 | 0.622333 |
| Dipp$_3$AsO | O–H$_b$ | 0.01884 | 0.06796 | 0.164366 | 0.604333 |
| Dipp$_3$AsO | O–H$_t$ | 0.011732 | 0.044857 | 0.312139 | 0.588 |
| Dipp$_3$AsO | O–H$_b$ | 0.01601 | 0.057627 | 0.180082 | 0.597333 |
| Dipp$_3$AsO | O–H$_t$ | 0.00933 | 0.035151 | 0.352238 | 0.584 |
| Dipp$_3$AsO | O–H$_b$ | 0.017945 | 0.065737 | 0.048447 | 0.599667 |
| Dipp$_3$AsO | O–H$_t$ | 0.010691 | 0.040523 | 0.258594 | 0.589333 |
| Dipp$_3$PO | O–H$_b$ | 0.018748 | 0.069759 | 0.083155 | 0.6 |
| Dipp$_3$PO | O–H$_t$ | 0.012736 | 0.050405 | 0.299645 | 0.588666 |
| Dipp$_3$PO | O–H$_b$ | 0.016223 | 0.060218 | 0.091032 | 0.593333 |
| Dipp$_3$PO | O–H$_t$ | 0.009108 | 0.035358 | 0.402915 | 0.581 |
| Dipp$_3$PO | O–H$_b$ | 0.017205 | 0.064809 | 0.071469 | 0.592667 |
| Dipp$_3$PO | O–H$_t$ | 0.010698 | 0.041732 | 0.286604 | 0.586667 |

**Table B.13.** Values of $\rho$ ($e^- \text{ Å}^{-3}$), $\nabla^2\rho$ ($e^- \text{ Å}^{-5}$), $\varepsilon$, and normalized distance at the $O\cdots H$ bond critical points for compounds $Dipp_3SbO$, $Dipp_3SbO\cdot H_2NPhF$, $Dipp_3SbOCuCl$, $(Dipp_3SbO)_2Ag^+$, $Dipp_3SbOAuPPh_3{}^+$-bent, and $Dipp_3SbOAuPPh_3{}^+$-linear.

| Compound | Bond | Density | Laplacian | Ellipticity | Distance |
|---|---|---|---|---|---|
| $Dipp_3SbO$ | $O–H_b$ | 0.018671 | 0.061694 | 0.63093 | 0.613 |
| $Dipp_3SbO$ | $O–H_t$ | 0.012762 | 0.047758 | 0.161681 | 0.599667 |
| $Dipp_3SbO$ | $O–H_b$ | 0.023615 | 0.081046 | 0.057021 | 0.622333 |
| $Dipp_3SbO\cdot H_2NPhF$ | $O–H$ | 0.007079 | 0.02545 | 0.510233 | 0.579 |
| $Dipp_3SbO\cdot H_2NPhF$ | $O–H$ | 0.016597 | 0.056964 | 0.187168 | 0.606 |
| $Dipp_3SbO\cdot H_2NPhF$ | $O–H$ | 0.011361 | 0.040819 | 0.128828 | 0.598333 |
| $Dipp_3SbO\cdot H_2NPhF$ | $O–H$ | 0.012608 | 0.041409 | 0.450714 | 0.595 |
| $Dipp_3SbO\cdot H_2NPhF$ | $O–H$ | 0.022207 | 0.07324 | 0.150897 | 0.622667 |
| $Dipp_3SbOCuCl$ | $O–H$ | 0.010153 | 0.038057 | 0.164826 | 0.590333 |
| $Dipp_3SbOCuCl$ | $O–H$ | 0.011889 | 0.040616 | 0.635793 | 0.590667 |
| $Dipp_3SbOCuCl$ | $O–H$ | 0.010164 | 0.038137 | 0.441307 | 0.588667 |
| $Dipp_3SbOCuCl$ | $O–H$ | 0.016469 | 0.055848 | 0.582978 | 0.612333 |
| $(Dipp_3SbO)_2Ag^+$ | $O–H$ | 0.016853 | 0.059598 | 0.201279 | 0.604333 |
| $(Dipp_3SbO)_2Ag^+$ | $O–H$ | 0.01618 | 0.054692 | 0.317991 | 0.610667 |
| $(Dipp_3SbO)_2Ag^+$ | $O–H$ | 0.00648 | 0.022634 | 0.296603 | 0.579667 |
| $(Dipp_3SbO)_2Ag^+$ | $O–H$ | 0.013719 | 0.044987 | 0.882015 | 0.599667 |
| $Dipp_3SbOAuPPh_3{}^+$-linear | $O–H$ | 0.015856 | 0.05566 | 0.259779 | 0.602333 |
| $Dipp_3SbOAuPPh_3{}^+$linear | $O–H$ | 0.015854 | 0.055679 | 0.259967 | 0.602333 |
| $Dipp_3SbOAuPPh_3{}^+$-linear | $O–H$ | 0.015858 | 0.055662 | 0.25959 | 0.602333 |
| $Dipp_3SbOAuPPh_3{}^+$-bent | $O–H$ | 0.019006 | 0.066428 | 0.139138 | 0.615 |
| $Dipp_3SbOAuPPh_3{}^+$-bent | $O–H$ | 0.007431 | 0.027378 | 0.310596 | 0.580667 |
| $Dipp_3SbOAuPPh_3{}^+$-bent | $O–H$ | 0.022128 | 0.07885 | 0.163286 | 0.614334 |

**Table B.14.** Select donor–acceptor interactions found from 2$^{nd}$ order perturbation theory analysis (DKH-PBE0/old-DKH-TZVPP//PBE0/def2-TZVPP) for $Dipp_3SbO$.

| Donor NBO | Acceptor NBO | Energy of stabilization (kcal/mol) |
|---|---|---|
| 62. LP ( 2) O  2 | 165. BD*( 1)Sb  1- C  3 | 4.04 |
| 62. LP ( 2) O  2 | 166. BD*( 1)Sb  1- C 15 | 11.30 |
| 62. LP ( 2) O  2 | 167. BD*( 1)Sb  1- C 27 | 2.61 |
| 63. LP ( 3) O  2 | 165. BD*( 1)Sb  1- C  3 | 8.46 |
| 63. LP ( 3) O  2 | 167. BD*( 1)Sb  1- C 27 | 9.45 |
| 63. LP ( 3) O  2 | 248. BD*( 1) C 33- H 73 | 3.38 |
| 62. LP ( 2) O  2 | 184. BD*( 1) C  9- H 41 | 1.46 |
| 62. LP ( 2) O  2 | 220. BD*( 1) C 23- H 61 | 0.68 |

**Table B.15.** Select results from NBO analysis of compounds.

| Compound | NPA Pn[a] | NPA O[b] | NPA A[c] | WBI PnO[d] | WBI OA[e] | NLMO %Pn[f] | NLMO %O[g] | NLMO Pn%s[h] | NLMO Pn%p[i] | NLMO O%s[j] | NLMO O%p[k] | E2 PnC[l] | E2 CH[m,q] | E2 OA[n] |
|---|---|---|---|---|---|---|---|---|---|---|---|---|---|---|
| Dipp₃PO | 1.913 | -1.126 | NA | 1.09 | NA | 25 | 74 | 32 | 67 | 38 | 62 | 62 | 0 | NA |
| Dipp₃AsO | 1.844 | -1.144 | NA | 1.03 | NA | 28 | 71 | 34 | 65 | 25 | 75 | 46 | 0.50 | NA |
| Dipp₃SbO | 2.157 | -1.241 | NA | 0.94 | NA | 25 | 74 | 39 | 61 | 21 | 79 | 36 | 5.52 | NA |
| Dipp₃SbO·H₂NPhF | 2.218 | -1.278 | 0.441 | 0.88 | 0.04 | 24 | 75 | 37 | 62 | 21 | 78 | 31 | 4.65 | 13 |
| Dipp₃SbOCuCl | 2.235 | -1.331 | 0.675 | 0.75 | 0.18 | 20 | 79 | 33 | 66 | 26 | 74 | 22 | 1.06 | 63 |
| (Dipp₃SbO)₂Ag⁺[o] | 1.975 | -1.139 | 0.766 | 0.85 | 0.21 | 24 | 74 | 36 | 64 | 18 | 82 | 21 | 3.05 | 39 |
| Dipp₃SbOAuPPh₃⁺-linear | 2.252 | -1.350 | 0.466 | 0.65 | 0.25 | 17 | 81 | 31 | 68 | 21 | 79 | 21 | 1.23 | 58 |
| Dipp₃SbOAuPPh₃⁺-bent | 2.228 | -1.276 | 0.437 | 0.70 | 0.26 | 20 | 79 | 32 | 68 | 24 | 76 | 18 | 4.16 | 79 |
| [Dipp₃AsOH][O₃SPh] | 1.844 | -0.944 | 0.504 | 0.76 | 0.71 | 24 | 75 | 25 | 74 | 25 | 75 | 17 | 0 | NA |
| [Dipp₃SbOH][O₃SPh] | 2.208 | -1.097 | 0.539 | 0.65 | 0.64 | 20 | 79 | 28 | 72 | 25 | 75 | 14 | 0 | NA |
| cis-Sb(OH)(OAc)Dipp₃ | 2.269 | -1.125 | 0.510 | 0.61 | 0.61 | 19 | 80 | 31 | 69 | 25 | 75 | 15 | 3.11 | NA |
| **A** | 2.405 | -1.274 | 2.405 | 0.61 | 0.38 | 19 | 80 | 39 | 61 | 18 | 82 | 19 | 0 | 107[r] |
| **B**[p] | 2.341 | -1.133 | 0.467 | 0.42 | 0.77 | 11 | 86 | 31 | 68 | 26 | 74 | 33 | 2.32 | NA |

[a] Natural population of pnictogen. [b] Natural population of oxygen. [c] Natural population of A (coordinated Lewis acid atom). [d] Wiberg bond index of Pn–O bond. [e] Wiberg bond index of O–A bond. [f] Pn-atom contribution to the pnictoryl bonding NLMO. [g] O-atom contribution to the pnictoryl bonding NLMO. [h] %s character of the Pn-atom contribution to the pnictoryl bonding NLMO. [i] %p character of the Pn-atom contribution to the pnictoryl bonding NLMO. [j] %s character of the O-atom contribution to the pnictoryl bonding NLMO. [k] %p character of the O-atom contribution to the pnictoryl bonding NLMO. [l] Energy of stabilization afforded by delocalization of electron density from O-centered lone pairs to Pn–C σ* orbitals. [m] Energy of stabilization afforded by delocalization of electron density from O-centered lone pairs to C–H σ* orbitals. [n] Energy of stabilization afforded by delocalization of electron density from O-centered lone pairs to A orbitals (Rydburg orbitals not included). [o] NBO analysis of (Dipp₃SbO)₂Ag⁺ was performed at BP86/def2-SVP level of theory. [p] No Pn–O bonding orbital is present; the primary O-centered lone pair is described. [q] No delocalizations below 0.50 kcal/mol printed. [r] Delocalizations from O-centered lone pairs to Sb–C and Sb–O σ* orbitals.

**Table B.16.** Deletion energies of $Dipp_3PnO$.

| Compound | $Dipp_3PO$ | $Dipp_3AsO$ | $Dipp_3SbO$ |
|---|---|---|---|
| Deletion Energy (kcal/mol)[a] | 172.11 | 116.68 | 92.28 |

[a] Energy of destabilization upon deleting non-covalent interactions between the O atom and $Dipp_3Pn$ molecular fragments.

**Table B.17.** Force constants of Pn–O bond stretch in $Dipp_3PnO$.

| Compound | $Dipp_3PO$ | $Dipp_3AsO$ | $Dipp_3SbO$ |
|---|---|---|---|
| Force constant (mdyne/Å)[a] | 9.014 | 6.852 | 5.656 |
| Force constant (mdyne/Å)[b] | 8.293 | 6.338 | 5.362 |

[a] Force constants obtained by fitting a quadratic function to a rigid surface scan of Pn–O stretching (DKH-PBE0/old-DKH-TZVPP). [b] Force constants obtained by diagonalization of the Hessian matrix with respect to potential energy (PBE0/def2-TZVPP).

**Table B.18.** Selected bond lengths and angles for $Dipp_3SbOCuCl·(CHCl_3)_2$, $[Ag(Dipp_3SbO)_2](CF_3SO_3)·OEt_2$, $[Dipp_3SbOAuPPh_3][CF_3SO_3]$-linear, and $[Dipp_3SbOAuPPh_3][CF_3SO_3]$-bent.

| | $Dipp_3SbOCuCl·$ $(CHCl_3)_2$ | $[Ag(Dipp_3SbO)_2](CF_3SO_3)·$ $OEt_2$ | $[Dipp_3SbOAuPPh_3][CF_3SO_3]$-linear | $[Dipp_3SbOAuPPh_3][CF_3SO_3]$-bent |
|---|---|---|---|---|
| Sb–O–M angle (°) | 145.40(9) | 130.42(10)/ 130.51(9) | 180.0 | 122.15(8) |
| O–M–X angle (°)[a] | 175.27(5) | 166.78(7) | 180.0 | 179.89(6) |
| Sb–O distance (Å) | 1.8591(14) | 1.8716(17)/ 1.8670(17) | 1.850(7) | 1.8932(17) |
| O–M distance (Å) | 1.8286(14) | 2.0939(17)/ 2.0926(17) | 1.982(7) | 2.0582(16) |

[a] X denotes the coordinated atom of the second ligand; Cl in the case of $Dipp_3SbOCuCl·(CHCl_3)_2$, O in the case of $[Ag(Dipp_3SbO)_2](CF_3SO_3)·OEt_2$, P in the case of $[Dipp_3SbOAuPPh_3][CF_3SO_3]$-linear and $[Dipp_3SbOAuPPh_3][CF_3SO_3]$-bent.

**References**

1.      NIST, NIST Computational Chemistry Comparison and Benchmark Database; NIST Standard Reference Database Number 101, Release 21 (August 2020). <http://cccbdb.nist.gov/>.

**Appendix C**

**Supplementary data for**

**Chapter 4: Variation in pnictogen–oxygen bonding unlocks greatly enhanced Brønsted**

**basicity for the monomeric stibine oxide**
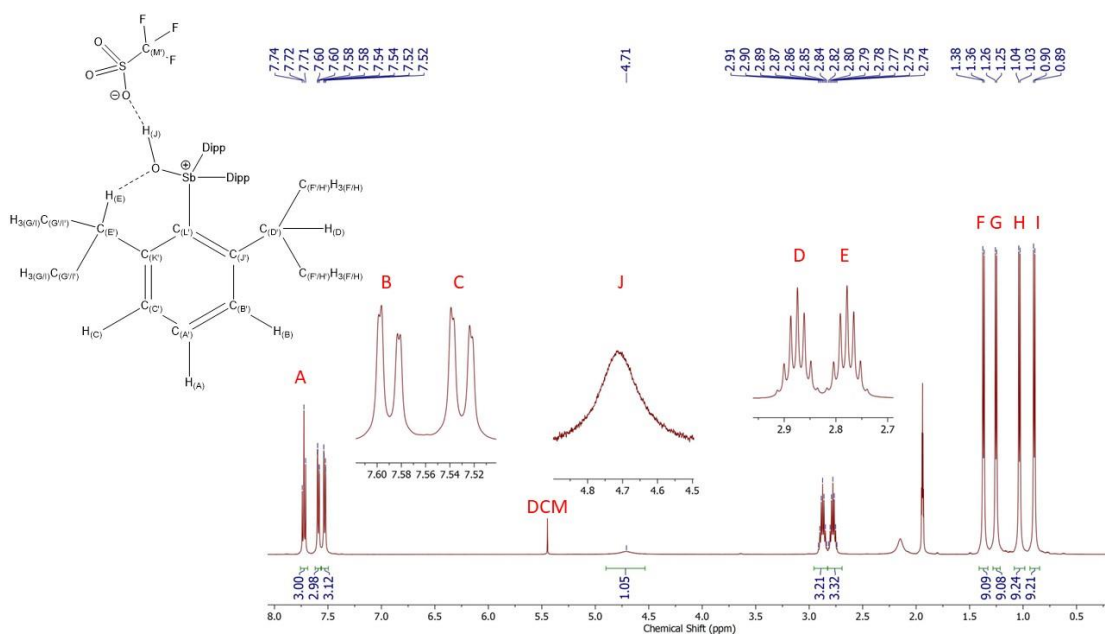
**Figure C.1.** $^1$H NMR spectrum (CD$_3$CN, 500 MHz) of [Dipp$_3$SbOH][CF$_3$SO$_3$] at room temperature.
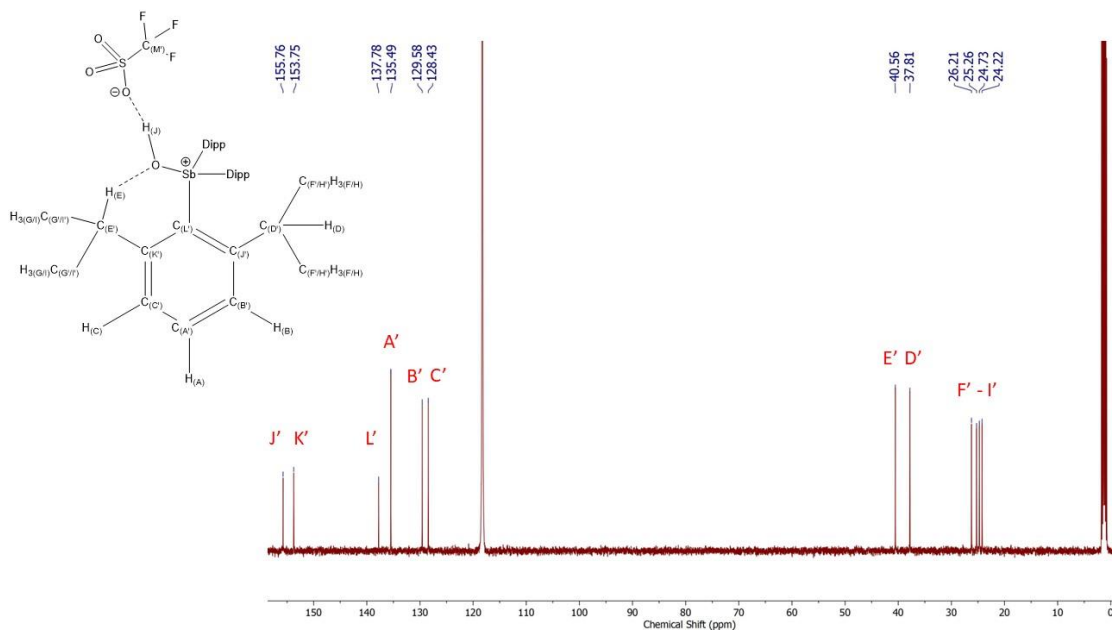


**Figure C.2.** $^{13}$C{$^1$H} NMR spectrum (CD$_3$CN, 125 MHz) of [Dipp$_3$SbOH][CF$_3$SO$_3$] at room temperature.
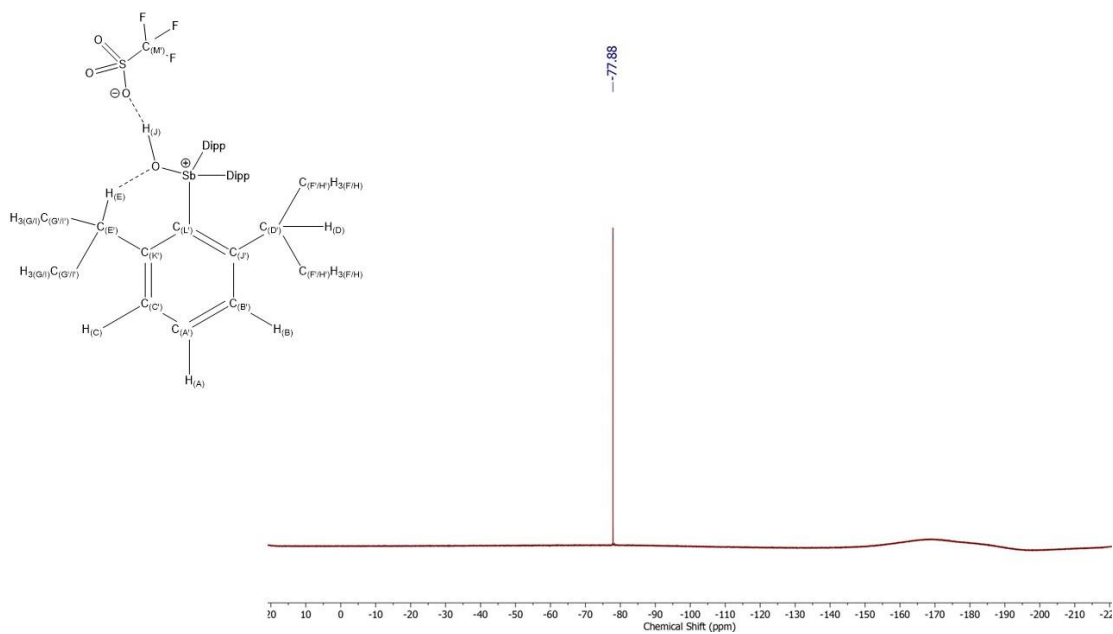
**Figure C.3.** $^{19}F$ NMR spectrum (CDCl$_3$, 470 MHz) of [Dipp$_3$SbOH][CF$_3$SO$_3$] at room temperature.
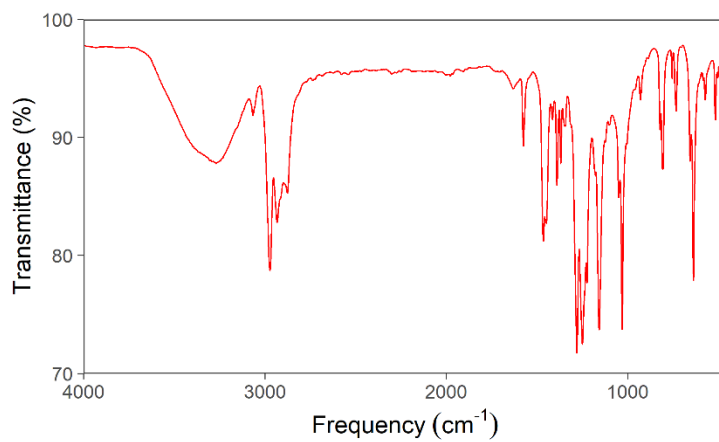


**Figure C.4.** Experimental IR spectrum (KBr pellet) of [Dipp$_3$SbOH][CF$_3$SO$_3$].
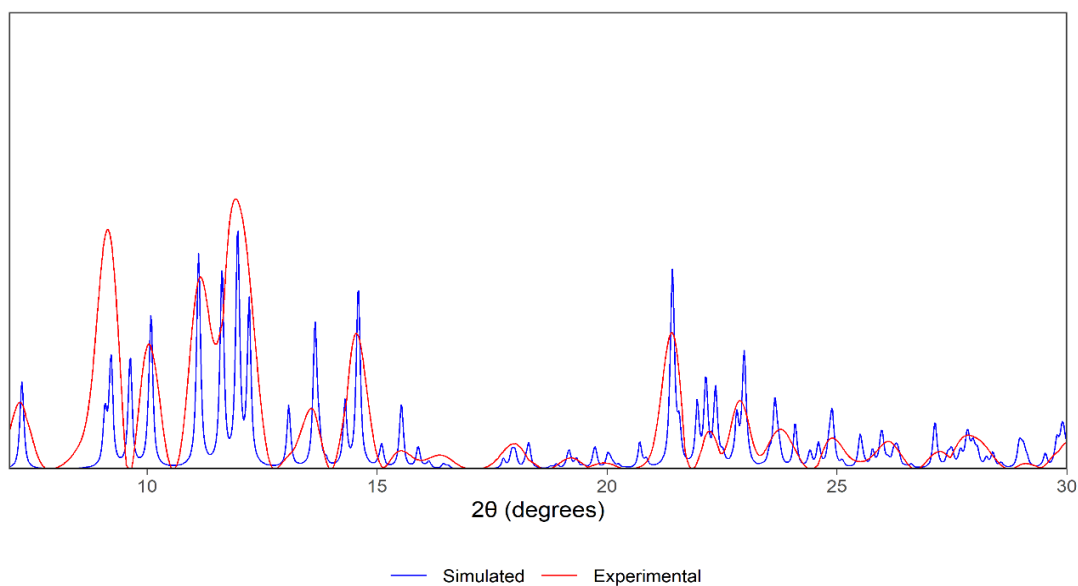
**Figure C.5.** Simulated and experimental PXRD diffractograms of [Dipp$_3$SbOH][CF$_3$SO$_3$].
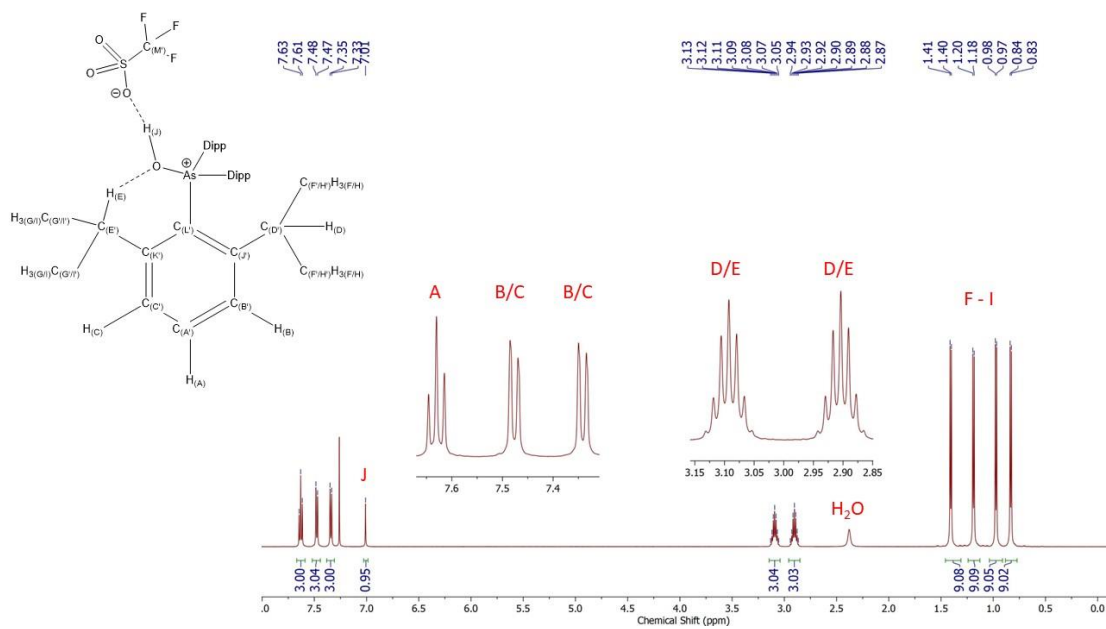


**Figure C.6.** $^1$H NMR spectrum (CDCl$_3$, 500 MHz) of [Dipp$_3$AsOH][CF$_3$SO$_3$]·CHCl$_3$ at room temperature.
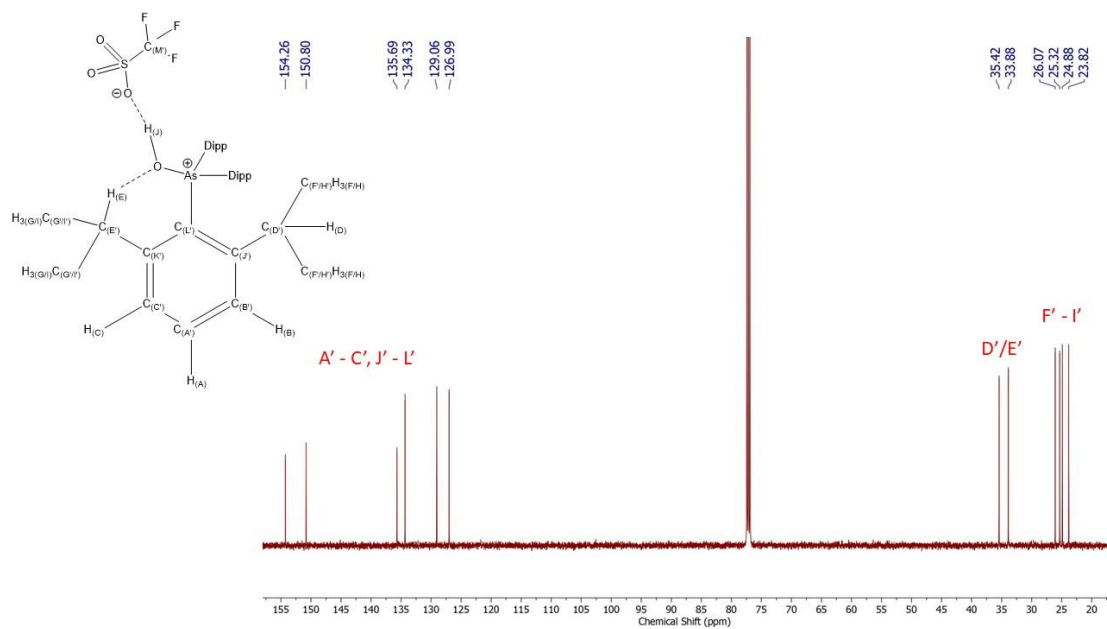
**Figure C.7.** $^{13}C\{^1H\}$ NMR spectrum (CDCl$_3$, 125 MHz) of [Dipp$_3$AsOH][CF$_3$SO$_3$]·CHCl$_3$ at room temperature.
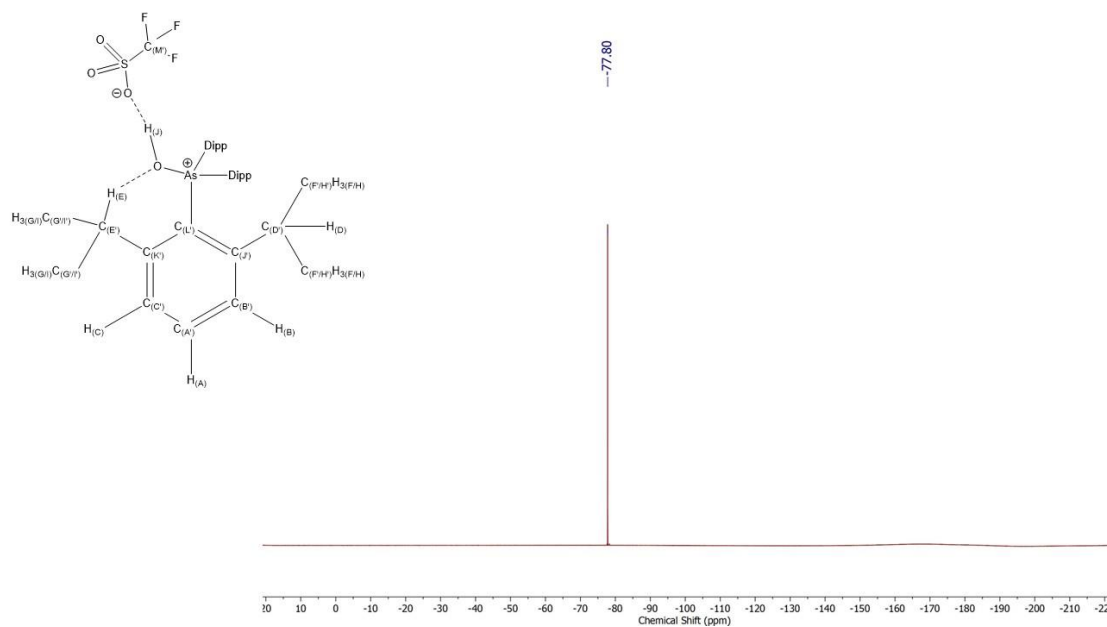


**Figure C.8.** $^{19}F$ NMR spectrum (CDCl$_3$, 470 MHz) of [Dipp$_3$AsOH][CF$_3$SO$_3$]·CHCl$_3$ at room temperature.
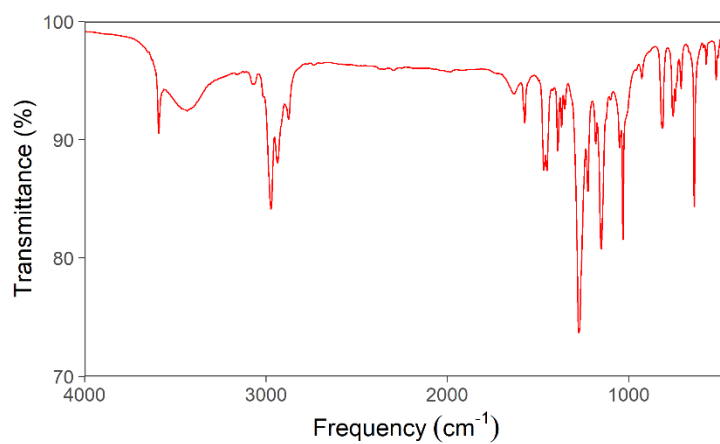
**Figure C.9.** Experimental IR spectrum (KBr pellet) of [Dipp$_3$AsOH][CF$_3$SO$_3$]·CHCl$_3$.
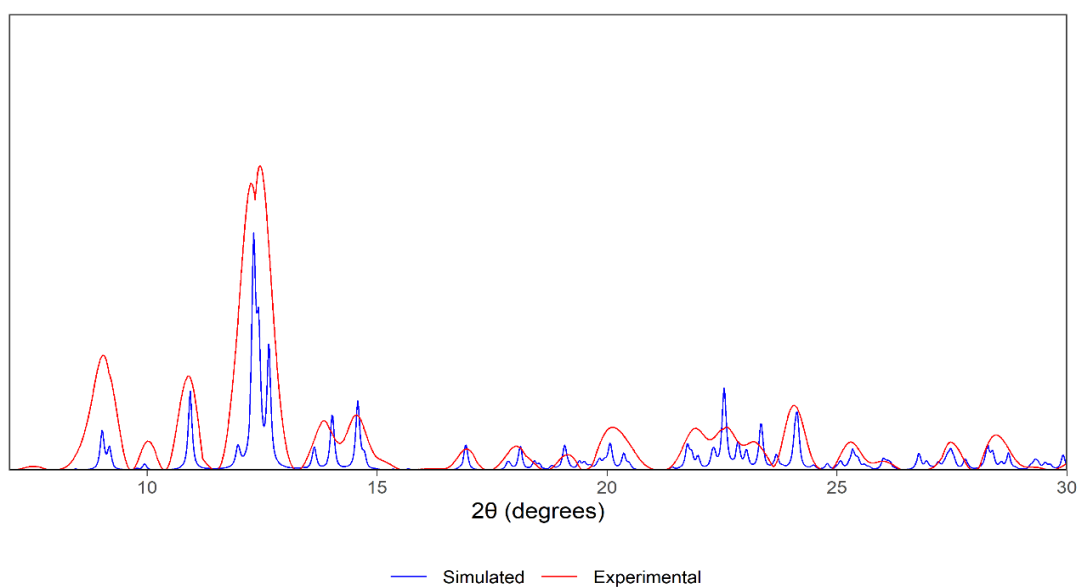


**Figure C.10.** Simulated and experimental PXRD diffractogram of [Dipp$_3$AsOH][CF$_3$SO$_3$]·CHCl$_3$. The simulated diffractogram is of the triclinic polymorph of [Dipp$_3$AsOH][CF$_3$SO$_3$]·CHCl$_3$.
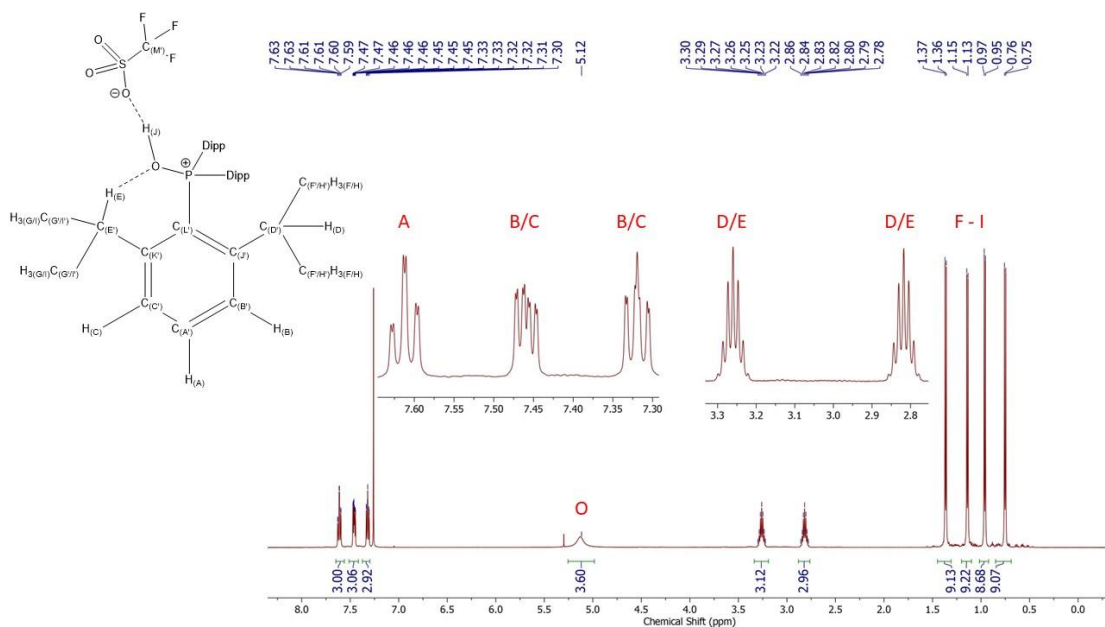
**Figure C.11.** $^1$H NMR spectrum (CDCl$_3$, 500 MHz) of [Dipp$_3$POH][O$_3$SCF$_3$] at room temperature.
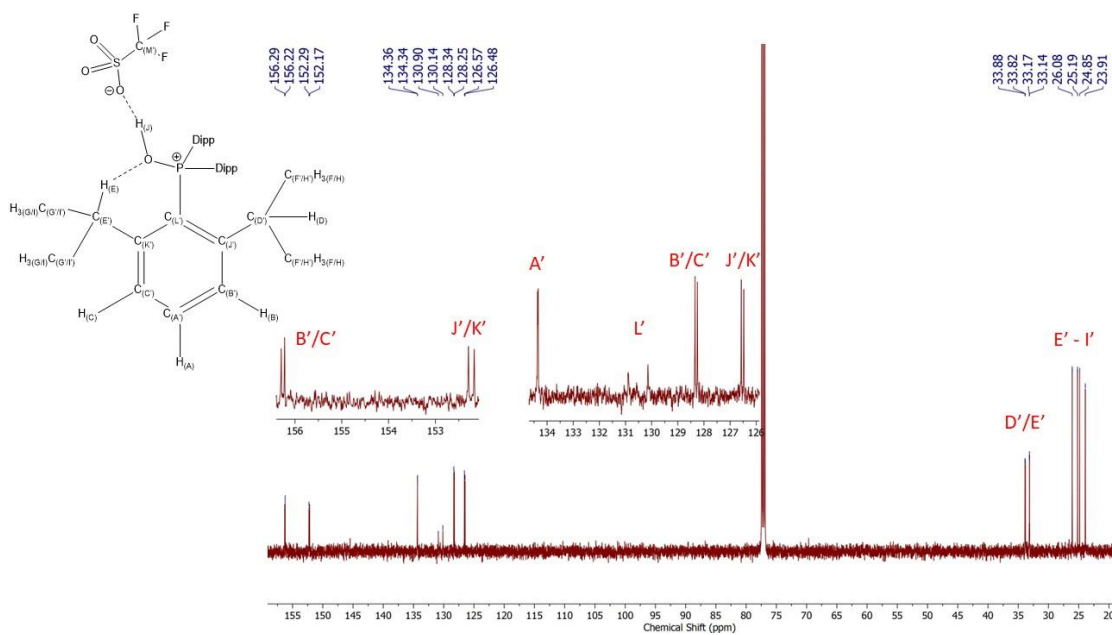


**Figure C.12.** $^{13}$C{$^1$H} NMR spectrum (CDCl$_3$, 125 MHz) of [Dipp$_3$POH][O$_3$SCF$_3$] at room temperature. Aryl signals were assigned positions relative to $^{31}$P nucleus based on coupling constants.
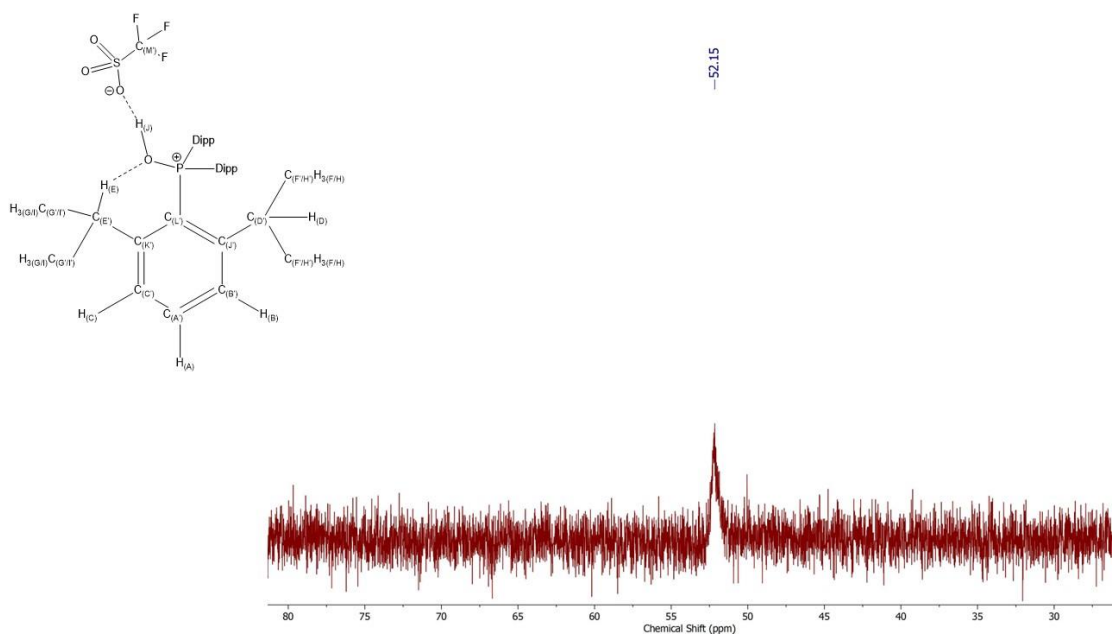
**Figure C.13.** $^{31}P$ NMR spectrum (CDCl$_3$, 470 MHz) of [Dipp$_3$POH][O$_3$SCF$_3$] at room temperature.
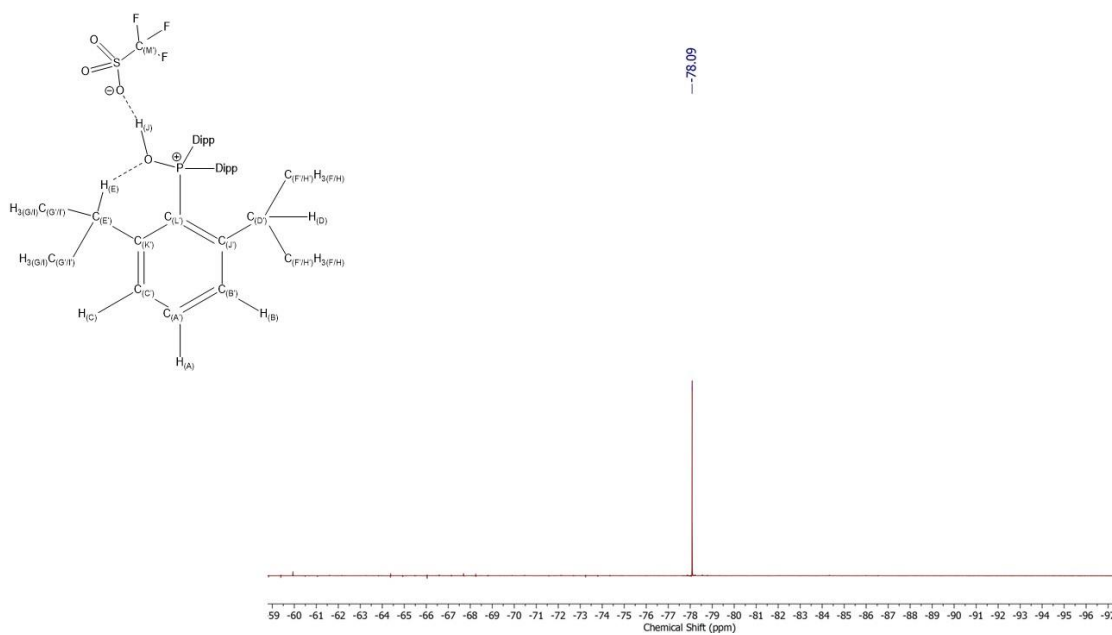


**Figure C.14.** $^{19}F\{^1H\}$ NMR spectrum (CDCl$_3$, 470 MHz) of [Dipp$_3$POH][O$_3$SCF$_3$] at room temperature.
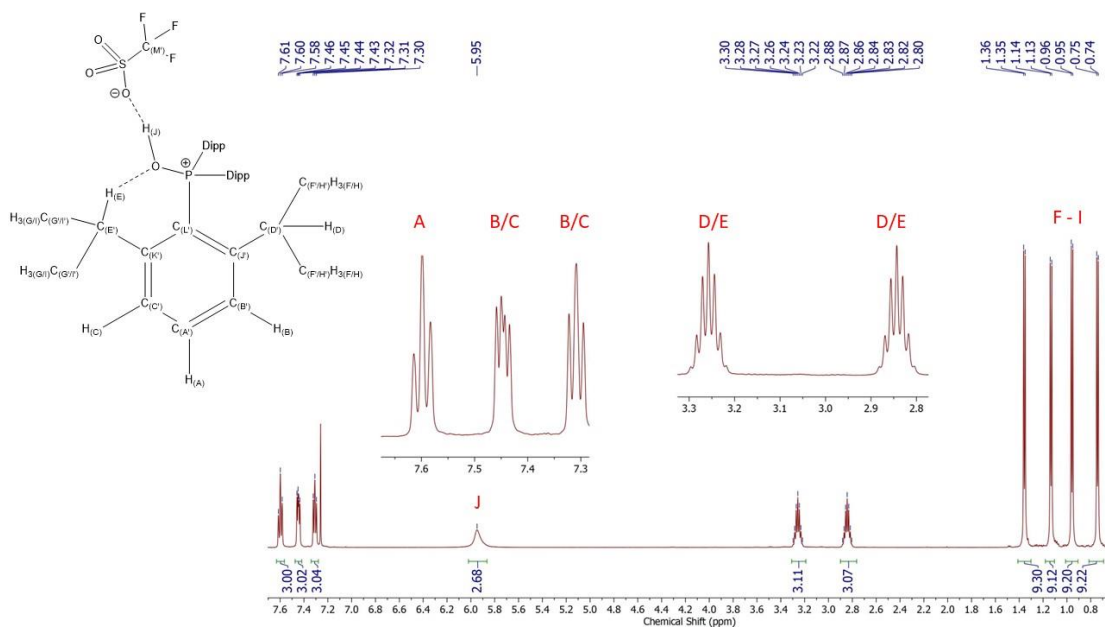
**Figure C.15.** $^{1}$H NMR spectrum (CDCl$_3$, 500 MHz) of a 1:1 mixture of Dipp$_3$PO and triflic acid at room temperature.
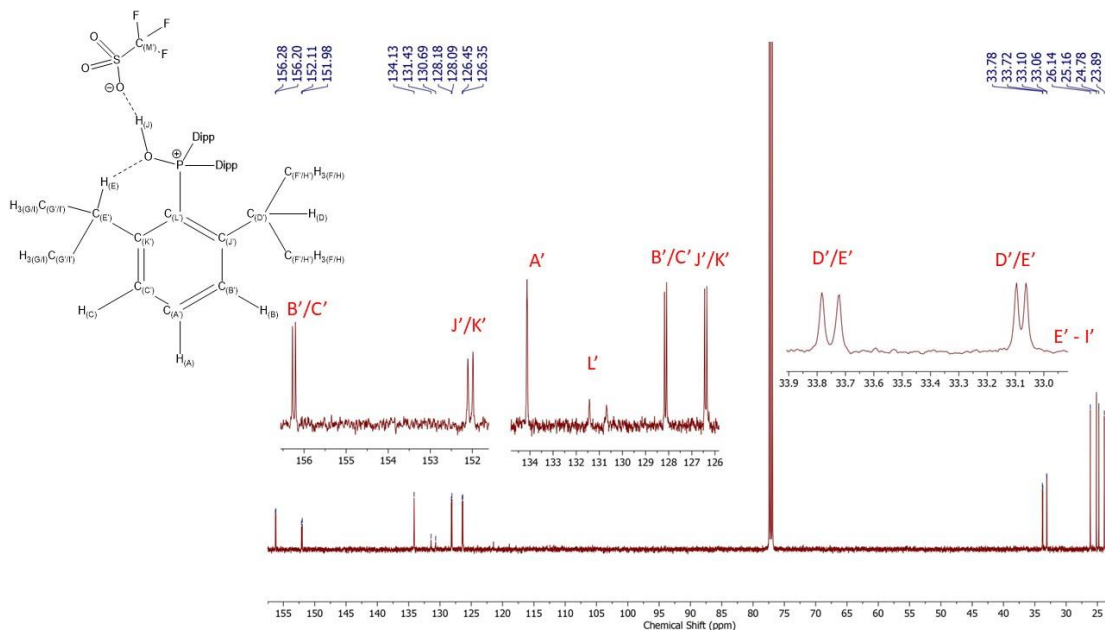


**Figure C.16.** $^{13}$C{$^{1}$H} NMR spectrum (CDCl$_3$, 125 MHz) of a 1:1 mixture of Dipp$_3$PO and triflic acid at room temperature. Aryl signals were assigned positions relative to $^{31}$P nucleus based on coupling constants.
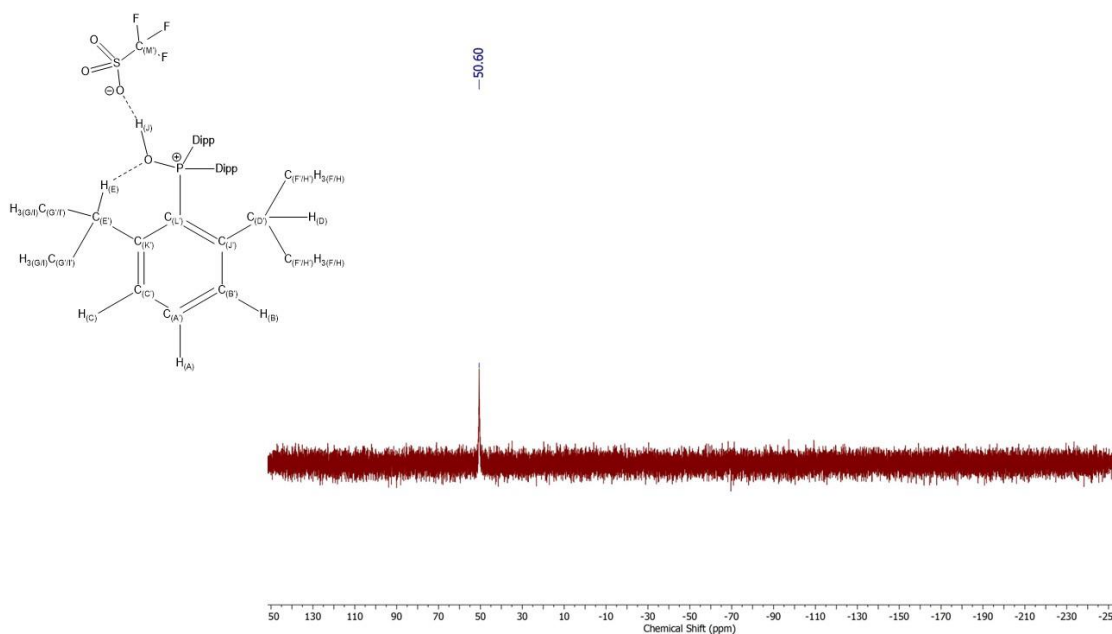
**Figure C.17.** $^{31}P$ NMR spectrum (CDCl$_3$, 470 MHz) of 1:1 mixture of Dipp$_3$PO and triflic acid at room temperature.
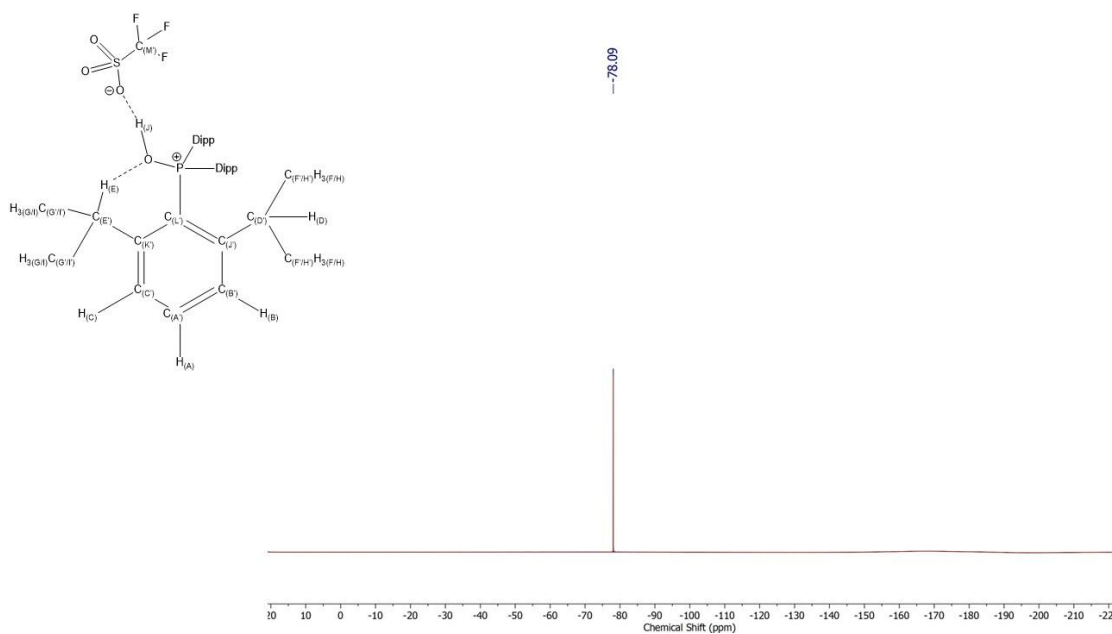


**Figure C.18.** $^{19}F$ NMR spectrum (CDCl$_3$, 470 MHz) of a 1:1 mixture of Dipp$_3$PO and triflic acid at room temperature.
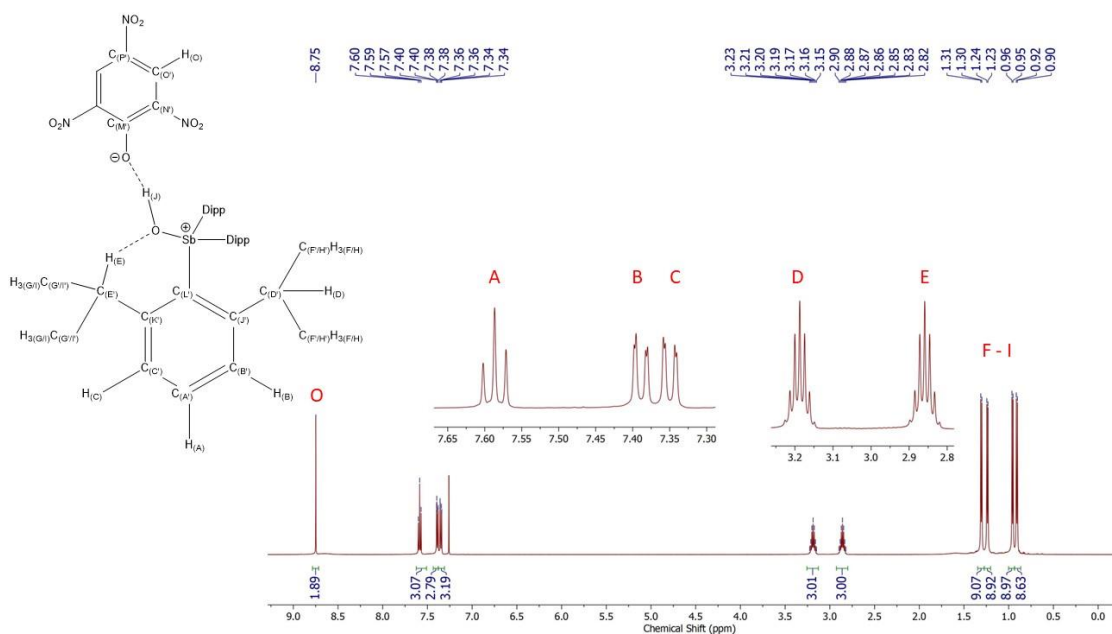
**Figure C.19.** $^1$H NMR spectrum (CDCl$_3$, 500 MHz) of [Dipp$_3$SbOH][OPh(NO$_2$)$_3$] at room temperature.
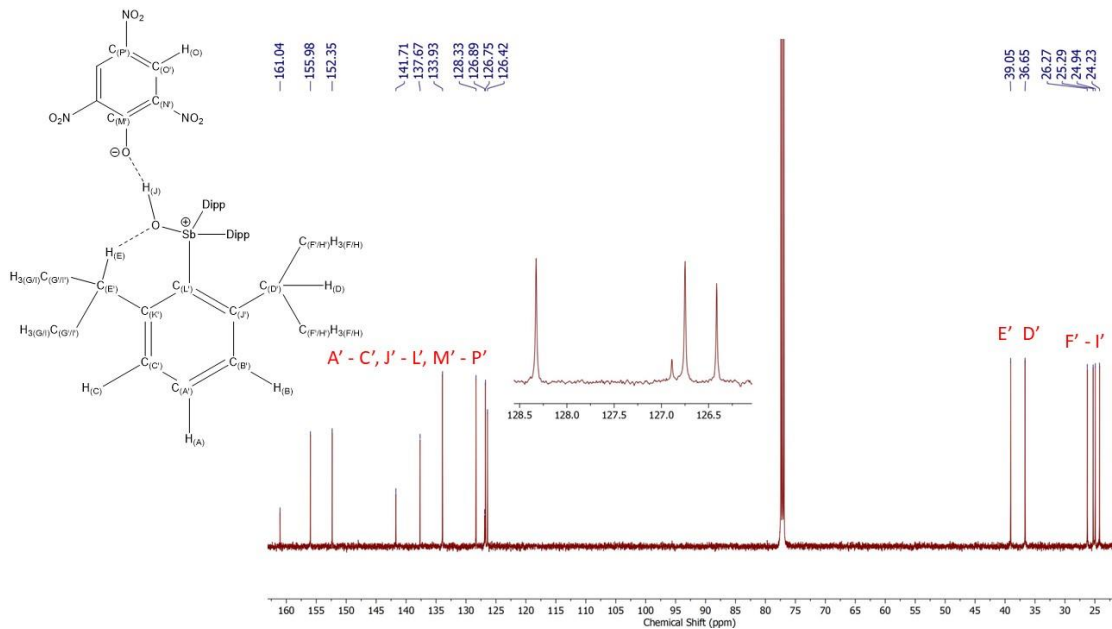


**Figure C.20.** $^{13}$C{$^1$H} NMR spectrum (CDCl$_3$, 125 MHz) of [Dipp$_3$SbOH][OPh(NO$_2$)$_3$] at room temperature.
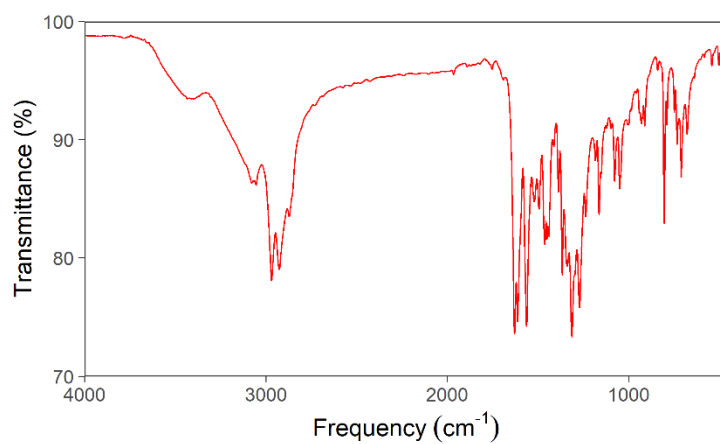
**Figure C.21.** Experimental IR spectrum (KBr pellet) of [Dipp$_3$SbOH][OPh(NO$_2$)$_3$].



Simulated — Experimental
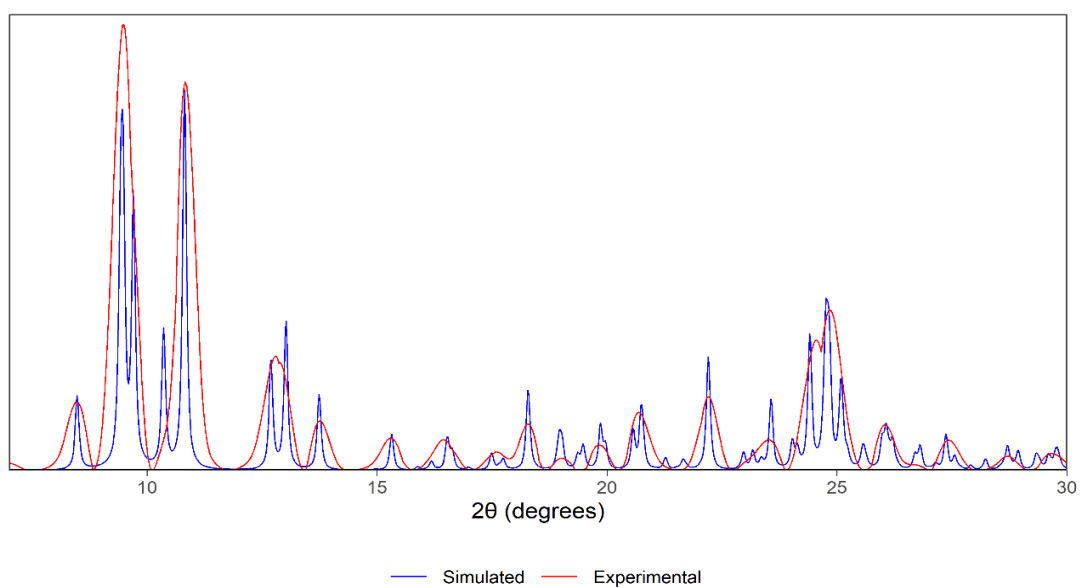
**Figure C.22.** Simulated and experimental PXRD diffractogram of [Dipp$_3$SbOH][OPh(NO$_2$)$_3$].
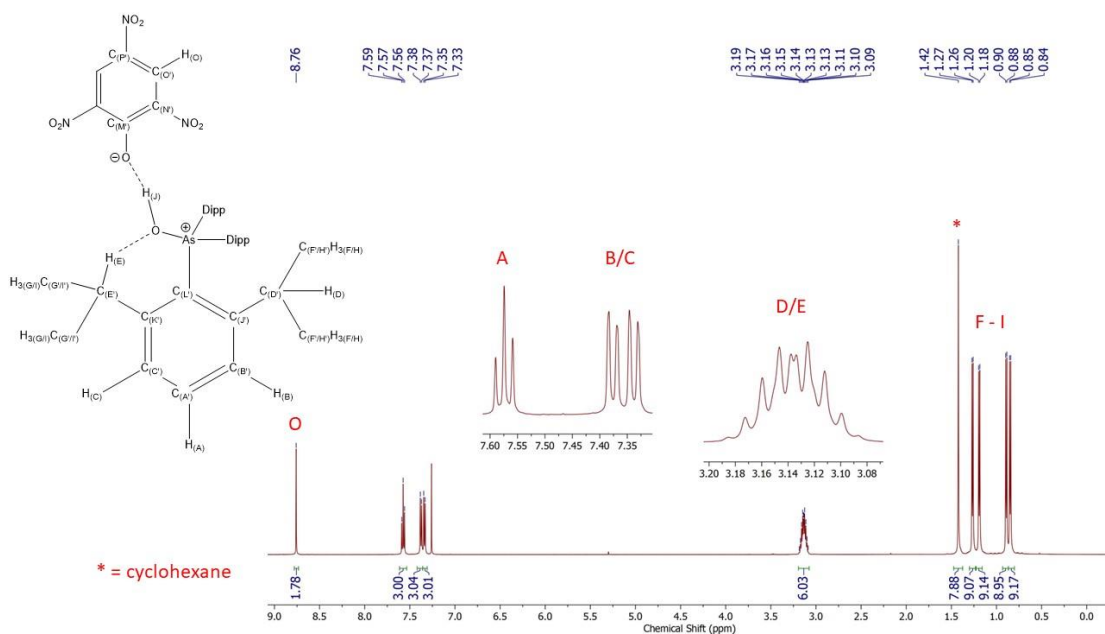
**Figure C.23.** $^1$H NMR spectrum (CDCl$_3$, 500 MHz) of [Dipp$_3$AsOH][OPh(NO$_2$)$_3$]·¾(C$_6$H$_{12}$) at room temperature.
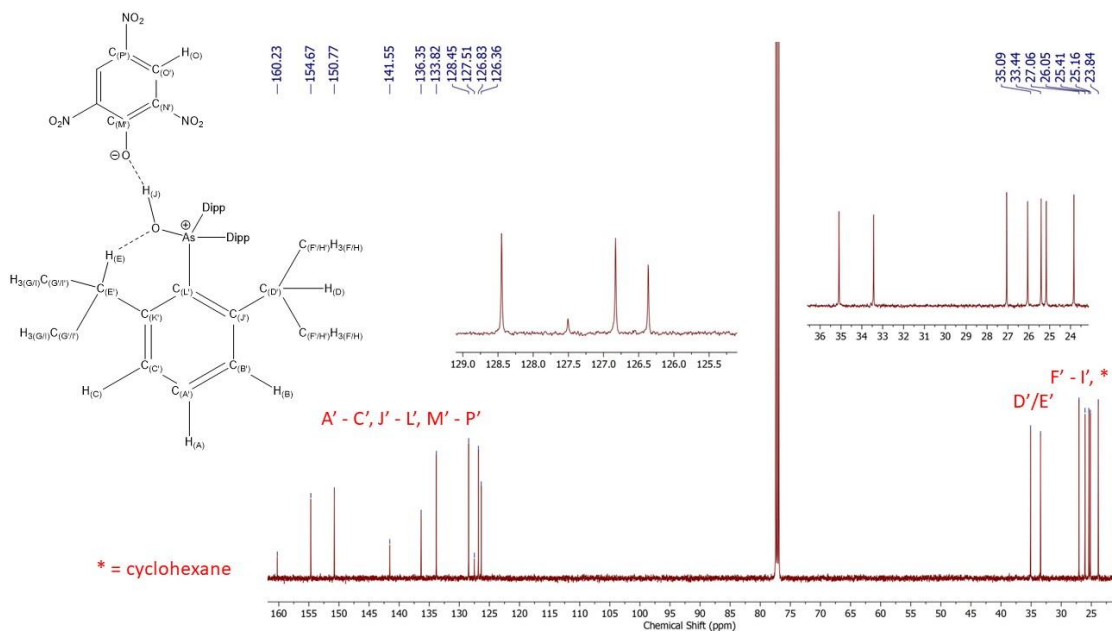


**Figure C.24.** $^{13}$C{$^1$H} NMR spectrum (CDCl$_3$, 125 MHz) of [Dipp$_3$AsOH][OPh(NO$_2$)$_3$]·¾(C$_6$H$_{12}$) at room temperature.
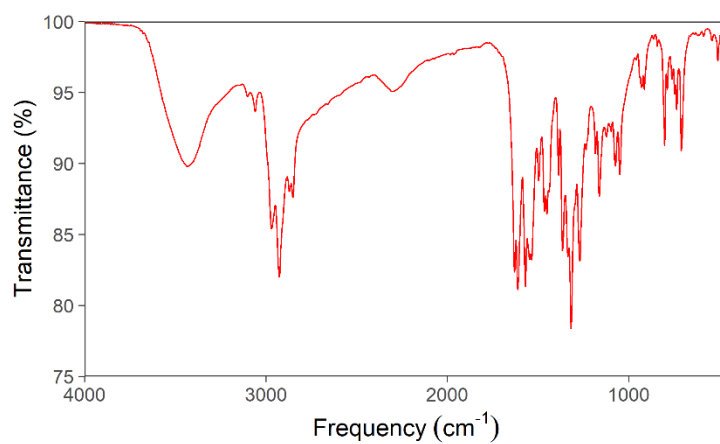
**Figure C.25.** Experimental IR spectrum (KBr pellet) of [Dipp$_3$AsOH][OPh(NO$_2$)$_3$]·¾(C$_6$H$_{12}$).
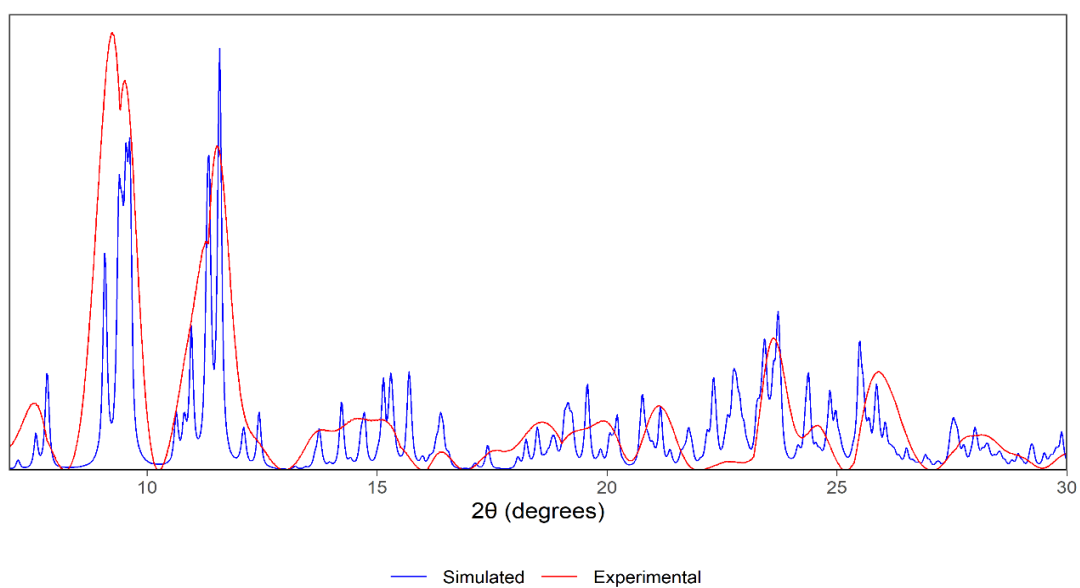


**Figure C.26.** Simulated and experimental PXRD diffractogram of [Dipp$_3$AsOH][OPh(NO$_2$)$_3$]·¾(C$_6$H$_{12}$).
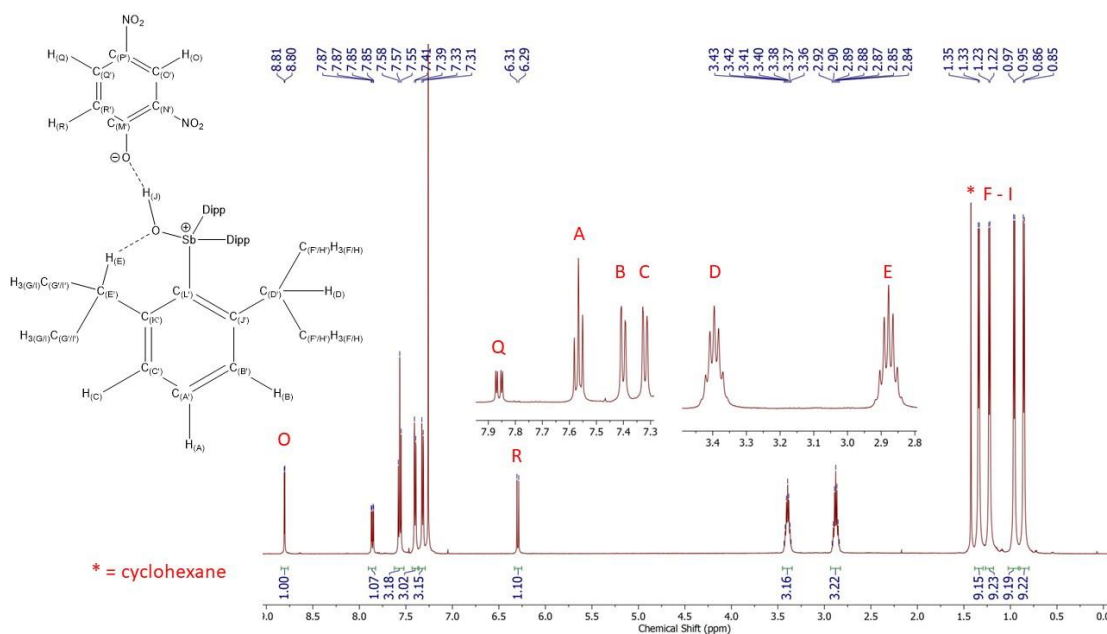
**Figure C.27.** ^{1}H NMR spectrum (CDCl₃, 500 MHz) of [Dipp₃SbOH][OPh(NO₂)₂]·2(CHCl₃) at room temperature.
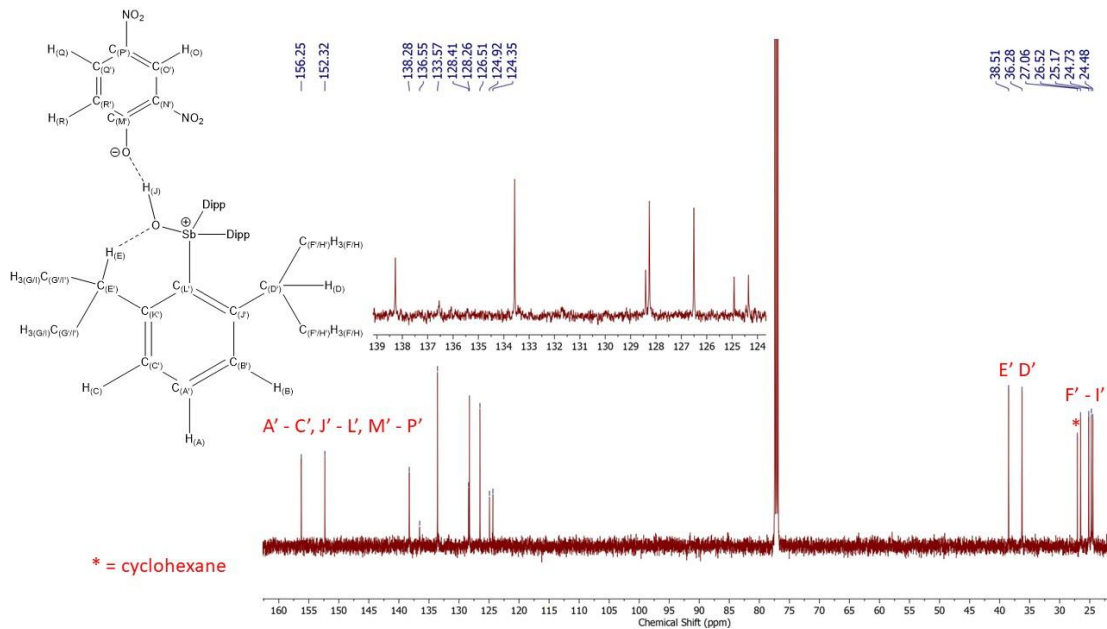


**Figure C.28.** ^{13}C{^{1}H} NMR spectrum (CDCl₃, 125 MHz) of [Dipp₃SbOH][OPh(NO₂)₂]·2(CHCl₃) at room temperature.

329
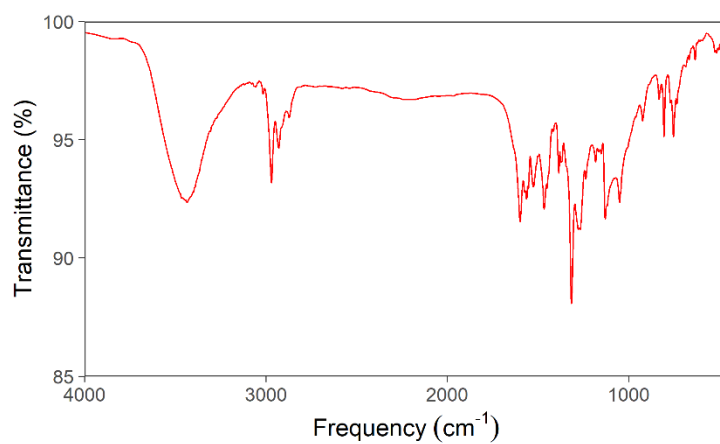
**Figure C.29.** Experimental IR spectrum (KBr pellet) of [Dipp$_3$SbOH][OPh(NO$_2$)$_2$]·2(CHCl$_3$).



Simulated     Experimental
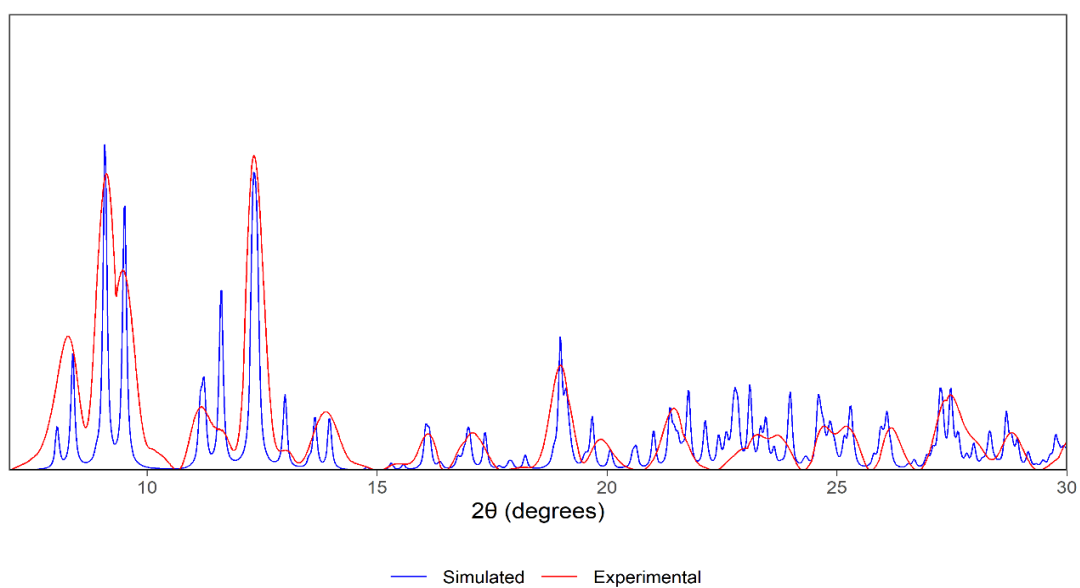
**Figure C.30.** Simulated and experimental PXRD diffractogram of [Dipp$_3$SbOH][OPh(NO$_2$)$_2$]·2(CHCl$_3$).
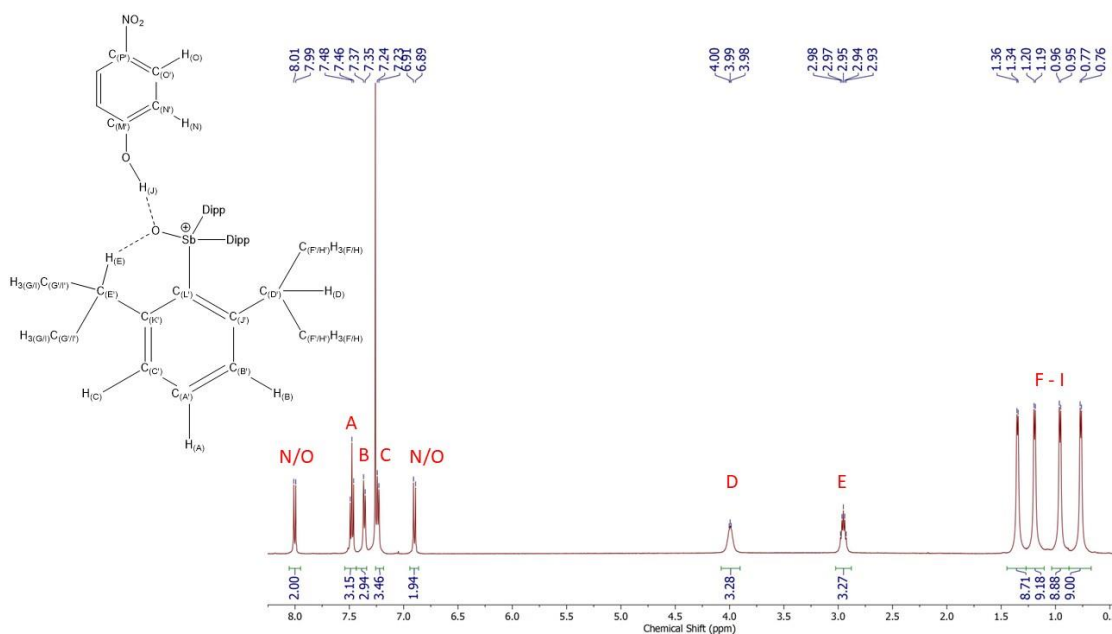
**Figure C.31.** $^1$H NMR spectrum (CDCl$_3$, 500 MHz) of Dipp$_3$SbO·HOPhNO$_2$ at room temperature.
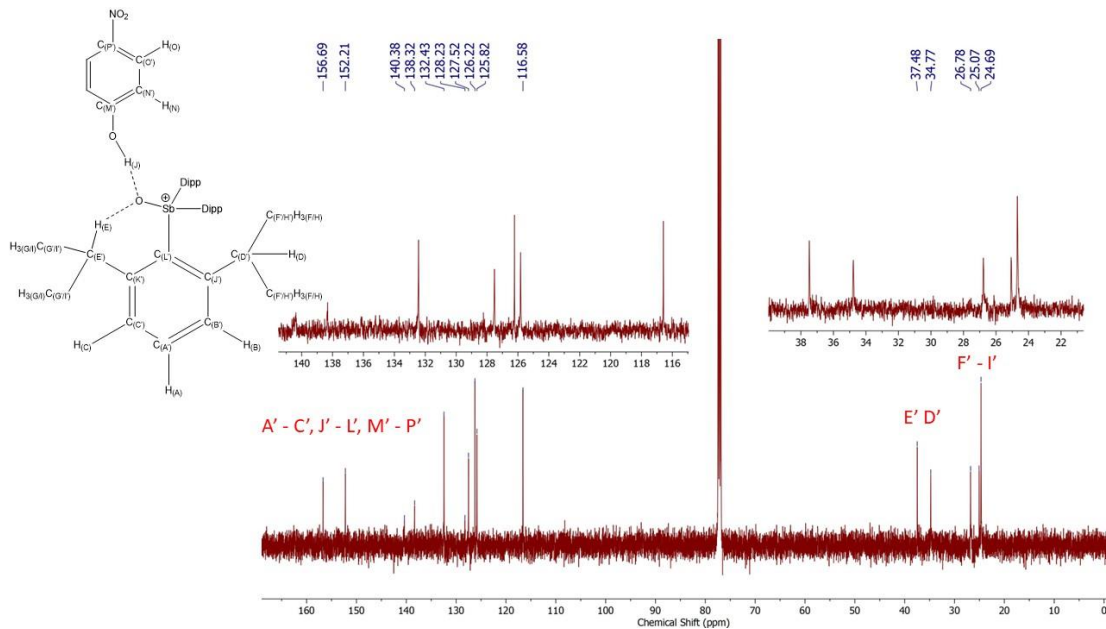


**Figure C.32.** $^{13}$C{$^1$H} NMR spectrum (CDCl$_3$, 125 MHz) of Dipp$_3$SbO·HOPhNO$_2$ at room temperature.
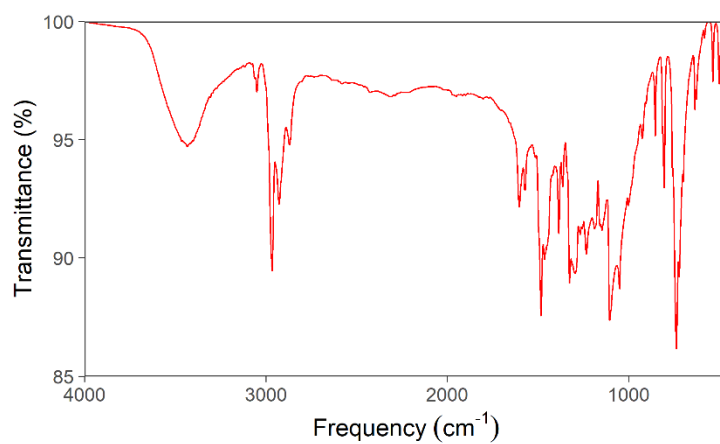
**Figure C.33.** Experimental IR spectrum (KBr pellet) of Dipp$_3$SbO·HOPhNO$_2$.
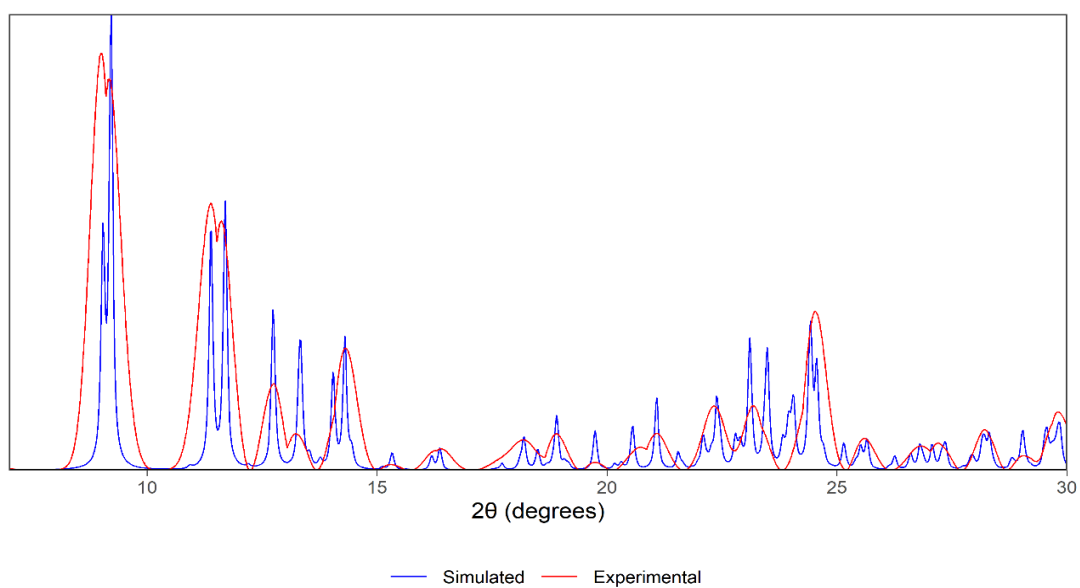


**Figure C.34.** Simulated and experimental PXRD diffractogram of Dipp$_3$SbO·HOPhNO$_2$.
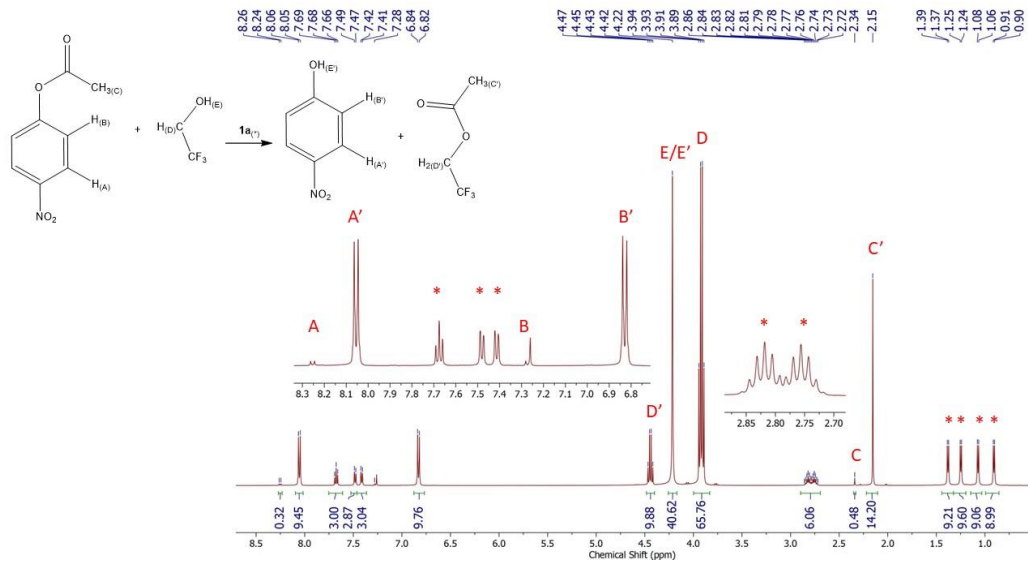
**Figure C.35.** $^1$H NMR spectrum (CDCl$_3$, 500 MHz) of Dipp$_3$SbO-catalyzed transesterification between *p*-nitrophenyl acetate and 2,2,2-trifluoroethanol reaction mixture at room temperature. Signals arising from pnictine oxide catalyst are denoted with an asterisk. The percent conversion was calculated by dividing the integral of peak C by the sum of the integrals of peaks A and A'. We note that a portion of the original 10 equivalents of 2,2,2-trifluoroethanol added to the mixture evaporated during the reaction.
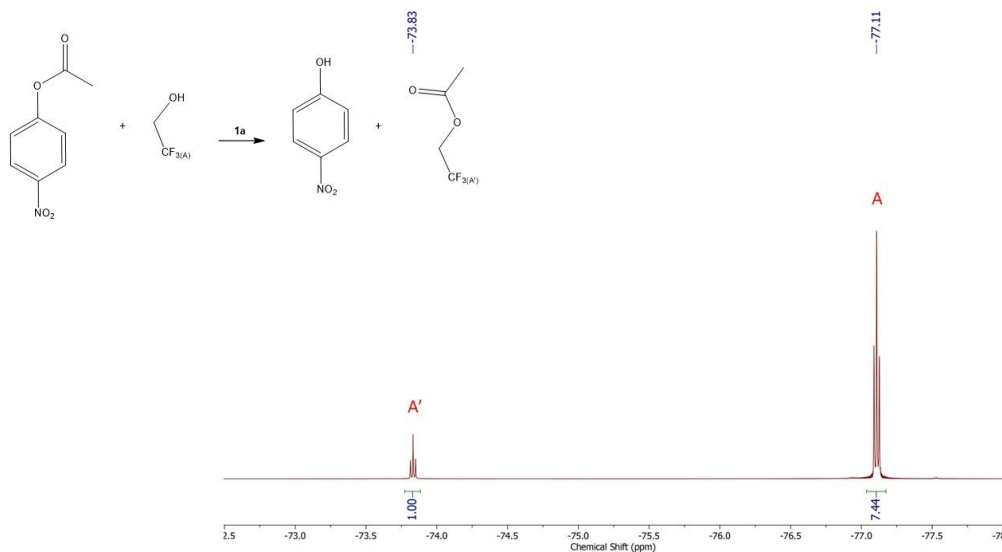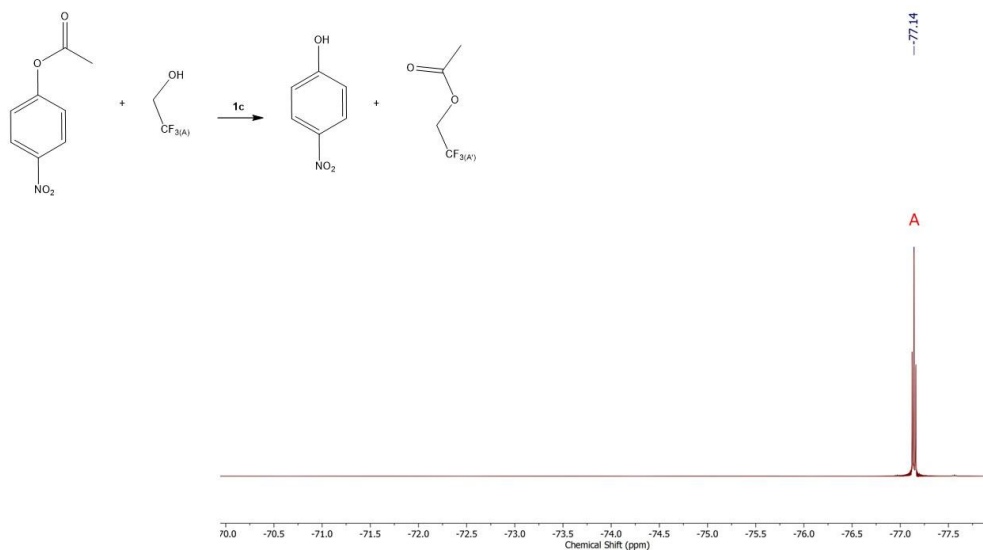


**Figure C.36.** $^{19}$F NMR spectrum (CDCl$_3$, 470 MHz) of Dipp$_3$SbO-catalyzed transesterification between *p*-nitrophenyl acetate and 2,2,2-trifluoroethanol reaction mixture at room temperature. We note that a portion of the original 10 equivalents of 2,2,2-trifluoroethanol added to the mixture evaporated during the reaction.
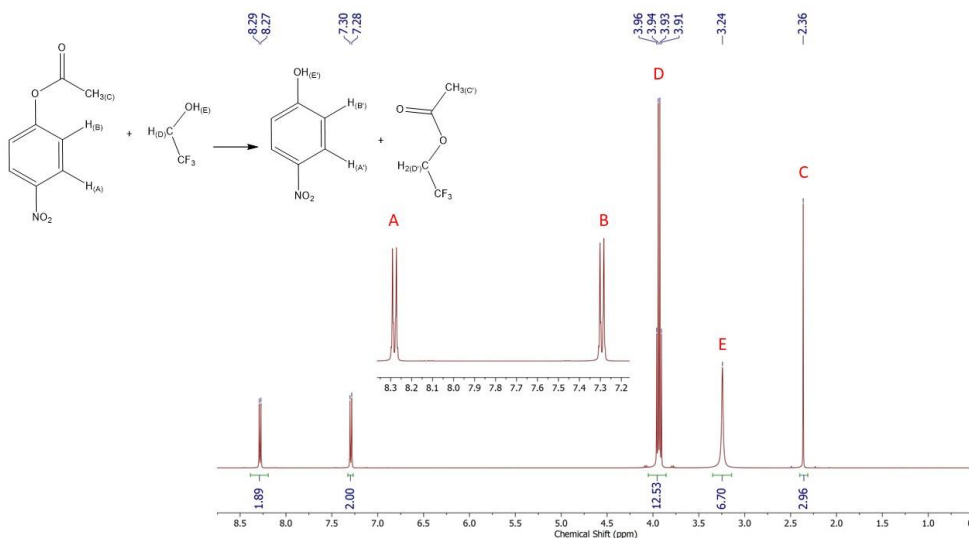
333
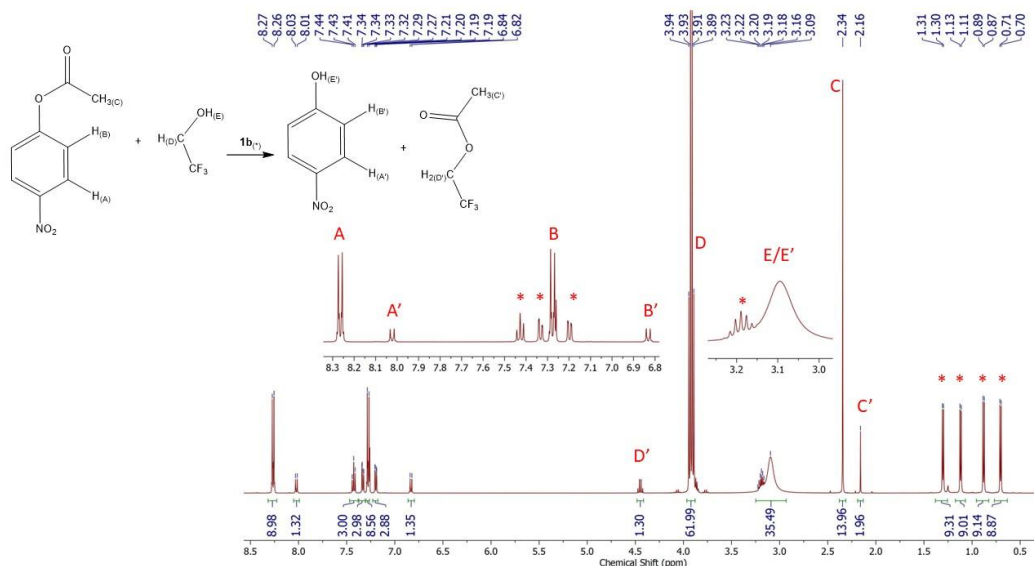
**Figure C.37.** $^1$H NMR spectrum (CDCl$_3$, 500 MHz) of Dipp$_3$AsO-catalyzed transesterification between *p*-nitrophenyl acetate and 2,2,2-trifluoroethanol reaction mixture at room temperature. Signals arising from pnictine oxide catalyst are denoted with an asterisk. The percent conversion was calculated by dividing the integral of peak C by the sum of the integrals of peaks A and A'. We note that a portion of the original 10 equivalents of 2,2,2-trifluoroethanol added to the mixture evaporated during the reaction.
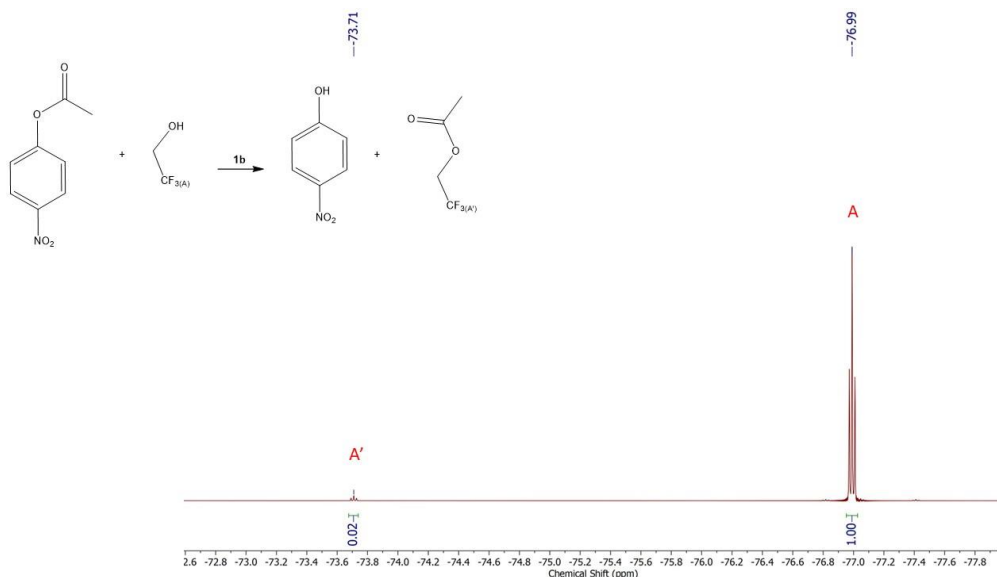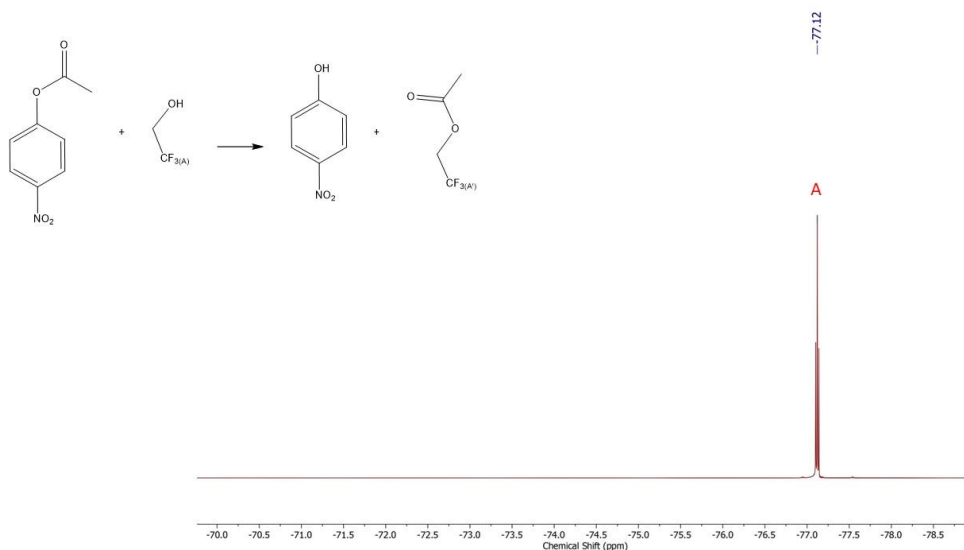


**Figure C.38.** $^{19}$F NMR spectrum (CDCl$_3$, 470 MHz) of Dipp$_3$AsO-catalyzed transesterification between *p*-nitrophenyl acetate and 2,2,2-trifluoroethanol reaction mixture at room temperature. We note that a portion of the original 10 equivalents of 2,2,2-trifluoroethanol added to the mixture evaporated during the reaction.
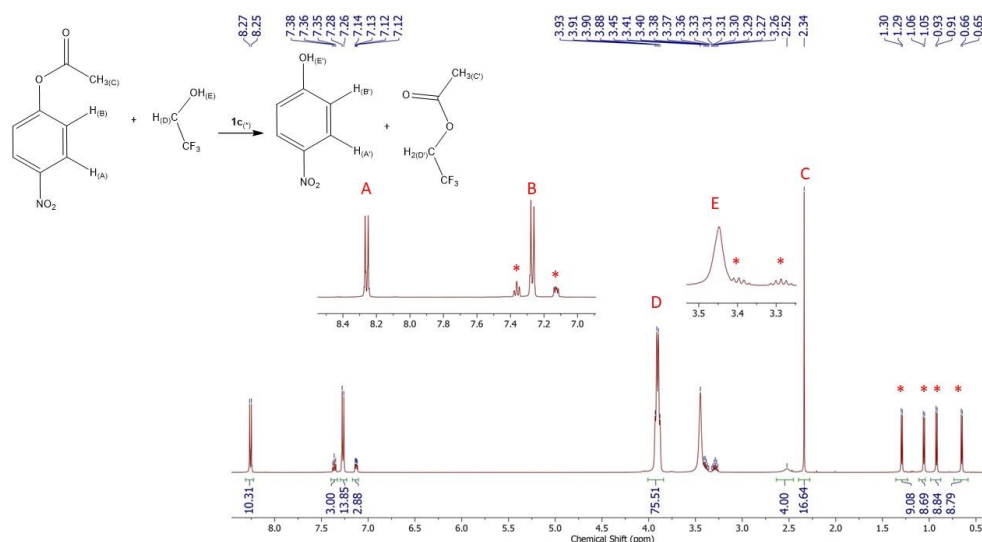
**Figure C.39.** ^{1}H NMR spectrum (CDCl$_3$, 500 MHz) of Dipp$_3$PO-catalyzed transesterification between *p*-nitrophenyl acetate and 2,2,2-trifluoroethanol reaction mixture at room temperature. Signals arising from pnictine oxide catalyst are denoted with an asterisk. The percent conversion was calculated by dividing the integral of peak C by the sum of the integrals of peaks A and A'. We note that a portion of the original 10 equivalents of 2,2,2-trifluoroethanol added to the mixture evaporated during the reaction.



**Figure C.40.** ^{19}F NMR spectrum (CDCl$_3$, 470 MHz) of Dipp$_3$PO-catalyzed transesterification between *p*-nitrophenyl acetate and 2,2,2-trifluoroethanol reaction mixture at room temperature. We note that a portion of the original 10 equivalents of 2,2,2-trifluoroethanol added to the mixture evaporated during the reaction.

**Figure C.41.** $^1$H NMR spectrum (CDCl$_3$, 500 MHz) of uncatalyzed transesterification between *p*-nitrophenyl acetate and 2,2,2-trifluoroethanol reaction mixture at room temperature. The percent conversion was calculated by dividing the integral of peak C by the sum of the integrals of peaks A and A'. We note that a portion of the original 10 equivalents of 2,2,2-trifluoroethanol added to the mixture evaporated during the reaction.



**Figure C.42.** $^{19}$F NMR spectrum (CDCl$_3$, 470 MHz) of uncatalyzed transesterification between *p*-nitrophenyl acetate and 2,2,2-trifluoroethanol reaction mixture at room temperature. We note that a portion of the original 10 equivalents of 2,2,2-trifluoroethanol added to the mixture evaporated during the reaction.
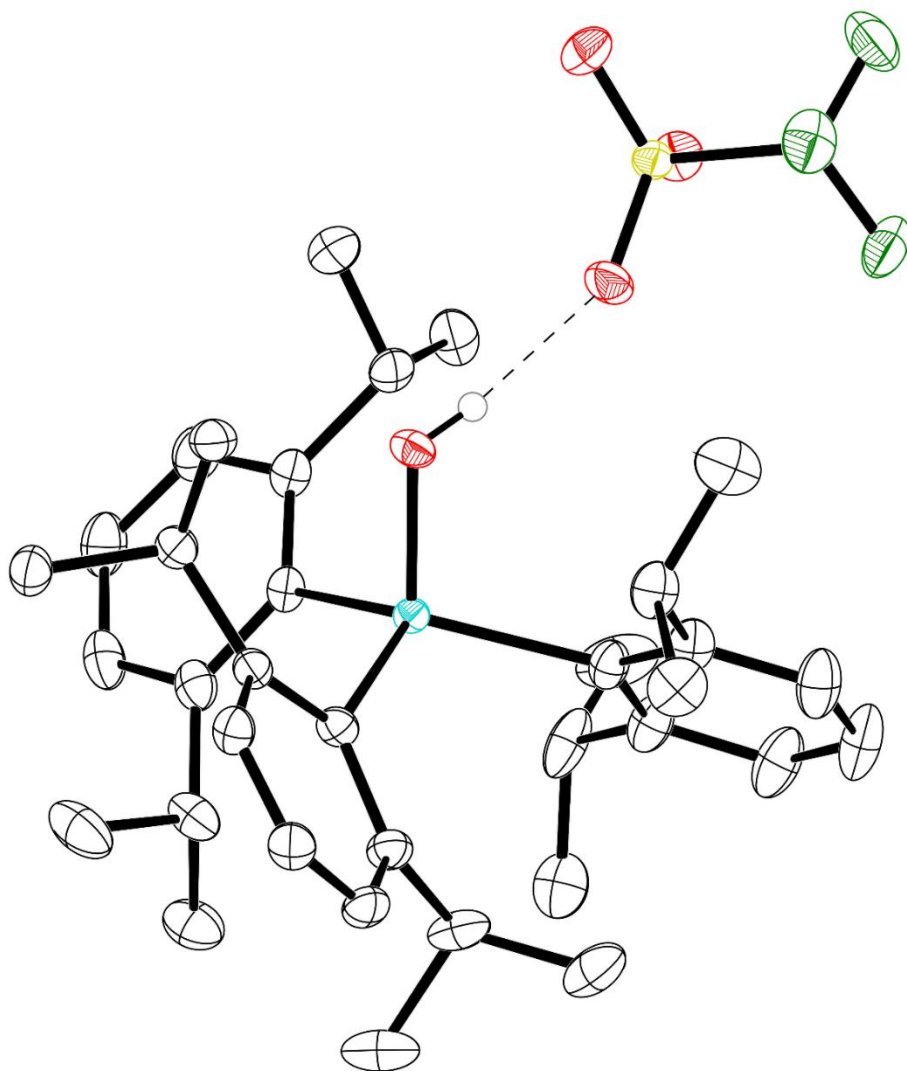
**Figure C.43.** Thermal ellipsoid plot (50% probability) of [Dipp₃SbOH][CF₃SO₃]. Color code: Sb teal, O red, C black, S yellow, F green, and H grey sphere of arbitrary radius. Non-protic H atoms are omitted for clarity.
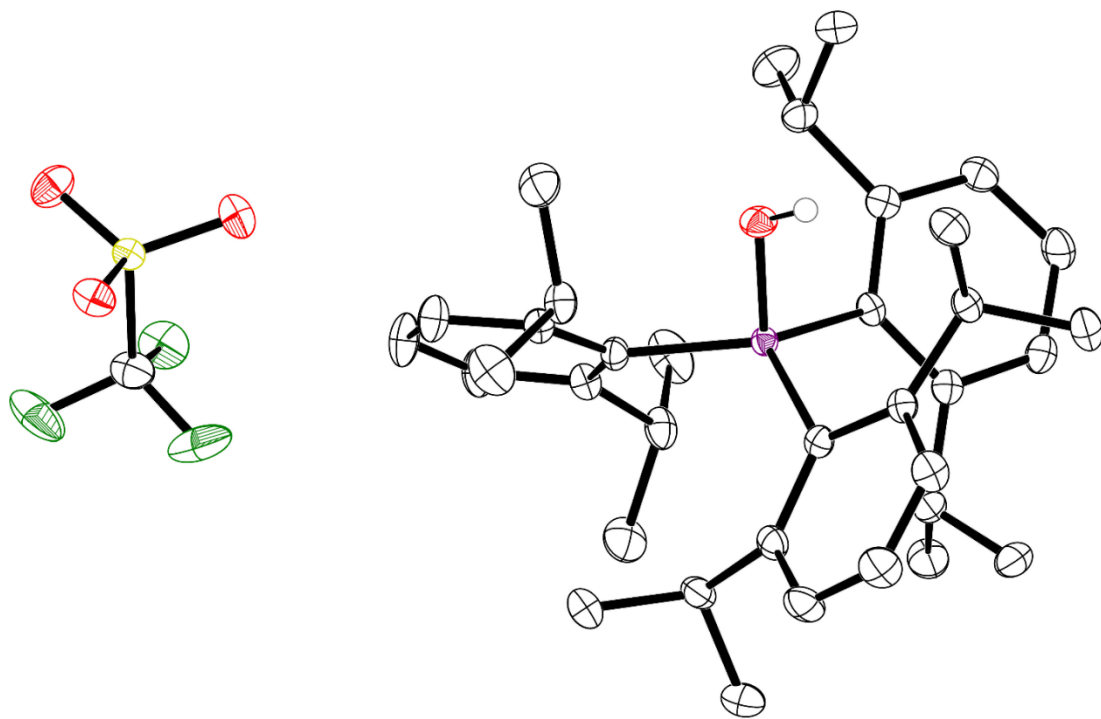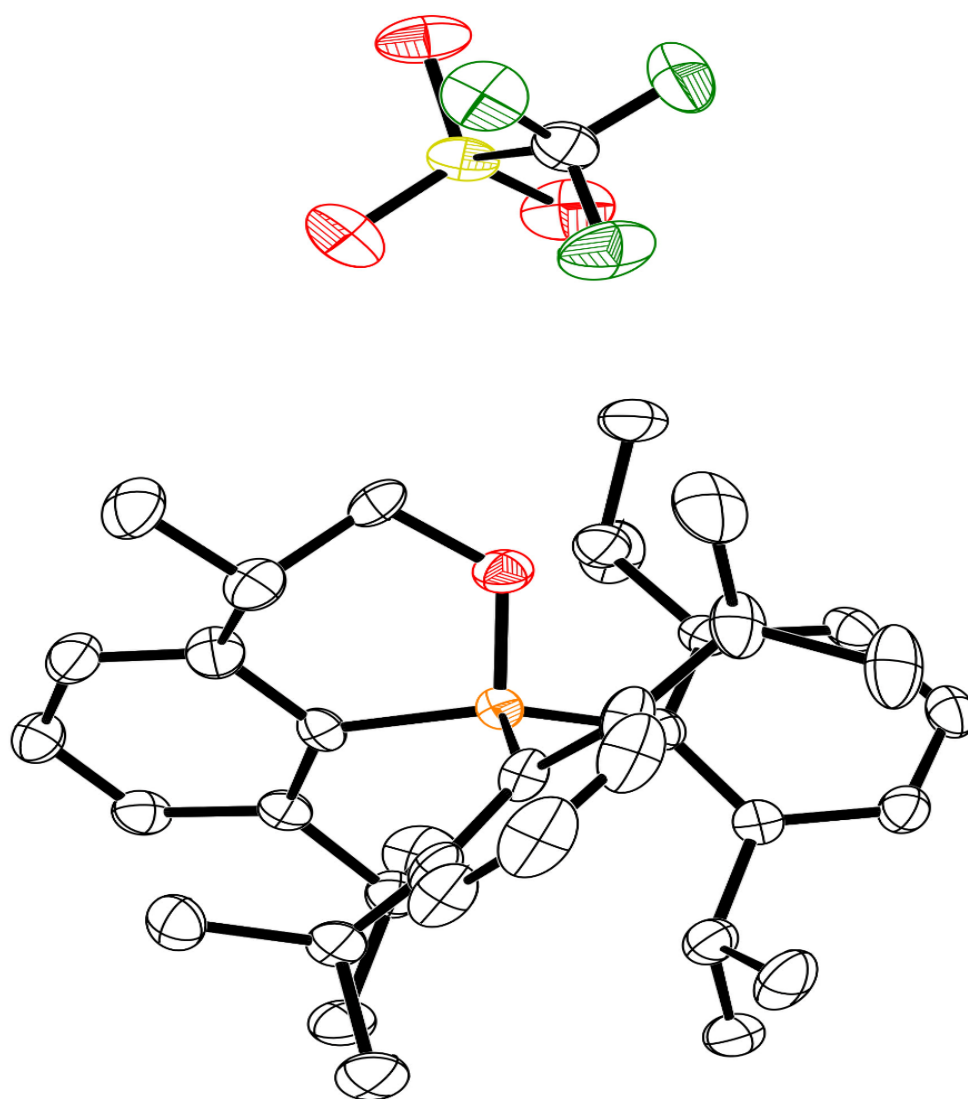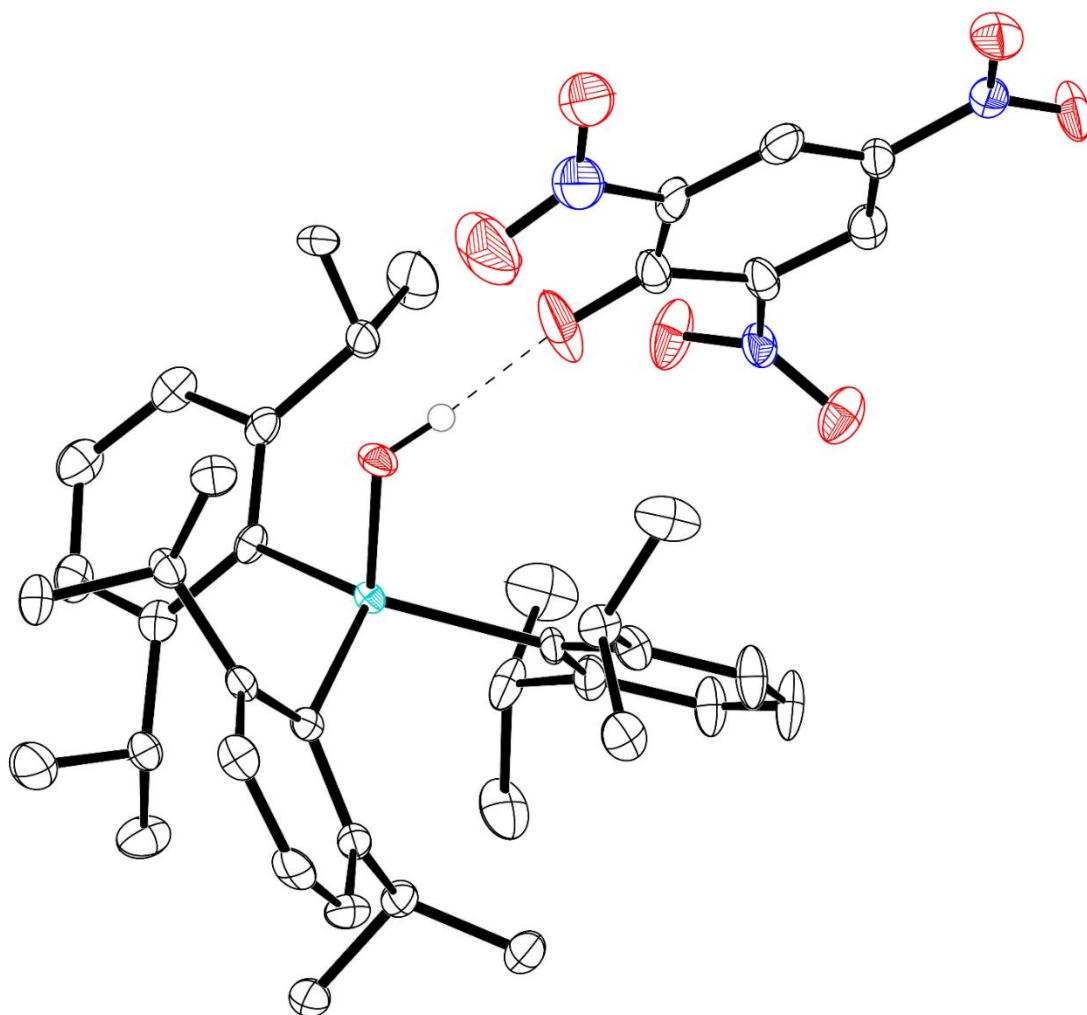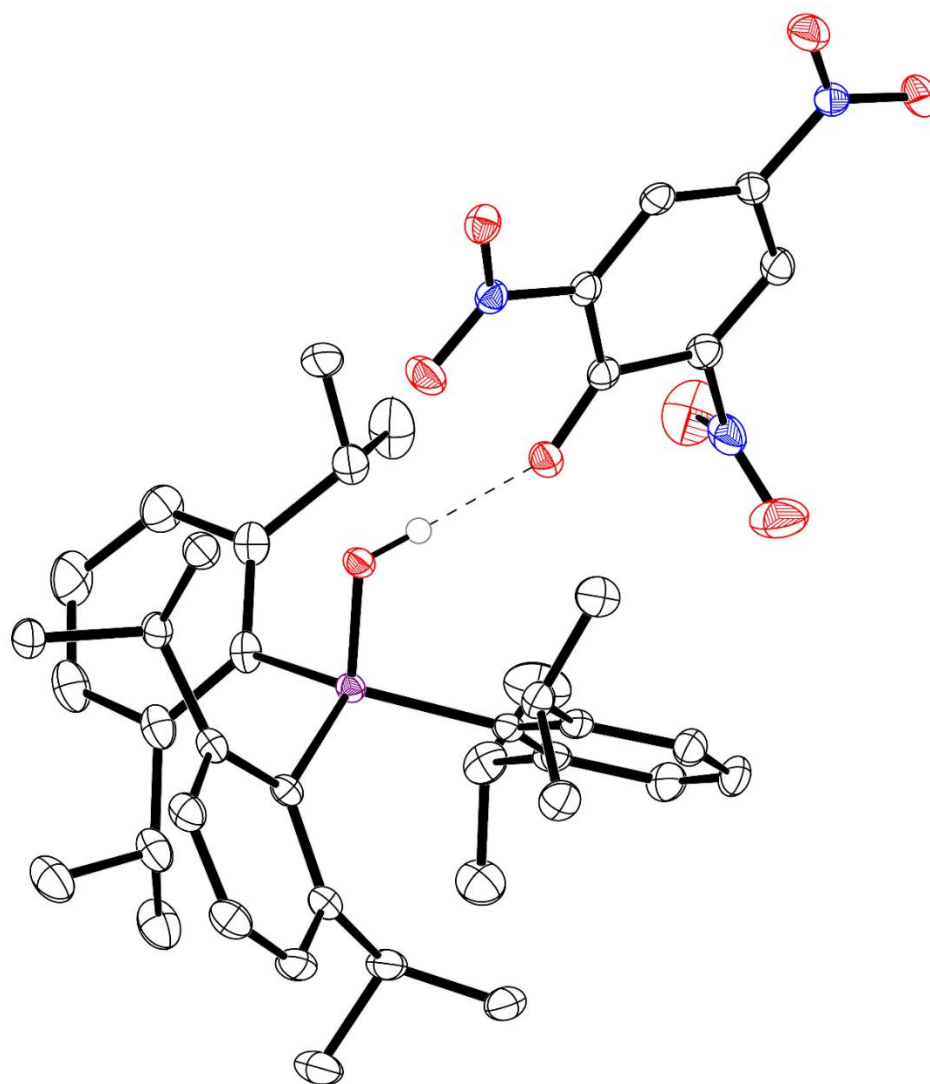
**Figure C.44.** Thermal ellipsoid plot (50% probability) of [Dipp$_3$AsOH][CF$_3$SO$_3$] triclinic. Color code: As purple, O red, C black, S yellow, F green, and H grey sphere of arbitrary radius. Non-protic H atoms are omitted for clarity.
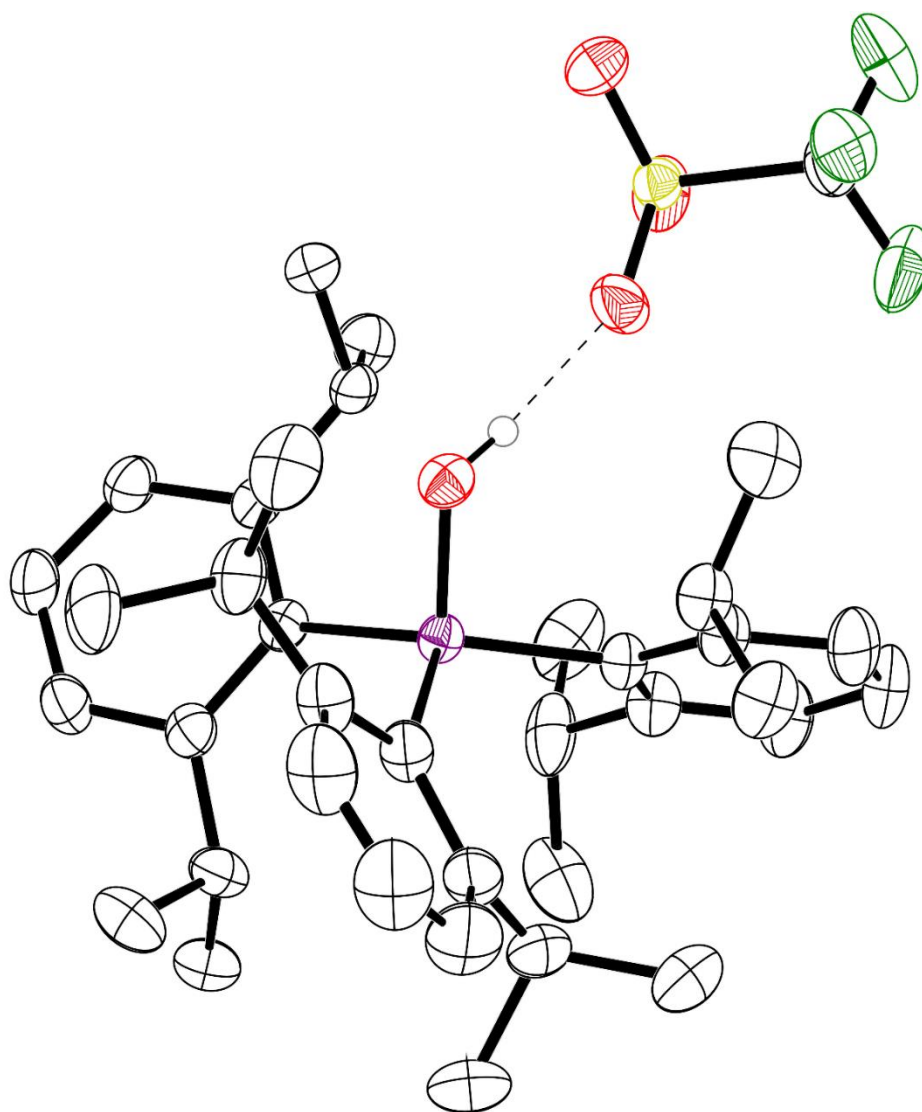
**Figure C.45.** Thermal ellipsoid plot (50% probability) of [Dipp$_3$AsOH][CF$_3$SO$_3$] monoclinic. Color code: As purple, O red, C black, S yellow, F green, and H grey sphere of arbitrary radius. Non-protic H atoms are omitted for clarity.
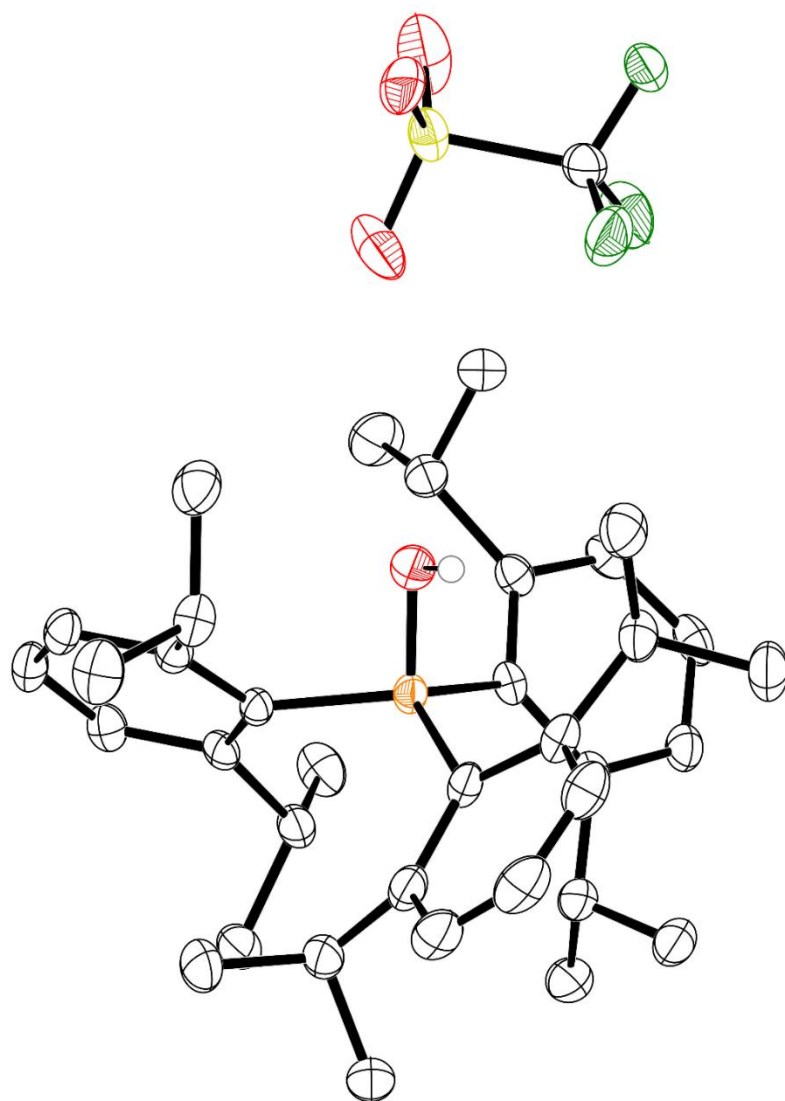
**Figure C.46.** Thermal ellipsoid plot (50% probability) of one of the crystallographically independent copies of [Dipp₃POH][O₃SCF₃] in the asymmetric unit. Color code: P orange, O red, C black, S yellow, F green, and H grey sphere of arbitrary radius. Non-protic H atoms are omitted for clarity.

**Figure C.47.** Thermal ellipsoid plot (50% probability) of **1**. Color code: P orange, O red, C black, S yellow, F green. Non-protic H atoms are omitted for clarity.

**Figure C.48.** Thermal ellipsoid plot (50% probability) of [Dipp₃SbOH][OPh(NO₂)₃]. Color code: Sb teal, O red, C black, N blue, and H grey sphere of arbitrary radius. Non-protic H atoms are omitted for clarity.
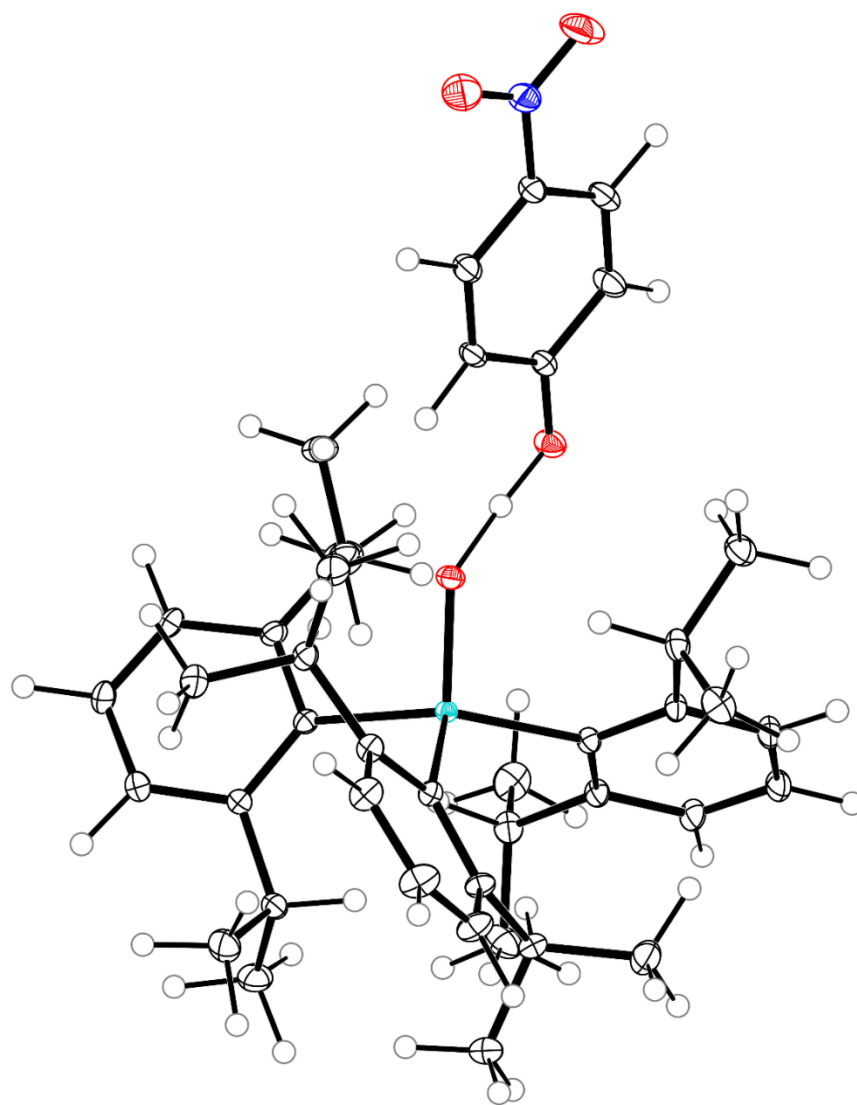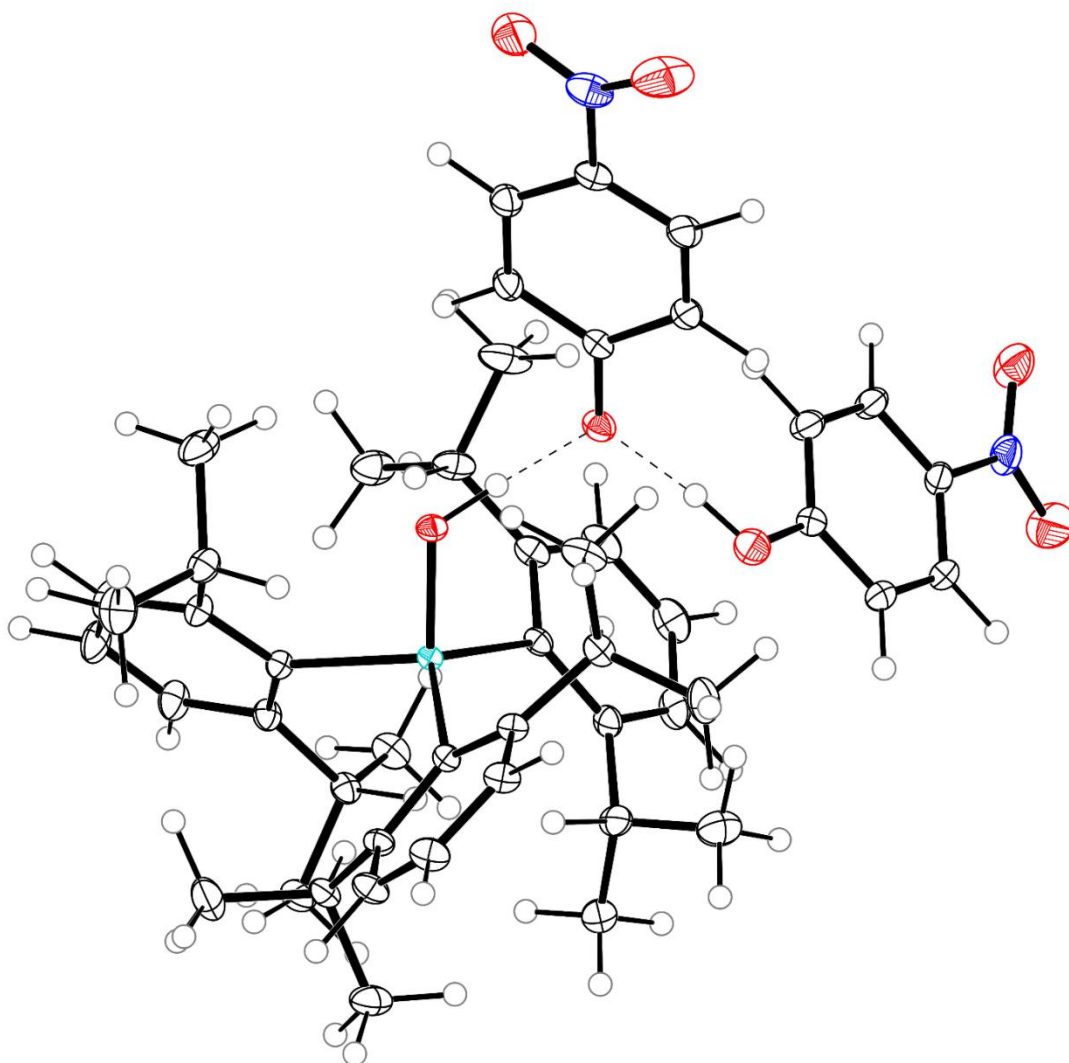
**Figure C.49.** Thermal ellipsoid plot (50% probability) of one of the crystallographically independent copies of [Dipp₃AsOH][OPh(NO₂)₃] present in the asymmetric unit of crystals of [Dipp₃AsOH][OPh(NO₂)₃]·¾(C₆H₁₂). Color code: As purple, O red, C black, N blue, and H grey sphere of arbitrary radius. Non-protic H atoms are omitted for clarity.
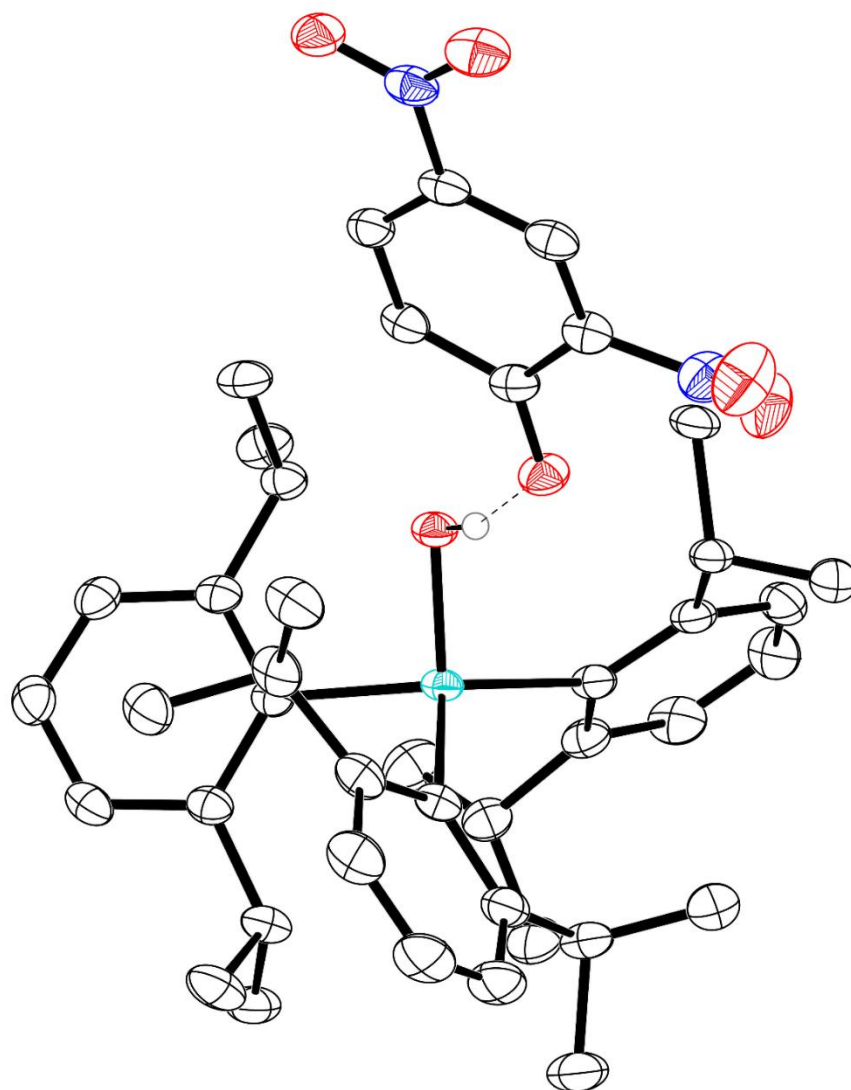
**Figure C.50.** Thermal ellipsoid plot (50% probability) of [Dipp₃SbOH][OPh(NO₂)₂]. Color code: Sb teal, O red, C black, N blue, and H grey sphere of arbitrary radius. Non-protic H atoms are omitted for clarity.

**Figure C.51.** Thermal ellipsoid plot (50% probability) of Dipp$_3$SbO·HOPhNO$_2$. Color code: Sb teal, O red, C black, N blue, and H grey spheres of arbitrary radius. Structure was obtained by Hirshfeld atom refinement.
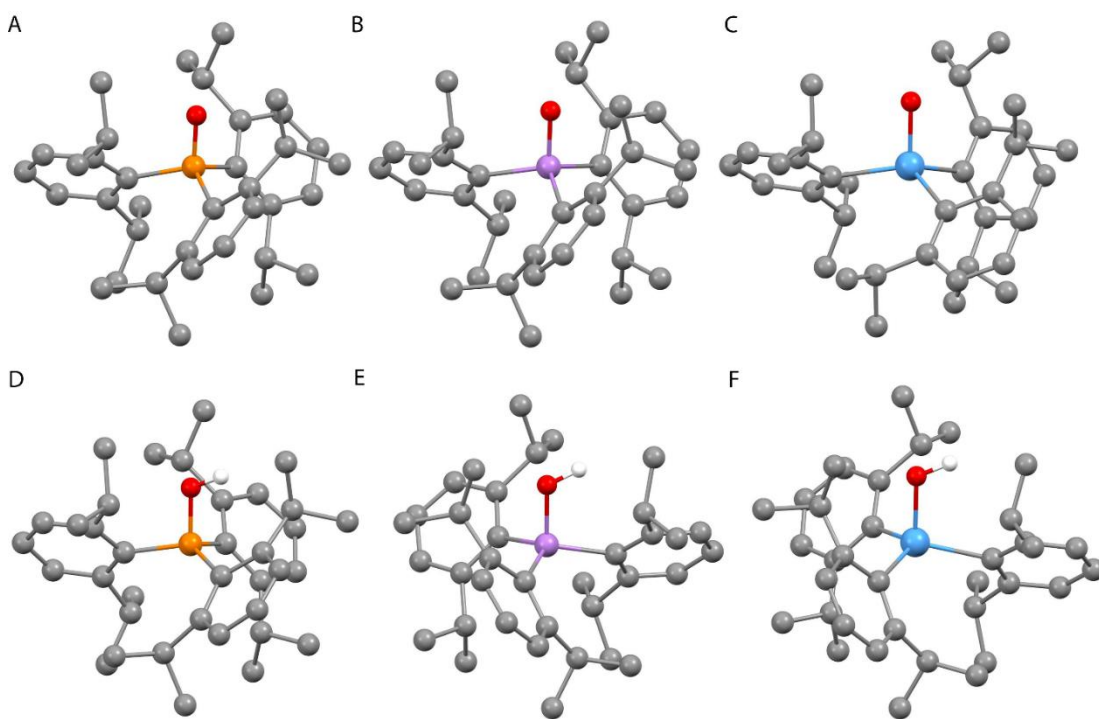
**Figure C.52.** Thermal ellipsoid plot (50% probability) of [Dipp₃SbOH][OPhNO₂]·*p*-nitrophenol. Color code: Sb teal, O red, C black, N blue, and H grey spheres of arbitrary radius. Structure was obtained by Hirshfeld atom refinement.
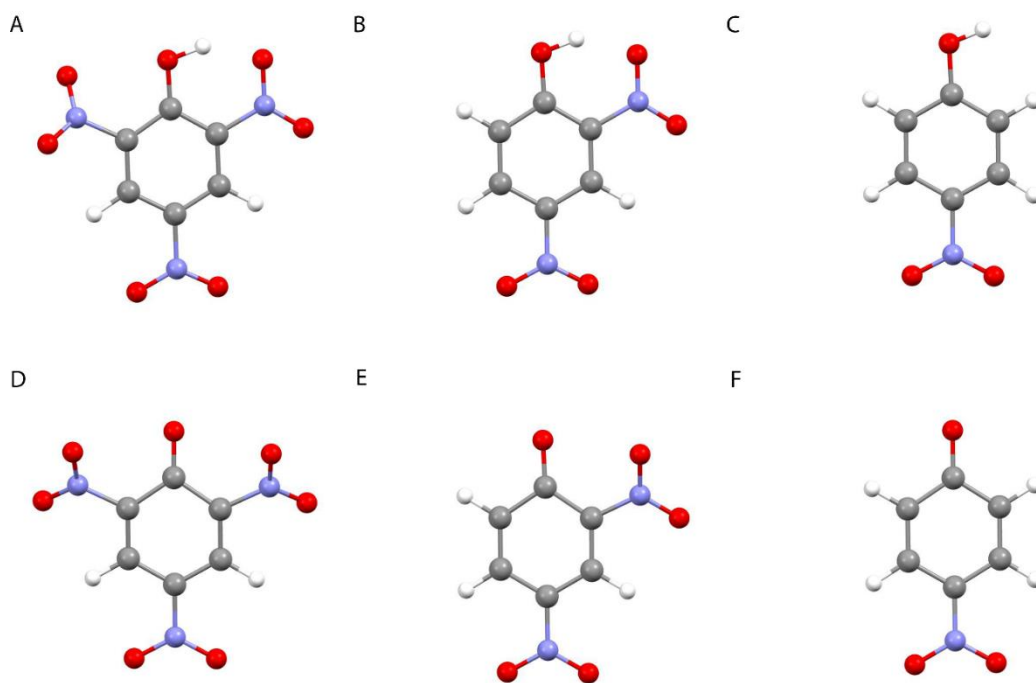
**Figure C.53.** Ball-and-stick representations of atomic coordinates of molecules used in theoretical studies. Geometry optimized (PBE0/def2-TZVPP) structure of (A) Dipp$_3$PO, (B) Dipp$_3$AsO, (C) Dipp$_3$SbO, (D) Dipp$_3$POH$^+$, (E) Dipp$_3$AsOH$^+$, (F) Dipp$_3$SbOH$^+$. Color code: C grey, H white, O red, Sb teal, As violet, P orange. Non-protic H atoms are omitted for clarity.

**Figure C.54.** Ball-and-stick representations of atomic coordinates of molecules used in theoretical studies. Geometry optimized (PBE0/def2-TZVPP) structure of (A) 2,4,6-trinitrophenol, (B) 2,4-dinitrophenol, (C) 4-nitrophenol, (D) 2,4,6-trinitrophenoxide, (E) 2,4-dinitrophenoxide, (F) 4-nitrophenoxide. Color code: C grey, H white, O red, N blue.
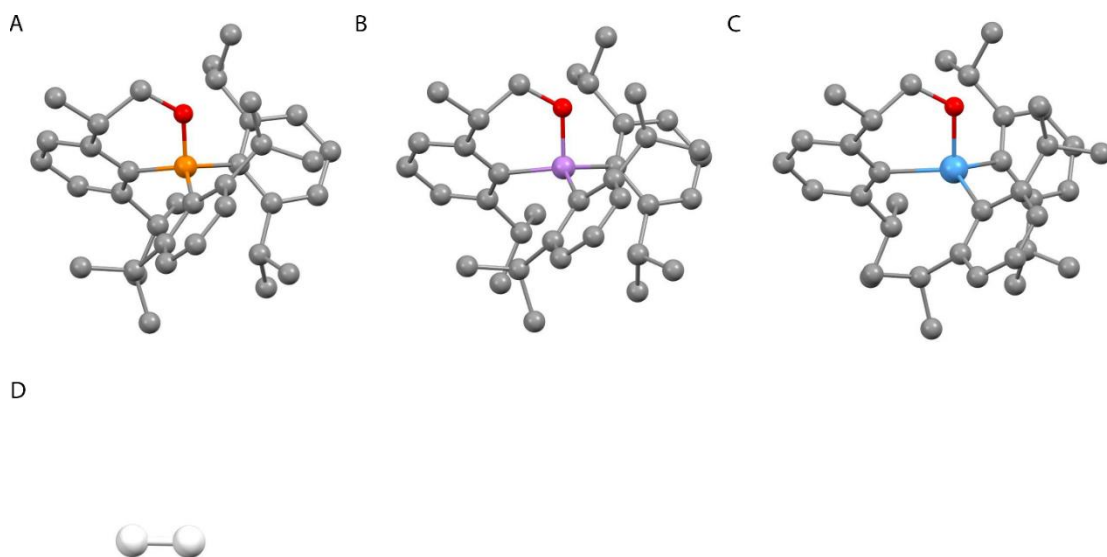
**Figure C.55.** Ball-and-stick representations of atomic coordinates of molecules used in theoretical studies. Geometry optimized (PBE0/def2-TZVPP) structure of (A) **1$^+$**, (B) **1$^+$**(As), (C) **1$^+$**(Sb), and (D) H$_2$. Color code: C grey, H white, O red, Sb teal, As violet, P orange. H atoms are omitted for clarity from the depictions of the pnictogen compounds.
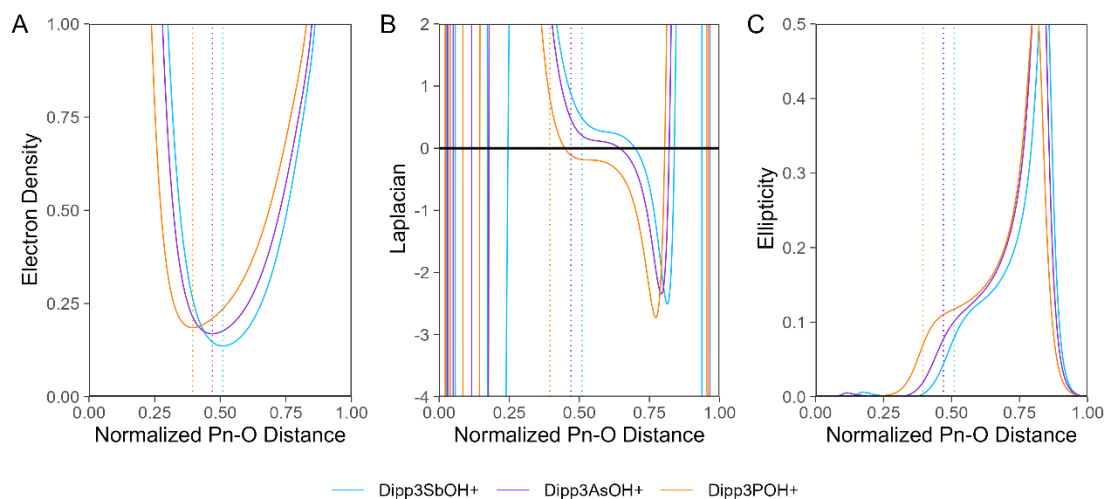


**Figure C.56.** Plots of ρ (e$^-$ Å$^{-3}$), ∇$^2$ρ (e$^-$ Å$^{-5}$), and ε along the Pn–O interatomic vector in Dipp$_3$PnOH$^+$.
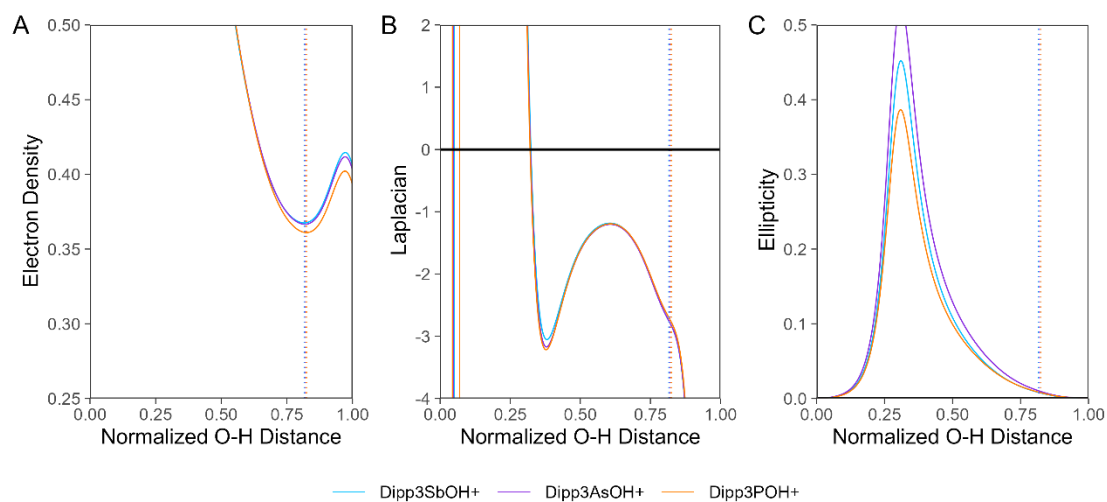
**Figure C.57.** Plots of $\rho$ ($e^-$ $\text{Å}^{-3}$), $\nabla^2\rho$ ($e^-$ $\text{Å}^{-5}$), and $\varepsilon$ along the O–H interatomic vector in $Dipp_3PnOH^+$.
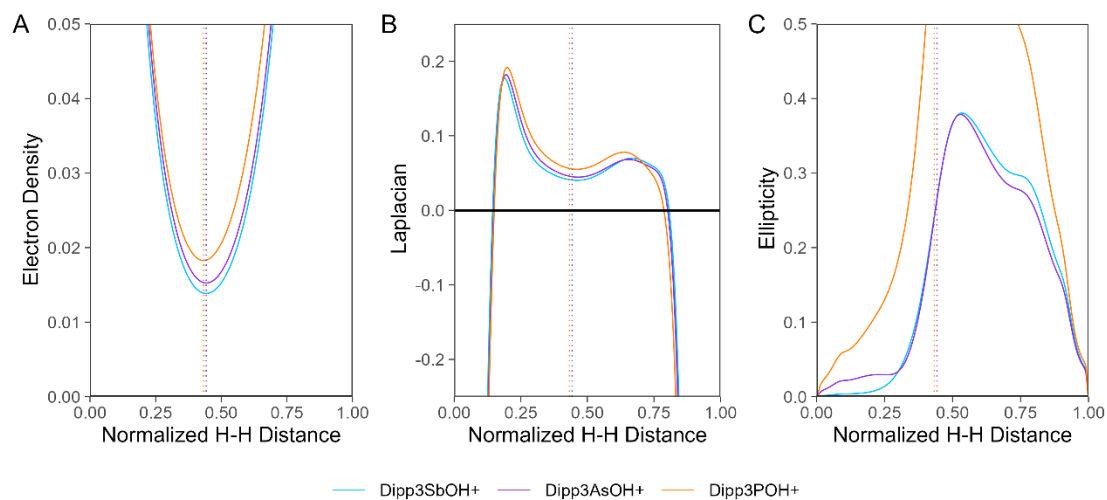


**Figure C.58.** Plots of $\rho$ ($e^-$ $\text{Å}^{-3}$), $\nabla^2\rho$ ($e^-$ $\text{Å}^{-5}$), and $\varepsilon$ along the OH$\cdots$HC$_{methyl}$ interatomic vector for the primary dihydrogen bonding interaction in $Dipp_3PnOH^+$.
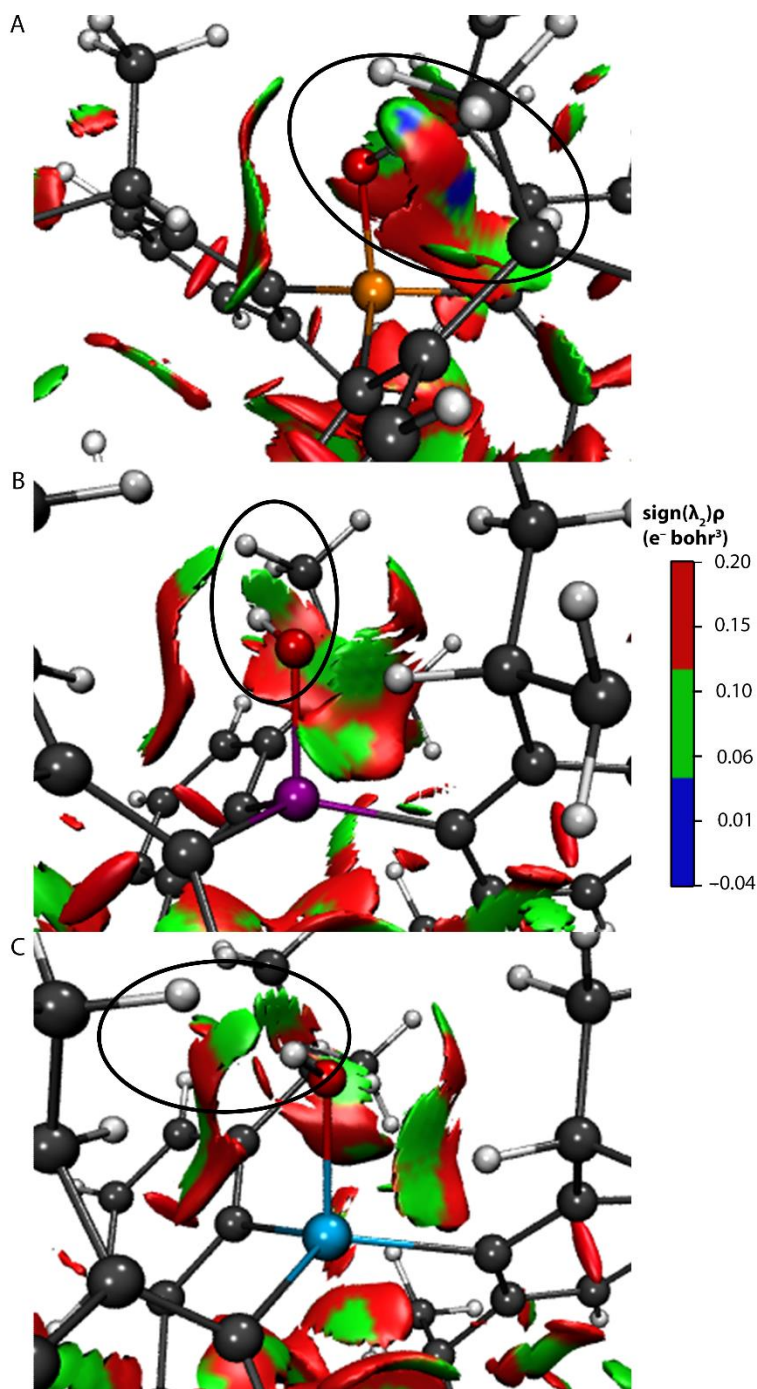
**Figure C.59.** NCI analysis of Dipp$_3$POH$^+$ (*top*), Dipp$_3$AsOH$^+$ (*middle*), and Dipp$_3$SbOH$^+$ (*bottom*) depicting reduced gradient surfaces (isovalue = 0.45 a.u.) with the function sign($\lambda_2$)$\rho$ where $\lambda_2$ is the second-largest eigenvalue of the Laplacian color-mapped on the surface. Blue is indicative of H-bonding interactions, green is indicative of van der Waals interactions, and red is indicative of steric repulsions. Color code: C black, H grey, O red, Sb teal, As violet, P orange.
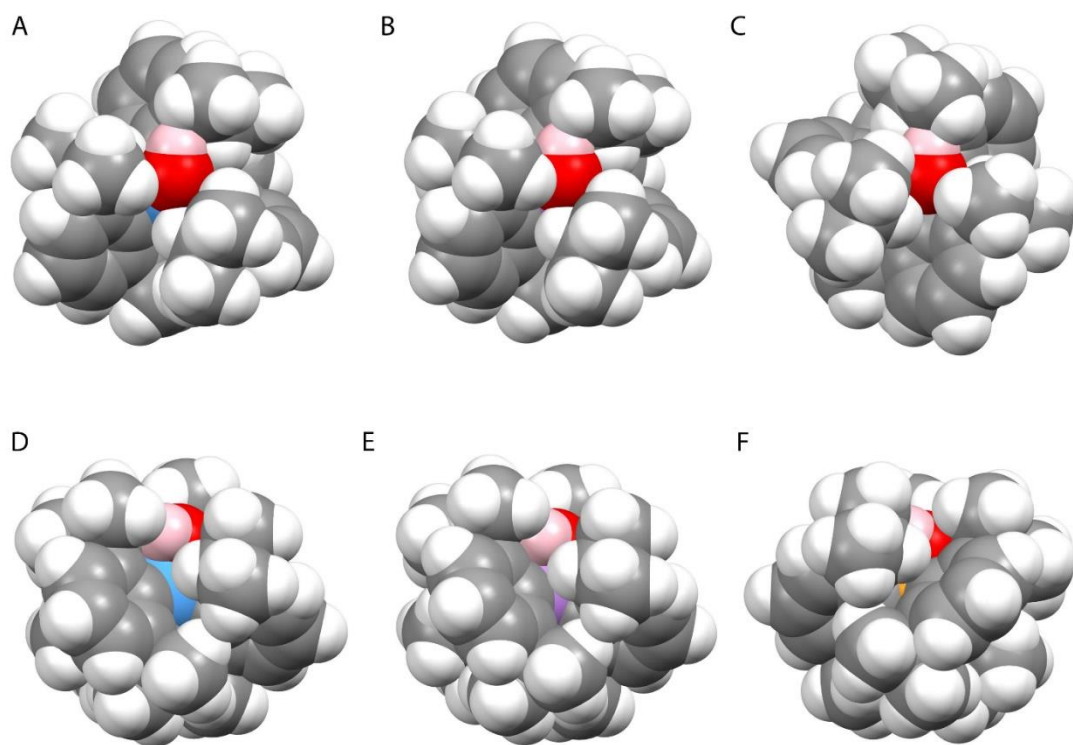
**Figure C.60.** Space-filling diagrams of optimized geometries (PBE0/def2-TZVPP) of Dipp$_3$SbOH$^+$ (A, D), Dipp$_3$AsOH$^+$ (B, E) and Dipp$_3$POH$^+$ (C, F) viewed along Pn–O bond axis (A-C) and perpendicular to Pn–O bond axis (D-F) (Pn = Sb, As, P). Color code: Sb teal, As purple, P orange, C grey, H white, protic H atom pink.

**Table C.1.** Calculated reaction enthalpies and Gibbs free energies of elimination of $H_2$ from hydroxypnictonium cations $Dipp_3PnOH^+$ to form cyclized alkoxypnictonium cations $\mathbf{1}^+$(Sb), $\mathbf{1}^+$(As), and $\mathbf{1}^+$, respectively.



(**1**⁺(Sb)) Pn = Sb
(**1**⁺(As)) Pn = As
(**1**⁺) Pn = P
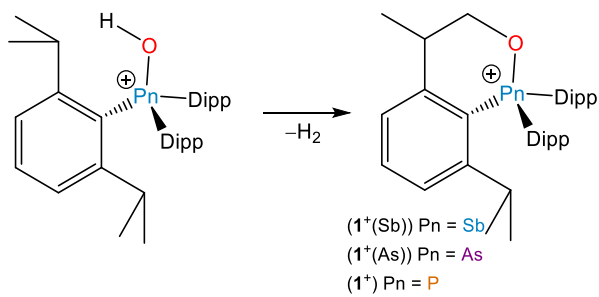
| Compound | $\Delta H$ (kcal/mol) | $\Delta G$ (kcal/mol) |
|---|---|---|
| $Dipp_3SbOH^+$ | 16.3 | 9.6 |
| $Dipp_3AsOH^+$ | 13.5 | 6.6 |
| $Dipp_3POH^+$ | 12.4 | 5.3 |

**Table C.2.** Crystallographic details for [Dipp$_3$SbOH][CF$_3$SO$_3$], [Dipp$_3$AsOH][CF$_3$SO$_3$]·CHCl$_3$ triclinic, [Dipp$_3$AsOH][CF$_3$SO$_3$]·CHCl$_3$ monoclinic, and [Dipp$_3$POH][O$_3$SCF$_3$].

| Compound | [Dipp$_3$SbOH][CF$_3$SO$_3$] | [Dipp$_3$AsOH][CF$_3$SO$_3$]·CHCl$_3$ | [Dipp$_3$AsOH][CF$_3$SO$_3$]·CHCl$_3$ monoclinic | [Dipp$_3$POH][O$_3$SCF$_3$] |
|---|---|---|---|---|
| Empirical Formula | C$_{37}$H$_{52}$F$_3$O$_4$SSb | C$_{38}$H$_{53}$F$_3$Cl$_3$O$_4$SAs | C$_{38}$H$_{53}$F$_3$Cl$_3$O$_4$SAs | C$_{37}$H$_{52}$F$_3$O$_4$S |
|  | 771.59 | 844.13 | 844.13 | 680.81 |
| Temperature | 100.0(1) | 100.0(1) | 100.0(1) | 100.0(1) |
| Wavelength | 1.54184 | 1.54184 | 1.54184 | 1.54184 |
| Crystal | Triclinic | Triclinic | Monoclinic | Triclinic |
| Space group | $P\bar{1}$ | $P\bar{1}$ | $P2_1/n$ | $P\bar{1}$ |
| $a$ (Å) | 10.19520(10) | 10.1956(2) | 10.06410(10) | 14.3959(2) |
| $b$ (Å) | 12.58260(10) | 14.2779(2) | 17.7940(3) | 16.0784(2) |
| $c$ (Å) | 14.95020(10) | 14.7095(2) | 23.5660(3) | 16.8118(2) |
| $\alpha$ (°) | 90.2560(10) | 92.4510(10) |  | 106.2340(1 |
| $\beta$ (°) | 98.4430(10) | 101.6540(10) | 98.6020(10) | 99.4490(10 |
| $\gamma$ (°) | 105.1700(10) | 100.5970(10) |  | 97.5890(10 |
| Volume (Å$^3$) | 1829.10(3) | 2054.26(6) | 4172.74(10) | 3619.84(8) |
| $Z$ | 2 | 2 | 4 | 4 |
| $\rho_{calc}$ (Mg/m$^3$) | 1.401 | 1.365 | 1.344 | 1.249 |
| Crystal size (mm$^3$) | 0.09 × 0.08 × 0.06 | 0.23 × 0.15 × 0.13 | 0.23 × 0.06 × 0.05 | 0.21 × 0.12 × 0.07 |
| $\theta$ range (°) | 2.991 to | 3.078 to 67.078 | 3.125 to 67.074 | 2.801 to |
| Total | 52573 | 25894 | 35950 | 49143 |
| Unique | 6525 | 7326 | 7436 | 12911 |
| Method | IAM | IAM | IAM | IAM |
| Parameters | 431 | 467 | 504 | 928 |
| Completeness | 100 | 100 | 100 | 99.9 |
| $R_{int}$ | 0.0480 | 0.0335 | 0.0394 | 0.0339 |
| $R_1$ (I > 2σ) | 0.0198 | 0.0362 | 0.0535 | 0.0435 |
| $R_1$ (all data) | 0.0209 | 0.0383 | 0.0573 | 0.0486 |
| $wR_2$ (I > 2σ) | 0.0489 | 0.0942 | 0.1154 | 0.1207 |
| $wR_2$ (all data) | 0.0494 | 0.0957 | 0.1170 | 0.1247 |
| Goodness of fit, $S$ | 1.031 | 1.056 | 1.164 | 1.037 |

**Table C.3.** Crystallographic details for **1**, [Dipp$_3$SbOH][OPh(NO$_2$)$_3$], [Dipp$_3$AsOH][OPh(NO$_2$)$_3$]·¾(C$_6$H$_{12}$), and [Dipp$_3$SbOH][OPh(NO$_2$)$_2$]·(CHCl$_3$)$_2$.

| Compound | **1** | [Dipp$_3$SbOH][OPh(NO$_2$)$_3$] [†] | [Dipp$_3$AsOH][OPh(NO$_2$)$_3$]·¾(C$_6$H$_{12}$ | [Dipp$_3$SbOH][OPh(NO$_2$)$_2$]·(CHCl$_3$)$_2$ |
|---|---|---|---|---|
| Empirical Formula | C$_{37}$H$_{50}$F$_3$O | C$_{42}$H$_{54}$N$_3$O$_8$Sb | C$_{46.5}$H$_{63}$AsN$_3$O$_8$ | C$_{44}$H$_{57}$Cl$_6$N$_2$O$_6$Sb |
| | 678.80 | 850.63 | 866.92 | 1044.36 |
| Temperature | 100.0(1) | 100.0(1) | 100.0(1) | 100.0(1) |
| Wavelength (Å) | 1.54184 | 0.71073 | 1.54184 | 1.54184 |
| Crystal system | Monoclin | Monoclinic | Triclinic | Triclinic |
| Space group | $P2_1/n$ | $Pn$ | $P\bar{1}$ | $P\bar{1}$ |
| $a$ (Å) | 9.49870(10) | 10.4423(2) | 11.82030(10) | 11.1814(2) |
| $b$ (Å) | 25.1021(3) | 20.8325(5) | 15.2864(2) | 14.1312(3) |
| $c$ (Å) | 14.9869(2) | 18.7820(4) | 24.9112(2) | 16.4708(4) |
| $\alpha$ (°) | | | 87.8670(10) | 79.673(2) |
| $\beta$ (°) | 101.4440 | 93.444(2) | 80.2660(10) | 74.232(2) |
| $\gamma$ (°) | | | 88.6100(10) | 76.038(2) |
| Volume (Å$^3$) | 3502.39(7) | 4078.44(15) | 4432.59(8) | 2412.49(10) |
| $Z$ | 4 | 4 | 4 | 2 |
| $\rho_{calc}$ (Mg/m$^3$) | 1.287 | 1.385 | 1.299 | 1.438 |
| Crystal size (mm$^3$) | 0.11 × 0.08 × 0.06 | 0.27 × 0.21 × 0.14 | 0.19 × 0.13 × 0.08 | 0.19 × 0.08 × 0.05 |
| θ range (°) | 3.486 to 67.077 | 2.185 to 25.123 | 2.893 to 67.077 | 2.809 to 67.080 |
| Total | 48293 | 32156 | 60318 | 30917 |
| Unique | 6253 | 12674 | 15821 | 8624 |
| Method | IAM | IAM | IAM | IAM |
| Parameters | 455 | 1087 | 1086 | 621 |
| Completeness | 100 | 99.9 | 100.0 | 100.0 |
| $R_{int}$ | 0.0372 | 0.0338 | 0.0359 | 0.0457 |
| $R_1$ (I > 2σ) | 0.0491 | 0.0310 | 0.0311 | 0.0346 |
| $R_1$ (all data) | 0.0524 | 0.0344 | 0.0345 | 0.0367 |
| $wR_2$ (I > 2σ) | 0.1282 | 0.0693 | 0.0779 | 0.0908 |
| $wR_2$ (all data) | 0.1307 | 0.0709 | 0.0799 | 0.0925 |
| Goodness of fit, $S$ | 1.039 | 1.079 | 1.048 | 1.048 |

**Table C.4.** Crystallographic parameters for Dipp$_3$SbO·HOPhNO$_2$·*p*-nitrophenol and Dipp$_3$SbO·HOPhNO$_2$.

| Compound | Dipp$_3$SbO·HOPhNO$_2$·*p*-nitrophenol | | Dipp$_3$SbO·HOPhNO$_2$ | |
|---|---|---|---|---|
| Empirical | C$_{48}$H$_{61}$N$_2$O$_7$Sb | | C$_{42}$H$_{56}$NO$_4$Sb | |
| Formula Weight | 899.788 | | 760.677 | |
| Temperature (K) | 100.0(1) | | 99.95(17) | |
| Wavelength (Å) | 0.71073 | | 0.71073 | |
| Crystal system | Monoclinic | | Triclinic | |
| Space group | *P*2$_1$/*n* | | *P*$\bar{1}$ | |
| *a* (Å) | 15.7304(3) | | 9.8747(2) | |
| *b* (Å) | 18.4840(3) | | 12.6935(3) | |
| *c* (Å) | 15.7610(3) | | 15.4719(3) | |
| α (°) | | | 87.478(2) | |
| β (°) | 101.383(2) | | 77.760(2) | |
| γ (°) | | | 83.096(2) | |
| Volume (Å$^3$) | 4492.54(14) | | 1881.15(7) | |
| *Z* | 4 | | 2 | |
| ρ$_{calc}$ (Mg/m$^3$) | 1.330 | | 1.343 | |
| Crystal size | 0.21 × 0.14 × 0.1 | | 0.22 × 0.08 × 0.06 | |
| θ range (°) | 2.32 to 33.73 | | 2.08 to 33.73 | |
| Total reflections | 69536 | | 62483 | |
| Unique | 17515 | | 15034 | |
| Method | IAM | HAR | IAM | HAR |
| Parameters | 541 | 706 | 448 | 601 |
| Completeness | 97.8 | 97.79 | 100.0 | 99.96 |
| R$_{int}$ | 0.0388 | 0.0412 | 0.0487 | 0.0515 |
| R$_1$ (I > 2σ) | 0.0296 | 0.0255 | 0.0308 | 0.0276 |
| R$_1$ (all data) | 0.0403 | 0.0362 | 0.0374 | 0.0341 |
| wR$_2$ (I > 2σ) | 0.0677 | 0.0471 | 0.0664 | 0.0488 |
| wR$_2$ (all data) | 0.0708 | 0.0496 | 0.0720 | 0.0535 |
| Goodness of fit, *S* | 1.059 | 1.0040 | 1.061 | 0.9511 |

**Table C.5.** Select data from NMR monitoring of titration (replicate 1) of [Dipp$_3$SbOH][CF$_3$SO$_3$] with triethylamine (TEA).

| Volume TEA added (mL) | Chemical Shift (ppm) | Total volume sample (mL) | Deprotonated (%) | [Dipp$_3$SbO] (mM) | [Dipp$_3$SbOH$^+$] (mM) | [TEA] (mM) | Equivalents of TEA added |
|---|---|---|---|---|---|---|---|
| 0.05 | 2.89 | 600.5 | 1.4 | 0.08 | 5.32 | 0.5 | 0.1 |
| 0.1 | 2.93 | 601 | 3.8 | 0.20 | 5.19 | 1.0 | 0.2 |
| 0.15 | 2.96 | 601.5 | 6.3 | 0.34 | 5.05 | 1.4 | 0.3 |
| 0.2 | 2.98 | 602 | 7.5 | 0.40 | 4.98 | 2.0 | 0.4 |
| 0.25 | 3.01 | 602.5 | 9.8 | 0.53 | 4.85 | 2.4 | 0.6 |
| 0.35 | 3.07 | 603.5 | 14.5 | 0.78 | 4.59 | 3.4 | 0.8 |
| 0.5 | 3.12 | 605 | 17.6 | 0.94 | 4.41 | 5.0 | 1.1 |
| 0.75 | 3.22 | 607.5 | 24.8 | 1.33 | 4.01 | 7.5 | 1.7 |
| 1 | 3.27 | 610 | 28.6 | 1.52 | 3.79 | 10.2 | 2.2 |
| 1.5 | 3.38 | 610.5 | 37.1 | 1.97 | 3.34 | 15.7 | 3.3 |
| 2 | 3.46 | 611 | 42.3 | 2.25 | 3.06 | 21.2 | 4.4 |
| 3 | 3.59 | 612 | 51.8 | 2.74 | 2.55 | 32.4 | 6.6 |
| 4.5 | 3.70 | 613.5 | 60.1 | 3.17 | 2.11 | 49.5 | 10.0 |
| 7 | 3.81 | 616 | 68.4 | 3.60 | 1.66 | 77.9 | 15.5 |
| 10 | 3.90 | 619 | 74.6 | 3.90 | 1.33 | 112.0 | 22.1 |
| 15 | 3.99 | 624 | 81.0 | 4.20 | 0.99 | 168.3 | 33.2 |
| 25 | 4.07 | 634 | 87.0 | 4.45 | 0.66 | 278.5 | 55.4 |
| 35 | 4.11 | 644 | 89.9 | 4.52 | 0.51 | 385.4 | 77.5 |
| 45 | 4.14 | 654 | 91.7 | 4.54 | 0.41 | 489.1 | 99.7 |
| 55 | 4.15 | 664 | 93.0 | 4.54 | 0.34 | 589.7 | 121.8 |
| 65 | 4.17 | 674 | 94.0 | 4.52 | 0.29 | 687.4 | 143.9 |
| 85 | 4.18 | 694 | 95.2 | 4.44 | 0.23 | 874.3 | 188.2 |

**Table C.6.** Select data from NMR monitoring of titration (replicate 2) of [Dipp$_3$SbOH][CF$_3$SO$_3$] with triethylamine (TEA).

| Volume TEA added (mL) | Chemical Shift (ppm) | Total volume sample (mL) | Deprotonated (%) | [Dipp$_3$SbO] (mM) | [Dipp$_3$SbOH$^+$] (mM) | [TEA] (mM) | Equivalents of TEA added |
|---|---|---|---|---|---|---|---|
| 0.05 | 2.93 | 600.5 | 4.1 | 0.22 | 5.17 | 0.5 | 0.1 |
| 0.1 | 2.96 | 601 | 6.6 | 0.36 | 5.03 | 1.0 | 0.2 |
| 0.15 | 3.00 | 601.5 | 9.3 | 0.50 | 4.89 | 1.4 | 0.3 |
| 0.2 | 3.02 | 602 | 10.7 | 0.58 | 4.81 | 2.0 | 0.4 |
| 0.25 | 3.05 | 602.5 | 12.5 | 0.67 | 4.71 | 2.4 | 0.6 |
| 0.35 | 3.08 | 603.5 | 15.3 | 0.82 | 4.55 | 3.4 | 0.8 |
| 0.5 | 3.14 | 605 | 19.1 | 1.02 | 4.33 | 5.0 | 1.1 |
| 0.75 | 3.21 | 607.5 | 24.8 | 1.32 | 4.01 | 7.5 | 1.7 |
| 1 | 3.28 | 610 | 29.4 | 1.56 | 3.75 | 10.2 | 2.2 |
| 1.5 | 3.38 | 610.5 | 36.9 | 1.96 | 3.35 | 15.7 | 3.3 |
| 2 | 3.49 | 611 | 44.5 | 2.36 | 2.94 | 21.2 | 4.4 |
| 3 | 3.61 | 612 | 53.5 | 2.83 | 2.46 | 32.4 | 6.6 |
| 4.5 | 3.73 | 613.5 | 62.4 | 3.29 | 1.99 | 49.5 | 10.0 |
| 7 | 3.86 | 616 | 71.4 | 3.75 | 1.51 | 77.9 | 15.5 |
| 10 | 3.94 | 619 | 77.3 | 4.04 | 1.19 | 112.0 | 22.1 |
| 15 | 4.01 | 624 | 82.8 | 4.30 | 0.89 | 168.3 | 33.2 |
| 25 | 4.10 | 634 | 89.1 | 4.55 | 0.56 | 278.5 | 55.4 |
| 35 | 4.14 | 644 | 91.7 | 4.62 | 0.42 | 385.4 | 77.5 |
| 45 | 4.16 | 654 | 93.4 | 4.62 | 0.33 | 489.1 | 99.7 |
| 55 | 4.17 | 664 | 94.5 | 4.61 | 0.27 | 589.7 | 121.8 |
| 65 | 4.18 | 674 | 95.3 | 4.58 | 0.23 | 687.4 | 143.9 |
| 85 | 4.20 | 694 | 96.5 | 4.50 | 0.16 | 874.3 | 188.2 |

**Table C.7.** Select data from NMR monitoring of titration (replicate 3) of [Dipp$_3$SbOH][CF$_3$SO$_3$] with triethylamine (TEA).

| Volume TEA added (mL) | Chemical Shift (ppm) | Total volume sample (mL) | Deprotonated (%) | [Dipp$_3$SbO] (mM) | [Dipp$_3$SbOH$^+$] (mM) | [TEA] (mM) | Equivalents of TEA added |
|---|---|---|---|---|---|---|---|
| 0.05 | 2.95 | 600.5 | 5.8 | 0.31 | 5.08 | 0.5 | 0.1 |
| 0.1 | 2.99 | 601 | 8.6 | 0.47 | 4.93 | 1.0 | 0.2 |
| 0.15 | 3.04 | 601.5 | 12.0 | 0.64 | 4.74 | 1.4 | 0.3 |
| 0.2 | 3.07 | 602 | 14.1 | 0.76 | 4.62 | 2.0 | 0.4 |
| 0.25 | 3.10 | 602.5 | 16.6 | 0.89 | 4.48 | 2.4 | 0.6 |
| 0.35 | 3.16 | 603.5 | 20.5 | 1.10 | 4.27 | 3.4 | 0.8 |
| 0.5 | 3.21 | 605 | 24.3 | 1.30 | 4.06 | 5.0 | 1.1 |
| 0.75 | 3.27 | 607.5 | 28.6 | 1.53 | 3.81 | 7.5 | 1.7 |
| 1 | 3.32 | 610 | 32.3 | 1.71 | 3.60 | 10.2 | 2.2 |
| 1.5 | 3.36 | 610.5 | 35.6 | 1.89 | 3.42 | 15.7 | 3.3 |
| 2 | 3.45 | 611 | 42.2 | 2.24 | 3.06 | 21.2 | 4.4 |
| 3 | 3.59 | 612 | 51.8 | 2.74 | 2.55 | 32.4 | 6.6 |
| 4.5 | 3.71 | 613.5 | 60.6 | 3.20 | 2.08 | 49.5 | 10.0 |
| 7 | 3.82 | 616 | 69.0 | 3.63 | 1.63 | 77.9 | 15.5 |
| 10 | 3.91 | 619 | 75.0 | 3.93 | 1.31 | 112.0 | 22.1 |
| 15 | 3.99 | 624 | 81.0 | 4.20 | 0.99 | 168.3 | 33.2 |
| 25 | 4.07 | 634 | 87.1 | 4.45 | 0.66 | 278.5 | 55.4 |
| 35 | 4.11 | 644 | 90.1 | 4.53 | 0.50 | 385.4 | 77.5 |
| 45 | 4.14 | 654 | 91.9 | 4.55 | 0.40 | 489.1 | 99.7 |
| 55 | 4.15 | 664 | 93.1 | 4.54 | 0.34 | 589.7 | 121.8 |
| 65 | 4.17 | 674 | 94.0 | 4.52 | 0.29 | 687.4 | 143.9 |
| 85 | 4.19 | 694 | 95.4 | 4.45 | 0.22 | 874.3 | 188.2 |

**Table C.8.** Select data from NMR monitoring of titration (replicate 1) of [Dipp$_3$AsOH][CF$_3$SO$_3$] with acridine (ACR).

| Mass ACR added (mg) | Chemical Shift (ppm) | Total volume sample (mL) | Deprotonated (%) | [Dipp$_3$AsO] (mM) | [Dipp$_3$AsOH$^+$] (mM) | [ACR] (mM) | Equivalents of ACR added |
|---|---|---|---|---|---|---|---|
| 0.05 | 2.79 | 501 | 2.3 | 0.08 | 3.28 | 0.5 | 0.2 |
| 0.07 | 2.82 | 501.5 | 4.6 | 0.16 | 3.20 | 0.7 | 0.2 |
| 0.12 | 2.85 | 502.5 | 8.0 | 0.27 | 3.08 | 1.1 | 0.4 |
| 0.17 | 2.87 | 503.5 | 10.1 | 0.34 | 3.01 | 1.6 | 0.6 |
| 0.25 | 2.90 | 505 | 12.7 | 0.42 | 2.91 | 2.3 | 0.8 |
| 0.37 | 2.94 | 507.5 | 16.7 | 0.55 | 2.76 | 3.5 | 1.2 |
| 0.49 | 2.98 | 510 | 20.0 | 0.66 | 2.64 | 4.8 | 1.6 |
| 0.74 | 3.04 | 515 | 25.3 | 0.83 | 2.44 | 7.2 | 2.5 |
| 0.99 | 3.08 | 520 | 29.4 | 0.95 | 2.29 | 9.7 | 3.3 |
| 1.24 | 3.12 | 525 | 33.1 | 1.06 | 2.15 | 12.1 | 4.1 |
| 1.73 | 3.18 | 535 | 39.2 | 1.23 | 1.91 | 16.8 | 5.7 |
| 2.47 | 3.26 | 550 | 45.9 | 1.41 | 1.65 | 23.7 | 8.2 |
| 3.96 | 3.36 | 580 | 55.7 | 1.62 | 1.29 | 36.5 | 13.1 |
| 5.94 | 3.44 | 620 | 62.9 | 1.71 | 1.01 | 51.7 | 19.7 |
| 8.90 | 3.53 | 680 | 72.1 | 1.79 | 0.69 | 71.3 | 29.5 |
| 12.37 | 3.61 | 750 | 79.2 | 1.78 | 0.47 | 90.3 | 41.0 |
| 17.31 | 3.67 | 850 | 84.6 | 1.67 | 0.31 | 112.0 | 57.4 |
| 22.26 | 3.70 | 950 | 88.1 | 1.56 | 0.21 | 129.2 | 73.8 |
| 27.21 | 3.73 | 1050 | 90.6 | 1.45 | 0.15 | 143.2 | 90.2 |
| 32.15 | 3.75 | 1150 | 92.4 | 1.35 | 0.11 | 154.7 | 106.6 |
| 42.05 | 3.77 | 1150 | 94.4 | 1.38 | 0.08 | 202.7 | 139.4 |
| 51.94 | 3.78 | 1150 | 95.6 | 1.40 | 0.06 | 250.7 | 172.2 |

**Table C.9.** Select data from NMR monitoring of titration (replicate 2) of [Dipp$_3$AsOH][CF$_3$SO$_3$] with acridine (ACR).

| Mass ACR added (mg) | Chemical Shift (ppm) | Total volume sample (mL) | Deprotonated (%) | [Dipp$_3$AsO] (mM) | [Dipp$_3$AsOH$^+$] (mM) | [ACR] (mM) | Equivalents of ACR added |
|---|---|---|---|---|---|---|---|
| 0.05 | 2.81 | 501 | 4.6 | 0.15 | 3.21 | 0.5 | 0.2 |
| 0.07 | 2.84 | 501.5 | 6.8 | 0.23 | 3.13 | 0.7 | 0.2 |
| 0.12 | 2.88 | 502.5 | 10.9 | 0.37 | 2.99 | 1.1 | 0.4 |
| 0.17 | 2.91 | 503.5 | 13.3 | 0.44 | 2.90 | 1.6 | 0.6 |
| 0.25 | 2.93 | 505 | 15.8 | 0.53 | 2.81 | 2.3 | 0.8 |
| 0.37 | 2.99 | 507.5 | 20.6 | 0.68 | 2.63 | 3.5 | 1.2 |
| 0.49 | 3.02 | 510 | 23.9 | 0.79 | 2.51 | 4.8 | 1.6 |
| 0.74 | 3.08 | 515 | 29.5 | 0.96 | 2.31 | 7.2 | 2.5 |
| 0.99 | 3.12 | 520 | 33.3 | 1.08 | 2.16 | 9.7 | 3.3 |
| 1.24 | 3.17 | 525 | 37.5 | 1.20 | 2.01 | 12.1 | 4.1 |
| 1.73 | 3.22 | 535 | 43.1 | 1.35 | 1.79 | 16.8 | 5.7 |
| 2.47 | 3.29 | 550 | 49.4 | 1.51 | 1.55 | 23.7 | 8.2 |
| 3.96 | 3.40 | 580 | 59.1 | 1.71 | 1.19 | 36.5 | 13.1 |
| 5.94 | 3.49 | 620 | 68.0 | 1.85 | 0.87 | 51.7 | 19.7 |
| 8.90 | 3.56 | 680 | 74.7 | 1.85 | 0.63 | 71.3 | 29.5 |
| 12.37 | 3.63 | 750 | 81.3 | 1.82 | 0.42 | 90.3 | 41.0 |
| 17.31 | 3.70 | 850 | 87.3 | 1.73 | 0.25 | 112.0 | 57.4 |
| 22.26 | 3.73 | 950 | 90.4 | 1.60 | 0.17 | 129.2 | 73.8 |
| 27.21 | 3.75 | 1050 | 92.4 | 1.48 | 0.12 | 143.2 | 90.2 |
| 32.15 | 3.76 | 1150 | 93.3 | 1.37 | 0.10 | 154.7 | 106.6 |
| 42.05 | 3.78 | 1150 | 95.4 | 1.40 | 0.07 | 202.7 | 139.4 |
| 51.94 | 3.79 | 1150 | 96.5 | 1.41 | 0.05 | 250.7 | 172.2 |

**Table C.10.** Select data from NMR monitoring of titration (replicate 3) of [Dipp$_3$AsOH][CF$_3$SO$_3$] with acridine (ACR).

| Mass ACR added (mg) | Chemical Shift (ppm) | Total volume sample (mL) | Deprotonated (%) | [Dipp$_3$AsO] (mM) | [Dipp$_3$AsOH$^+$] (mM) | [ACR] (mM) | Equivalents of ACR added |
|---|---|---|---|---|---|---|---|
| 0.05 | 2.77 | 501 | 0.2 | 0.01 | 3.35 | 0.5 | 0.2 |
| 0.07 | 2.78 | 501.5 | 1.6 | 0.05 | 3.30 | 0.7 | 0.2 |
| 0.12 | 2.81 | 502.5 | 3.8 | 0.13 | 3.22 | 1.1 | 0.4 |
| 0.17 | 2.84 | 503.5 | 6.8 | 0.23 | 3.12 | 1.6 | 0.6 |
| 0.25 | 2.86 | 505 | 8.6 | 0.29 | 3.05 | 2.3 | 0.8 |
| 0.37 | 2.90 | 507.5 | 12.4 | 0.41 | 2.90 | 3.5 | 1.2 |
| 0.49 | 2.93 | 510 | 15.1 | 0.50 | 2.80 | 4.8 | 1.6 |
| 0.74 | 2.98 | 515 | 19.7 | 0.64 | 2.63 | 7.2 | 2.5 |
| 0.99 | 3.02 | 520 | 23.7 | 0.77 | 2.47 | 9.7 | 3.3 |
| 1.24 | 3.05 | 525 | 26.5 | 0.85 | 2.36 | 12.1 | 4.1 |
| 1.73 | 3.12 | 535 | 33.1 | 1.04 | 2.11 | 16.8 | 5.7 |
| 2.47 | 3.18 | 550 | 39.0 | 1.19 | 1.87 | 23.7 | 8.2 |
| 3.96 | 3.29 | 580 | 49.2 | 1.43 | 1.48 | 36.5 | 13.1 |
| 5.94 | 3.39 | 620 | 58.3 | 1.58 | 1.13 | 51.7 | 19.7 |
| 8.90 | 3.48 | 680 | 67.5 | 1.67 | 0.80 | 71.3 | 29.5 |
| 12.37 | 3.55 | 750 | 74.1 | 1.66 | 0.58 | 90.3 | 41.0 |
| 17.31 | 3.63 | 850 | 80.8 | 1.60 | 0.38 | 112.0 | 57.4 |
| 22.26 | 3.67 | 950 | 84.6 | 1.50 | 0.27 | 129.2 | 73.8 |
| 27.21 | 3.70 | 1050 | 87.4 | 1.40 | 0.20 | 143.2 | 90.2 |
| 32.15 | 3.72 | 1150 | 89.6 | 1.31 | 0.15 | 154.7 | 106.6 |
| 42.05 | 3.75 | 1150 | 92.1 | 1.35 | 0.12 | 202.7 | 139.4 |
| 51.94 | 3.77 | 1150 | 93.8 | 1.37 | 0.09 | 250.7 | 172.2 |

**Table C.11.** Natural population analysis (DKH-PBE0/old-DKH-TZVPP//PBE0/def2-TZVPP) for Dipp₃PnOH⁺.

| Compound | NPA Pn$^a$ (e⁻) | NPA O$^b$ (e⁻) | NPA H$^c$ (e⁻) |
|---|---|---|---|
| Dipp₃SbOH⁺ | 2.17761 | −1.07558 | 0.49758 |
| Dipp₃AsOH⁺ | 1.84652 | −0.98745 | 0.50877 |
| Dipp₃POH⁺ | 1.91694 | −0.99183 | 0.53603 |

$^a$ Natural population of pnictogen atom. $^b$ Natural population of O atom. $^c$ Natural population of protic H atom.

**Appendix D**

**Supplementary data for**

**Chapter 5: Steric congestion in heavy pnictines alters oxidative halogenation pathways**
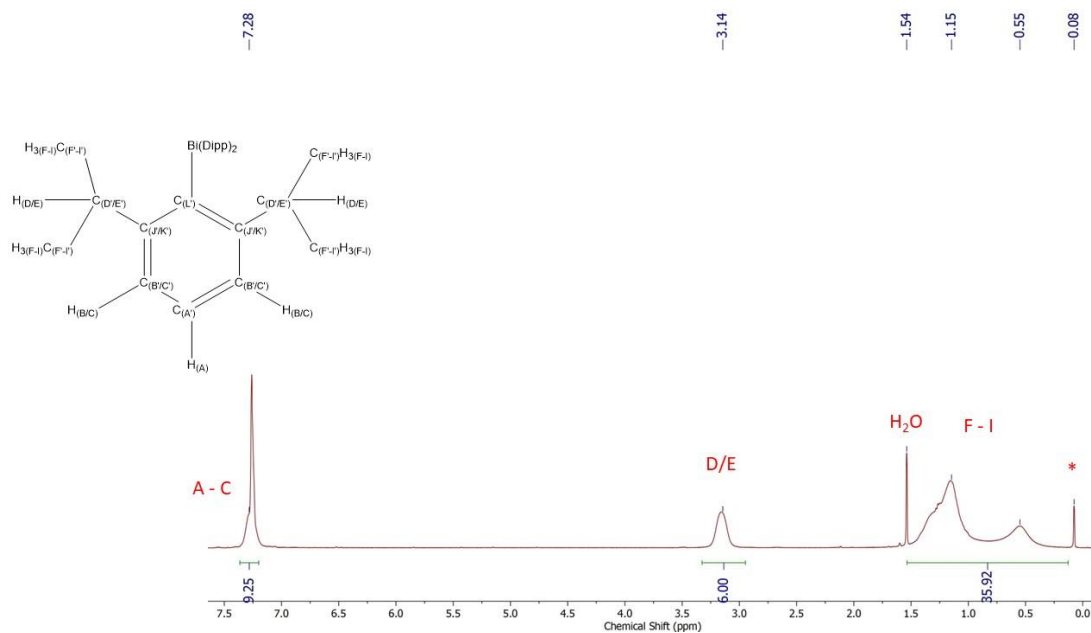
**Figure D.1.** $^1$H NMR spectrum (CDCl$_3$, 500 MHz) of Dipp$_3$Bi at room temperature. The asterisk denotes a grease signal.
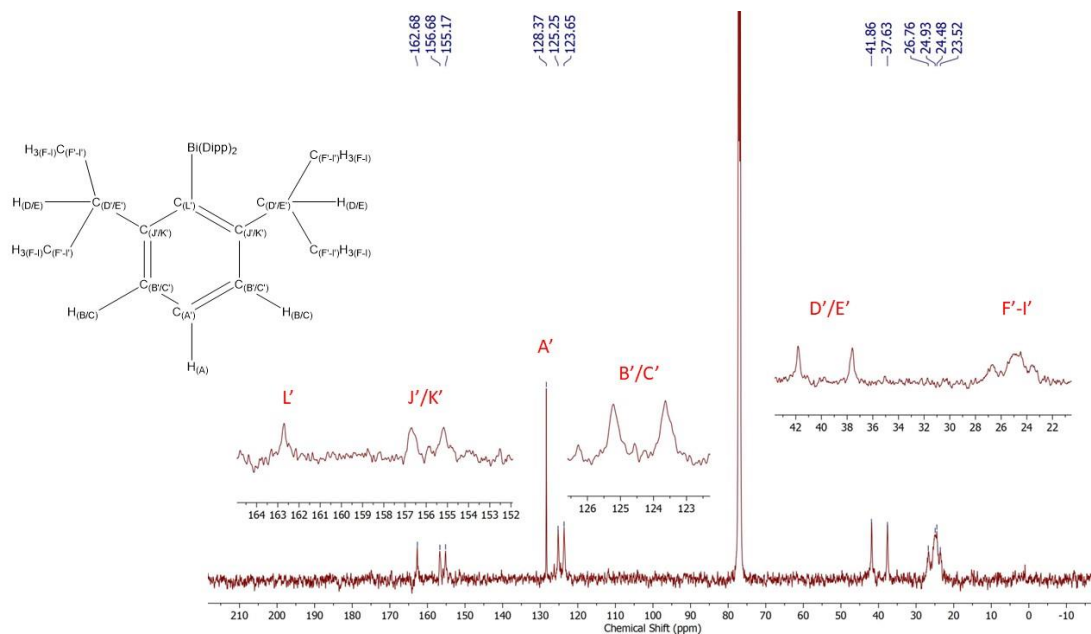


**Figure D.2.** $^{13}$C{$^1$H} NMR spectrum (CDCl$_3$, 125 MHz) of Dipp$_3$Bi at room temperature.
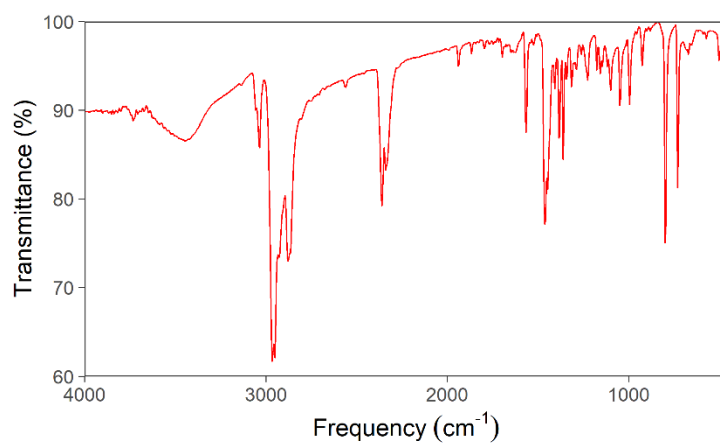
**Figure D.3.** Experimental IR spectrum (KBr pellet) of Dipp$_3$Bi.
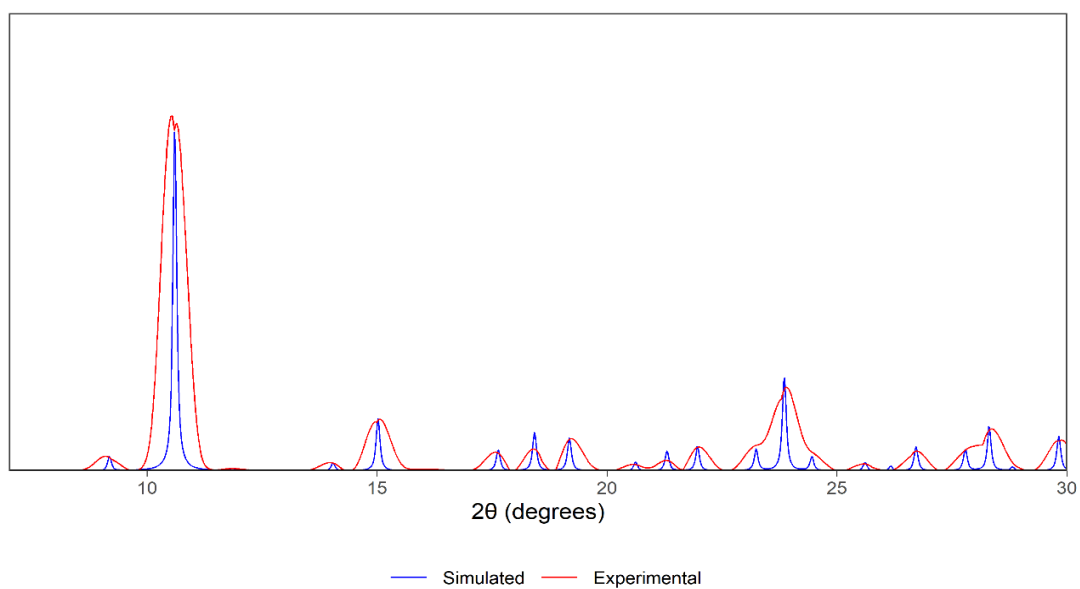


**Figure D.4.** Simulated and experimental PXRD diffractogram of Dipp$_3$Bi.
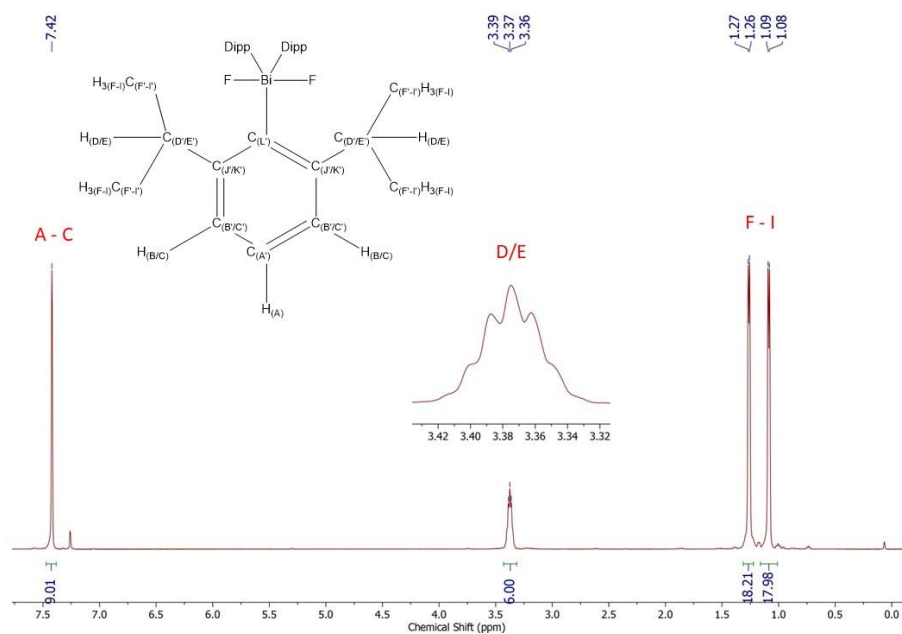
**Figure D.5.** $^1$H NMR spectrum (CDCl$_3$, 500 MHz) of Dipp$_3$BiF$_2$ at room temperature.
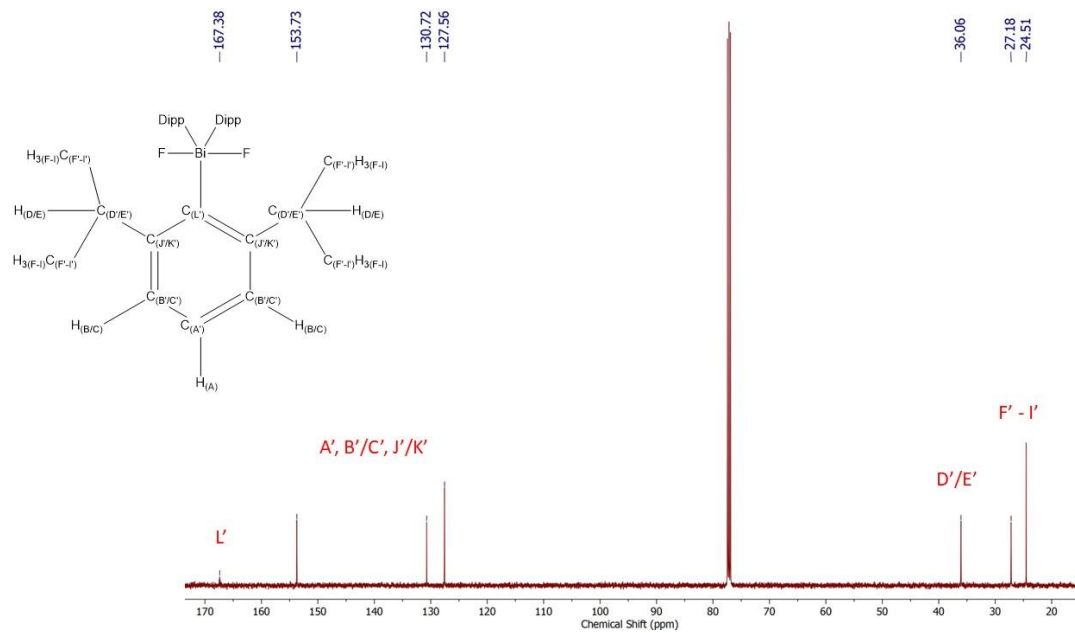


**Figure D.6.** $^{13}$C{$^1$H} NMR spectrum (CDCl$_3$, 125 MHz) of Dipp$_3$BiF$_2$ at room temperature.
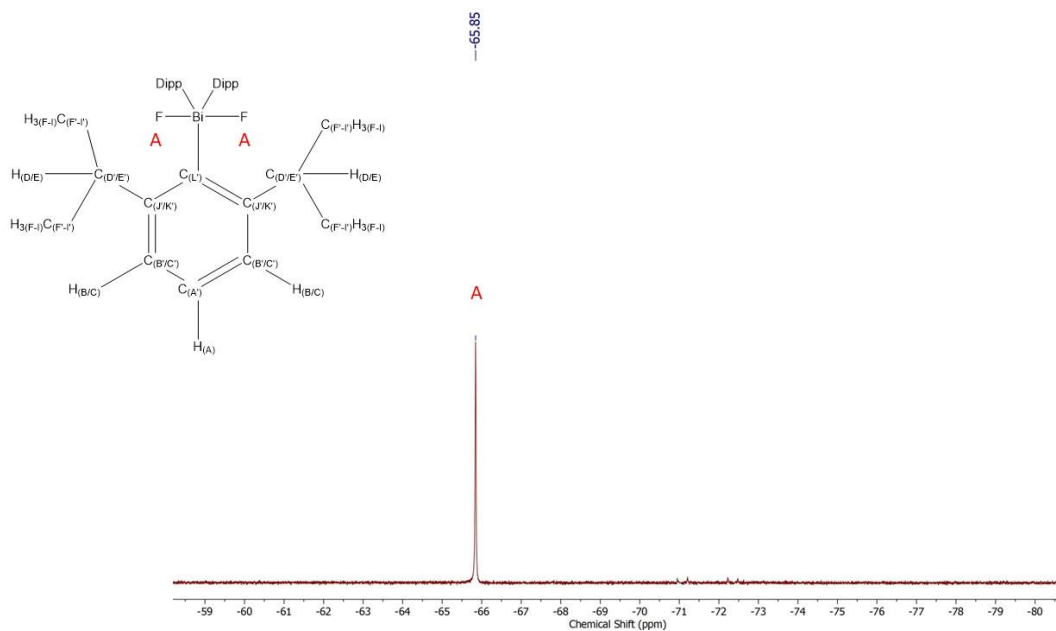
**Figure D.7.** $^{19}$F NMR spectrum (CDCl$_3$, 470 MHz) of Dipp$_3$BiF$_2$ at room temperature.
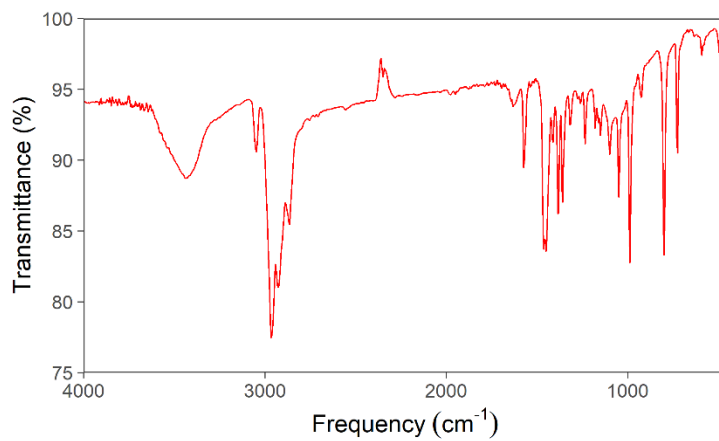


**Figure D.8.** Experimental IR spectrum (KBr pellet) of Dipp$_3$BiF$_2$.
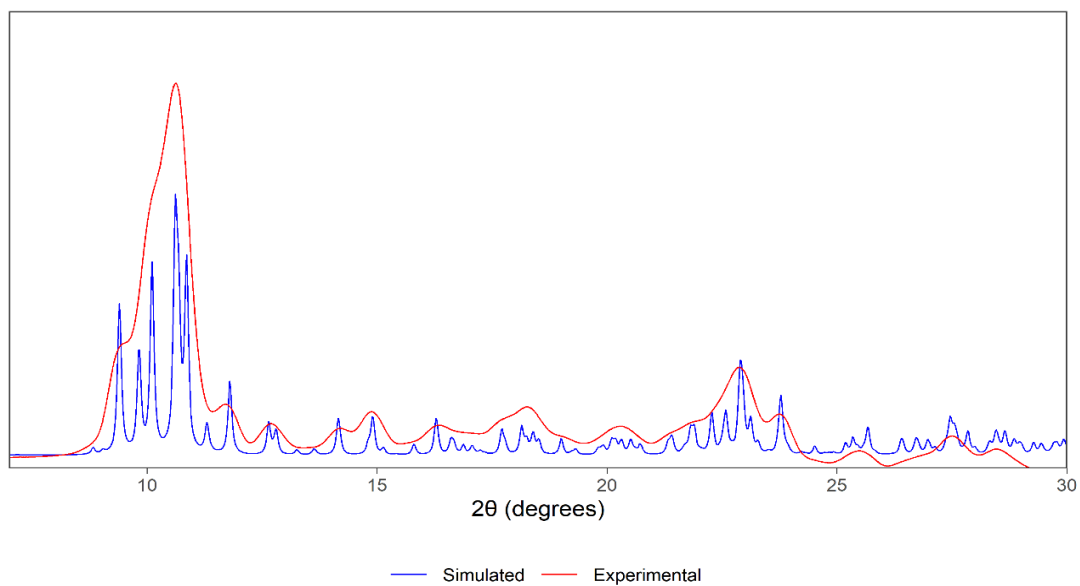
**Figure D.9.** Simulated and experimental PXRD diffractogram of Dipp$_3$BiF$_2$.
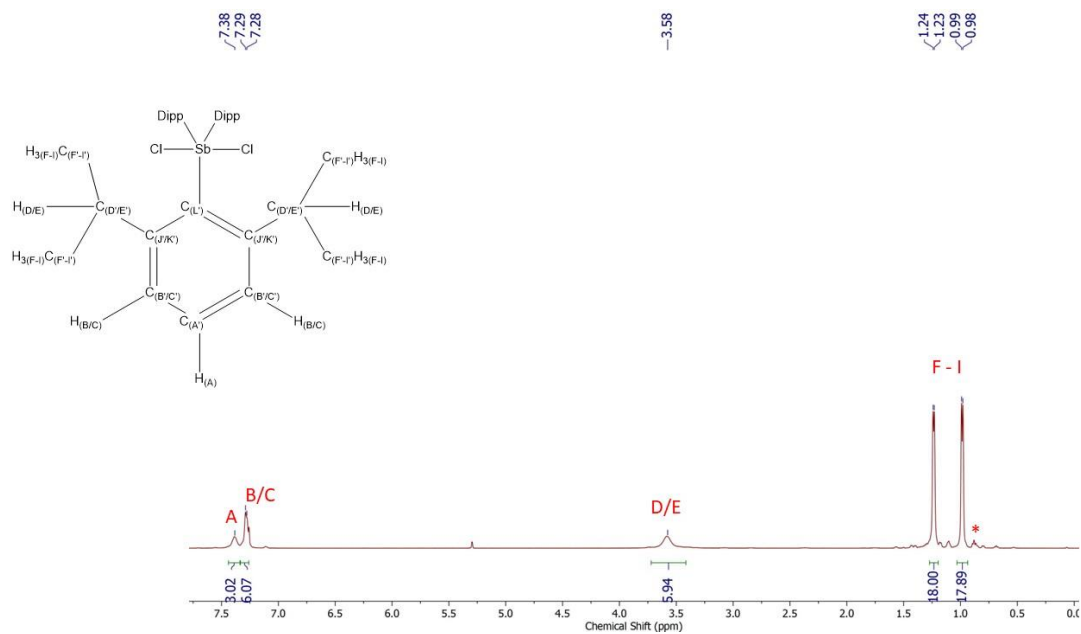


**Figure D.10.** $^1$H NMR spectrum (CDCl$_3$, 500 MHz) of Dipp$_3$SbCl$_2$ at room temperature. Asterisks denote pentane signals.
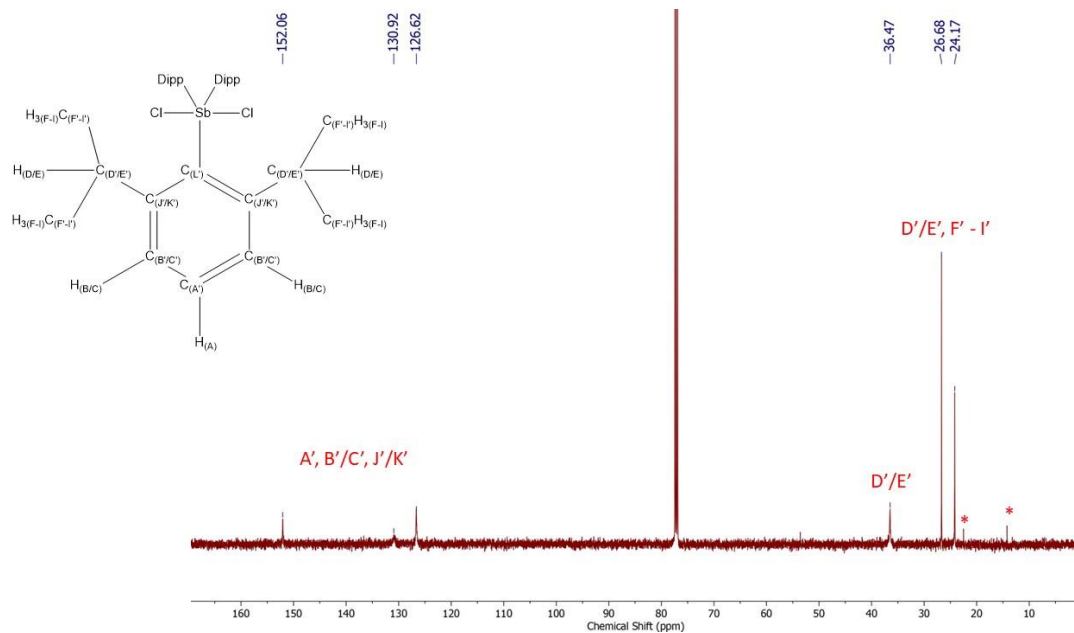
**Figure D.11.** $^{13}C\{^1H\}$ NMR spectrum (CDCl$_3$, 125 MHz) of Dipp$_3$SbCl$_2$ at room temperature. Asterisks denote pentane signals.
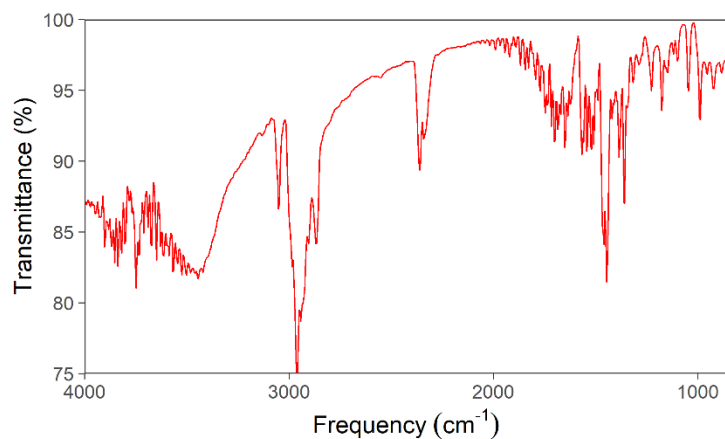


**Figure D.12.** Experimental IR spectrum (KBr pellet) of Dipp$_3$SbCl$_2$.
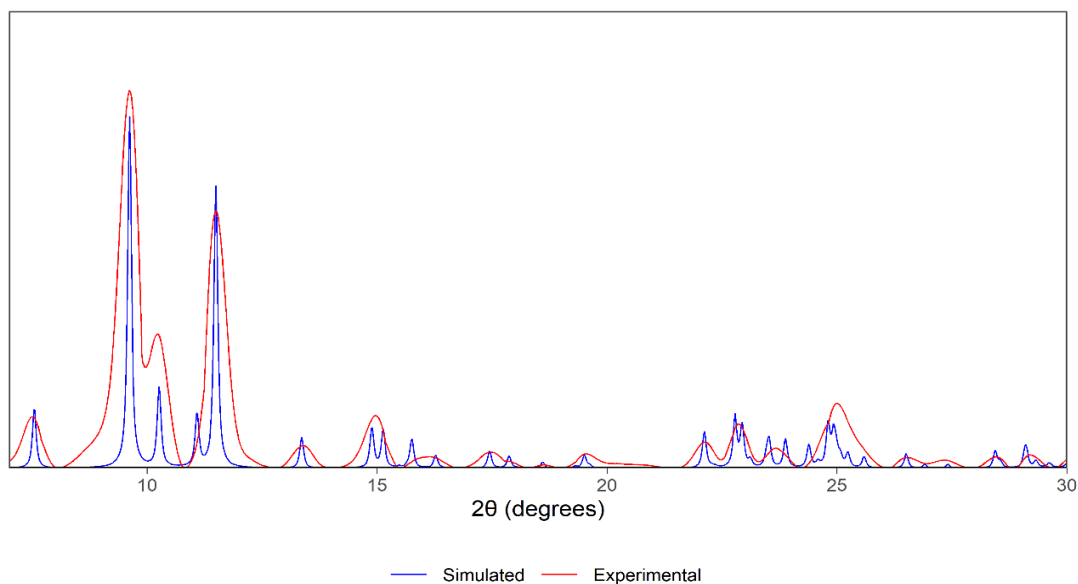
**Figure D.13.** Simulated and experimental PXRD diffractogram of Dipp$_3$SbCl$_2$.
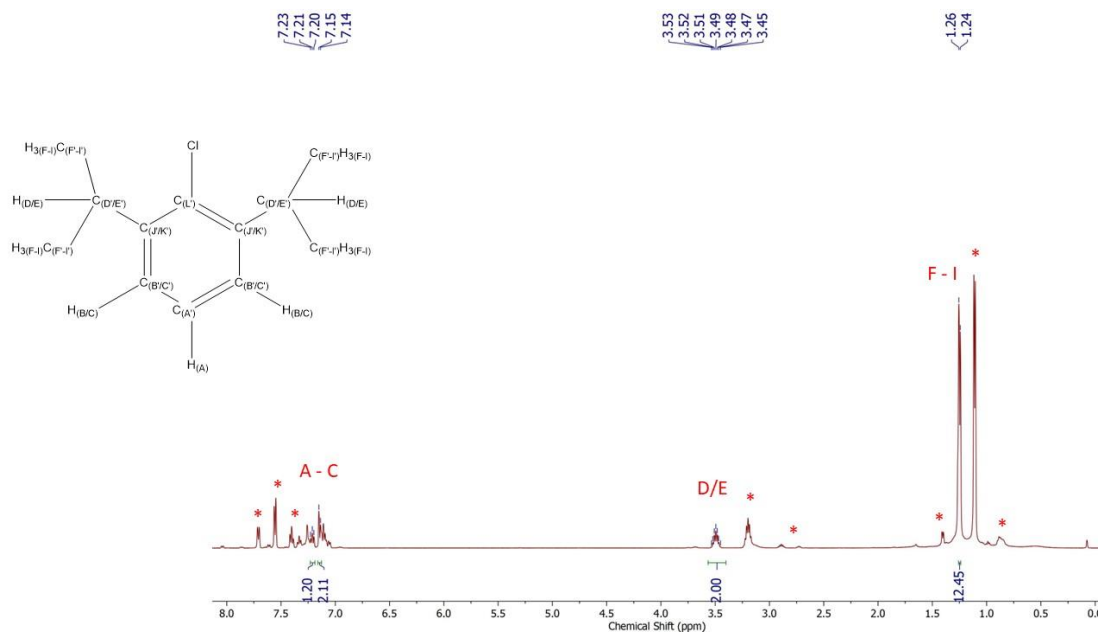


**Figure D.14.** ^{1}H NMR spectrum (CDCl$_3$, 500 MHz) of a reaction mixture from Dipp$_3$Bi and PhICl$_2$ starting materials at room temperature. Assigned signals match previous literature report of DippCl.[1] Asterisks denote unassigned decomposition products.
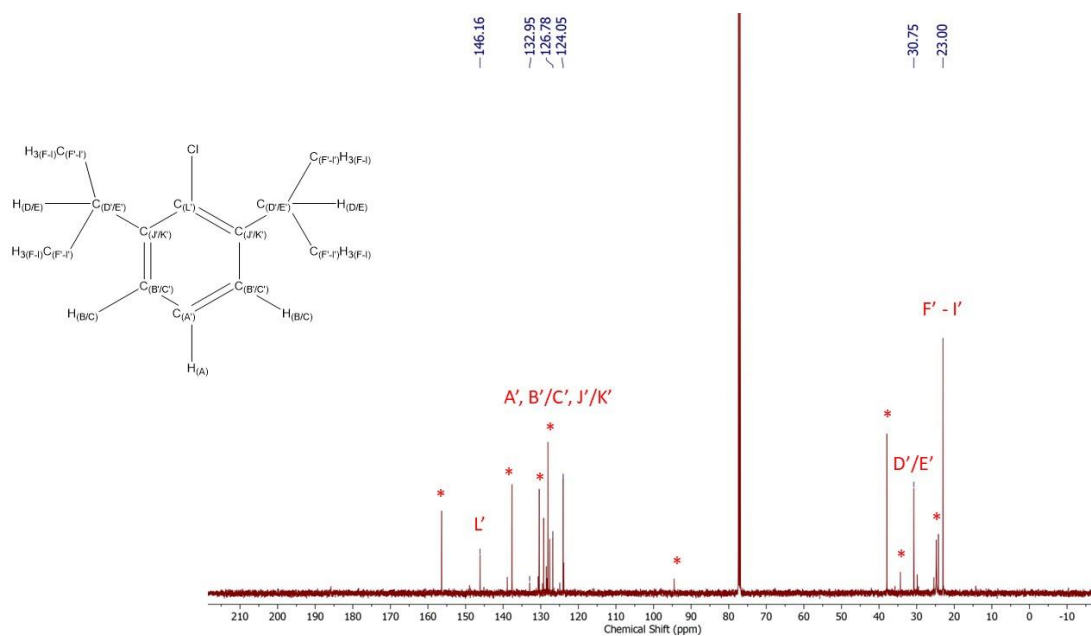
**Figure D.15.** $^{13}$C{$^1$H} NMR spectrum (CDCl$_3$, 125 MHz) of a reaction mixture from Dipp$_3$Bi and PhICl$_2$ starting materials at room temperature. Assigned signals match previous literature report of DippCl.[1] Asterisks denote unassigned decomposition products.
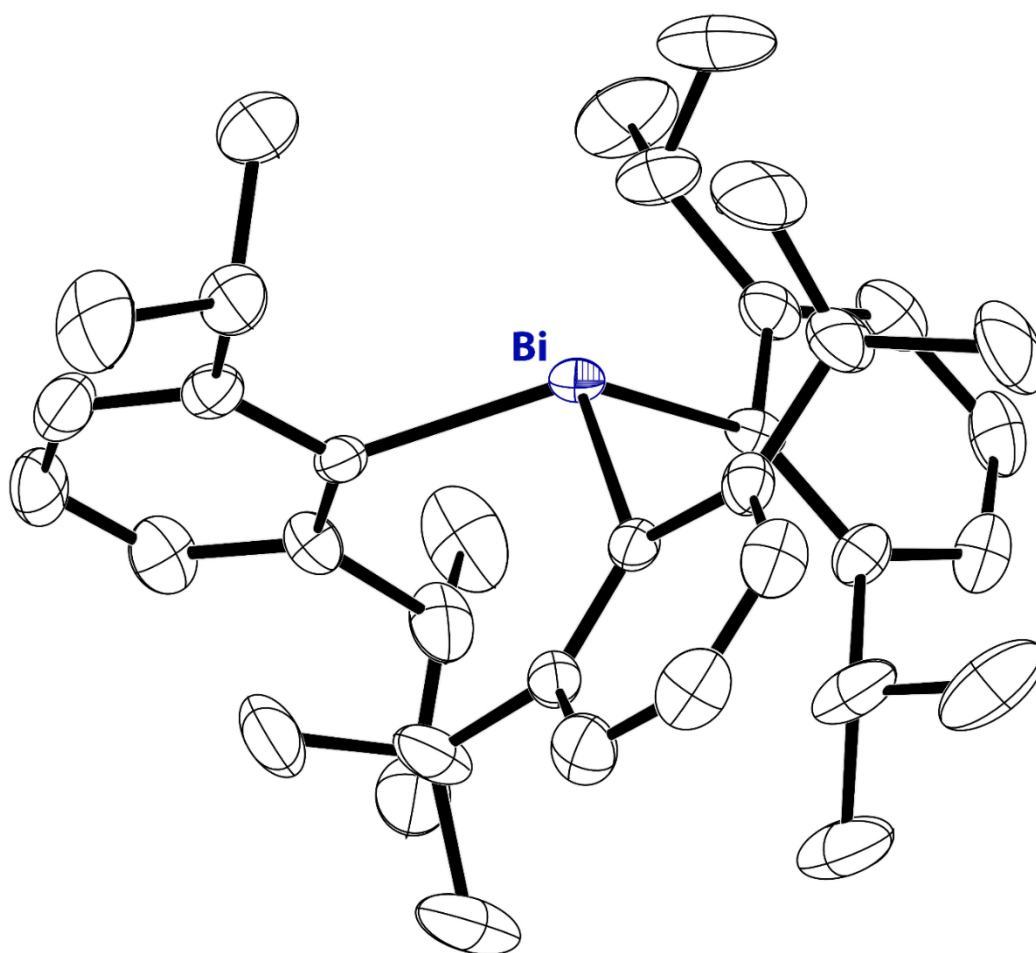
**Figure D.16.** Thermal ellipsoid plot (50% probability) of Dipp₃Bi. Color code: Bi navy and C black. Hydrogen atoms are omitted for clarity.
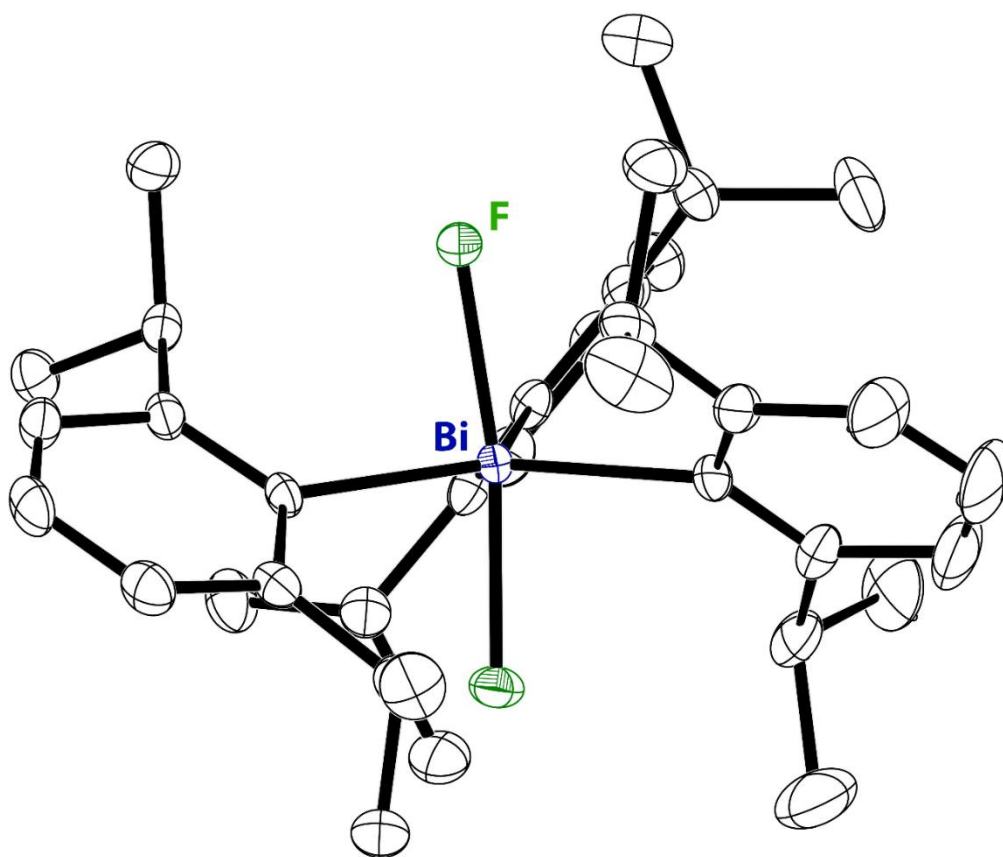
**Figure D.17.** Thermal ellipsoid plot (50% probability) of Dipp$_3$BiF$_2$. Color code: Bi navy, F light-green, and C black. Hydrogen atoms are omitted for clarity and only one of the crystallographically inequivalent molecules of Dipp$_3$BiF$_2$ is depicted.
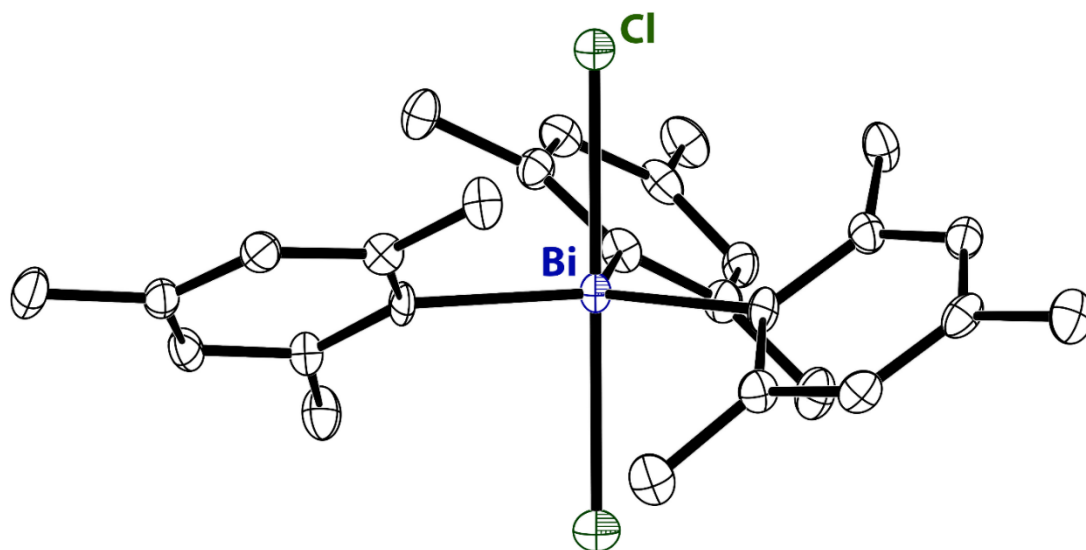
**Figure D.18.** Thermal ellipsoid plot (50% probability) of Mes$_3$BiCl$_2$. Color code: Bi navy, Cl dark-green, and C black. Hydrogen atoms are omitted for clarity.
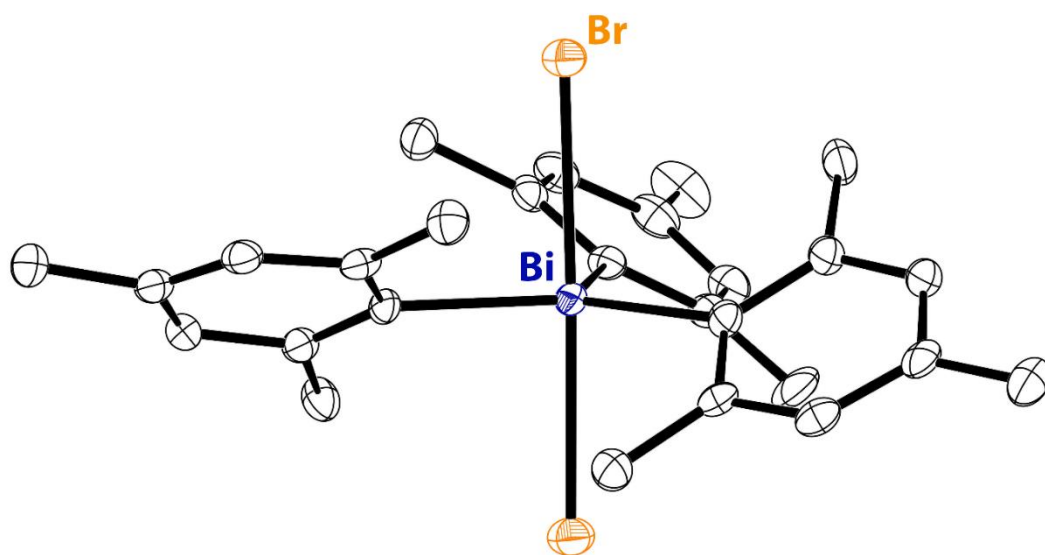
**Figure D.19.** Thermal ellipsoid plot (50% probability) of Mes$_3$BiBr$_2$. Color code: Bi navy, Br orange, and C black. Hydrogen atoms are omitted for clarity.
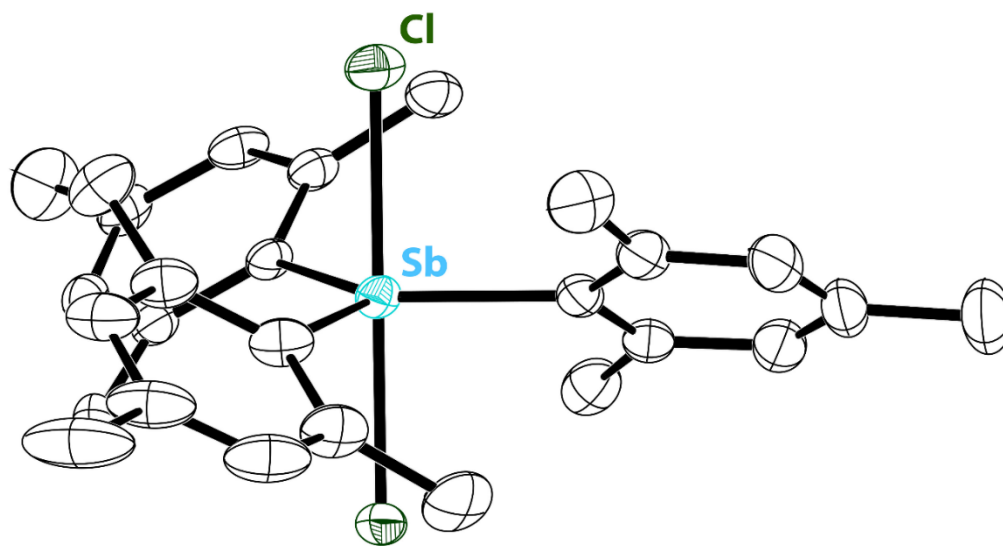
**Figure D.20.** Thermal ellipsoid plot (50% probability) of Mes$_3$SbCl$_2$. Color code: Sb teal, Cl dark-green, and C black. Hydrogen atoms are omitted for clarity and only one of the crystallographically inequivalent molecules of Mes$_3$SbCl$_2$ is depicted.
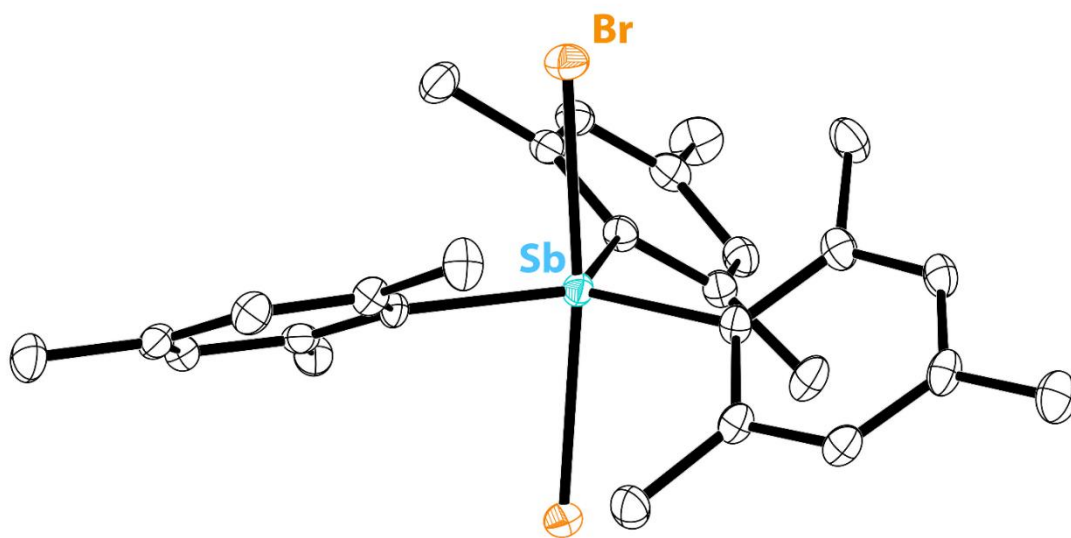
**Figure D.21.** Thermal ellipsoid plot (50% probability) of Mes$_3$SbBr$_2$. Color code: Sb teal, Br orange, and C black. Hydrogen atoms are omitted for clarity and only one of the crystallographically inequivalent molecules of Mes$_3$SbBr$_2$ is depicted.
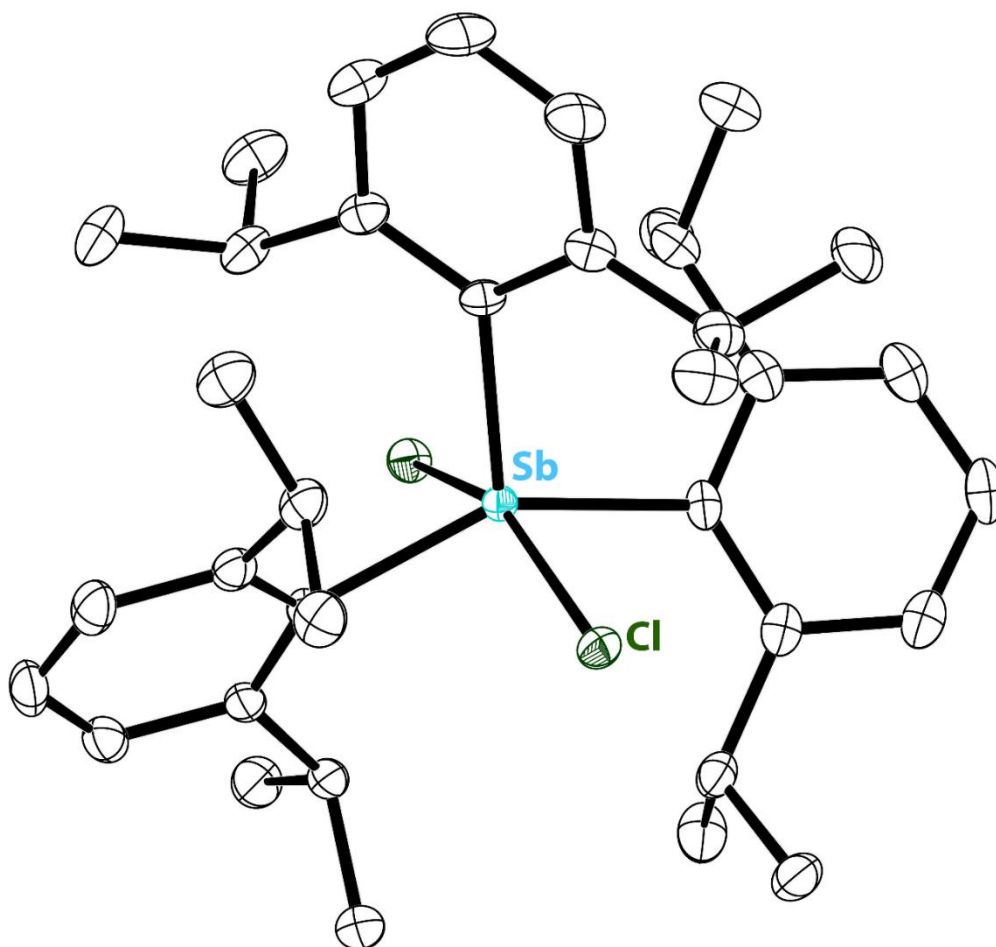
**Figure D.22.** Thermal ellipsoid plot (50% probability) of Dipp$_3$SbCl$_2$. Color code: Sb teal, Cl dark-green, and C black. Hydrogen atoms are omitted for clarity.
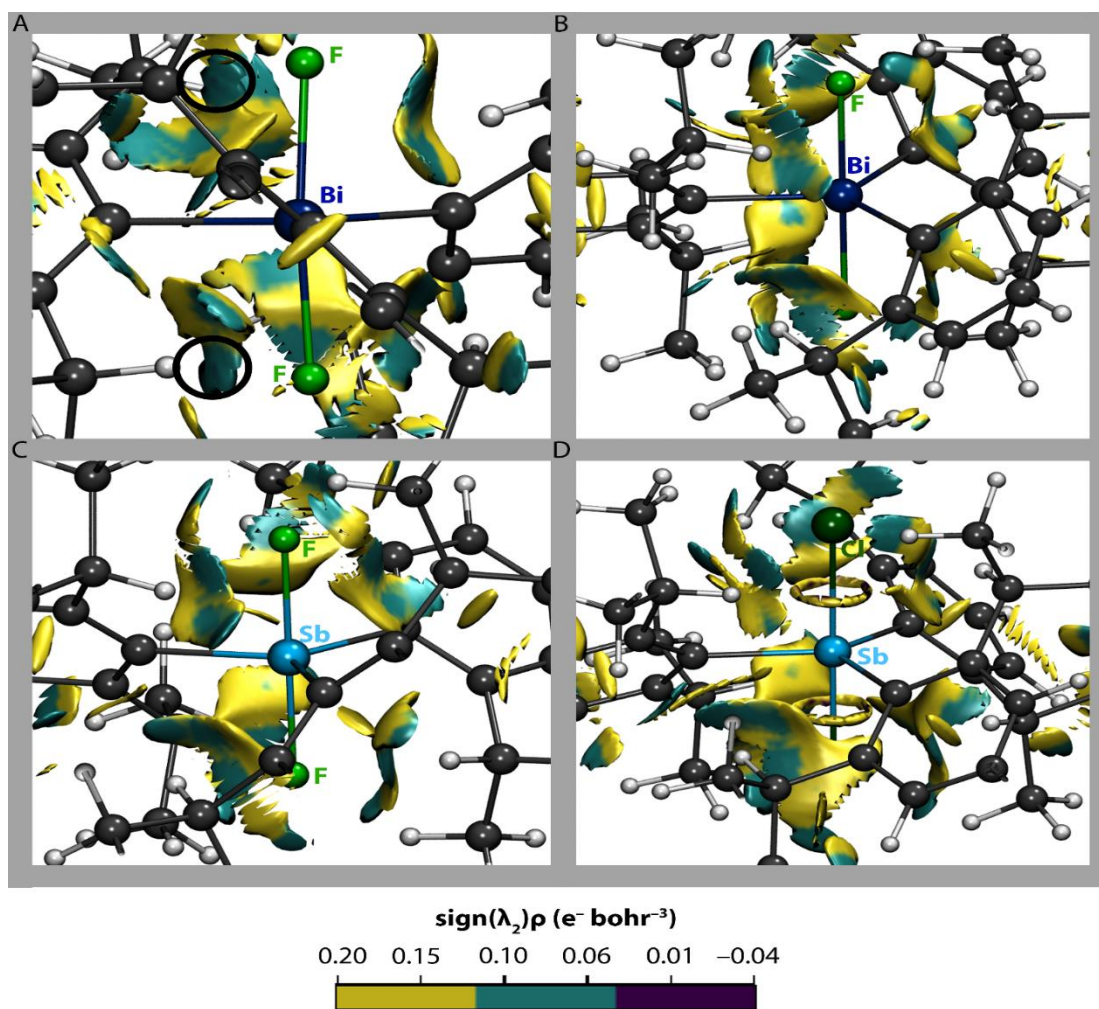
**Figure D.23.** NCI analysis of (A) $Dipp_3BiF_2$, (B) $Dipp_3BiF_2$(linear), (C) $Dipp_3SbF_2$, and (D) $Dipp_3SbCl_2$(linear) depicting reduced gradient surfaces (isovalue = 0.45 a.u.) with the function $sign(\lambda_2)\rho$ (where $\lambda_2$ is the second-largest eigenvalue of the Laplacian) color-mapped on the surface. Purple is indicative of H-bonding interactions, aqua is indicative of van der Waals interactions, and yellow is indicative of steric repulsions. H-bonding interactions are highlighted with a black circle for clarity. Color code: Bi navy, Sb teal, Cl dark-green, F light-green, C black, H grey.
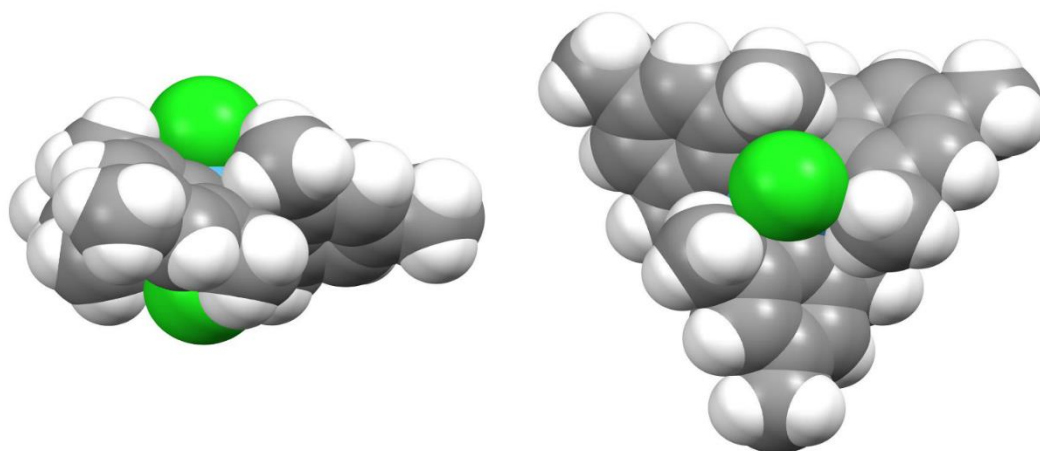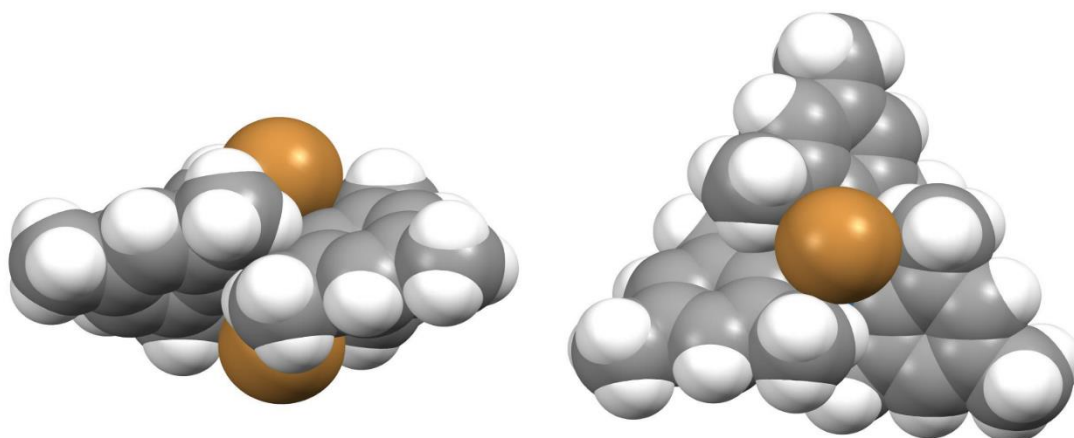
**Figure D.24.** Space-filling diagrams from crystallographic coordinates of (A) Mes$_3$SbCl$_2$ and (B) Mes$_3$SbBr$_2$ depicting two orientations of a single molecule from the asymmetric unit.

**Table D.1.** Crystallographic details for $Dipp_3Bi$, $Dipp_3BiF_2$, $Mes_3BiCl_2 \cdot C_6H_{12}$, and $Mes_3BiBr_2 \cdot CHCl_3$.

| Compound | $Dipp_3Bi$ | $Dipp_3BiF_2$ | $Mes_3BiCl_2 \cdot C_6H_{12}$ | $Mes_3BiBr_2 \cdot CHCl_3$ |
|---|---|---|---|---|
| Empirical | $C_{36}H_{51}Bi$ | $C_{36}H_{51}BiF_2$ | $C_{33}H_{45}BiCl_2$ | $C_{28}H_{34}BiBr_2Cl_3$ |
| Formula | 692.74 | 730.74 | 721.57 | 845.70 |
| Temperature | 100.0 | 100.0 | 100.0 | 100.0 |
| Wavelength (Å) | 1.54184 | 1.54184 | 1.54184 | 1.54184 |
| Crystal system | Cubic | Triclinic | Trigonal | Monoclinic |
| Space group | $I\bar{4}3d$ | $P\bar{1}$ | $P31c$ | $P2_1/n$ |
| $a$ (Å) | 23.57390(10) | 10.10880(10) | 13.24860(10) | 12.0446(2) |
| $b$ (Å) | | 16.6488(2) | | 14.4667(3) |
| $c$ (Å) | | 20.3613(2) | 10.07740(10) | 17.2702(3) |
| $\alpha$ (°) | | 84.9560(10) | | |
| $\beta$ (°) | | 79.9160(10) | | 101.723(2) |
| $\gamma$ (°) | | 78.3720(10) | | |
| Volume (Å$^3$) | 13100.69(17) | 3299.69(6) | 1531.86(3) | 2946.49(10) |
| $Z$ | 16 | 4 | 2 | 4 |
| $\rho_{calc}$ (Mg/m$^3$) | 1.405 | 1.471 | 1.564 | 1.906 |
| Crystal size | 0.1 × 0.08 × | 0.13 × 0.1 × | 0.1 × 0.1 × 0.07 | 0.13 × 0.1 × 0.04 |
| $\theta$ range (°) | 4.595 to | 2.207 to | 3.853 to 67.059 | 4.021 to 67.079 |
| Total | 15828 | 47510 | 14900 | 20910 |
| Unique | 1955 | 12087 | 1821 | 5274 |
| Method | IAM | IAM | IAM | IAM |
| Parameters | 116 | 727 | 113 | 316 |
| Completeness | 100 | 100 | 100 | 99.9 |
| $R_{int}$ | 0.0355 | 0.0405 | 0.0601 | 0.0469 |
| $R_1$ ($I > 2\sigma$) | 0.0186 | 0.0190 | 0.0186 | 0.0284 |
| $R_1$ (all data) | 0.0190 | 0.0217 | 0.0195 | 0.0325 |
| $wR_2$ ($I > 2\sigma$) | 0.0447 | 0.0434 | 0.0437 | 0.0763 |
| $wR_2$ (all data) | 0.0450 | 0.0444 | 0.0442 | 0.0790 |
| Goodness of fit | 1.058 | 1.045 | 1.021 | 1.040 |

**Table D.2.** Crystallographic details for $Dipp_3SbCl_2$, $Mes_3SbCl_2$, and $Mes_3SbBr_2$.

| Compound | $Dipp_3SbCl_2$ | $Mes_3SbCl_2$ | $Mes_3SbBr_2$ |
|---|---|---|---|
| Empirical formula | $C_{36}H_{51}Cl_2Sb$ | $C_{27}H_{33}Cl_2Sb$ | $C_{27}H_{33}Br_2Sb$ |
| Formula Weight | 676.41 | 550.18 | 639.10 |
| Temperature (K) | 100.0 | 100.0 | 100.0 |
| Wavelength (Å) | 1.54184 | 1.54184 | 1.54184 |
| Crystal system | Monoclinic | Triclinic | Triclinic |
| Space group | $C2/c$ | $P\bar{1}$ | $P\bar{1}$ |
| $a$ (Å) | 17.8308(3) | 8.6350(2) | 11.1928(2) |
| $b$ (Å) | 15.9452(2) | 16.4857(3) | 15.5266(3) |
| $c$ (Å) | 12.3095(2) | 19.4253(3) | 15.6681(3) |
| $\alpha$ (°) | | 107.4700(10) | 82.834(2) |
| $\beta$ (°) | 105.011(2) | 97.505(2) | 70.207(2) |
| $\gamma$ (°) | | 99.301(2) | 87.413(2) |
| Volume ($Å^3$) | 3380.36(9) | 2555.47(9) | 2542.01(9) |
| $Z$ | 4 | 4 | 4 |
| $\rho_{calc}$ ($Mg/m^3$) | 1.329 | 1.430 | 1.670 |
| Crystal size ($mm^3$) | 0.13 × 0.08 × 0.04 | 0.1 × 0.03 × 0.03 | 0.18 × 0.15 × 0.06 |
| $\theta$ range (°) | 3.778 to 67.072 | 2.429 to 67.077 | 2.868 to 70.073 |
| Total reflections | 23380 | 54313 | 41157 |
| Unique reflections | 3027 | 9125 | 9658 |
| Method | IAM | IAM | IAM |
| Parameters | 184 | 559 | 559 |
| Completeness | 100.0 | 100.0 | 100.0 |
| $R_{int}$ | 0.0582 | 0.0575 | 0.0337 |
| $R_1$ ($I > 2\sigma$) | 0.0207 | 0.0300 | 0.0208 |
| $R_1$ (all data) | 0.0215 | 0.0361 | 0.0218 |
| $wR_2$ ($I > 2\sigma$) | 0.0545 | 0.0740 | 0.0495 |
| $wR_2$ (all data) | 0.0549 | 0.0762 | 0.0500 |
| Goodness of fit, $S$ | 1.068 | 1.051 | 1.025 |

**Table D.3.** Results from thermochemical analysis (PBE0/def2-TZVPP) of $Dipp_3SbCl_2$ and $Dipp_3BiF_2$.

| Compound | ΔH (kcal/mol) | ΔH Difference[a] (kcal/mol) | ΔG (kcal/mol) | ΔG Difference[b] (kcal/mol) |
|---|---|---|---|---|
| $Dipp_3BiF_2$ | −1138749.117 | 0 | −1138822.357 | 0 |
| $Dipp_3BiF_2$ (linear) | −1138750.239 | −1.122 | −1138820.99 | 1.367 |
| $Dipp_3SbCl_2$ | −1606983.806 | 0 | −1607056.249 | 0 |
| $Dipp_3SbCl_2$ (linear) | −1606974.506 | 9.300 | −1607043.925 | 12.323 |

[a] Difference between the ΔH of the compound in the listed geometry and the structure optimized starting from crystallographic coordinates. [b] Difference between the ΔG of the compound in the listed geometry and the structure optimized starting from crystallographic coordinates.

**Table D.4.** Energy Decomposition Analysis (PBE0/QZVP) of $Dipp_3SbCl_2$.[h]

| | $E_{SCF}$(first, $Dipp_3SbCl_2$)[a] | $E_{SCF}$(last $Dipp_3SbCl_2$)[b] | $E_{SCF}$($Dipp_3Sb$)[c] | $E_{SCF}$(2Cl)[d] | $\Delta E_{tot}$[e] | $\Delta E_{orb}$[f] | $\Delta E_{steric}$[g] |
|---|---|---|---|---|---|---|---|
| **Energy (a.u)** | −4395.78 | −4398.25 | −3476.01 | −920.015 | −2.2208 | −2.46494 | 0.24414 |
| **Energy (kJ/mol)** | −2758368 | −2759915 | −2181209 | −577312 | −1393.56 | −1546.76 | 153.199 |

[a] Energy of $Dipp_3SbCl_2$ with no orbital interaction between 2Cl and $Dipp_3Sb$ fragments. [b] Energy of $Dipp_3SbCl_2$. [c] Energy of $Dipp_3Sb$ at optimized coordinates for $Dipp_3SbCl_2$. [d] Energy of 2Cl at optimized coordinates for $Dipp_3SbCl_2$. [e] Difference in energy of $Dipp_3SbCl_2$ and the sum of the 2Cl and $Dipp_3SbCl_2$ fragments; the total energy afforded by interaction of the fragments. [f] Difference in energy between **$E_{SCF}$(last, $Dipp_3SbCl_2$)** and **$E_{SCF}$(first, $Dipp_3SbCl_2$)**; the energy of stabilization afforded by orbital interaction between the $Dipp_3Sb$ and 2Cl fragments. [g] Difference between $\Delta E_{tot}$ and $\Delta E_{orb}$. [h] $\Delta E_{orb}/\Delta E_{tot}$ = 1.1099.

**Table D.5.** Energy Decomposition Analysis (PBE0/QZVP) of $Dipp_3SbCl_2$(linear).[h]

| | $E_{SCF}$(first, $Dipp_3SbCl_2$ (linear))[a] | $E_{SCF}$(last $Dipp_3SbCl_2$, (linear))[b] | $E_{SCF}$($Dipp_3Sb$)[c] | $E_{SCF}$(2Cl)[d] | $\Delta E_{tot}$[e] | $\Delta E_{orb}$[f] | $\Delta E_{steric}$[g] |
|---|---|---|---|---|---|---|---|
| **Energy (a.u)** | −4394.69 | −4397.28 | −3474.96 | −919.975 | −2.33729 | −2.58827 | 0.25098 |

| Energy (kJ/mol) | −2757680 | −2759304 | −2180550 | −577287 | −1466.66 | −1624.15 | 157.487 |
|---|---|---|---|---|---|---|---|

[a] Energy of Dipp$_3$SbCl$_2$(linear) with no orbital interaction between 2Cl and Dipp$_3$Sb fragments. [b] Energy of Dipp$_3$SbCl$_2$(linear). [c] Energy of Dipp$_3$Sb at optimized coordinates for Dipp$_3$SbCl$_2$(linear). [d] Energy of 2Cl at optimized coordinates for Dipp$_3$SbCl$_2$(linear). [e] Difference in energy of Dipp$_3$SbCl$_2$(linear) and the sum of the 2Cl and Dipp$_3$SbCl$_2$ fragments; the total energy afforded by interaction of the fragments. [f] Difference in energy between **E$_{SCF}$(last, Dipp$_3$SbCl$_2$(linear))** and **E$_{SCF}$(first, Dipp$_3$SbCl$_2$(linear))**; the energy of stabilization afforded by orbital interaction between the Dipp$_3$Sb and 2Cl fragments. [g] Difference between $\Delta$**E$_{tot}$** and $\Delta$**E$_{orb}$**. [h] $\Delta$**E$_{orb}$**/$\Delta$**E$_{tot}$** = 1.1073.

### References

1.  Hoshi, T.; Honma, T.; Mori, A.; Konishi, M.; Sato, T.; Hagiwara, H.; Suzuki, T., An Active, General, and Long-Lived Palladium Catalyst for Cross-Couplings of Deactivated (Hetero)aryl Chlorides and Bromides with Arylboronic Acids. *J. Org. Chem.* **2013,** *78*, 11513-11524.

**Appendix E**

**Supplementary data for**

**Chapter 6: A sterically accessible monomeric stibine oxide activates organotetrel(IV)**

**halides, including C–F and Si–F bonds**
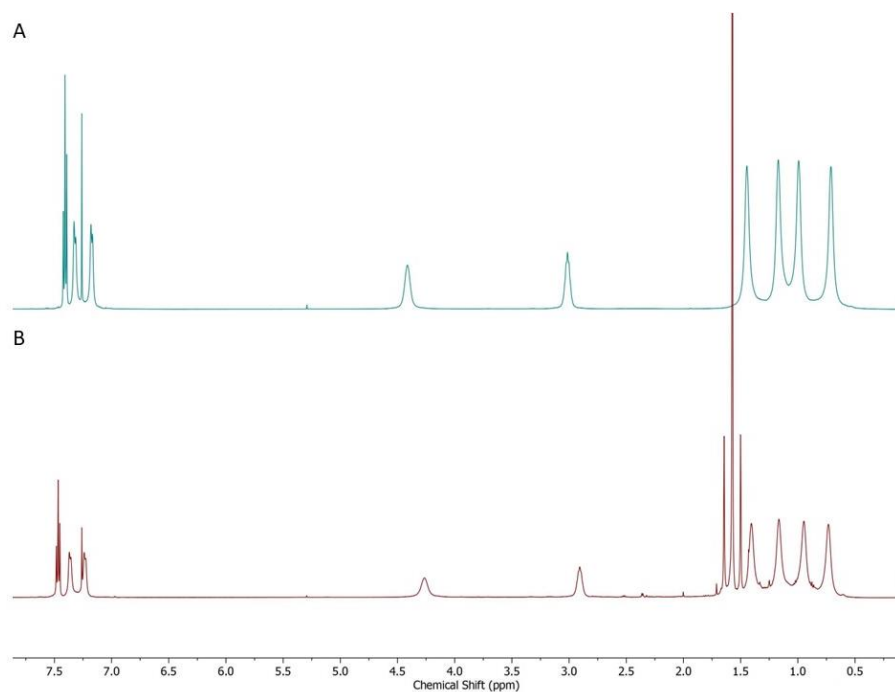
**Figure E.1.** (A) ^{1}H NMR spectrum (CDCl$_3$, 500 MHz) of Dipp$_3$SbO at room temperature.[1] (B) ^{1}H NMR spectrum (CDCl$_3$, 500 MHz) of a mixture of Dipp$_3$SbO and PbMe$_3$Cl in a 1 : 3 molar ratio at room temperature.
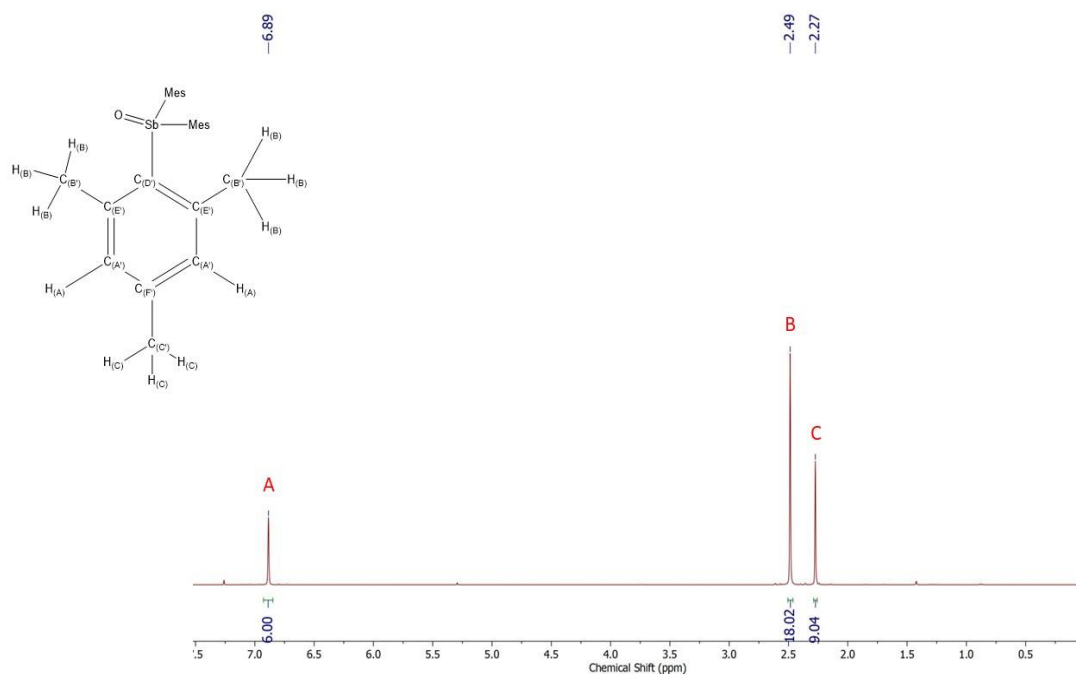
**Figure E.2.** $^1$H NMR spectrum (CDCl$_3$, 500 MHz) of Mes$_3$SbO at room temperature.
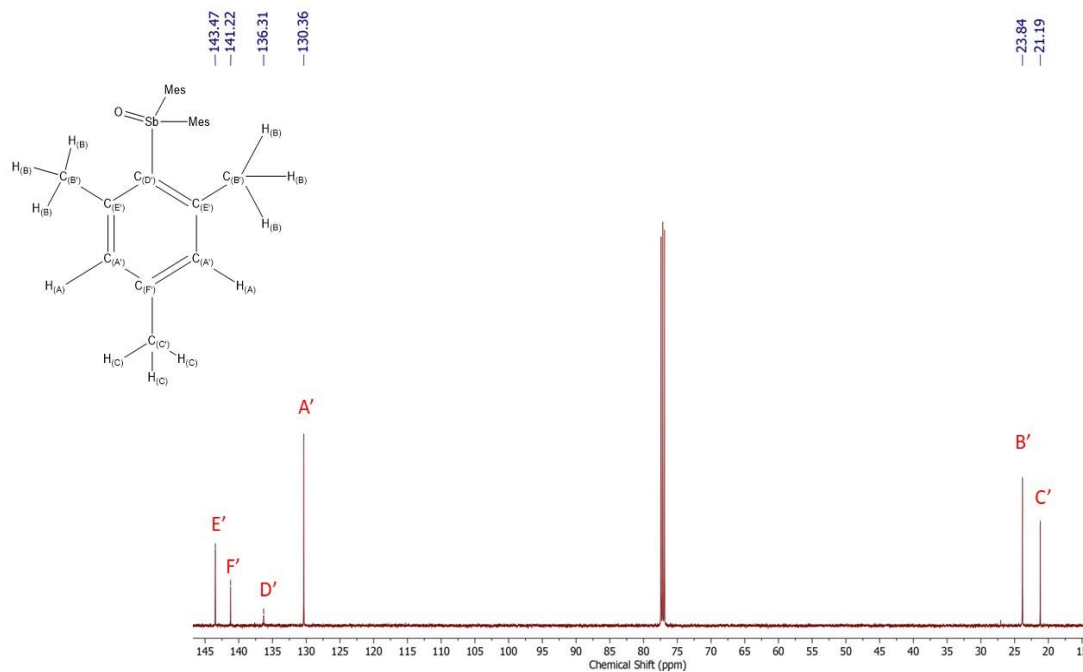


**Figure E.3.** $^{13}$C{$^1$H} NMR spectrum (CDCl$_3$, 125 MHz) of Mes$_3$SbO at room temperature.

388
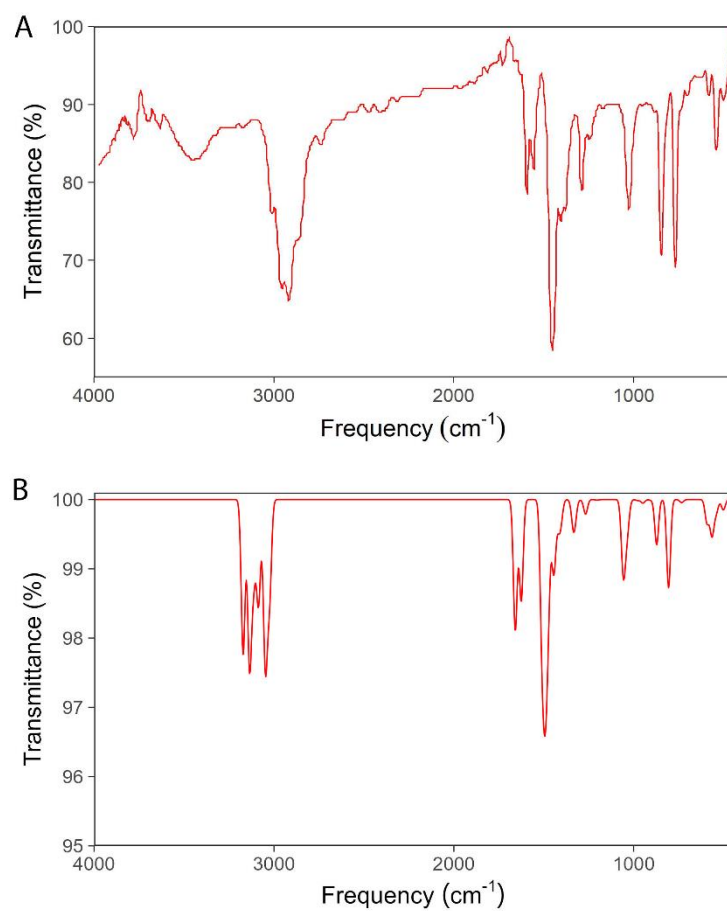
**Figure E.4.** (A) Experimental IR spectrum (KBr pellet) of Mes$_3$SbO. A rolling average with a 6 data point span was applied to smooth the data. (B) Calculated IR spectrum (PBE0/def2-TZVPP) of Mes$_3$SbO.
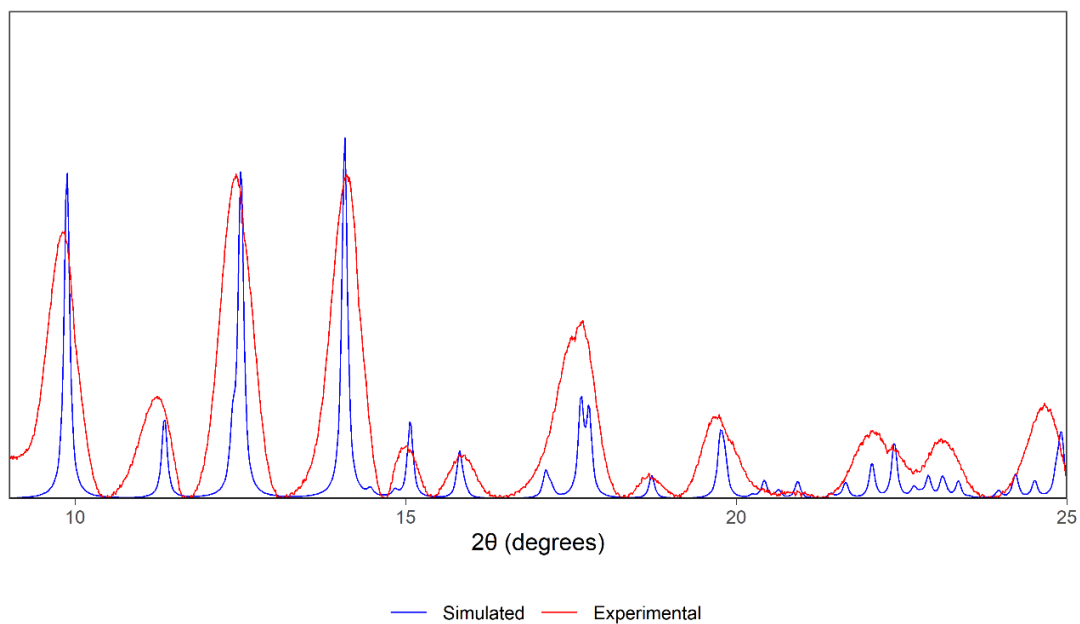
**Figure E.5.** Simulated and experimental PXRD diffractogram of Mes₃SbO.
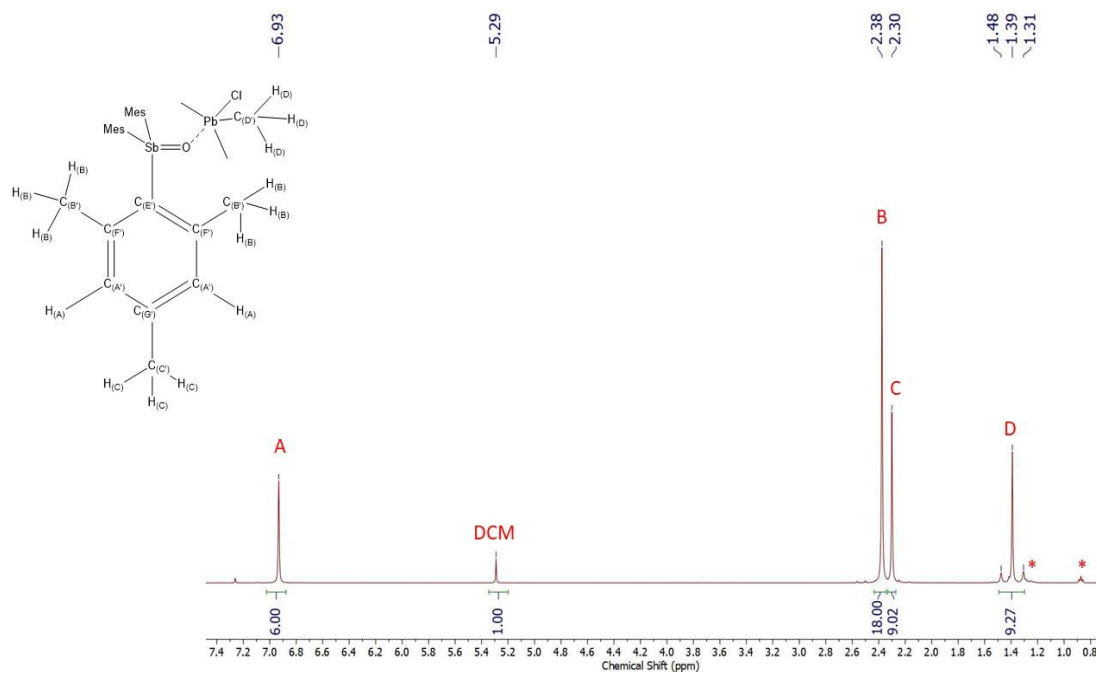


**Figure E.6.** $^1$H NMR spectrum (CDCl$_3$, 500 MHz) of Mes$_3$SbO→PbMe$_3$Cl·(CH$_2$Cl$_2$)$_{0.5}$ at room temperature. The asterisks denote pentane signals.
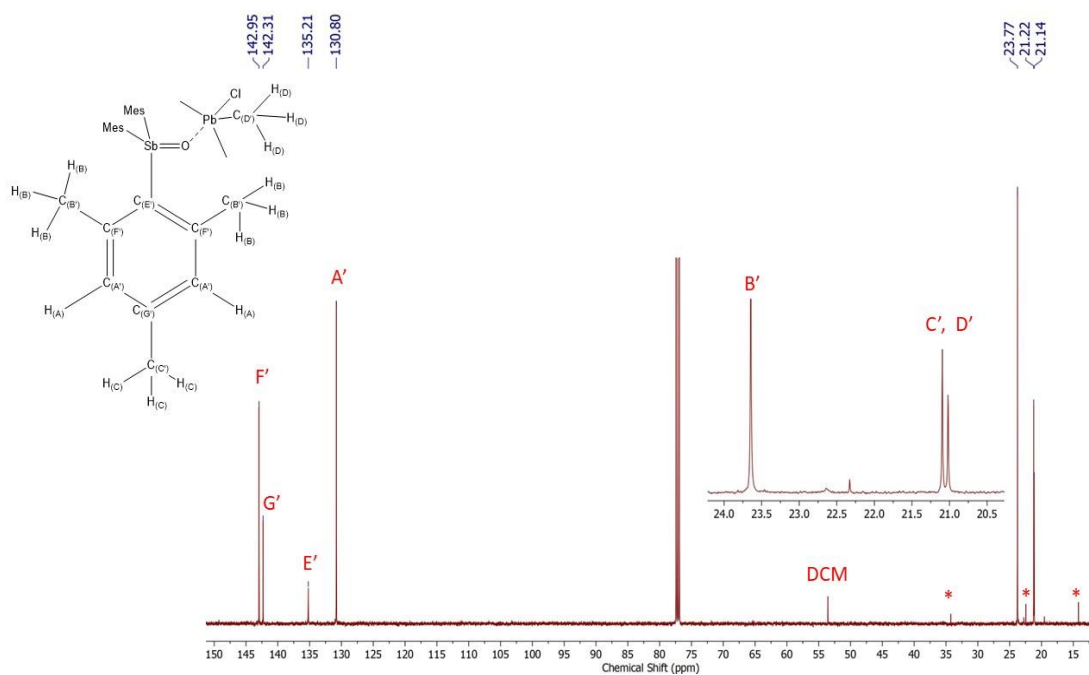
**Figure E.7.** $^{13}C\{^1H\}$ NMR spectrum (CDCl$_3$, 125 MHz) of Mes$_3$SbO→PbMe$_3$Cl·(CH$_2$Cl$_2$) at room temperature. The asterisks denote pentane signals.
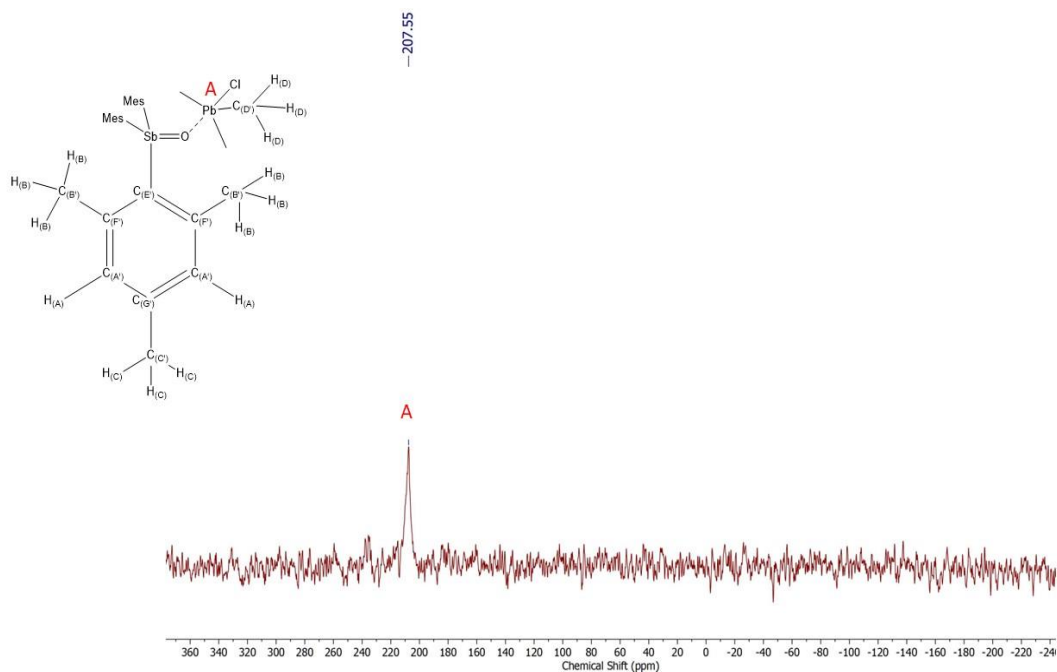


**Figure E.8.** $^{207}Pb\{^1H\}$ NMR spectrum (CDCl$_3$, 105 MHz) of Mes$_3$SbO→PbMe$_3$Cl·(CH$_2$Cl$_2$) at room temperature.
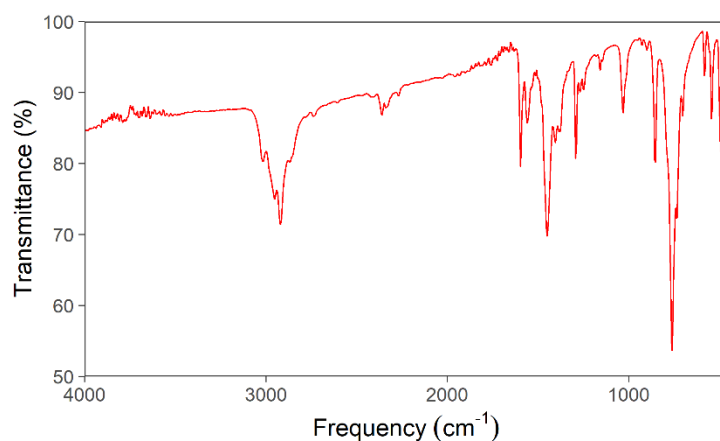
**Figure E.9.** Experimental IR spectrum (KBr pellet) of Mes$_3$SbO→PbMe$_3$Cl·(CH$_2$Cl$_2$).
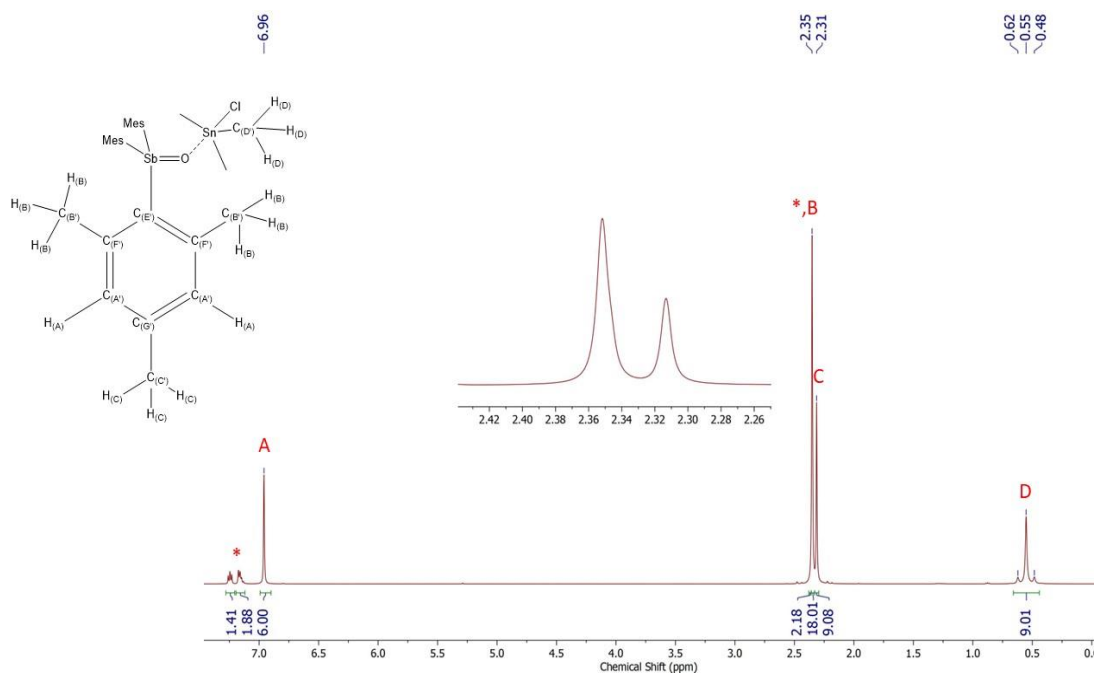


**Figure E.10.** $^1$H NMR spectrum (CDCl$_3$, 500 MHz) of Mes$_3$SbO→SnMe$_3$Cl·(C$_7$H$_8$) at room temperature. The asterisks denote toluene signals.
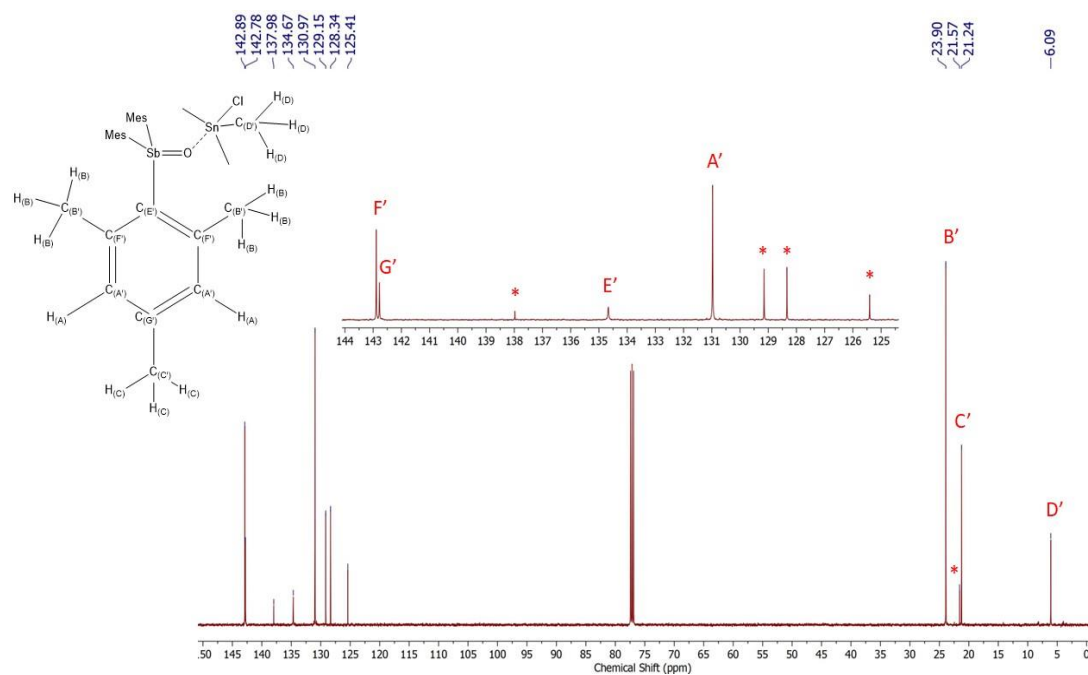
**Figure E.11.** $^{13}C\{^1H\}$ NMR spectrum (CDCl$_3$, 125 MHz) of Mes$_3$SbO→SnMe$_3$Cl·(C$_7$H$_8$) at room temperature. The asterisks denote toluene signals.
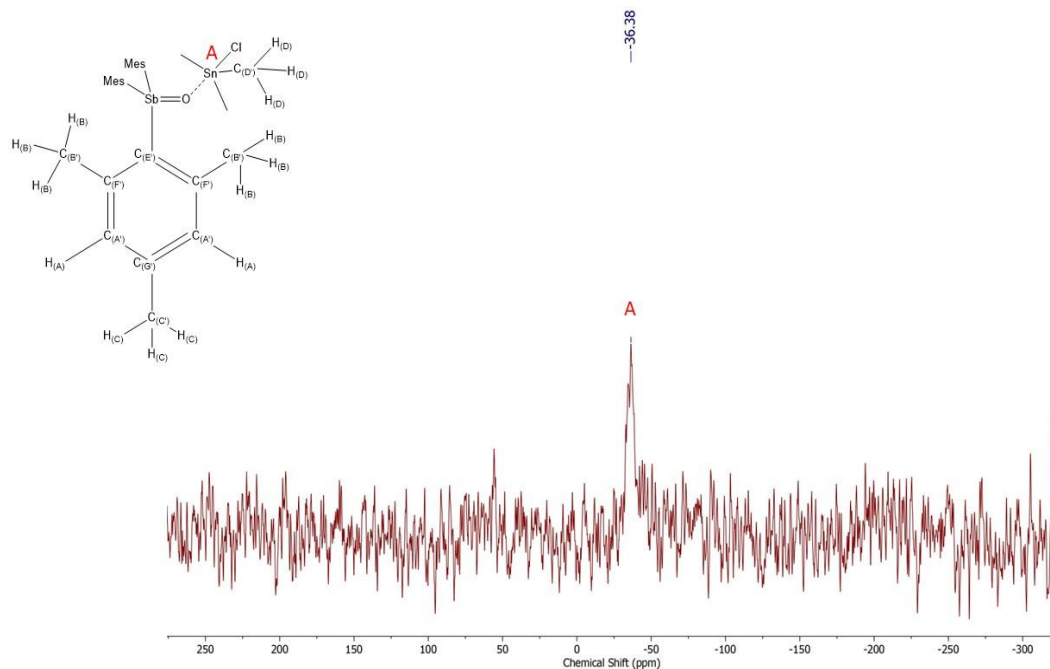


**Figure E.12.** $^{119}Sn\{^1H\}$ NMR spectrum (CDCl$_3$, 164 MHz) of Mes$_3$SbO→SnMe$_3$Cl·(C$_7$H$_8$) at room temperature.
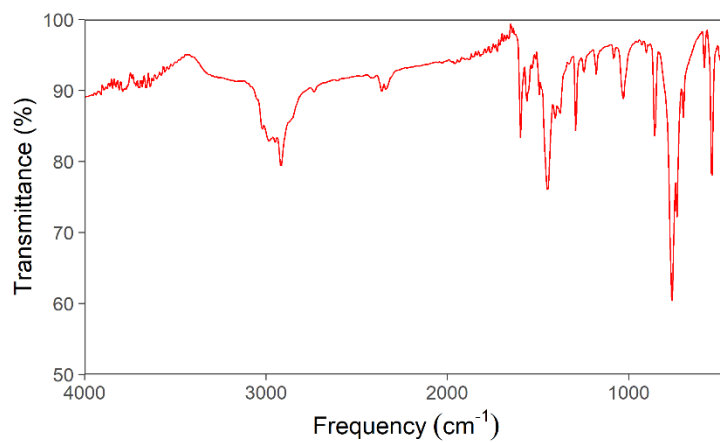
**Figure E.13.** Experimental IR spectrum (KBr pellet) of Mes$_3$SbO→SnMe$_3$Cl·(C$_7$H$_8$).



Simulated — Experimental —
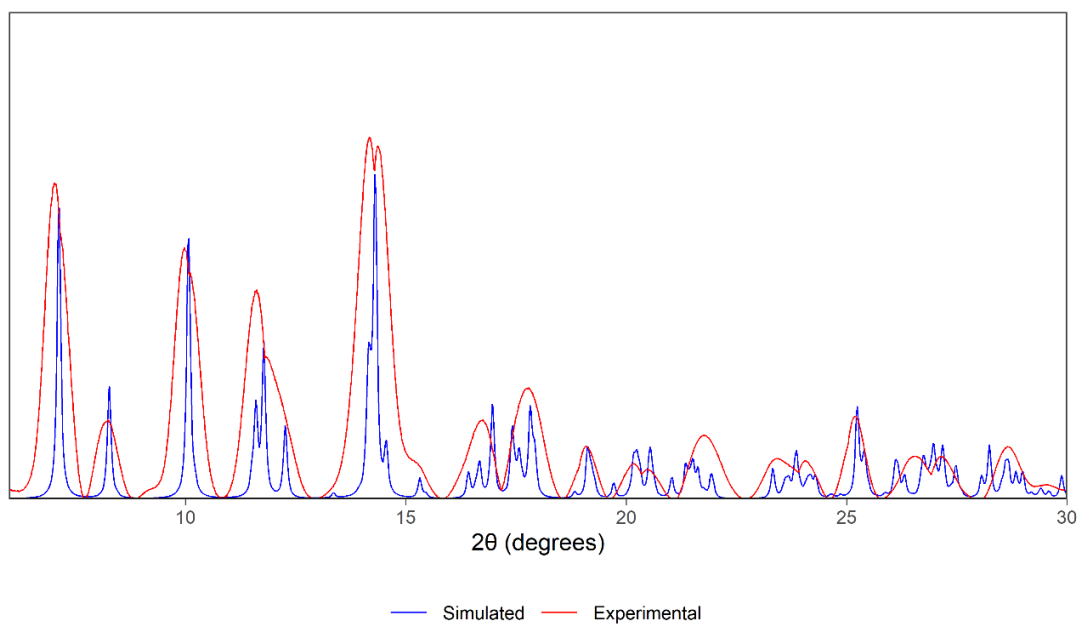
**Figure E.14.** Simulated and experimental PXRD diffractogram of Mes$_3$SbO→SnMe$_3$Cl·(C$_7$H$_8$).
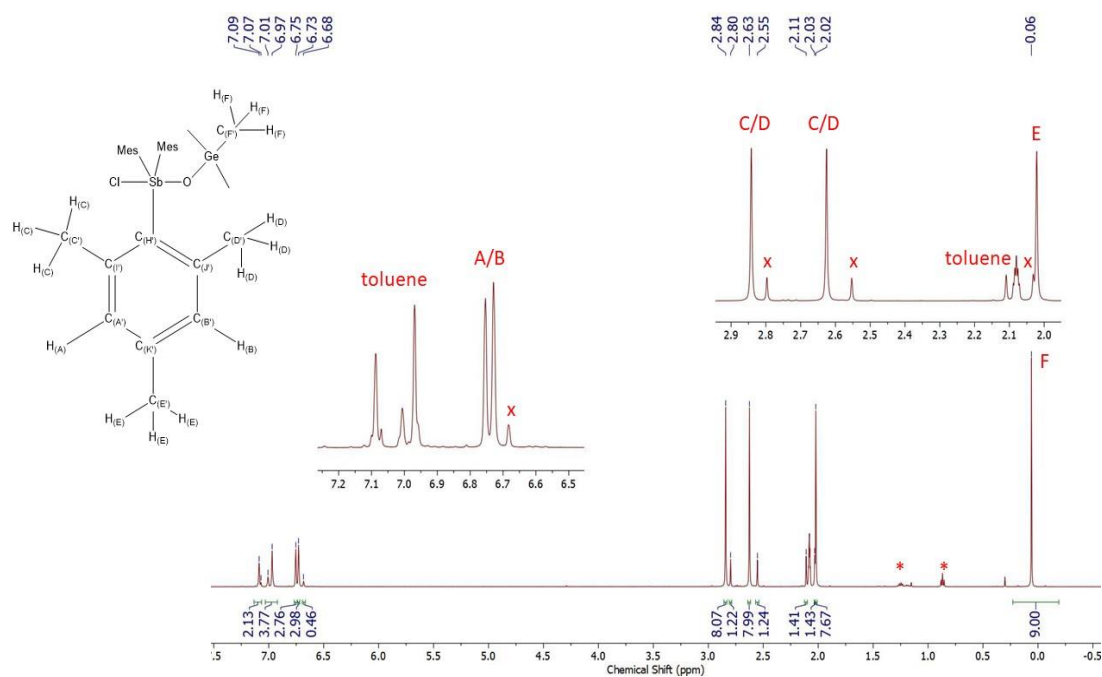
**Figure E.15.** $^1$H NMR spectrum (toluene-$d_8$, 500 MHz) of Mes$_3$Sb(OGeMe$_3$)Cl·(C$_7$H$_8$)$_{0.5}$ at room temperature. The asterisks denote pentane signals. The "x" symbols denote signals arising from the minor isomer.
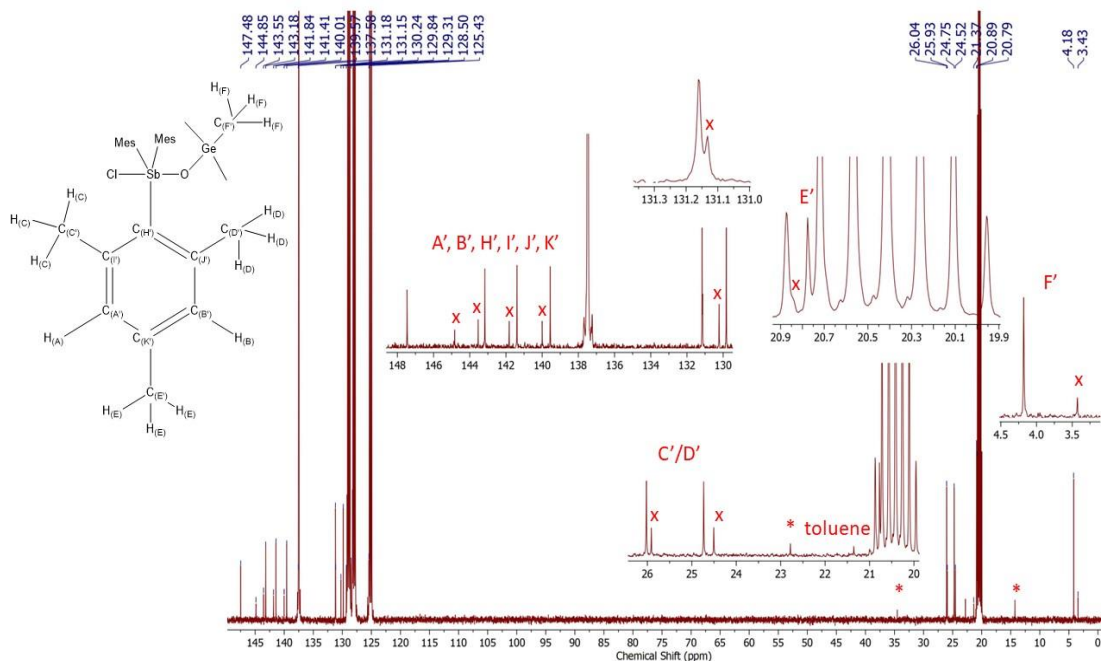


**Figure E.16.** $^{13}$C{$^1$H} NMR spectrum (toluene-$d_8$, 125 MHz) of Mes$_3$Sb(OGeMe$_3$)Cl·(C$_7$H$_8$)$_{0.5}$ at room temperature. The asterisks denote pentane signals. The "x" symbols denote signals arising from the minor isomer.
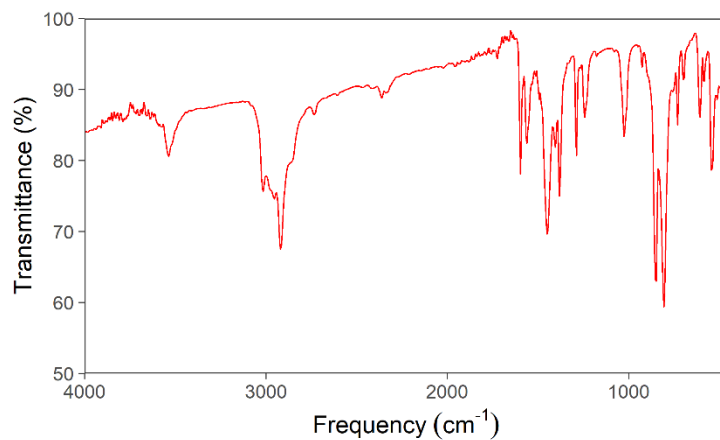
**Figure E.17.** Experimental IR spectrum (KBr pellet) of $Mes_3Sb(OGeMe_3)Cl \cdot (C_7H_8)_{0.5}$.
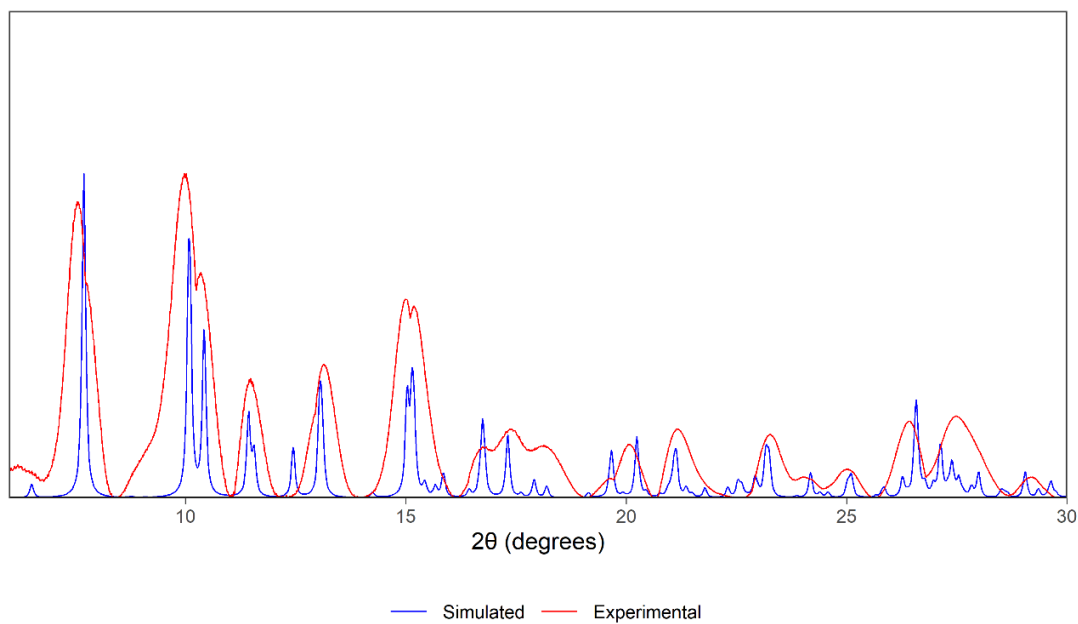


**Figure E.18.** Simulated and experimental PXRD diffractogram of $Mes_3Sb(OGeMe_3)Cl \cdot (C_7H_8)_{0.5}$.
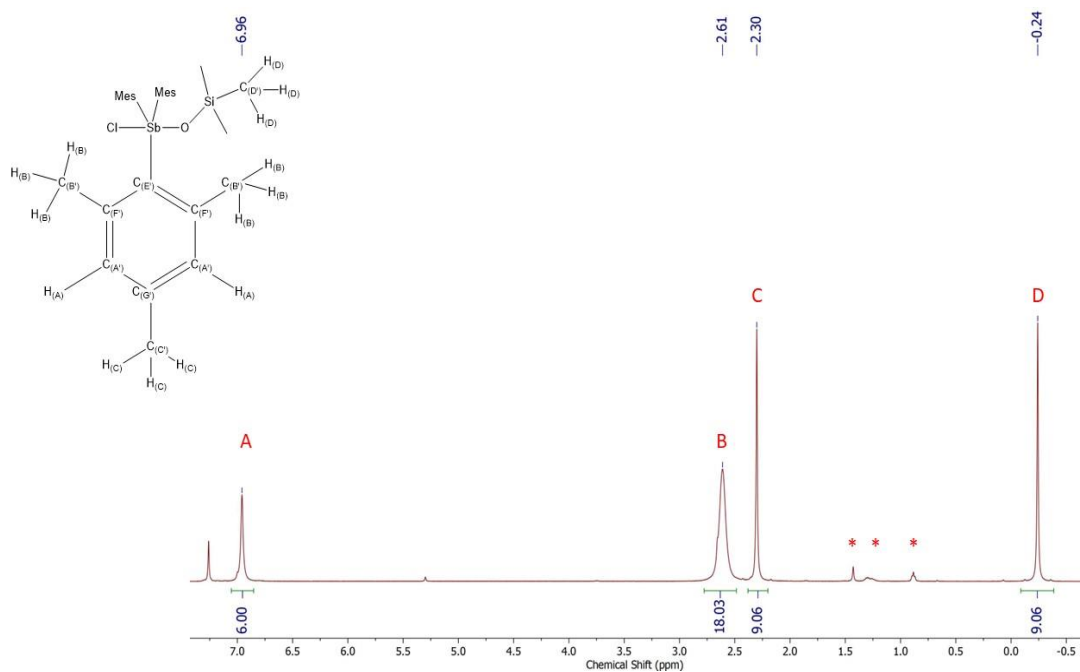
**Figure E.19.** $^1$H NMR spectrum (CDCl$_3$, 500 MHz) of Mes$_3$Sb(OSiMe$_3$)Cl at room temperature. The asterisks denote pentane and cyclohexane signals.
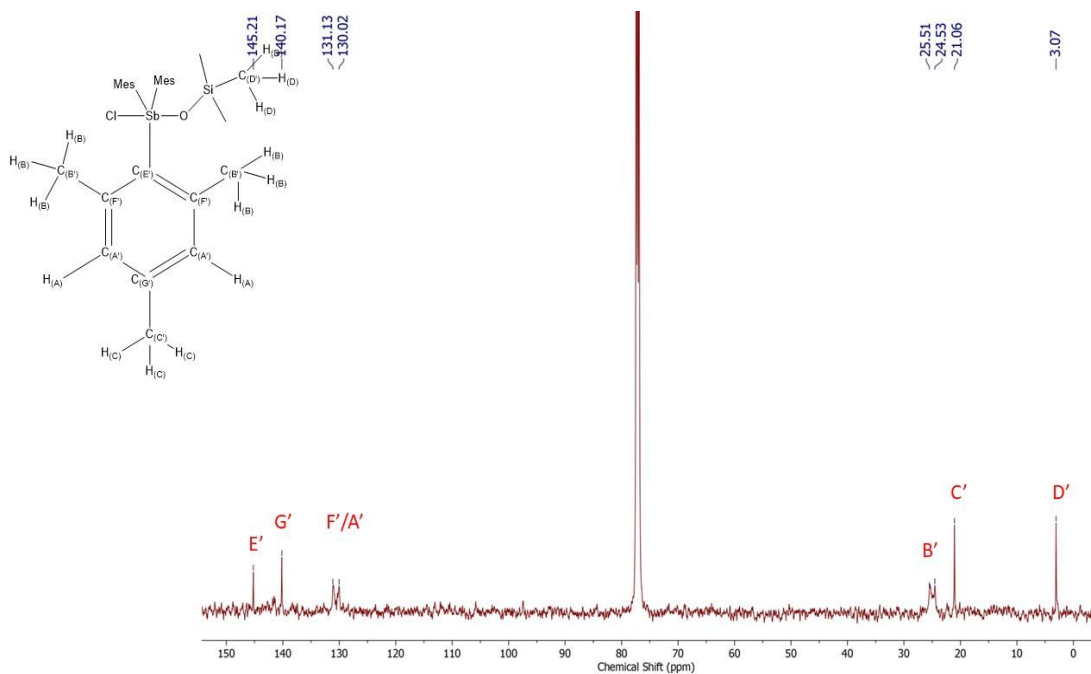


**Figure E.20.** $^{13}$C{$^1$H} NMR spectrum (CDCl$_3$, 125 MHz) of Mes$_3$Sb(OSiMe$_3$)Cl at room temperature.
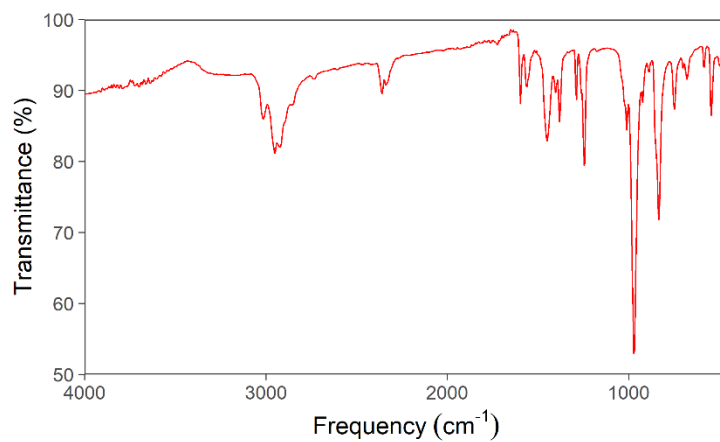
**Figure E.21.** Experimental IR spectrum (KBr pellet) of Mes$_3$Sb(OSiMe$_3$)Cl.
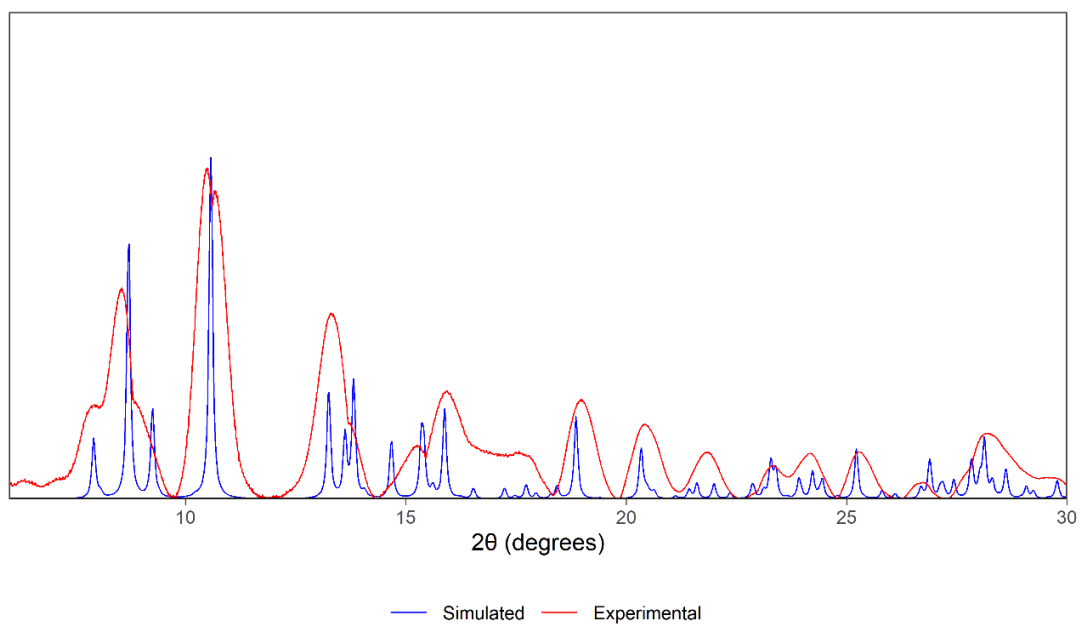


**Figure E.22.** Simulated and experimental PXRD diffractogram of Mes$_3$Sb(OSiMe$_3$)Cl.

398
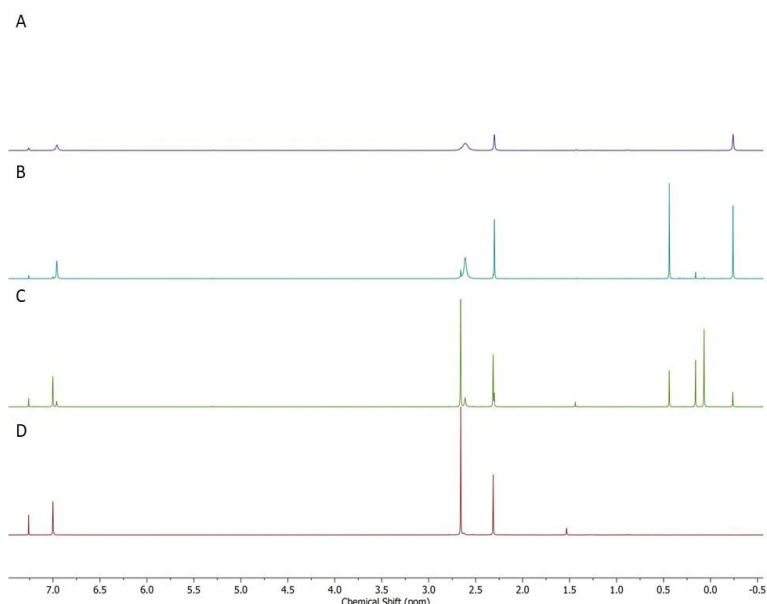
**Figure E.23.** [^1]H NMR spectrum (CDCl$_3$, 500 MHz) at room temperature of (A) Mes$_3$Sb(OSiMe$_3$)Cl, (B) a mixture of Mes$_3$SbO and two equivalents of Me$_3$SiCl collected minutes after mixing in CDCl$_3$, (C) a mixture of Mes$_3$SbO and two equivalents of Me$_3$SiCl after heating at 50 °C for 24 h, and (D) Mes$_3$SbCl$_2$. In part C, the signals at 0.16 ppm and 0.07 ppm are assigned to (Me$_3$Si)$_2$O and Me$_3$SiOH, respectively.[2-3]
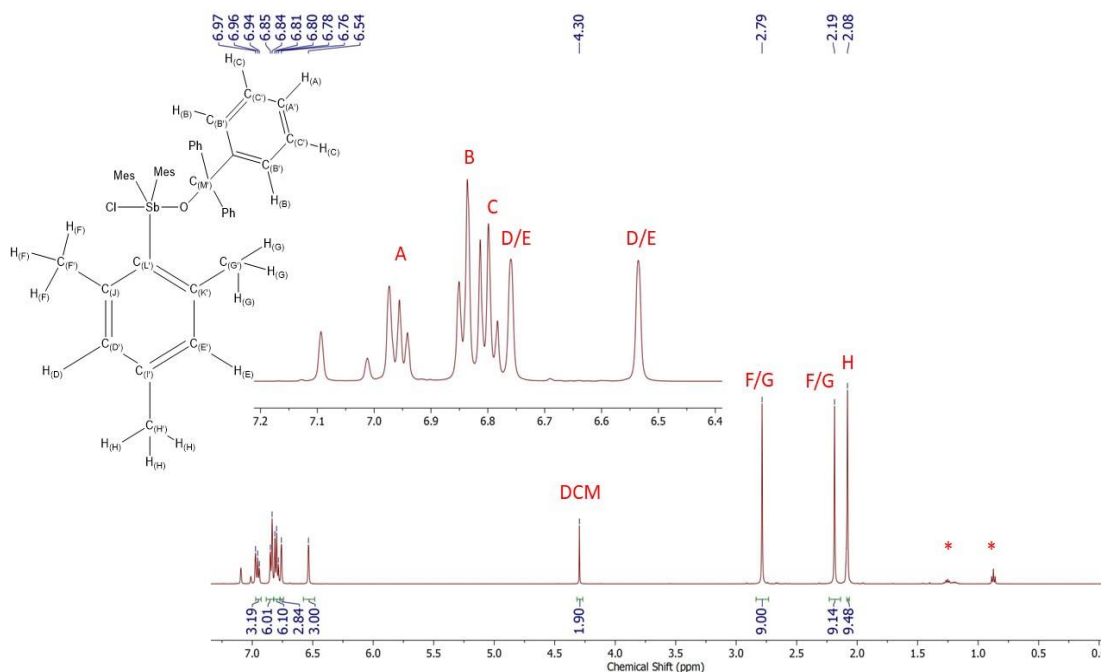


**Figure E.24.** [^1]H NMR spectrum (toluene-$d_8$, 500 MHz) of Mes$_3$Sb(OCPh$_3$)Cl·(CH$_2$Cl$_2$)$_{1.5}$ at room temperature. The asterisks denote pentane signals.

399
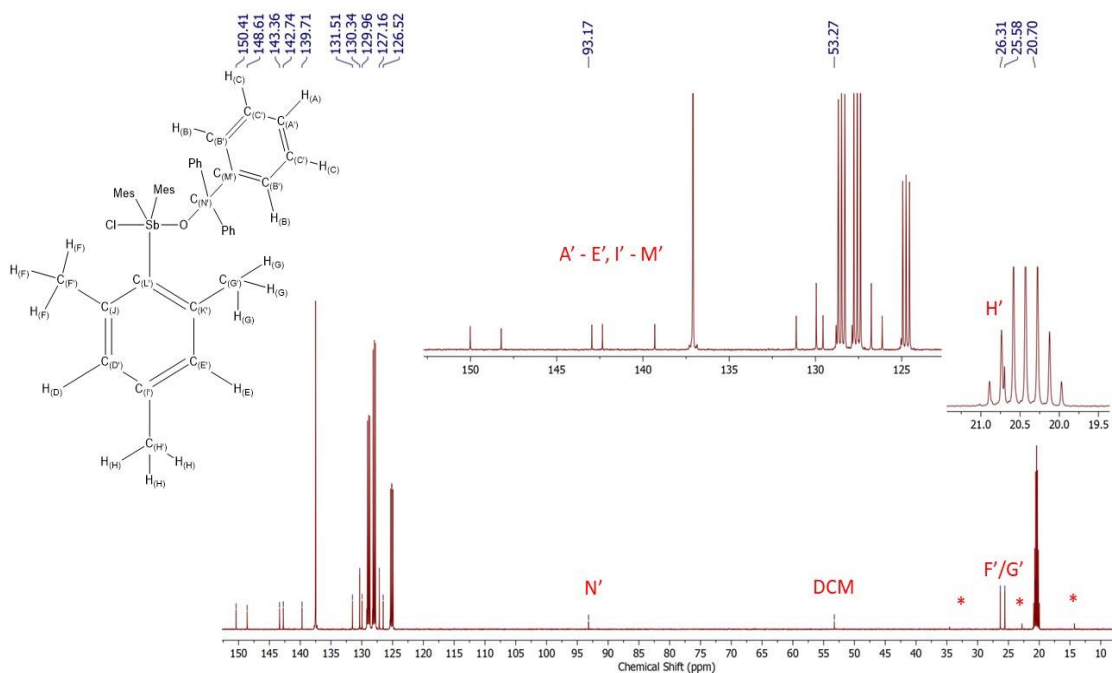
**Figure E.25.** $^{13}C\{^1H\}$ NMR spectrum (toluene-$d_8$, 125 MHz) of Mes$_3$Sb(OCPh$_3$)Cl·(CH$_2$Cl$_2$)$_{1.5}$ at room temperature. The asterisks denote pentane signals.
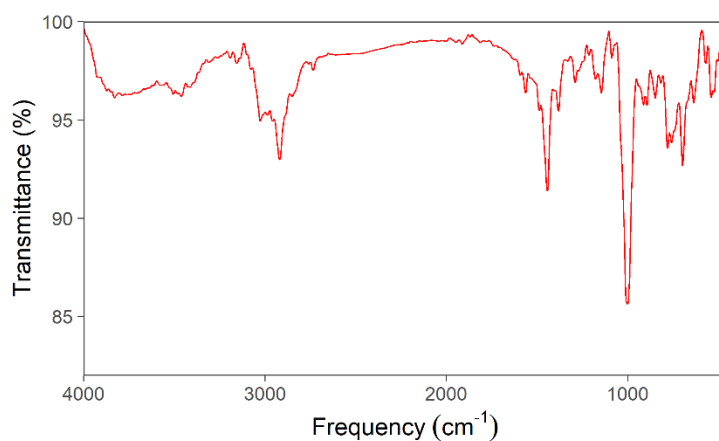


**Figure E.26.** Experimental IR spectrum (KBr pellet) of Mes$_3$Sb(OCPh$_3$)Cl·(CH$_2$Cl$_2$)$_{1.5}$.
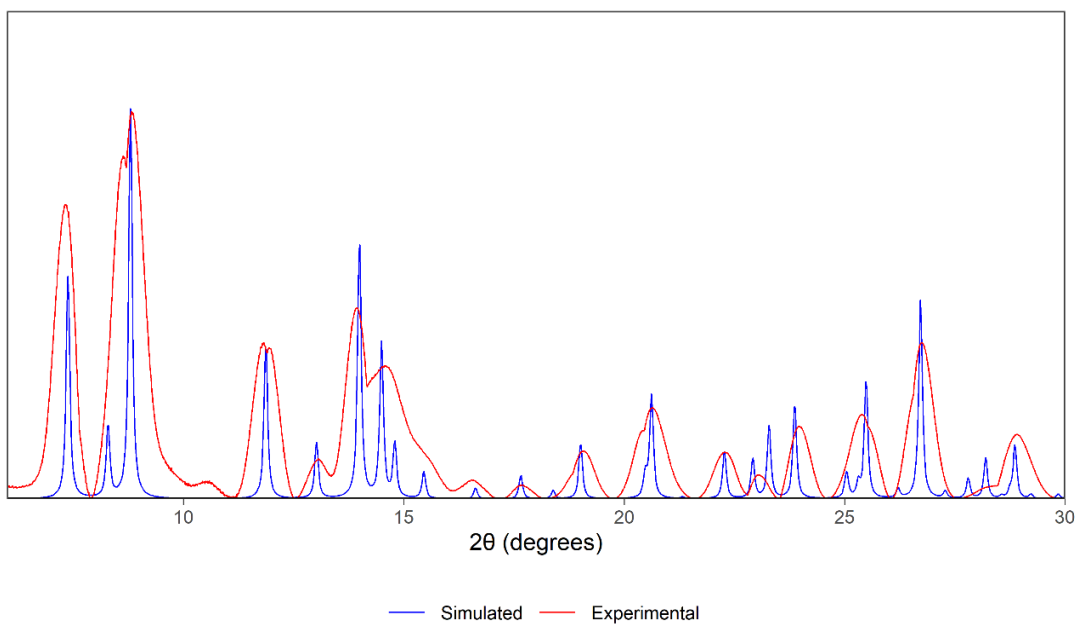
**Figure E.27.** Simulated and experimental PXRD diffractogram of $Mes_3Sb(OCPh_3)Cl\cdot(CH_2Cl_2)_{1.5}$.
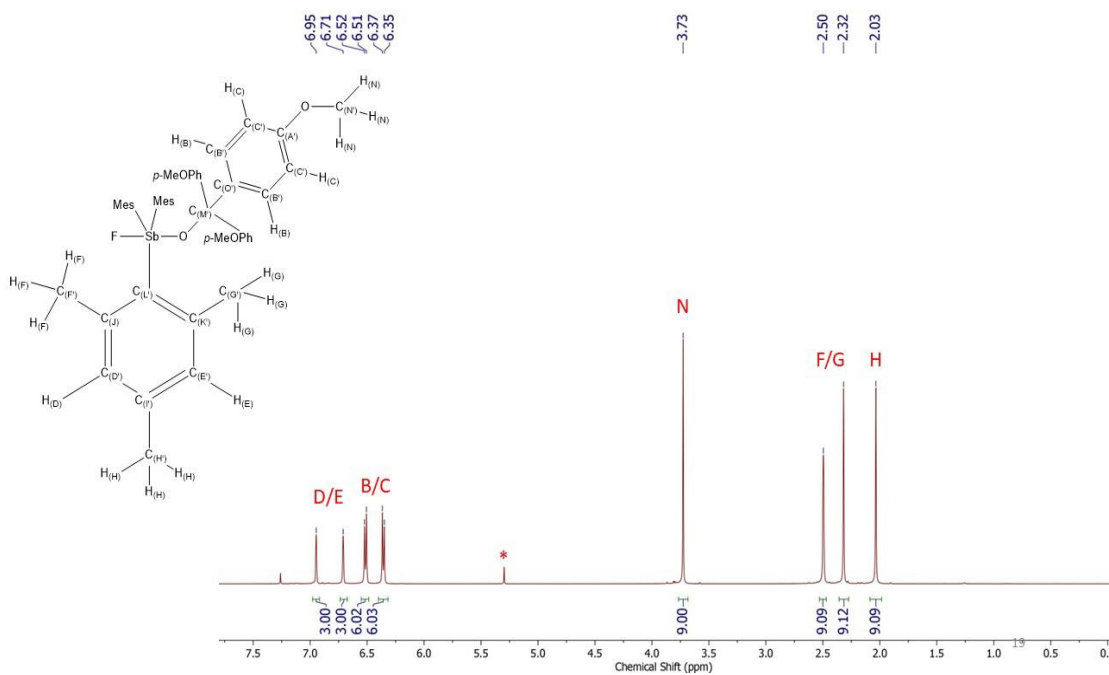


**Figure E.28.** $^1H$ NMR spectrum ($CDCl_3$, 500 MHz) of $Mes_3Sb(OC(p\text{-}MeOPh)_3)F$ at room temperature. The asterisk denotes a DCM signal.

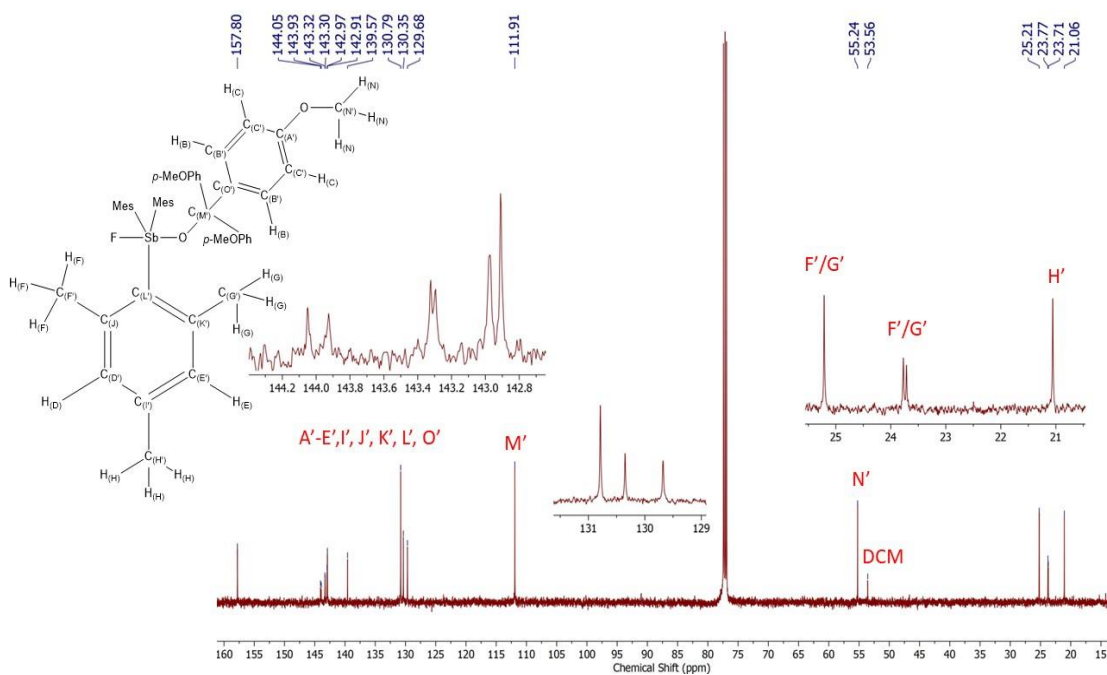**Figure E.29.** $^{13}$C{$^1$H} NMR spectrum (CDCl$_3$, 125 MHz) of Mes$_3$Sb(OC(p-MeOPh)$_3$)F at room temperature.
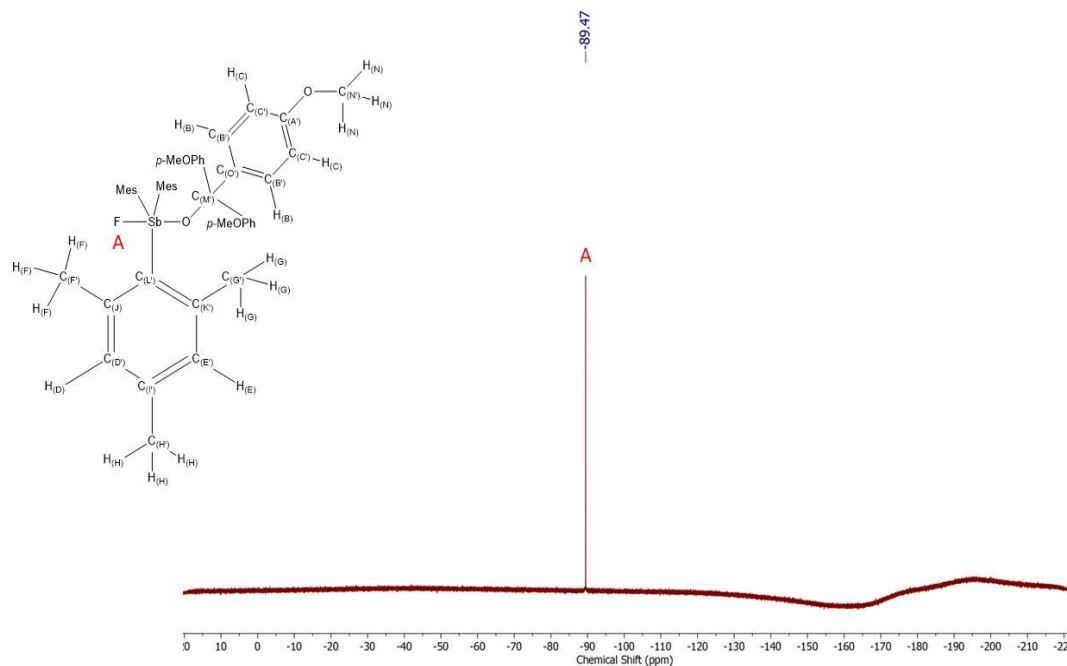


**Figure E.30.** $^{19}$F{$^1$H} NMR spectrum (CDCl$_3$, 471 MHz) of Mes$_3$Sb(OC(p-MeOPh)$_3$)F at room temperature.
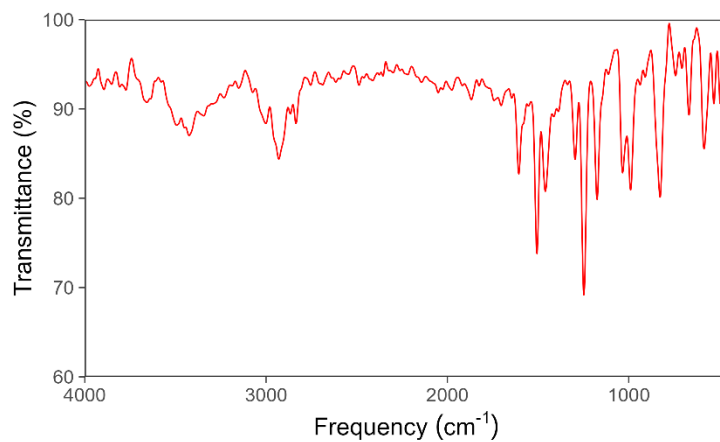
**Figure E.31.** Experimental IR spectrum (KBr pellet) of Mes$_3$Sb(OC($p$-MeOPh)$_3$)F. A rolling average with an 8 data point span was applied to smooth the data.
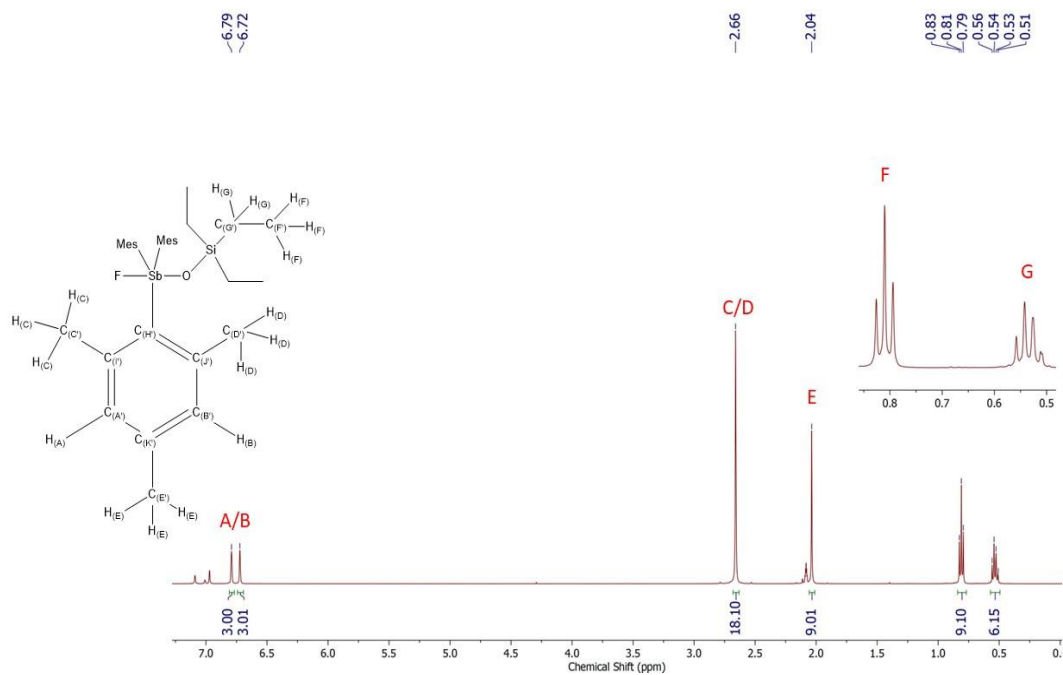


**Figure E.32.** $^1$H NMR spectrum (toluene-$d_8$, 500 MHz) of Mes$_3$Sb(OSiEt$_3$)F at room temperature.
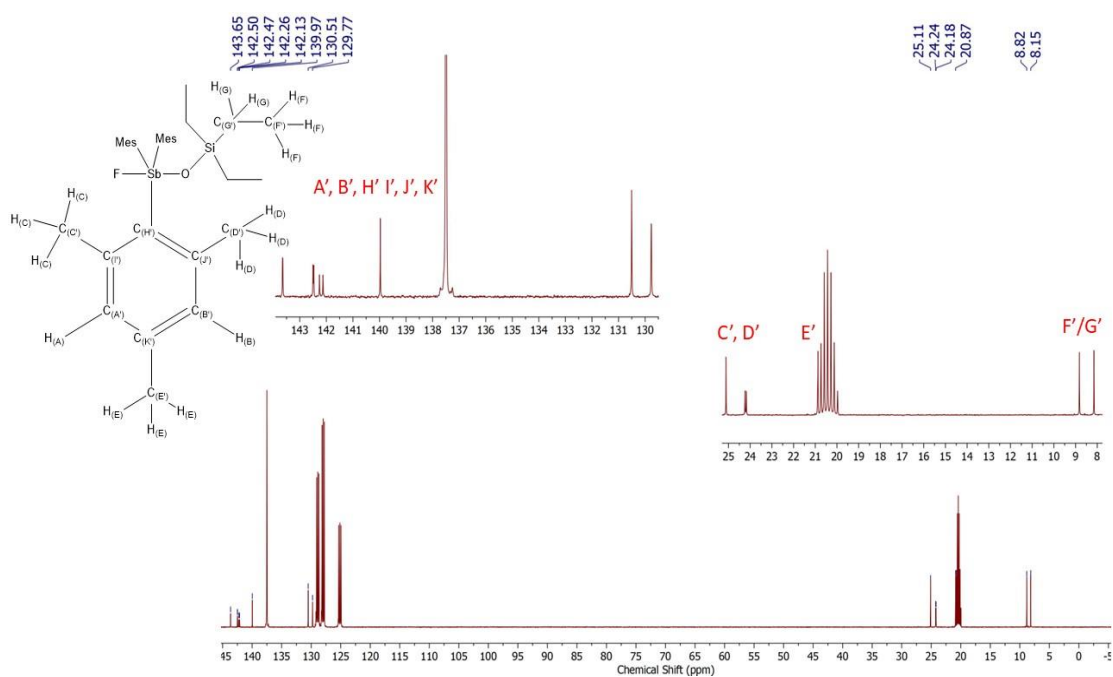
**Figure E.33.** $^{13}C\{^1H\}$ NMR spectrum (toluene-$d_8$, 125 MHz) of Mes$_3$Sb(OSiEt$_3$)F at room temperature.
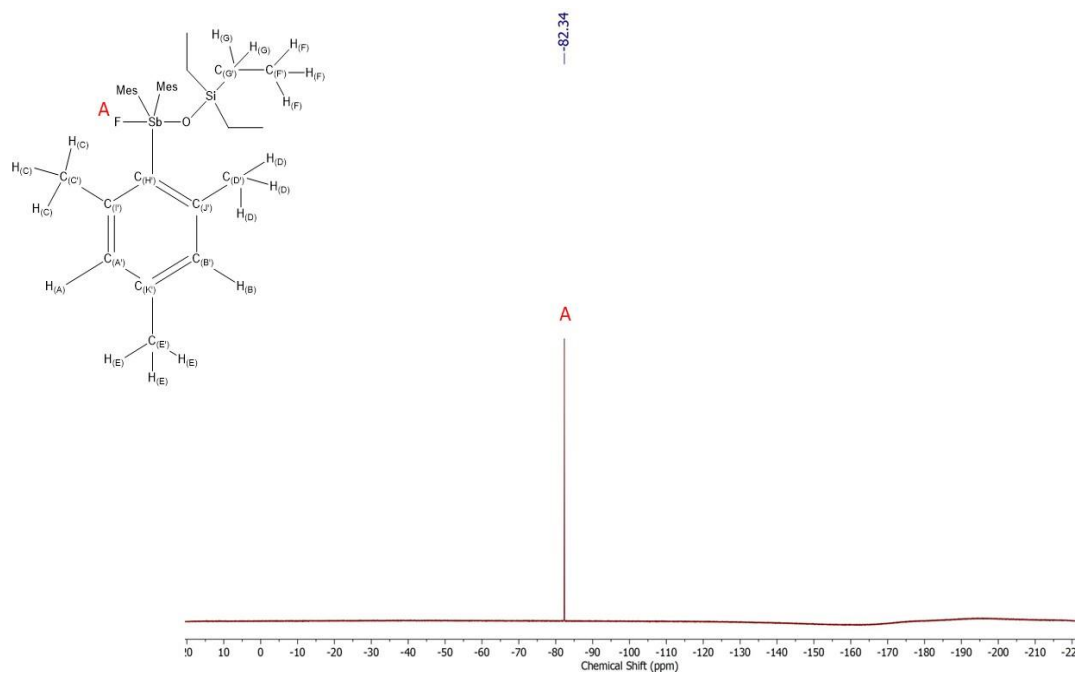


**Figure E.34.** $^{19}F\{^1H\}$ NMR spectrum (toluene-$d_8$, 471 MHz) of Mes$_3$Sb(OSiEt$_3$)F at room temperature.

404
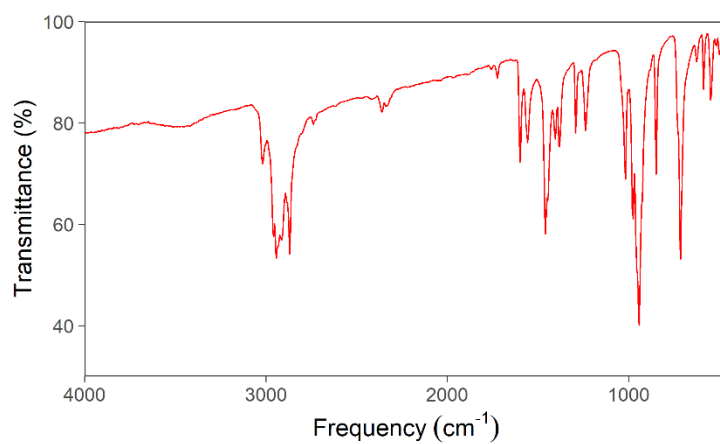
**Figure E.35.** Experimental IR spectrum (KBr pellet) of Mes$_3$Sb(OSiEt$_3$)F.
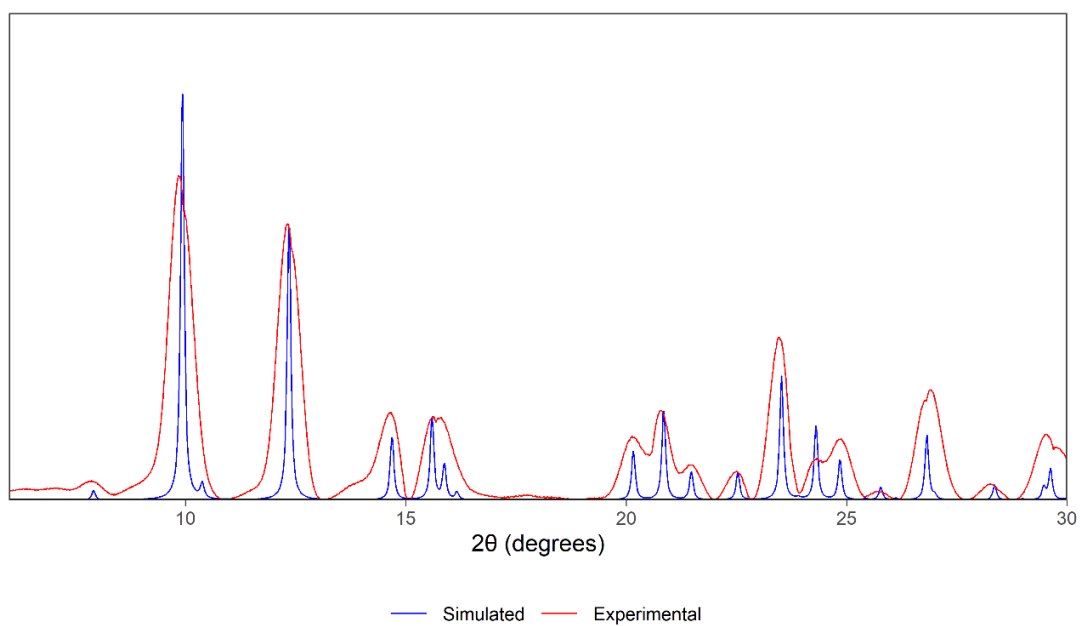


**Figure E.36.** Simulated and experimental PXRD diffractogram of Mes$_3$Sb(OSiEt$_3$)F.
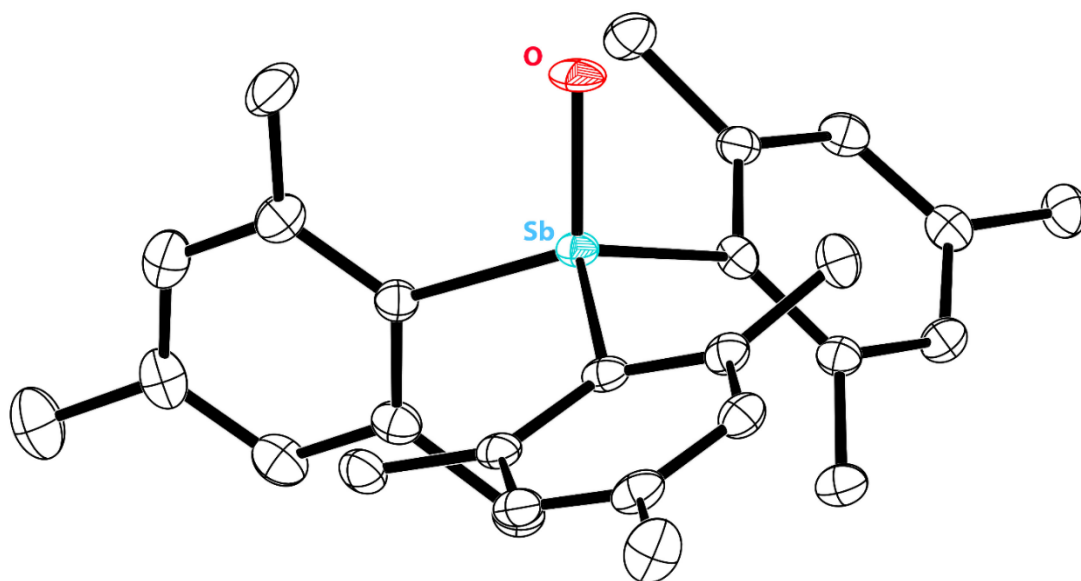
**Figure E.37.** Thermal ellipsoid plot (50% probability) of Mes$_3$SbO. Color code: Sb teal, O red, and C black. Hydrogen atoms are omitted for clarity.
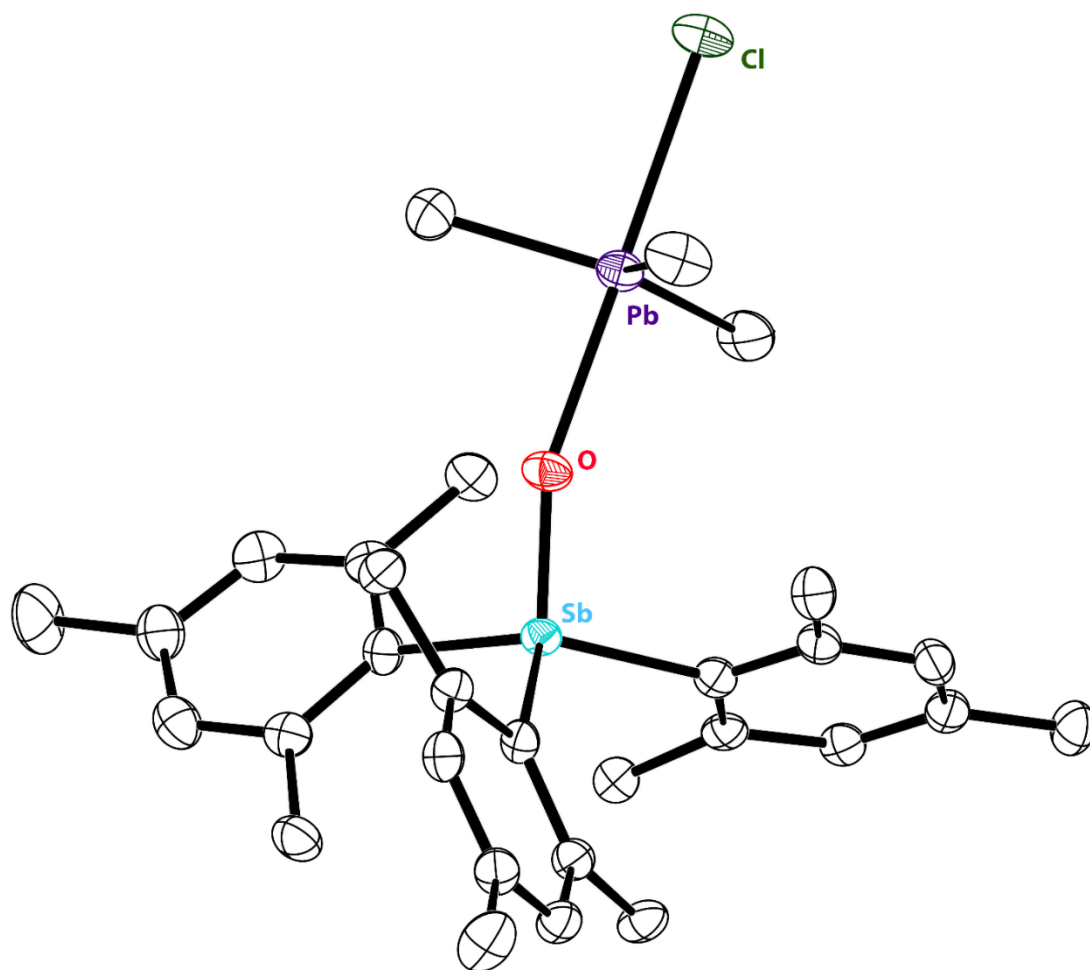
**Figure E.38.** Thermal ellipsoid plot (50% probability) of Mes$_3$SbO→PbMe$_3$Cl·(CH$_2$Cl$_2$). Color code: Sb teal, Pb purple, Cl dark-green, O red, and C black. Hydrogen atoms and solvent molecules are omitted for clarity.

**Figure E.39.** Thermal ellipsoid plot (50% probability) of Mes$_3$SbO→SnMe$_3$Cl·(C$_7$H$_8$). Color code: Sb teal, Sn blue, Cl dark-green, O red, and C black. Hydrogen atoms and solvent molecules are omitted for clarity.

**Figure E.40.** Thermal ellipsoid plot (50% probability) of Mes$_3$Sb(OGeMe$_3$)Cl·(C$_7$H$_8$)$_{0.5}$. Color code: Sb teal, Ge light-green, Cl dark-green, O red, and C black. Hydrogen atoms and solvent molecules are omitted for clarity.

**Figure E.41.** Thermal ellipsoid plot (50% probability) of Mes₃Sb(OSiMe₃)Cl. Color code: Sb teal, Si yellow, Cl dark-green, O red, and C black. Hydrogen atoms are omitted for clarity.
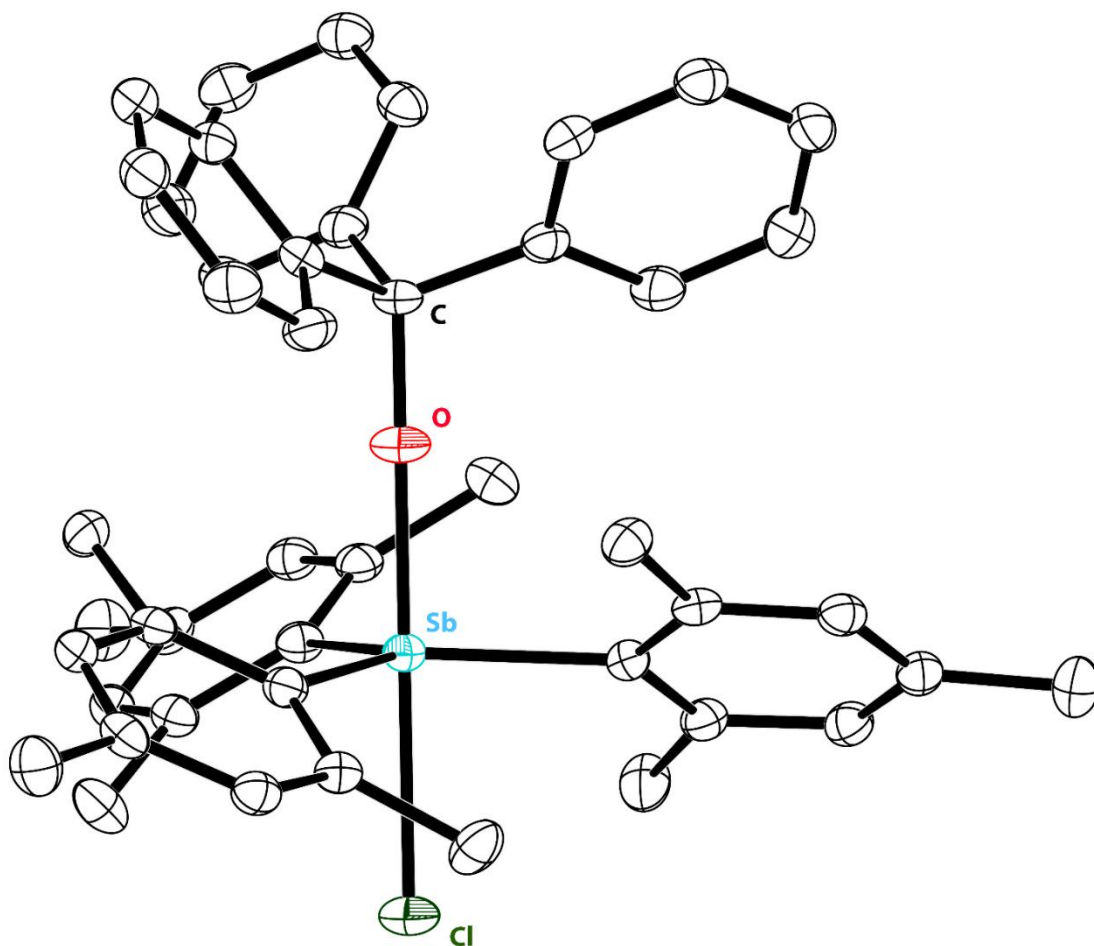
**Figure E.42.** Thermal ellipsoid plot (50% probability) of Mes$_3$Sb(OCPh$_3$)Cl·(CH$_2$Cl$_2$)$_{1.5}$. Color code: Sb teal, Cl dark-green, O red, and C black. Hydrogen atoms and solvent molecules are omitted for clarity.

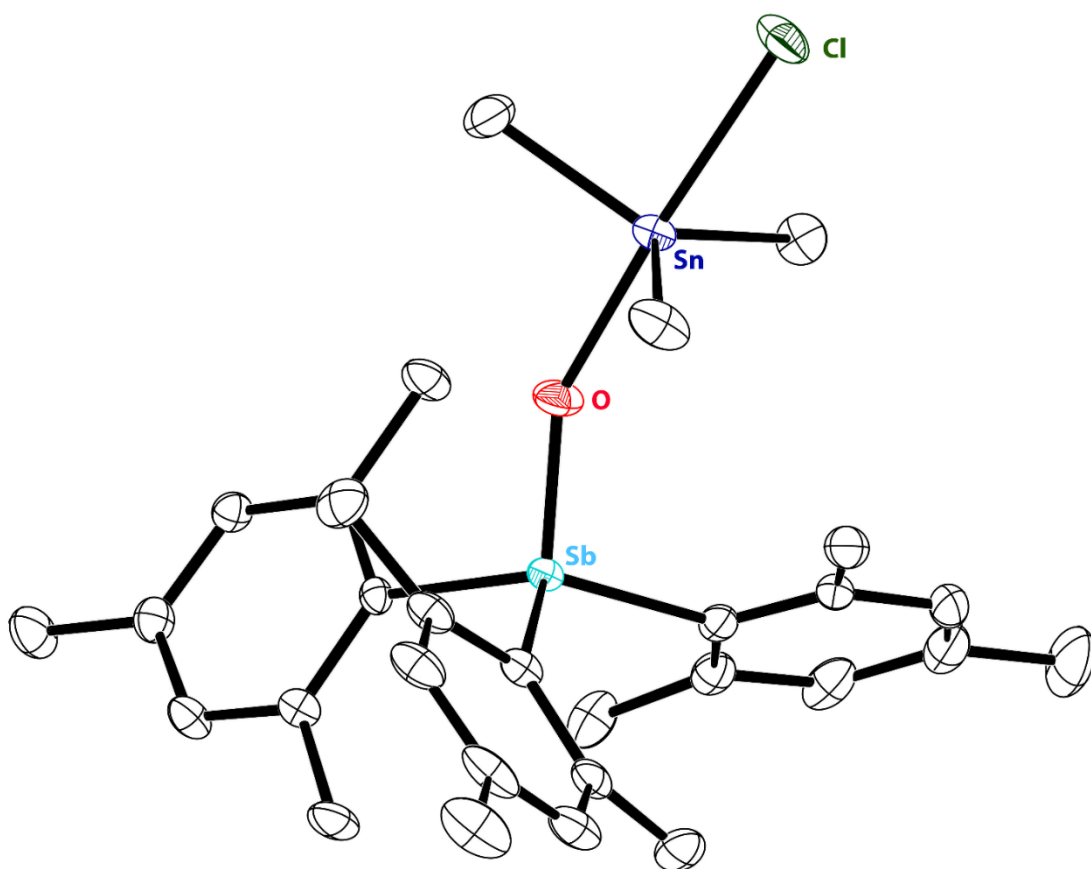**Figure E.43.** Thermal ellipsoid plot (50% probability) of Mes$_3$Sb(OC($p$-MeOPh)$_3$)F·(CH$_2$Cl$_2$)$_2$. Color code: Sb teal, F green, O red, and C black. Hydrogen atoms and solvent molecules are omitted for clarity.
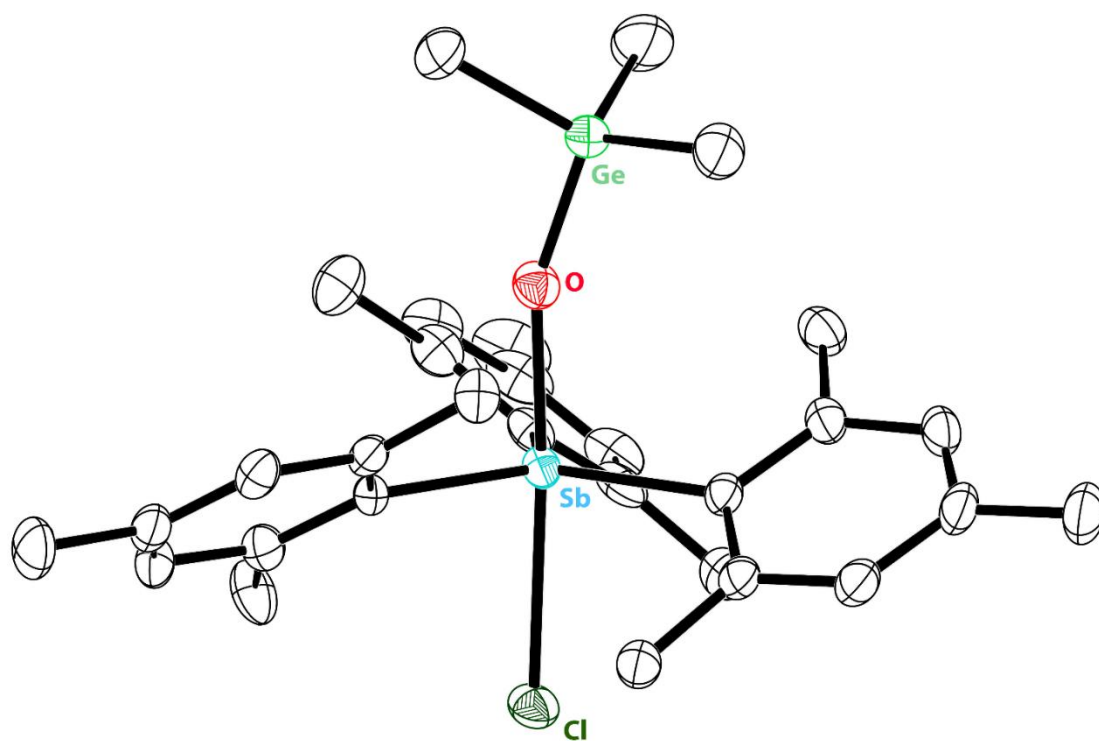
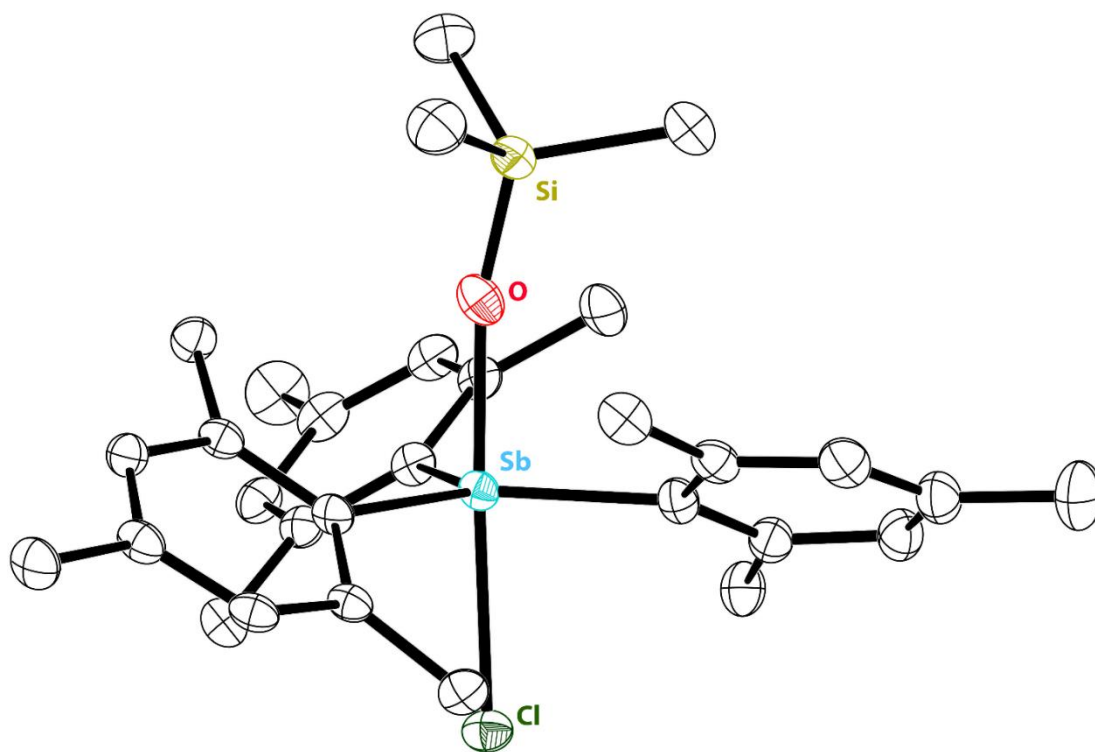**Figure E.44.** Thermal ellipsoid plot (50% probability) of Mes$_3$Sb(OSiEt$_3$)F. Color code: Sb teal, Si yellow, F green, O red, and C black. Hydrogen atoms are omitted for clarity.

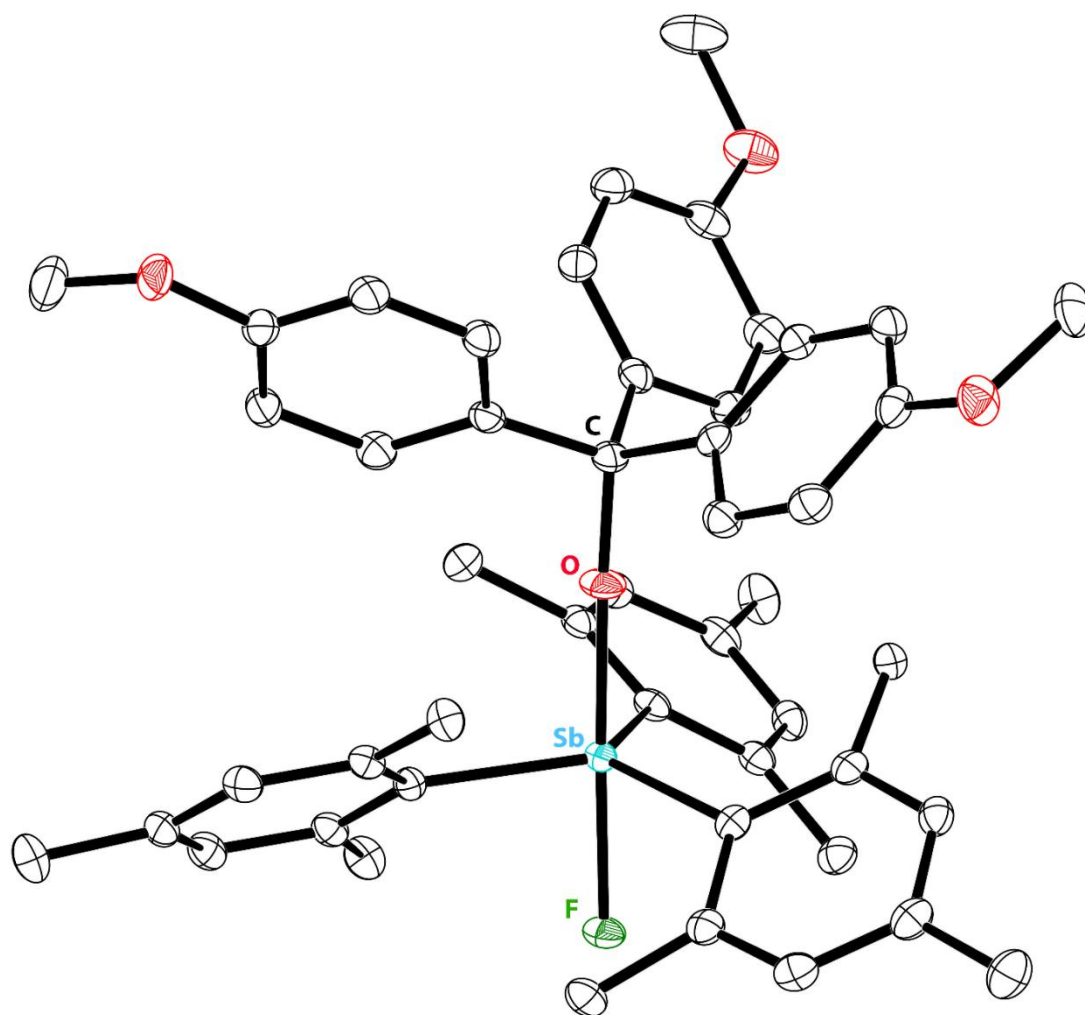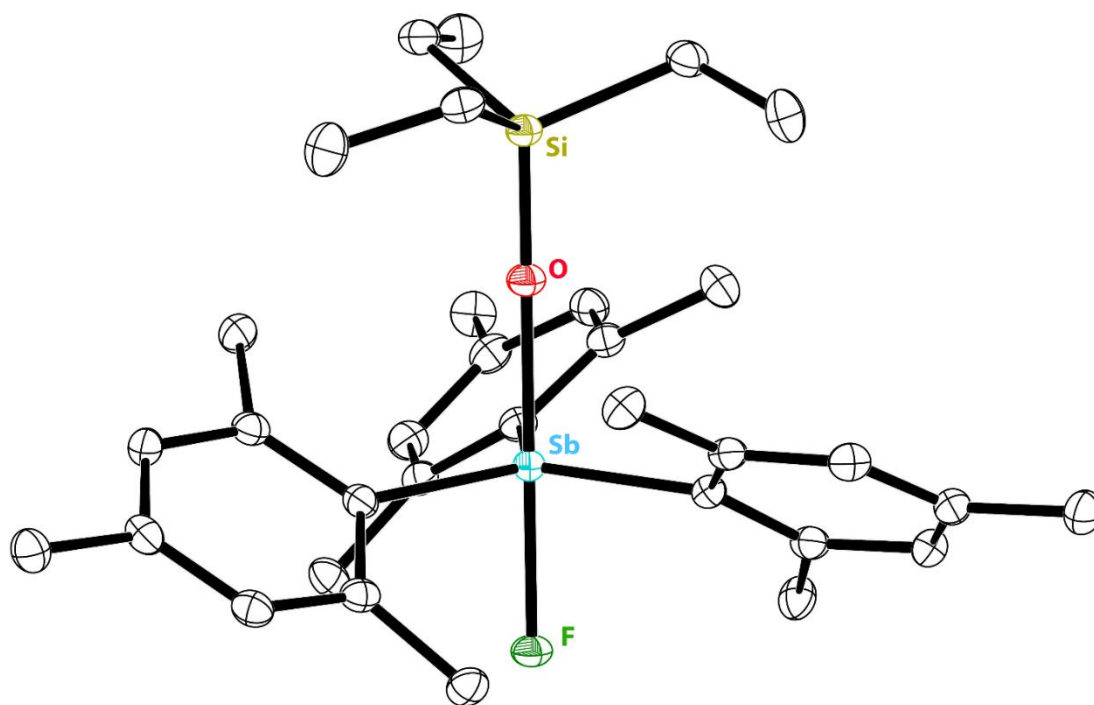**Table E.1.** Crystallographic details for Mes$_3$SbO, Mes$_3$SbO→PbMe$_3$Cl·(CH$_2$Cl$_2$), Mes$_3$SbO→SnMe$_3$Cl·(C$_7$H$_8$), Mes$_3$Sb(OGeMe$_3$)Cl·(C$_7$H$_8$)$_{0.5}$.

| Compound | Mes$_3$SbO | Mes$_3$SbO→ PbMe$_3$Cl· (CH$_2$Cl$_2$) | Mes$_3$SbO→ SnMe$_3$Cl· (C$_7$H$_8$) | Mes$_3$SbO GeMe$_3$Cl· (C$_7$H$_8$)$_{0.5}$ |
|---|---|---|---|---|
| Empirical Formula | C$_{27}$H$_{33}$SbO | C$_{31}$H$_{44}$SbOPbCl$_3$ | C$_{37}$H$_{50}$SbOSnCl | C$_{33.5}$H$_{46}$SbOGe |
| Formula | 495.28 | 867.95 | 786.66 | 694.49 |
| Temperature | 100.0(3) | 107(4) | 99.98(13) | 104(5) |
| Wavelength (Å) | 1.54184 | 1.54184 | 1.54184 | 1.54184 |
| Crystal system | Monoclinic | Monoclinic | Monoclinic | Triclinic |
| Space group | $P2_1/c$ | $P2_1/c$ | $P2_1/n$ | $P\overline{1}$ |
| $a$ (Å) | 18.2342(3) | 13.2454(2) | 11.1055(2) | 10.4635(2) |
| $b$ (Å) | 15.5777(2) | 14.60770(10) | 15.3570(2) | 11.8795(3) |
| $c$ (Å) | 8.20730(10) | 17.4505(2) | 21.5584(3) | 13.6256(2) |
| $\alpha$ (°) | | | | 88.753(2) |
| $\beta$ (°) | 101.023(2) | 95.1220(10) | 103.747(2) | 84.364(2) |
| $\gamma$ (°) | | | | 75.016(2) |
| Volume (Å$^3$) | 2288.25(6) | 3362.92(7) | 3571.40(10) | 1628.17(6) |
| $Z$ | 4 | 4 | 4 | 2 |
| $\rho_{calc}$ (Mg/m$^3$) | 1.438 | 1.714 | 1.463 | 1.417 |
| Crystal size | 0.1 x 0.08 x | 0.17 x 0.14 x 0.05 | 0.21 x 0.16 x 0.12 | 0.06 x 0.05 x |
| $\theta$ range (°) | 2.469 to | 3.953 to 68.241 | 3.569 to 68.240 | 3.259 to |
| Total | 17162 | 24813 | 26667 | 21321 |
| Unique | 4185 | 6165 | 6550 | 5968 |
| Method | IAM | IAM | IAM | IAM |
| Parameters | 271 | 374 | 383 | 383 |
| Completeness | 100.0 | 100.0 | 100.0 | 99.9 |
| R$_{int}$ | 0.0422 | 0.0443 | 0.0560 | 0.0348 |
| R$_1$ (I > 2$\sigma$) | 0.0290 | 0.0320 | 0.0324 | 0.0265 |
| R$_1$ (all data) | 0.0319 | 0.0344 | 0.0350 | 0.0294 |
| wR$_2$ (I > 2$\sigma$) | 0.0749 | 0.0840 | 0.0836 | 0.0650 |
| wR$_2$ (all data) | 0.0769 | 0.0860 | 0.0858 | 0.0664 |
| Goodness of fit, $S$ | 1.047 | 1.034 | 1.030 | 1.050 |

**Table E.2.** Crystallographic details for Mes₃Sb(OSiMe₃)Cl , Mes₃Sb(OCPh₃)Cl·(CH₂Cl₂)₁.₅, Mes₃Sb(OSiEt₃)F, Mes₃Sb(OC(*p*-MeOPh)₃)F·(CH₂Cl₂)₂.

| Compound | Mes₃Sb (OSiMe₃)Cl | Mes₃Sb (OCPh₃)Cl· (CH₂Cl₂)₁.₅ | Mes₃Sb (OSiEt₃)F | Mes₃Sb (OC(*p*-MeOPh)₃)F ·(CH₂Cl₂)₂ |
|---|---|---|---|---|
| Empirical | $C_{30}H_{42}SbOSiCl$ | $C_{47.5}H_{51}SbOCl_4$ | $C_{33}H_{48}SbOSiF$ | $C_{51}H_{58}Cl_4FO_4Sb$ |
| Formula | 603.92 | 901.43 | 629.55 | 1017.52 |
| Temperature | 100.0(2) | 99.97(12) | 105(2) | 105(7) |
| Wavelength | 1.54184 | 1.54184 | 1.54184 | 1.54184 |
| Crystal system | Monoclinic | Trigonal | Trigonal | Triclinic |
| Space group | $I2/a$ | $R\overline{3}$ | $R\overline{3}$ | $P\overline{1}$ |
| $a$ (Å) | 21.4322(3) | 14.8986(2) | 14.3212(2) | 14.4860(4) |
| $b$ (Å) | 13.35190(10) | | | 14.5779(3) |
| $c$ (Å) | 22.7677(3) | 31.9666(6) | 25.5412(3) | 14.6616(3) |
| $\alpha$ (°) | | | | 94.931(2) |
| $\beta$ (°) | 117.018(2) | | | 115.637(2) |
| $\gamma$ (°) | | | | 117.037(2) |
| Volume (Å³) | 5804.17(15) | 6144.9(2) | 4536.60(14) | 2327.21(11) |
| $Z$ | 8 | 6 | 6 | 2 |
| $\rho_{calc}$ (Mg/m³) | 1.382 | 1.462 | 1.383 | 1.452 |
| Crystal size | 0.12 x 0.08 x | 0.16 x 0.07 x | 0.23 x 0.19 x | 0.16 x 0.09 x 0.06 |
| θ range (°) | 3.964 to 68.237 | 3.694 to | 3.962 to | 3.572 to 68.245 |
| Total | 46943 | 16072 | 11877 | 29674 |
| Unique | 5298 | 2509 | 1858 | 8525 |
| Method | IAM | IAM | IAM | IAM |
| Parameters | 319 | 178 | 116 | 590 |
| Completeness | 99.9 | 99.9 | 100.0 | 99.9 |
| $R_{int}$ | 0.0518 | 0.0520 | 0.0442 | 0.0362 |
| $R_1$ (I > 2σ) | 0.0215 | 0.0241 | 0.0189 | 0.0245 |
| $R_1$ (all data) | 0.0240 | 0.0255 | 0.0192 | 0.0264 |
| $wR_2$ (I > 2σ) | 0.0554 | 0.0618 | 0.0470 | 0.0624 |
| $wR_2$ (all data) | 0.0567 | 0.0626 | 0.0473 | 0.0633 |
| Goodness of fit, $S$ | 1.043 | 1.074 | 1.097 | 1.068 |

**Table E.3.** Select structural parameters of Mes$_3$SbO and Dipp$_3$SbO.

| | Sb–O distance (Å) | Average Sb–C$_{ipso}$–C$_{para}$ angle (°) | Sum of C$_{ipso}$–Sb–C$_{ipso}$ angles (°) |
|---|---|---|---|
| **Mes$_3$SbO** [a] | 1.848(2) | 173.06(7) | 333.08(18) |
| **Mes$_3$SbO (DFT)** [b] | 1.831 | 174.26 | 332.01 |
| **Dipp$_3$SbO(monoclinic)** [c,f] | 1.8371(4) | 169.46(2) | 338.73(03) |
| **Dipp$_3$SbO(orthorhombic)** [d,f] | 1.8428(14) | 172.76(6) | 336.98(13) |
| **Dipp$_3$SbO (DFT$ca$)** [e,f] | 1.827 | 169.17 | 339.62 |

[a] Crystallographic coordinates of Mes$_3$SbO. [b] Computationally optimized coordinates of Mes$_3$SbO (PBE0/def2-TZVPP). [c] Crystallographic coordinates of Dipp$_3$SbO within monoclinic polymorph. [d] Crystallographic coordinates of Dipp$_3$SbO within orthorhombic polymorph. [e] Computationally optimized coordinates of Dipp$_3$SbO (PBE0/def2-TZVPP). [f] These values are reproduced from a prior report.[1]

**Table E.4.** Select properties of Dipp$_3$PnO and Mes$_3$PnO calculated at the DKH-PBE0/old-DKH-TZVPP//PBE0/def2-TZVPP level of theory.

| | $\rho_{bcp}$(Pn–O) [b] (e$^-$/Å$^3$) | HOMO [c] (eV) | LUMO [d] (eV) | NPA O [e] (e$^-$) | NPA Pn [f] (e$^-$) | E$_{del}$ [g] (kcal/mol) |
|---|---|---|---|---|---|---|
| **Dipp$_3$SbO** [a] | 0.173 | −6.29 | −0.82 | −1.24 | 2.16 | 92 |
| **Dipp$_3$AsO** [a] | 0.216 | −6.55 | −0.72 | −1.14 | 1.84 | 117 |
| **Dipp$_3$PO** [a] | 0.232 | −6.77 | −0.79 | −1.13 | 1.91 | 172 |
| **Mes$_3$SbO** | 0.172 | −6.32 | −0.74 | −1.23 | 2.22 | 91 |
| **Mes$_3$AsO** | 0.214 | −6.52 | −0.68 | −1.13 | 1.88 | 117 |
| **Mes$_3$PO** | 0.232 | −6.69 | −0.72 | −1.11 | 1.93 | 171 |

[a] These values are reproduced from a prior report.[4] [b] Electron density at the Pn–O bond critical point. [c] Energy of HOMO. [d] Energy of LUMO. [e] Natural charge of the O atom. [f] Natural charge of the pnictogen atom. [g] Energy of destabilization upon deletion of non-covalent interactions between the O atom and Dipp$_3$Pn/Mes$_3$Pn molecular fragments.

**Table E.5.** Calculated total enthalpies (PBE0/def2-TZVPP) of molecules employed in FIA determinations.

| | H (kJ/mol) |
|---|---|
| **Mes$_3$SbO** | -3577798.614 |
| **Mes$_3$SbOF$^-$** | -3840017.168 |
| **COF$_3^-$** | -1083548.896 |
| **COF$_2$** | -821337.7622 |
| **Et$_3$Si$^+$** | -1382025.936 |
| **Et$_3$SiF** | -1644938.002 |

## References

1.    Wenger, J. S.; Weng, M.; George, G. N.; Johnstone, T. C., Isolation, bonding and reactivity of a monomeric stibine oxide. *Nat. Chem.* **2023,** *15*, 633-640.

2.    Chulsky, K.; Dobrovetsky, R., Metal-Free Catalytic Reductive Cleavage of Enol Ethers. *Org. Lett.* **2018,** *20*, 6804-6807.

3.    Zafrani, Y.; Gershonov, E.; Columbus, I., Efficient and Facile Ar–Si Bond Cleavage by Montmorillonite KSF: Synthetic and Mechanistic Aspects of Solvent-Free Protodesilylation Studied by Solution and Solid-State MAS NMR. *J. Org. Chem.* **2007,** *72*, 7014-7017.